

# **Large Scale Earthquake Simulation of a Hybrid Lead Rubber Isolation System Designed with Consideration of Nuclear Seismicity**

## AVAILABILITY OF REFERENCE MATERIALS IN NRC PUBLICATIONS

### NRC Reference Material

As of November 1999, you may electronically access NUREG-series publications and other NRC records at NRC's Library at [www.nrc.gov/reading-rm.html](http://www.nrc.gov/reading-rm.html). Publicly released records include, to name a few, NUREG-series publications; *Federal Register* notices; applicant, licensee, and vendor documents and correspondence; NRC correspondence and internal memoranda; bulletins and information notices; inspection and investigative reports; licensee event reports; and Commission papers and their attachments.

NRC publications in the NUREG series, NRC regulations, and Title 10, "Energy," in the *Code of Federal Regulations* may also be purchased from one of these two sources.

#### 1. The Superintendent of Documents

U.S. Government Publishing Office  
Mail Stop IDCC  
Washington, DC 20402-0001  
Internet: [bookstore.gpo.gov](http://bookstore.gpo.gov)  
Telephone: (202) 512-1800  
Fax: (202) 512-2104

#### 2. The National Technical Information Service

5301 Shawnee Rd., Alexandria, VA 22312-0002  
[www.ntis.gov](http://www.ntis.gov)  
1-800-553-6847 or, locally, (703) 605-6000

A single copy of each NRC draft report for comment is available free, to the extent of supply, upon written request as follows:

Address: **U.S. Nuclear Regulatory Commission**  
Office of Administration  
Publications Branch  
Washington, DC 20555-0001  
E-mail: [distribution.resource@nrc.gov](mailto:distribution.resource@nrc.gov)  
Facsimile: (301) 415-2289

Some publications in the NUREG series that are posted at NRC's Web site address [www.nrc.gov/reading-rm/doc-collections/nuregs](http://www.nrc.gov/reading-rm/doc-collections/nuregs) are updated periodically and may differ from the last printed version. Although references to material found on a Web site bear the date the material was accessed, the material available on the date cited may subsequently be removed from the site.

### Non-NRC Reference Material

Documents available from public and special technical libraries include all open literature items, such as books, journal articles, transactions, *Federal Register* notices, Federal and State legislation, and congressional reports. Such documents as theses, dissertations, foreign reports and translations, and non-NRC conference proceedings may be purchased from their sponsoring organization.

Copies of industry codes and standards used in a substantive manner in the NRC regulatory process are maintained at—

#### The NRC Technical Library

Two White Flint North  
11545 Rockville Pike  
Rockville, MD 20852-2738

These standards are available in the library for reference use by the public. Codes and standards are usually copyrighted and may be purchased from the originating organization or, if they are American National Standards, from—

#### American National Standards Institute

11 West 42nd Street  
New York, NY 10036-8002  
[www.ansi.org](http://www.ansi.org)  
(212) 642-4900

Legally binding regulatory requirements are stated only in laws; NRC regulations; licenses, including technical specifications; or orders, not in NUREG-series publications. The views expressed in contractor-prepared publications in this series are not necessarily those of the NRC.

The NUREG series comprises (1) technical and administrative reports and books prepared by the staff (NUREG-XXXX) or agency contractors (NUREG/CR-XXXX), (2) proceedings of conferences (NUREG/CP-XXXX), (3) reports resulting from international agreements (NUREG/IA-XXXX), (4) brochures (NUREG/BR-XXXX), and (5) compilations of legal decisions and orders of the Commission and Atomic and Safety Licensing Boards and of Directors' decisions under Section 2.206 of NRC's regulations (NUREG-0750).

**DISCLAIMER:** This report was prepared as an account of work sponsored by an agency of the U.S. Government. Neither the U.S. Government nor any agency thereof, nor any employee, makes any warranty, expressed or implied, or assumes any legal liability or responsibility for any third party's use, or the results of such use, of any information, apparatus, product, or process disclosed in this publication, or represents that its use by such third party would not infringe privately owned rights.



# **Large Scale Earthquake Simulation of a Hybrid Lead Rubber Isolation System Designed with Consideration of Nuclear Seismicity**

Manuscript Completed: April 2013  
Date Published: August 2015

Prepared by:  
K. L. Ryan, C. B. Coria, N. D. Dao

Center for Civil Engineering Earthquake Research  
(CCEER) University of Nevada, Reno/MS 0258  
Reno, Nevada 89557-0258

Hernando Candra, NRC Project Manager

Office of Nuclear Regulatory Research



## ABSTRACT

Seismic isolation systems have been proven to provide superior performance and meet continued functionality performance objectives for many facilities around the world, and are thus being considered for the future generation of nuclear power plants in the United States. Experimental simulation of a hybrid lead-rubber isolation system for a 5-story steel moment frame was performed at Hyogo Earthquake Engineering Research Center (E-Defense) of the National Institute for Earth Science and Disaster Prevention in Japan. The isolation system was developed for the seismicity of a potential nuclear site in Central and Eastern United States (CEUS). The isolation system was tested to displacements representing beyond design basis ground motions at the CEUS site and design basis ground motions for a Western United States. Forces in the lead-rubber (LR) bearings were measured by an assembly of load cells.

The design of the isolation system was constrained by the experimental setup. The light axial loads on the system, which are not representative of a nuclear facility, necessitated the use of a hybrid system of bearings and flat sliders, known as cross linear (CL) bearings. The CL bearings support beneath some of the columns without contributing to the system base shear, so that the desired isolation period could be provided at the target displacement. Additionally, the CL bearings provided substantial resistance against the tensile demands generated by overturning as a result of the light axial loads. Thus, the suitability of a hybrid isolation system for nuclear power plant was evaluated as part of the test program.

A numerical simulation model was developed for the isolation system and the structure. The lead-rubber bearings were modeled with a bilinear force-displacement relation. Due to the amplitude dependence of the bearing response, the parameters of the bilinear model were calibrated independently for each simulation. Using the calibrated model, the predicted displacement demand of the isolators was within 10% of the observed experimental displacement.

For typical XY (horizontal only) input excitation, the horizontal accelerations at the roof level were reduced by a factor of 10 relative to the fixed-base building. Under 3D input excitation which included vertical shaking, the vertical accelerations of all floor slabs were amplified by a factor of 4-6 relative to the input vertical excitation, but the vertical amplification factor was essentially the same for the isolated and the fixed-base building; thus the isolation system did not increase vertical acceleration relative to the fixed-base building. Horizontal-vertical coupling was detected in the vibration modes of the structure (both fixed-base and base-isolated). The coupling was attributed partially to a mass irregularity. The majority of the coupling effects were replicated by a well-crafted numerical simulation model that accounted for slab-frame interaction and refined distribution of mass over the floor system. The design of the base isolation system and structure should consider and accommodate these predictable horizontal-vertical coupling effects.



## FOREWORD

This NUREG/CR-7196 was prepared by the University of Nevada in Reno through commercial contract NRC-HQ-11-C-04-0067 (JCN V6274) with the Seismic Geotechnical Structural Engineering Branch, Division of Engineering Office of Nuclear Regulatory Research. This research was part of a larger collaboration between the National Science Foundation (NSF) Network for Earthquake Engineering Simulation (NEES) and Japan's National Research Institute for Earth Science and Disaster Prevention (NIED). This collaboration created the opportunity and a cost effective way to test and investigate Hybrid Lead Rubber Isolation System isolation system focused on nuclear applications.

Through pre-application meetings between NRC staff and vendors, staff identified the body of research and development already done in the seismic isolation (SI) area. Based on those meetings NRC staff anticipates that the types of isolators investigated by this research are those that would be used in design applications. The data that this testing program was designed to acquire are anticipated to address a gap in the NRC staff's ability to review applications that include the use of rubber bearing SI devices and the performance of these isolators under the extreme beyond-design-basis ground motions for the staff review of seismic safety margins. The resulting data produced by this research can also be used to verify the confirmatory numerical models for SI devices in the new NRC ESSI Simulator code, a seismic soil-structure interaction tool under development by the NRC and the University of California at Davis.

This report provides the technical information and comprehensive test data that can be used by the NRC staff to support new regulatory guidance related to seismic isolation (SI) technology on future nuclear power plant structures. Despite the light weight and the application of cross linear (CL) bearings on the test system (hybrid system), which are not representative of a nuclear facility, the CL bearings provided substantial resistance against the tensile demands and large displacement stability without contributing to the system base shear. Thus, these test data can be used for numerical confirmatory analysis and benchmarking for SI, and advance the steps toward the solution of key technical issues that must be addressed before base isolation systems can safely be implemented for the economical seismic protection of nuclear facilities.

A numerical simulation with OpenSees code was used for this isolation system and the structure. Due to OpenSees lacks of features compared with commercial software (Ansys, Abaqus, or LS Dyna), many assumptions and approximations were used in this analysis. The CL bearings were represented by a combination of spring elements due to lack of contact algorithm, this approximation is not strictly accurate since the CL bearing is a friction device which can slide in two directions, and its resistant is proportional to the instantaneous axial force.

The lead-rubber bearings that were modeled with a bilinear force-displacement relation needs to be re-calibrated independently for each simulation to match the test data. This indicates the need of improved models that can capture others nonlinear parameters such as the effects of heating of the lead core, pressure variation, and rate dependence (research on this device is under development by the NRC and the University of Buffalo). Because of the difficulties in modeling the response of the tested LR bearings, the simulation results should be carefully studied before using them in supporting the regulatory guidance, however the analysis still provides some useful insight and the test data can be used for confirmatory analysis and simulation benchmark.



# TABLE OF CONTENTS

ABSTRACT .....	iii
FOREWORD .....	v
TABLE OF CONTENTS .....	vii
LIST OF FIGURES .....	xi
LIST OF TABLES.....	xxi
EXECUTIVE SUMMARY.....	xxiii
ACKNOWLEDGMENT .....	xxv
NOMENCLATURES.....	xxvii
1. INTRODUCTION.....	1
1.1 Potential for Seismic Isolation of Safety Related Nuclear Facilities.....	1
1.2 State of Knowledge and Motivation for Full Scale Testing.....	3
1.3 Opportunity for Testing at E-Defense .....	4
1.4 Report Organization .....	7
2. DESIGN AND CONFIGURATION OF THE 5-STORY STEEL MOMENT FRAME TESTBED STRUCTURE.....	9
2.1 Description of Testbed Structure .....	9
2.1.1 Basic Dimensions.....	9
2.1.2 Design Spectra and Design Criteria.....	10
2.1.3 Framing System .....	10
2.1.4 Slabs .....	13
2.1.5 Material Properties .....	13
2.2 Non-Structural Components and Contents.....	14
2.3 Weights.....	15
2.4 System Identification .....	17
2.5 Condition of the Testbed Prior to Testing .....	18
3. DESIGN OF THE ISOLATION SYSTEM.....	19
3.1 Target Response of a Nuclear Site.....	19
3.2 Isolation System Design.....	21
3.2.1 Estimated Displacement Demands.....	21
3.2.2 Configuration of Lead-Rubber Bearings.....	22
3.2.3 Selection of the Bearing Dimensions .....	26
3.2.4 Selection of the Lead Plug Dimensions .....	27
3.2.5 Cross Linear Bearings.....	28
3.2.6 Summary of Design Properties.....	30
3.3 Selection and Scaling of Ground Motions.....	32

3.3.1	Imposed Limitations for Safety .....	33
3.3.2	Vogtle and Diablo Canyon Motions.....	34
3.3.3	Remainder of the Test Program .....	38
4.	EXPERIMENTAL PROGRAM .....	41
4.1	Design of Connection Assembly .....	41
4.2	Instrumentation .....	44
4.2.1	Load Cells .....	45
4.2.2	Displacement Transducers.....	45
4.2.3	Accelerometers .....	48
4.3	Installation of the Specimen on the Earthquake Simulator.....	50
4.4	Test Schedule .....	54
4.5	Table Motions.....	58
4.6	Derived Responses .....	64
4.6.1	Horizontal Displacement of the Isolation System.....	64
4.6.2	Isolator Forces.....	67
4.6.3	Horizontal Acceleration and Story Drifts.....	68
5.	SUMMARY OF EXPERIMENTAL SIMULATION RESULTS FOR THE HYBRID LR ISOLATED BUILDING.....	71
5.1	Isolator Displacements .....	71
5.2	Torsional Response .....	74
5.3	System Base Shear.....	75
5.4	Axial Forces in LR Bearings .....	78
5.5	Isolation System Re-Centering.....	81
5.6	Floor Accelerations in the Testbed Building.....	84
5.7	Story Drifts in Testbed Building .....	87
6.	TECHNICAL RESPONSE OF HYBRID LR ISOLATION SYSTEM.....	89
6.1	Bolt Slip in LR Bearings.....	89
6.2	Transfer of Load Between Bearings .....	96
6.3	Repeatability of Isolation System Response after Many Tests .....	108
7.	MODEL FOR ISOLATION BEARINGS AND BEARING CHARACTERIZATION .....	121
7.1	Lead-Rubber Bearings .....	121
7.1.1	Horizontal Direction Modeling Assumptions.....	121
7.1.2	Vertical Direction Modeling Assumptions .....	122
7.2	Cross Linear Bearing.....	123
7.2.1	Horizontal Direction Modeling Assumptions.....	123
7.2.2	Vertical Direction .....	124
7.3	Composite Vertical Properties of the Isolation System .....	125
7.4	Characterization of Lead-Rubber Bearings.....	125



7.4.1	Characterization by Dynamic Isolation Systems (DIS)	126
7.4.2	Characterization Based on Experimental Data	129
7.4.3	Trilinear Characterization	136
7.4.4	Final Bearing Parameter Selection for Numerical Simulation	139
8.	NUMERICAL SIMULATION MODEL OF TESTBED STRUCTURE	141
8.1	Modeling Beams and Columns	142
8.2	Modeling Panel Zones	144
8.3	Modeling Gravity Load and Mass	146
8.4	Modeling Damping	147
9.	COMPARISON OF EXPERIMENTAL AND NUMERICAL SIMULATION	151
9.1	Isolator Response	151
9.2	Modal Analysis	161
9.3	Structural Response	168
10.	INFLUENCE OF VERTICAL EXCITATION ON THE STRUCTURAL RESPONSE	181
10.1	Response of LR Bearings under Axial Force Variation	181
10.2	Horizontal and Vertical Floor System Vibration	185
10.3	Source of Amplification of Horizontal Floor Acceleration under 3D Input	189
10.4	Influence of Supplementary Roof Mass on Vertical Slab Vibration and Horizontal-Vertical Coupling	195
10.5	Implications for Design	201
11.	STRUCTURAL AND ISOLATOR RESPONSE FOR THREE BUILDING CONFIGURATIONS	203
11.1	Structural Response	205
11.2	Isolation System Response	211
12.	CONCLUSIONS AND CONSIDERATIONS FOR NUCLEAR POWER PLANTS	221
12.1	Characteristics of Lead-Rubber Bearing Response	221
12.2	Predictability of the System Response	221
12.3	Hybrid Lead-Rubber (LR) and Cross-Linear (CL) Bearing System	223
12.4	Comparison of the Three Building Configurations	224
12.5	Influence of Vertical Excitation on the Structural Response	225
13.	REFERENCES	227

APPENDIX A	DESIGN & CONSTRUCTION DRAWING FOR TESTING OF VALUE-ADDED DAMPED BUILDING .....	A-1
APPENDIX B	DRAWINGS AND SPECIFICATIONS FOR LEAD-RUBBER BEARINGS AND CROSS LINEAR BEARINGS.....	B-1
APPENDIX C	DRAWINGS FOR LOAD CELL ASSEMBLIES AND CONNECTION TO THE SIMULATOR PLATFORM .....	C-1
APPENDIX D	DRAWINGS FOR STRUCTURAL INSTRUMENTATION PLAN.....	D-1
APPENDIX E	ISOLATOR TEST REPORT FOR LEAD-RUBBER BEARINGS .....	E-1

## LIST OF FIGURES

Figure 1-1	E-Defense earthquake simulator parameters .....	5
Figure 2-1	The 5-story steel moment frame specimen .....	9
Figure 2-2	Basic dimensions of the specimen: (a) typical plan view from floors 2 to 5, and (b) elevation view .....	10
Figure 2-3	Design spectrum for Japanese Level II and Level III earthquakes.....	11
Figure 2-4	Beam, beam to column connection and slab.....	11
Figure 2-5	Column base: (a) view from top (b) view from bottom, (c) rendering of stiffeners .....	12
Figure 2-6	Horizontal braces at base level .....	13
Figure 2-7	Hospital room .....	15
Figure 2-8	Office room.....	15
Figure 2-9	Location of steel weights at roof .....	16
Figure 2-10	Transfer function during white noise excitation in fixed-base configuration: (a) x-direction and (b) y-direction .....	17
Figure 2-11	Cracks in concrete slab and rust on steel member.....	18
Figure 3-1	5% damped URS for the DBE at the Vogtle site. (Source: Huang et al.2009).....	20
Figure 3-2	5% damped response spectra for the 30 sets of spectrum compatible maximum-minimum motions: (a) maximum component, (b) minimum component and (c) vertical component. (Source: Huang et al. 2009) .....	20
Figure 3-3	Idealized bilinear force-displacement relationship for LR bearings, determined by post-yield stiffness $K_d$ (stiffness of rubber), characteristic strength $Q_d$ (strength of lead plug) and initial stiffness $K_1$ or yield displacement $D_y$ . An effective or secant stiffness $K_{eff}$ is determined as the peak-to-peak stiffness based on maximum force $F_{max}$ and displacement $D_{max}$ .....	21
Figure 3-4	Displacement demand representing (a) median response to maximum- minimum motions and (b) 90% percentile response to 150% maximum- minimum motions for Vogtle site .....	22
Figure 3-5	Drawing of testbed base plan with column labels (N = North, E = East, S = South, W = West, C = Center) .....	23
Figure 3-6	Illustration of a connection assembly with triaxial load cells to measure bearing forces .....	23
Figure 3-7	(a) Configuration Option 1 with LR bearings beneath 4 corner columns, (b) Configuration Option 2 with LR bearings (circles) beneath 4 edge columns and flat sliders (squares) beneath remaining columns. The supported weights (in units of kN) at the isolators based on tributary loads are also indicated .....	25
Figure 3-8	Proposed design options for LR bearings .....	26
Figure 3-9	Axial force capacity of proposed LR bearings versus lateral displacement .....	27
Figure 3-10	Photo of installed CL bearing illustrating orthogonal LM guides assemblies on top and bottom .....	29

Figure 3-11	Total base shear ( $V_b$ ) and overturning forces ( $F_{OT}$ ) acting on an elevation view of the testbed building.....	30
Figure 3-12	(a) Final plan drawing of the hybrid LR isolation system, (b) photo of LR bearing, and (c) photo of CL bearing.....	31
Figure 3-13	Calculated displacement trace of the isolation system for 6 Vogtle motions by SDOF analysis.....	34
Figure 3-14	Calculated displacement histories of the isolation system in x and y-directions for 6 Vogtle motions by SDOF analysis.....	35
Figure 3-15	Predicted displacement trace of each isolator for the OpenSees building model subjected to 150% Vogtle #13.....	36
Figure 3-16	Predicted displacement trace of each isolator for the OpenSees building model subjected to 150% Vogtle #13, with input ground excitation components rotated by 11.25 degrees.....	37
Figure 3-17	Predicted displacement trace of each isolator for the OpenSees building model subjected to 100% Diablo Canyon #15.....	38
Figure 4-1	Load cell connection assemblies used for: (a) East bearing and (b) North, South and West bearings.....	42
Figure 4-2	Connection assembly.....	42
Figure 4-3	Load cell drawings with bolt patterns and elevation views: (a) Type A and (b) Type B.....	43
Figure 4-4	Connection of Type A and Type B load cells to top and bottom connection plates.....	44
Figure 4-5	Magnitude of low-pass Butterworth Filter transfer function.....	45
Figure 4-6	Load cell channels for the hybrid LR isolation configuration.....	46
Figure 4-7	Layout of displacement transducers at base.....	47
Figure 4-8	Instrumentation for measuring story drift.....	47
Figure 4-9	Layout of displacement transducers to measure story drift in 2 <sup>nd</sup> to 5 <sup>th</sup> stories.....	48
Figure 4-10	Accelerometers at the top connection plates to estimate inertia forces.....	49
Figure 4-11	Layout of accelerometers at the 5 <sup>th</sup> floor.....	49
Figure 4-12	Connection assembly.....	50
Figure 4-13	Connection assemblies on the simulator platform.....	51
Figure 4-14	Installing the LR bearings to the connecting assemblies and the CL bearings to the simulator platform.....	51
Figure 4-15	Lowering the testbed building over the isolation system.....	52
Figure 4-16	Bolt holes for connecting the testbed structure to the isolation system.....	52
Figure 4-17	Drilling and tapping holes at the bottom of the specimen.....	53
Figure 4-18	Acceleration history of target and realized RRS88 motion in the hybrid LR isolation configuration test.....	61
Figure 4-19	Ratio of realized to target motion 5% damped spectral accelerations – hybrid LR configuration.....	62
Figure 4-20	Ratio of realized to target motion 5% damped spectral accelerations – fixed-based configuration.....	63
Figure 4-21	Configurations for solving displacement of the isolation system. (a) original configuration, (b) displaced configuration.....	66
Figure 4-22	Free body diagram illustrating derivation of isolator reaction.....	67

Figure 4-23	Diagram illustrating the computation of drift at the geometric center.....	69
Figure 5-1	Peak vector sum displacement recorded in any LR bearing for each earthquake simulation .....	72
Figure 5-2	X-direction, y-direction and overall peak (vector sum) displacement of each LR bearing for each earthquake simulation .....	72
Figure 5-3	Displacement trace (x vs y-direction displacement) of the East LRB for (a) WSM80, (b) DIA95(XY), (c) VOG100 and (d) VOG175.....	73
Figure 5-4	Peak rotation angle of the base for each earthquake simulation.....	74
Figure 5-5	Displacement trace of each isolator during the Vogtle 175% simulation .....	75
Figure 5-6	Base shear coefficient for all simulations: total, x and y-directions.....	77
Figure 5-7	Base shear coefficient for each simulation alongside the design backbone curve.....	78
Figure 5-8	Peak compressive force in any LR bearing for each earthquake simulation .....	80
Figure 5-9	Peak tensile force in any LR bearing for each earthquake simulation. (A tensile force of zero indicates that tension was not observed) .....	80
Figure 5-10	Peak axial forces in each LR bearing for each simulation: (a) Peak compression force, (b) peak normalized compression force, (c) peak tension force, and (d) normalized peak tension force .....	81
Figure 5-11	X-direction, y-direction, and total (vector sum) displacement recorded in each LR bearing at the end of every earthquake simulation .....	82
Figure 5-12	Permanent displacement of around 1.1 cm on the East bearing due to sliding of the bottom steel plate.....	83
Figure 5-13	Permanent displacement at the location of each LR bearing at the end of one simulation compared to the beginning of the next.....	84
Figure 5-14	Peak acceleration profile for all simulations in both horizontal directions.....	86
Figure 5-15	Peak floor acceleration profiles for increasing intensity of Vogtle input excitation (75% - 175%) .....	86
Figure 5-16	Peak absolute and normalized acceleration profile comparing XY and 3D excitations for Diablo (95% and 80% respectively) and Rinaldi (88%) .....	87
Figure 5-17	Peak story drift throughout the height of the building for all excitations in x and y directions .....	88
Figure 6-1	Movement of (a) East LR bearing relative to (b) top and (c) bottom plates. ....	90
Figure 6-2	Horizontal force history of the East bearing (LRB-E) in the x- and y-directions for a subset of the trials.....	91
Figure 6-3	X and y-direction hysteresis loops (horizontal force vs. displacement) of the East bearing (LRB-E) during Vogtle 125% and Vogtle 150% .....	93
Figure 6-4	Horizontal ( $F_x$ and $F_y$ ) and vertical ( $F_z$ ) force history of all four LR bearings during Vogtle 150%.....	94
Figure 6-5	Propagation of bolt slip through the height of the structure in x-direction during Vogtle 150%; unfiltered horizontal force in LRB-E and 1 <sup>st</sup> – 6 <sup>th</sup> floor acceleration in SE column.....	95
Figure 6-6	Resultant action on LR bearings as a result of CL bearings and base diaphragm constraint.....	96
Figure 6-7	History of average horizontal displacement (x, y and vector sum), and axial force in individual LR bearings and summed over all LR bearings for Sine Wave (XY) .....	97

Figure 6-8	History of average horizontal displacement (x, y and vector sum), and axial force in individual LR bearings and summed over all LR bearings for Diablo 95% (XY) .....	98
Figure 6-9	History of average horizontal displacement (x, y and vector sum), and axial force in individual LR bearings and summed over all LR bearings for Rinaldi 88% (XY).....	99
Figure 6-10	History of axial force in individual LR bearings and summed over all LR bearings for Rinaldi 88% .....	101
Figure 6-11	History of axial force in individual LR bearings and summed over all LR bearings comparing Rinaldi 88% – dashed line – and Rinaldi 88% (XY) – solid line. A low pass filter with a cutoff frequency of 2 Hz was applied to the total axial force for Rinaldi 88% and is superimposed over the total, shown as a red dashed line .....	102
Figure 6-12	History of average vector sum displacement at building center, axial force in individual LR bearings and axial force summed over all LR bearings comparing Diablo 95% – dashed line – and Diablo 80% (XY) – solid line. A low pass filter with a cutoff frequency of 2 Hz was applied to the total axial force for Diablo 80% and is superimposed over the total, shown as a red dashed line.....	103
Figure 6-13	History of average vector sum displacement at building center, axial force in individual LR bearings and axial force summed over all LR bearings for Vogtle 175%. A low pass filter with a cutoff frequency of 2 Hz was applied to the total axial force and is superimposed over the total, shown as a red dashed line .....	104
Figure 6-14	(a) Relative change in compressive force and (b) Total compressive force summed over LR bearings at the start and end of all simulations.....	106
Figure 6-15	Sample feedback acceleration at the center of the earthquake simulator (averaged over several accelerometers) in the x and y-directions compared for the first and second Sine 100% (Y) and Vogtle 75% simulations .....	109
Figure 6-16	5% damped response spectra for the feedback acceleration at the center of the earthquake simulator (averaged over several accelerometers) in the x, y and z-directions compared for the first and second Sine 100% (Y) and Vogtle 75% simulations .....	110
Figure 6-17	Y-direction force vs. displacement (hysteresis loops) for the 1 <sup>st</sup> and 2 <sup>nd</sup> simulation of Sine 100%(Y) .....	112
Figure 6-18	Y-direction displacement and force histories for the 1 <sup>st</sup> and 2 <sup>nd</sup> simulation of Sine 100% (Y).....	113
Figure 6-19	X-direction force vs. displacement (hysteresis loops) for the 1 <sup>st</sup> and 2 <sup>nd</sup> simulation of Vogtle 75%.....	114
Figure 6-20	Y-direction force vs. displacement (hysteresis loops) for the 1 <sup>st</sup> and 2 <sup>nd</sup> simulation of Vogtle 75%.....	115
Figure 6-21	X-direction displacement and force histories for the 1 <sup>st</sup> and 2 <sup>nd</sup> simulation of Vogtle 75% .....	116
Figure 6-22	Y-direction displacement and force histories for the 1 <sup>st</sup> and 2 <sup>nd</sup> simulation of Vogtle 75% .....	117

Figure 6-23	X vs. y-direction displacement (displacement trace) for the 1 <sup>st</sup> and 2 <sup>nd</sup> simulation of Vogtle 75%.....	118
Figure 6-24	Y-direction force vs. displacement (hysteresis loops) identified by cycle for the 1 <sup>st</sup> and 2 <sup>nd</sup> simulation of Sine 100% (Y).....	119
Figure 7-1	Horizontal force-displacement of LR bearing for numerical simulation.....	122
Figure 7-2	Vertical force-deformation of LR bearing for analytical model: (a) elastic-no tension, (b) elastic, and (c) combined .....	122
Figure 7-3	Horizontal force-displacement of CL bearing for numerical simulation.....	124
Figure 7-4	Vertical force-deformation of CL bearing for analytical model: (a) elastic-no tension, (b) elastic, and (c) combined.....	125
Figure 7-5	Comparison of fitted hysteresis loop and parameters to test data.....	127
Figure 7-6	Hysteresis loop of Test A and D for one of the isolation pairs.....	128
Figure 7-7	Projection of displacement trace to main axis for Vogtle 100%.....	129
Figure 7-8	Selection of cycle for characterization for Vogtle 100% .....	130
Figure 7-9	Hysteresis loop of peak cycle for the projected-direction for East bearing for Vogtle 100%.....	131
Figure 7-10	Analytical and experimental hysteresis loop using (a),(c) isolator design parameters and (b),(d) characterized parameters .....	134
Figure 7-11	Y-direction hysteresis and force history of test data of the East bearing compared to (a - b) characterization model,and (c - d) design model for Sine 100%(Y)-1. ....	135
Figure 7-12	X and y-direction displacement history of experimental data compared to (a) characterized model and (b) design model for Vogtle 175%, East bearing .....	136
Figure 7-13	Force vs. displacement loop for the East LRB in Sine 100%(Y)-1 .....	137
Figure 7-14	Conceptual force vs. displacement of lead plug for monotonic loading (courtesy of Dynamic Isolation Systems) .....	137
Figure 7-15	Comparison of numerical and experimental simulation force versus displacement of the East bearing for SIN100(Y)-1 and VOG100 using (a), (c) a trilinear hysteretic model and (b), (d) a bilinear hysteretic model.....	139
Figure 7-16	Comparison of numerical simulation with 100% and 85% characterized values of $Q_d$ to the experimental data for Vogtle 100%; displacement history and hysteresis loop in the y-direction for the East bearing .....	140
Figure 8-1	(a) Photo and (b) OpenSees model of the testbed building without isolators....	141
Figure 8-2	Primary beam, beam-to-column connection, and slab .....	142
Figure 8-3	Behavior of a representative composite fiber section beam with and without axial restraint: (a) fiber section geometry and (b) force-displacement relationship.....	143
Figure 8-4	Composite section behavior: (a) moment-curvature relationship of the section, (b) component 1 of resultant section modeled by steel material model, and (c) component 2 of resultant section modeled by hysteresis model.....	144
Figure 8-5	Panel zone model for beam to column connection. (a) beam to column connection, (b) numerical model of panel zone .....	145
Figure 8-6	Gusset plate and its finite element model: (a) gusset plate, (b) Von-Mises stress due to gravity load .....	146

Figure 8-7	Rayleigh damping model for the fixed-base and hybrid LR isolated building model.....	148
Figure 8-8	Additional damper for adjusting the damping coefficient of the 2 <sup>nd</sup> mode in the X direction .....	149
Figure 9-1	Comparison of numerical and experimental simulation for El Centro 130%; displacement trace and displacement histories (x and y) in each LR bearing, labeled by position (E, S, N, W). Numerical simulation uses the characterized model with 85% of the characterized value for $Q_d$ .....	153
Figure 9-2	Comparison of numerical and experimental simulation for El Centro 130%; bearing force vs. displacement or hysteresis loops (x and y) in each LR bearing, labeled by position (E, S, N, W). Numerical simulation uses the characterized model with 85% of the characterized value for $Q_d$ .....	154
Figure 9-3	Comparison of numerical and experimental simulation for Vogtle 100%; displacement trace and displacement histories (x and y) in each LR bearing, labeled by position (E, S, N, W). Numerical simulation uses the characterized model with 85% of the characterized value for $Q_d$ .....	155
Figure 9-4	Comparison displacement (x and y) histories of numerical and experimental simulation for Vogtle 100% in each LR bearing labeled by position (E, S, N, W). Numerical simulation uses the characterized model with 85% of the characterized value for $Q_d$ .....	156
Figure 9-5	Comparison of numerical and experimental simulation for Vogtle 175%; displacement trace and displacement histories (x and y) in each LR bearing, labeled by position (E, S, N, W). Numerical simulation uses the characterized model with 85% of the characterized value for $Q_d$ .....	157
Figure 9-6	Comparison of numerical and experimental simulation for Vogtle 175%; displacement trace and displacement histories (x and y) in each LR bearing, labeled by position (E, S, N, W). Numerical simulation uses the characterized model with 85% of the characterized value for $Q_d$ .....	158
Figure 9-7	Comparison of numerical and experimental simulation for Diablo 95%; displacement trace and displacement histories (x and y) in each LR bearing, labeled by position (E, S, N, W). Numerical simulation uses the characterized model with 85% of the characterized value for $Q_d$ .....	159
Figure 9-8	Comparison displacement (x and y) histories of numerical and experimental simulation for Diablo 95% in each LR bearing, labeled by position (E, S, N, W). Numerical simulation uses the characterized model with 85% of the characterized value for $Q_d$ .....	160
Figure 9-9	Comparison of numerical and experimental simulation for Vogtle 175%; history of base rotation angle. Analysis uses the characterized model with 85% of the characterized value for $Q_d$ .....	161
Figure 9-10	Modes 1-4 deflected shape of all the frames in 3-dimensional, x- and y-direction, along with their associated frequencies and periods. The undeflected shape of the system is shown in dashed lines .....	163
Figure 9-11	Modes 5-8 deflected shape of all the frames in 3-dimensional, x- and y-direction, along with their associated frequencies and periods. The undeflected shape of the system is shown in dashed lines .....	164



Figure 9-12	Modes 9-12 deflected shape of all the frames in 3-dimensional, x- and y-direction, along with their associated frequencies and periods. The undeflected shape of the system is shown in dashed lines. ....	165
Figure 9-13	Modes 13-16 deflected shape of all the frames in 3-dimensional, x- and y-direction, along with their associated frequencies and periods. The undeflected shape of the system is shown in dashed lines .....	166
Figure 9-14	Modes 17-20 deflected shape of all the frames in 3-dimensional, x- and y-direction, along with their associated frequencies and periods. The undeflected shape of the system is shown in dashed lines .....	167
Figure 9-15	Comparison of numerical and experimental simulation for El Centro 130%; x and y-direction roof acceleration histories, peak acceleration profiles, 2nd story drift histories, and peak drift profiles. Numerical simulation uses the characterized model with 85% of the characterized value for $Q_d$ .....	169
Figure 9-16	Comparison of numerical and experimental simulation for Vogtle 100%; x and y-direction roof acceleration histories, peak acceleration profiles, 2nd story drift histories, and peak drift profiles. Numerical simulation uses the characterized model with 85% of the characterized value for $Q_d$ .....	170
Figure 9-17	Comparison of numerical and experimental simulation for Vogtle 175%; x and y-direction roof acceleration histories, peak acceleration profiles, 2nd story drift histories, and peak drift profiles. Numerical simulation uses the characterized model with 85% of the characterized value for $Q_d$ .....	171
Figure 9-18	Comparison of numerical and experimental simulation for Diablo 95%; x and y-direction roof acceleration histories, peak acceleration profiles, 2nd story drift histories, and peak drift profiles. Numerical simulation uses the characterized model with 85% of the characterized value for $Q_d$ .....	172
Figure 9-19	Comparison of numerical and experimental simulation for El Centro 130%; x and y-direction spectral accelerations for 1st through 6th floors. Numerical simulation uses the characterized model with 85% of the characterized value for $Q_d$ .....	174
Figure 9-20	Comparison of numerical and experimental simulation for Vogtle 100%; x and y-direction spectral accelerations for 1st through 6th floors. Numerical simulation uses the characterized model with 85% of the characterized value for $Q_d$ .....	175
Figure 9-21	Comparison of numerical and experimental simulation for Vogtle 175%; x and y-direction spectral accelerations for 1st through 6th floors. Numerical simulation uses the characterized model with 85% of the characterized value for $Q_d$ .....	176
Figure 9-22	Comparison of numerical and experimental simulation for Diablo 95% (XY); x and y-direction spectral accelerations for 1st through 6th floors. Numerical simulation uses the characterized model with 85% of the characterized value for $Q_d$ .....	177
Figure 10-1	Bearing force vs. displacement (hysteresis loops) in x-direction for a single large displacement cycle compared for Rinaldi 88% (XY) and Rinaldi 88% (V-PGA = 1.21g) excitations .....	182

Figure 10-2	Bearing force vs. displacement (hysteresis loops) in y-direction for a single large displacement cycle compared for Rinaldi 88% (XY) and Rinaldi 88% (V-PGA = 1.21g) excitations.....	182
Figure 10-3	History of shear force and axial force variation in LRB-S compared for Rinaldi 88% (XY) and Rinaldi 88% (V-PGA = 1.21g) excitations .....	183
Figure 10-4	Bearing force vs. displacement (hysteresis loops) in x-direction for a single cycle compared for Diablo 80% (V-PGA = 0.44g) and Diablo 95% (XY) excitations.....	184
Figure 10-5	Bearing force vs. displacement (hysteresis loops) in y-direction for a single cycle compared for Diablo 80% (V-PGA = 0.44g) and Diablo 95% (XY) excitations.....	184
Figure 10-6	History of shear force and axial force variation in LRB-N compared for Diablo 80% (V-PGA = 0.44g) and Diablo 95% (XY) excitations.....	185
Figure 10-7	Comparison of vertical roof slab acceleration (blue), 5 <sup>th</sup> floor slab acceleration (red), and ground acceleration (black) for (a) Vogtle 100%, (b) Diablo 80%, and (c) Rinaldi 88%. Peak values indicated on graph .....	186
Figure 10-8	Comparison of numerical simulation to experimental data for vertical slab acceleration; (a) roof floor and (c) 5 <sup>th</sup> floor for Diablo 80%, and (b) roof floor and (d) 5 <sup>th</sup> floor for Rinaldi 88% .....	187
Figure 10-9	Comparison of x and y-direction roof acceleration histories and peak acceleration profiles for Diablo 80% and Diablo 95% (XY) .....	188
Figure 10-10	Comparison of x and y-direction roof acceleration histories and peak acceleration profiles for Rinaldi 88% (XY) and Rinaldi 88%.....	189
Figure 10-11	Comparison of x and y-direction 5% damped spectral accelerations for 1 <sup>st</sup> through 6 <sup>th</sup> floors for Diablo 80% and Diablo 95% (XY). These spectra were derived from the experimentally recorded signals.....	190
Figure 10-12	Comparison of x and y-direction 5% damped spectral accelerations for 1 <sup>st</sup> through 6 <sup>th</sup> floors for Rinaldi 88% (XY) and Rinaldi 88%. These spectra were derived from the experimentally recorded signals.....	191
Figure 10-13	Comparison of numerical simulation to experimental data for Diablo 80%; x and y-direction 5% damped spectral accelerations for 1st through 6th floors. Numerical simulation uses the characterized bearing model with 85% of the characterized value for $Q_d$ .....	193
Figure 10-14	Comparison of numerical simulation to experimental data for Rinaldi 88%; x and y-direction 5% damped spectral accelerations for 1 <sup>st</sup> through 6 <sup>th</sup> floors. Numerical simulation uses the characterized bearing model with 85% of the characterized value for $Q_d$ .....	194
Figure 10-15	Numerically simulated vertical slab acceleration for Diablo 80% and Rinaldi 88%; comparison using the testbed building model and the augmented model with supplementary mass removed from the roof and replaced at the base. ....	196
Figure 10-16	Comparison of numerically simulated x and y-direction roof acceleration histories and peak acceleration profiles for Diablo 80% and Diablo 95% (XY) using the augmented model with supplementary mass removed from the roof and replaced at the base.....	197

Figure 10-17	Comparison of numerically simulated x and y-direction roof acceleration histories and peak acceleration profiles for Rinaldi 88% XY and Rinaldi 88% using the augmented model with supplementary mass removed from the roof and replaced at the base.....	198
Figure 10-18	Comparison of numerically simulated x and y-direction 5% damped spectral accelerations in 1 <sup>st</sup> through 6 <sup>th</sup> floors for Diablo 80% and Diablo 95% (XY) using the augmented model with supplementary mass removed from the roof and replaced at the base.....	199
Figure 10-19	Comparison of numerically simulated x and y-direction 5% damped spectral accelerations in 1 <sup>st</sup> through 6 <sup>th</sup> floors for Rinaldi 88% XY and 3D using the augmented model with supplementary mass removed from the roof and replaced at the base.....	200
Figure 11-1	Normalized backbone curves (base shear vs. displacement) for the Long Period TP isolation system and the Moderate Period LR isolation system, based on design properties of the bearings and measured mass.....	203
Figure 11-2	Peak floor acceleration (vector sum) vs. floor level of the three building configurations for (a) WSM 80%, (b) IWA 100%/70%, (c) Rinaldi 88%/35% (XY) and (d) Rinaldi 88%/35% records. Accelerations are absolute on the left graph and normalized by PGA on the right.....	206
Figure 11-3	History of total base shear in x and y-directions compared for the 3 system configurations in (a) Rinaldi 88% (XY) and (b) Rinaldi 88%. The bottom graphs provide a close-up of the isolated configurations; peak values are indicated .....	208
Figure 11-4	Comparison of x and y-direction 5% damped spectral accelerations in the TP isolation configuration for 1 <sup>st</sup> through 6 <sup>th</sup> floors for Rinaldi 88% XY and Rinaldi 88%.....	209
Figure 11-5	Vertical acceleration history of floor slab (recorded at middle of the NE quadrant), column average, and ground acceleration average (recorded at simulator platform) for Rinaldi 88% for (a,d) TP isolation configuration, (b,e) hybrid LR isolation configuration, and (c,f) fixed-base configuration; (a-c) = 5 <sup>th</sup> floor slab and (d-f) = roof slab .....	210
Figure 11-6	Peak story drift (max in x or y-direction) vs. story level of the three building configurations for (a) WSM 80%, (b) IWA 100%/70%, (c) Rinaldi 88%/35% (XY) and (d) Rinaldi 88%/35% records.....	211
Figure 11-7	Comparison of Moderate Period LR and Long Period TP systems for WSM 80%; displacement trace and displacement histories (x and y) in each bearing, labeled by position (E, S, N, W) .....	214
Figure 11-8	Comparison of Moderate Period LR and Long Period TP systems for Rinaldi 88% (XY); displacement trace and displacement histories (x and y) in each bearing, labeled by position (E, S, N, W).....	215
Figure 11-9	Comparison of the base shear coefficient for Moderate Period LR and Long Period TP systems in the x- and y-directions for the East bearing; WSM 80% and Rinaldi 88% (XY) .....	216
Figure 11-10	Rotation angle at the base for Moderate Period LR and Long Period TP isolated configurations for (a) WSM 80% and (b) Rinaldi 88% (XY) .....	216

Figure 11-11	Qualitative illustration of expected weight distribution (calculated by natural distribution of the weight) and observed weight distribution (measured in load cells) on TP isolation system.....	217
Figure 11-12	Maximum residual displacement in the Long Period and Moderate Period isolation systems after each simulation .....	218
Figure 11-13	Displacement of the SW bearing in the Moderate Period isolation system over the course of a single test day, illustrating the residual displacement after each record.....	219
Figure 11-14	Displacement of the SE bearing in the Long Period isolation system over the course of a single test day, illustrating the residual displacement after each record.....	219

## LIST OF TABLES

Table 2-1	Yield and ultimate strength of steel from coupon tests.....	14
Table 2-2	Estimated weight in kN of the specimen by component and floor level.....	16
Table 2-3	Experimentally determined natural periods and damping ratios of the fixed-base building.....	18
Table 3-1	Required Diameter of the Lead Plug.....	28
Table 3-2	Ratio of Lead Plug Diameter to Bearing Diameter ( $D_{LP}/D$ ).....	28
Table 3-3	Lead Rubber Bearing Properties.....	32
Table 3-4	Cross Linear Bearing Properties.....	32
Table 3-5	Predicted x, y and Vector Peak Displacement in the different Isolator for the Building Model Subjected to 150% Vogtle #13 Record, with Rotated Horizontal Components of Input Motion.....	37
Table 3-6	Common Earthquake Records Considered for Three Test Configurations.....	39
Table 4-1	Properties of load cells.....	43
Table 4-2	Vertical load on each bearing after installation.....	53
Table 4-3	Simulation schedule for the TP isolation configuration.....	55
Table 4-4	Simulation schedule for the hybrid LR isolation configuration.....	56
Table 4-5	Simulation schedule for the fixed-base building.....	57
Table 4-6	Peak acceleration of target and realized motions for the TP isolation configuration.....	59
Table 4-7	Peak acceleration of target and realized motions for hybrid LR isolation and fixed-base configurations.....	60
Table 5-1	List of ground motion (GM) simulations by number, name, abbreviation and the directions considered.....	73
Table 5-2	Peak base shear for all simulations: total, x and y directions.....	76
Table 5-3	Peak base shear coefficient for all simulations: total, x and y directions.....	76
Table 7-1	Compression Shear Test Schedule.....	127
Table 7-2	Recorded and fitted parameters for Test A.....	128
Table 7-3	Characterized isolator parameters for all tests in the sequence.....	128
Table 7-4	Characterized bearing parameters for each earthquake simulation.....	132
Table 8-1	Weight and eccentricity (distance from geometric center to center of mass) of numerical simulation model.....	147
Table 8-2	Experimentally determined natural periods and damping ratios of the fixed-base building.....	148
Table 11-1	Ground Motions, Scale Factors and Peak Accelerations Common to 3 Configurations.....	204



## EXECUTIVE SUMMARY

Seismic isolation systems have been proven to provide superior performance and meet continued functionality performance objectives for many facilities around the world, and are thus being considered for the future generation of nuclear power plants in the United States. Experimental simulation of a hybrid lead-rubber isolation system for a 5-story steel moment frame was performed at Hyogo Earthquake Engineering Research Center (E-Defense) of the National Institute for Earth Science and Disaster Prevention in Japan. The isolation system was developed for the seismicity of a potential nuclear site in Central and Eastern United States (CEUS). The isolation system was tested to displacements representing beyond design basis ground motions at the CEUS site and design basis ground motions for a Western United States. Forces in the lead-rubber (LR) bearings were measured by an assembly of load cells. The design of the isolation system was constrained by the experimental setup. The light axial loads on the system, which are not representative of a nuclear facility, necessitated the use of a hybrid system of bearings and flat sliders, known as cross linear (CL) bearings. The CL bearings provide support beneath some of the columns without contributing to the system base shear, so that the desired isolation period could be provided at the target displacement. Additionally, the CL bearings provided substantial resistance against the tensile demands generated by overturning as a result of the light axial loads. Thus, the suitability of a hybrid isolation system for nuclear power plant was evaluated as part of the test program.

The following behaviors, many of which have been observed before, were observed in the response of LR bearings during this test program.

1. Pinching near the center of the measured bearing hysteresis loop, attributed to the small size of the lead plug;
2. Loss of characteristic strength over the duration of an excitation, associated with heating of the lead plug;
3. Slight fluctuation of shear force during high frequency axial force variation; thought to be insignificant;
4. Small (negligible) permanent displacements at the end of the records;
5. Significant base rotation demands due to the inability to configure the system appropriately for torsion;
6. No loss of shear resistance at large displacements due to the stabilizing influence of the CL bearings;
7. Transfer of axial forces from LR bearings to CL bearings at large displacements, causing the LR bearings to sustain tension that was not induced by overturning.

While the hybrid system overcame stability issues, the vertical force demands in individual bearings were difficult to predict due to lack of compliance and subsequent load transfer between the two types of devices (LR bearings and CL bearings). Thus, the compliance issues suggest that the hybrid system should not be used in nuclear facilities. If it had been possible to design an isolation system for this experiment using only LR bearings, the response of the bearings would have been similar but without the load transfer effects.

A numerical simulation model was developed for the isolation system and the structure. The numerical simulation and its comparison to experimental data cannot be directly applied to nuclear facilities due to difficulties in modeling the response of the tested LR bearings, and differences between the tested superstructure and a nuclear facility, but still provides some useful insight. The lead-rubber bearings were modeled with a bilinear force-displacement relation. Due to the amplitude dependence of the bearing response, the parameters of the bilinear model were calibrated independently for each simulation. Using the calibrated model, the predicted displacement demand of the isolators was within 10% of the observed experimental displacement. Improved models that can capture the effects of heating of the lead core, pressure variation, and rate dependence were not used here.

For typical XY (horizontal only) input excitation, the horizontal accelerations at the roof level were reduced by a factor of 10 relative to the fixed-base building. Under 3D input excitation which included vertical shaking, the vertical accelerations of all floor slabs were amplified by a factor of 4-6 relative to the input vertical excitation, but the vertical amplification factor was essentially the same for the isolated and the fixed-base building; thus the isolation system did not increase vertical acceleration relative to the fixed-base building. Horizontal-vertical coupling was detected in the vibration modes of the structure (both fixed-base and base-isolated), which caused horizontal accelerations to be amplified somewhat in a strong 3D excitation compared to an XY excitation. The coupling was attributed partially to a mass irregularity; a large supplemental mass was placed at the roof level in an asymmetric configuration in plan. The spectral peaks associated with the coupling modes computed from analysis decreased significantly when the supplemental mass in the numerical model was moved from the roof and distributed in a regular configuration at the base level. Other sources of coupling in the hybrid LR isolation system were hypothesized but not confirmed. The majority of the coupling effects were replicated by a well-crafted numerical simulation model that accounted for slab-frame interaction and refined distribution of mass over the floor system. The design of the base isolation system and structure should consider and accommodate these predictable horizontal- vertical coupling effects.

All data from the experiments is permanently archived and publicly accessible in the NEES Project Warehouse (Ryan et al. 2013a, 2013b, 2013c).



## ACKNOWLEDGMENT

This report was prepared as an account of work sponsored by an agency of the U.S. Government. Neither the U.S. Government nor any agency thereof, nor any of their employees, makes any warranty, expressed or implied, or assumes any legal liability or responsibility for any third party's use, or the results of such use, of any information, apparatus, product, or process disclosed in this report, or represents that its use by such third party would not infringe privately owned rights. The views expressed in this report are not necessarily those of the U.S. Nuclear Regulatory Commission.

This report was based on work under the primary sponsorship of the U.S. Nuclear Regulatory Commission through Contract NRC-HQ-11-C-04-0067. The work was part of a larger collaboration between the National Science Foundation (NSF) Network for Earthquake Engineering Simulation (NEES) through NSF Grants CMMI-1113275 and CMMI-0721399 and Japan's National Research Institute for Earth Science and Disaster Prevention (NIED). The NEES/NIED collaboration created the opportunity to test an additional isolation system focused on nuclear applications. Financial support, product donations and in-kind technical support were provided by Earthquake Protection Systems, Dynamic Isolation Systems, Aseismic Devices Company, Takenaka, USG Building Systems, Victaulic, Tolco, Hilti, CEMCO steel, and Allan Automatic Sprinkler. The authors are grateful for all that led to the success of the project. The authors also acknowledge and thank the following individuals for reviewing and providing input on a draft version of the report: Andrew Whittaker, Ron Mayes, Robert Kennedy, Amarnath Kasalanati, and Hernando Candra.



## NOMENCLATURES

$A_b$	Crass-sectional area of the bearing
$a_{cX}$	Horizontal acceleration of the compound including top connecting plate and bottom half of the isolator
$a_{cZ}$	Vertical acceleration of the compound including top connecting plate and bottom half of the isolator
$a_{xC}$	Acceleration at the geometric center of the floor in x-direction
$a_{xSE}$	X component of the horizontal acceleration at the South-East corner
$a_{yC}$	Acceleration at the geometric center of the floor in y-direction
$a_{ySE}$	Y component of the horizontal acceleration at the South-East corner
$b$	Plate width
$b_{cf}$	Flange width of column
$c$	Damping coefficient of additional damper
$c_{nn}$	Constant dependent on nth mode shape
$c_s$	Side cover rubber thickness
$d$	Given horizontal displacement of the bearing
$D$	Overall diameter
$D_D$	Design displacement
$D_{LP}$	Diameter of the lead plug
$D_{max}$	Maximum isolator displacement
$D_{min}$	Minimum isolator displacement
$D_p$	Lead diameter
$D_{peak}$	Absolute peak displacement for selected cycle
$D_{TM}$	Maximum displacement
$DX_{A'}$	Displacement component at the center bearing in X direction
$d_{xC}$	Story drift in the x-direction at the geometric center
$d_{xSE}$	Story drift in the x-direction at the South-East corner
$D_y$	Yield displacement
$D_{y,rub}$	Yield displacement of rubber
$DY_{A'}$	Displacement component at the center bearing in Y direction
$E$	Elastic modulus
$EDC$	Energy dissipated per cycle
$EDC_{bilin}$	Energy dissipated per cycle for a bilinear force-displacement loop
$EDC_{test}$	Energy dissipated per cycle for experimental data

$e_u$	Rubber's elongation-at-break
$f$	Frequency
$F_{max}$	Maximum force
$F_{min}$	Minimum force
$F_{OT}$	Overturning force
$F_{peak}$	Absolute peak force for selected cycle
$f_{pn}$	Horizontal displacement at base in the nth mode shape
$f_{qn}$	Horizontal displacement at roof in the nth mode shape
$F_y$	Yield force
$G$	Shear modulus
$g$	Gravitational acceleration
$h$	Plate height
$I$	Moment of inertia
$k$	Horizontal stiffness
$K_1$	Initial stiffness of bearing
$K_{1\_char}$	Characterized initial stiffness
$K_{1\_lead}$	Initial stiffness of lead
$K_{1\_rub}$	Initial stiffness of rubber
$K_{1s}$	Initial stiffness of the CL bearing
$K_b$	Horizontal stiffness of low-damping natural rubber
$K_d$	Post-yield stiffness of bearing
$K_{d, char}$	Characterized post-yield stiffness
$K_{eff}$	Effective or secant stiffness
$K_H$	Kinematic hardening modulus
$K_{LC}$	Vertical stiffness of load cell
$K_{L1}$	First stiffness of the lead-plug for trilinear model (Figure 7-14)
$K_{L2}$	Second stiffness of the lead-plug for trilinear model (Figure 7-14)
$K_{L3}$	Third stiffness of the lead-plug for trilinear model (Figure 7-14)
$K_t$	Tension vertical stiffness for LR bearing
$K_{plate}$	Plate bending stiffness
$K_{total}$	Total vertical stiffness
$k_{truss}$	Equivalent elastic stiffness of axial element
$K_v$	Compressive vertical stiffness for LR bearing

$K_{vc}$	Compressive vertical stiffness for CL bearing
$K_{vt}$	Tension vertical stiffness for CL bearing
$L_{clear}$	Clear length between adjacent load cells
$L$	Length of element
$L_A$	Distance between a and A' measured by the displacement transducer
$m$	Coefficient of friction
$m_{nn}^*$	Modal mass of the nth mode
$m_c$	Mass of the compound including top connecting plate and bottom half of the isolator
$M_{yF}$	Yield strength of spring representing bending of the flanges
$M_{yp}$	Yield strength of spring representing shear behavior of panel zone
$N$	Number of rubber layers
$N_{LR}$	Number of lead-rubber bearings
$P_{allow}$	Allowable axial load at a lateral displacement of zero
$Q_d$	Characteristic yield strength of bearing or system
$Q_{d,char}$	Characterized characteristic strength
$Q_{d,lead}$	Characteristic strength of lead
$Q_{d,rub}$	Characteristic strength of rubber
$QL_R$	Total characteristic strength of lead rubber bearings
$Q_{Slider}$	Total characteristic strength of flat sliders
$R$	Radius of curvature of friction pendulum bearing
$R_{cX}$	Dynamic reaction component in x-direction at the load cell level
$R_{cZ}$	Dynamic reaction component in z-direction at the load cell level
$R_X$	Dynamic reaction component in x-direction at the isolator level
$R_Z$	Dynamic reaction component in z-direction at the isolator level
$R_{Z,init}$	Initial static vertical reaction
$S_F$	Initial stiffness of spring representing bending of the flanges
$S_p$	Initial stiffness of spring representing shear behavior of panel zone
$T$	Period
$t_{bp}$	Bottom mounting plate thickness
$t_{cf}$	Flange thickness of column
$T_d$	Post-yield period of bearing or system
$T_{eff}$	Effective period of bearing or system
$t_{ip}$	Internal plate thickness

$T_r$	Total thickness of rubber
$t_r$	Layer thickness
$t_s$	Shim thickness
$t_{tp}$	Top mounting plate thickness
$v$	Equivalent uniform load on the beam element
$V_b$	Total base shear in the isolator system
$V_i$	Shear force at the $i^{\text{th}}$ node
$V_j$	Shear force at the $j^{\text{th}}$ node
$V_p$	Volume of panel zone web
$W$	Estimated weight on each CL bearing
$W_i$	Tributary weight supported by the $i^{\text{th}}$ isolator
$W_{LRBs}$	Total weight carried by the LR bearings
$W_{total}$	Total weight of the structure
$x$	Length of the gusset plate
$X_a$	X- coordinate of node a
$X_{A'}$	X-coordinate of displaced node A'
$y$	Width of the gusset plate
$Y_a$	Y-coordinate of node a
$Y_{A'}$	Y-coordinate of displaced node A'
$\beta$	Equivalent damping ratio
$\gamma$	Calibration factor
$\Delta x$	Displacement of center bearing in x-direction computed by data processing
$\Delta y$	Displacement of center bearing in y-direction computed by data processing
$\zeta_n$	Additional damping ratio
$\mu$	Coefficient of friction of a sliding bearing
$\sigma_u$	Ultimate strength
$\sigma_y$	Yield strength
$\sigma_{y,LP}$	Dynamic yield strength of the lead plug
$\phi$	Rotation of center bearing computed by data processing
$\phi_{pn}$	Horizontal displacement at base in the nth mode shape
$\phi_{qn}$	Horizontal displacement at roof in the nth mode shape
$\omega_n$	Angular frequency of the nth mode
$\omega_{z,rigid}$	Vertical frequency of a "rigid body"

# 1. INTRODUCTION

## 1.1 Potential for Seismic Isolation of Safety Related Nuclear Facilities

Seismic base isolation is a technology used to protect structures from the damaging effects of earthquake ground motion by decoupling the structure from the foundation through the incorporation of a flexible interface between the two. Flexible isolation devices are incorporated to shift or elongate the natural period of the structure in the horizontal direction away from the typical dominant energy of the earthquake, thereby significantly reducing the accelerations, inertial forces, and subsequently base shear demands on the structure. Increased displacements are accommodated in the isolation system, while structural deformations are substantially reduced such that the structural system practically moves “rigidly” above the isolators.

Seismic isolation has been shown to successfully protect the structural system and content of numerous structures in prior earthquakes. Most recently, many isolated buildings were shaken in the 2011 Tohoku Earthquake and Tsunami, with isolator displacement demands ranging from 20 to 40 cm (Nishiyama et al. 2011). Seismic isolated structures around the world now number in the several thousands, and seismic isolation systems have been incorporated into the design of nuclear power plants in France and South Africa (Malushte and Whittaker 2005). As a result, seismic isolation is being considered for the future generation of nuclear power plants in the United States.

The structures, systems, and components of nuclear power plants are required to be designed for natural phenomena (such as earthquakes) without loss of capability to perform their safety functions (10 CFR 50, 2011). Seismic isolation is most effective for stiff, short period structures. Safety related nuclear structures fit this description since their horizontal period is on the order of 0.1 to 0.25 sec. If designed to remain elastic under strong ground motions, a short period structure attracts high acceleration demands that must be accommodated by internal equipment. If, on the other hand, a short period structure is designed to yield, it can experience large ductility demands relative to a longer period structure with a comparable strength reduction factor (e.g. Chopra 2012). Fortunately, the flexibility of the isolation system shifts the natural period of the building to significantly reduce both force demands to the structural system and acceleration demands to internal equipment. Thus, seismic isolation could be considered for safety related nuclear facilities if the overall system is analyzable and the response is predictable.

Two major classes of isolation devices have been used in the United States: elastomeric bearings and friction pendulum bearings. Elastomeric bearings are composed of alternating layers of natural, or synthetic, rubber bonded to intermediate steel shim plates. A rubber cover is provided to protect the internal rubber layers and steel plates from environmental degradation and corrosion. Elastomeric bearings can be categorized as: (1) low-damping natural or synthetic rubber and (2) high-damping rubber. Low-damping natural rubber material exhibits nearly linear shear stress-strain behavior up to approximately 150% shear strain, wherein the horizontal stiffness  $K_b$  is calculated as:

$$K_b = \frac{GA_b}{T_r} \quad (1.1)$$

where  $G$  is the shear modulus,  $A_b$  is the cross-sectional area of the bearing, and  $T_r$  is the total thickness of rubber. A typical range of  $G$  for seismic applications is 0.4-0.9 MPa (60-130 psi).

The equivalent damping ratio,  $\beta$ , for low-damping natural rubber ranges between 2% and 3% at 100% shear strain. To limit displacements across the isolation interface, external supplemental damping devices or alternative isolation devices are typically used in parallel with low-damping natural rubber bearings. A higher level of damping can be achieved through the addition of fillers to the rubber; however, recently such devices are rarely used in the United States. Another type of elastomeric bearing is the lead rubber bearing. From a construction perspective, lead-rubber bearings differ from low-damping natural rubber bearings only by the addition of a lead-plug that is press-fit into a central hole in the bearing. The lead-plug deforms plastically under shear deformation, enhancing the energy dissipation capabilities compared to the low-damping natural rubber bearing. The horizontal force-deformation relationship of a lead-rubber bearing is characterized using bilinear behavior with an effective, or secant stiffness ( $K_{eff}$ ) calculated as:

$$K_{eff} = \frac{Q_d}{d} + K_d \quad (1.2)$$

where  $Q_d$  is the bearing characteristic strength, which is controlled by the yield strength of the lead in shear and the area of the lead-plug;  $K_d$  is the post-yield stiffness and  $d$  is a given horizontal displacement of the bearing. The vertical stiffness of all types of elastomeric bearings (low damping rubber, high damping rubber, and lead rubber) is typically thousands of times larger than the horizontal stiffness so that isolation systems composed of elastomeric bearings provide isolation only from the horizontal components of ground shaking.

The Friction Pendulum™ (FP) bearing, developed by Earthquake Protection Systems, Inc. is a sliding bearing that supports the weight of the structure on a bearing that rests on a sliding interface. A single FP bearing consists of a single sliding interface, while a Triple Pendulum™ (TP) bearing consists of multiple sliding interfaces. The sliding interface is designed with a low coefficient of friction, which limits the resistance to horizontal forces. The single FP bearing consists of a base-plate, an articulated slider and a spherical concave dish. Under horizontal motion, the spherical concave dish displaces horizontally relative to the articulated slider and base-plate. Friction between the two surfaces provides frictional resistance and energy dissipation, whereas the radius of curvature of the spherical concave dish provides a restoring force. The shear force-horizontal deformation behavior of FP bearings is characterized using a bilinear relationship. The horizontal strength, or zero-displacement force-intercept,  $Q_d$ , is controlled by the bearing material and the weight  $W$  carried by the isolators, according to:

$$Q_d = \mu W \quad (1.3)$$

where  $\mu$  is the sliding coefficient of friction of the bearing interface. The sliding coefficient of friction can range between 0.03 and 0.2. The post-yield stiffness of the FP bearing is controlled by weight acting on the isolator and the radius of curvature,  $R$ , of the spherical concave dish. The TP bearing consists of four spherical sliding surfaces and three independent pendulum mechanisms. The internal pendulum mechanism with two concave plates and a rigid slider determines the response during low intensity shaking. The outer stainless steel concave surfaces, when designed with different curvatures and friction coefficients, provide two independent pendulum mechanisms that determine the response during medium to high intensity shaking. Both the single FP and the TP bearings provide no resistance to tensile forces and thus are free to uplift. In certain situations uplift in the bearings could occur, e.g. bearings



on the perimeter of slender structures or those located under braced frames. For these situations resistance to uplift is considered desirable.

## 1.2 State of Knowledge and Motivation for Full Scale Testing

The following briefly summarizes the research and development that has led to the modern seismic isolation systems used today. Early proof of concept earthquake simulator or “shake table” tests are discussed, as well as later tests that examined system level technical concerns. Then, analytical modeling capabilities for elastomeric isolation bearings that have been developed mostly in conjunction with device level testing are reviewed. Finally, the need for full scale earthquake simulator testing of isolated structures is addressed.

Initial development and proof-of-concept earthquake simulator testing was carried out in the United States on elastomeric and friction pendulum isolators in the 1980’s and 1990’s (e.g., Kelly et al. 1980a, 1980b; Kelly and Hodder 1981; Zayas et al. 1987; Mokha et al. 1988, 1990; Kelly and Chalhoub 1990; Constantinou et al. 1990; Al-Hussaini et al. 1994). In Japan, research and development was also carried out at construction companies that built several demonstration buildings to be tested by earthquakes (Kelly 1988).

Earthquake simulator testing eventually progressed beyond basic validation to examine performance of the overall isolation system under challenging loading conditions, and elastomeric bearings have been tested to various limit states under dynamic loading. For example, a series of uplift experiments were performed on slender structures isolated with elastomeric bearings (Griffith et al. 1988a, 1988b), and researchers have developed and tested several uplift restraint devices suitable for elastomeric isolation systems (e.g. Griffith et al. 1990; Kasalanati and Constantinou 2005). Uplift restraint in elastomeric bearings is often provided through limited engagement of the elastomers in tension by providing a fully bolted connection detail for the elastomeric bearing. One project designed a series of experiments to drive an isolated structure out to its ultimate capacity, including large isolator displacement demands and structural yielding (Clark et al. 1997). The experiment showed that design strategies can be adopted to ensure that the isolation system is not the weak link, and that isolators can withstand significant tension due to structure overturning. At least two studies performed earthquake simulator tests where the intensity of the excitation was increased until the bearings ruptured (Sato et al. 2002; Takaoka et al. 2011). A more detailed review of the history of earthquake simulator or “shake table” testing of isolated building structures was provided in Warn and Ryan (2012).

Recently, much progress has been made in understanding and modeling the macro-mechanical behavior of natural rubber and lead-rubber bearings. Bidirectionally coupled bilinear or Bouc-Wen models are frequently used by commercial software to represent the hysteretic behavior of lead-rubber bearings. These models are incapable of representing the amplitude dependence of the hysteretic properties and the lateral-axial interaction of the response, which may or may not be significant. In lead-rubber bearings, the characteristic strength of the lead plug has been observed to degrade with repeated cycling (Constantinou et al. 2007), which is a result of viscous heating of the lead plug. Theoretical models to account for heating effects have been developed and experimentally verified (Kalpakidis and Constantinou 2009a, 2009b), as well as a numerical modeling approach for implementation in finite element software for dynamic analysis (Kalpakidis et al. 2010). A theory of scaling based on similitude and recommendations for testing reduced scaled bearings to properly account for the effects of heating was then developed (Kalpakidis and Constantinou 2010). Constantinou et al. (2007) also evaluated the effects of history of loading, aging, and environmental conditions (such as extreme temperature variation) on the behavior of elastomeric isolation hardware, but concluded that rational procedures to account for these effects in design have yet to be developed. They also

concluded that current property modification factors – used to establish probable maximum and minimum values of key mechanical properties over the lifetime of the bearings – are probably conservative.

The influence of axial load on the horizontal force-deformation behavior of elastomeric bearings leads to complexity that can affect the analyzability of the overall system; however much recent research has been completed to evaluate the critical load capacity and post-buckling behavior of the bearings. The overlapping area approximation was developed to estimate the reduction in critical load capacity with increasing displacement (Buckle and Liu 1994). Several studies have experimentally evaluated stability and post-buckling behavior of elastomeric bearings (Buckle et al. 2002; Warn and Whittaker 2006; Weisman and Warn 2012; Sanchez et al. 2012). They all concluded that the overlapping area approximation is conservative, and improvements have been proposed. Experimental studies also evaluated the reduction in vertical stiffness at large horizontal displacements (Warn and Whittaker 2007).

A simple two-spring model that include the influence of vertical load on the horizontal response was developed by Koh and Kelly (1987) for linear material behavior and extended by Ryan et al. (2005) for nonlinear material behavior. Another extension of the two-spring model considered large displacement/rotation theory to predict the stable post-critical behavior that has been observed in test data (Nagarajaiah and Ferrell 1999). More advanced distributed spring models accounting for these second-order effects have been developed that are also capable of exhibiting zero or negative tangential horizontal stiffness (Yamamoto et al. 2009, Kikuchi et al. 2010).

Most of the aforementioned studies (especially earthquake simulator tests) involved reduced scale structural models and reduced scale isolation bearings. Despite the wealth of data on reduced-scale systems, the following knowledge gaps still need to be addressed.

- Dynamic test data of full-scale elastomeric bearings is not available for a system earthquake simulator test. A full scale system test is necessary to verify that the complex phenomena observed in reduced-scale bearings under realistic earthquake loading (e.g. velocity effects, temperature effects, horizontal and vertical interaction) are scalable to much larger devices. Earthquake simulator tests of a full scale building isolated with high damping rubber bearings and natural rubber bearings with dampers were performed (Sato et al. 2011), but bearing force data was not recorded as part of that particular program.
- Larger scale tests are needed to evaluate the influence and analyzability of complex isolator-structure interaction effects that are affiliated with full-scale structures. Most reduced scale tests are bare frame tests with supplementary mass pieces bolted to the frame. Such tests have not examined the influence of a composite floor system, mass and stiffness irregularities, and nonstructural components – all of which may interact with the structure – on the effectiveness of the seismic isolation system.
- Similar to the previous item, earthquake simulator testing of isolated building models under combined horizontal and vertical loading is somewhat limited. Full scale testing should be performed that emphasizes realistic three-dimensional input and strong vertical input recorded in near-fault ground motions.

### **1.3 Opportunity for Testing at E-Defense**

The Hyogo Earthquake Engineering Research Center of Miki, Japan, also known as E-Defense, contains the world's largest single earthquake simulator facility, and the only facility in the world

capable of reproducing three-dimensional earthquake excitation to test full scale structures (<http://www.bosai.go.jp/hyogo/ehyogo/>). The 15 x 20 meter (49 x 66.6 ft) table platform is driven by 5 actuators in each horizontal direction and 14 actuators in the vertical direction (Figure 1-1). At the payload capacity of 1200 metric tons (2646 kips), the table can replicate motions with horizontal accelerations up to 0.9g and vertical accelerations up to 1.5g (Figure 1-1). The E-Defense earthquake simulator facility can uniquely meet the testing needs for full scale isolated structures.

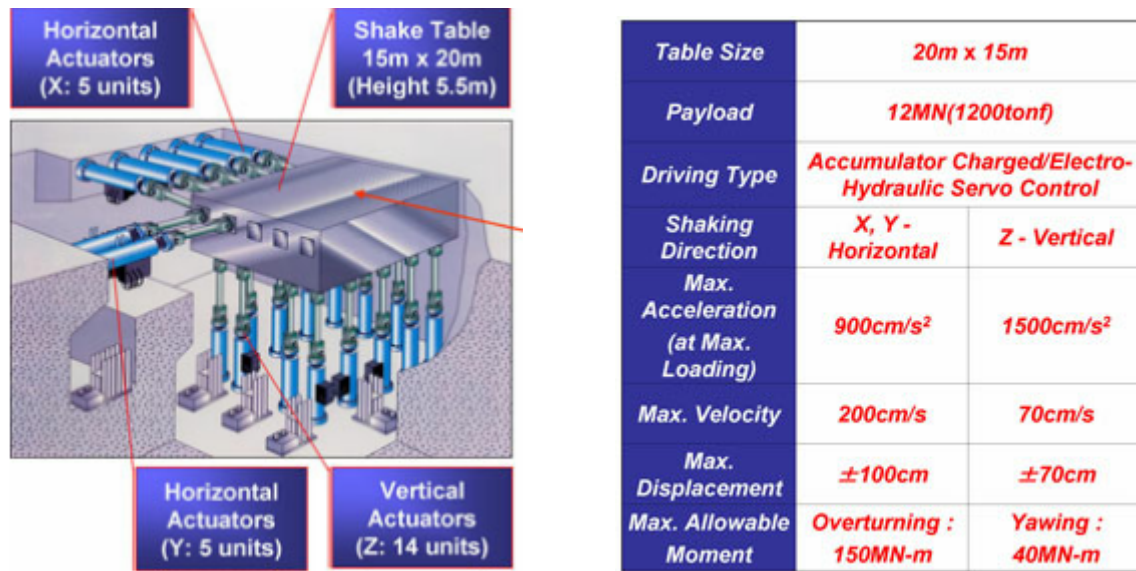


**Figure 1-1 E-Defense earthquake simulator parameters (Source: <http://www.bosai.go.jp/hyogo/ehyogo/>)**

Collaborative research between United States and Japan investigators utilizing the E-Defense earthquake simulator was made possible through a Memorandum of Understanding (MOU) between the National Science Foundation (NSF) funded Network for Earthquake Engineering Simulation (NEES) program and Japan's National Research Institute for Earth Science and Disaster Prevention (NIED). The NEES Tools for Isolation and Protective Systems (TIPS) project was funded by NSF to conduct basic and applied research to overcome some of the technical, cost and procedural barriers to the wider implementation of seismic isolation in the United States. One of the perceived barriers to implementation was the lack of full scale validation of seismic isolation of a realistic full scale structure to demonstrate both structural and content protection in very large earthquakes. Thus, the NEES TIPS project included collaboration with Japan to test a full scale isolated building at E-Defense.

Planning of the NEES TIPS/E-Defense test program began in earnest in May of 2010, with a projected test date of fall 2011. The development of the test program initially prioritized the testing of TP bearings for several reasons. The TP bearing has been regarded as an innovative isolation device that can be designed under the Performance Based Earthquake Engineering (PBEE) paradigm to target various levels of protection under multiple earthquakes scenarios (Fenz and Constantinou, 2008; Morgan and Mahin, 2011). The isolation period of TP bearings are insensitive to the weight of the supported structure above, and the displacement capacity of the device is not limited by stability considerations. This allowed the following design strategy to be employed: the period of the isolation system was lengthened beyond the pulse period of several well known and challenging near fault motions, while sufficient displacement capacity was provided to meet the displacement demands of the strongest long period motions that could

be found in the Pacific Earthquake Engineering Research (PEER) Next Generation Attenuation (NGA) database (Chiou et al. 2008). Finally, strong in-kind support from the manufacturer helped to overcome financial-based limitations on scope.

The developed test program made use of an existing 5-story steel moment frame building structure that had been tested at E-Defense in early 2009 as part of a program on value-added buildings (Kasai et al. 2010). This building was stored in the fabrication yard at E-Defense from 2009 to 2011. Over the course of 2010 and early 2011, the members of the NSF funded NEES Research Nonstructural Grand Challenge project (<http://www.nees-nonstructural.org>) were recruited as collaborators. The test plans evolved to include installation and testing of an integrated interior partition wall – suspended ceiling – and sprinkler piping system on the 4<sup>th</sup> and 5<sup>th</sup> stories of the building; and the moment frame building would be tested in the fixed-base configuration as well as the isolated configuration. As a nontrivial part of the program, a support assembly was designed for the isolated building utilizing 73 of 76 of the triaxial load cells owned by E-Defense to measure the shear and axial forces in each of 9 TP bearings.

The TP isolation system designed for testing at E-Defense was not ideal for a safety related nuclear structure, because (a) 1 meter displacement demand across the isolation interface is rather large for a nuclear structure, (b) the design strategy using a very long isolation period may lead to undesirable residual displacements in the isolators, and (c) the low friction force of the inner sliders may activate the isolation system more than desired in small motions (say 1/6 of design basis). The design was developed without considering the expected seismicity of a representative nuclear site and the needs of a safety related nuclear structure. Furthermore, given the history of investigation of elastomeric bearings for nuclear applications, verification of the stability and load-carrying capacity of elastomeric bearings at displacements representative of extended design basis ground motions was a top objective.

The planned test program at E-Defense offered a payload opportunity to design and test an additional isolation system tailored to the needs of the nuclear industry at low incremental cost. Thus, on June 1, 2011 (about 2.5 months before the planned start of testing at E-Defense), the project team, with product and in-kind support from Dynamic Isolation Systems, Inc. made the decision to proceed with the design and manufacture of an additional isolation system using lead rubber (LR) bearings to be tested at E-Defense on the potential of a future contract from the United States Nuclear Regulatory Commission.

The main objective for the payload project was to evaluate the performance of the elastomeric isolation system designed for a safety related nuclear structure in *beyond design basis* earthquake (DBE) shaking. Ground motions were developed for a representative central and eastern United States soil site. The test program was developed considering the performance objectives of ASCE 43-05 (ASCE 2008), that the isolation system has less than 1% probability of unacceptable performance for 100% DBE shaking and less than 10% probability of unacceptable performance for 150% DBE shaking. For acceptable performance, individual isolators are expected to (1) sustain no damage during DBE shaking; (2) sustain gravity and earthquake induced axial loads at 90<sup>th</sup> percentile lateral displacements consistent with 150% DBE shaking; and (3) have 1% or less probability of impacting surrounding structure for 100% DBE shaking and 10% for 150% DBE shaking. The third objective was not directly assessed in the test program, but relates to the predictability of the isolation system.

The E-Defense test setup provided an excellent opportunity to test an isolation system at large scale, but the following should be noted:

- The isolation system was to be designed for the existing (flexible) moment frame structure, which is unlike most nuclear structures that are extremely stiff.

- The moment-frame structure was light, which precluded the use of only elastomeric bearings to simultaneously provide sufficient period elongation and meet the displacement demands at a representative United States nuclear site. This led to the pairing of LR bearings with near frictionless tension-capable Cross Linear (CL) bearings manufactured by THK, referred to as the hybrid LR isolation system. LR and CL bearings have been used together in over 100 projects in Japan. Thus, the hybrid system was found to be a reasonable solution for the test. This report examines whether a hybrid system is a feasible solution for a nuclear facility.
- The test setup was constrained to use load cell connection assemblies that had been designed for the TP isolation system. This led to the decision not to place load cells beneath the CL bearings because the designed connection assembly was too flexible.
- The payload project was limited to 2 days of testing with an expected limit of 7 simulations per test day. Thus, the testing needs had to be prioritized with recognition that all needs could not be met.
- The objectives of other interested parties, including E-Defense collaborators, Dynamic Isolation Systems, Inc. and partner Aseismic Devices Co., Ltd. - provider of the CL bearings – were also considered in planning the test program.
- Several constraints on the test program were imposed due to safety considerations of the facility, such as limitations on the displacement, a slow ramp up (3-5 simulations) to the largest anticipated motion to ensure the target displacement limit was not exceeded, etc.

## 1.4 Report Organization

This report is organized as follows. Chapter 2 describes the 5-story steel moment frame building, for which the hybrid LR isolation system was designed, as well as the nonstructural components and building content that were monitored during the tests. The design of the hybrid LR isolation system, including the iterative thought process through which the final selections were derived, is described in Chapter 3. This chapter also explains the consideration for selection and scaling of ground motions during the 2 days of testing on the hybrid LR isolation system. Chapter 4 summarizes the test program, including the assembly and connection of isolators and building to the earthquake simulator, instrumentation to measure structural and bearing responses, shaking test schedule, amplitude of realized table motions relative to the targets, and algorithms to generate derived data. For completeness, the shaking test schedule includes the test days for the TP configuration and the fixed-base configuration, although the test results for these systems are discussed only briefly in this report. A statistical summary of the test results for the hybrid LR building configuration is given in Chapter 5, where peak values of key response quantities are identified for every simulation. Chapter 6 examines the technical response and unique aspects of the hybrid LR isolation system.

The latter part of the report furthers the understanding of the test data through development, validation and synthesis of a robust analytical model of the hybrid LR isolation system and building. In Chapter 7, the analytical models for the LR bearings and CL bearings are presented, and the parameters of the model are calibrated to the bearing test data. Chapter 8 describes the analytical model of the superstructure. The analytically predicted responses of the LR bearings and the structural system are compared to the test data for four representative excitations in Chapter 9, including a synthesis of modal participation through interpretation of the floor spectra. Chapter 10 examines the influence of vertical excitation on the system response by comparing the isolator and structural responses to two pairs of ground motions that were

applied with and without vertical excitation, with further corroboration through analytical modeling. The response of the other building configurations (isolated with TP bearings and fixed-base) is briefly described and compared to the response of the hybrid LR configuration in Chapter 11. Chapter 12 summarizes the major findings from this test program.

## 2. DESIGN AND CONFIGURATION OF THE 5-STORY STEEL MOMENT FRAME TESTBED STRUCTURE

### 2.1 Description of Testbed Structure

The testbed structure used in this experiment program was designed by Hyogo Earthquake Engineering Research Center in 2008 and used in a test in March 2009 (Kasai et al., 2010). The authors of this report were not involved in its design. Hereafter is description of the testbed structure to enable later interpretation of results. The complete structural drawings of the building with hybrid LR isolation system are given in Appendix A.

#### 2.1.1 Basic Dimensions

The testbed specimen was a five-story steel moment frame building with rectangular plan (Figure 2-1). The building was 10 x 12 m (32.8 x 39.4 ft) in plan and approximately 16 m (52.5 ft) in height, with 2 bays in each direction. The bay widths in the long direction – 12 m or 39.4 ft – were 7 m (23 ft) and 5 m (16.4 ft) to promote torsion, which is typical of asymmetric structures. Figure 2-2 shows the basic dimensions of the building and the assumed coordinate system for presentation of results, where the Z-axis is the vertical axis. The previous researchers chose to simulate a 5-story steel specimen because it is on the high side of the typical building stock in Japan and without added damping, would be susceptible to more significant demands than comparable taller buildings (Kasai et al. 2010).



Figure 2-1 The 5-story steel moment frame specimen

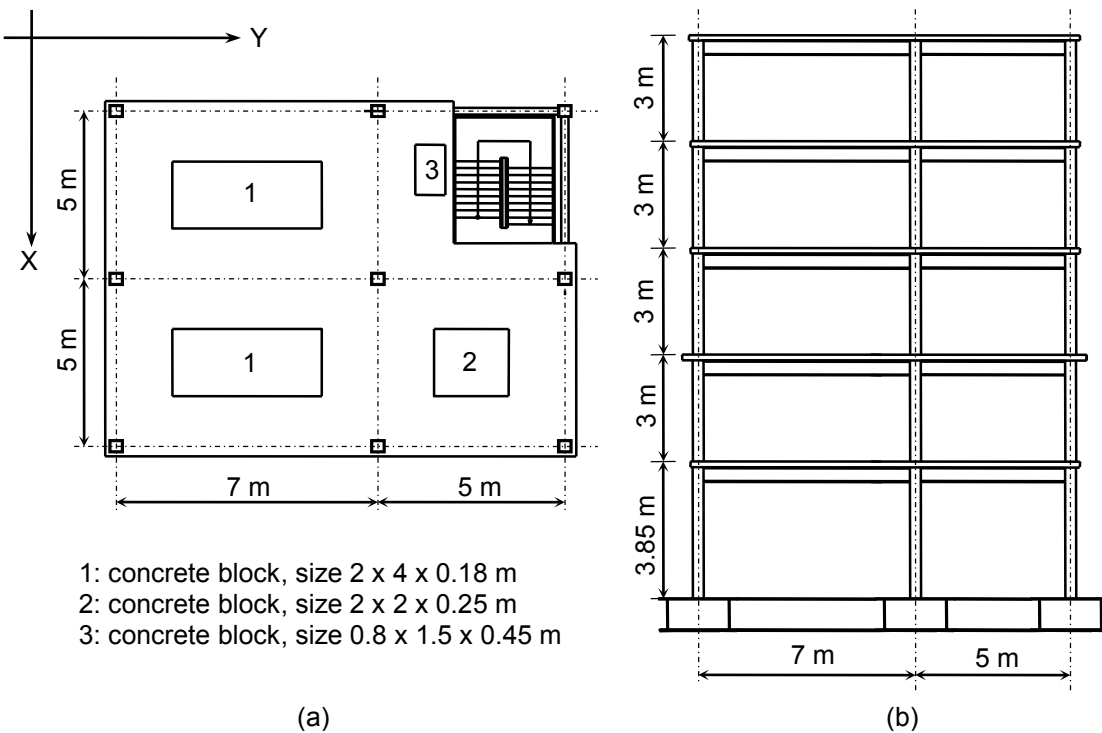


**Figure 2-2 Basic dimensions of the specimen: (a) typical plan view from floors 2 to 5, and (b) elevation view**

### 2.1.2 Design Spectra and Design Criteria

The design of the lateral system was based on Japanese Level II and Level III earthquake design spectra (Figure 2-3). Because the testbed was designed to be a “value-added” building (Kasai et al. 2008), whose structural components and non-structural components are protected for major earthquakes, the story drift angle of the frame was limited to 0.005 rad for a Level II earthquake, whereas the drift angle limit for conventional frames would be 0.01 rad. The structure was also required to remain elastic for a drift angle up to 0.01 rad (Kasai et al. 2008).

### 2.1.3 Framing System

The lateral system was designed and detailed according to Japanese code and construction practice. The framing system was a three dimensional steel moment frame where the columns were engaged in flexure about both their principal axes. The columns were made of 35 cm x 35 cm (13.8 in x 13.8 in) hollow box sections with thickness varying from story to story. The beams were either rolled or built-up I-sections. The primary beams, which were connected to the columns, consisted of a small-section segment at the middle and two large-section segments at the ends (Figure 2-4). These 3 segments were all 40 cm (15.7 in) height and bolted together at the approximate inflection points determined from gravity loading. Connections between columns and beams were all fully restrained moment connections, with both flanges and web of the beam welded to the column. Generally, the flanges of the primary beams were haunched at their ends to form plastic hinges away from the columns and improve the beam-to-column connection. Continuity plates were also provided to protect the panel zones (Figure 2-4).



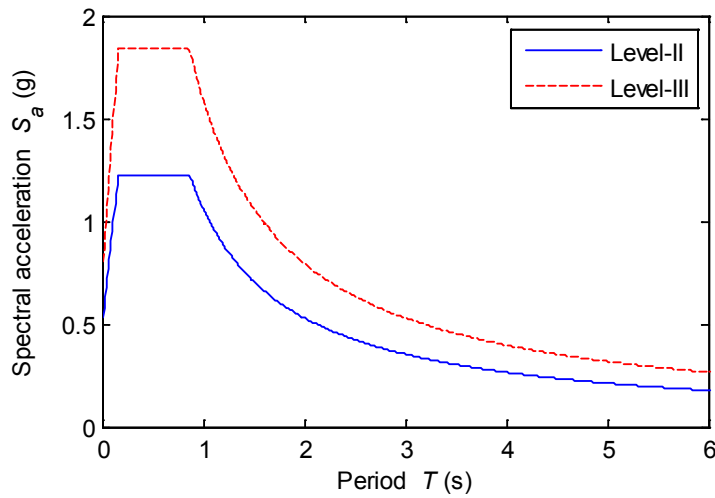


**Figure 2-3 Design spectrum for Japanese Level II and Level III earthquakes**

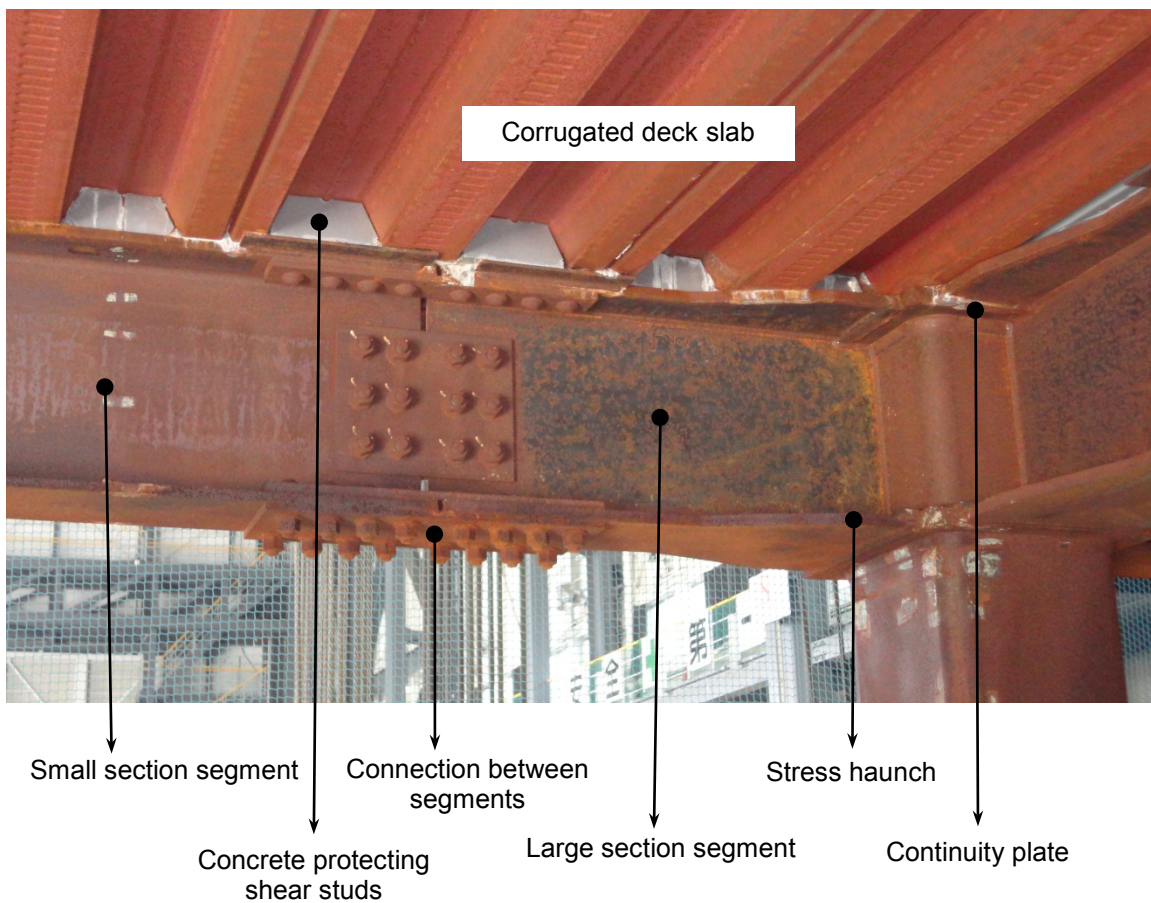


**Figure 2-4 Beam, beam to column connection and slab**

To connect the testbed to the shaking table and provide the stiffness required to “fix” the testbed at its base, column bases and grade girders were designed with special details. The column bases were detailed as steel boxes with dimension of 2.5 m x 2.5 m x 0.9 m (8.2 ft x 8.2 ft x 3 ft) (Figure 2-5). Vertical stiffeners were installed inside the boxes. The grade girders were bolted to

the column bases and were the same height as the column bases (0.9 m or 3 ft). The foundation framing was braced in its plane as shown in Figure 2-6.

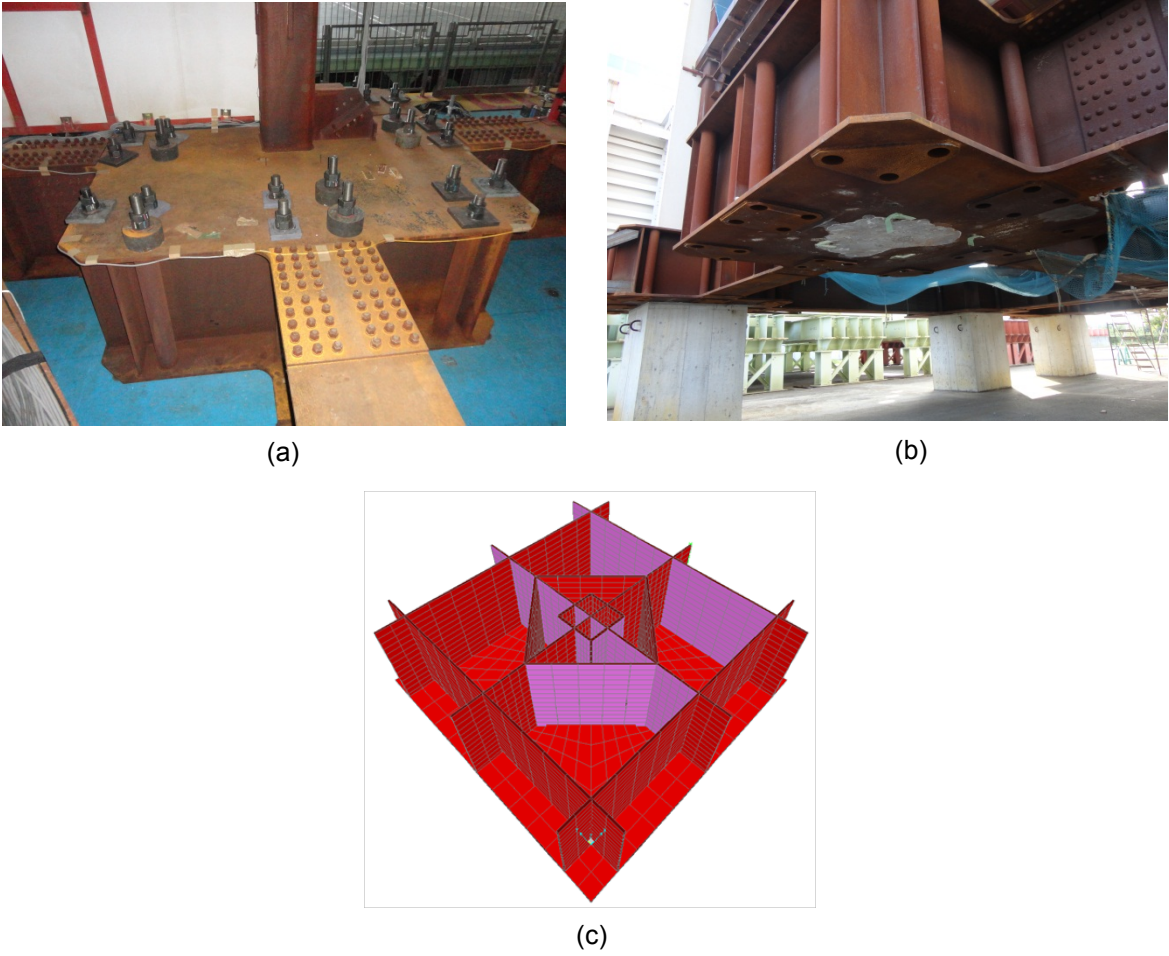


**Figure 2-5** Column base: (a) view from top (b) view from bottom, (c) rendering of stiffeners



**Figure 2-6 Horizontal braces at base level**

#### **2.1.4 Slabs**

The composite floor slabs were formed from 7.5 cm (3 in) high corrugated (ribbed) steel decking and 8 cm (3.1 in) thick normal weight concrete cast over the ribs of the deck. The corrugated steel deck (Figure 2-4) was 1.2 mm (0.05 in) thick and oriented parallel to the Y-direction. Typical reinforcement in the floor slabs was a single layer of  $\phi 1$  cm @ 15 cm ( $\phi 0.4$  in @ 5.9 in) rebar in both directions placed at the slab mid-thickness.

The roof slabs were 15 cm (5.9 in) normal weight concrete slabs cast on a 1.2 mm (0.05 in) flat steel deck. Reinforcement for the roof slab included layers of  $\phi 1.3$  cm @ 20 cm ( $\phi 0.5$  in @ 7.9 in) rebar in each direction at the top and bottom of the slab. The roof slab was nearly twice as thick as the floor slabs as it was designed to carry roof mounted equipment (e.g., air conditioning system, water tanks) and a penthouse.

Shear studs connected the concrete slabs to the primary beams to provide a fully composite connection (Figure 2-4).

#### **2.1.5 Material Properties**

The specified yield strengths of steel were 295 MPa (42.8 ksi) and 325 MPa (47.1 ksi) for the columns and beams, respectively. The expected ultimate tensile strengths were 400 MPa (58 ksi) for columns and 490 MPa (71 ksi) for beams. Coupon tests showed that yield and ultimate strengths of the steel varied from member to member and the average ratio of measured to nominal strength was 1.2 (Kasai et al. 2010). Table 2-1 presents the range of observed yield strength  $\sigma_y$  and ultimate strength  $\sigma_u$  of steel used for the beams and columns.

**Table 2-1 Yield and ultimate strength of steel from coupon tests.**

<b>Member</b>	<b><math>\sigma_y</math>(MPa)</b>	<b><math>\sigma_u</math>(MPa)</b>
Columns	346 – 398	430 – 470
Beams	331 – 422	510 – 557

(Source: Kasai et al. 2010)

The compressive strength of the normal weight concrete used in the slabs was 21 MPa (3 ksi); the measured compressive strength of standard samples was 24 MPa (3.5 ksi). The concrete slabs were reinforced by SD295A grade rebar. The nominal yield stress for the rebar was 295 MPa (42.8 ksi); measured rebar strengths were unavailable.

## **2.2 Non-Structural Components and Contents**

Nonstructural components, including an integrated system of interior walls, suspended ceilings, and sprinkler piping were installed in the 4<sup>th</sup> and 5<sup>th</sup> stories, where the floor acceleration was expected to be maximized. The overview of the nonstructural component response in both isolated and fixed-base building configurations is discussed briefly in this report; however, the detailed analysis of the nonstructural response will be reported elsewhere. Preliminary observations of the nonstructural response are available in Soroushian et al. (2012).

To investigate the response of non-anchored contents in the isolated and fixed-base buildings for different earthquake excitation, furnishings representing a hospital room on the 4<sup>th</sup> floor (Figure 2-7) and an office room on the 5<sup>th</sup> floor (Figure 2-8) were installed in specially designed enclosed areas. Both rooms were 2 m x 4 m (6.6 ft x 13.1 ft) in plan and were constructed on top of the concrete mass blocks already present on the floors (Figure 2-2(a)). Contents in the hospital room included a wheeled patient bed, a dresser containing medical equipment, a medical cart, a storage cart, IV poles, a mobile lamp, medical bottles and boxes. Many of these items were wheeled. The office room was furnished with desks, chairs, computer system, bookcases and a photocopy machine.





**Figure 2-7 Hospital room**



**Figure 2-8 Office room.**

## 2.3 Weights

In addition to the weight of structural components, nonstructural components and contents, additional mass in the form of concrete and steel blocks were installed to simulate permanent live load. Concrete weights, whose typical size and position on the floors are shown in Figure 2-2(a), were built as a permanent part of structure on floors 2 to 5, while steel blocks were tied to the roof as shown in Figure 2-9. The categorized weights of the testbed components are listed in Table 2-2. This information was used to design the isolation system, model the structure and compute inertia forces from recorded accelerations.

In the 2009 experimental program that first used the testbed building (Kasai et al. 2010), steel blocks were distributed uniformly to the roof level to represent additional weight of equipment such as an air conditioning unit, water tank, or even a small penthouse. Each block included either 7 or 8 steel plates of size 2.1 m x 4.3 m x 0.025 m (6.9 ft x 14.1 ft x 0.08 ft). The roof slab was specifically designed to accommodate the additional weight, which summed to 820 kN (184 kips). For this experimental program, the weight at the roof was altered from that used in 2009 experiments to introduce additional mass eccentricity and increase torsional response; specifically, about one third of the steel plates were removed on the West side of the building (Figure 2-9). The altered weight of the steel plates for this experimental program was 535 kN (120 kips). The intent of the added weight as designed for the original experiments was to

simulate equipment weight in a typical building lacking a basement (Kasai 2011). However, this supplementary weight far exceeds the concentrated weight introduced by a typical single piece of roof mounted equipment, such as a chiller (about 80 kN or 18 kips), and thus might be considered atypical or even unrealistic. The issue is noteworthy because the supplementary weight influenced the seismic response of the building, which is discussed throughout the report.

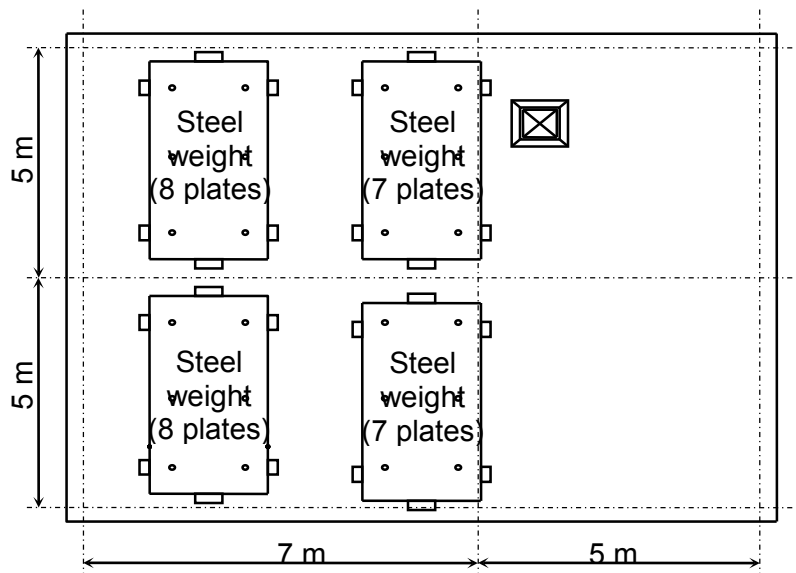


**Figure 2-9 Location of steel weights at roof**

**Table 2-2 Estimated weight in kN of the specimen by component and floor level.**

Floor	Structural	Conc. Weight	Steel weight	Non-structural	Total
Roof	599	0	535	19.4	1153
5F	478	258	0	35.5	771
4F	497	268	0	16.2	781
3F	528	213	0	41.2	782
2F	527	176	0	89.6	792
Base	794 (*)	0	0	48.4	842
Sum w/ base	3422	914	535	250	5122
Sum w/o base	2628	914	535	202	4279

(\*) Before the test, the weight of structural component at base was estimated at 256 kN. This low value did not account the weight of column bases. The total weight of the specimen corresponding to this value was 4585 kN.

The estimated total weight of the testbed, about 5122 kN (1151 kips), was well below the maximum capacity of the E-Defense earthquake simulator, which is 12000 kN (2700 kips) (Tagawa and Kajiwara 2007). The actual weight of the specimen measured during testing was 5220 kN (1174 kips) as reported in Section 4.3.

## 2.4 System Identification

The experimental response of the fixed base building to white noise excitations was analyzed (Sasaki et al., 2012) to find the periods and damping ratios of natural modes of the structure. Figure 2-10 shows examples of transfer functions determined from the white noise excitation on the fixed-based building conducted prior to the primary earthquake excitation. The period and damping ratio corresponding to the fundamental response modes were evaluated by curve fitting theoretical transfer functions to the measured transfer functions using a least square algorithm. Table 2-3 summarizes the periods and damping ratios of first 3 modes in both directions determined from this process. Rocking of the earthquake simulator has been observed to affect the natural frequencies and mode shapes (Kasai et al., 2011; Sasaki et al., 2012); however, the effect of rocking was ignored in the modes presented in Table 2-3.

With a natural period in the range of 0.65 to 0.70 seconds, the tested moment frame building is much more flexible than a nuclear facility, which has a natural period in the range of 0.1 to 0.25 sec. Thus, the response of the structural system in this experiment is not representative of a nuclear facility. In the presentation of the superstructure response, commentary is offered to explain how the response of a stiffer structure might differ from the response of the test frame. Although the superstructure is not representative of a nuclear facility, the experiments still provide useful information about the dynamic response of large scale elastomeric bearings (designed for nuclear seismicity) in a system level test.

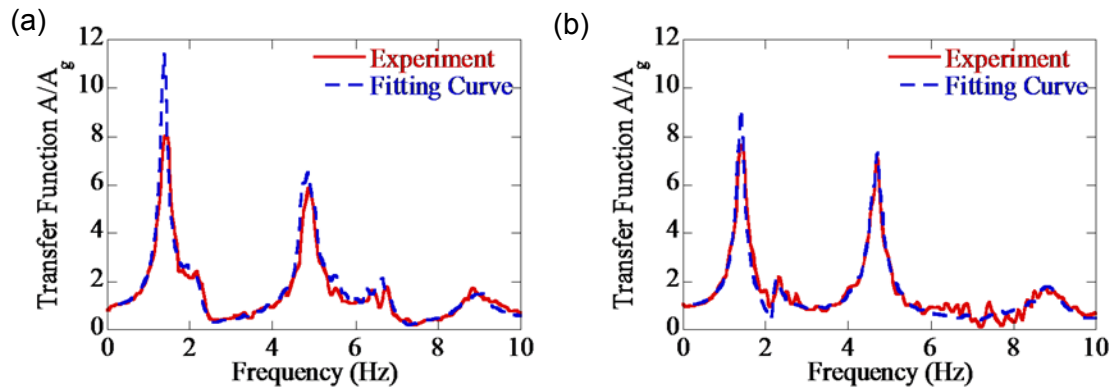


**Figure 2-10** Transfer function during white noise excitation in fixed-base configuration: (a) x-direction and (b) y-direction

**Table 2-3 Experimentally determined natural periods and damping ratios of the fixed-base building.**

	White noise X		White noise Y		White noise 3D	
	Period (s)	Damping ratio (%)	Period (s)	Damping ratio (%)	Period (s)	Damping ratio (%)
Mode 1 X	0.65	3.3	n/a	n/a	0.68	4.1
Mode 2 X	0.20	1.6	n/a	n/a	0.21	2.0
Mode 3 X	0.11	3.3	n/a	n/a	0.11	3.7
Mode 1 Y	n/a	n/a	0.68	2.5	0.69	3.5
Mode 2 Y	n/a	n/a	0.21	1.7	0.21	1.9
Mode 3 Y	n/a	n/a	0.11	2.6	0.11	3.6

## 2.5 Condition of the Testbed Prior to Testing

The testbed was built in 2008 and tested first in March 2009 equipped with several types of damping devices (Kasai et al. 2010). The testbed was stored outdoors and unprotected between April 2009 and July 2011.

Several cracks in concrete slabs formed during the March 2009 test (Kasai et al. 2010). Examples of these cracks are shown in Figure 2-11. Steel beams and columns had not been painted and some corrosion was present in August 2011 (Figure 2-11). We did not quantify the effects of this damage but suspect they are insignificant.



**Figure 2-11 Cracks in concrete slab and rust on steel member.**



### 3. DESIGN OF THE ISOLATION SYSTEM

#### 3.1 Target Response of a Nuclear Site

A main objective of the test program was to demonstrate the stable response of an isolation system subjected to *beyond design basis* shaking at a representative nuclear site. Extensive prior work was performed by Huang *et al.* (2009) to characterize the site specific response spectra and displacement demands of representative isolation systems for three potential United States nuclear sites: North Anna, Vogtle and Diablo Canyon. North Anna represents a Central and Eastern United States (CEUS) rock site, Vogtle represents a CEUS soil site, and Diablo Canyon represents a Western United States (WUS) rock site. During an initial consultation, the external Advisory Board recommended designing an isolation system suitable for one of the three sites. The options were quickly narrowed down to focus on the Vogtle site while eliminating the other two sites from consideration. Even in beyond design basis shaking, the displacement demands for the North Anna site were too small to fully realize the shaking potential of both present isolation hardware and the E-Defense earthquake simulator facility in Japan. On the other hand, the displacement demands for the Diablo Canyon site were quite large, making it extremely difficult to size the lead-rubber bearings to provide sufficient flexibility, displacement capacity, and stability for the lightweight structure. Because of these difficulties, it is recognized that isolation of a safety related nuclear facility may be more likely to come to fruition on a CEUS site; thus, the Vogtle site was deemed a more appropriate selection.

The development of site specific response spectra and spectrum matched motions for the Vogtle site, as utilized in this study, was described in detail in Huang *et al.* (2009) and is hereby summarized. Spectra representing the design basis earthquake (DBE) were developed by Southern Nuclear Operating Company. The uniform risk spectrum (URS) was developed by a combination of probabilistic seismic hazard analysis (PSHA), site response analysis, and conversion of the uniform hazard spectrum (UHS) to a URS. The seismic hazard was de-aggregated for a mean annual frequency of exceedance (MAFE) of  $10^{-4}$  and  $10^{-5}$ . Spectral shapes were developed for both high and low frequency spectral ranges using the attenuation relationship of McGuire *et al.* (2001) for Central and Eastern United States.. Site response analysis was conducted to determine the amplification of rock motion to the free field surface. Site class factors and resulting spectra for the high and low frequency sets were merged into one, which led to the site specific UHS. The UHS was converted to a URS according to the procedure of ASCE 43-05 (ASCE 2008). These site specific spectra for horizontal and vertical response are shown in Figure 3-1.

Thirty spectrum matched motions were developed using seed ground motions selected based on the controlling magnitude  $M_w$  and distance  $r$  pair ( $M_w = 7.2$  and  $r = 130$  km) for the low frequency spectral range. Each set of ground motions included two horizontal components and a vertical component. These seed motions were spectrally matched to the Vogtle site specific URS for the DBE to get 30 spectrum compatible motions. These motions were then amplitude scaled to develop maximum-minimum spectrum compatible motions. The maximum and minimum components consider the effects of directionality, wherein the minimum demand occurs at an orientation perpendicular to the maximum demand. The 5% damped response spectra for the 30 sets of developed maximum-minimum motions for the Vogtle site (Huang *et al.* 2009) are shown in Figure 3-2.

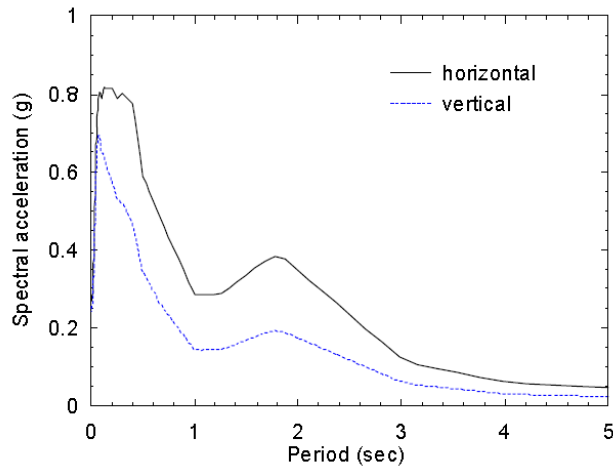


Figure 3-1 5% damped URS for the DBE at the Vogtle site. (Source: Huang et al. 2009)

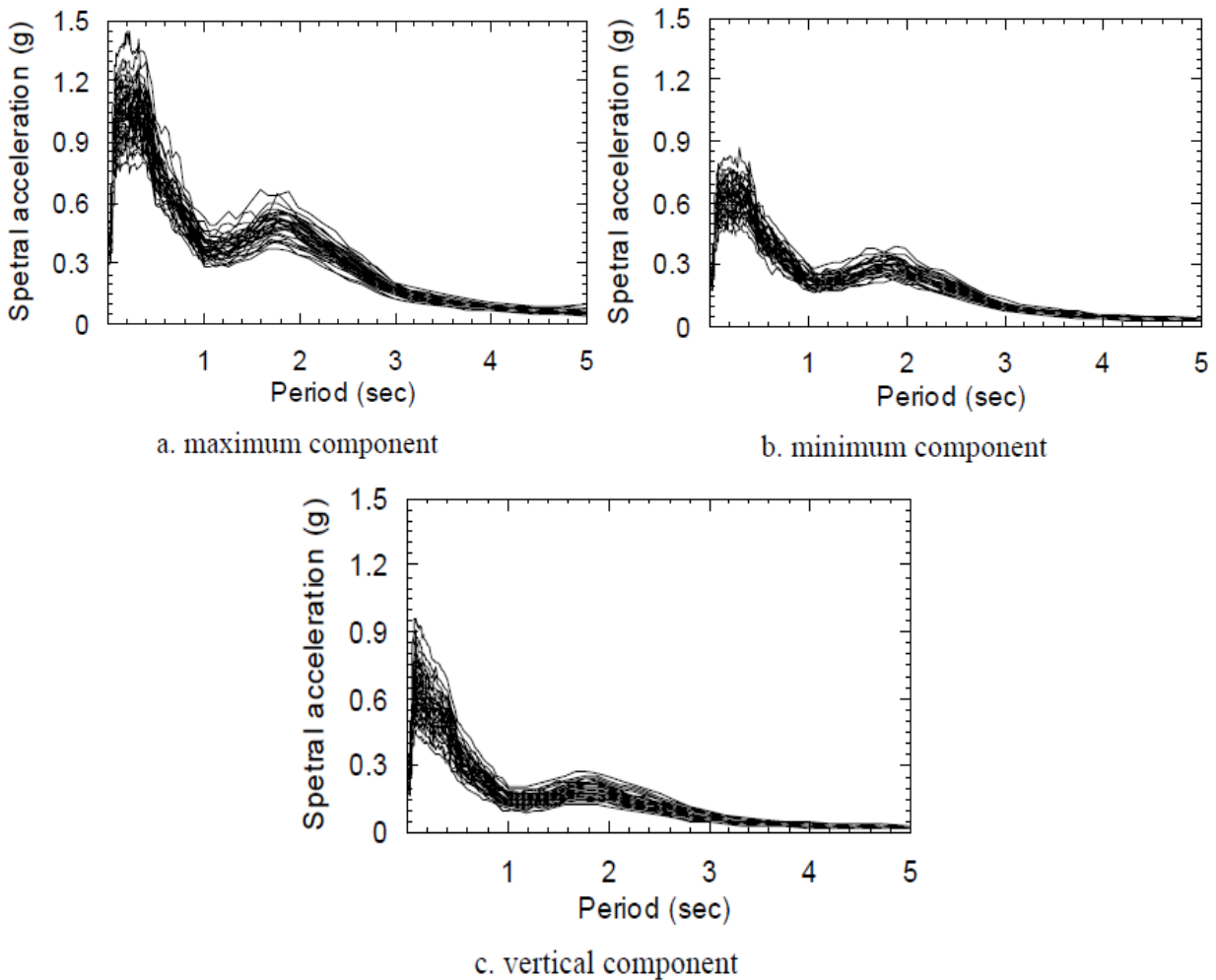


Figure 3-2 5% damped response spectra for the 30 sets of spectrum compatible maximum-minimum motions: (a) maximum component, (b) minimum component and (c) vertical component. (Source: Huang et al. 2009)

## 3.2 Isolation System Design

The design properties of the LR bearings to be used in the test program were selected with the following considerations in mind. First, as mentioned above, the isolation system was to be tested under beyond design basis ground motions. Thus, the general procedure utilized was to scale the record(s) for the Vogtle site (Huang et al. 2009) to an intensity level corresponding to beyond design basis, estimate the displacement demands in the isolation system, and size the isolators accordingly. Second, the configuration and force demands in the isolators were to be selected such that connection assemblies designed for the complementary tests on the TP bearings could also be used to measure the shear and axial forces in the LR bearings. Third, safety requirements were imposed by the facility to protect the equipment.

### 3.2.1 Estimated Displacement Demands

To obtain an approximate estimate of the isolator demands, the isolated building was modeled as a simple spring-mass system (rigid structure supported by a flexible isolator driven by bidirectional pairs of ground motions), consistent with the assumptions in Huang et al. (2009). The spring, or isolator, was modeled with a bi-directionally coupled bilinear force-displacement relationship (Figure 3-3) characterized by the post-yield stiffness  $K_d$  (corresponding to the period  $T_d$ ), and the yield strength normalized by the weight ( $Q_d/W$ ). The post-yield stiffness is generally associated with the horizontal stiffness of the rubber while the yield strength is associated with the shear strength of the lead plug. Additional 2% viscous damping was assigned to the isolator model in each horizontal direction based on the post-yield stiffness of the isolator (Huang et al. 2009). The weight of the building was estimated to be 4540 kN (1020 kips) for design.

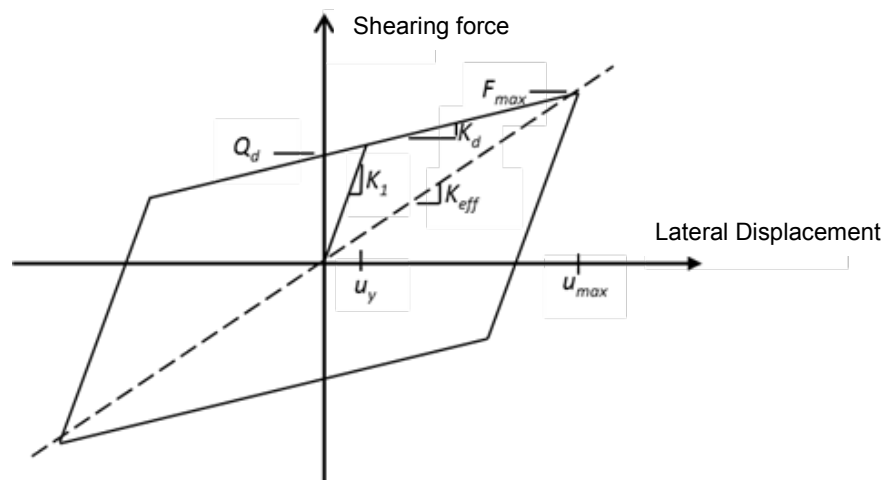


**Figure 3-3 Idealized bilinear force-displacement relationship for LR bearings, determined by post-yield stiffness  $K_d$  (stiffness of rubber), characteristic strength  $Q_d$  (strength of lead plug) and initial stiffness  $K_1$  or yield displacement  $D_y$ . An effective or secant stiffness  $K_{eff}$  is determined as the peak-to-peak stiffness based on maximum force  $F_{max}$  and displacement  $D_{max}$**

A subset of the parameters considered by Huang et al. (2009) was used as a starting point for this project, namely  $T_d = 2$  and 3 sec, and  $Q_d/W = 0.06$  and 0.09. The systems with  $Q_d/W = 0.06$  and 0.09 are hereafter referred to as Q6 and Q9. Other values of  $T_d$ , between 2 and 3 sec, were considered. The isolation period was desired to be greater than 2 sec to maximize the isolation effect and go beyond the soil-column related peak in the Vogtle spectrum just below 2 sec. A challenge with this testbed was to provide both the flexibility and the displacement

capacity required at  $T_d = 3$  sec due to the relatively low weight of the building. Figure 3-4(a) shows the median displacement demands of the maximum-minimum motions (Figure 3-2) predicted for a Q6 and Q9 system at different periods, determined by statistical analysis of the responses of the single degree-of-freedom (SDOF) system; the values at 2 and 3 sec are identical to those in Huang et al. (2009). Reducing the period for the Q6 system below 3 sec did not reduce the displacement demand, which is likely related to the local maximum in the response spectrum near 2 sec. The peak displacement demand of the Q6 nonlinear system occurred between periods of 2.4 and 2.6 sec. For the Q9 system, the displacement demand decreased monotonically as the period was reduced below 3 sec. Figure 3-4(b) shows the 90% percentile displacement demand of the maximum-minimum motions scaled to 150% – representative of beyond DBE shaking – for a Q6 and Q9 system. For this case, reducing the period below 3 sec caused the 90<sup>th</sup> percentile displacements to increase for both Q6 and Q9 systems. Based on these observations, a target period of 3 sec was selected for initial design and both Q6 and Q9 systems were considered.

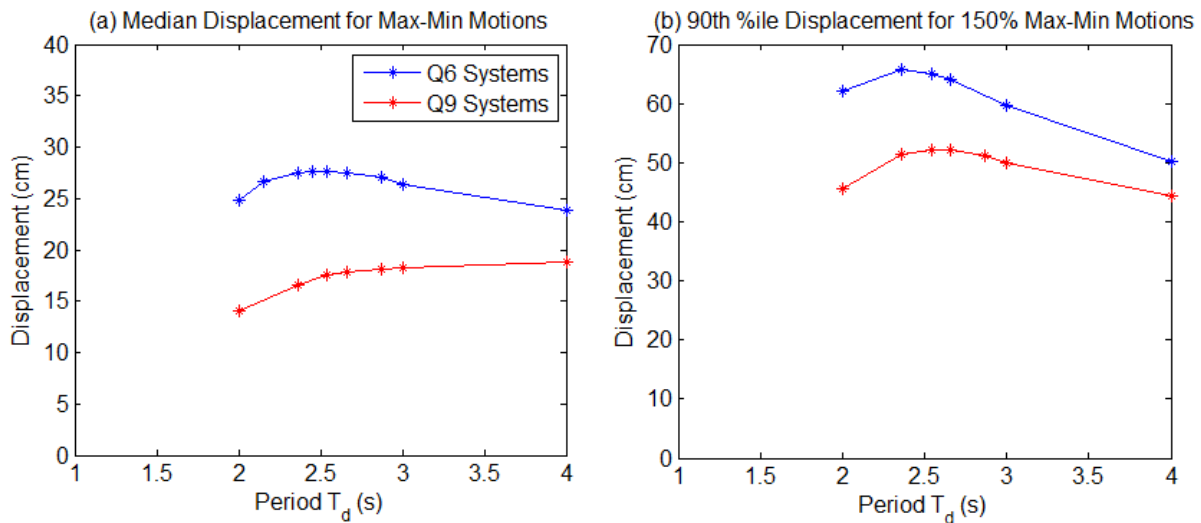


**Figure 3-4 Displacement demand representing (a) median response to maximum-minimum motions and (b) 90% percentile response to 150% maximum-minimum motions for Vogtle site**

### 3.2.2 Configuration of Lead-Rubber Bearings

As mentioned previously, the testbed was a 2 bay frame in each direction with 9 columns. The configuration of columns at the base labeled by direction coordinates is shown in Figure 3-5. Forces in LR bearings could potentially be obtained by bolting the bearings to connection assemblies. The connection assemblies, which were designed for the TP isolation system, consisted of 7 to 9 load cells sandwiched between two steel plates (e.g. Figure 3-6). Further details of the connection assemblies are provided in Chapter 4.

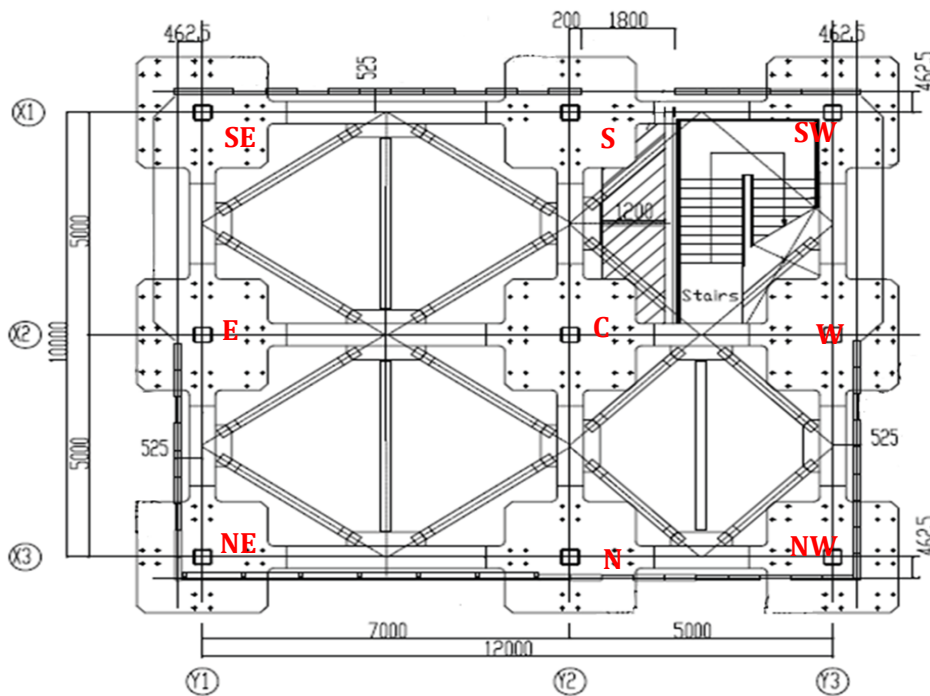


**Figure 3-5 Drawing of testbed base plan with column labels (N = North, E = East, S = South, W = West, C = Center)**

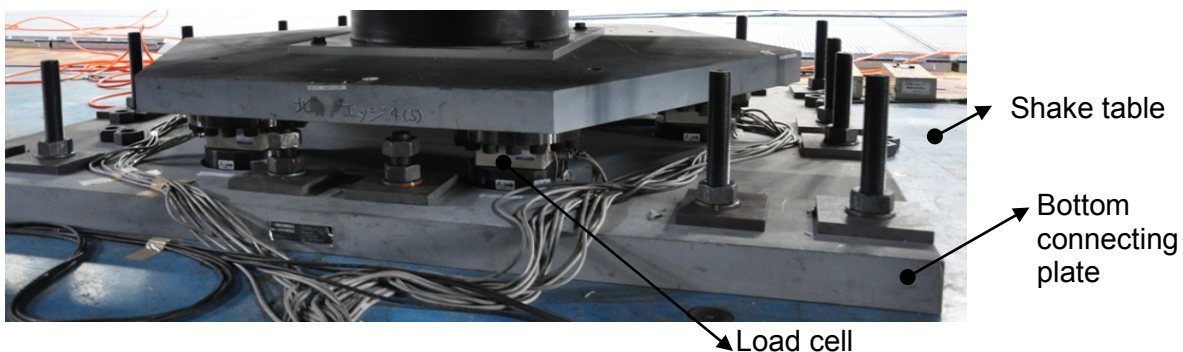
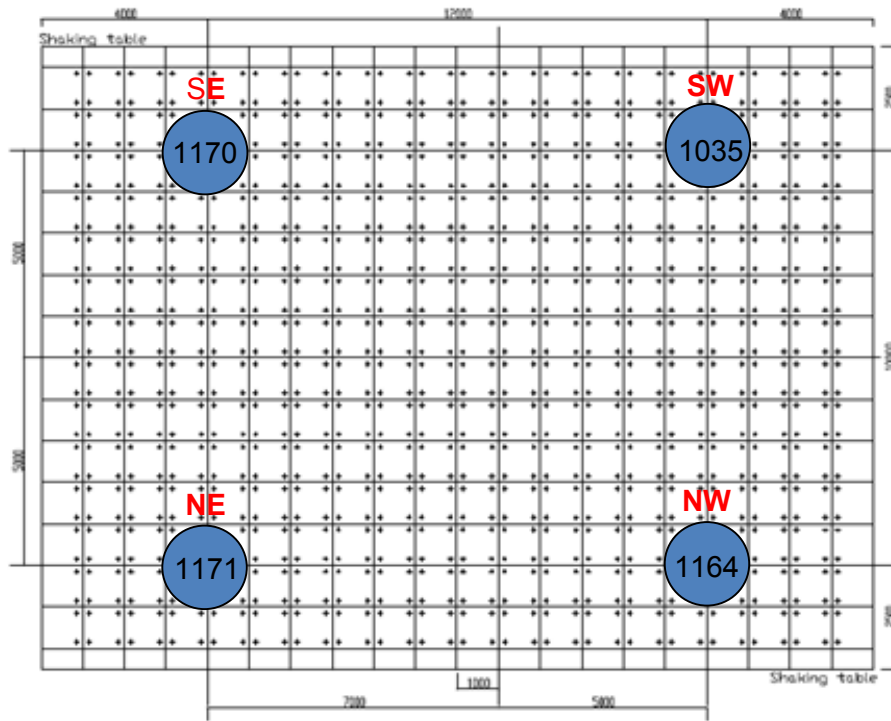


**Figure 3-6 Illustration of a connection assembly with triaxial load cells to measure bearing forces**

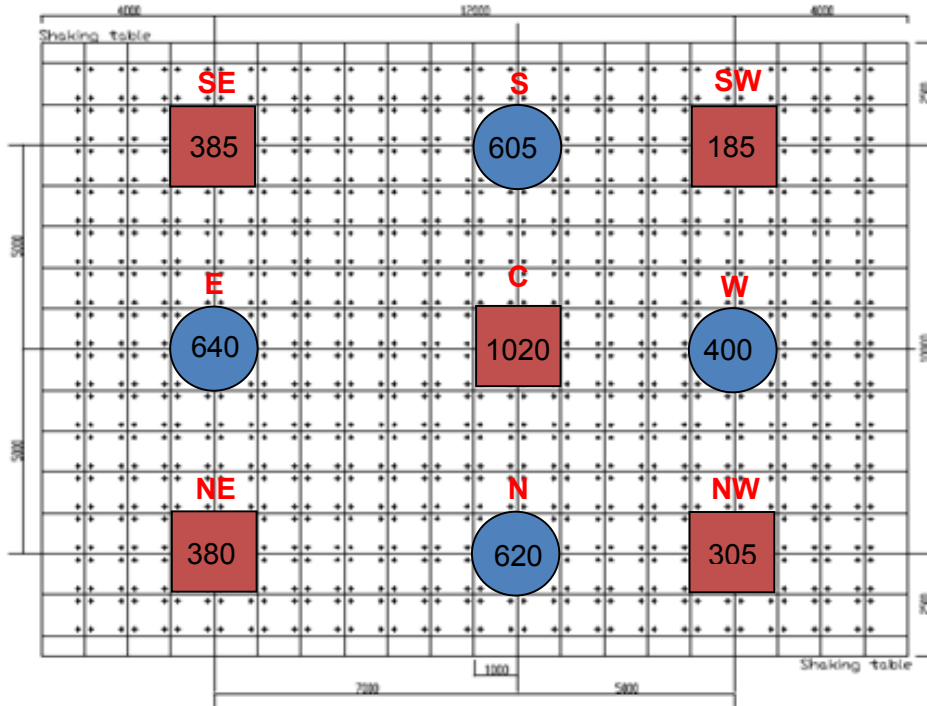
The target design parameters of the system could only be achieved with a small number of LR bearings. Thus, a design using four LR bearings was proposed. Given that LR bearings would not be placed beneath every column, two alternatives were considered. In Configuration Option 1, LR bearings were to be placed at the four corner columns (SE, SW, NE and NW) with no isolators beneath the remaining 5 columns (Figure 3-7(a)). In Configuration Option 2 (Figure 3-7(b)), LR bearings were to be placed beneath the four edge columns (S, E, W and N), and complementary flat sliders were to be placed beneath the remaining 5 columns, comprising a hybrid isolation system as introduced in Chapter 1. (Note that the selected CL bearings were one of several types of flat sliders that could have been used for this purpose.) The weight supported by each isolator based on tributary load calculation is indicated for each configuration option. Configuration Option 1 was preferred since the LR bearings were to carry the total

weight of the building, leading to a good test of the isolator stability, which was related to the test objectives. Configuration Option 1 was ultimately eliminated because the base diaphragm was not believed to be sufficiently stiff to suppress bouncing of the unsupported columns, and the expected loads on individual isolators exceeded the capacities of the designed connection assemblies (Figure 3-6).

Thus, Configuration Option 2 was selected. The LR bearings were located at the edge columns in Configuration Option 2 (Figure 3-7(b)) where they were expected to carry larger axial forces, which was desirable for a better test of the stability of the bearings at large displacements. A drawback to this arrangement was that it decreased the torsional resistance of the isolation system from Configuration Option 1. We note that a typical isolation solution for a large structure or nuclear power plant would not be affected by these constraints.



(a)



(b)

**Figure 3-7** (a) Configuration Option 1 with LR bearings beneath 4 corner columns, (b) Configuration Option 2 with LR bearings (circles) beneath 4 edge columns and flat sliders (squares) beneath remaining columns. The supported weights (in units of kN) at the isolators based on tributary loads are also indicated

### 3.2.3 Selection of the Bearing Dimensions

Based on the target period  $T_d = 3$  sec and a displacement demand of 60 cm (24 in) for a Q6 system and 50 cm (20 in) for a Q9 system (Figure 3-4(b)), three alternative isolators were proposed by Dynamic Isolation Systems, who provided the bearings for this project. The parameters for each alternative are shown in Figure 3-8, where  $D$  is the overall diameter,  $N$  is the number of rubber layers,  $P_{allow}$  is the allowable axial load at a lateral displacement of zero, and  $D_{max}$  is the maximum displacement capacity of the bearing at the anticipated axial load demand. All options assumed 0.6 cm (0.236 in) thick rubber layers and a shear modulus  $G = 0.41$  MPa (0.06 ksi). The post-yield stiffness  $K_d$  was calculated from

$$K_d = \frac{GA_b}{T_r} \quad (3.1)$$

where  $A_b$  is the area of the bearing, and  $T_r$  is the total thickness of rubber.  $P_{allow}$  was computed as the maximum axial load of the bearing in the undeformed configuration divided by a factor of 3, which is standard industry practice in the United States to provide a high margin of safety under gravity loads. Figure 3-9 illustrates the theoretical axial load capacity (computed as a minimum of buckling, elastomer limit or stress limit) for each proposed bearing design as a function of lateral isolator displacement (Constantinou et al. 2007). The peak axial load demand was estimated for the trial calculations as the peak dead weight supported by any isolator (based on tributary area) increased by a factor of 1/3 for overturning: 850 kN (191 kip). For the trial design the displacement capacity was estimated as the displacement at an axial load of 850 kN (191 kip) on the axial force-lateral displacement curve (Figure 3-9).

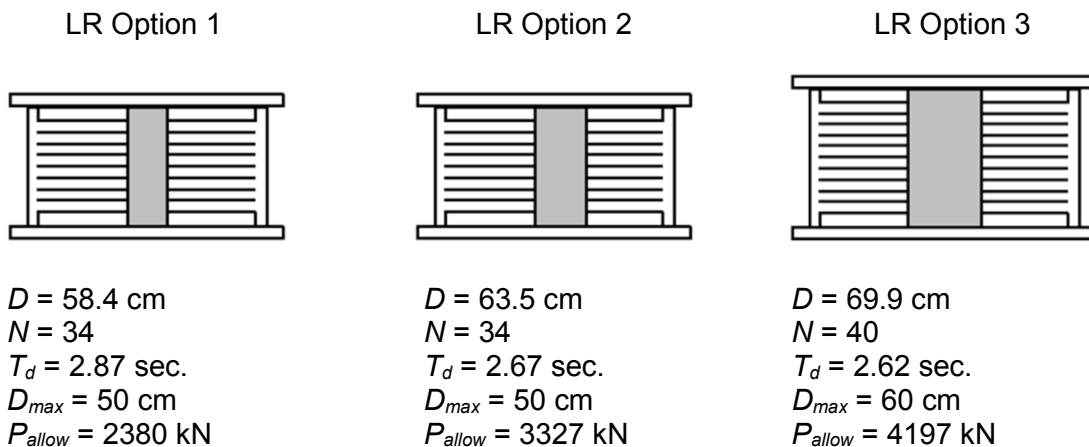


**Figure 3-8 Proposed design options for LR bearings**



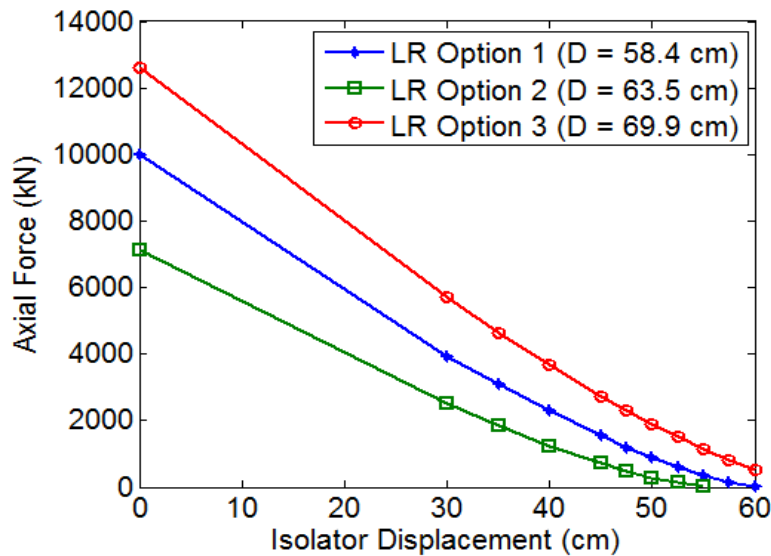


**Figure 3-9 Axial force capacity of proposed LR bearings versus lateral displacement**

LR Option 1 was the most flexible of the three ( $T_d = 2.87$  sec) and it nearly met the target period, but its displacement capacity was limited. The target displacement could only be achieved for Q9. LR Options 2 and 3 provided nearly the same effective period, but LR Option 3 had a substantially higher displacement capacity, which was achieved by increasing the diameter and height of the bearing. LR Option 3 was preferred to LR Option 2.

### 3.2.4 Selection of the Lead Plug Dimensions

Initially, lead plugs were sized for Q6, Q9 and an intermediate option Q7.5 ( $Q_d/W = 0.075$ ), where contributions to the zero-displacement force intercept were to be made by flat sliders with a friction coefficient  $\mu = 0.06$  and the lead plugs in the LR bearings. Recall that LR bearings were to be installed under the edge columns (columns S, E, W and N in Figure 3-7(b)) and flat sliders were to be installed under the remaining 5 columns. The sliders alone would have provided a yield force of approximately 120 kN (27 kips) based on the tributary weight and a coefficient of sliding friction of 0.06. The lead plugs were sized to provide the remainder, based on the following equation:

$$\begin{aligned}
 Q_{LR} &= \left( \frac{Q_d}{W} \right) W - Q_{Slider} \\
 &= N_{LR} \sigma_{y,LP} (\pi/4) D_{LP}^2
 \end{aligned}
 \tag{3.2}$$

where  $Q_{LR}$  and  $Q_{Slider}$  are the characteristic strength of the LR bearings and flat sliders, respectively.  $N_{LR}$  is the number of LR bearings (4),  $\sigma_{y,LP}$  is the dynamic yield strength of the lead plug and  $D_{LP}$  is the diameter of the lead plug. For this calculation,  $\sigma_{y,LP}$  was taken as 7.94 MPa (1.15 ksi), which is the value recommended by Dynamic Isolation Systems for their products. Table 3-1 lists the required diameter of the lead plug for Q6, Q7.5 and Q9, tabulated from Equation (3.2). The required diameter of the lead plug increased by about 33% (from 7.7 cm (3.0 in) to 10.6 cm (4.2 in)) from a Q6 to a Q9 design.

**Table 3-1 Required Diameter of the Lead Plug.**

Label	Yield strength $\sigma_{y,LP}$ in MPa (ksi)	Strength required Q in kN (kip)	Strength required per bearing in kN (kip)	Area lead plug in cm <sup>2</sup> (in <sup>2</sup> )	Diameter lead plug $D_{LP}$ in cm (in)
Q6	7.94 (1.15)	146.8 (33)	36.7 (8.25)	46.2 (7.2)	7.7 (3.0)
Q7.5	7.94 (1.15)	213.5 (48)	53.4 (12.00)	67.2 (10.4)	9.3 (3.6)
Q9	7.94 (1.15)	280.2 (63)	70.0 (15.75)	88.5 (13.7)	10.6 (4.2)

If the diameter of the lead plug is small, then the hysteresis may be pinched as seen in later figures. Importantly, if the plug is too small, little energy dissipation is achieved. If the diameter of the lead plug is too great, then the isolator may not provide sufficient confinement of the core during repeated cycling. The rule of thumb, based on years of experimentation and analysis is that the ratio of the diameter of the lead plug to the bonded diameter of the bearing is between 1/6 and 1/3. Table 3-2 presents the ratio of  $D_{LP}/D$  for the different combinations of bearing and lead plug sizes. For most combinations, the ratio did not meet the minimum of 1/6. The diameter ratios were lowest for LR Option 3, which provided the largest displacement capacity. Based on Table 3-2, the combination of LR Option 3 and Q9 almost met the minimum diameter ratio requirement, but the displacement demand would be lower for a Q9 design, such that the provided capacity of the bearing would not be fully utilized in the test. Thus, an alternative low friction slider was considered, as described in the next section.

**Table 3-2 Ratio of Lead Plug Diameter to Bearing Diameter ( $D_{LP}/D$ ).**

Bearing Diameter	Q6 ( $D_{LP} = 7.67$ cm)	Q7.5 ( $D_{LP} = 9.25$ cm)	Q9 ( $D_{LP} = 10.62$ cm)
LR Option 1 ( $D = 58.4$ cm)	0.13	0.16	0.18
LR Option 2 ( $D = 63.5$ cm)	0.12	0.15	0.17
LR Option 3 ( $D = 69.9$ cm)	0.11	0.13	0.15

### 3.2.5 Cross Linear Bearings

The cross-linear (CL) bearing manufactured by THK allows nearly resistance-free linear motion. The LM Guide technology allows free rolling motion of a weight supporting part on a rail, where the part and the rail are internally separated by recirculating ball bearings. The CL bearing uses two orthogonally mounted LM Guide assemblies (Figure 3-11). The CL bearing can be combined with traditional isolation devices to support the weight of the building without increasing the total base shear of the isolation system. The coefficient of friction of the sliders varies from 0.48-0.62%, leading to a negligible contribution to the base shear for a reasonable value of the supported weight.

Making use of the CL bearings means that  $Q_{Slider}$  in Equation (3.2) can be taken to zero; thus allowing the lead plugs to provide the yield strength in entirety. Opting for a Q6 design, the required diameter of the lead plug was 10.16 cm (4.0 in), which provided the estimated total yield strength of 267 kN (60 kip) or 66.75 kN (15 kip) per bearing.

Besides its low friction sliding capability, the CL bearing provides significant resistance to tensile forces. A more careful evaluation of overturning on the hybrid isolation system suggested that the LR bearings alone would be unable to resist the tensile demands. The tensile force demands in the system at a displacement of 60 cm (24 in) were estimated as follows. First, the total base shear  $V_b$  in the isolation system was estimated as:



**Figure 3-10 Photo of installed CL bearing illustrating orthogonal LM guides assemblies on top and bottom**

$$\begin{aligned}
 V_b &= N_{LR}(Q_d + K_d D_{\max}) \\
 &= 4(66.75 \text{ kN} + 0.65 \text{ kN/mm} \cdot 600 \text{ mm}) \\
 &= 1827 \text{ kN} (411 \text{ kip})
 \end{aligned}
 \tag{3.3}$$

The post-yield stiffness  $K_d$  and strength  $Q_d$  assumed LR Option 3 with a lead plug diameter  $D_{LP} = 10.16 \text{ cm}$  (4 in). The base shear was assumed to act at 9 m, which is about half the height of the building (Figure 3-11). The overturning moment generated by the base shear was balanced by an overturning force  $F_{OT}$  times the shortest base dimension of the building (10 m). Thus,  $F_{OT}$  was calculated as 9/10 of the base shear  $V_b$  ( $F_{OT} = 1644 \text{ kN}$  or 370 kip). The overturning demand was assumed to be carried by tension on the more lightly loaded South side of the building (Figure 3-7(b)). The total tension  $T$  carried by the three isolators (SE, S and SW) was computed as:

$$\begin{aligned}
 T &= F_{OT} - \sum_i W_i \\
 &= 1644 \text{ kN} - (385+605+185)\text{kN} \\
 &= 469 \text{ kN} (105 \text{ kip})
 \end{aligned}
 \tag{3.4}$$

where  $W_i$  is the tributary weight supported by the  $i^{\text{th}}$  isolator, summed over the SE, S and SW isolators. Without CL bearings, the 469 kN (105 kip) of tension would be carried by a single LR bearing. Since CL bearings were utilized, the CL bearings were expected to carry the

overturning induced tension and each CL would be subjected to about 235 kN (53 kip) tension. In reality, the tensile demands may not be equally balanced by the CL bearings, since the SW bearing carries significantly less weight than the SE bearing according to tributary area (Figure 3-7(b)).

Equation (3.4) suggested that peak compressive force on a given side of the building could increase by a factor of 2 or more due to overturning. The initial estimate of axial force demand (850 kN or 191 kip) used to estimate the displacement capacity of the LR bearings would then be unconservative. However, the CL bearings were much stiffer in compression than the LR bearings, and the vertical movements of LR and CL bearings were coupled together by the rigidity of the base diaphragm. This base diaphragm constraint was expected to prevent individual LR bearings from shortening or buckling, thus enhancing the overall stability of the isolation system such that the projected axial force limits would not be relevant. The interaction and load transfer between LR bearings and CL bearings is a unique aspect of this isolation system, which is evaluated extensively later in this report. The suitability of the tested hybrid system for nuclear facilities is also evaluated based on a synthesis of the experimental data.

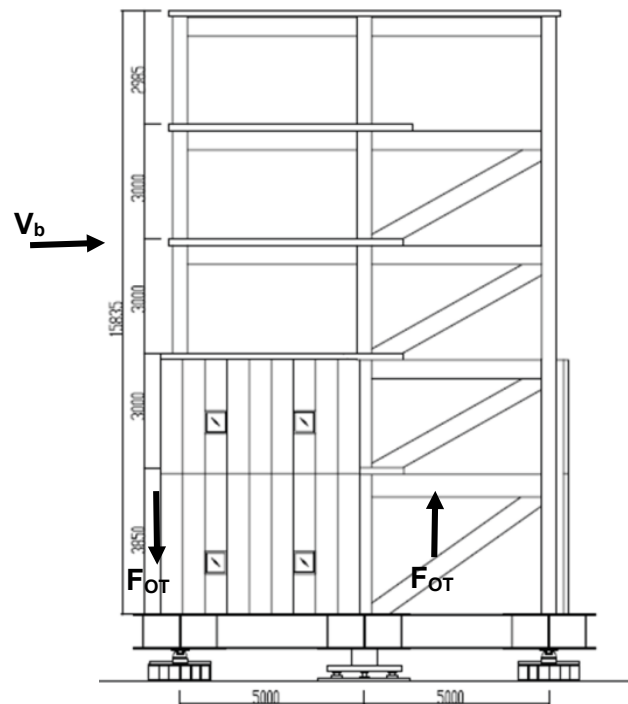


**Figure 3-11 Total base shear ( $V_b$ ) and overturning forces ( $F_{OT}$ ) acting on an elevation view of the testbed building**

### 3.2.6 Summary of Design Properties

The final hybrid LR isolation system design included four LR bearings and five CL bearings. The configuration of the bearings (LR bearings at edge columns and CL bearings at center and corner columns) is shown in Figure 3-12, along with photographs of the devices taken prior to installation. LR Option 3 was used for the LR ( $D = 69.9$  cm or 27.5 in, 40 rubber layers, post yield stiffness  $K_d = 6.5$  kN/cm or 3.71 kip/in and  $T_d = 2.6$  sec) and the lead plug was sized for Q6 ( $D_{LP} = 10.16$  cm or 4 in). The estimated displacement capacity of the LR bearings based on a stability limit was 60 cm (23.6 in). The CL bearings were designed with a displacement capacity of 60 cm (23.6 in) imposed by a low force capacity stopper at the end of travel in each perpendicular direction that was not intended to be reached.

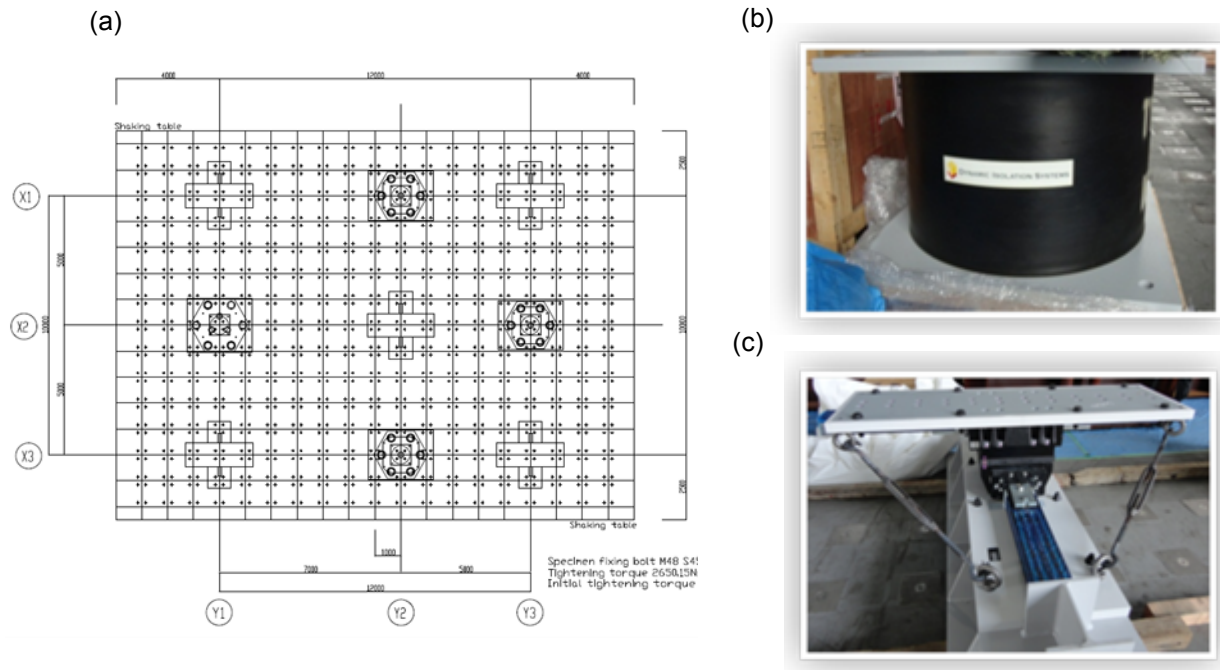


**Figure 3-12 (a) Final plan drawing of the hybrid LR isolation system, (b) photo of LR bearing, and (c) photo of CL bearing**

The dimensions and target stiffness and strength parameters of the LR bearings are listed in Table 3-3. All parameters were provided by the manufacturers. Several of the parameters are modeling parameters recommended for a bilinear representation of the force-deformation relation, as shown in Figure 3-3. The bearings were tested by Dynamic Isolation Systems prior to shipment to E-Defense. Force-deformation characterization was generated for cycles of amplitude 30 cm (11.8 in), 50 cm (19.7 in) and 65 cm (25.6 in) at different axial loads. Pseudo-static tests were performed and dynamic material properties were not provided. The results of this characterization are reported in Chapter 7.

The main properties of the CL bearings are listed in Table 3-4. The vertical stiffness of the CL bearings in compression and tension was provided by Aseismic Devices Co. Design drawings and specification sheets for both LR and CL bearings provided by the manufacturers are included in Appendix B.

**Table 3-3 Lead Rubber Bearing Properties.**

<b>Bearing Dimensions</b>		
Overall Diameter, $D$	=	69.85 cm (27.5 in)
Number of Rubber Layers, $N$	=	40
Lead Diameter, $D_p$	=	10.16 cm (4.0 in)
Shim Thickness, $t_s$	=	0.3 cm (0.1196 in)
Layer Thickness, $t_r$	=	0.6 cm (0.236 in)
Side Cover Rubber Thickness, $c_s$	=	1.27 cm (0.5 in)
Top Mounting Plate Thickness, $t_{tp}$	=	2.54 cm (1in)
Bottom Mounting Plate Thickness, $t_{bp}$	=	2.54 cm (1in)
Internal Plate Thickness, $t_{ip}$	=	2.54 cm (1in)
<b>Isolator Properties</b>		
Effective Period, $T_{eff}$	=	2.27 sec
Post Yield Period, $T_d$	=	2.62 sec
Design Displacement, $D_D$	=	30 cm
Maximum Displacement, $D_{TM}$	=	60 cm
Post-Yield Stiffness, $K_d$	=	6.5 kN/cm (3.7 kip/in)
Initial Stiffness, $K_1$	=	65 kN/cm (37 kip/in)
Characteristic Strength, $Q_d$	=	65.7 kN (14.8 kip)
Yield Force, $F_y$	=	73 kN (16.4 kip)
Yield Displacement $D_y$	=	1.128 cm (0.44 in)
Vertical Stiffness, $K_v$	=	15000 kN/cm (8566 kip/in)
Shear Modulus, $G$	=	0.414 MPa (0.06 ksi)
Rubber Ultimate Strain (at-break), $\epsilon_u$	=	5.5

**Table 3-4 Cross Linear Bearing Properties.**

<b>Isolator Properties</b>		
Coefficient of friction, $\mu$	=	0.48%-0.62%
Yield displacement, $D_y$	=	0.01 cm
Compressive Vertical Stiffness, $K_{vc}$	=	34710 kN/cm (19821 kip/in)
Tension Vertical Stiffness, $K_{vt}$	=	2450 kN/cm (1399 kip/in)

### 3.3 Selection and Scaling of Ground Motions

The test program for the hybrid LR isolation system was developed based on the recommendations and interests of several different parties, including the research sponsor, the Advisory Board members, the manufacturers, the project team and Japanese collaborators. Two days of testing were planned for the hybrid LR isolation system configuration, where 7 independent trials (in extreme cases 8) could be executed each day.

Demonstrating the stable performance of elastomeric isolation systems in design or beyond design basis earthquakes is an important step to enable the use of base isolation for safety related nuclear structures. The seismic hazard at the Vogtle site is well known to the nuclear engineering community, and thus a record representing the seismic hazard at the Vogtle site was prioritized for the test program. A Vogtle record was sought from among the set of 30 maximum-minimum spectrum compatible ground motion pairs developed by Huang et al. (2009) that would produce a peak LR bearing displacement demand of about 60 cm (23.6 in) when scaled to 150%, in accordance with the beyond design basis target. Extensive pre-test analysis

was conducted to identify the best Vogtle record for this purpose. While the isolation system was designed specifically for beyond design basis motions at the Vogtle site, its capabilities also permitted the system to be subjected to a Diablo Canyon record, representative of a WUS rock site, scaled to about 100%. The Diablo Canyon record was selected from a set of 30 maximum-minimum spectrum compatible ground motion pairs developed by Huang et al. (2009) using a procedure similar to the one described for the Vogtle site. The sponsor requested that the maximum displacement demands on the LR bearings be imposed in as few trials as possible so that the bearings were in their virgin state. The performance of bearings made from natural rubber has generally been found to be stable after repeated cyclic testing, although the hysteresis of LR bearings can be affected by heating of the lead plug and strain hardening induced by cumulative travel effects (Constantinou et al. 2007). An additional objective evolved from these considerations, which was to repeat one of the early trials at the end of the test program to evaluate the consistency of the LR bearing response.

Once the sponsor objectives had been met, other objectives could be entertained. For example, the project team aimed to identify a service level, design level, and maximum considered earthquake (MCE) level motion to be replicated on all three building configurations (TP isolation system, hybrid LR isolation system, and fixed base). The Japanese collaborators aimed to identify a strong Japanese motion that could be replicated on all three building configurations. Dynamic Isolation Systems requested a sine wave characterization test to be repeated at the beginning and the end of the test program.

The test facility imposed additional constraints on the test program based on safety considerations, which are described next.

### **3.3.1 Imposed Limitations for Safety**

The following limitations related to target demands and test sequence were imposed.

1. The target displacement demand of the LR bearings was limited to 55 cm (21.6 in). In initial discussions, Japanese collaborators imposed a displacement limit equal to the design displacement of 30 cm (11.8 in), which was comparable to displacements permitted in previous tests at E-Defense. A compromise was reached after a) it was demonstrated that shear rupture was not expected before displacements of 80-90 cm (31.5-35.4 in), b) it was demonstrated that the CL bearings would stabilize the entire isolation system, and c) Dynamic Isolation Systems agreed to in-house characterization tests of the LR bearings to displacements of 65 cm (25.6 in) prior to shipment of the bearings to Japan.
2. The target displacement demand of the CL bearings was limited to about 40 cm (15.7 in) in each of the x and y perpendicular directions, which is a factor of safety of about 1.5 relative to the displacement limit of the CL bearings. This agreement was reached after Aseismic Devices Co. agreed to add a safety stop at the end of travel in each direction. The safety stop was not intended to stop the momentum of the building if a high impact collision of the sliders with the safety stop were to occur.
3. The largest displacement was to be approached over a series of 3 or 4 incremented trials that gradually increased the intensity of the earthquake shaking. This incremental approach was intended to validate the analytical model and allow adjustment to the intensity of the largest imposed record as necessary. This constraint conflicted with the objective to impose the largest intensity record early in the test sequence, but could not be avoided.

### 3.3.2 Vogtle and Diablo Canyon Motions

Substantial effort was expended to identify the best Vogtle record and best Diablo Canyon record for the testing program. Six Vogtle records were considered; these records were identified by evaluating the peak bidirectional displacement demand of the SDOF system to all 30 pairs of Vogtle records scaled by 150%, and selecting those that predicted a peak displacement closest to 55 cm (21.6 in). Displacement traces (x vs y-direction displacement) and displacement histories for the 6 records that were considered are shown in Figure 3-13 and 3-14. Preference was given to the records that included multiple cycles of large displacement (Figure 3-14), and followed a partially circular trace rather than a linear trace in a given direction (Figure 3-13). Vogtle #13 and Vogtle #9 were considered to meet these criteria better than the other records.

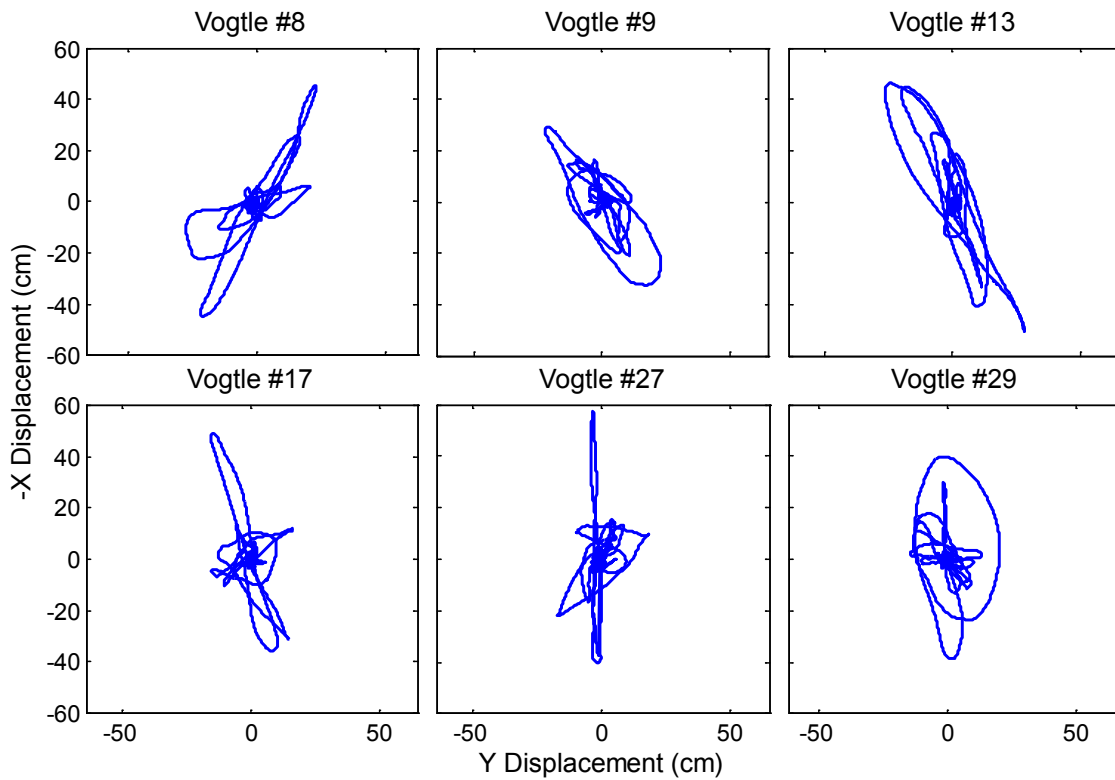


**Figure 3-13** Calculated displacement trace of the isolation system for 6 Vogtle motions by SDOF analysis



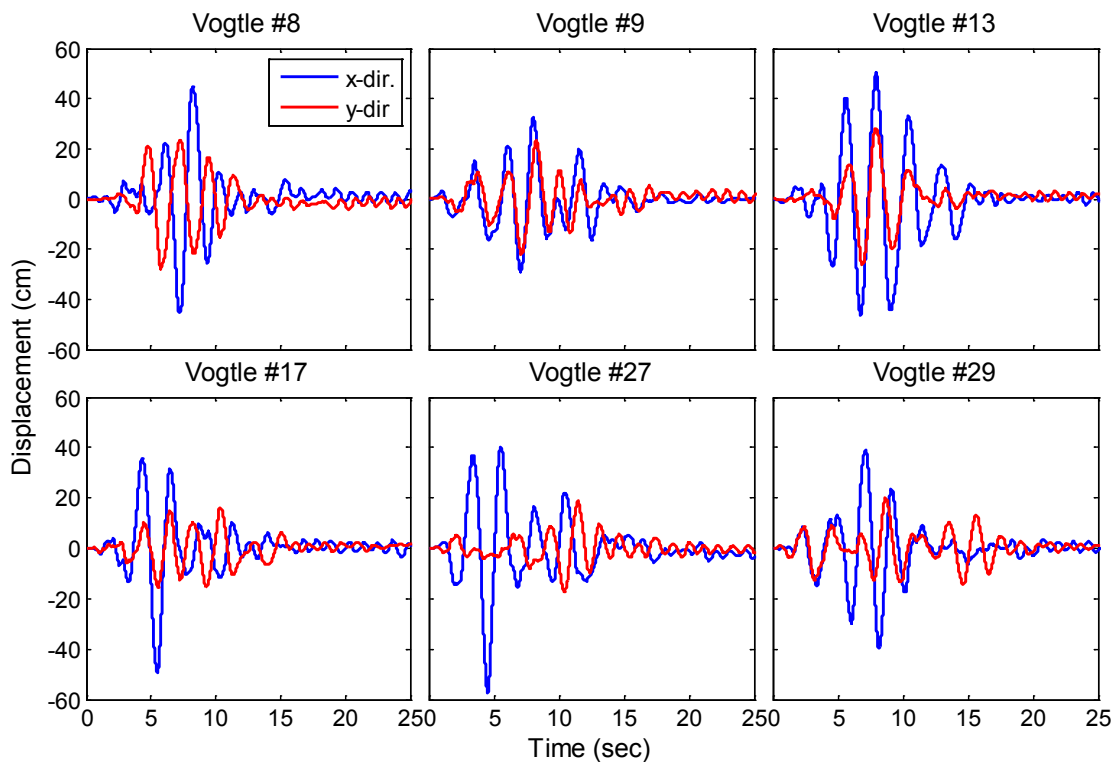


**Figure 3-14** Calculated displacement histories of the isolation system in x and y-directions for 6 Vogtle motions by SDOF analysis

Next, the records were applied to the isolated building model that was developed in OpenSees (described in Chapter 8) to obtain a more accurate assessment of the displacement and force demands. In general, the peak displacement demands of the isolators in the building model were somewhat larger than in the SDOF model. Upon examining the data, two sources of discrepancy were identified. First, the building model did not contain viscous damping alongside the isolation system. Displacements in the SDOF model were re-evaluated after removing this damping (2% of critical calibrated to the isolator post-yield stiffness), and they increased substantially, which indicated that the response was sensitive to the seemingly small additional damping. Although some viscous energy dissipation may be present, the damping was removed from the SDOF model to err on the side of conservatism.

Second, substantial rotational demands at the base level were predicted by the analysis of the building model, which caused amplification of the displacement on one side or corner of the building compared to the other. To illustrate this, the displacement traces of each bearing are presented in Figure 3-15. Due to the rotation, the peak displacement in one bearing was predicted to be 54 cm (21.3 in), while the peak displacement predicted in the opposite corner was only 46 cm (18.1 in). The project team was skeptical about the significant amount of torsion predicted by the analysis, and experimented with the modeling assumptions to develop confidence in the prediction and possibly identify a cause. Several alternative assumptions were considered, including bearing placement at the corners rather than on the edges, and accounting for the rotational stiffness of both the LR and CL bearings. None of the modifications significantly altered the amplitude of the rotational demands, and the experimental data later validated the torsion predicted by numerical simulation (see Chapters 5 and 9). The rotational demands observed in the isolation system resulted from limitations on the number and placement of LR bearings for the testbed structure. In a large building or safety related nuclear structure with hundreds of isolators, isolation system asymmetries and rotational demands could be eliminated or minimized by strategic placement of bearings with and without lead plugs.

With the exception of Vogtle #13, the peak displacements predicted by the building model exceeded those predicted by the SDOF model without viscous damping. Thus, Vogtle #13 was selected since the displacement predicted by the building model was closest to that predicted by SDOF model for the desired scale factor of 150%.

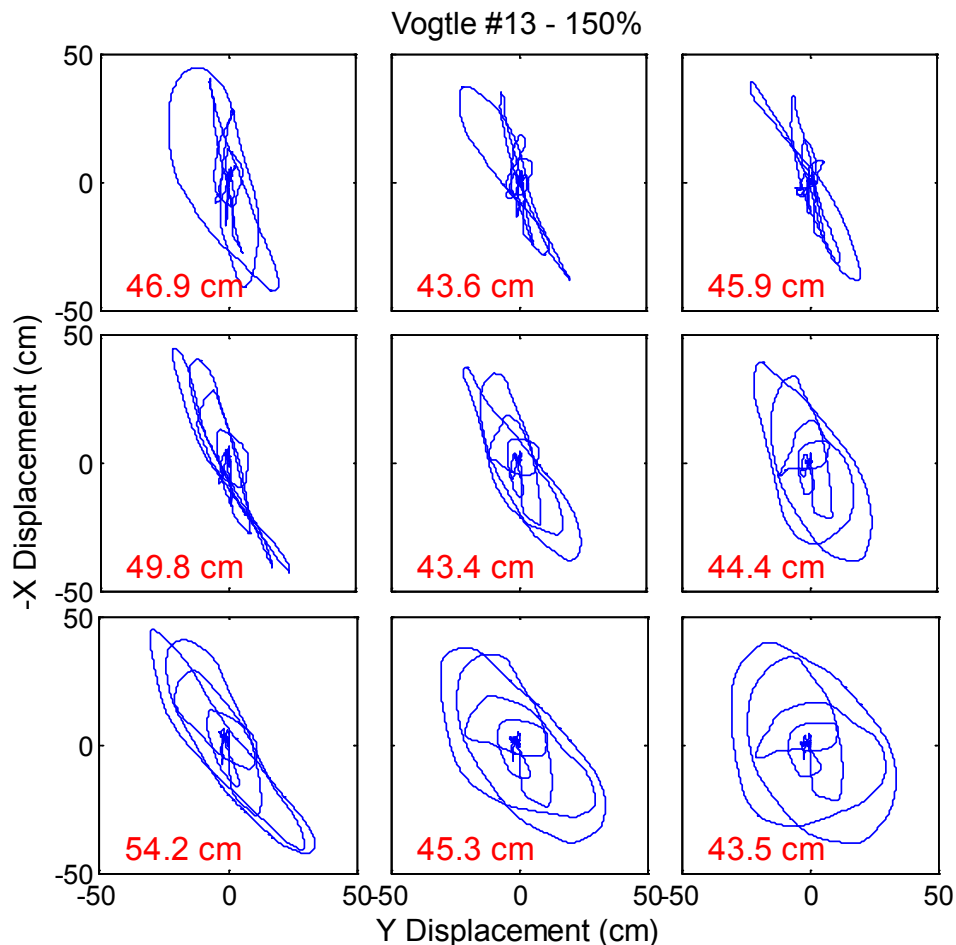


**Figure 3-15 Predicted displacement trace of each isolator for the OpenSees building model subjected to 150% Vogtle #13**

While the LR bearings could be subjected to displacements of up to 55 cm (21.7 in), the CL bearings were not permitted to exceed displacements of 40 cm (15.7 in) in the x and y-directions. Thus, we proposed to rotate the components of the input ground motion such that the peak displacement demand occurred at approximately 45 degrees, which would simultaneously minimize the demands in x and y-directions and maximize the vector displacement. To determine the rotation of the input motion, the building model was analyzed to the Vogtle #13 input excitation rotated at increments of 11.25 deg. Thus, rotated inputs at 0, 11.25, 22.5, 37.75, and 45 degree were considered. Based on this analysis (summarized in Table 3-5), a rotation angle of 11.25 degrees was selected. The anticipated peak displacement demand in any LR bearing for Vogtle #13 rotated by 11.25 degrees and scaled to 150% was 49 cm (19 in), while the peak displacement in any CL bearing in the x or y direction was 40 cm (16 in). Adjustments to the scale factors were made on the day of testing, and the actual peak scale factor applied was 175%. The complete final schedule of simulations actually conducted is summarized in Chapter 4.

**Table 3-5 Predicted x, y and Vector Peak Displacement in the different Isolator for the Building Model Subjected to 150% Vogtle #13 Record, with Rotated Horizontal Components of Input Motion.**

Bearing	Rotation Angle (degrees)	X - Peak Displacement (cm)	Y - Peak Displacement (cm)	Vector Peak Displacement (cm)
Lead Rubber	0	34	45	50
	11.25	39	40	49
	22.5	44	33	49
	37.75	47	27	50
	45	50	21	51
Cross Linear	0	34	45	54
	11.25	39	40	55
	22.5	44	33	54
	37.75	47	27	53
	45	50	21	52

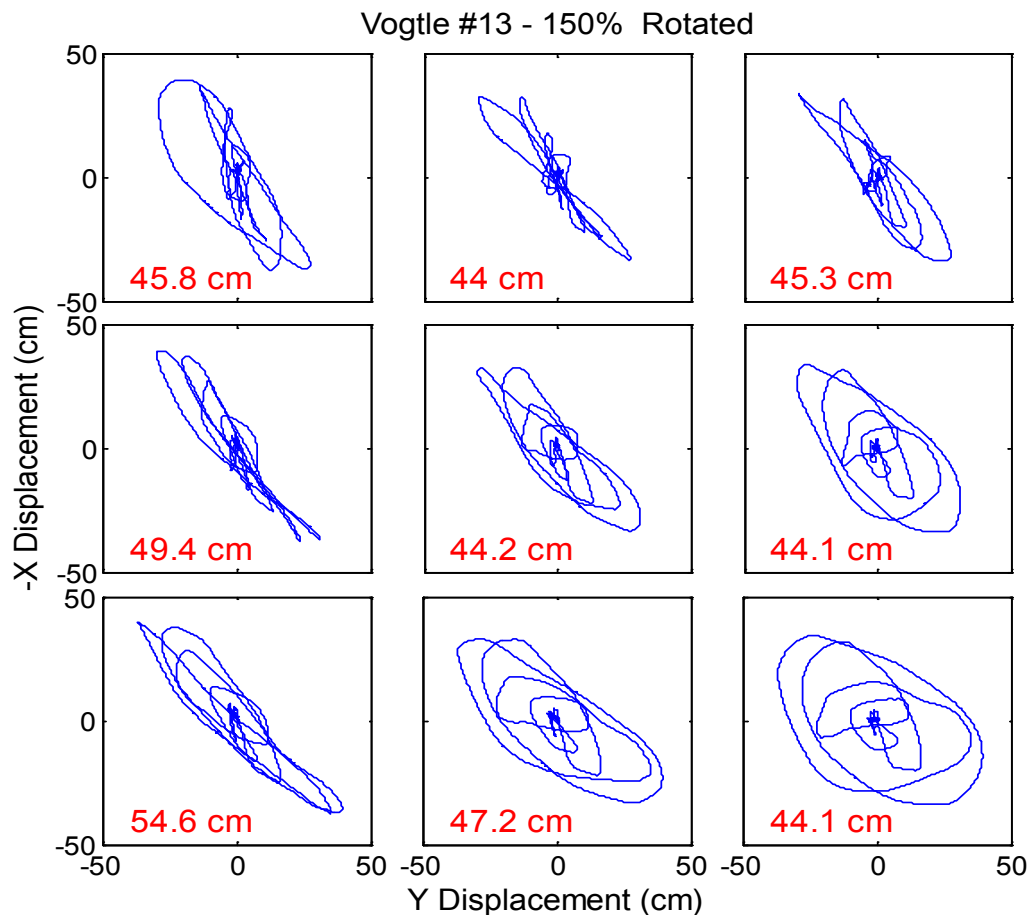


**Figure 3-16 Predicted displacement trace of each isolator for the OpenSees building model subjected to 150% Vogtle #13, with input ground excitation components rotated by 11.25 degrees**

A similar process was used to select the input motion to represent the design ground shaking at the Diablo Canyon site, with a target scale factor of 100%. The Diablo Canyon #15 record was selected for the test program. The predicted displacement trace of the isolators for Diablo Canyon #15 scaled to 100% is shown in Figure 3-17. Rotation was not required for this input motion since the vector displacement was approximately maximized without rotation. The actual scale factor applied to Diablo Canyon #15 during testing was 95%.

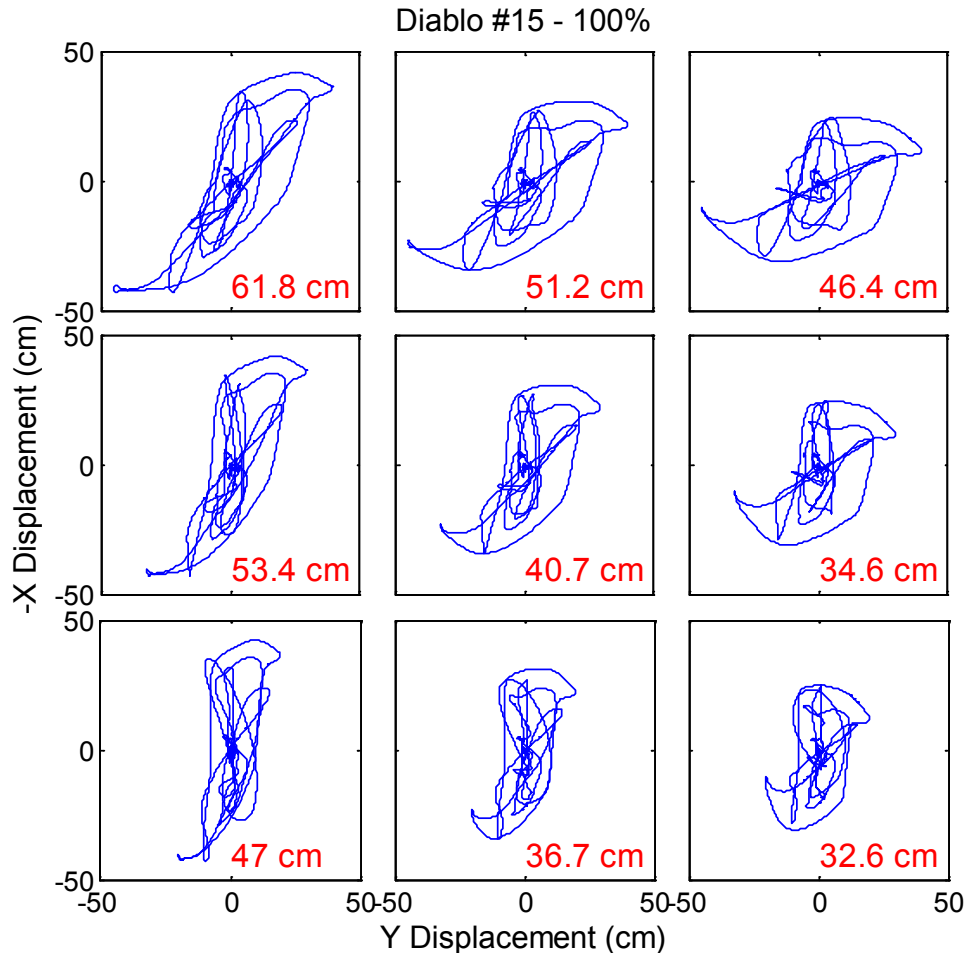


**Figure 3-17 Predicted displacement trace of each isolator for the OpenSees building model subjected to 100% Diablo Canyon #15**

### 3.3.3 Remainder of the Test Program

As mentioned previously, the objectives of the sponsor were prioritized in the planning of the test program. These objectives were to simulate the response of LR bearings to motions representing the seismicity at a potential nuclear site, and impose design basis and extended design basis demands on the system. Once these objectives had been satisfied, objectives of other interested parties could be entertained.

For comparative purposes, the project team (United States and Japan collaborators) proposed to include in the test program 3 ground motions, one each representing a service level, design level and MCE as defined by the United States building code (ASCE 2010), that would be commonly applied to each of the three building configurations. The assumed seismic hazard associated with these events is presented in Dao (2012). In addition, Japan side collaborators

requested that a large motion recorded during a Japan earthquake be commonly applied to each of the three building configurations. The preliminary selections are shown in Table 3-6. During the testing of the TP isolation configuration, which was chronologically first in the sequence, the response of the building was particularly affected by the strong vertical excitation of the 1994 Northridge recorded at Rinaldi Receiving Station. This excitation was not part of the planned test program for the hybrid LR isolation or fixed-base configurations. However, late modifications to the planned test program were accommodated to repeat this excitation as a 3D excitation and an XY excitation (omitting the vertical component) in each building configuration to better comprehend the response of isolated and non-isolated buildings to strong vertical excitation.

In the end, not all objectives were met due to safety considerations (see Table 3-6) and compromises were made. The imposed safety limits were analytically predicted isolator displacements  $\leq 55$  cm for the hybrid LR isolation system and analytically predicted structural drift limits  $\leq 1.2\%$  for all configurations. A suitable MCE level earthquake that met the safety limitations for the hybrid LR isolated and fixed-base configurations could not be identified, and the MCE comparison was removed from the test program. The selected design event (El Centro) was never applied to the fixed-base configuration, and the selected Japan motion (Iwanuma) as well as Rinaldi were applied to the fixed-base building at reduced scale factors in the horizontal direction.

**Table 3-6 Common Earthquake Records Considered for Three Test Configurations.**

Objective	Earthquake Record	Scale Factor	Simulation Considered Safe?		
			TP Config.	Hybrid LR Config.	Fixed-Base Config.
Service Earthquake	1987 Superstition Hills, Westmorland Sta. (3D)	80%	Yes	Yes	Yes
Design Earthquake	1940 Imperial Valley, El Centro Sta. (3D)	130%	Yes	Yes	Safety questions
MCE Earthquake	1994 Northridge, Sylmar OR 1995 Kobe, Takatori (3D)	100%	Yes	No, safety imposed displacement limit	No, safety imposed story drift limit
Japan Earthquake	2011 Tohoku Earthquake, Iwanuma (XY)	100%	Yes	Yes	No, Scaled to 70%
XY vs 3D Input Comparison	1994 Northridge, Rinaldi Rec. Sta. (XY)	88%	Yes	Yes	No, Scaled to 35%
XY vs 3D Input Comparison	1994 Northridge, Rinaldi Rec. Sta. (3D)	88%	Yes	Yes	No, Scaled to 35% (88% in vertical)



## 4. EXPERIMENTAL PROGRAM

### 4.1 Design of Connection Assembly

A plan was developed and executed for securely connecting the isolation devices (both LR bearings and CL bearings) to the structure and to the earthquake simulator. As described in Chapter 3, the connection design for the hybrid LR isolation system made use of connection assemblies, each consisting of a layer of load cells sandwiched between a square or rectangular base plate and a hexagonal shaped top plate, that were designed for the TP isolation configuration. Details of the assembly design calculations and supporting finite element analysis were described in Dao (2012). The assemblies were used at the N, S, E and W column locations to measure the forces in the LR bearings.

The connection assemblies were not used at CL bearing locations, for several reasons. First, the axial force demands on the CL bearings were expected to be high since the CL bearings would carry all overturning induced axial forces. Second, Aseismic Design Corporation, the provider of the CL bearings, calculated that the supporting plates of the connection assembly were too flexible to prevent rotation (bending) of the bearings about the horizontal axes, and thus ensure their proper function. Although very small, the contribution of the CL bearings to the total base shear could not be measured.

Three distinctly configured load cell connection assemblies had been devised for the TP isolation configuration tests according to expected tributary weight carried by the bearings at different plan locations: one for the center column, one for the edge columns, and one for the corner columns. For the hybrid LR isolation system, we used the edge connection assembly for three of the four bearings. However, the center connection assembly was substituted at the East edge location, because erratic measurements were observed in the assembly used at that location in the prior TP configuration tests.

The plan drawings of the two connection assemblies utilized for the hybrid LR configuration are shown in Figure 4-1, and a photograph of a constructed assembly is shown in Figure 4-2. The center column assembly placed 3 Type A load cells on a circle 35 cm (13.8 in) from the center of both plates and 6 Type B load cells on a circle 90 cm (35.4 in) from the center of both plates, both with equal angular spacing. The edge column assemblies placed 1 Type A load cell at the center of both plates, and 6 Type B load cells on a circle 75 cm (29.5 in) from the center of both plates with equal angular spacing. The Type A and Type B load cells differed in their capacities as listed in Table 4-1. Drawings of the load cells are shown in Figure 4-3, which indicate the bolt pattern for the top and bottom rings and the elevation. The connection plates were produced by milling a steel plate with thickness = 10.2 cm (4 in) down to 9.5 cm (3.7 in), which leveled the surface. Because the two types of load cells differed in height, the thickness of each bottom connection plate was milled down to 9.1 cm (3.6 in) at Type A locations and 7.6 cm (3.0 in) at Type B locations (see Figure 4-4). The load cells were installed upside down between the top and bottom connection plates. The complete set of drawings for connection the load cell assemblies, LR bearings and testbed building to the simulator platform are given in Appendix C.

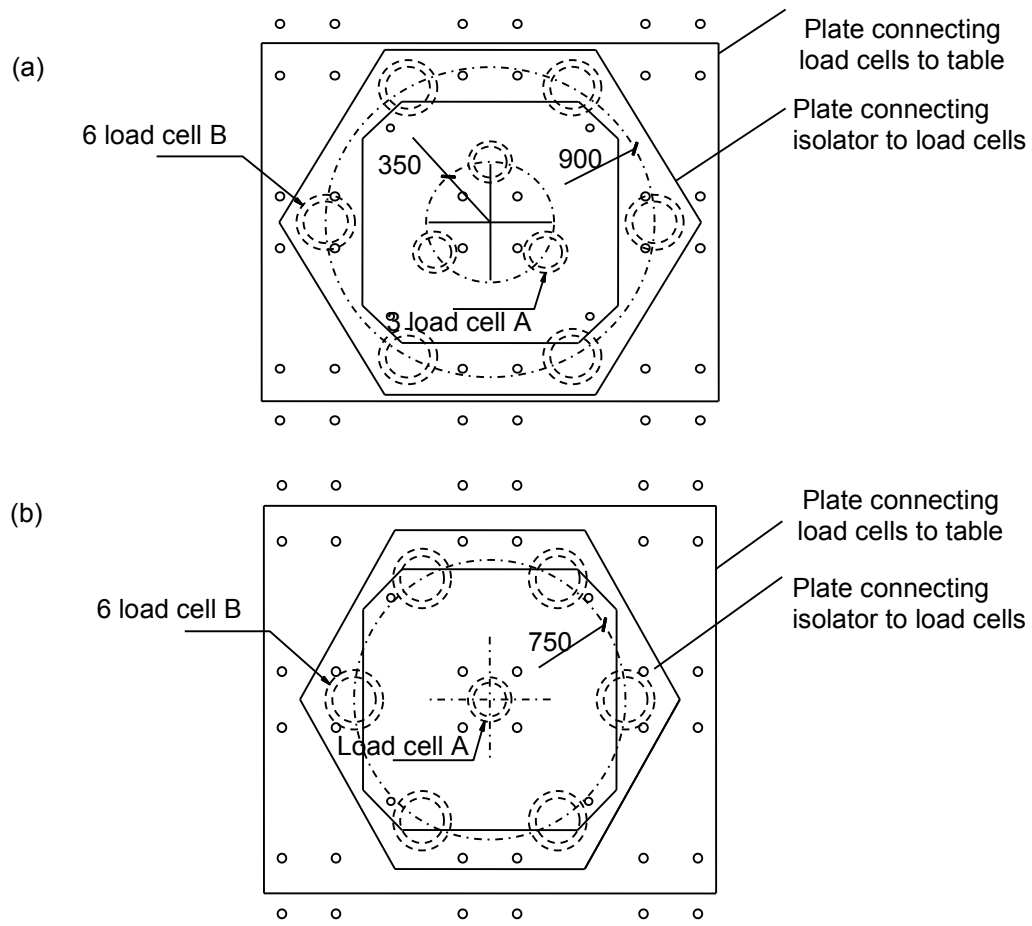


**Figure 4-1 Load cell connection assemblies used for: (a) East bearing and (b) North, South and West bearings**

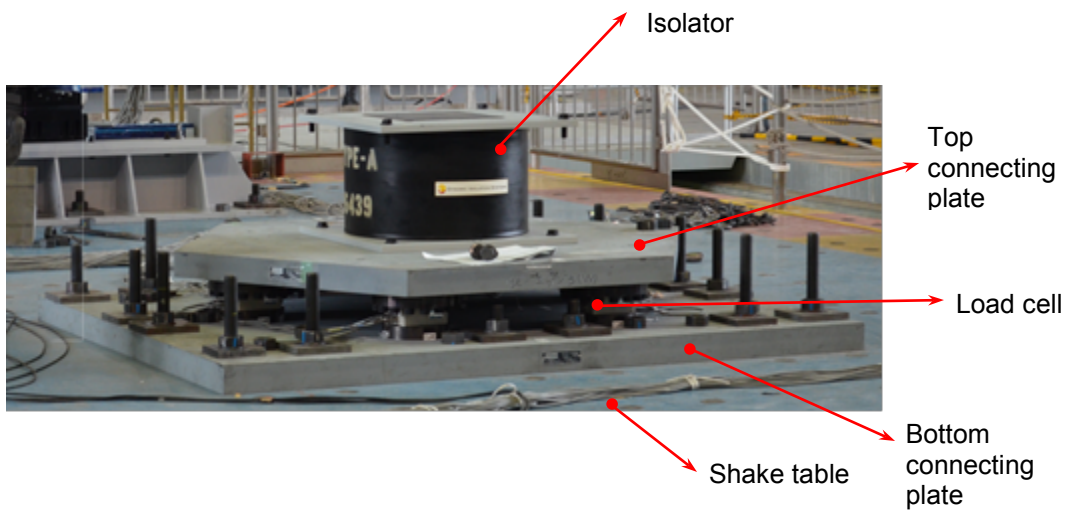


**Figure 4-2 Connection assembly**



**Table 4-1 Properties of load cells.**

Type	Number (units)	Height (cm)	Vertical capacity (kN)	Horizontal capacity (kN)	Vertical stiffness (kN/cm)	Horizontal stiffness (kN/cm)
A	44	18	400	250	85000	24000
B	32	19.5	700	400	140000	35000

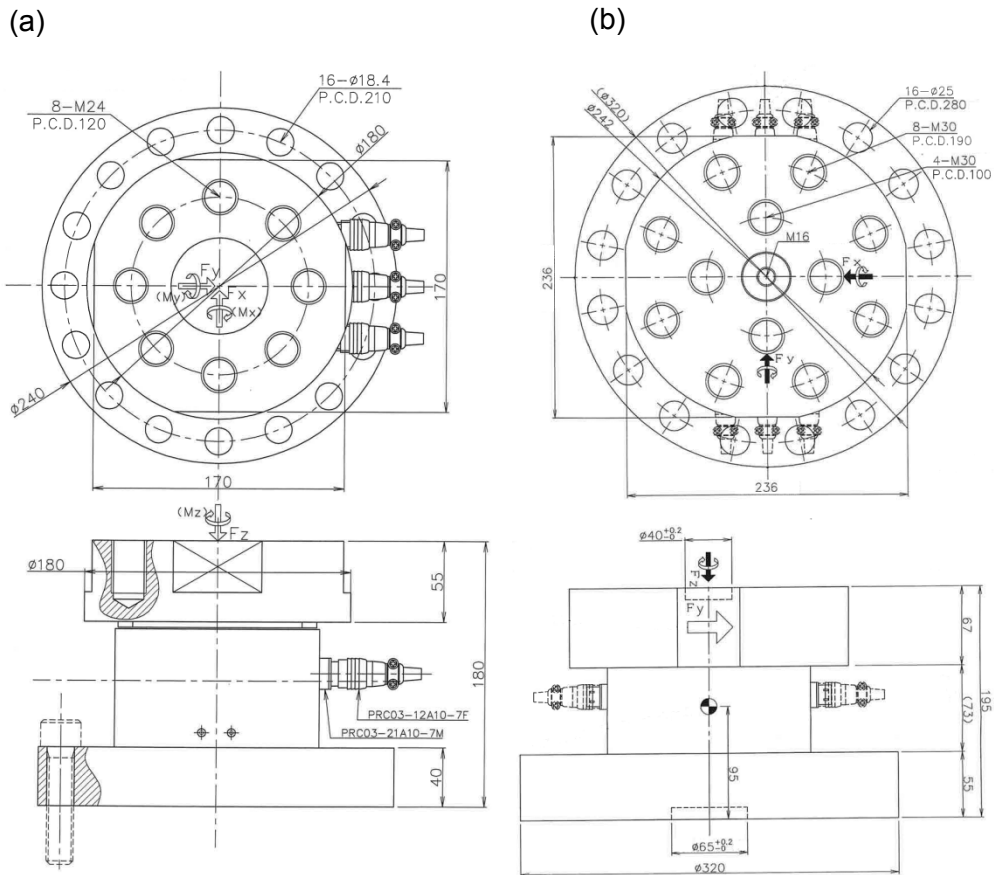


**Figure 4-3 Load cell drawings with bolt patterns and elevation views: (a) Type A and (b) Type B**

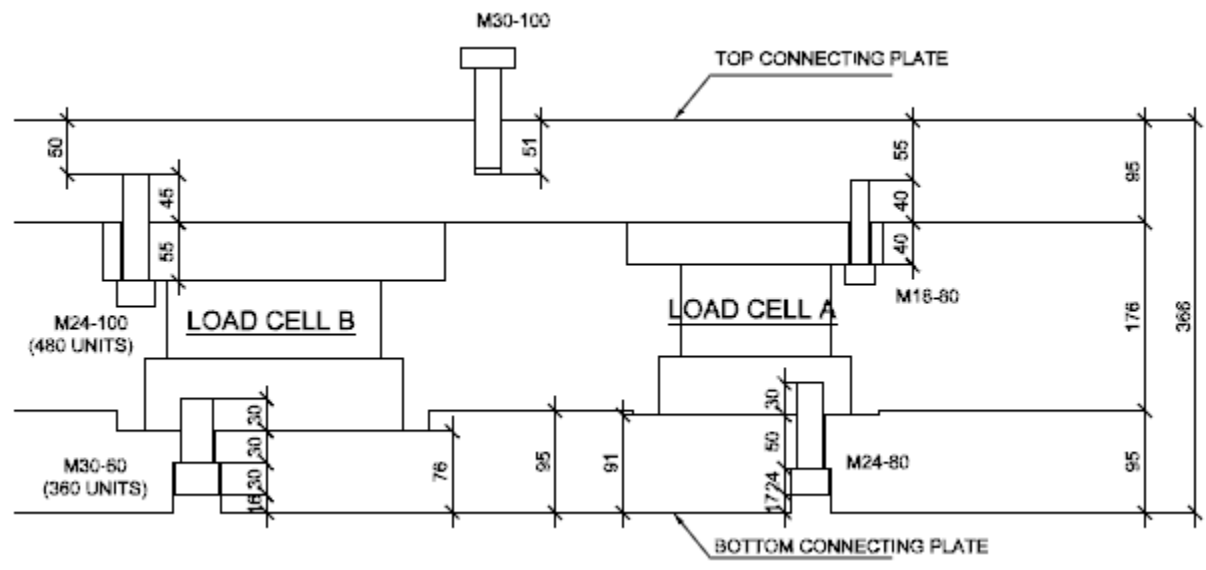


**Figure 4-4 Connection of Type A and Type B load cells to top and bottom connection plates**

## 4.2 Instrumentation

Approximately 470 channels were used for measuring the responses of structural and nonstructural components in the building with the hybrid LR isolation system. The sampling frequency of all channels was 1000 Hz. The results included in this report were based on measurements from the following three types of sensors:

- Sensors for measuring force: load cells (90 channels)
- Sensors for measuring displacement: displacement transducers (26 channels)
- Sensors for measuring acceleration: accelerometers (100 channels)
- The following describes the details of each sensor type.

Unless otherwise mentioned, all recorded data of the structural responses presented in the report was filtered using a Low-Pass Butterworth filter with a cut off frequency of 50 Hz. The filter shape as a function of normalized frequency is shown in Figure 4-5. The low pass filter “filtered out” or eliminated the high frequency components of the signal while preserving lower frequency components, including the dominant isolation frequency. The shape of the Butterworth filter provides a smooth transition from filtered to preserved frequencies. The cutoff frequency of 50 Hz was selected to eliminate noise that would not affect structural or equipment response and performance.

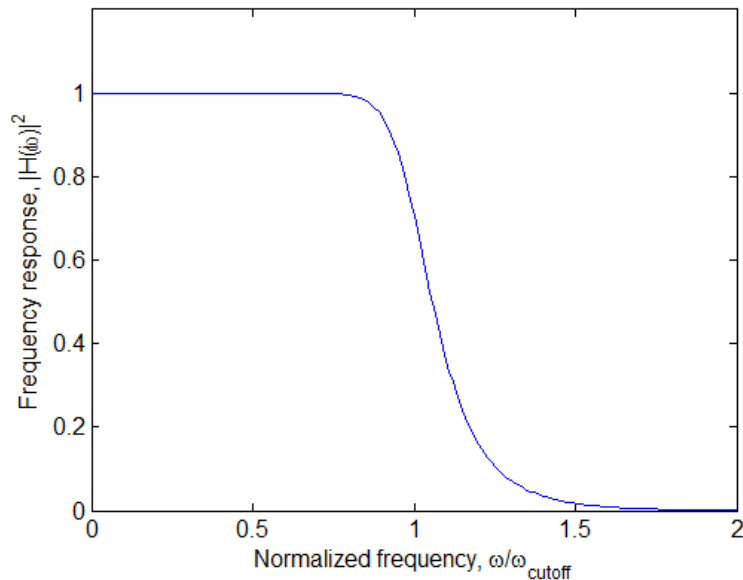


**Figure 4-5 Magnitude of low-pass Butterworth Filter transfer function**

#### 4.2.1 Load Cells

Triaxial load cells were used to measure the forces in the LR bearings in all three directions. Figure 4-6 illustrates the load cell channels for each of the North, South, East and West bearings. The East bearing used a configuration of 9 load cells while the other bearings used only 7 load cells.

#### 4.2.2 Displacement Transducers

Displacement transducers were used to measure the displacement of the isolation system and story drift. Figure 4-7 shows the layout of displacement transducers (wire pots) at base level for measuring the displacement of the isolation system. Three wire pots each were installed at the column bases at the North side and East side to measure the displacement in the x and y-directions, respectively. Three transducers were required to uniquely determine the translation and rotation of the isolation system and three additional channels were included for redundancy.

Laser-based transducers were used to measure story drift. Each sensor was attached to a vertical instrumentation frame and its reflecting plate was attached to the floor above as shown in Figure 4-8. A pair of transducers measured the relative displacement between the two floors in each direction at 2 locations (Figure 4-9). Assuming a rigid floor diaphragm, 3 unique displacement transducers were needed for determining relative displacement between the adjacent floors. An additional displacement transducer was added in each story for redundancy. The layout of the 4 displacement transducers in the 2<sup>nd</sup> to 5<sup>th</sup> story is shown Figure 4-9. In the 1st story, the 4 displacement transducers were installed at the SE and NW columns.

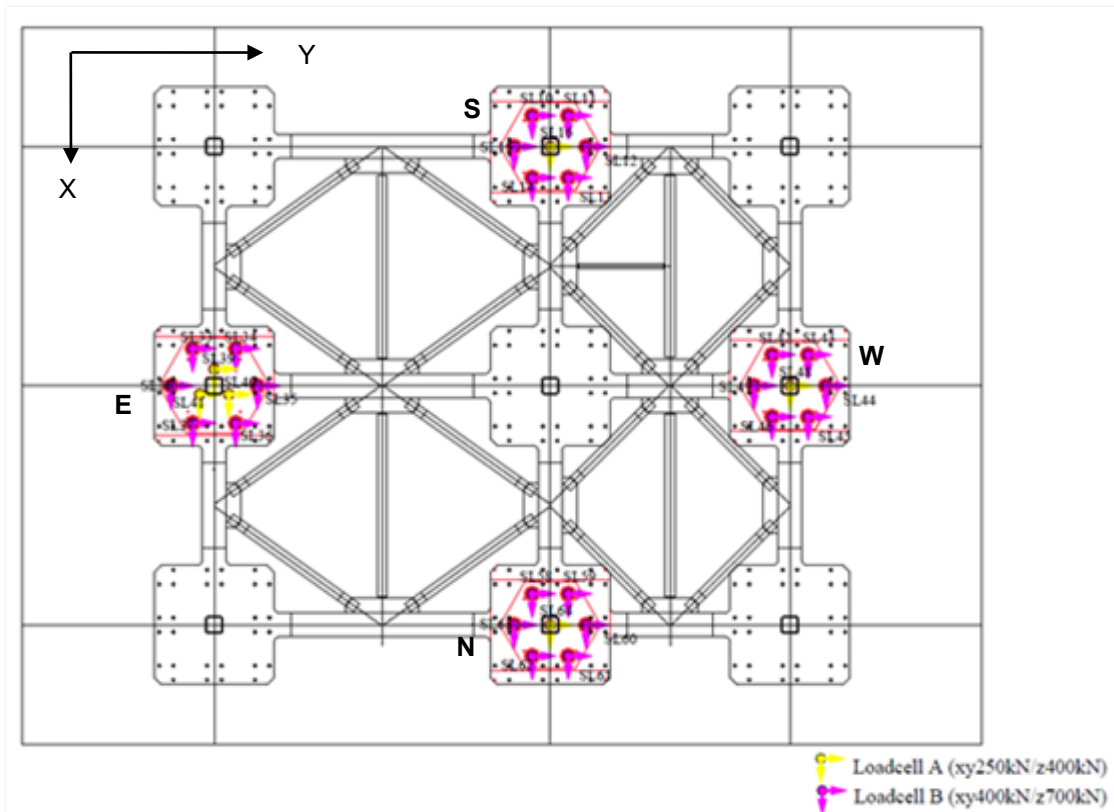
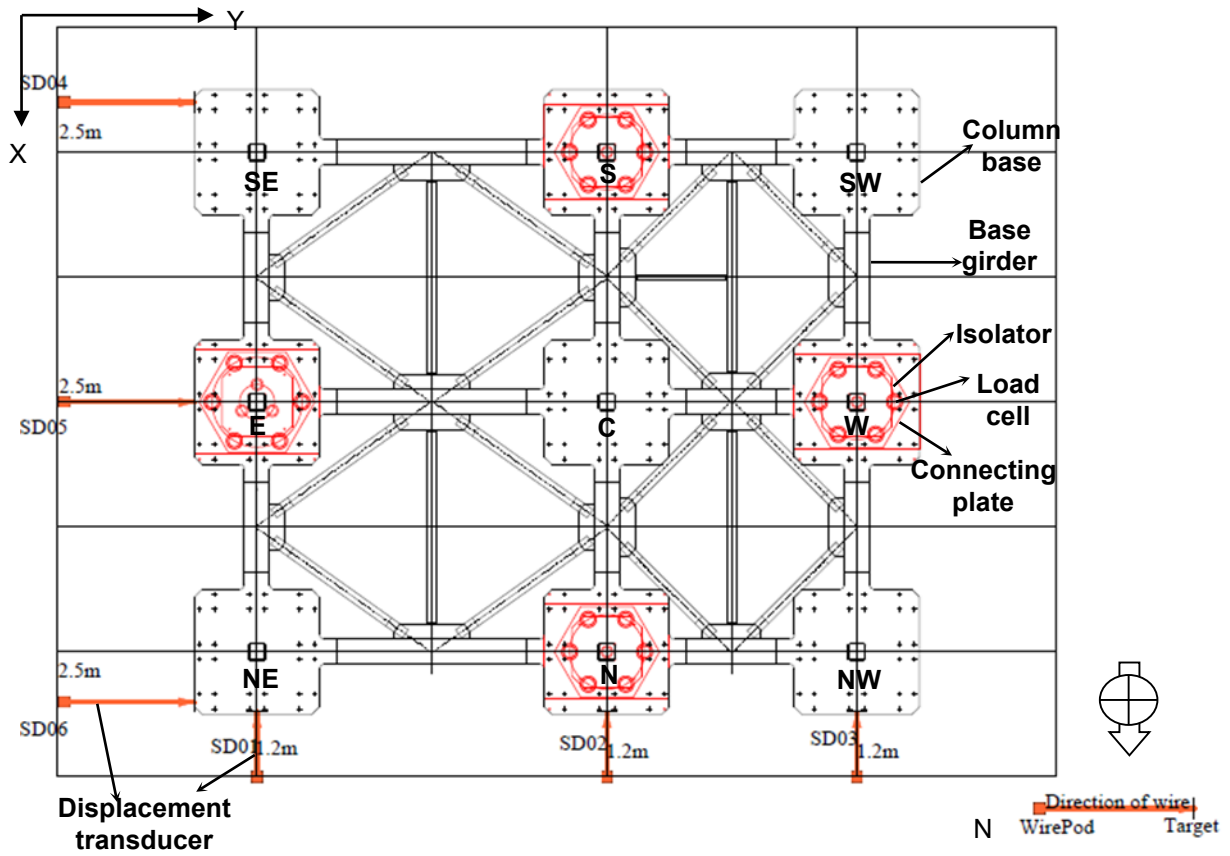


Figure 4-6 Load cell channels for the hybrid LR isolation configuration



**Figure 4-7** Layout of displacement transducers at base



**Figure 4-8** Instrumentation for measuring story drift

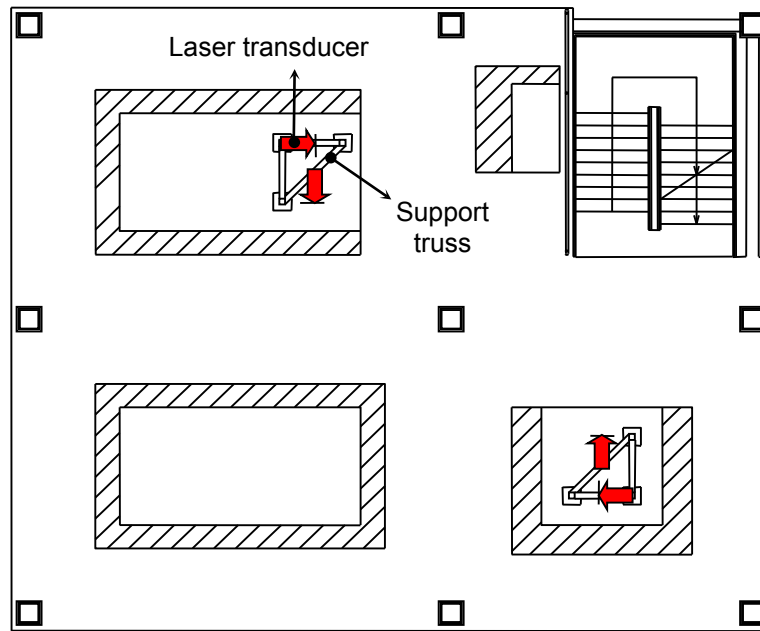


**Figure 4-9** Layout of displacement transducers to measure story drift in 2<sup>nd</sup> to 5<sup>th</sup> stories

### 4.2.3 Accelerometers

Three triaxial accelerometers were installed to measure the 3 components of acceleration at the 4 corners of the earthquake simulator platform. Accelerations at the center of the platform were also measured by permanent sensors integrated into the simulator control system. The measured acceleration at the center of the table included all 6 six components (3 translational components and 3 rotational components) of motion.

Two uniaxial accelerometers were also installed on the top plates of the connection assemblies (Section 4.1) to measure the horizontal acceleration of the plates (Figure 4-10). The recorded acceleration is used to derive the bearing forces. The load cells described in Section 4.2.1 did not measure the isolator force but rather the force just beneath the top connection plate. These forces differed by the inertia force associated with the top connection plate and the bottom half of the isolator. Since the total mass separating these two locations was large (about 4 tons) depending on location and the expected acceleration was also large (approximately equal to the input acceleration, about 1 g), the inertia force, which was significant compared to the isolator force, was accounted for.

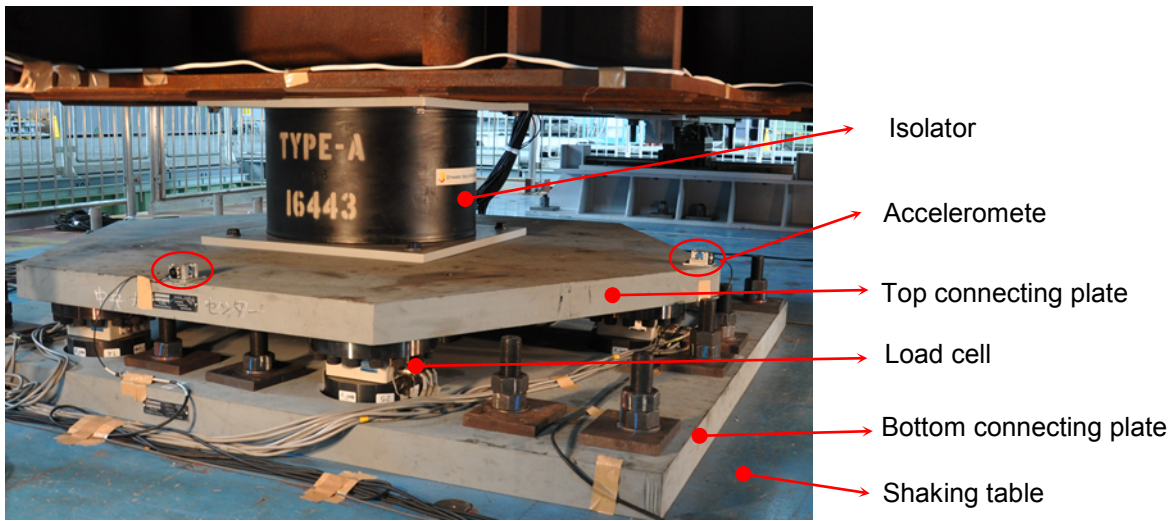


**Figure 4-10 Accelerometers at the top connection plates to estimate inertia forces**

Floor accelerations (2 horizontal and vertical components) were measured using 3 triaxial accelerometers installed at the SE, NE and NW corners of every floor. These triaxial accelerometers were attached to the column face just above the floor slab. Vertical accelerations at other locations on the floor slab were also recorded. Figure 4-11 shows the layout of accelerometers on the 5<sup>th</sup> floor, which was a typical layout for all floors. The vertical accelerometers were attached to the bottoms of the slabs.

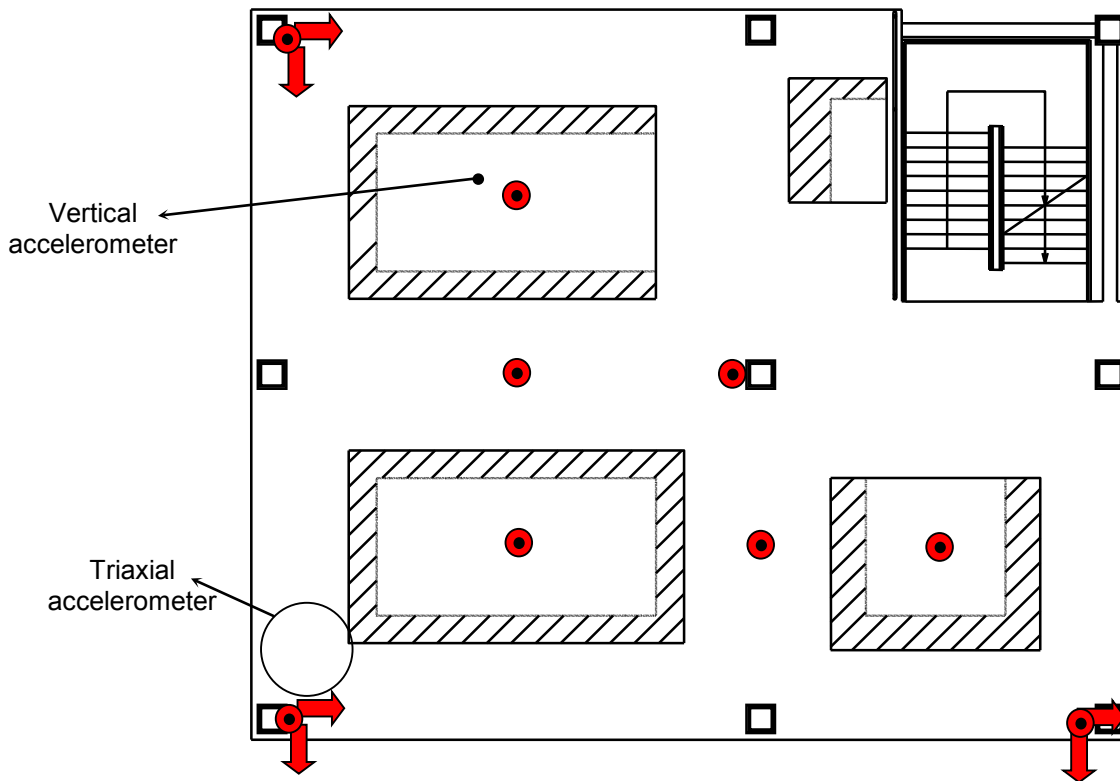


**Figure 4-11 Layout of accelerometers at the 5<sup>th</sup> floor**

### 4.3 Installation of the Specimen on the Earthquake Simulator

The connection assemblies were put together using the following process. Holes were drilled and tapped in the steel connection plates as needed. The load cells were first bolted to the top hexagonal shaped plate of the connection assembly (Figure 4-2). The bottom plate was then added to the assembly (Figure 4-12). The connection assemblies were then turned over and bolted to the earthquake simulator platform using 48 mm (1.9 in) diameter threaded rods (see Figure 4-13). The installation of the testbed building with the hybrid LR isolation system, immediately followed testing and removal of the TP isolation system. After removal of the TP bearings and rearrangement of the connection assemblies, the LR bearings were bolted to the connection assemblies while CL bearings were bolted directly to the simulator platform (Figure 4-14). The building was then transported across the laboratory using two 400-ton-cranes and lowered over the isolation system (Figure 4-15).

The testbed building was connected to the isolation system through bolt holes in the column bases that had been drilled and tapped from below (Figure 4-16). Drilling and tapping these holes in the overhead position was a laborious and expensive process (Figure 4-17). As such, measures were taken to limit the number and size of connecting bolts. Four M24 bolts were used to connect each LR bearing to the structure above and the connecting plates below. These bolts were attached through 30 mm (1.2 in) oversized holes in the top connecting plates and 33 mm (1.3 in) oversized holes in the bottom connecting plate. The oversized holes were used to help align the testbed building with the isolators.

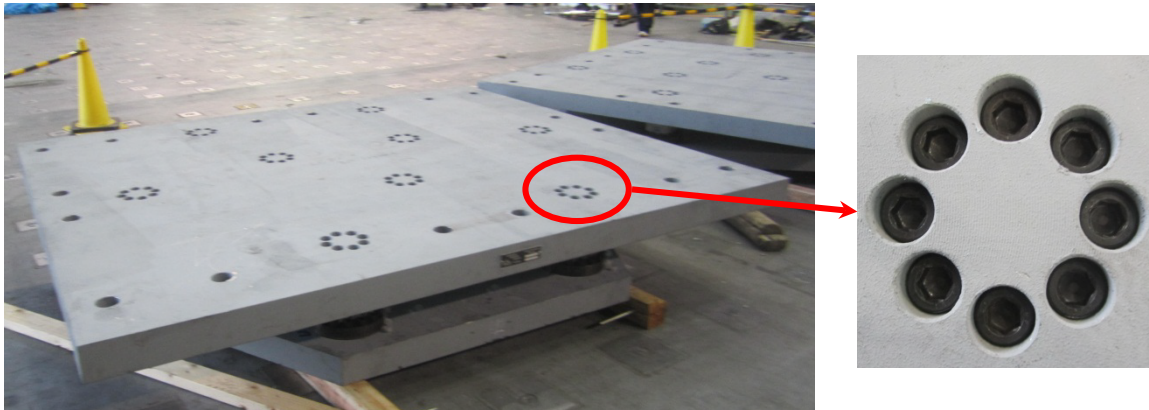


Figure 4-12 Connection assembly





**Figure 4-13 Connection assemblies on the simulator platform**



**Figure 4-14 Installing the LR bearings to the connecting assemblies and the CL bearings to the simulator platform**



**Figure 4-15 Lowering the testbed building over the isolation system**

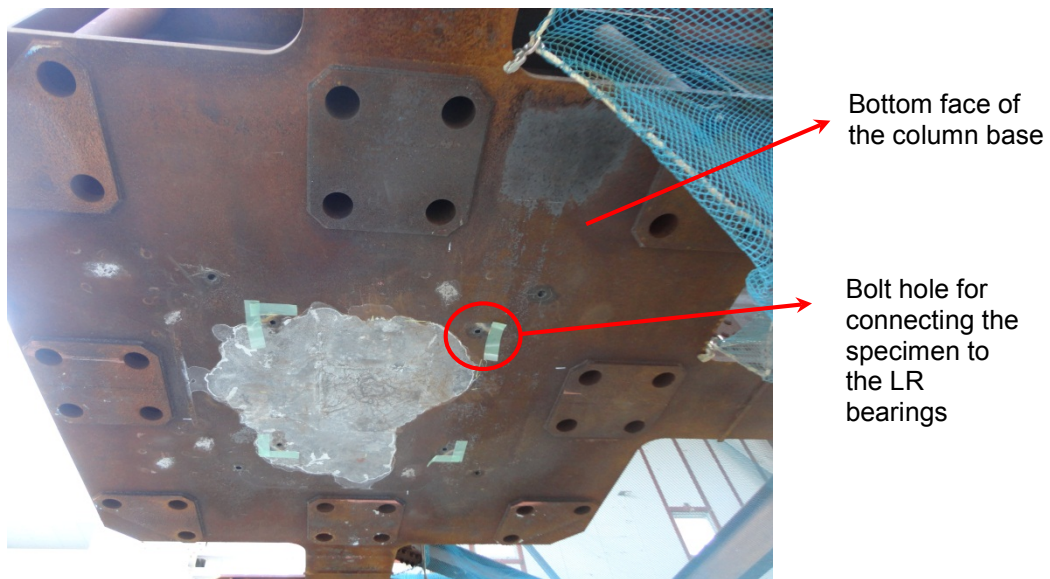


**Figure 4-16 Bolt holes for connecting the testbed structure to the isolation system**





**Figure 4-17 Drilling and tapping holes at the bottom of the specimen**

The measured weight of the building (excluding the isolators) was 5220 kN (1173 kip). This weight was determined during the testing of the TP isolation configuration, as described in Dao (2012), since static forces were measured in every bearing. The measured weight of the testbed was about 17% greater than the 4540 kN (1020 kips) anticipated in the design (Section 3.2). The change in weight affected the realized stiffness and strength of the isolation system. However, since the properties of the LR bearings are highly amplitude dependent (see Section 7.4), the influence of this change in supported weight was not explored in detail.

The static vertical load on an isolator is expected to be proportional to the mass of the tributary area. This condition could have been obtained if the testbed had been erected directly on the isolation system (similar to the expected construction process). However, the testbed had been built and stored outside for more than 2 years before testing so that its base was warped and the distribution of vertical load on all isolators deviated from the calculated values. Table 4-2 shows the measured vertical load on each LR bearing after the building was bolted to the isolation system and the expected vertical load on the isolators based on the pre-test simulation model. The expected vertical load on each isolator was scaled by 1.17 compared to the values reported earlier (Figure 3-7) to adjust for the actual weight (=5220 kN or 1174 kips) of the testbed. The table shows that most of the LR bearings were carrying less gravity load than expected based on tributary area. The static load in the West bearing was very small at 235 kN (53 kip). Shims were installed to achieve a distribution of gravity load similar to that assumed for design, with limited success.

**Table 4-2 Vertical load on each bearing after installation.**

<b>Bearing</b>	<b>E</b>	<b>S</b>	<b>N</b>	<b>W</b>	<b>Percent of Total</b>
Actual load (kN)	435	755	490	235	37%
Expected load (kN) (*)	749	708	725	468	51%
Difference (%)	-41.9	6.6	-32.4	-49.9	

(\*) The expected load was linearly scaled such that the total vertical load matches the measured load

#### 4.4 Test Schedule

The test schedule included 3 days of shaking (21 simulations) for the TP isolation configuration, 2 days of shaking (15 simulations) for the hybrid LR configuration, and 1 day of shaking (5 simulations along with white noise and sine sweep) for the fixed-base configuration. Dao (2012) discussed the selection of the ground motions for the TP configuration, while Chapter 3 described the selection of ground motions for the hybrid LR configuration. Since only a minimal number of simulations could be included for the fixed-base configuration, motions were selected that would allow a broad comparison between the three different configurations, and to provide insight into the influence of vertical excitation.

Although the majority of the inputs were 3D, some of the earthquake motions were applied as horizontal (XY) only, which enables a study of the effect of vertical excitation. Other reasons for not including the vertical component of excitation for some simulations included: 1) lack of access to the vertical record, 2) the capacity of the earthquake simulator limited the application of all 3 components at full scale, and 3) test-day decisions to limit damage to nonstructural components.

For the isolation configurations, the floors containing nonstructural components and contents were inspected only at the end of the test day, with one exception. On the first test day (TP isolation configuration), nonstructural components and contents were inspected after Rinaldi 88%, which generated some unexpected ceiling damage and disruption to contents. The shaking of the fixed-base building, completed in 1 day, included 5 earthquake excitations. For the fixed-base configuration only, nonstructural components were inspected and partially repaired after every simulation, thus 3D white noise excitation preceded and followed every earthquake simulation for system identification before and after the repairs. Unidirectional white noise excitations were also applied at the beginning and end of the day. Damage to nonstructural components and content disruption was observed in all system configurations under large intensity vertical excitation, and the damage was similar in all configurations. The nature of the damage is not discussed in this report, as the tested nonstructural components were not nuclear qualified, and the observations could be misleading. Rather the performance of safety related nuclear structures should be judged on the basis of the reported seismic demand parameters. Further information about the response of the nonstructural components is provided in Soroushian et al. (2012).

For completeness, the simulation schedule for all three building configurations is listed in Tables 4-3 to 4-5. In Tables 4-3 and 4-4, the shaded simulations are 3D excitations and the rest are XY simulations. Color coded groups of simulations represent the same input at different scale factors; for instance, red = the Vogtle suite of motions in Table 4-4. In the shaking schedule for the fixed-base building (Table 4-5), the earthquake simulations are shaded and the motion in red use the same input with different scale factors. The nomenclature introduced in Table 4-4 (simulation abbreviation) is used throughout the report to refer to different simulations in the hybrid LR system. The abbreviation consists of the first three letters of the station name with the scale factor. If the input excitation is not 3D, then "(XY)" is added for bidirectional horizontal input and "(Y)" is added for unidirectional input in the y-direction. If the simulation is repeated with the same input, the repetitions are labeled "-1" and "-2". Thus, "SIN100(Y)-1" reflects the first repetition of a sine wave input scaled to 100% and the input is unidirectional in the y-direction; "VOG150" reflects the Vogtle record scaled to 150% and the input is 3D.

**Table 4-3 Simulation schedule for the TP isolation configuration.**

Date dd/mm/y	Time	Simulation Abbreviation	Motion	Scale Factor			Damage Inspection
				X	Y	Z	
17/08/11	12:01:46	SIN65(X)	Sine-wave	0.65	0	0	
	12:49:54	SIN100(X)	Sine-wave	1.00	0	0	
	13:42:20	WSM80	Superstition Hills,	0.80	0.80	0.80	
	14:30:21	ELC130	Westmorland, Imperial Valley,	1.30	1.30	1.30	
	15:20:16	RRS88	El Centro Northridge,	0.88	0.88	0.88	Yes
	17:16:16	SYL100	Rinaldi Rec. Sta. Northridge, Sylmar	1.00	1.00	1.00	
	17:48:56	TAB50	Tabas, Tabas Sta.	0.50	0.50	0.50	Yes
18/08/11	11:35:31	LGP70	Loma Prieta  Los Gatos Pres. Ctr.	0.70	0.70	0.70	
	12:25:40	TCU50(XY)	ChiChi, TCU065	0.50	0.50	0	
	13:55:30	TCU70(XY)	ChiChi, TCU065	0.70	0.70	0	
	14:31:59	IWA100(XY)	Tohoku, Iwanuma	1.00	1.00	0	
	15:45:46	SAN100(XY)	Sannomaru	1.00	1.00	0	
	16:34:58	TAK100	Kobe, JMA Takatori	1.00	1.00	1.00	
	17:05:03	KJM100	Kobe, Kobe JMA	1.00	1.00	1.00	Yes
19/08/11	11:29:55	RRS88(XY)	Northridge,  Rinaldi Rec. Sta.	0.88	0.88	0	
	12:16:55	TCU80(XY)	ChiChi, TCU065	0.80	0.80	0	
	13:08:07	TAB80	Tabas, Tabas Sta.	0.80	0.80	0.80	
	14:02:19	TAB90(XY)	Tabas, Tabas Sta.	0.90	0.90	0	
	14:50:46	TAB100(XY)	Tabas, Tabas Sta.	1.00	1.00	0	
	15:28:19	SCT100(XY)	Michoacan, SCT	1.00	1.00	0	
	16:19:03	TAK115	Kobe, JMA Takatori	1.15	1.15	1.00	Yes

**Table 4-4 Simulation schedule for the hybrid LR isolation configuration.**

Date dd/mm/y	Time	Simulation Abbreviation	Motion	Scale Factor			Damage Inspection
				X	Y	Z	
25/08/11	11:19:52	WSM80	Superstition Hills, Westmorland	0.80	0.80	0.80	
	12:21:52	SIN100(Y)-1	Sine-wave	0	1.00	0	
	13:06:04	VOG75-1	Vogle #13	0.75	0.75	0.75	
	13:56:09	VOG100	Vogle #13	1.00	1.00	1.00	
	14:33:53	VOG125	Vogle #13	1.25	1.25	1.25	
	15:15:09	VOG150	Vogle #13	1.50	1.50	1.50	
	16:17:50	VOG175	Vogle #13	1.75	1.75	1.75	
	16:52:49	DIA80	Diablo #15	0.80	0.80	0.80	Yes
	12:03:09	DIA95(XY)	Diablo #15	0.95	0.95	0	
26/08/11	12:48:49	ELC130	Imperial Valley, El Centro	1.30	1.30	1.30	
	13:44:36	IWA100(XY)	Tohoku, Iwanuma	1.00	1.00	0	
	14:37:30	RRS88(XY)	Northridge Rinaldi Rec. Sta.	0.88	0.88	0	
	15:20:52	RRS88	Northridge Rinaldi Rec. Sta.	0.88	0.88	0.88	
	16:15:12	VOG75-2	Vogle #13	0.75	0.75	0.75	
	16:59:19	SIN100(Y)-2	Sine-wave	0	1.00	0	Yes

**Table 4-5 Simulation schedule for the fixed-base building.**

Date (dd/mm/yy)	Time	Simulation abbreviation	Motion	Scale factor			Damage inspection
				X	Y	Z	
31/08/11	10:19:52	WHT100(X)-1	White noise	1.00	0	0	
	10:30:02	WHT100(Y)-1	White noise	0	1.00	1.00	
	10:38:32	WHT100(Z)-1	White noise	1.00	1.00	1.00	
	10:50:35	WSM80	Superstition Hills, Westmorland	0.80	0.80	0.80	
	11:02:50	WHT100-1	White noise	1.00	1.00	1.00	Yes
	12:06:31	WHT100-2	White noise	1.00	1.00	1.00	
	12:18:47	RRS35(XY)	Northridge, Rinaldi Rec. Sta.	0.35	0.35	0	
	12:28:02	WHT100-3	White noise	1.00	1.00	1.00	Yes
	13:37:34	WHT100-4	White noise	1.00	1.00	1.00	
	13:51:20	RRS35	Northridge, Rinaldi Rec. Sta.	0.35	0.35	0.35	
	14:03:01	WHT100-5	White noise	1.00	1.00	1.00	Yes
	15:12:50	WHT100-6	White noise	1.00	1.00	1.00	
	15:24:53	RRS35(XY)88(Z)	Northridge, Rinaldi Rec. Sta.	0.35	0.35	0.88	
	15:33:51	WHT100-7	White noise	1.00	1.00	1.00	Yes
	17:07:04	WHT100-8	White noise	1.00	1.00	1.00	
	17:22:33	IWA70(XY)	Tohoku, Iwanuma	0.70	0.70	0	
	17:35:28	WHT100(X)-2	White noise	1.00	0	0	
	17:43:12	WHT100(Y)-2	White noise	0	1.00	0	
	17:52:47	WHT100(Z)-2	White noise	1.00	1.00	1.00	Yes

## 4.5 Table Motions

The peak accelerations of the target motions and the actual motions generated by the earthquake simulator are compared in Tables 4-6 and 4-7. The target records were obtained from various sources such as the PEER NGA database (Chiou et al. 2008), Huang et al. (2009), and sources within E-Defense; and scaled by the scaled factors given in Tables 4-3 to 4-5. The realized input motions to the structure were generally amplified by the earthquake simulator relative to the target motions, and amplification factors of 50% were not uncommon. Amplification occurred because the recommended iterative response modification technique, which involves gradually increasing the intensity of the motions while making modifications to the control settings, was not used in favor of performing more simulations with a wider variety of earthquakes. We observed, however, that ground motion excitations were replicated consistently when repeated for the different system configurations.

Amplification was notable during the Northridge-Rinaldi (RRS88) simulation due to its effect on the vertical response of the system. The motion was reproduced similarly for all three building configurations. The acceleration histories of the 3 components of this motion for the hybrid LR configuration are plotted in Figure 4-18. The horizontal amplification occurred at the instant of the large horizontal pulse in the record and the vertical acceleration was amplified at the same instant. Thus, the realized intensity of the Rinaldi motion was much stronger than the intended design level earthquake, and in particular the vertical component of excitation might be considered extreme. On the other hand, motions with similar vertical intensity can be found in the PEER NGA database (Chiou et al. 2008). Note that the realized intensity of vertical excitation in RRS88(XY) was non-negligible (vertical peak ground acceleration or PGA = 0.05g for the hybrid LR configuration and 0.10g for TP configuration).

The 5% damped response spectra are compared for the target motions and the realized input motions. The ratio between these spectra at periods ranging from 0.01 sec to 5 sec is plotted in Figures 4-19 and 4-20. At periods longer than 0.7 sec, the spectral amplitudes of the realized motions did not differ much from the target motions. At periods less than 0.7 sec, the spectral amplitude of the realized motions in the horizontal direction was generally larger than that of the target motions. The isolation system is controlled by the post-yield properties of the bearings, so that the isolator displacement demands would not be significantly affected by the difference between the realized motions and the target motions. However, the contribution of higher mode effects to structural accelerations may have been amplified in the simulations compared to typical ground motions. The earthquake simulator appeared to amplify the horizontal period components at around 0.2 sec more strongly than components at neighboring periods.



**Table 4-6 Peak acceleration of target and realized motions for the TP isolation configuration.**

	Trial	Peak $a_x$ (g)		Peak $a_y$ (g)		Peak $a_z$ (g)	
		Target	Table	Target	Table	Target	Table
TP Configuration	80WSM	0.171	0.169	0.135	0.147	0.174	0.140
	130ELC	0.278	0.293	0.408	0.484	0.263	0.261
	88RRS	0.427	0.586	0.730	1.213	0.722	1.241
	100SYL	0.601	0.674	0.869	1.145	0.519	0.543
	50TAB	0.450	0.585	0.418	0.463	0.327	0.357
	70LGP	0.415	0.445	0.391	0.628	0.641	0.687
	50TCU	0.408	0.453	0.304	0.278	0.000	0.015
	70TCU	0.571	0.648	0.425	0.378	0.000	0.027
	100IWA	0.364	0.409	0.418	0.580	0.000	0.031
	100SAN	0.190	0.231	0.167	0.161	0.000	0.020
	100TAK	0.747	0.789	0.619	0.922	0.288	0.259
	100KJM	0.595	0.680	0.822	0.893	0.340	0.408
	88RRSXY	0.427	0.532	0.730	1.194	0.000	0.098
	80TCU	0.653	0.747	0.486	0.418	0.000	0.034
	80TAB	0.720	0.870	0.670	0.836	0.523	0.593
	90TAB	0.810	0.930	0.753	1.011	0.000	0.102
	100TAB	0.901	0.995	0.837	1.139	0.000	0.120
	100SCT	0.171	0.177	0.101	0.106	0.000	0.017
	115TAK	0.859	0.936	0.712	1.088	0.288	0.278

**Table 4-7 Peak acceleration of target and realized motions for hybrid LR isolation and fixed-base configurations.**

	Trial	Peak $a_x$ (g)		Peak $a_y$ (g)		Peak $a_z$ (g)	
		Target	Table	Target	Table	Target	Table
Hybrid Configuration	WSM80	0.170	0.195	0.138	0.150	0.209	0.145
	VOG75-1	0.329	0.391	0.213	0.259	0.215	0.214
	VOG100	0.438	0.521	0.284	0.346	0.286	0.297
	VOG125	0.548	0.687	0.355	0.451	0.358	0.368
	VOG150	0.657	0.857	0.426	0.549	0.429	0.437
	VOG175	0.767	1.025	0.497	0.639	0.501	0.493
	DIA80	0.783	0.917	0.543	0.662	0.455	0.452
	DIA95(XY)	0.930	1.118	0.645	0.808	0.000	0.063
	ELC130	0.278	0.300	0.406	0.497	0.259	0.277
	IWA100(XY)	0.363	0.429	0.420	0.590	0.000	0.021
	RRS88(XY)	0.430	0.524	0.733	1.180	0.000	0.051
	RRS88	0.430	0.521	0.733	1.193	0.738	1.257
	VOG75	0.329	0.393	0.213	0.246	0.215	0.220
Fixed-base configuration	80WSM	0.171	0.219	0.135	0.175	0.174	0.136
	35RRSXY	0.170	0.201	0.290	0.398	0.000	0.011
	35RRS	0.170	0.201	0.290	0.406	0.287	0.350
	88RRS	0.170	0.228	0.290	0.409	0.722	1.062
	70IWA	0.255	0.270	0.292	0.373	0.000	0.013

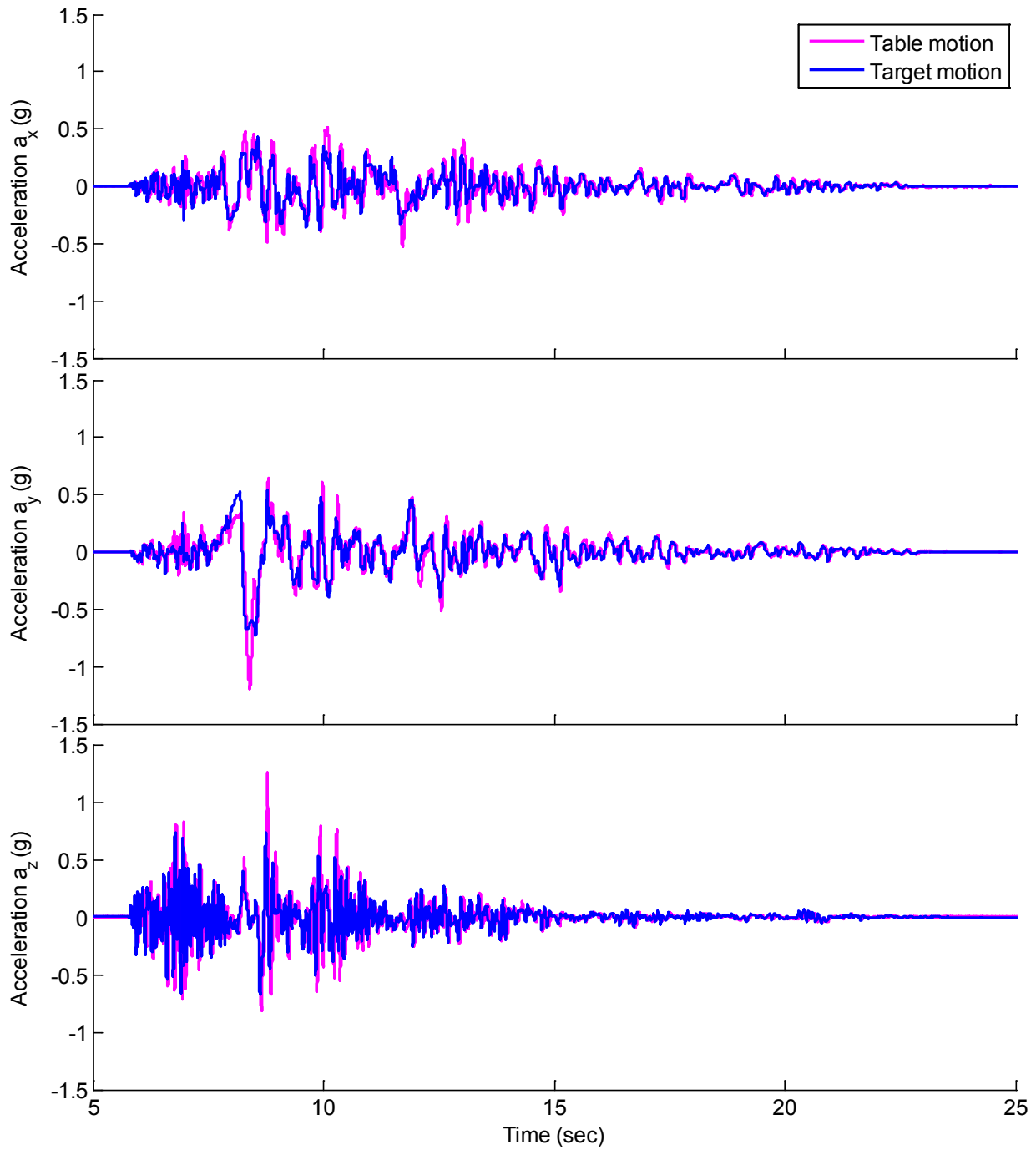


**Figure 4-18 Acceleration history of target and realized RRS88 motion in the hybrid LR isolation configuration test**

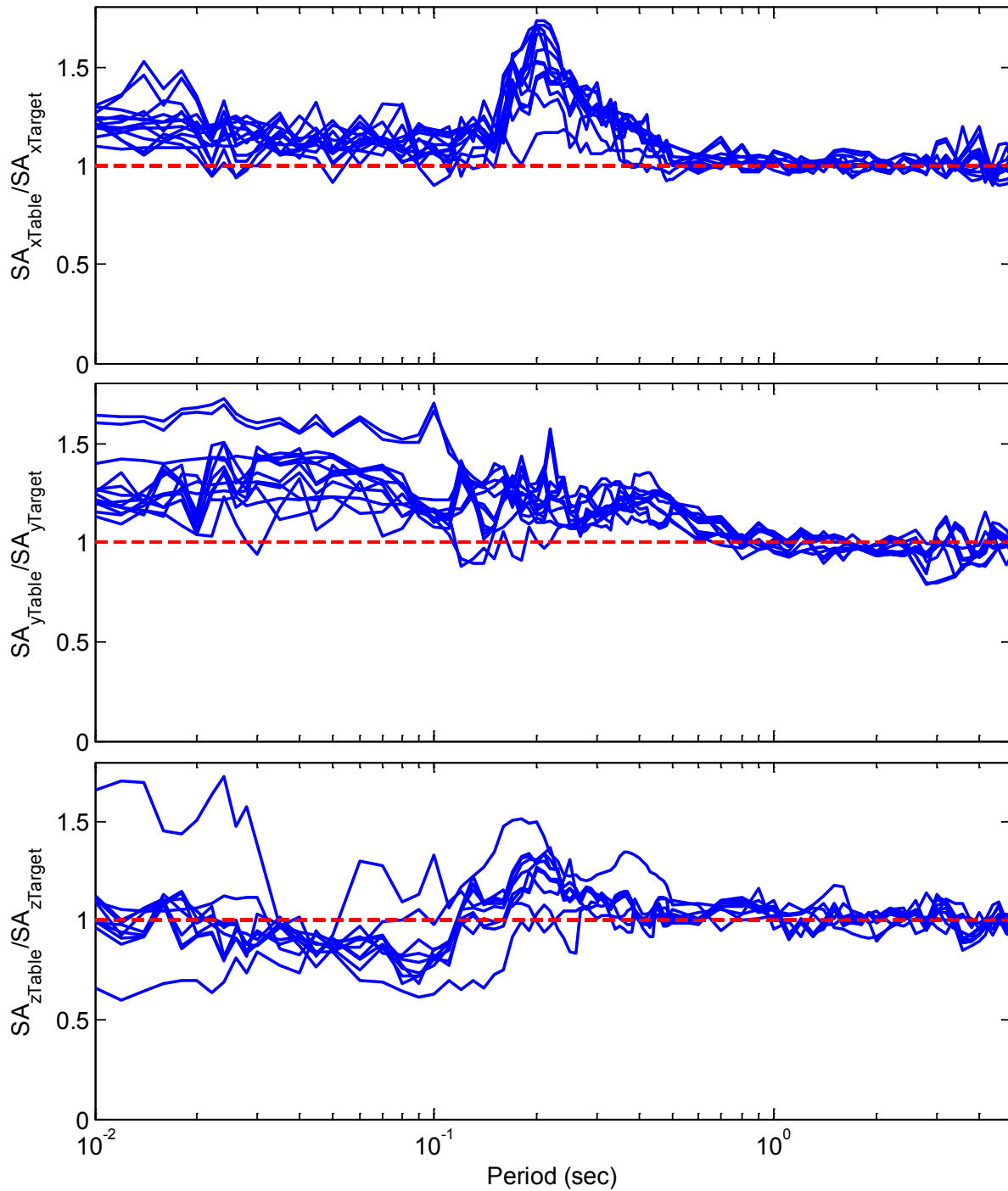


**Figure 4-19 Ratio of realized to target motion 5% damped spectral accelerations – hybrid LR configuration**

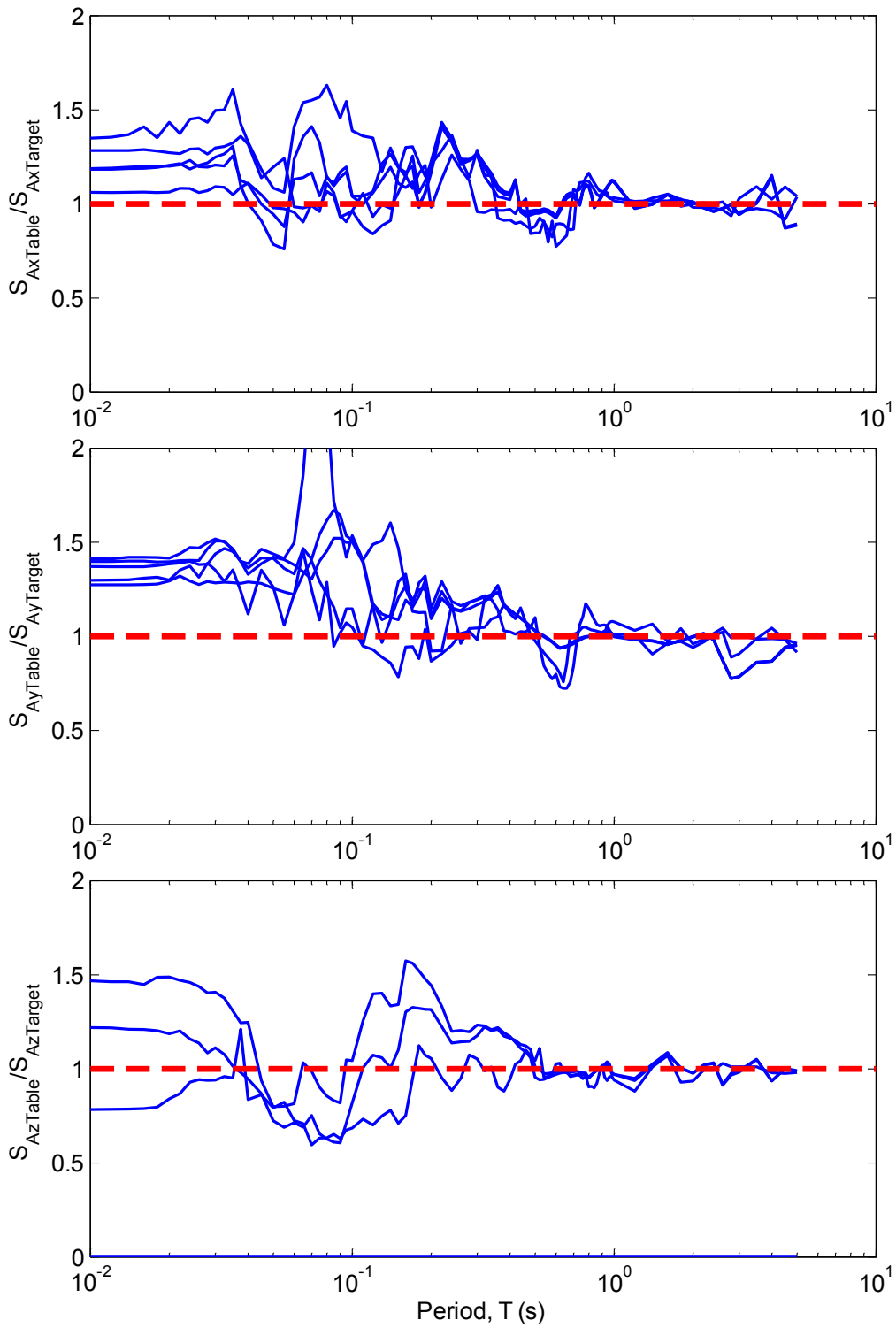


**Figure 4-20 Ratio of realized to target motion 5% damped spectral accelerations – fixed-base configuration**

## 4.6 Derived Responses

### 4.6.1 Horizontal Displacement of the Isolation System

An algorithm to compute the displacements in each isolator from the measured displacements in the string pots is described next. The algorithm accounts for large displacement geometric effects as a result of the large displacement demand in the bearings. From the original and displaced configurations of the isolation system in Figure 4-21, the coordinates  $X_{A'}, Y_{A'} \dots$  of displaced nodes A', B', D', F', G' and H' are:

$$\begin{aligned}X_{A'} &= \Delta X + X_A \cos \phi - Y_A \sin \phi \\Y_{A'} &= \Delta Y + X_A \sin \phi + Y_A \cos \phi \\X_{B'} &= \Delta X + X_B \cos \phi - Y_B \sin \phi \\Y_{B'} &= \Delta Y + X_B \sin \phi + Y_B \cos \phi \\X_{D'} &= \Delta X + X_D \cos \phi - Y_D \sin \phi \\Y_{D'} &= \Delta Y + X_D \sin \phi + \\&Y_D \cos \phi \\(4.1) \\X_{F'} &= \Delta X + X_F \cos \phi - Y_F \sin \phi \\Y_{F'} &= \Delta Y + X_F \sin \phi + Y_F \cos \phi \\X_{G'} &= \Delta X + X_G \cos \phi - Y_G \sin \phi \\Y_{G'} &= \Delta Y + X_G \sin \phi + Y_G \cos \phi \\X_{H'} &= \Delta X + X_H \cos \phi - Y_H \sin \phi \\Y_{H'} &= \Delta Y + X_H \sin \phi + Y_H \cos \phi\end{aligned}$$

where  $\Delta X, \Delta Y$  and  $\phi$  are the displacements and rotation at the center bearing in moving from the original configuration C to the displaced configuration C', with sign convention shown in Figure 4-21(b);  $X_A, Y_A$  are coordinates of the original point A, and so on.

From the displaced configuration in Figure 4-21(b):

$$\begin{aligned}(X_{A'} - X_a)^2 + (Y_{A'} - Y_a)^2 &= L_A^2 \\(X_{B'} - X_b)^2 + (Y_{B'} - Y_b)^2 &= L_B^2 \\(X_{D'} - X_d)^2 + (Y_{D'} - Y_d)^2 &= L_D^2 \\(4.2) \\(X_{F'} - X_f)^2 + (Y_{F'} - Y_f)^2 &= L_F^2 \\(X_{G'} - X_g)^2 + (Y_{G'} - Y_g)^2 &= L_G^2 \\(X_{H'} - X_h)^2 + (Y_{H'} - Y_h)^2 &= L_H^2\end{aligned}$$

where  $X_a, Y_a$  are coordinate of node  $a$ ;  $L_A = L_{A0} + \Delta L_A$  is the distance between  $a$  and  $A'$ ;  $L_{A0}$  is the original length of the transducer and  $\Delta L_A$  is the change in length measured by the transducer.

Substituting Equation (4.1) into Equation (4.2) leads to a system of 6 nonlinear equations to solve for 3 unknown  $\Delta X, \Delta Y$  and  $\phi$ . The system of equations was solved using the `lsqnonlin` command in Matlab, which is applicable to nonlinear least-squares (nonlinear data-fitting) problems. After solving for  $\Delta X, \Delta Y$  and  $\phi$ , the coordinate of the displaced isolators were determined from Equation (4.1). These displacements were determined by subtracting the original coordinates from the displaced coordinates.

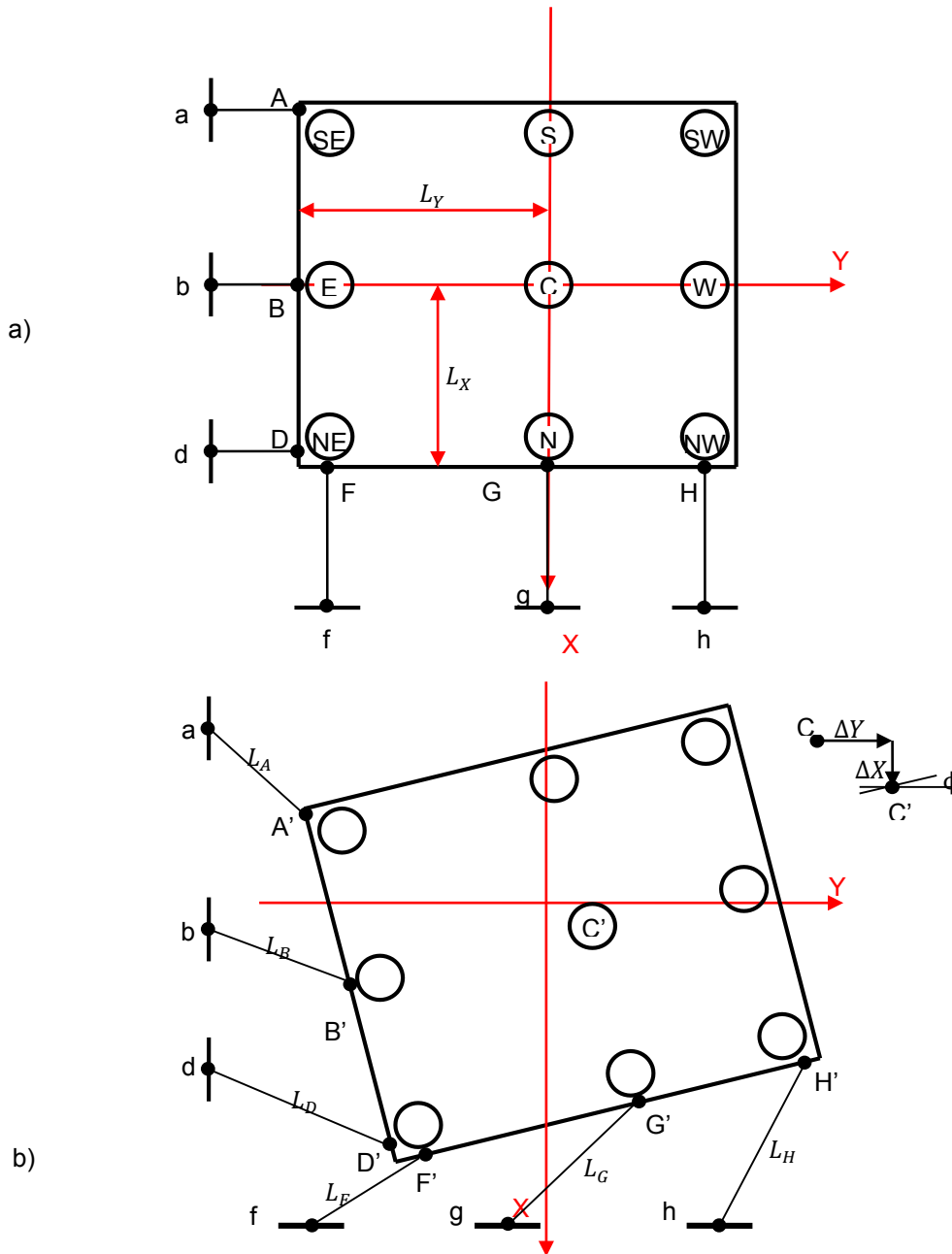


**Figure 4-21** Configurations for solving displacement of the isolation system. (a) original configuration, (b) displaced configuration



#### 4.6.2 Isolator Forces

The X, Y and Z components of the recorded dynamic force from all load cells of an isolator were added to get the X, Y and Z components of the dynamic reaction at the load cells level. This reaction was then modified by the inertia forces of the connection plate and the bottom concave plate of the bearing to get the dynamic reaction at the isolator level. From the free body diagram in Figure 4-22 the relationships between the dynamic reaction components  $R_X, R_Z$  at the isolator level and the dynamic reaction components  $R_{cX}, R_{cZ}$  at the load cell level are:

$$\begin{aligned} R_X &= R_{cX} - m_c a_{cX} \\ R_Y &= R_{cY} - m_c a_{cY} \\ R_Z &= R_{cZ} - m_c a_{cZ} \end{aligned} \quad (4.3)$$

where  $m_c$  is the mass of the top plate in the bearing connection assemblies plus the bottom half of the bearing; and  $a_{cX}, a_{cY}$  and  $a_{cZ}$  represent the horizontal and vertical accelerations recorded at the top connection plate. The reactions  $R_X$  and  $R_Z$  in Equation (4.3) represent the forces at mid-height of the LR bearing. These reactions are dynamic reactions so that the participation of the gravity load is not included in the equations.

Since vertical acceleration in the top connection plate was not recorded, the vertical acceleration in the earthquake simulator was used for  $a_{cZ}$ , which approximates the load cells as vertically rigid. The vertical acceleration of the simulator platform at every isolator was extrapolated from the measured acceleration at the center of the platform including the effect of roll and pitch components. The validity of these extrapolation accelerations was checked by comparing the extrapolated acceleration at the 4 corners of the platform to the accelerations recorded at these locations.

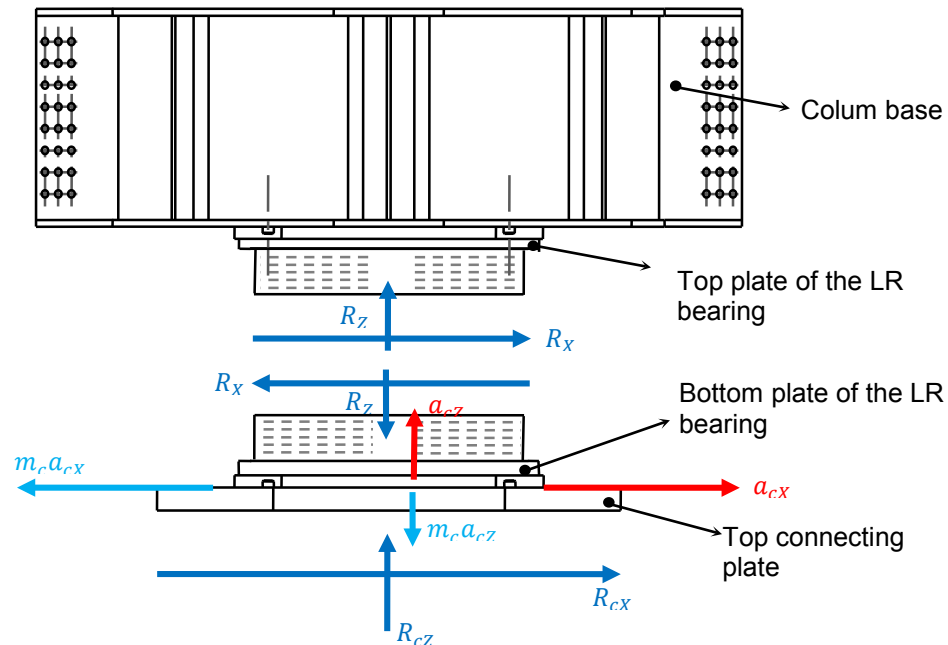


Figure 4-22 Free body diagram illustrating derivation of isolator reaction

The vertical force in all load cells was measured before each test series. The load cells were then zeroed before the first simulation of the test series so that only the dynamic force variation was measured during the simulations. The forces were only sampled during the simulation so that any redistribution of forces on the bearings from the original static state were reflected as offsets in the vertical forces at the beginning of each new simulation. The procedure used to measure the initial static forces in the LR bearings was found to be unreliable; thus, the computed static loads may have errors in them. Fortunately, interpretation of the LR bearing response was not sensitive to the measured vertical force.

### 4.6.3 Horizontal Acceleration and Story Drifts

As shown in Figure 4-11, the horizontal accelerations were measured at the SE, NW and NE corners of each floor. These recorded accelerations were processed to get an average acceleration in each direction, computed as:

$$\begin{aligned} a_{x,avg} &= \frac{1}{3}(a_{xSE} + a_{xNE} + a_{xNW}) \\ a_{y,avg} &= \frac{1}{3}(a_{ySE} + a_{yNE} + a_{yNW}) \end{aligned} \quad (4.4)$$

where  $a_{xSE}$ ,  $a_{ySE}$  are  $X$  and  $Y$  –components of the horizontal acceleration at the SE corner, and so on. Physically, the average acceleration represents a plan location one third of the way from the geometric center to the NE corner of the building.

The story drift in  $X$ - and  $Y$ -direction at the geometric center were also interpolated from the measured story drift at the 2 locations shown in Figure 4-23. For instance, the story drifts  $\delta_{xC}$  at (Figure 4-23) or  $\delta_{yC}$  the geometric center were extrapolated from the story drifts at the SE and NW corners  $\delta_{xSE}$ ,  $\delta_{xNW}$ ,  $\delta_{ySE}$ ,  $\delta_{yNW}$  as follows:

$$\begin{aligned} \delta_{xC} &= \delta_{xSE} + \frac{L_1}{L_2}(\delta_{xNW} - \delta_{xSE}) \\ \delta_{yC} &= \delta_{ySE} + \frac{L_1}{L_2}(\delta_{yNW} - \delta_{ySE}) \end{aligned} \quad (4.5)$$

Inconsistencies were observed in the drift sensor measurements, especially under vertical excitation. The vertical slab vibration is believed to have produced rocking of the measurement towers, which distorted the recorded drifts.

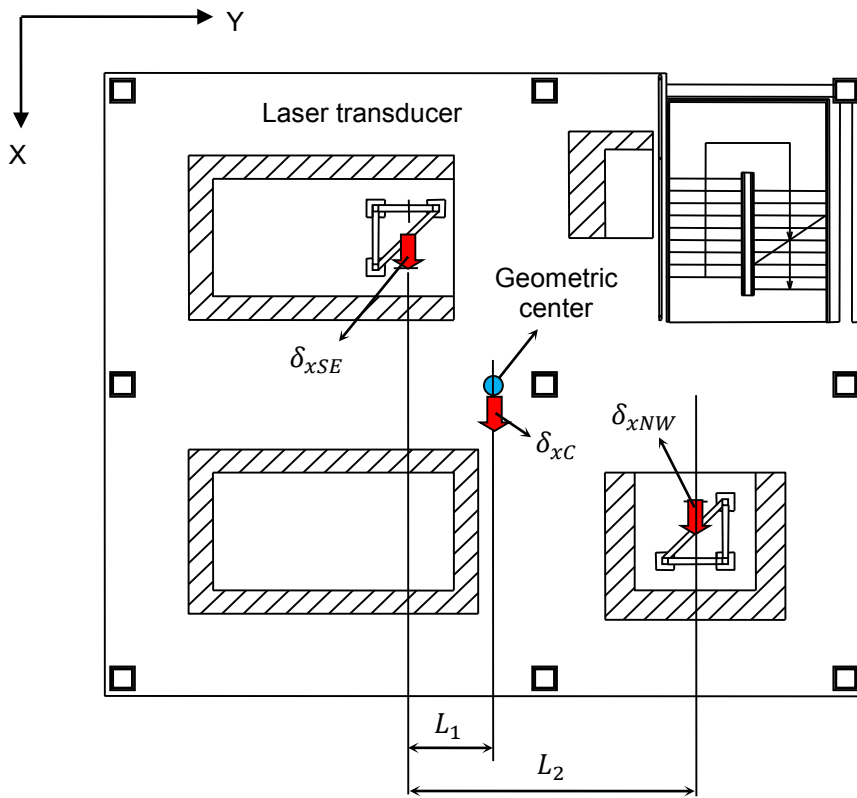


Figure 4-23 Diagram illustrating the computation of drift at the geometric center



## 5. SUMMARY OF EXPERIMENTAL SIMULATION RESULTS FOR THE HYBRID LR ISOLATED BUILDING

This chapter summarizes the overall response of the building with hybrid LR isolation system, with emphasis on the peak demands of various response parameters observed throughout the experimental program. Response quantities examined include displacement, rotation, shear force, axial force in compression and tension, and residual displacement of the isolators; and floor accelerations and story drifts in the structure.

### 5.1 Isolator Displacements

The target isolator displacements were 30 cm (11.8 in) for the design base earthquake (DBE) and 60 cm (23.6 in) for the maximum credible earthquake (MCEbeyond DBE). However, as mentioned previously, the maximum isolator displacement targeted in the test program was 55 cm (21.6 in) due to the various safety-related limitations imposed by the test facility (see Section 3.3.1). The DBE motion, VOG100, produced a peak vector sum displacement of 26.5 cm (10.4 in) and the MCE beyond DBE motion, VOG175, produced a peak vector sum displacement of 50.5 cm (19.9 in) as shown in Figure 5-1. The peak displacements observed during the Vogtle suite of simulations were slightly lower than analytically predicted, and did not reach the target. However, the displacement demands for the Diablo Canyon suite of simulations were slightly greater than predicted. The scale factor for the largest Diablo Canyon simulation (DIA95(XY)), originally planned for 100%, was adjusted on the day of testing to achieve the target displacement of 55 cm (21.6 in). The peak displacement observed in any LR bearing during DIA95(XY) was 54.7 cm (21.5 in). The smallest displacement (8.8 cm or 3.5 in) was observed during the service level simulation WSM80. The peak displacement increased approximately linearly as the simulation intensity was increased from VOG75 to VOG175. Because of the nonlinearity of the isolation system, the displacement demand would not normally be expected to increase linearly with excitation intensity.

The maximum displacements observed in each LR bearing (East (E), South (S), North (N) and West (W)) are summarized in Figure 5-2 for the x-direction, y-direction, and overall peak in any direction, determined as the peak of the vector sum displacement history. The simulation names are abbreviated by numbers in the figure, in order of their sequence, where the correspondence between number and simulation name, the directions that the excitations were applied and the input scale factor is summarized in Table 5-1 for convenience. By way of the small rotation assumption used to process the sensor data and derive individual isolator displacements (Section 4.6.1), the x-direction displacements were identical for the North and South bearings, which had the same y-coordinate, and the y-direction displacements were identical for the East and West bearings, which had the same x-coordinate. The East bearing experienced the largest displacement for most of the simulations (Figure 5-2(c)) due to the observed base rotation (see Section 5.2). The displacement traces (displacement in x-direction versus displacement in y-direction) of the East LRB are compared for four simulations in Figure 5-3: (a) WSM80, which produced the smallest displacement demand, (b) DIA95(XY), which produced the largest displacement demand, (c) VOG100, which was scaled to DBE intensity, and (d) VOG175, which was scaled to MCE intensity. The displacement observed in WSM80 was trivially small compared to the other simulations, and the large discrepancy in displacements affected the ability to model the LR bearings with a single set of physical parameters (discussed in Chapter 7). The simulations produced both linear and circular displacement orbits in the bearings, the latter of which would be more affected by bidirectional coupling. As mentioned in Section 3.3.2, the Vogtle ground excitation was rotated 11.25 degrees to induce the maximum displacement in a diagonal direction, as observed in Figure 5-3(d).

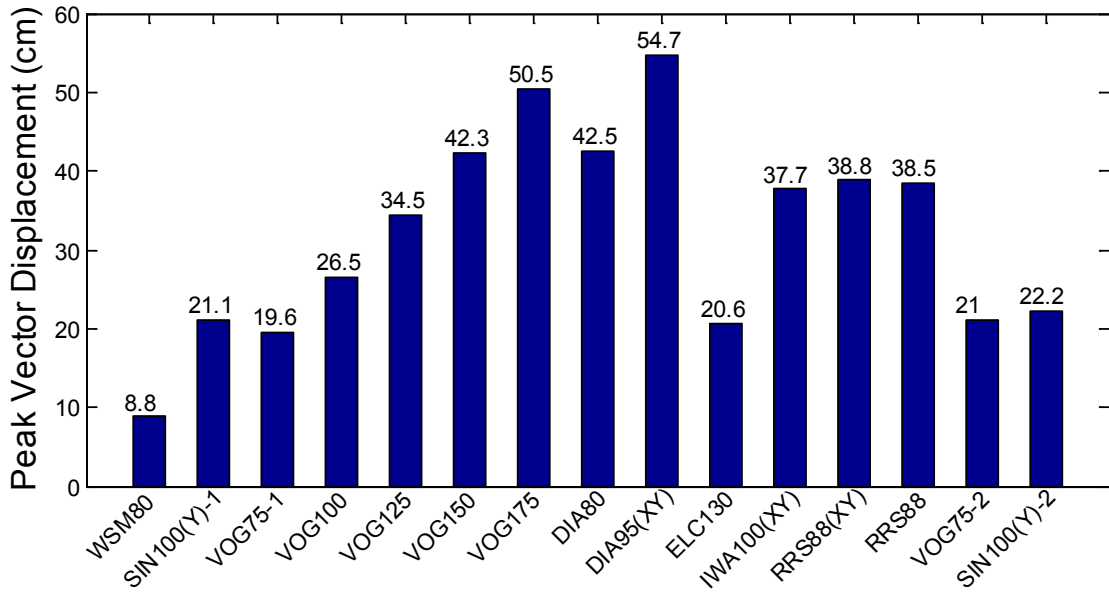


**Figure 5-1 Peak vector sum displacement recorded in any LR bearing for each earthquake simulation**

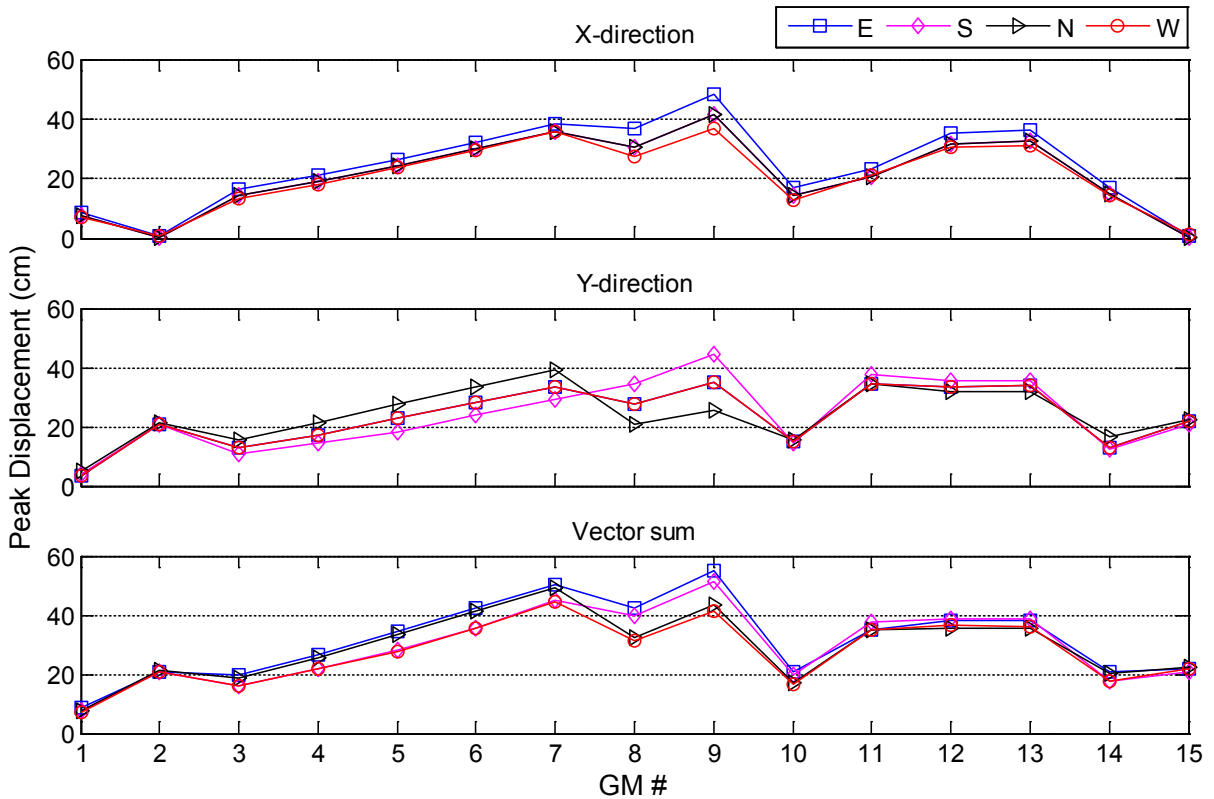


**Figure 5-2 X-direction, y-direction and overall peak (vector sum) displacement of each LR bearing for each earthquake simulation**

**Table 5-1 List of ground motion (GM) simulations by number, name, abbreviation and the directions considered.**

GM #	GM Name	GM Abbreviation	Input Direction	Scale Factor (%)
1	Superstition Hills, Westmorland	WSM80	X, Y, Z	80
2	Sine-wave	SIN100(Y)-1	Y	100
3	Vogtle #13	VOG75-1	X, Y, Z	75
4	Vogtle #13	VOG100	X, Y, Z	100
5	Vogtle #13	VOG125	X, Y, Z	125
6	Vogtle #13	VOG150	X, Y, Z	150
7	Vogtle #13	VOG175	X, Y, Z	175
8	Diablo #15	DIA80	X, Y, Z	80
9	Diablo #15	DIA95(XY)	X, Y	95
10	Imperial Valley, El Centro	ELC130	X, Y, Z	130
11	Tohoku, Iwanuma	IWA100	X, Y, Z	100
12	Northridge, Rinaldi Rec. Sta.	RRS88(XY)	X, Y	88
13	Northridge, Rinaldi Rec. Sta.	RRS88	X, Y, Z	88
14	Vogtle #13	VOG75-2	X, Y, Z	75
15	Sine-wave	SIN100(Y)-2	Y	100

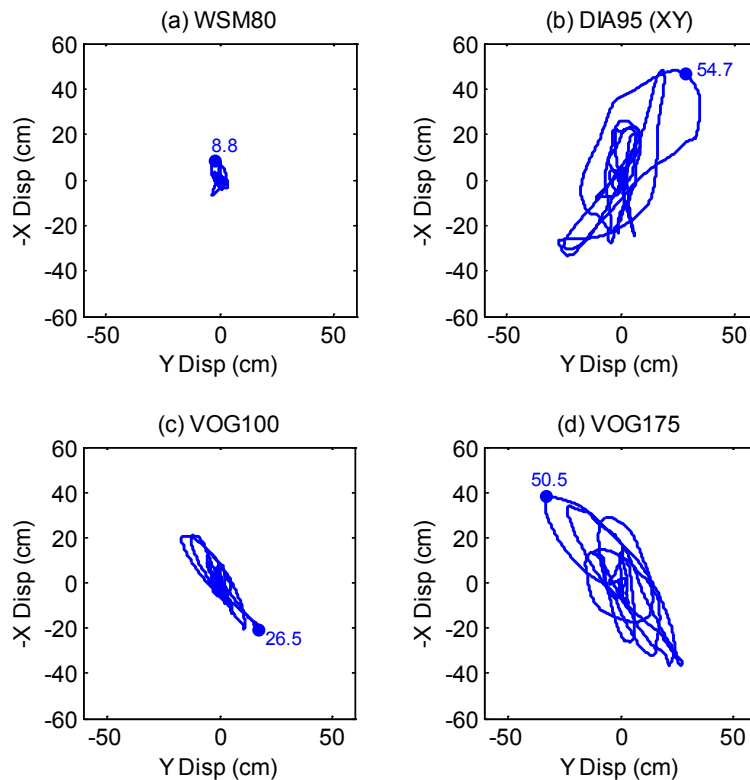


**Figure 5-3 Displacement trace (x vs y-direction displacement) of the East LRB for (a) WSM80, (b) DIA95(XY), (c) VOG100 and (d) VOG175**

## 5.2 Torsional Response

The dynamic characteristics of the testbed building were affected by stiffness asymmetry resulting from the unequal bays widths (equal to 7 m or 23 ft and 5 m or 16.4 ft) in the y-direction (Section 2.1, Figure 2-2), and various sources of mass eccentricity, the most notable being the asymmetrically configured steel blocks at the roof level (Section 2.3). The level of eccentricity is later quantified while discussing the model development for numerical simulation (Section 8.3). Aside from the supplementary roof weight, the sources of eccentricity were mild and typical of practice. However, as discussed in Section 3.3.2, the restrictions on the experimental setup did not allow for the isolation system to be configured to minimize torsion, unlike the design of a realistic structure with hundreds of isolators. Thus, non-negligible rotation was observed in the hybrid LR isolation system.

The peak rotation angle at the base (isolation system) level for each simulation is summarized in Figure 5-4. The rotation angle observed during the sine wave simulation (SIN100-1 and SIN100-2) was negligible, since the sine wave was applied unidirectionally in the y-direction (theoretically uncoupled) to minimize the torsional response for bearing characterization. During WSM 80%, which produced the smallest displacement demand, a peak rotation angle of 0.0019 rad was observed, and during VOG175 the largest peak rotation angle of 0.019 rad was observed. The peak rotation was not necessarily proportional to the peak displacement; for example, the greatest individual bearing displacement was observed in DIA95(XY) (Figure 5-1) but the greatest rotation angle was observed in VOG175 (Figure 5-4). The influence of this rotation on the bearing displacements can be observed from the displacement traces of all bearings during the VOG175 motion (Figure 5-5). From the SE to the NW isolator, the displacement traces transitioned from nearly linear (back and forth) motion to a circular displacement orbit. Furthermore, the peak displacement in the LR bearings varied from 50.5 cm in LRB-E to 44.6 cm in LRB-W, which is a 13% variation across the plan. Considering all isolation devices, the peak displacement varied from 53.1 cm (NE corner) to 42.7 cm (SW corner), a 24% variation from corner to corner. For the Rinaldi simulation that was repeated at the same scale factor for XY and 3D input, the peak rotation increased 7% from RRS88(XY) to RRS88 (Figure 5-4) while the peak displacement remained about the same, which may have been related to a residual rotation or displacement.

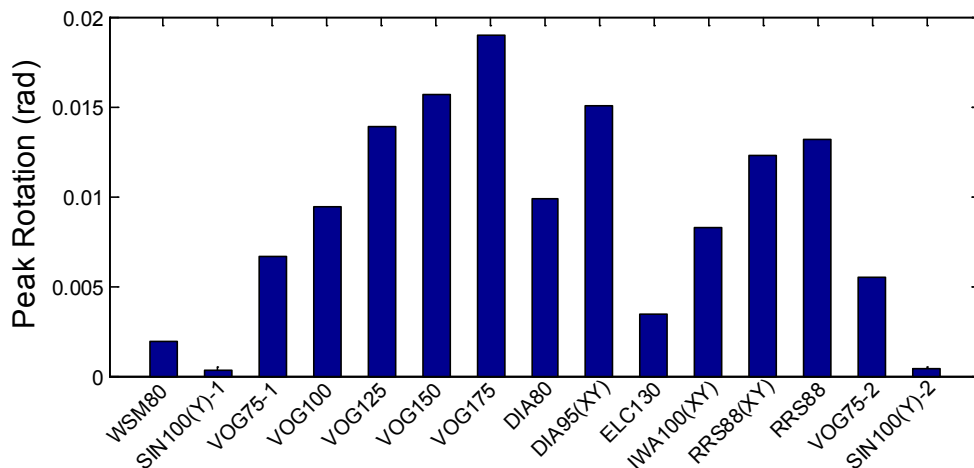
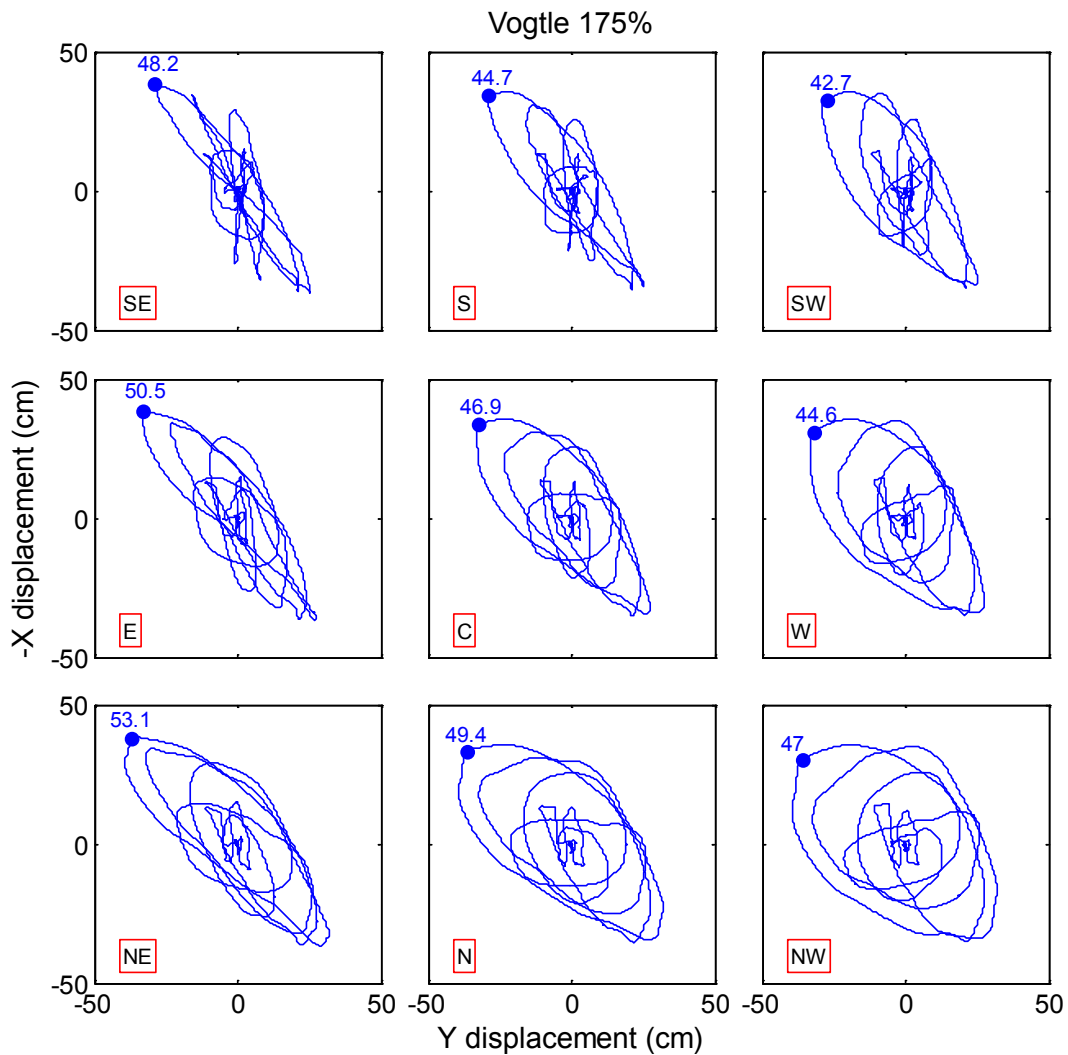


Figure 5-4 Peak rotation angle of the base for each earthquake simulation





**Figure 5-5 Displacement trace of each isolator during the Vogtle 175% simulation**

### 5.3 System Base Shear

The total base shear was computed by summing the recorded shear force of the four LR bearings in the x and y-directions, evaluating the vector sum of the x and y-components, and determining the peak over all times steps. This procedure was applied in the two horizontal directions, and from this the peak vector sum was determined. The calculation of the base shear does not include forces in the CL bearings, which were not recorded in this experiment. The forces in the CL bearings were assumed to be negligible as the rated friction coefficient was about 0.0025. Although we cannot be certain of the influence of the CL bearings on the base shear, there was no evidence to suggest that the forces in the CL bearings were significant. The peak values of total (vector sum), x and y-direction base shears are listed in Table 5-2 for each simulation. The corresponding values of normalized base shear or base shear coefficient, listed in Table 5-3, were obtained by dividing the total base shear by the total static weight of the building. Figure 5-6 illustrates the results of Table 5-2 graphically. The largest base shear of 1467 kN (328 kips), corresponding to a base shear coefficient of 0.28, was observed during VOG175. Among the other largest base shear coefficients observed were DIA95(XY) (0.28), DIA80 (0.24) and RRS88(XY) and RRS88 (both 0.26).

**Table 5-2 Peak base shear for all simulations: total, x and y directions.**

<b>GM #</b>	<b>GM Name</b>	<b>Peak Base Shear (kN)</b>	<b>Peak Base Shear - X (kN)</b>	<b>Peak Base Shear - Y (kN)</b>
1	WSM80	468	467	274
2	SIN100(Y)-1	996	9	996
3	VOG75-1	869	682	665
4	VOG100	1003	831	754
5	VOG125	1163	979	870
6	VOG150	1317	1109	967
7	VOG175	1467	1237	1058
8	DIA80	1271	1064	916
9	DIA95(XY)	1457	1245	965
10	ELC130	851	677	719
11	IWA100(XY)	1212	766	1211
12	RRS88(XY)	1365	1100	1240
13	RRS88	1355	1097	1214
14	VOG75-2	808	645	624
15	SIN100(Y)-2	926	13	926

**Table 5-3 Peak base shear coefficient for all simulations: total, x and y directions.**

<b>GM #</b>	<b>GM Name</b>	<b>Peak Base Shear Coeff.</b>	<b>Peak Base Shear Coeff. - X</b>	<b>Peak Base Shear Coeff. - Y</b>
1	WSM80	0.09	0.09	0.05
2	SIN100	0.19	0.002	0.19
3	VOG75	0.17	0.13	0.13
4	VOG100	0.19	0.16	0.14
5	VOG125	0.22	0.19	0.17
6	VOG150	0.25	0.21	0.18
7	VOG175	0.28	0.24	0.20
8	DIA80	0.24	0.20	0.17
9	DIA95_2D	0.28	0.24	0.18
10	ELC130	0.16	0.13	0.14
11	IWA100	0.23	0.15	0.23
12	RRS88_2D	0.26	0.21	0.24
13	RRS88	0.26	0.21	0.23
14	VOG75	0.15	0.12	0.12
15	SIN100	0.18	0.002	0.18

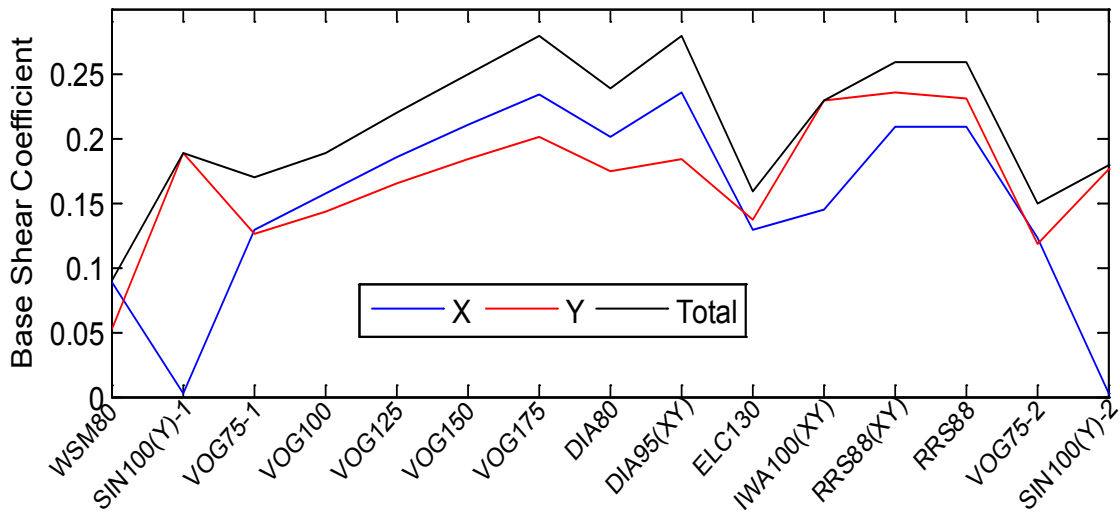


**Figure 5-6 Base shear coefficient for all simulations: total, x and y-directions**

In Figure 5-7, the base shear coefficient for each motion is superimposed over the backbone force-displacement relation of the LR bearings, using the assumed design properties in Table 3-3. The total force in the LR bearings was observed to exceed the design backbone for displacements less than 30 cm (12 in) and fall below the design backbone for displacements exceeding 30 cm (12 in). As an example, the base shear was approximately proportional to displacement as the intensity was increased from VOG75 to VOG175 simulations (simulations 3 to 7 in Figure 5-7), but with a slope slightly lower than the second slope post-yield stiffness  $K_d$ . The influence of ground motion intensity on the isolator response and modeling assumptions is addressed in Section 7.4.2.

Most simulations followed this trend with the exception of the Rinaldi motions (simulations 12 and 13, RRS88(XY) and RRS88, in Figure 5-7). Assuming the design backbone curve was an accurate reflection of the bearing response, the observed points should fall below the design curve since the base shear coefficient represented an average bearing shear, while the displacement represented a peak displacement recorded in any LR bearing. An explanation for the higher observed base shear in the Rinaldi motions could not be found.

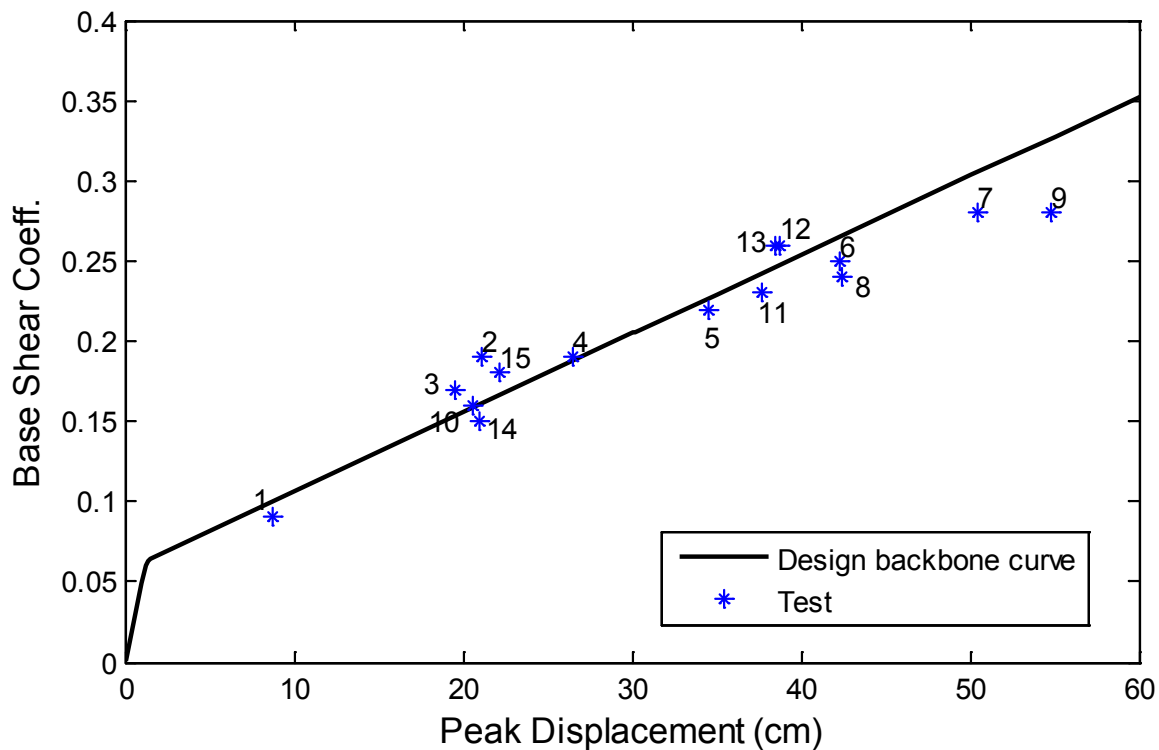


**Figure 5-7 Base shear coefficient for each simulation alongside the design backbone curve**

#### 5.4 Axial Forces in LR Bearings

The static forces on the LR bearings at the start of the experiments were measured as: East = 435 kN (98 kips), South = 755 kN (170 kips), North = 490 kN (110 kips), and West = 235 kN (53 kips). As discussed in Section 4.3, the measured static loads on the bearings at the beginning of the experiments differed from the expected loads according to tributary area calculations. The actual measured and expected static loads on the LR bearings were compared in Table 4-2. In summary, the portion of the building weight carried by the LR bearings (about 37%) was significantly less than portion of the weight that was expected to be carried by the LR bearings (about 51%). The sources of the discrepancy could not be identified with certainty, but we mention the following probable causes: 1) The base of the testbed building was warped due to weathering and storage conditions. This caused the weight of the building to be distributed in a different pattern than if the building had been erected on top of the isolation system. 2) The stiffer CL bearings attracted more weight, thus carrying a larger portion than if the weight was balanced on a single type of isolator. Both factors were thought to contribute to the static load distribution measured at the part of the experiment.

The axial forces in the LR bearings varied for each bearing and during each simulation due to a combination of factors including: variation in static forces, overturning, vertical excitation, and load transfer between LR bearings and CL bearings (discussed in Section 6.2). The peak compressive and tensile forces measured in any LR bearing for each simulation are shown in Figures 5-8 and 5-9, respectively. Tension was observed in at least one bearing for seven of the fifteen simulations (Figure 5-8). The largest compressive force in a single bearing was about 2000 kN or 450 kips (about 40% of the static weight of the building) and the largest tensile force was 453 kN (102 kips), both observed during RRS88. The variation in axial force during RRS88 was caused by the vertical excitation. In general, cavitation, or tensile rupture of the rubber

matrix, is expected at a negative pressure =  $3G$  (Constantinou et al. 2007), where  $G$  is the shear modulus of the rubber. Taking  $G$  to equal the design value of 0.41 MPa (0.06 ksi) (Table 3-3), the approximate tensile force for cavitation in these LR bearings is 476 kN (107 kips), which only slightly exceeds the peak tensile force observed. Thus, the East LR bearing may have been on the verge of cavitation, or cavitation may have actually occurred, preventing the peak tensile force from going beyond the observed value.

Figure 5-10 illustrates the peak axial force in compression and tension for each LR bearing in each simulation, both absolute and normalized by the static force in the bearing at the start of the test program. Throughout the simulations, the South bearing was generally subjected to the largest compressive force, and the West bearing was subjected to the smallest compressive force (Figure 5-10(a)), which was in proportion to the static weight carried on the bearings. However, the *normalized* compressive force was largest in the West bearing, which carried the smallest static force, and smallest in the South bearing, which carried the largest static force (Figure 5-10(b)). Thus, the variation in compressive force, computed as a percentage of the static load, increased as the static load decreased. The largest tensile force generally occurred in the East LR (Figure 5-10(c)), which did not carry the greatest or least static force, but was usually subjected to the largest displacement (Figure 5-2). At large lateral displacements, a portion of the axial forces in the LR bearings were observed to transfer to the CL bearings, in some cases causing the LR bearings to be subjected to tension. Since the displacement demands were largest in the East bearing, the largest tensile forces occurred in the East bearing. The phenomenon of load transfer between LR and CL bearings is documented in Section 6.2.

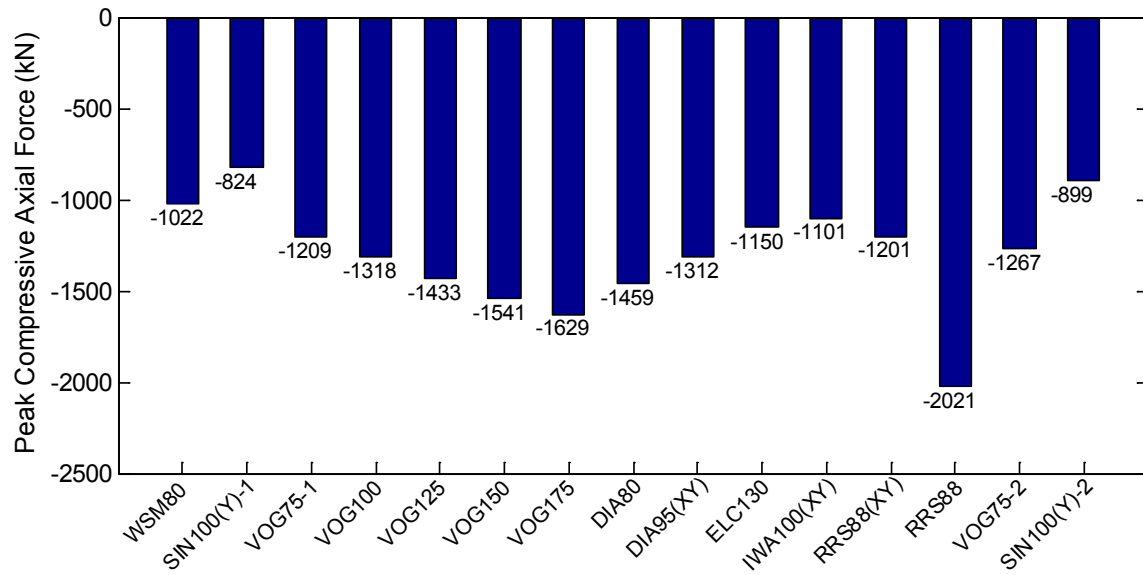


**Figure 5-8 Peak compressive force in any LR bearing for each earthquake simulation**

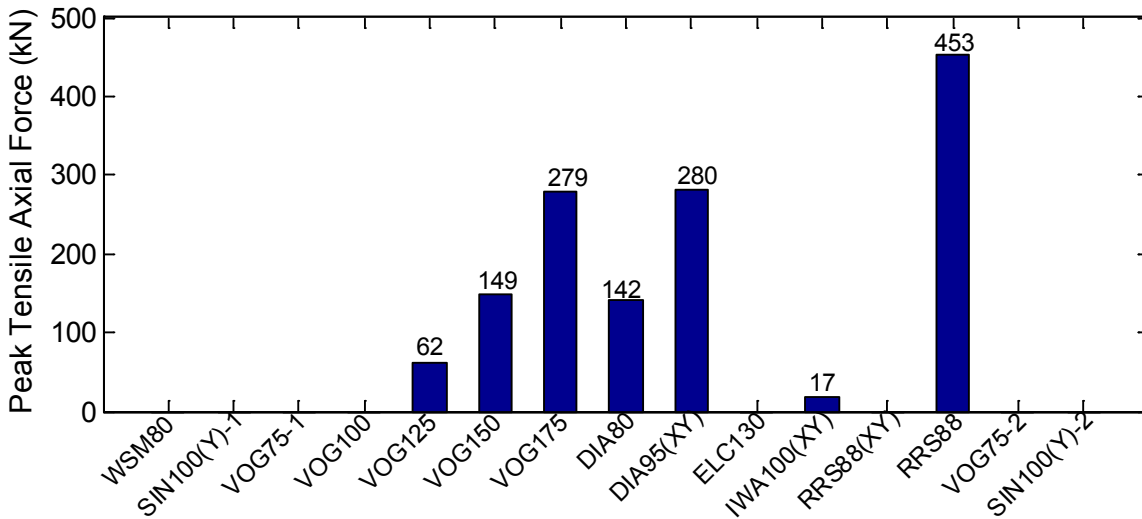


**Figure 5-9 Peak tensile force in any LR bearing for each earthquake simulation. (A tensile force of zero indicates that tension was not observed)**

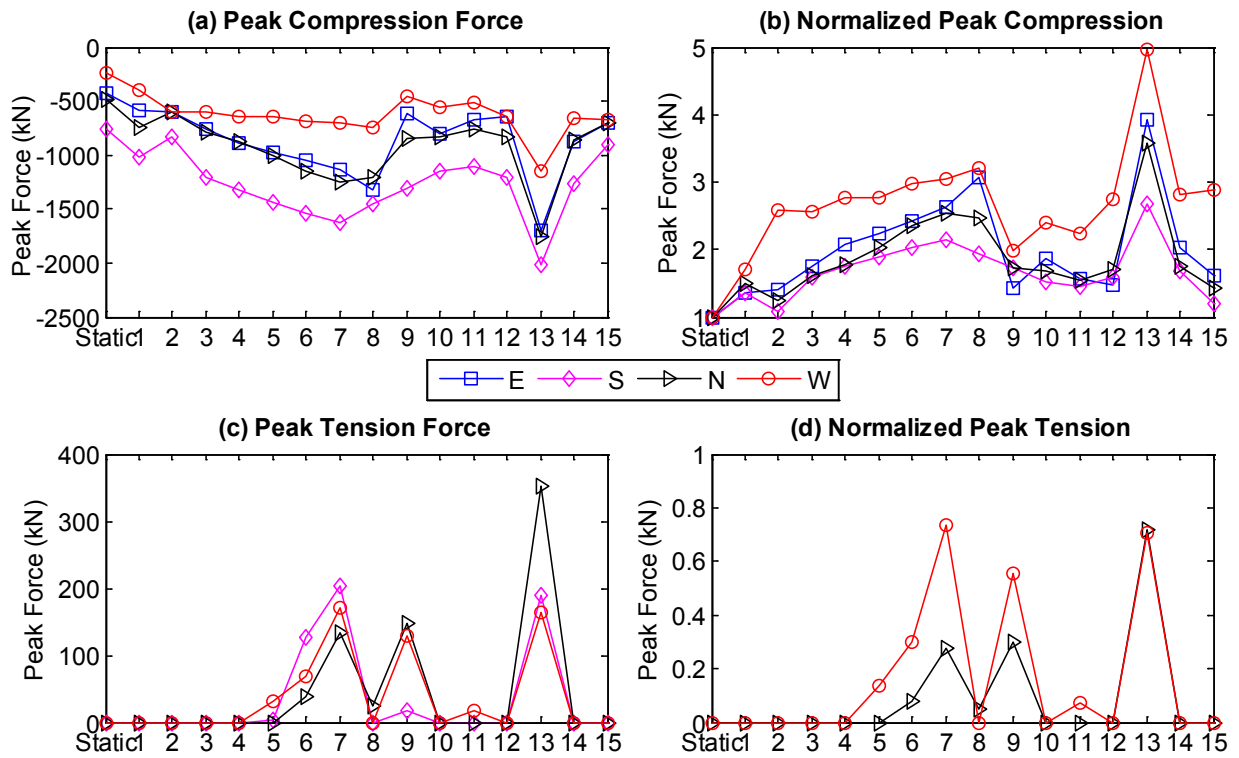


**Figure 5-10 Peak axial forces in each LR bearing for each simulation: (a) Peak compression force, (b) peak normalized compression force, (c) peak tension force, and (d) normalized peak tension force**

## 5.5 Isolation System Re-Centering

The displacement recorded at the location of each LR bearing at the end of every simulation – referred to as permanent displacement - is shown in Figure 5-11. Prior to the 8<sup>th</sup> simulation (DIA80), the peak permanent displacement at any isolator location was about 0.5 cm (0.2 in). A sudden increase in the permanent displacement was observed in the x and y directions at the East and North LRB locations, respectively, at simulation #8. This permanent displacement recorded in the sensors reflected is believed to be a combination of permanent deformation in the bearings and sliding of the steel connecting plate.

From the inspection pictures taken at the end of the 1<sup>st</sup> day of testing which directly followed DIA80 (Figure 5-12), the bottom steel plate of the East LRB slid about 1.1 cm (0.4 in). It cannot be determined whether the slippage occurred during trial 8 or trial 7. However, as later shown in Section 6.1, slippage of the bolts connecting the LRB bottom steel plate to the supporting steel hexagonal plate of the load cell occurred as early as the 5<sup>th</sup> trial (VOG125), which led to the sliding of the bottom plate seen in Figure 5-12. If the sliding of the steel plate had not occurred, we believe that the permanent displacement in the bearings would have been limited to that observed in the first few simulations - around 0.5 cm (0.2 in) - which is insignificant.

Prior relaxation tests performed on LR bearings (Constantinou et al. 2007) suggested that the characteristic strength of LR bearings drops markedly under static conditions. Specifically, a bearing was returned to zero displacement following a sequence of large velocity cyclic loading and an imposed permanent displacement. When returned to zero displacement, the characteristic dropped to about 1/3 of its starting value after 8 minutes and 1/4 of its starting

value after 30 minutes. The drop in characteristic strength due to relaxation suggests that residual permanent displacements in the bearings would disappear over time.

The relaxation effect was evaluated in the present test program by considering any changes looking for reductions in permanent displacement from the end of one simulation to the start of the next, which is illustrated separately for each bearing in Figure 5-13. Recall that the average time between simulations was about 50 minutes. Figure 5-13 does not indicate consistent reductions any significant changes in permanent displacements in the sensors from the end of one simulation to the start of the next that would be are consistent with a relaxation effect. Relaxation The changes in permanent displacement may have been inconsistent (sometimes increasing and sometimes decreasing) may not have been observed since the bearing displacements, as computed by the string pots, were not independent but rather constrained to move together through the assumed base diaphragm constraint. Nonetheless, the observed permanent displacements were not significant.

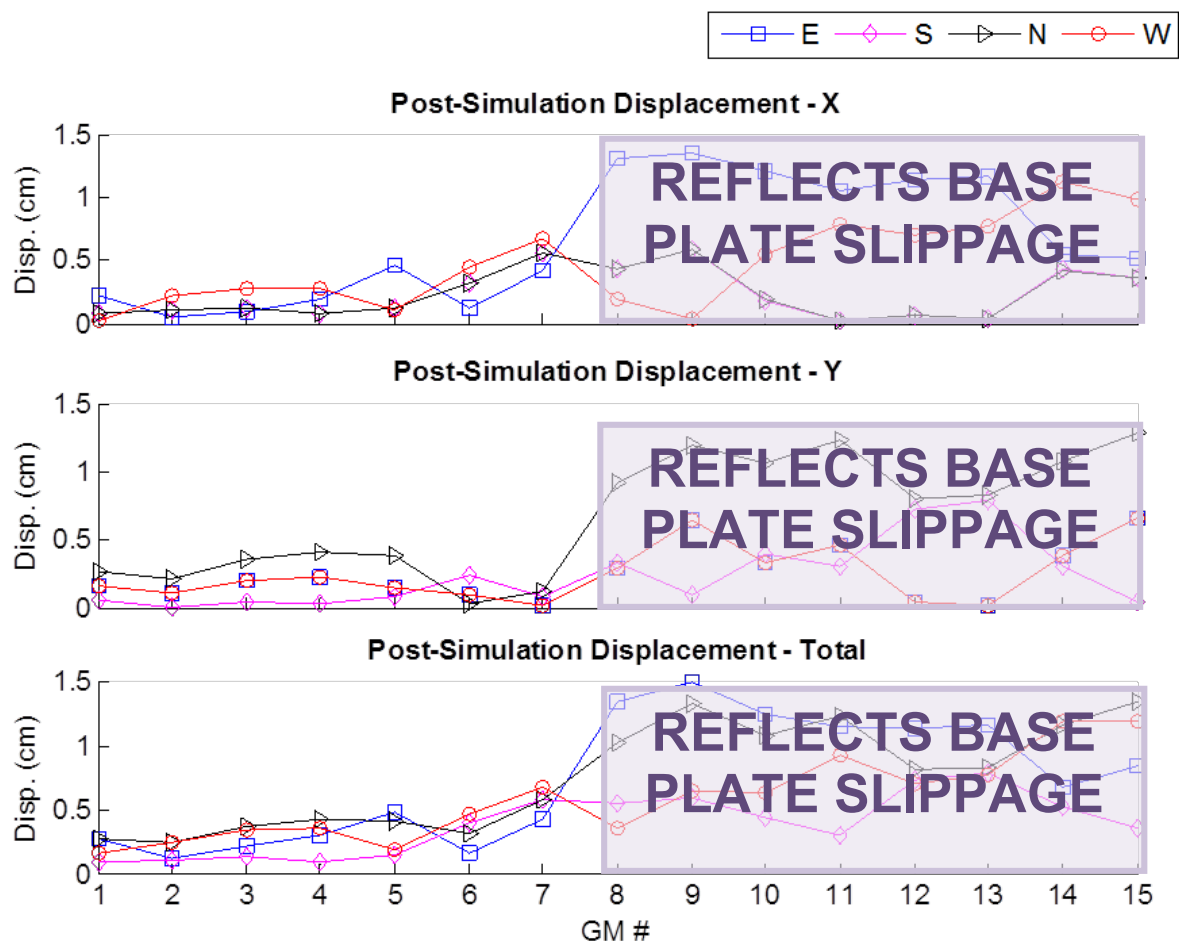


**Figure 5-11 X-direction, y-direction, and total (vector sum) displacement recorded in each LR bearing at the end of every earthquake simulation**



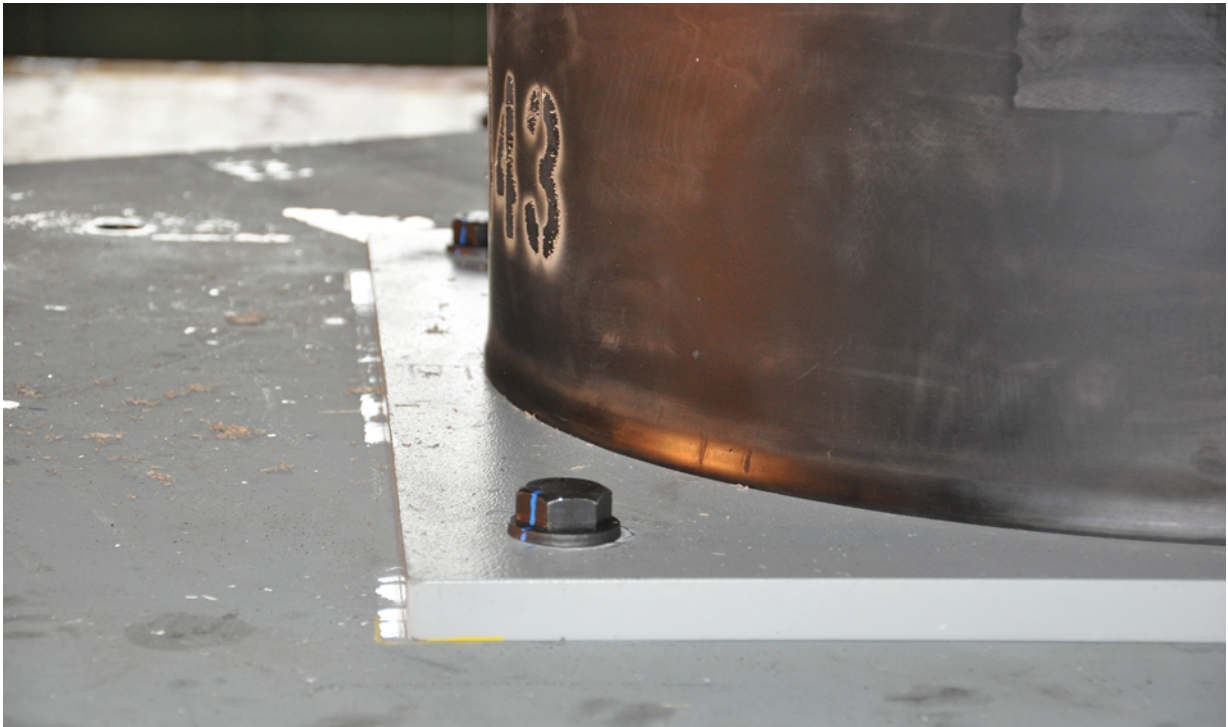


**Figure 5-12** Permanent displacement of around 1.1 cm on the East bearing due to sliding of the bottom steel plate

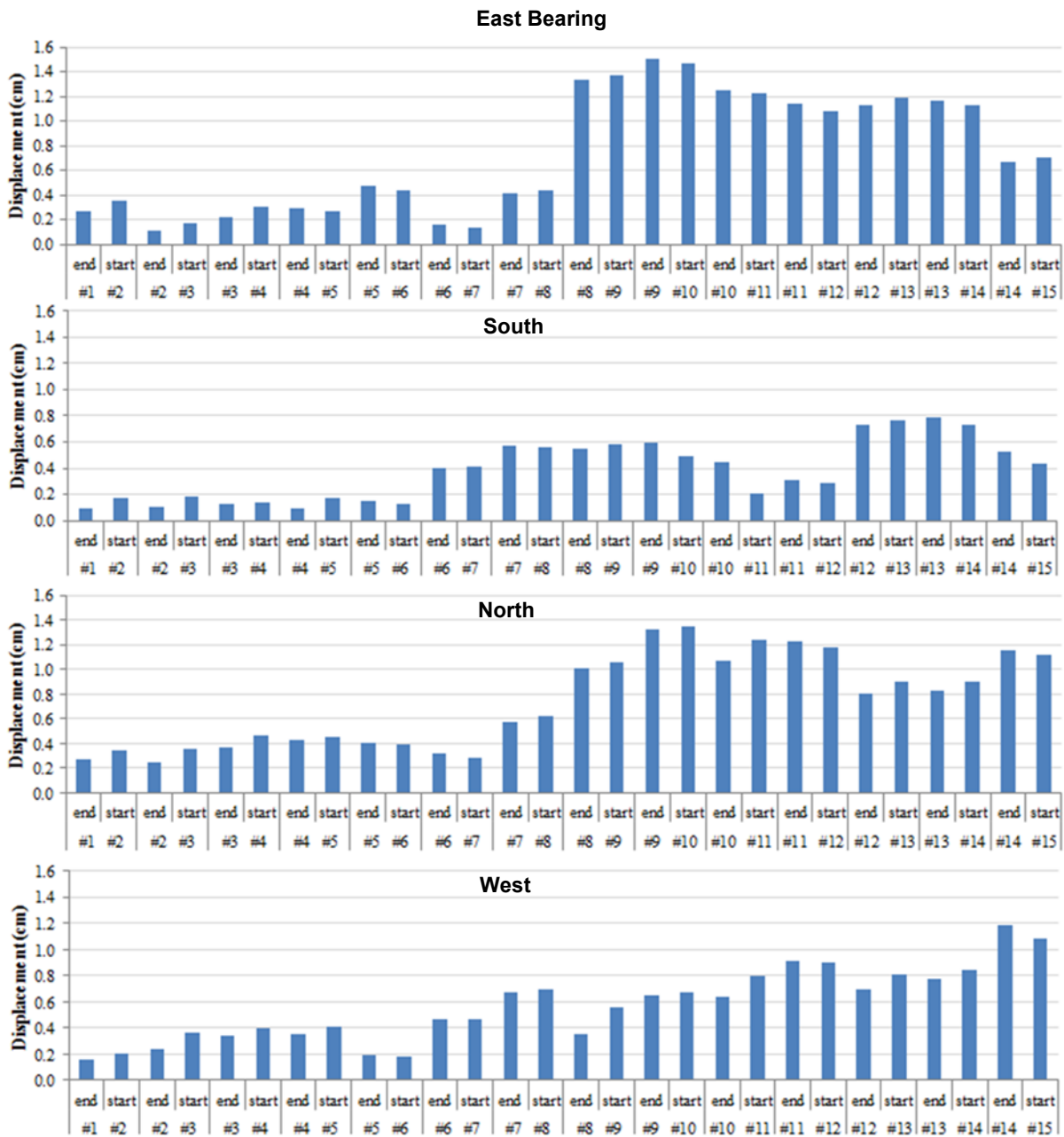


Figure 5-13 Permanent displacement at the location of each LR bearing at the end of one simulation compared to the beginning of the next

## 5.6 Floor Accelerations in the Testbed Building

The peak acceleration profile of the building (peak acceleration versus floor level) in both horizontal directions for all earthquake simulations is shown in Figure 5-14. Accelerations from multiple sensors were averaged as described in Section 4.6.3 based on the acceleration sensor layout in Figure 4-11. Although most individual simulations are not identified by input excitation, this plot format depicts the range of accelerations observed. The acceleration profile shape was similar for most excitations, which was almost linear from the base through the 4<sup>th</sup> floor followed by an increase in acceleration at the 5<sup>th</sup> and roof floors. The isolation system was very effective

in attenuating the acceleration in the superstructure. Outliers are identified in Figure 5-14, which include on the low side: the service level motion Westmorland (WSM80) in both horizontal directions, and the sine wave simulations (SIN100(Y)- 1 & SIN100(Y)-2)) in the x-direction due to the unidirectional input; on the high side: Rinaldi (RRS88) in the y-direction as a result of the strong vertical input. The influence of vertical excitation on the overall response of the structure, with special attention to the RRS88 simulation, is explored in Chapter 10.

With the exception of RRS88, larger peak ground accelerations led to greater attenuation of acceleration as expected. Although it cannot represent variability due to ground motion frequency content, the reduction in floor accelerations relative to PGA is often used to quantify the effectiveness of the isolation system. During Diablo 95%, one of the largest motions applied to the system with PGA in the x-direction = 1g, the observed peak roof acceleration was 0.45g, which was a 65% decrease relative to PGA. Excluding the outliers, PGA ranged from around 0.3g to 1g in the x-direction and 0.24g to 1.18g in the y-direction, while base level peak acceleration (just above the isolators) ranged from 0.19g to 0.5g in both directions. For Rinaldi 88, the roof acceleration in the y-direction was greater than the PGA.

To directly investigate the floor acceleration as a function of ground motion intensity, the floor acceleration profiles, both absolute and normalized by PGA, are plotted for the increasing intensity Vogtle excitations (VOG75, VOG100, VOG125, VOG150 and VOG175) in Figure 5-15. Recall that a low pass filter with a cutoff frequency of 50 Hz was applied to all signals (Figure 4-5). The absolute floor accelerations increased consistently with increasing ground intensity, but the normalized accelerations decreased with increasing ground intensity as expected. The influence of vertical excitation is considered by comparing the absolute and normalized acceleration profiles for Diablo 95% (XY), Diablo 80% and Rinaldi 88% (XY and 3D) (Figure 5-16). Even though the intensity of the Diablo 95% motion was substantially greater than the Diablo 80% motion, the floor accelerations were greater in Diablo 80%, which indicates that vertical excitation affected the recorded horizontal floor acceleration. For the Rinaldi motion, a significant amplification of horizontal floor acceleration was observed for 3D shaking relative to XY (horizontal only) shaking, which suggests a horizontal-vertical coupling phenomenon (see Chapter 10).

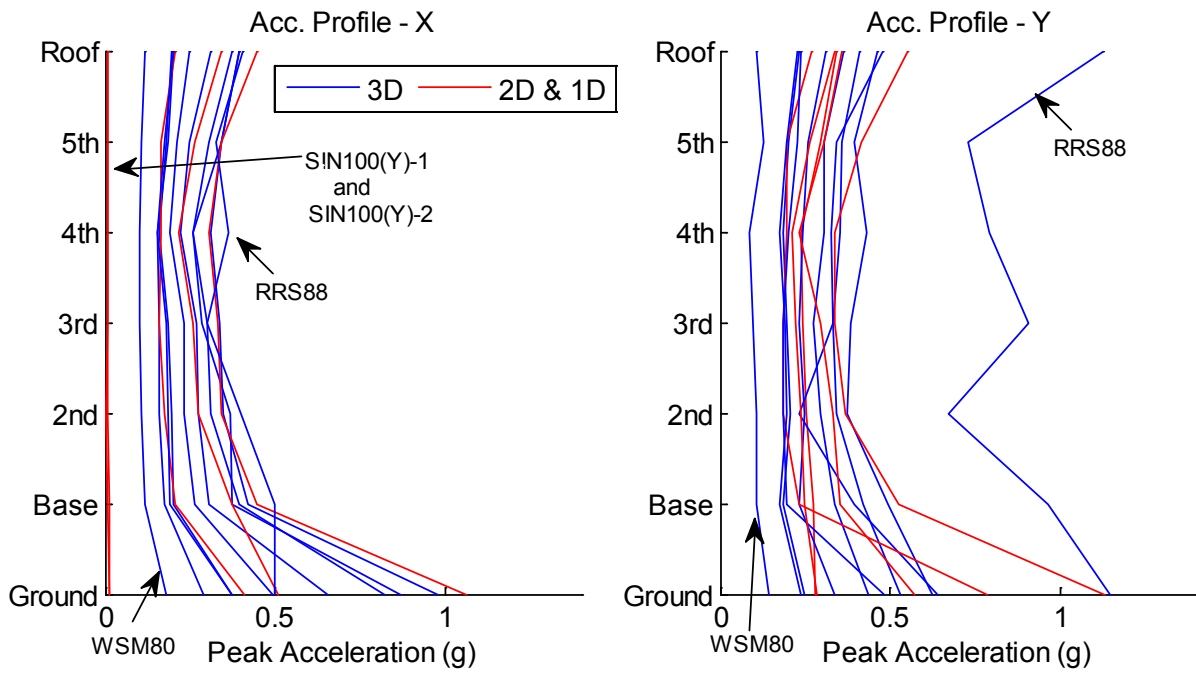


**Figure 5-14 Peak acceleration profile for all simulations in both horizontal directions**

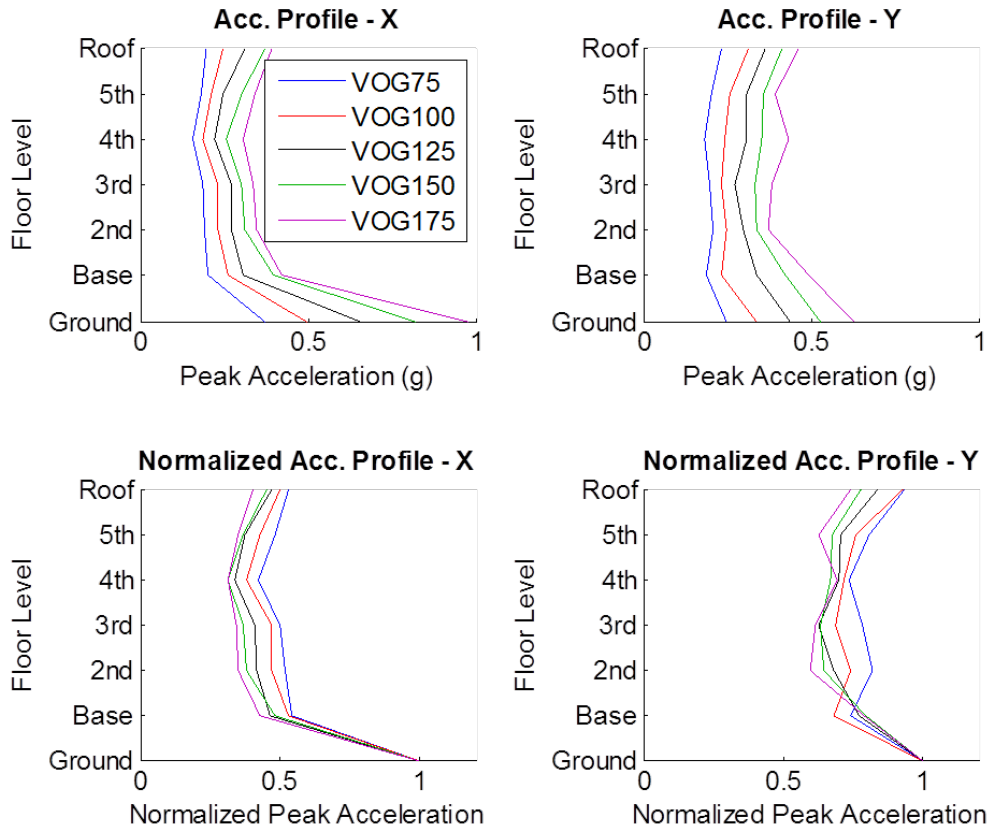


**Figure 5-15 Peak floor acceleration profiles for increasing intensity of Vogtle input excitation (75% - 175%)**

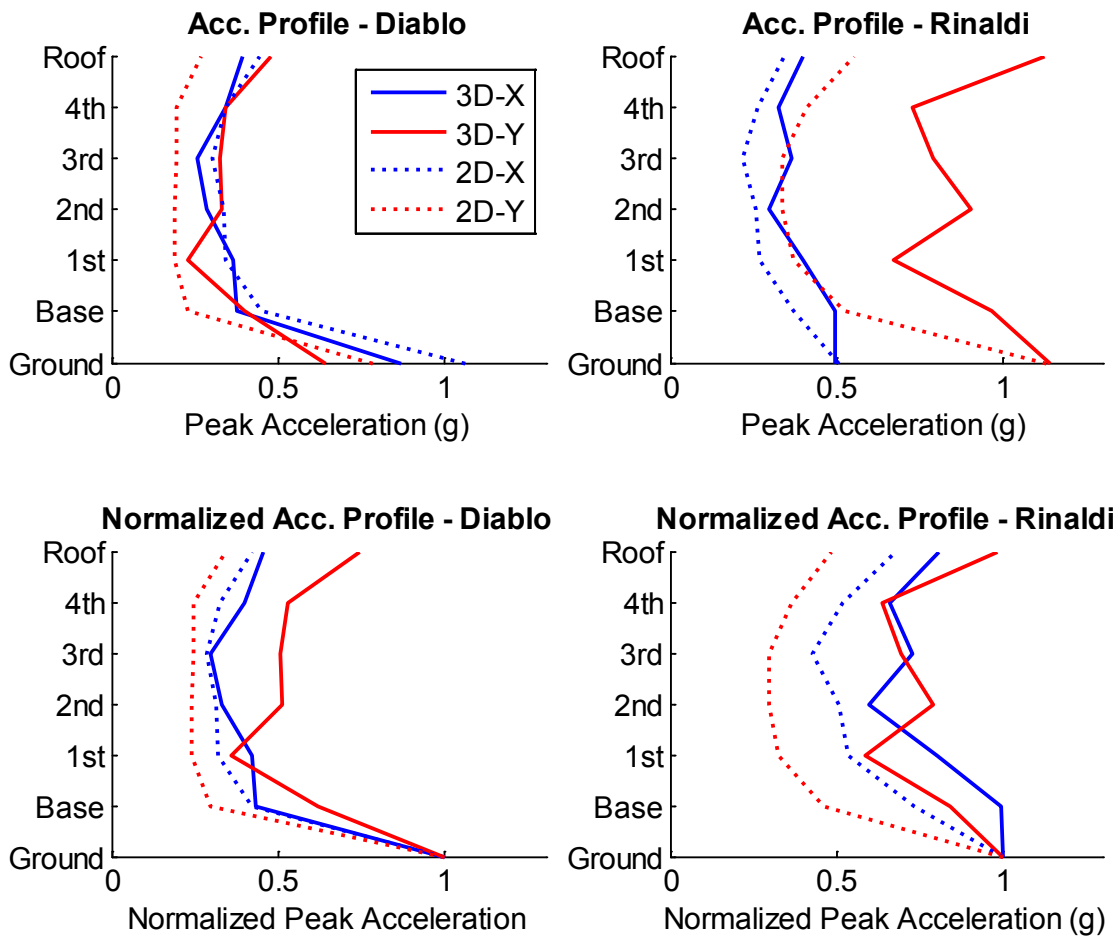


**Figure 5-16 Peak absolute and normalized acceleration profile comparing XY and 3D excitations for Diablo (95% and 80% respectively) and Rinaldi (88%)**

### 5.7 Story Drifts in Testbed Building

The peak story drift profiles (peak drift versus story level) in both horizontal directions for all earthquake simulations are shown in Figure 5-17. The drifts were calculated at the geometric center of each story level as described in Section 4.6.3. The peak drift in either direction occurred in the 2<sup>nd</sup> floor for all simulations, with the exception of both sine wave simulations, which incurred negligible drifts in the x-direction. The story drift decreased from the 2<sup>nd</sup> floor to the roof level, where the peak roof drift was generally less than the first story drift.

The drifts for both RRS88(XY) and RRS88 in the y-direction were noticeably larger than the drifts observed in any other motion. This increase in drift was due to the predominance of low frequency components associated with the near-fault motion. The input acceleration history for the RRS88 simulation, shown in Figure 4-18, contains a strong pulse with a duration of about 1 sec at the instant of peak acceleration in the y-direction. The relative intensity of ground acceleration in the x and y-directions was consistent with the trend of the drift profiles. Like the accelerations, the drifts increased significantly from RRS2D to RRS3D. The drift in the 5<sup>th</sup> floor was larger than the 4<sup>th</sup> floor in the y-direction for RRS3D, which is consistent with the acceleration profile of Figure 5-16.

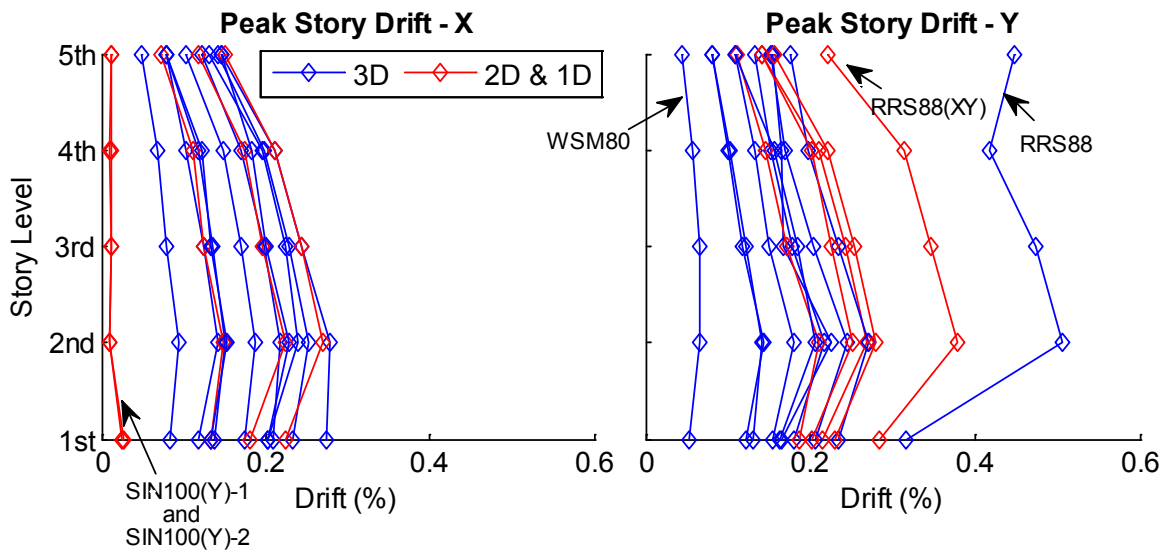


**Figure 5-17 Peak story drift throughout the height of the building for all excitations in x and y directions**



## 6. TECHNICAL RESPONSE OF HYBRID LR ISOLATION SYSTEM

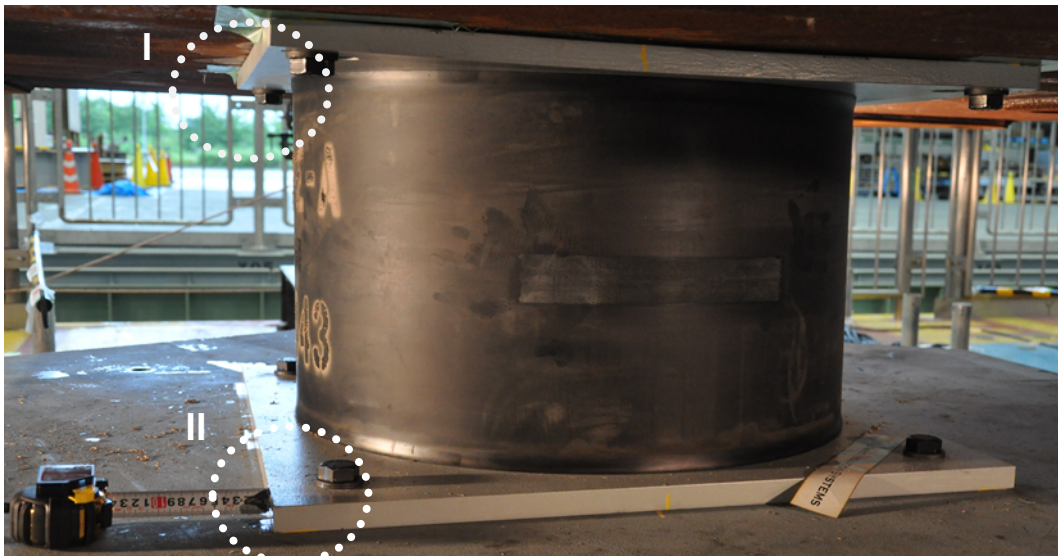
In this chapter, specific technical aspects germane to the response of the hybrid LR isolation system are explored. This is the first time that LR bearings and CL were tested as a hybrid isolation system on an earthquake simulator. Thus, unique load transfer between the two types of devices and stability aspects of the system are explored in depth. The topics discussed in this chapter include bolt slip, load transfer, and repeatability of the isolation system response after many tests.

### 6.1 Bolt Slip in LR Bearings

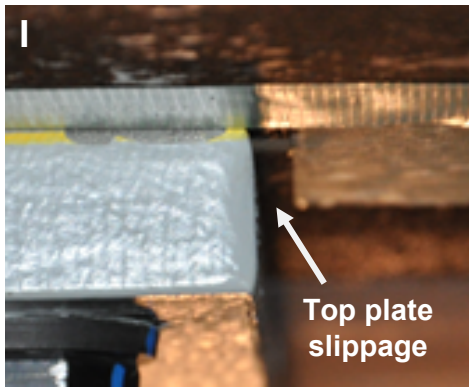
Due to a variety of conditions unique to this experimental program, the bolted connections securing the LR bearings to the structure above and steel connecting plates below did not satisfy slip critical criteria, and slippage of the bolts was observed. The connections were anticipated to reach the slip critical limit at bearing displacements of about 40 to 45 cm (16-18 in), but the bearings were tested out to displacements of 55 cm (22 in). In practice, the bearings would never be designed with low capacity at the connection level. The following factors influenced the connection design: 1) technical difficulties and prohibitive cost associated with drilling and tapping holes in the base of the testbed structure from beneath prompted the project team to select the smallest possible bolt size for the connection. 2) The bolt holes were oversized by 9 mm (0.4 in), deviating from standard practice, to accommodate ease of installation when lowering the testbed structure by crane over the 9 pre-installed isolators. 3) During pre-test planning and negotiation, when the connection design was finalized, it was doubtful that the bearings would be tested beyond 40 cm (16 in). Since bolt slip can easily be avoided in practice, its occurrence and subsequent influence on the response of the isolated building are documented briefly here for completeness.

As mentioned above, slippage was observed in the bolts that secured the LR bearing top connecting plate to the base of the structure above and the bottom connecting plate to the steel hex plate of the load cell assembly. Evidence of bolt slip included: 1) loud banging noise heard in-phase with the displacement cycles and subsequently observed instantaneous force drops and/or spikes in the LR bearing forces recorded by the load cells, and 2) movement of the LR bearings relative to the structure above and below observed in post-test inspection, which was shown in Figure 5-12 and is further illustrated in Figure 6-1 below.

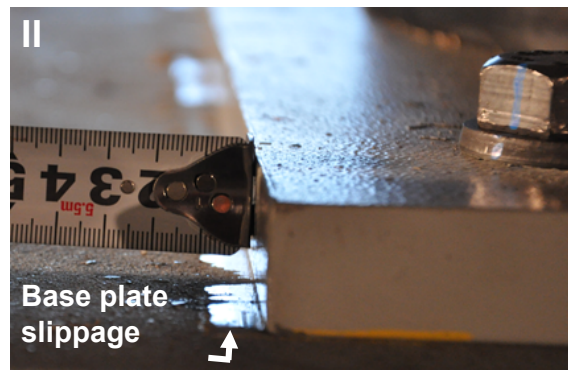
The bolt slip was first observed during Vogtle 125%, and continued to be observed throughout the simulation sequence, wherein larger displacements in the bearings increased the instances of bolt slip. Some slip was observed in all four LRBs, but the largest force spikes and drops occurred in the East bearing. Figures 6-2 plot snapshots of the *unfiltered* force history of the East bearing (LRB-E) in the x and y-directions for 8 of the 15 simulations, which are labeled by trial number, the 3 letter abbreviation for the ground motion, and the scale factor. (Recall that, as stated in Chapter 4, all data shown is filtered unless otherwise indicated.) In these figures, the force drops are first observed in Vogtle 125% around 11.5 sec and 12 sec. In the next trial (Vogtle 150%), additional drops are observed at other time instances, and spikes are observed at 11.5 and 12 seconds. Then, in Vogtle 175%, even more spikes and drops are observed. After Vogtle 175%, force drops and spikes continue to appear (e.g. Diablo 80% at about 15 sec) but with decreasing intensity. The drops and spikes are also observed in the bearing hysteresis loops, such as those plotted for LRB-E during Vogtle 125% and Vogtle 150% (Figure 6-3). The force drops and spikes tend to be observed during large displacement cycles just before the peak displacement is reached.



(a)



(b)



(c)

**Figure 6-1 Movement of (a) East LR bearing relative to (b) top and (c) bottom plates.**



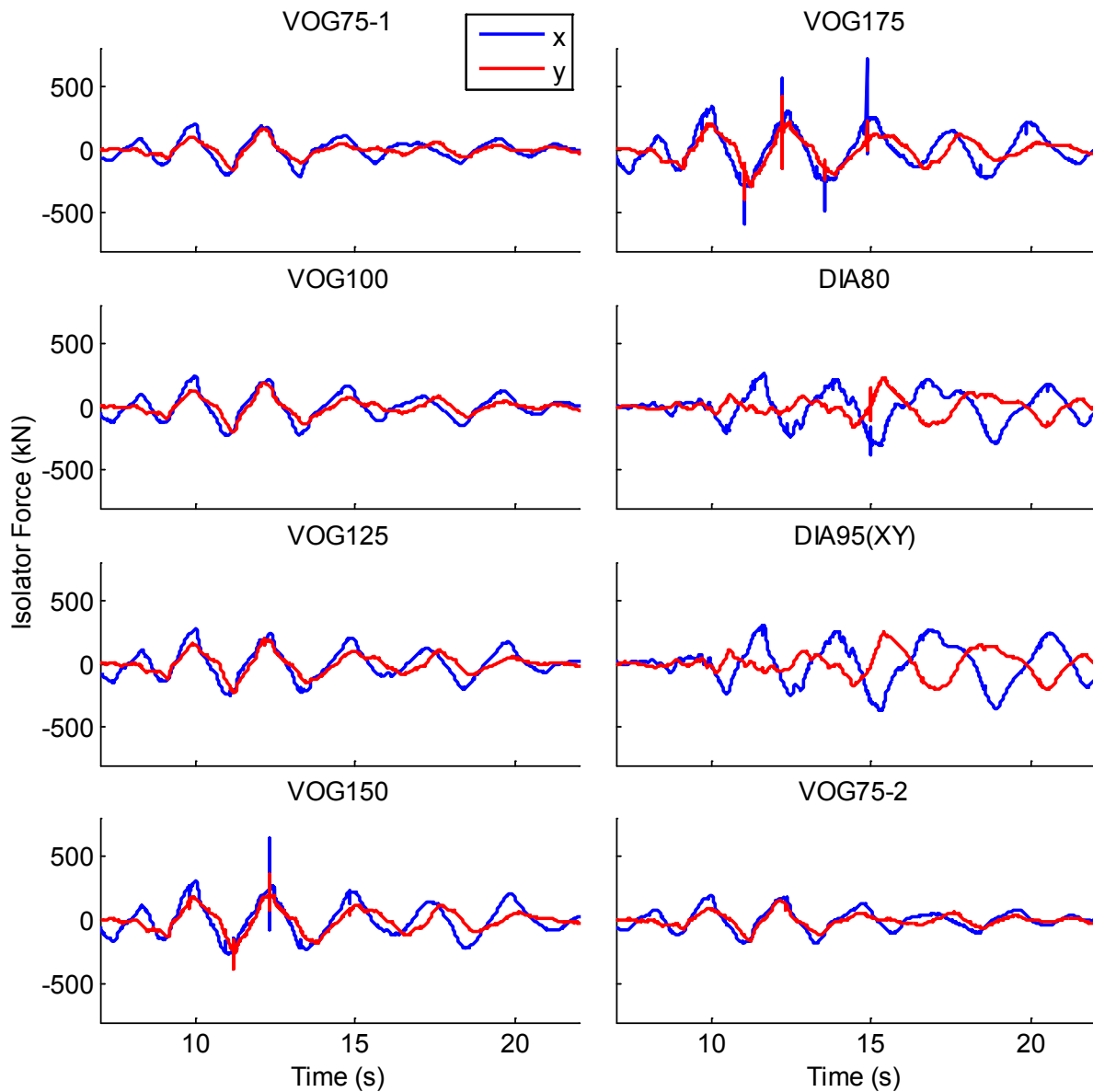


**Figure 6-2 Horizontal force history of the East bearing (LRB-E) in the x- and y-directions for a subset of the trials**

The horizontal and vertical force histories for all four LR bearings are shown in Figure 6-4 for Vogtle 150%, which demonstrates that the greatest amount of bolt slip occurred in LRB-E. During Vogtle 150%, LRB-E is the only bearing that experienced both substantial force spikes and force drops. Several force drops are observed in LRB-W, but they are small in intensity compared to LRB-E. Only one small drop/spike for LRB-N (around 12 sec), and two in LRB-S are evident (Figure 6-4).

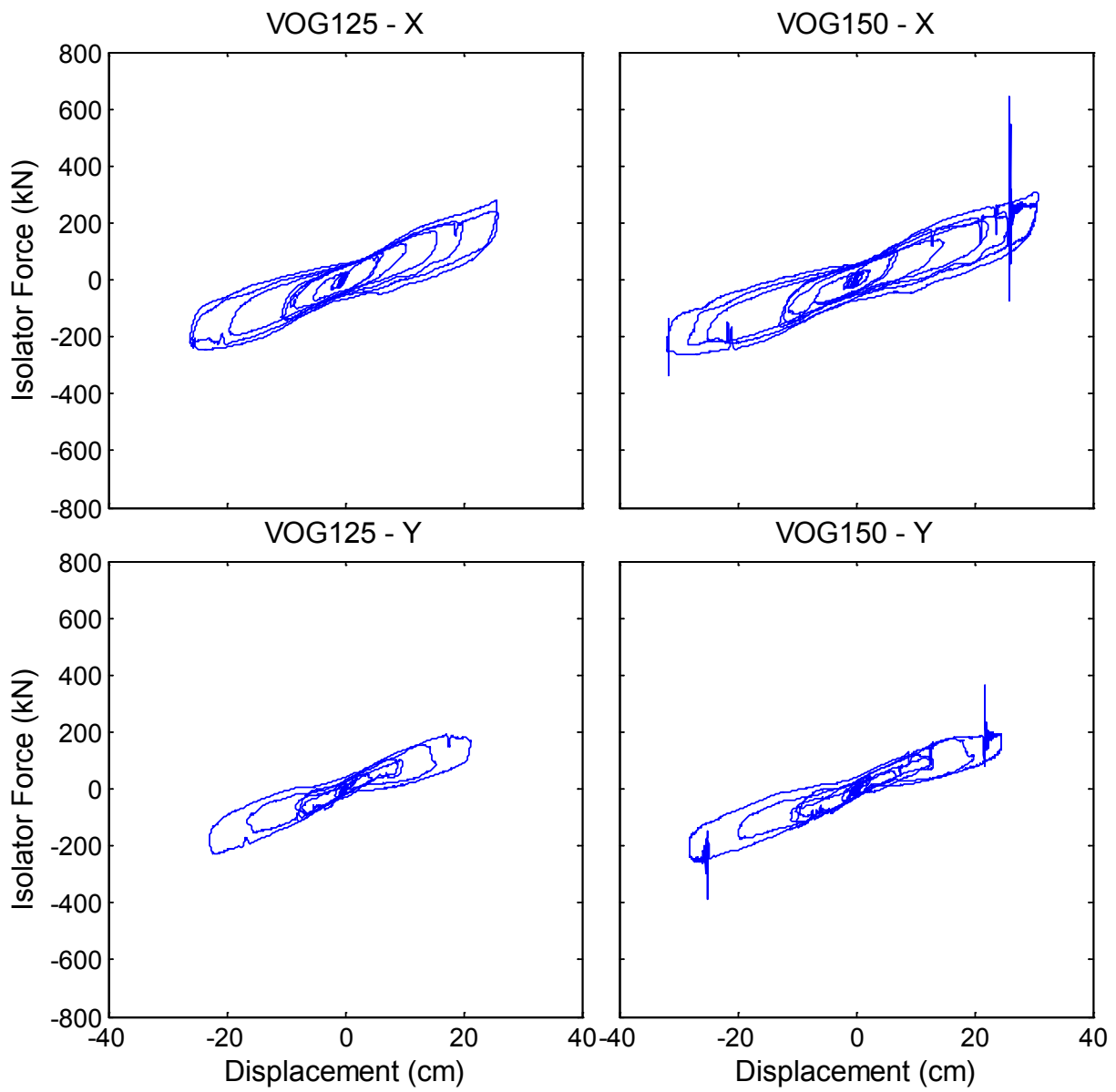
The synchronized vertical force histories of each bearing are also plotted in Figure 6-4 to provide additional insight as to why the bolt slip may have occurred. One proposed theory is that bearing tension contributed to the bolt slip. The addition of CL bearings to the isolation system did not entirely prevent tension in the LR bearings, which is discussed in the next section. During the Vogtle 150% record, tension (bearing vertical force greater than zero in Figure 6-4) is observed more frequently and with larger intensity in LRB-E and LRB-W, which also have the

most obvious horizontal force drops/spikes. The instances of bolt slip seen in this figure do not align with the instances of peak tension, but horizontal force drops/spikes always occur after tension has been observed in the bearing. At the same time, LRB-E is subjected to the largest displacement demands (42.3 cm (16.7 in) in Vogtle 150% compared to 35.7 cm (14.1 in) in LRB-W), and thus experiences a larger shear force that makes it more susceptible to bolt slip.

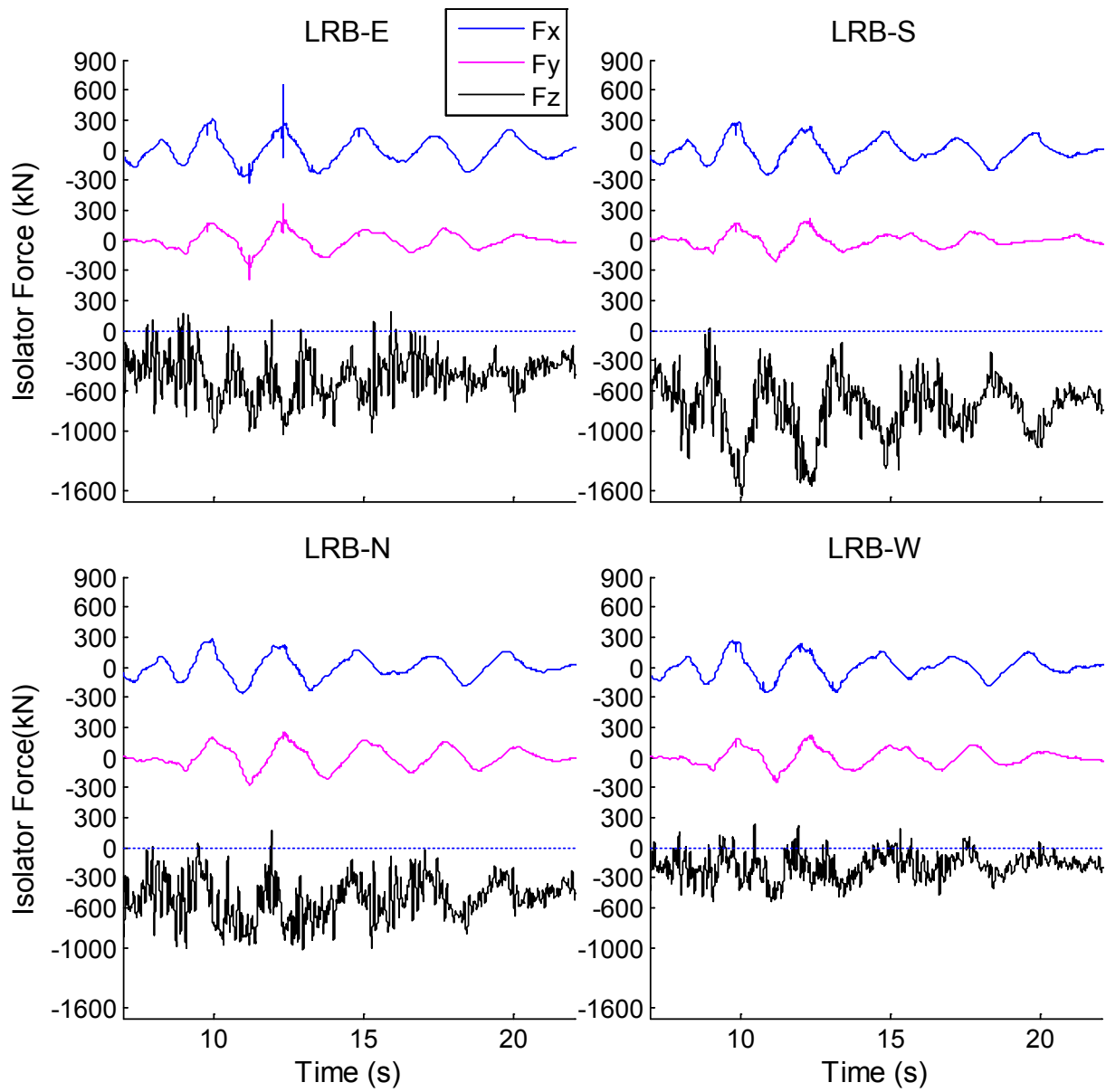
Figure 6-5 plots the unfiltered force in LRB-E and unfiltered accelerations in the SE column sensors at all floors in x and y-directions, respectively, for Vogtle 150%. In this figure, a spike in the bearing horizontal force is always preceded by a small force drop. The following explanation is consistent with the drop/spike pattern. After a large tension excursion, the bolts start to slip and move with respect to the oversized holes. The bolt movement stops the bearing movement, causing it to instantaneously unload, corresponding to the first drop in force. If the bolts reach the other side of the oversized hole, an impact occurs, resulting in a force spike and a loud banging noise. Due to the instantaneous nature of the impact, dynamic amplification occurs, causing what appears to be an instantaneous spike/drop, but is actually very high frequency oscillation.

Figure 6-5 also shows that the bolt slip induces a dynamic amplification in the floor accelerations that diminishes with increasing height in the building. The acceleration spikes appear to be timed with the first force drop associated with the start of bolt slip and not the second force spike/drop associated with impact of the bolt against the other side of the hole. In the overall test program, bolt slip (by itself) did not appear to affect the performance of nonstructural components or cause disruption of contents, located on the 4<sup>th</sup> floor and above. There is no evidence of whether nonstructural components on the lower floors would have been affected by the bolt slip. Filtering the recorded force and acceleration data significantly reduced the drops and spikes resulting from bolt slip, but did not completely eliminate them.

In summary, in this experimental program, the bolt slip did not appear to affect the response of the isolation system aside from the drops/spikes in force, and the adverse effects on the structural response were limited. However, the possibility that increased acceleration would affect the response of nonstructural components and contents or compromise performance in any way is an unnecessary risk. The observations from these experiments reinforce the conclusion that bearings should always be designed with slip critical connections, as they routinely are in practice.



**Figure 6-3 X and y-direction hysteresis loops (horizontal force vs. displacement) of the East bearing (LRB-E) during Vogtle 125% and Vogtle 150%**



**Figure 6-4 Horizontal ( $F_x$  and  $F_y$ ) and vertical ( $F_z$ ) force history of all four LR bearings during Vogtle 150%**

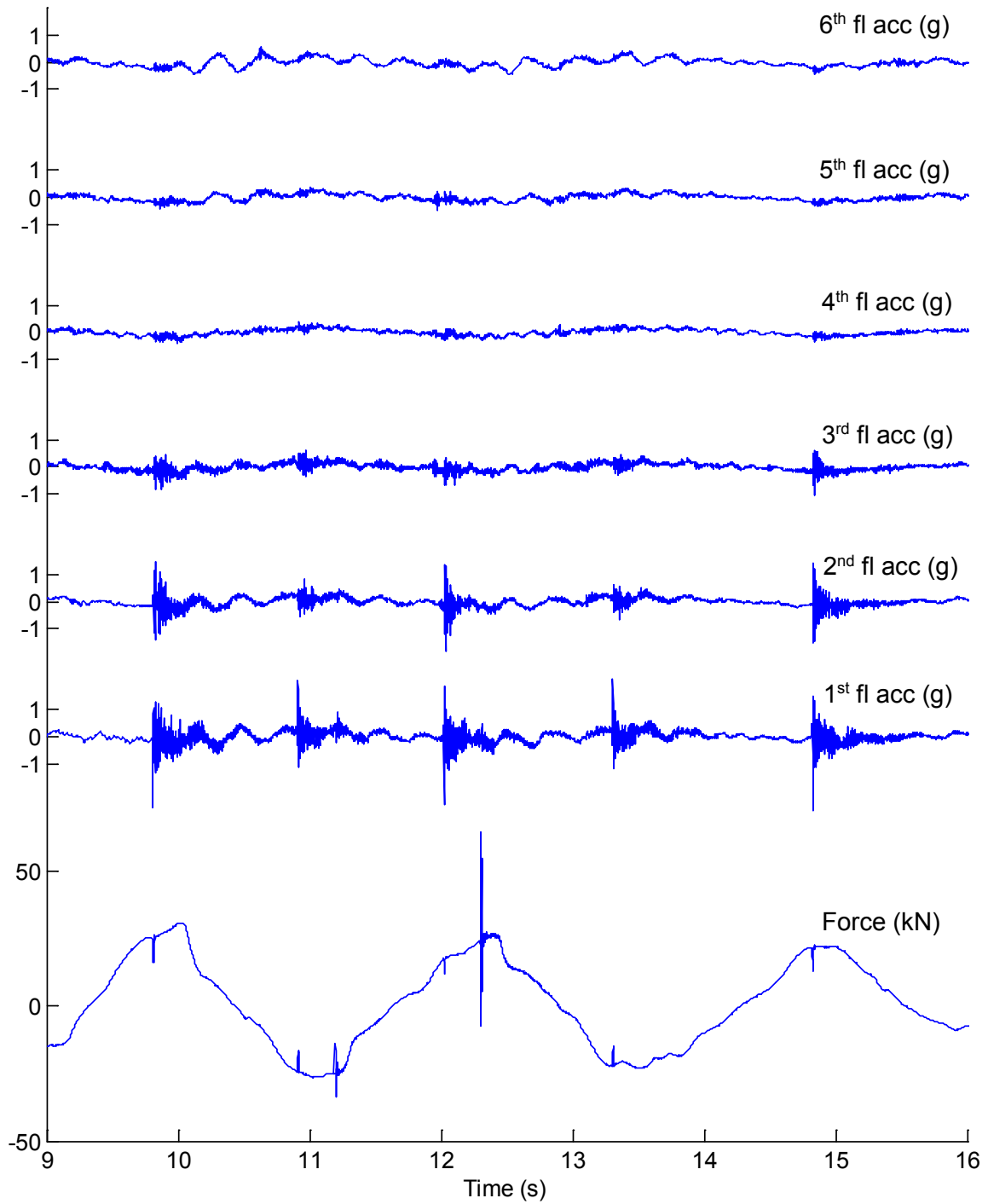


**Figure 6-5 Propagation of bolt slip through the height of the structure in x-direction during Vogtle 150%; unfiltered horizontal force in LRB-E and 1<sup>st</sup> – 6<sup>th</sup> floor acceleration in SE column**

## 6.2 Transfer of Load Between Bearings

Axial force transfer between the LR bearings and the CL bearings over the course of the simulations was expected. LR bearings, when subjected to combined compressive load and lateral displacement, reduce in height, as shown in Figure 6-6(a), where  $P$  is the axial force and  $\delta$  is the downward deflection or shortening. However, downward movement of the LR bearings is constrained by the rigidity of the base diaphragm and the axial stiffness of the CL bearings, which is about 2.5 times the stiffness of the LR bearings. The constraint generates an upward force  $F$  on the bearings (Figure 6-6(b)), which This causes load to redistribute from the LR bearings to other isolators. If  $P$  exceeds  $F$ , The net effect is a reduction in axial compressive force carried by the LR bearings occurs, while if  $F$  exceeds  $P$  and individual the LR bearings will may go into tension to satisfy the base diaphragm constraint. This type of behavior can occur at large displacements and is (unrelated to system overturning) to satisfy the base diaphragm constraint. We refer to this subsequently as the “load transfer” effect.

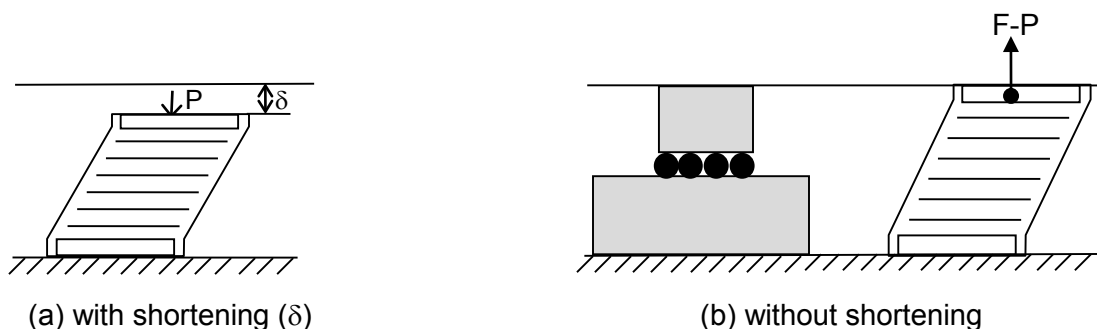


**Figure 6-6 Resultant action on LR bearings as a result of CL bearings and base diaphragm constraint**

Evidence of the load transfer effect was observed during the test program. Histories of isolator displacements and axial forces on individual LR bearings and summed over all LR bearings are shown for three different XY excitations: sine wave input (Figure 6-7), Diablo 95% (Figure 6-8) and Rinaldi 88% (Figure 6-9). The displacements shown have been computed by averaging displacements of LRB-E and LRB-W in the x-direction, and LRB-N and LRB-S in the y-direction; axial force is considered to be positive in tension. Recall that forces acting on the CL bearings were not measured during the experimental program. The sine wave simulation is the simplest to interpret because the input to the building was unidirectional in the y-direction, generating very little torsional response in the isolators. Vertical lines drawn through local (vector sum) peak displacements and extended through the axial force plots demonstrate that every time a peak displacement is reached (either local maximum or local minimum), a corresponding net reduction in total axial force of the 4 LR bearings (black line in Figure 6-7) is observed. The axial forces in individual LR bearings are more complex since overturning effects are present. LRB-N and LRB-S, which being close to the neutral axis of the building plan for y-direction input should not experience much overturning, also appear to consistently unload at every local displacement peak – max or min (Figure 6-7). The instant of least compressive axial force in the bearings does not exactly correspond to the instant of peak displacement shown, but is close enough that the load transfer trend is confirmed. With regard to individual bearings, LRB-W sustains maximum compression for displacements in the positive y-direction and minimum compression for displacements in the negative y-direction, while LRB-E experiences the opposite, which is the expected trend when subjected to overturning related axial force demands (Figure 6-7). Thus, for this excitation, the overturning effect in LRB-E and LRB-W is

stronger than the load transfer effect. However, fluctuation of the axial force between the displacement peaks suggests that both the overturning effect and the load transfer effect are contributing to the response.

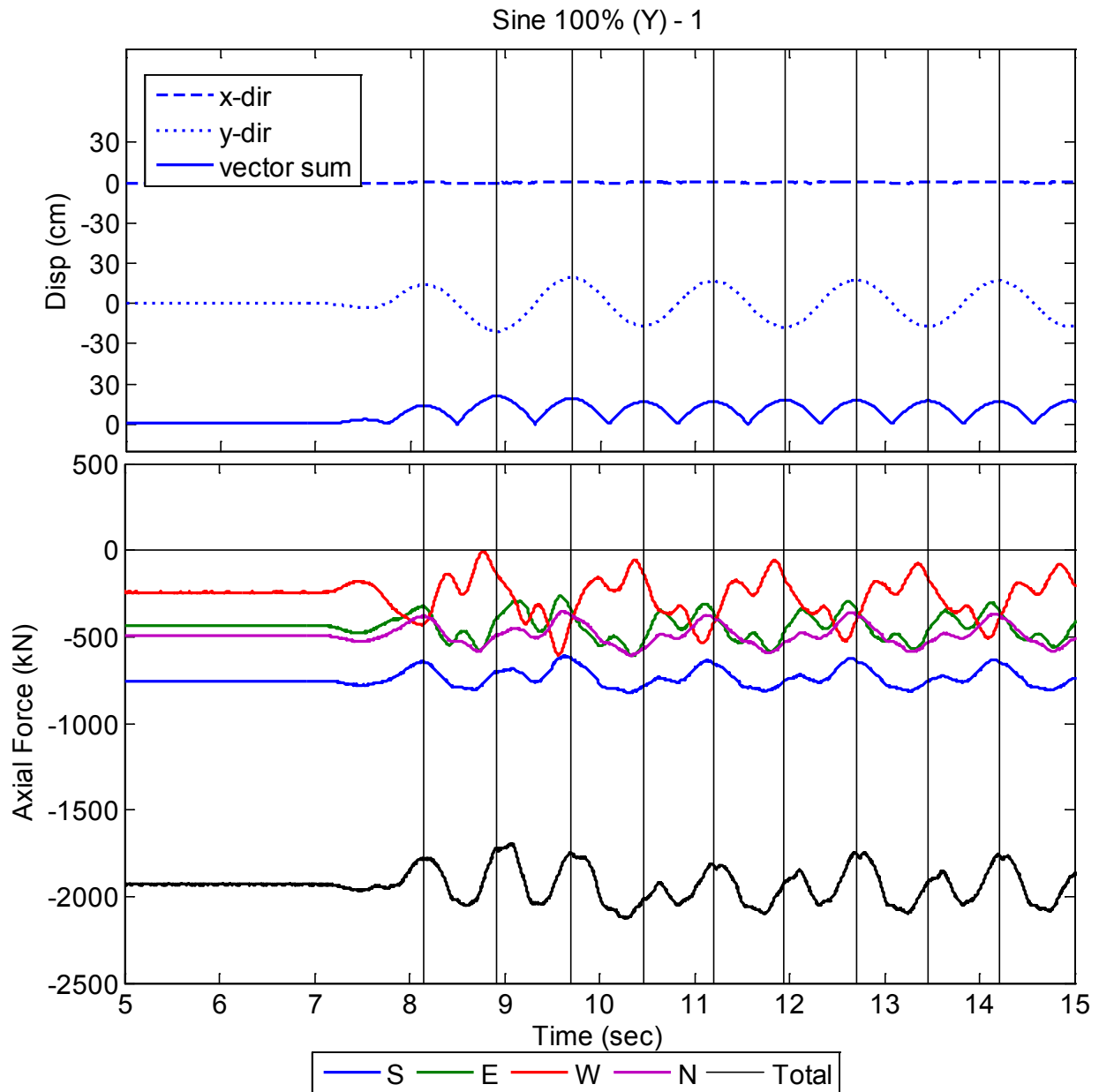


**Figure 6-7 History of average horizontal displacement (x, y and vector sum), and axial force in individual LR bearings and summed over all LR bearings for Sine Wave (XY)**

For Diablo 95% (XY) (Figure 6-8), substantial load transfer, as indicated by axial unloading of the LR bearings, occurs at 4 different time instants corresponding to peak displacements (combination of x and y-direction movement) observed at the center of the building. LRB-E sustains tension at every one of these time instants, and at two different instants (just after 15 sec and about 19 sec), the total axial force on the LR bearings exceeds 0, indicating that the entire weight of the building has shifted to the CL bearings. The load transfer effect is much

more significant for this simulation than the sine wave since the isolator displacement is much larger (55 cm or 22 in compared to 21 cm or 8 in, see Figure 5-1). As a result of the torsional demand on the isolation system discussed previously, the largest displacements are consistently observed in LRB-E, which is also subjected to the greatest tension.

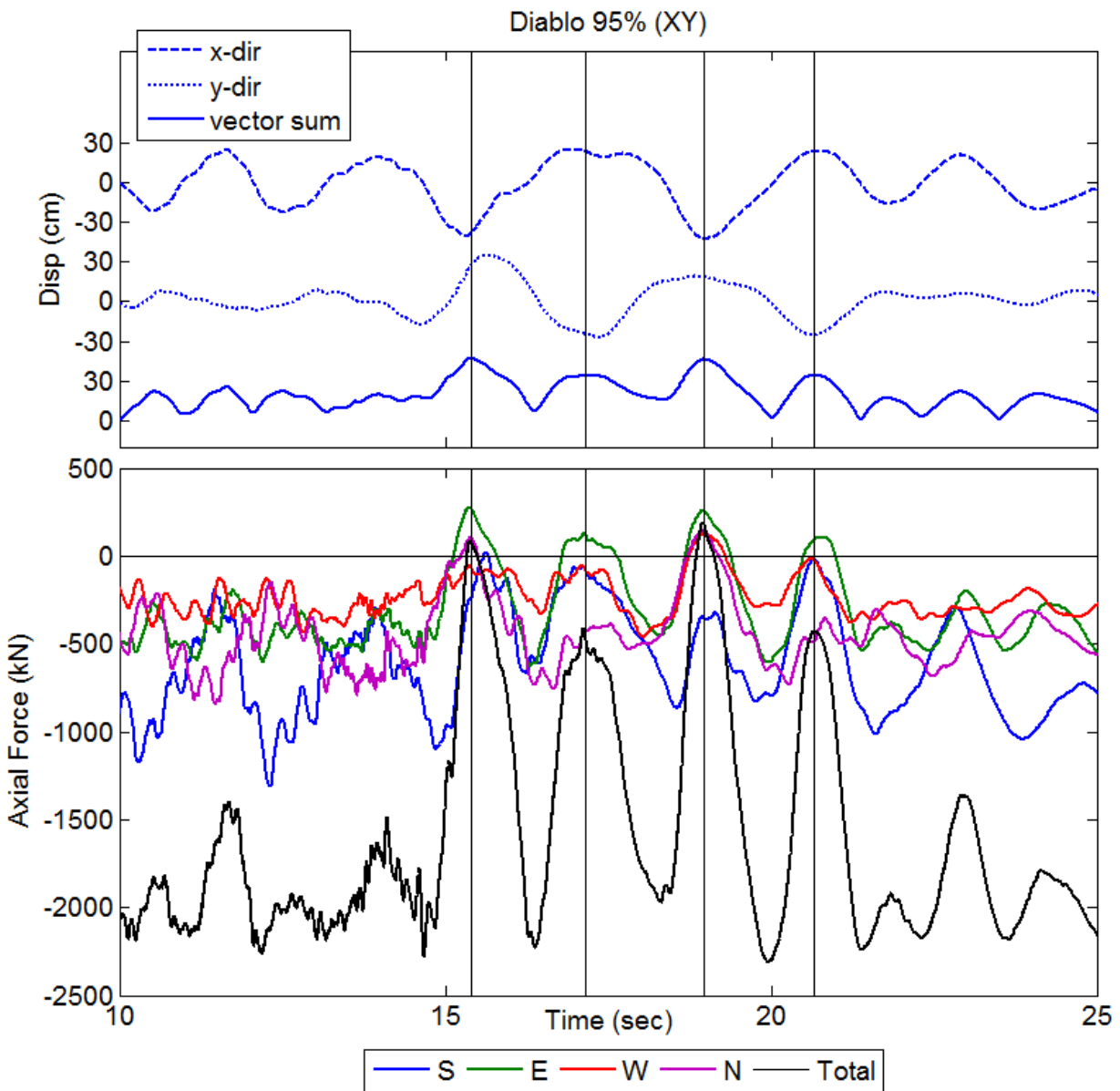


**Figure 6-8** History of average horizontal displacement (x, y and vector sum), and axial force in individual LR bearings and summed over all LR bearings for Diablo 95% (XY)



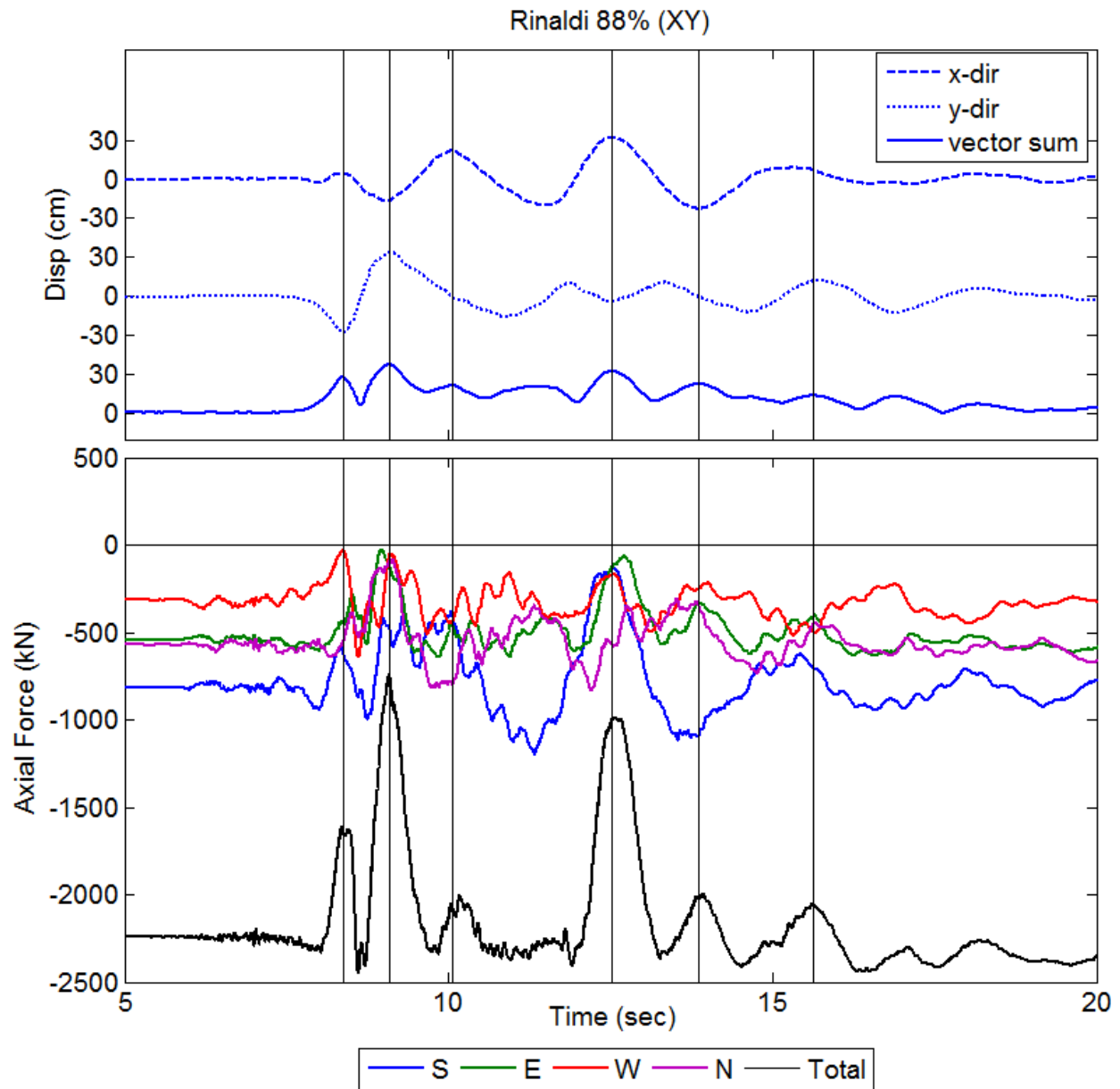


**Figure 6-9 History of average horizontal displacement (x, y and vector sum), and axial force in individual LR bearings and summed over all LR bearings for Rinaldi 88% (XY)**

To understand the extent of load transfer when the isolator displacement is 55 cm, consider that the overlapping area  $A_r$  between the top and bottom areas of a circular bearing at a given displacement is calculated by (AASHTO, 2010):

$$\delta = 2 \cos^{-1} \left( \frac{dD_{max}}{D} \right) = 2 * \cos^{-1} \left( \frac{55\text{cm}}{69.85\text{cm}} \right) = 1.34 \quad (6.1)$$

$$A_r = \frac{D^2}{4} (\delta - \sin\delta) = \frac{69.85^2}{4} (1.34 - \sin(1.34)) = 449.2\text{cm}^2 \quad (6.2)$$

where  $D$  is the bearing diameter and  $dD_{max}$  is the peak displacement. At the peak recorded displacement of 55 cm (22 in), the overlapping area is a small fraction – about 12% – of the total bonded area (3832 cm<sup>2</sup> or 592 in<sup>2</sup>). According to the overlapping area rule (Buckle and Liu

1994), the bearing has sustained an 88% loss in axial force capacity, which confirms that upward forces are generated to counteract the natural shortening in the bearing. The displacement pattern shown in the time series plots of Figure 6-8 (also in Figure 5-3) indicates that the peak displacement cycle occurs along a diagonal (from NE corner to SW corner). Since the load transfer is partially counteracted by the effects of overturning, LRB-N and LRB-E sustain less load transfer (axial unloading) for a positive excursion in x and a negative excursion in y, and LRB-S sustains less load transfer for a negative excursion in x and a positive excursion in y (Figure 6-8). The trend for LRB-W is inconclusive. The load transfer effect may be stronger than the overturning effect in LRB-W because it carries significantly less static weight than the rest of the LR bearings (Section 5.4). The load transfer effect is also observed during Rinaldi 88% (Figure 6-9), although the less axial force unloading occurs due to the lower peak displacement in Rinaldi (38 cm or 15 in from Figure 5-1).

While the transfer of load between LR bearings and CL bearings is evident for XY simulations, the trends are more difficult to ascertain in 3D simulations that include vertical excitation. In this series, Rinaldi 88% is the only excitation applied both with and without vertical input, thus allowing for the effects of vertical shaking to be directly assessed. Figure 6-10 shows the axial force histories for each of the four bearings and the total for Rinaldi 88%. By inspection, the axial force histories for 3D excitation are rich in higher frequency content compared to the force histories for XY excitation. Thus, instances of load transfer are less obvious. However, from a direct comparison of the axial forces in Rinaldi 88% (XY) and Rinaldi 88% (Figure 6-11), the 3D forces oscillate about the backbone of the XY forces. Thus, the 3D force variation is essentially equal to the XY force variation augmented by an additional high frequency component. To eliminate the force variation due to vertical excitation, and thus verify the pattern of load transfer for the 3D simulation, a low-pass Butterworth filter with a cutoff frequency of 2 Hz is applied to the total axial force for Rinaldi 88%. This filter has the same shape as that shown in Figure 4-5 when normalized with respect to the cutoff frequency. The 2 Hz cutoff frequency was selected since it preserves the frequencies related to horizontal vibration of the isolation system but eliminates typical frequency of vertical excitation and response. The resulting filtered axial force is shown in Figure 6-11 as a red dashed line superimposed over the unfiltered total axial force. The filtered total axial force for 3D excitation matches that for XY excitation very closely.

Knowing that the trend for 3D excitation can be identified, an XY versus 3D comparison is attempted for the Diablo excitation, where the 3D simulation data is available at a different scale factor (80%) than the XY simulation (95%). The total (vector sum) displacement (computed as described for Figures 6-7 to 6-9, axial forces in each LR bearing, and total axial force (with and without filtering for the 3D simulation) are compared for Diablo 95% (XY) and Diablo 80% in Figure 6-12. The peak displacement demand at the center of the building (Figure 6-12) is about 25% lower in Diablo 80% than Diablo 95% (XY). However, in Diablo 80%, about half of the load transfers from the LR bearings to the CL bearings, while in Diablo 95% (XY), all of the load transfers from the LR bearings to the CL bearings at two different time instances. This indicates a nonlinear or escalating trend in the amount of load transfer with increasing horizontal displacement. The bearing tensile force demands would need to be analyzed prior to executing Diablo 95% as a 3D simulation; as it stands, almost no tension was observed in Diablo 80% (Figure 6-12).

In the context of the previous information, horizontal displacement and axial force data is presented for Vogtle 175% (Figure 6-13), which represents the largest simultaneous horizontal displacement and vertical excitation. The pattern of load transfer for individual LR bearings is evident even without filtering, and applying filtering to the total force confirms the pattern. Peak tensile demands in individual bearings are not as great for Vogtle 175% as they were for Diablo 95% (XY), for which the bearing displacements are largest, or Rinaldi 88%, for which the vertical excitation input is largest.

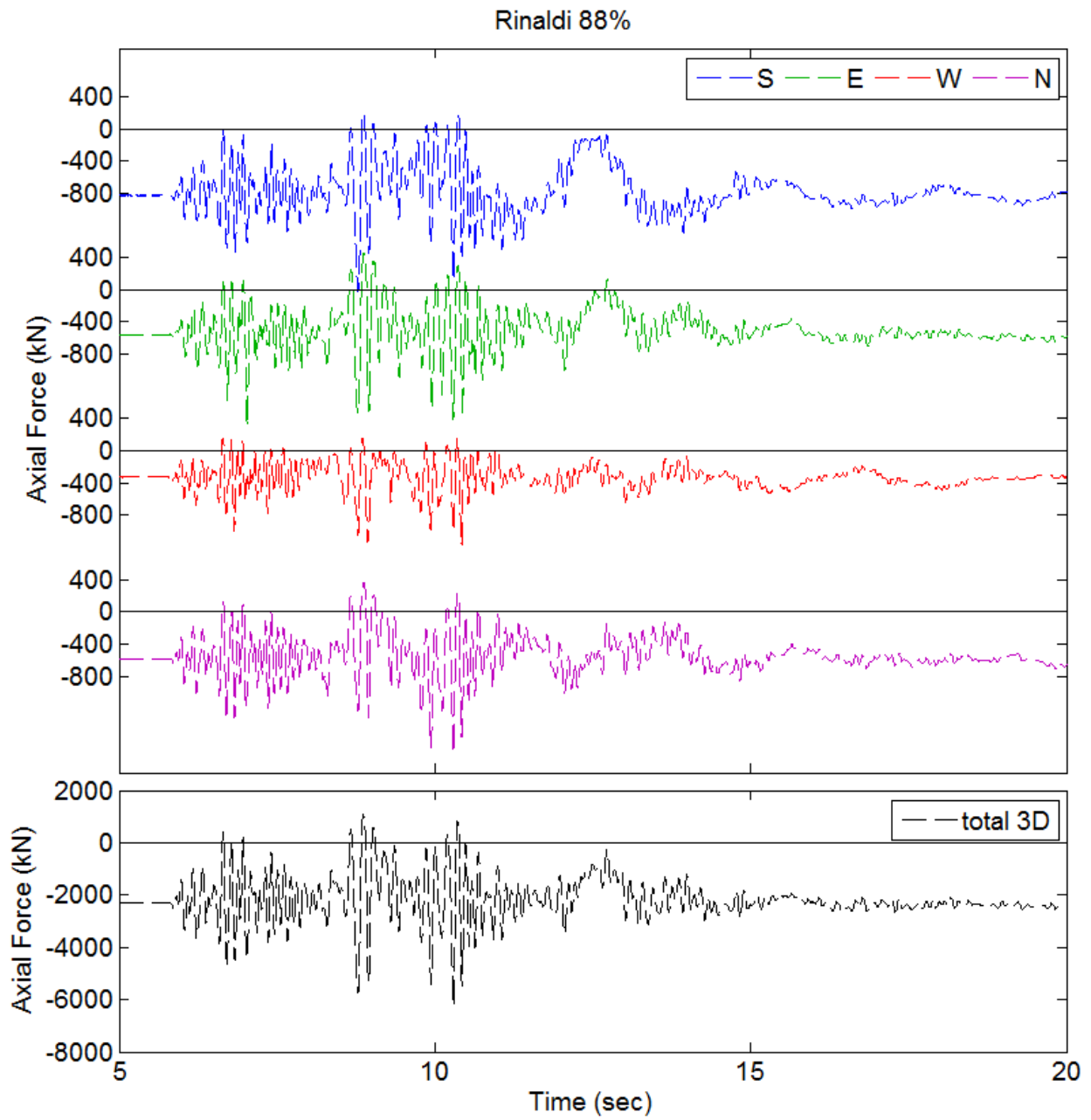


**Figure 6-10 History of axial force in individual LR bearings and summed over all LR bearings for Rinaldi 88%**

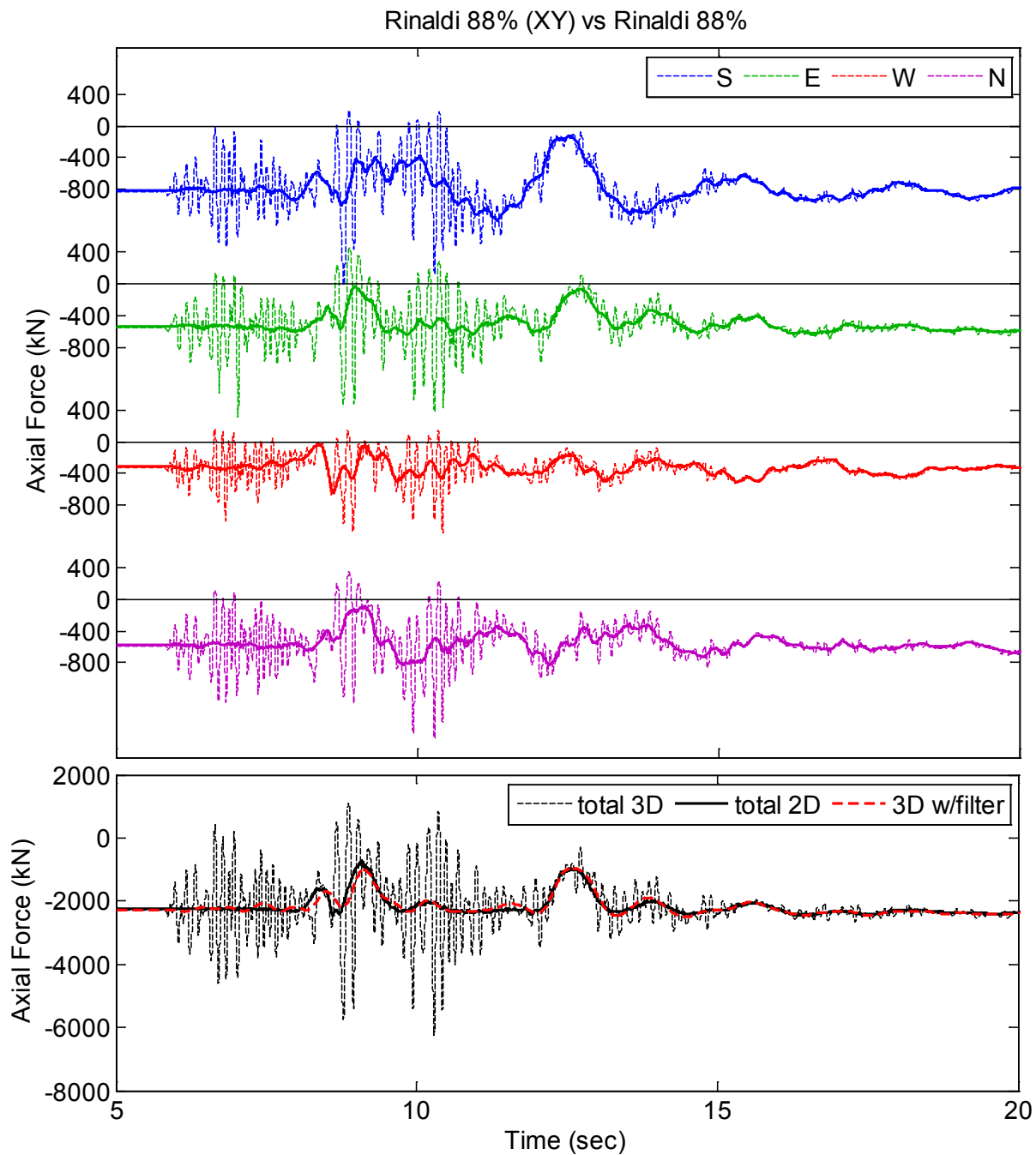


**Figure 6-11** History of axial force in individual LR bearings and summed over all LR bearings comparing Rinaldi 88% – dashed line – and Rinaldi 88% (XY) – solid line. A low pass filter with a cutoff frequency of 2 Hz was applied to the total axial force for Rinaldi 88% and is superimposed over the total, shown as a red dashed line

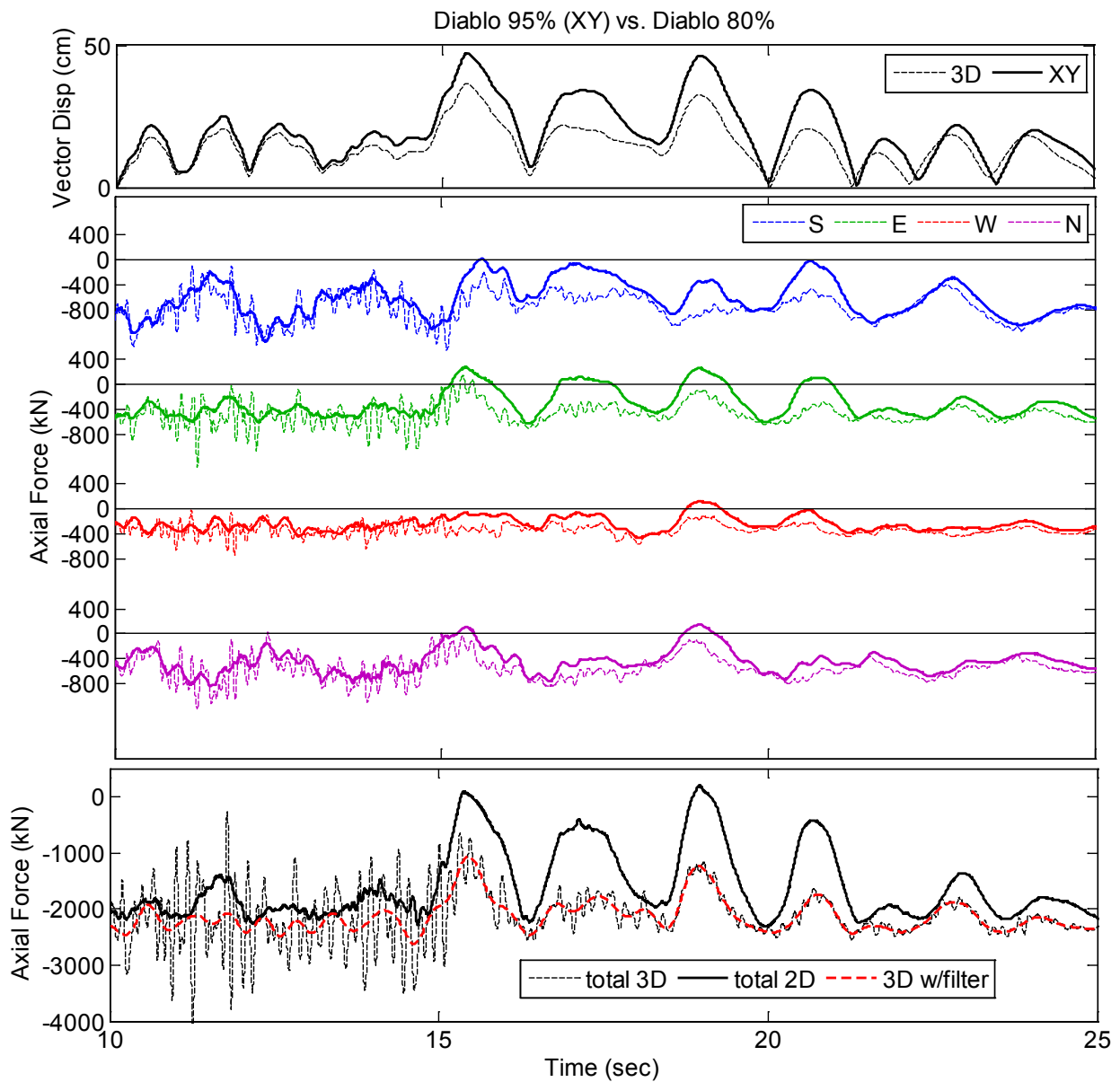


**Figure 6-12 History of average vector sum displacement at building center, axial force in individual LR bearings and axial force summed over all LR bearings comparing Diablo 95% – dashed line – and Diablo 80% (XY) – solid line. A low pass filter with a cutoff frequency of 2 Hz was applied to the total axial force for Diablo 80% and is superimposed over the total, shown as a red dashed line**

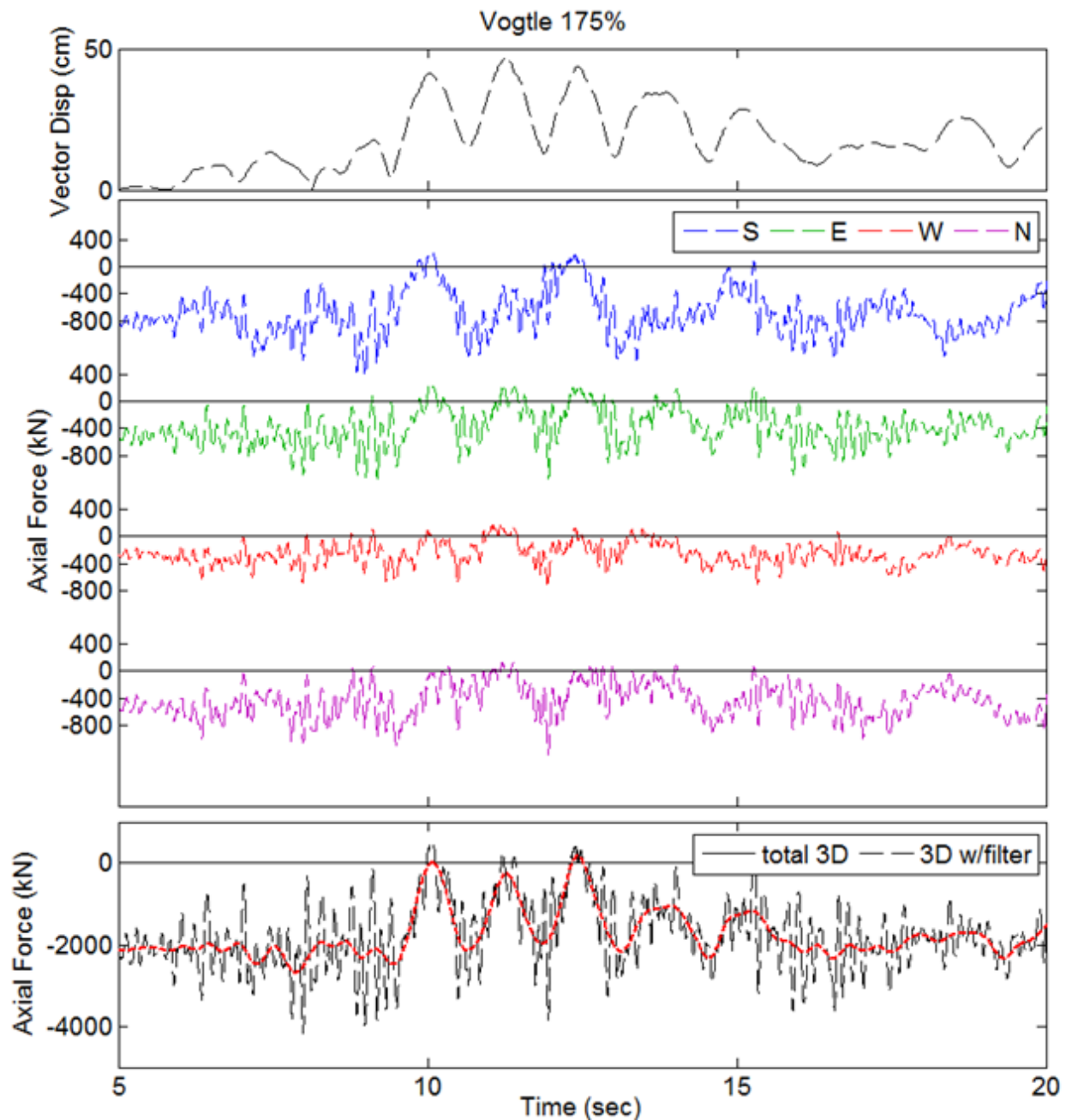


**Figure 6-13** History of average vector sum displacement at building center, axial force in individual LR bearings and axial force summed over all LR bearings for Vogtle 175%. A low pass filter with a cutoff frequency of 2 Hz was applied to the total axial force and is superimposed over the total, shown as a red dashed line

While we have demonstrated that force transfers between LR bearings and CL bearings over the course of a simulation, a different pattern emerged between simulations, which is illustrated in Figure 6-14. This figure shows that the total compressive force carried by the LR bearings always increases from the beginning to the end of the simulation, which means that a small amount of load transfers from the CL bearings to the LR bearings over the course of the simulation. However, from the end of one simulation to the beginning of the next, the total compressive force carried by the LR bearings is consistently observed to decrease (Figure 6-14(a)), which suggests that the original compressive force on the LR bearings would be restored

over time. As mentioned before, the time between simulations in a given day was about 50 minutes. At the end of Day 1, the total compressive force increase on the four LR bearings is about 430 kN or 97 kips (about 22% of the original total of 1915 kN or 431 kips). As confirmation of the relaxation effect, the original static load on the LRBs is nearly restored by the start of Day 2; only about 50 kN (11 kips) additional remained (Figure 6-14(a)). Nearly the same pattern is repeated on Day 2, except that additional compressive force accumulates more quickly as larger motions were executed earlier in the day.

Our hypothesis regarding the pattern of axial force transfer between simulations is as follows. When the bearings are constrained at large lateral displacements as depicted in Figure 6-6, the lead is sheared laterally and takes the shape of the slanted cylinder. The height of the slanted cylinder is longer than the height of the cylinder in the undeformed configuration. Upon return to the original position, the slanted cylinder tries to rotate, but the axial load and confinement from the shims force the lead cylinder back to its original height. Immediately upon return to the undeformed configuration, the lead plug exerts some force onto the upper and lower plates, or alternatively a slight height increase is maintained if the upper and lower plates are not confined. The confining force or height increase causes the LR bearings to temporarily take on additional load. After a short period of time, the force relaxes and the original state is restored. This effect would not be seen if a) the hybrid isolation system used elastomeric bearings instead of LR bearings, b) the base diaphragm was less stiff, or c) the system consisted entirely of LR bearings.

The maximum increase in the static compressive force in the LR bearings due to the effect described above is about 500 kN, which is about a 25% increase relative to the static load carried by the LR bearings at the start of the test program. Figure 6-14(b) provides a visual impression of the total static force variation throughout the test program.

As described in Section 3.2.2, the combination of LR and CL bearings was necessary in this program to provide a sufficient period shift and displacement capacity for the relatively lightweight structure. Chapters 8-10 describe numerical simulation to validate and demonstrate the predictability of the experimental response. However, we do not attempt to predict the axial forces in the bearings as part of this simulation. The forces in CL bearings cannot be validated since they were not measured.

The observed load transfer in these experiments suggests that the compliance of the devices in a hybrid system must be carefully considered. The experiments have demonstrated that when working with a high stiffness tension capable device, the LR bearings can be subjected to non-negligible tension due to a combination of load transfer and vertical excitation; the tension is not related to overturning. While the load transfer and the resulting tension observed in the LR bearings in these experiments is considered acceptable, the main drawback is that the peak force demands in the bearings (both tensile and compressive and in both types of devices) are difficult to predict; see Chapter 8-10 for further discussion. This is a concern since reliable numerical simulation is a requirement for the design of a nuclear structure.

Due to these concerns regarding the load transfer, it is pertinent to consider the likely differences in response between the tested hybrid system and an isolation system composed exclusively of LR bearings. First, suppose the CL bearings were removed from the test setup, and the as-designed LR bearings were located beneath the four corner columns. Further, suppose that the same DBE and beyond DBE motions were posed that produced displacement demands up to 30 cm and 55 cm, respectively. The likely differences in the response of the exclusive LR system and the hybrid LR are discussed as follows.

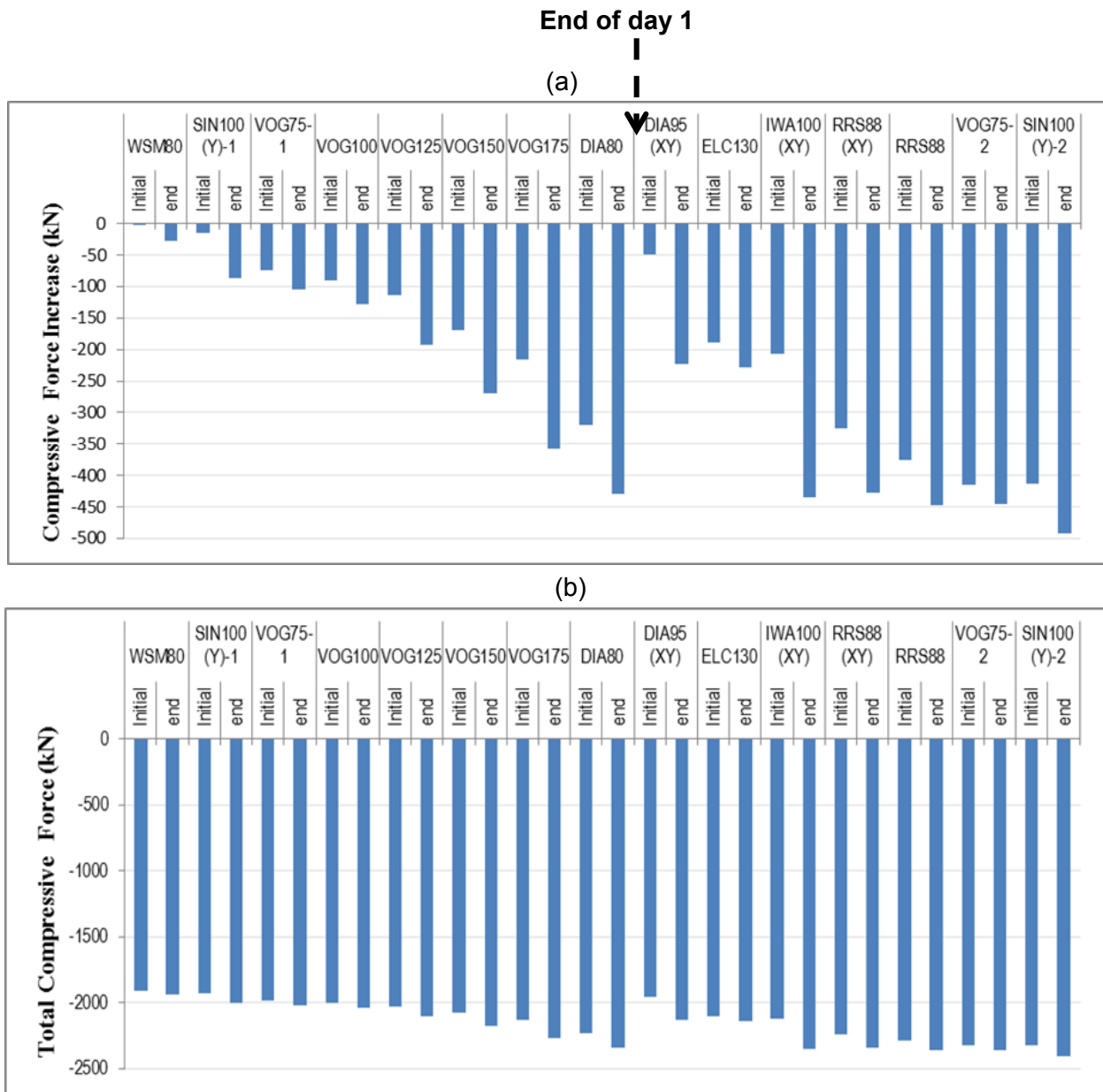


**Figure 6-14 (a) Relative change in compressive force and (b) Total compressive force summed over LR bearings at the start and end of all simulations**

The effective isolation properties and displacement demands for a DBE are expected to be essentially unchanged for an exclusive LR system. The bearing hysteresis loops in the exclusive LR system and the hybrid LR system are expected to look very similar.

Without CL bearings, individual LR bearings are estimated to sustain overturning induced tensile loads on the order of 200 kN (see Equation (3.4) and related discussion). Based on Figure 5-10, a tensile load on the order of 350 kN was observed in one bearing in this experiment due to the combined effects of load transfer and vertical excitation. Vertical excitation would also increase the peak tensile load in an exclusive LR system, such that the peak tensile demands on individual bearings in the hybrid LR system and in the exclusive LR system are expected to be similar.



If not constrained by the hybrid setup, a simple analysis predicts that one or more bearings may experience a complete loss of horizontal stiffness at the displacement demands of beyond DBE motions (55 cm). As discussed earlier, the bearing overlapping area at 55 cm of displacement is about 12% of the total bonded area (Equation (6.2)), and thus by the overlapping area rule is predicted to reduce to 12% of the bearing critical buckling load in the undeformed configuration (Buckle and Liu 1994). The nominal critical buckling load of the bearings is  $P_{cro} = 12,600$  kN (Figures 3-8 and 3-9 for LR Option 3), and thus the reduced buckling load is  $P_{cr} = 1500$  kN at a displacement of 55 cm. With only 4 LR bearings, the average static load of  $P = 1300$  kN per bearing nearly exceeds the reduced critical buckling load, and thus the bearings are expected to buckle if subjected to compressive force increase due to overturning. In this case, the reduced horizontal stiffness of the bearing  $K_b$  of the bearing as a function of the nominal stiffness  $K_{bo}$

$$K_b = K_{bo} \left( 1 - \left( \frac{P}{P_{cr}} \right)^2 \right) \quad (6.3)$$

would also tend to zero. As a worst case scenario, buckling and temporary loss of stiffness in one or more bearings could cause a global collapse of the system.

However, emerging studies suggest that the stability capacity of elastomeric bearings at large displacements is much larger than predicted by the overlapping area rule, and the isolation system has remarkable ability to recover from local instabilities in one or more bearings. For example, Sanchez et al. (2012) subjected a rigid block system with 4 one quarter scale natural rubber bearings to ground motions that imposed bearing displacements beyond their theoretical and experimentally observed stability limits. In one instance, one of the bearings was driven to a displacement 1.2 times its diameter and about twice the displacement at which loss of stiffness was observed, and the composite isolation system had a large negative stiffness. The isolation system successfully recovered from this and other excursions into the instability range. In an experimental study of a two-fifth scale 3-span horizontally curved girder bridge with two isolation bearings at each bent and abutment, isolators were shown to remain stable at displacements 1.33 times the bearing diameter (Monzon et al. 2013). At a slightly larger displacement (1.4 times the bearing diameter), both bearings at one abutment experienced a local instability. One bearing was observed to sit down on the bottom plate while the top plate touched the side of the bearing. The other isolators remained stable because the bent bearings were larger diameter and because the displacement demands at the abutment were larger due to asymmetry in the curved bridge. The system recovered from instability multiple times, and no change to the isolator hysteretic properties were observed following instability.

Relating these results to a hypothetical test of an exclusive LR isolation system at E-Defense, another possible scenario is that the isolated structure could survive excursions to displacements equal to the bearing diameter (70 cm) and beyond without collapse due to the ability to recover from local instabilities. The potential for recovery would be aided by the fact that displacements on one of the building were consistently observed to be substantially smaller than displacements on the other side due to torsion, and that axial loads on one side of the building would be less than the static loads due to overturning. Both of these variations increase the likelihood that the instabilities are localized, enhancing the chance of a global recovery. As a result of localized instabilities, the bearing hysteresis loops would change substantially compared to the ones observed in these tests, and exhibit negative stiffness loops at large displacements, similar to those observed in Sanchez et al. (2012).

Next, suppose instead that the isolation system were designed without the constraints of the test setup for an actual nuclear facility. Removal of the test constraints implies the following could be achieved. Individual bearings would carry greater static loads, and thus their size (both diameter and bearing height) could be increased without altering the design properties (period and damping) of the system. As a result of the size increase, the target displacement demand for the Vogtle site (about 60 cm) could easily be accommodated without approaching the stability limit of the bearing. As a result, stable hysteresis loops similar to the ones observed in these tests (discussed further in Chapters 7 and 9) would be expected. Assuming the nuclear facility is squat in plan compared to the tested 5-story steel frame building, the isolation system could feasibly be designed to eliminate overturning-induced tensile demands. Incidental bearing tension due to vertical excitation would still be likely, and the influence of vertical excitation on the response of the system (see Chapter 10) would be unaffected. Because a safety related nuclear facility could be designed exclusively with LR bearings without the need for CL bearings, the constraints encountered in the test program would not be encountered in the design of a nuclear facility, thus the hybrid LR isolation system tested at E-Defense need not be used for safety related nuclear facilities. As such, the load transfer issues that were apparent in the tests are of no consequence to practical applications.

### **6.3 Repeatability of Isolation System Response after Many Tests**

During the test program, repetitions were conducted for two of the input ground excitations: Sine 100% (Y) and Vogtle 75%. Each of these excitations was applied near the beginning of the test program and then again at the end of the test program for the hybrid LR isolation system. The repetitions were planned to assess the consistency of the isolation system response after the LR bearings had been subjected to many ground motions and to very large ground motions.

The variation in the input signals for these repetitions is assessed in Figures 6-15 and 6-16. Figure 6-15 compares the x and y-direction feedback acceleration at the center of the earthquake simulator (averaged over several accelerometers) for the first and second Sine 100% (Y) and Vogtle 75% simulations. This feedback acceleration is the input acceleration to the isolated structure. Figure 6-16 compares the comparable 5% damped response spectra for the feedback acceleration. Figures 6-15 and 6-16 demonstrate that the input accelerations for the first and second simulations are essentially identical for both Sine 100% (Y) and Vogtle 75%.

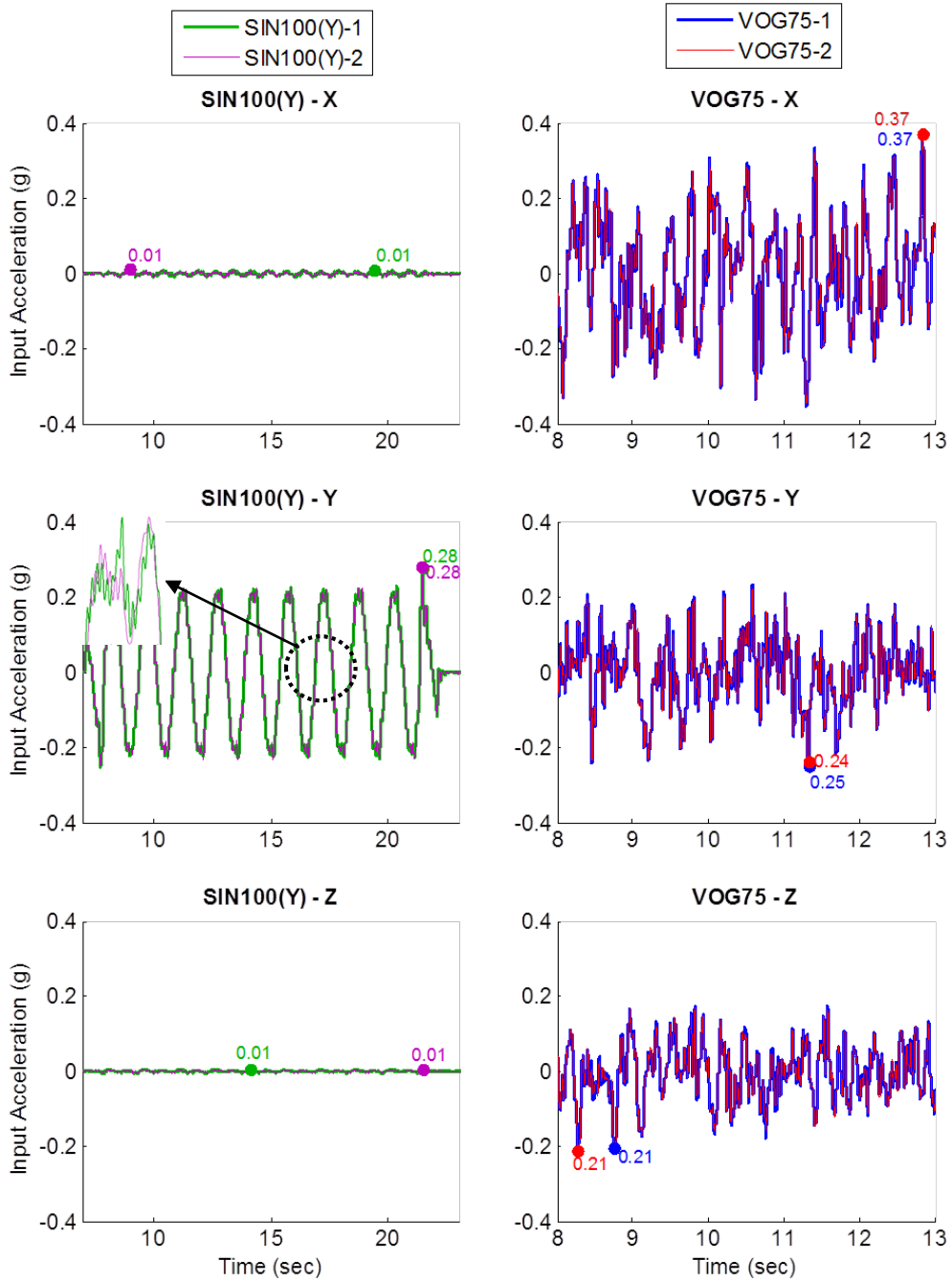


**Figure 6-15 Sample feedback acceleration at the center of the earthquake simulator (averaged over several accelerometers) in the x and y-directions compared for the first and second Sine 100% (Y) and Vogtle 75% simulations**

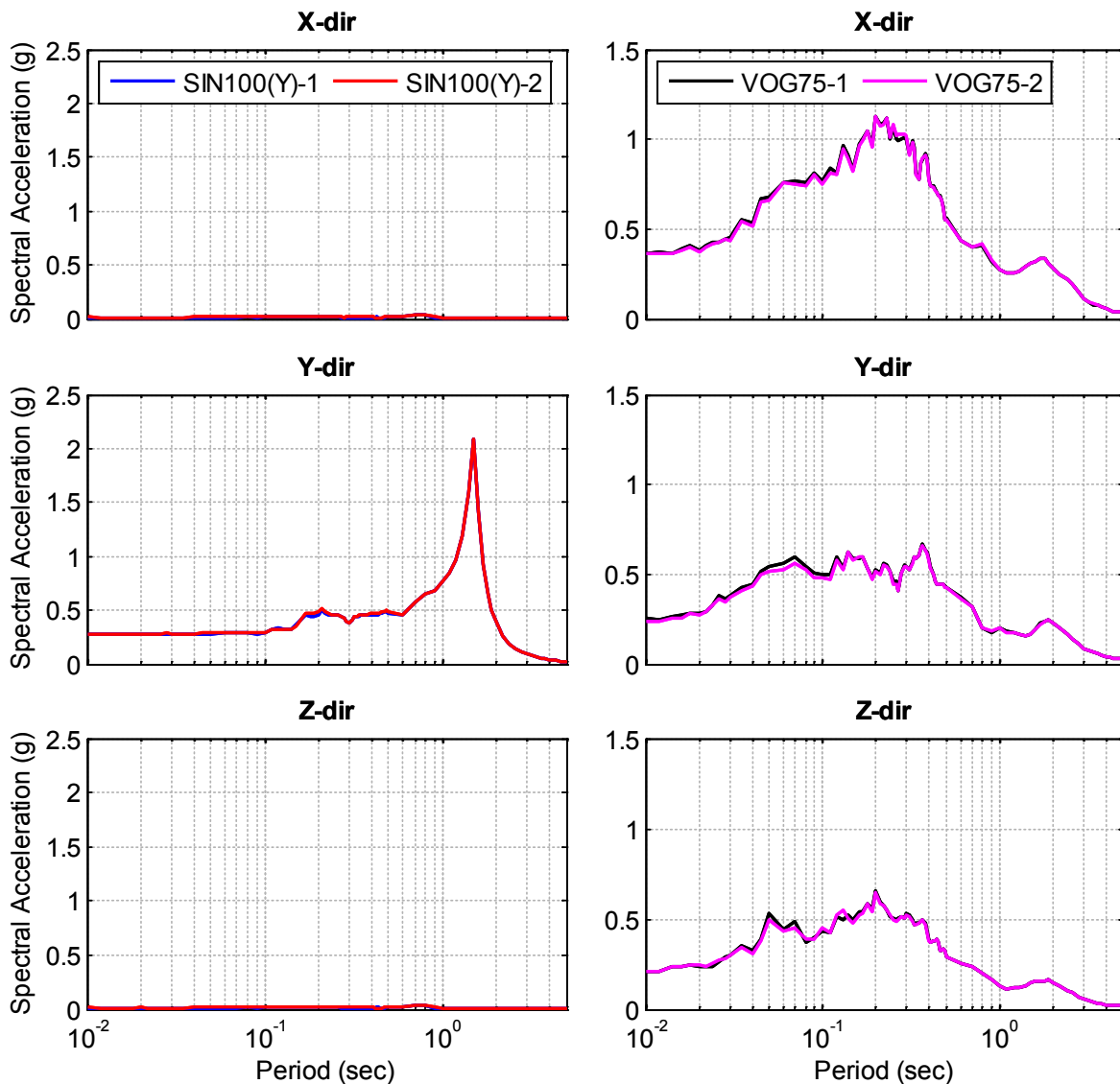


**Figure 6-16 5% damped response spectra for the feedback acceleration at the center of the earthquake simulator (averaged over several accelerometers) in the x, y and z-directions compared for the first and second Sine 100% (Y) and Vogtle 75% simulations**

The Sine 100% (Y) excitation is a unidirectional input consisting of several similar amplitude sinusoidal cycles used for characterization of the isolation system. As mentioned in the previous section, the input was applied in the y-direction to minimize torsional response. Minor displacements and forces in the x-direction were observed that had no distinguishable effects on the y-direction hysteresis loops. The y-direction bearing force versus displacement (hysteresis loops) and y-direction displacement/force histories of all LR bearings are compared for the two Sine 100% (Y) simulations in Figures 6-17 and 6-18, respectively. From the hysteresis loops, a small decrease in bearing force is observed in the second simulation relative to the first (Figure 6-17). This force decrease is most notable as the displacement peak is approached in the negative direction. The peak force cycle-by-cycle is also slightly lower for the second simulation than the first based on the force histories (Figure 6-18), which is true for all

LRBs. The observed decrease in the peak force is on the order of 5 to 11% when all LR bearings are considered, which is small.

The following hypothesis is offered to explain the mild variation in bearing response over the two simulations. The characteristic strength of LR bearings is affected by heating and temperature increase in the lead plug (Kalpakidis and Constantinou 2009a). Specifically, the characteristic strength of the lead plug decreases as the temperature increases under repeated cycling. While repetitions performed with the same starting temperature should produce identical response in the bearings, repetitions performed at different starting temperatures would produce slightly different response in the bearings. Since the test program consisted of many simulations in a single day with only 45-50 minutes between simulations, it is likely that 1) the bearings did not have time to cool to the starting temperature between simulations, and 2) the starting temperature for each simulation was different based on the recent simulation history. Consistent with the observations, the starting temperature for the second SIN100 simulation was likely higher than for the first SIN100 simulation, since the second followed a full day of testing including DIA95(XY), which generated the largest displacement demand, and IWA100(XY), which was more than 4 minutes long.

Although the forces decrease, the overall displacement demands do not increase in the second Sine 100% (Y) simulation. Rather, the hysteresis loop for each bearing shifts slightly to the left in the second simulation so that the negative direction peak increases but the positive direction peak decreases. This shift can be observed in every bearing hysteresis loop except for LRB-S (Figure 6-17), and in the displacement histories (Figure 6-18). The shift could be related to a small residual (permanent) displacement present at the beginning of the second Sine 100% (Y) simulation in some bearings; residual displacement is visible only in LRB-S and LRB-N in the opposite directions (Figure 6-18), which indicates that the permanent displacement is torsional. Recall that a portion of the permanent displacement is believed to be a result of sliding in the connection plates associated with bolt slip (see Sections 5.5 and 6.1). The absolute peak displacement (observed in the negative direction) increases on the order of 3 to 5% in the second simulation when all LR bearings are considered, which is insignificant.

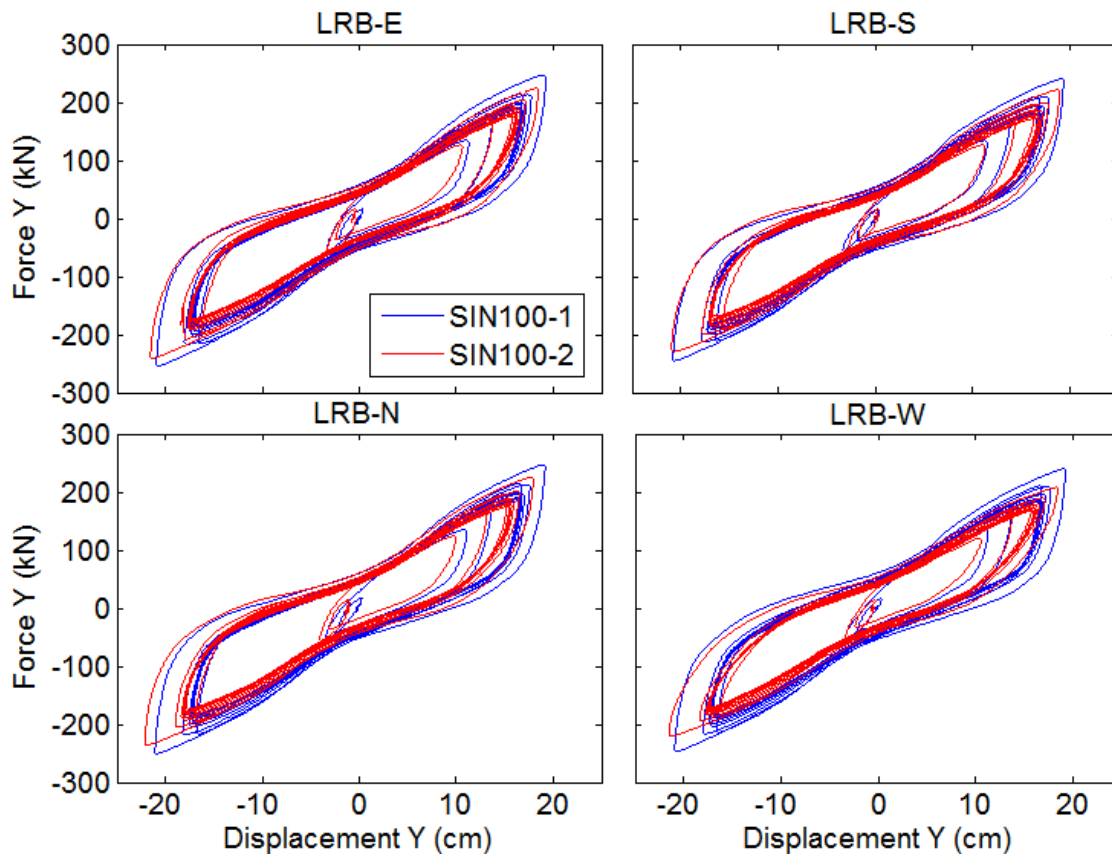


**Figure 6-17 Y-direction force vs. displacement (hysteresis loops) for the 1<sup>st</sup> and 2<sup>nd</sup> simulation of Sine 100%(Y)**

Additional plots are included to evaluate the consistency of the bearing response in the Vogtle 75% simulations, for responses in both directions. X and y-direction bearing force versus displacement (hysteresis loops) are compared for the Vogtle 75% simulations in Figures 6-19 and 6-20, while x and y-direction displacement/force histories of all LR bearings are compared in Figure 6-21 and 6-22. An additional figure (Figure 6-23) indicates the displacement traces (displacement in x versus displacement in y) of all LR bearings for the two Vogtle 75% repetitions. This figure is necessary to evaluate the consistency of the peak displacement, which is a vector quantity for bidirectional horizontal excitation, over the two Vogtle simulations.

Again, by visual inspection of the hysteresis loops, the forces in the LR bearings decrease slightly for the second repetition of Vogtle 75% relative to the first (Figures 6-19 and 6-20). This reduction in force seems to be smaller for Vogtle 75% than for Sine 100% (Y), but a statistical evaluation was not completed. The absolute peak displacement increases for each LR bearing in the second simulation relative to the first, but also appears to result from the entire hysteresis loop shifting to the direction of negative displacement rather than a true increase in the displacement demand. The increase in absolute peak displacement for the second simulation of Vogtle 75% relative to the first is about 8% in all LR bearings (determined from Figure 6-23). Force and displacement histories are very similar when superimposed over each other for the first and second simulations (Figures 6-21 and 6-22).

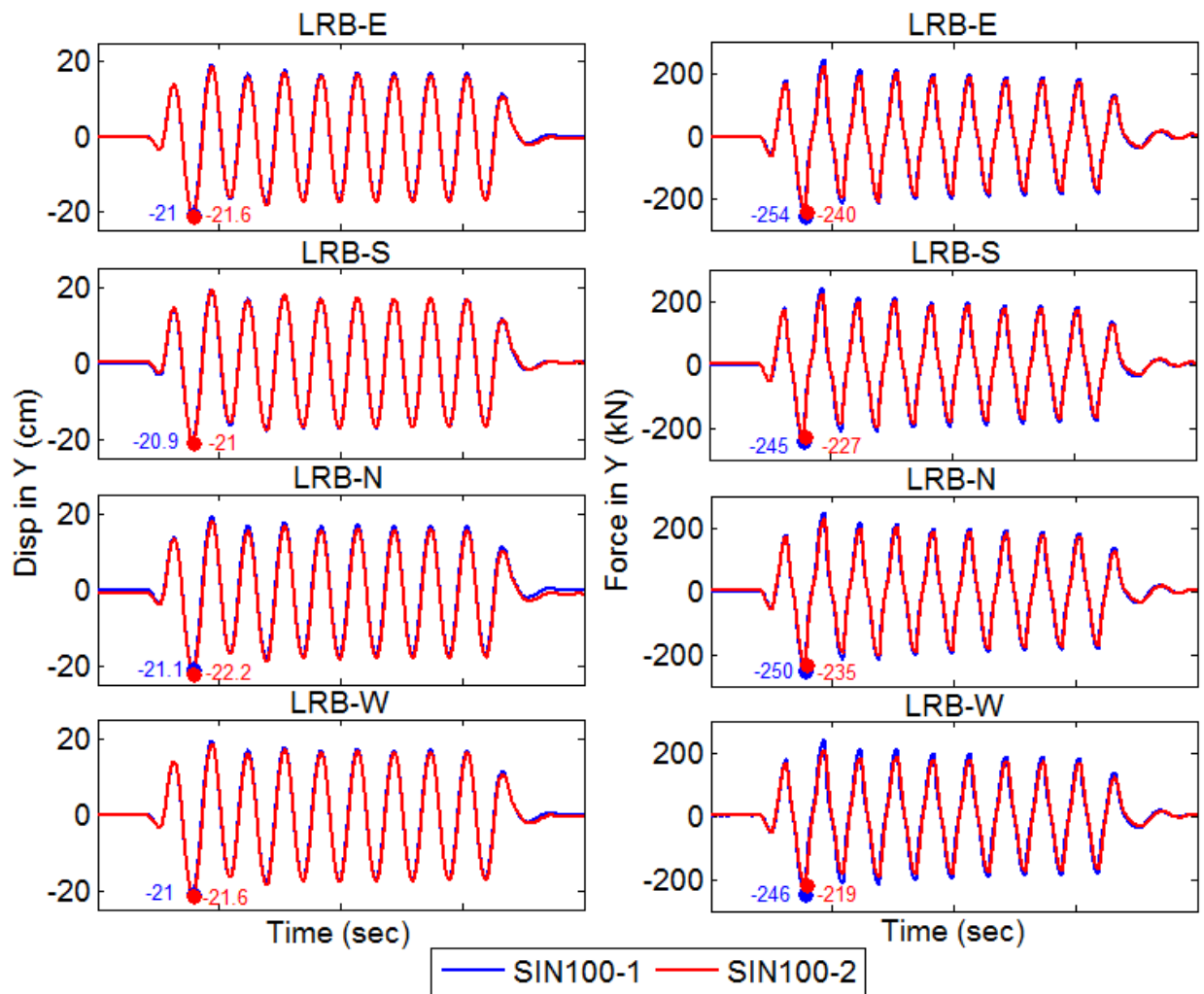


**Figure 6-18 Y-direction displacement and force histories for the 1<sup>st</sup> and 2<sup>nd</sup> simulation of Sine 100% (Y)**

The peak force in the LR bearings also decreases from cycle to cycle while the displacement remains approximately constant over the course of a simulation. This behavior is also indicative of dynamic reduction in yield strength due to heating of the lead plug. This behavior is observed most clearly during the Sine 100% (Y) simulation, which contains several regular displacement cycles of similar amplitude. The hysteresis loops generated during Sine 100% (Y), both first and second simulations, are plotted again for LRB-N in Figure 6-24, where the cycles are individually identified. In this figure, the forces decrease in every cycle, with the greatest reduction between the first and the second cycle. While the total reduction in strength over the 8 cycles of the sine wave is significant, a typical motion includes at most a few cycles of strong amplitude motion. Thus, a reduction in strength is not noticeable for the majority of the motions included in the test program, such as Vogtle 75% (Figures 6-19 and 6-20), which contains at most two large displacement amplitude cycles. The data for the two sine wave simulations suggests that much, but not all, of the force reduction is recovered between tests.

Related to these observations, predicting the change in characteristic strength of the lead plug over the history of the motion is of interest. Such effects have not been incorporated into our numerical simulation models, discussed in Chapters 7-9, but the following is noteworthy.

Kalpakidis and Constantinou (2009a) developed theoretical equations to compute the instantaneous strength and evolution of strength in the lead plug over the history of the excitation. Kalpakidis et al. (2010) presented a numerical algorithm to incorporate the temperature dependence into a bidirectionally coupled bilinear numerical model of the isolator. The algorithm to compute the temperature increase in a response simulation is based on the dimensions of the lead plug, density and specific heat of lead, thermal diffusivity and thermal conductivity of steel, and a few other calibrated parameters. To represent the simulation data from the series of tests discussed in this report, we have the added challenge of predicting the temperature at the start of a simulation, which normally would not be necessary. Incorporating heating of the lead plug into numerical simulation models for improved prediction of the data is a goal of our ongoing investigation.

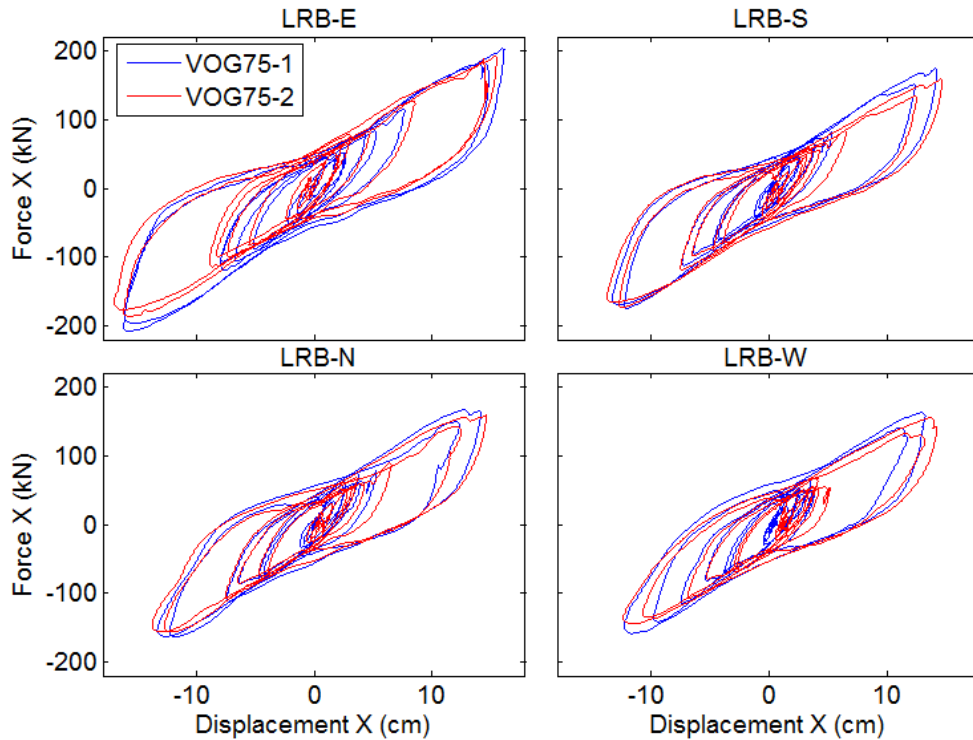


**Figure 6-19 X-direction force vs. displacement (hysteresis loops) for the 1<sup>st</sup> and 2<sup>nd</sup> simulation of Vogtle 75%**



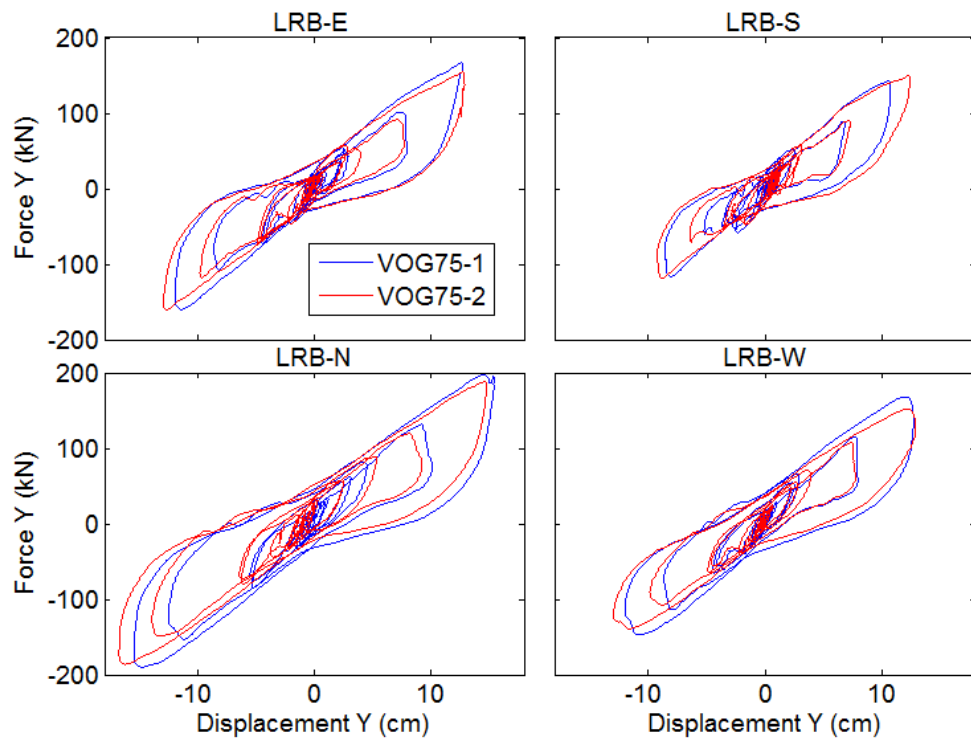


**Figure 6-20 Y-direction force vs. displacement (hysteresis loops) for the 1<sup>st</sup> and 2<sup>nd</sup> simulation of Vogtle 75%**

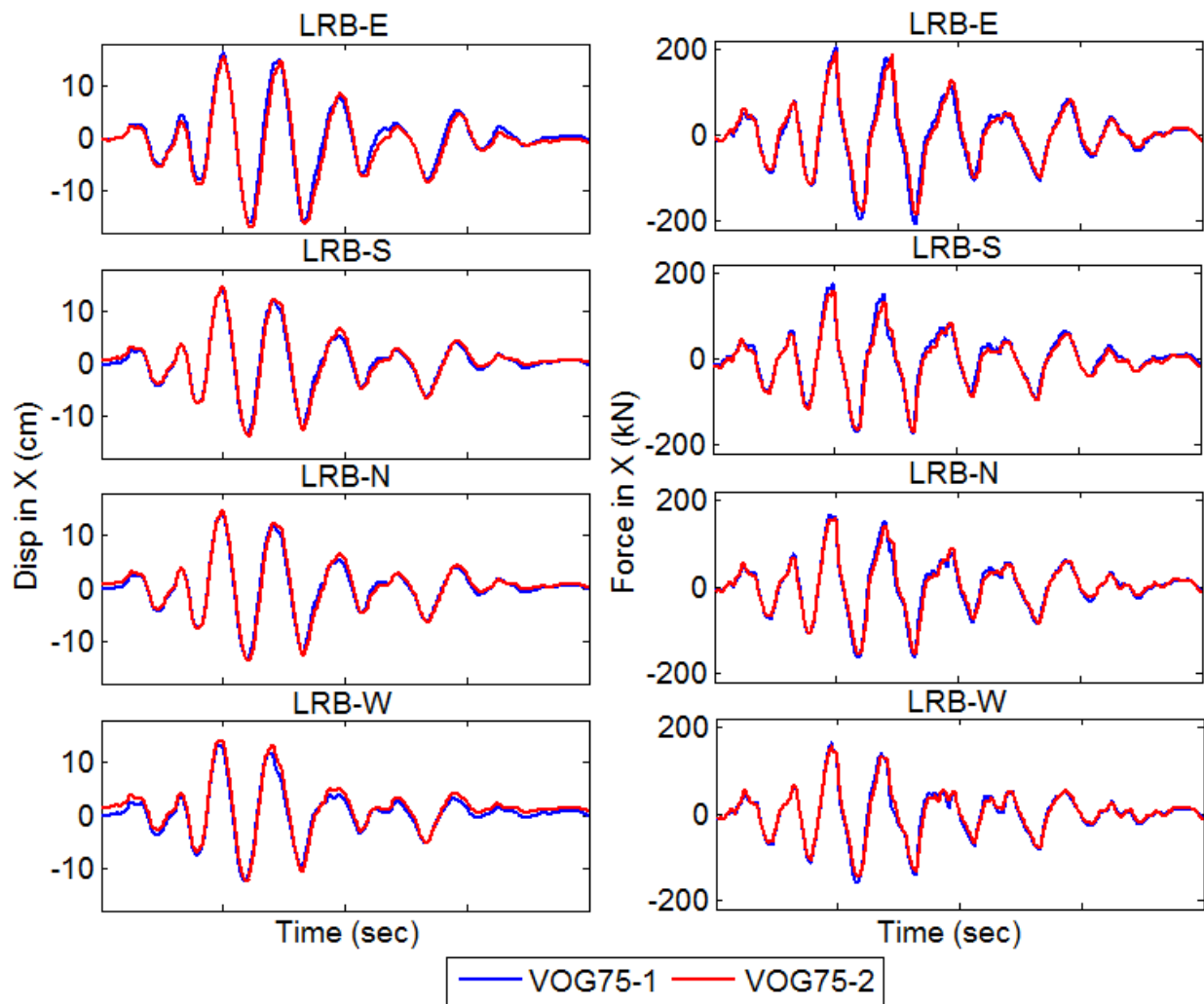


**Figure 6-21 X-direction displacement and force histories for the 1<sup>st</sup> and 2<sup>nd</sup> simulation of Vogtle 75%**

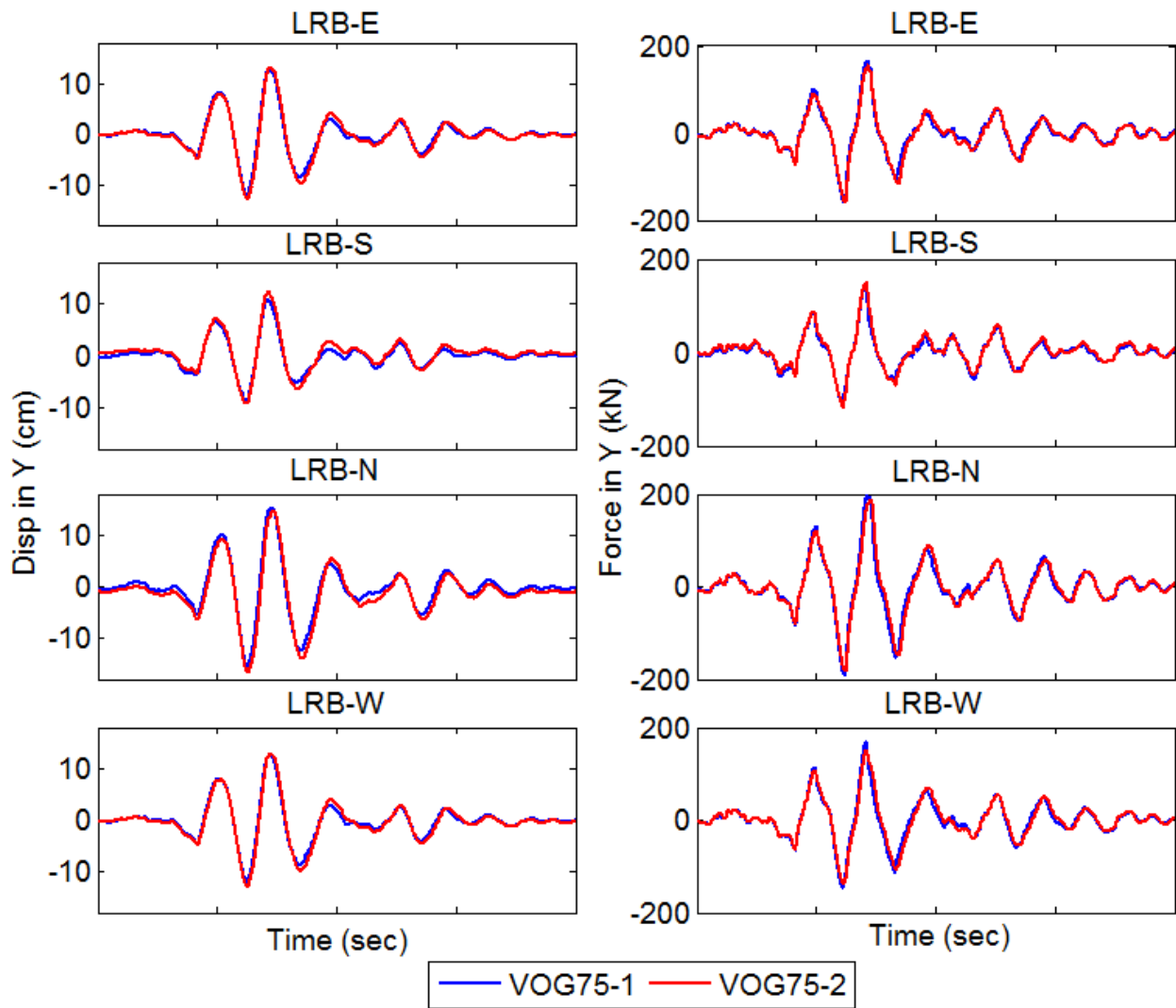
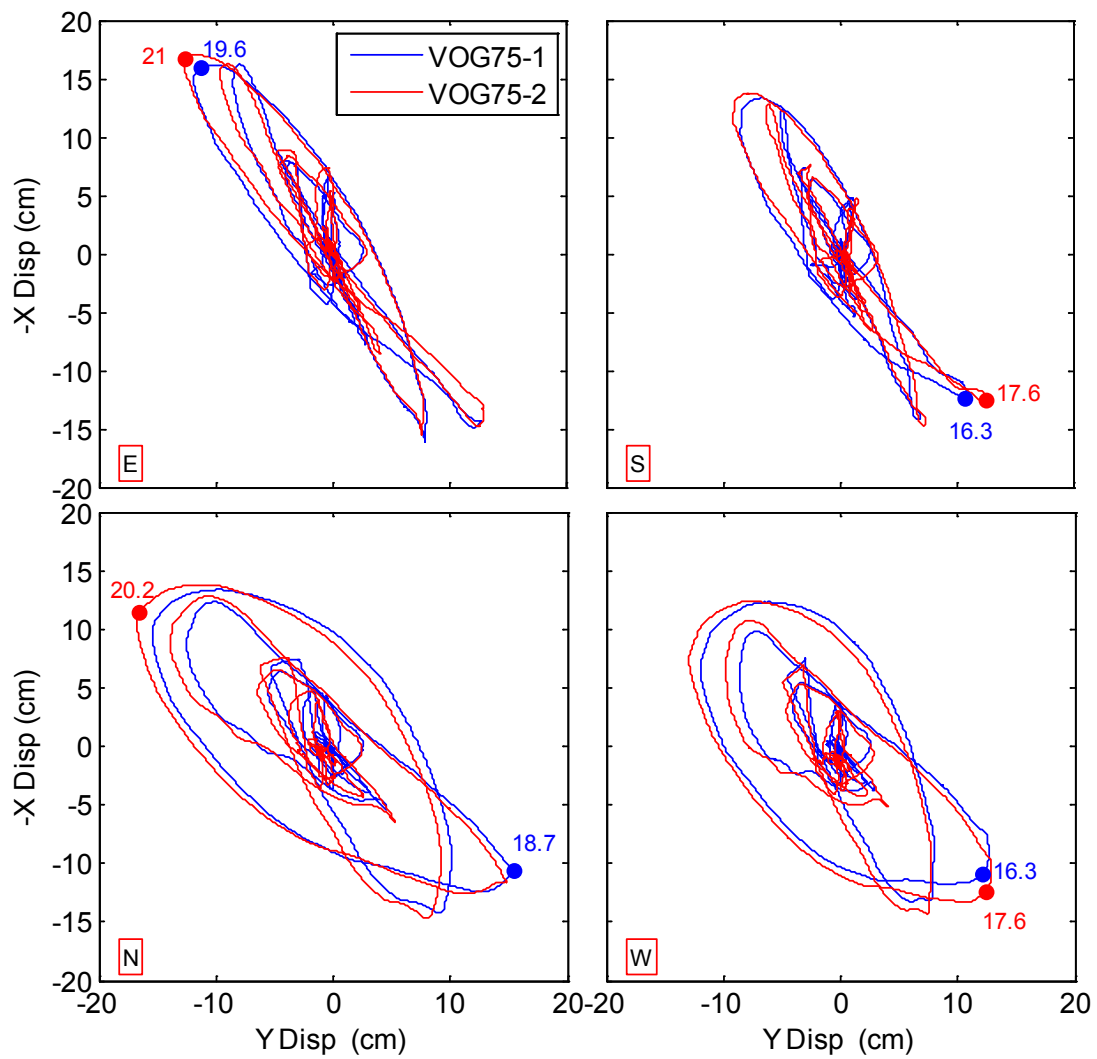
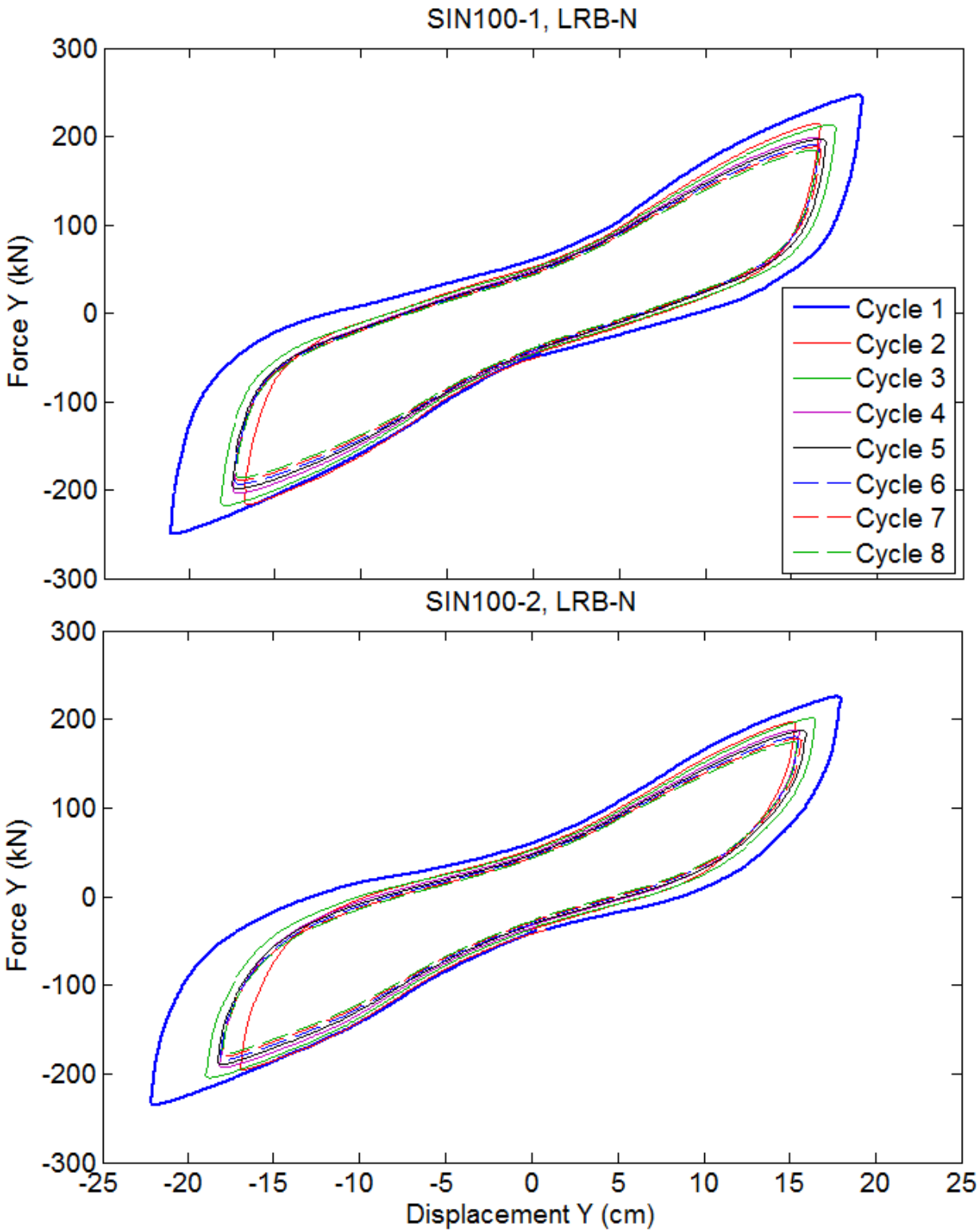


Figure 6-22 Y-direction displacement and force histories for the 1<sup>st</sup> and 2<sup>nd</sup> simulation of Vogtle 75%



**Figure 6-23 X vs. y-direction displacement (displacement trace) for the 1<sup>st</sup> and 2<sup>nd</sup> simulation of Vogtle 75%**



**Figure 6-24 Y-direction force vs. displacement (hysteresis loops) identified by cycle for the 1<sup>st</sup> and 2<sup>nd</sup> simulation of Sine 100% (Y)**



## 7. MODEL FOR ISOLATION BEARINGS AND BEARING CHARACTERIZATION

For further validation, a 3D frame model of the testbed building was developed for numerical simulation in the Open System for Earthquake Engineering Simulation v2.2.2 (OpenSees, 2010). The results of numerical simulation using this model are directly compared to experimental data in Chapters 9-10. In this chapter, we describe the modeling and characterization of the hybrid LR isolation system. The modeling assumptions for the LR bearings and CL bearings are described in Section 7.1 and 7.2, respectively. Section 7.3 estimates the vertical dynamic properties of the system considering the contribution of the load cell assemblies. Section 7.4 details the procedure used by Dynamic Isolation Systems to characterize the parameters of the LR bearings based on cyclic testing (Sec. 7.4.1), which is extended to the test data (Sec. 7.4.2).

### 7.1 Lead-Rubber Bearings

The force-deformation relation of the LR bearings was represented by a combination of spring elements. The horizontal and vertical behavior of the bearing was assumed to be uncoupled. Horizontal-vertical coupling, loss of lateral stiffness, and loss of axial load carrying capacity have been observed in elastomeric bearings under the combination of large horizontal displacements and axial forces (Buckle and Liu 1994, Buckle et al. 2002, Warn and Whittaker 2006). However, the constraint provided by the vertically stiff CL bearings and base diaphragm, documented in Chapter 6, prevented axial shortening and loss of lateral load carrying capacity of the isolation system, which supports the choice of an uncoupled bearing model.

#### 7.1.1 Horizontal Direction Modeling Assumptions

The force-displacement relation of the LR bearings in the horizontal direction was idealized as bilinear as shown in Figure 7-1. Numerically, this was implemented as a rate-independent plasticity model with kinematic hardening; defined by the elastic stiffness ( $K_1$ ), yield force ( $F_y$ ), and the kinematic ( $K_H$ ) hardening modulus. These parameters were calculated from the post yield stiffness ( $K_d$ ) and characteristic strength ( $Q_d$ ) according to:

$$K_1 = 10K_d \quad (7.1)$$

$$F_y = Q_d + K_d D_y \quad (7.2)$$

$$K_H = \frac{K_1 K_d}{K_1 - K_d} \quad (7.3)$$

where  $u_y$   $D_y$  is the yield displacement. The values of  $K_d$  and  $Q_d$  selected for numerical simulation are given in Section 7.4. Bidirectional coupling was accounted for through a circular yield surface. Physically, the element was implemented as a zero Length Section element in OpenSees (2010) incorporating a Bidirectional section to directly represent the force-deformation relation of the isolator.

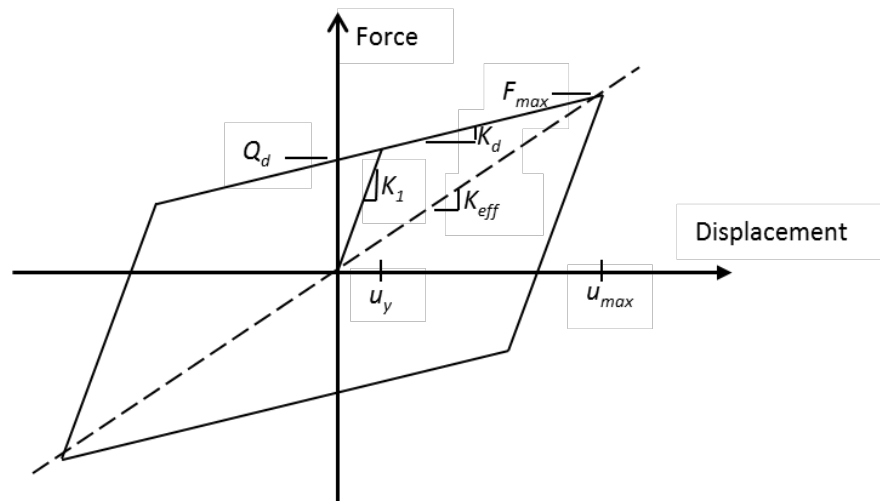


**Figure 7-1 Horizontal force-displacement of LR bearing for numerical simulation**

### 7.1.2 Vertical Direction Modeling Assumptions

In the vertical direction, the force-displacement relation of the LR bearings was idealized as bilinear elastic with different stiffness in tension and compression as recommended by Dynamic Isolation Systems. Physically, the bearings have nominal stiffness in tension but cavitate at relatively low values of tensile pressure (Constantinou et al. 2007). This behavior can be approximately simulated by assuming a low tensile stiffness. Numerically, an elastic-no tension model (Figure 7-2(a)) was combined in parallel with an elastic model (Figure 7-2(b)) to achieve the desired behavior shown in Figure 7-2(c). An effective tension stiffness was estimated to be of 2% of the compression stiffness was assumed. This approach was recommended by Dynamic Isolation Systems as an approximate way to capture the elastic-plastic tension behavior of the bearing and limited tensile capacity.

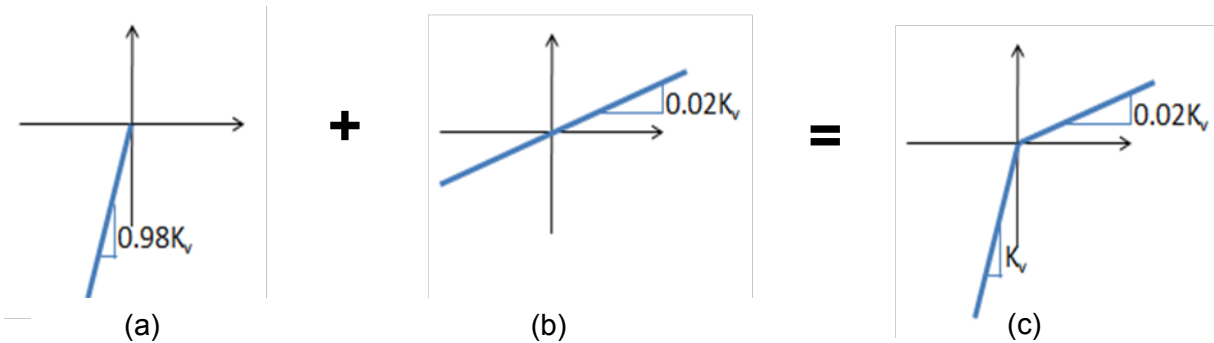


**Figure 7-2 Vertical force-deformation of LR bearing for analytical model: (a) elastic-no tension, (b) elastic, and (c) combined**

The nominal vertical stiffness of each LR bearing, as provided by DIS Dynamic Isolation Systems, was  $K_v = 15,000 \text{ kN/cm}$  (8,570 kip/in). The vertical stiffness of the bearings in the numerical simulation model was adjusted by trial and error to  $10,000 \text{ kN/cm}$  (5,710 kip/in) to indirectly account for the flexibility of the load cell support assemblies described in Section 4.1. This adjusted value was supported by the following approximate calculations. The vertical stiffness of a single Type A load cell – present under three of the four bearings – was given as  $K_{LC} = 85,000 \text{ kN/cm}$  (48,600 kip/in). The vertical stiffness of the steel plates was assumed to be



dominated by plate bending as the weight carried by the isolator was shifted to different locations on the steel plate. Assuming the plate acts as a continuous beam spanning several load cells, the plate bending stiffness was computed assuming fixed-fixed boundary conditions with a point load (the weight transferred through the isolator) acting midway between the supports (load cells):

$$K_{plate} = \frac{192EI}{L^3} \quad (7.4)$$

where  $E = 200$  GPa (29,000 ksi) is the elastic modulus of steel,  $L = 75$  cm (30 in) is the clear length between adjacent load cells, and  $I = bh^3/12$ , using  $b = L/2$  and  $h = 10$  cm (4 in) as the plate thickness. With these assumptions, the plate bending stiffness was computed to be  $K_{plate} = 28,000$  kN/cm (19,000 kip/in). Combining the stiffness of an LR bearing, plate, and load cell in series

$$\frac{1}{K_{total}} = \frac{1}{K_v} + \frac{1}{K_{plate}} + \frac{1}{K_{LC}} \quad (7.5)$$

the total vertical stiffness of the bearing load cell assembly was  $K_{total} = 8,800$  kN/cm (5,030 kip/in), which is close to the assumed value of 10,000 kN/cm (5,710 kip/in). The estimated stiffness of the bearing-load cell assembly was estimated similarly for a TP bearing-load cell assembly, which was in fact further corroborated by a detailed finite element analysis of the assembly (Dao 2012).

## 7.2 Cross Linear Bearing

Similar to the LR bearings, the force-displacement relation of the CL bearings was represented by a combination of spring elements, which were uncoupled in the horizontal and vertical directions. This assumption is not strictly accurate since the CL bearing is a friction device, and thus the horizontal force is proportional to the instantaneous axial force. However, the friction coefficient of the CL bearings was small so that their contribution to the overall base shear was negligible.

### 7.2.1 Horizontal Direction Modeling Assumptions

The force-displacement relation for the CL bearings was assumed to be elastic-perfectly plastic (with a post-yield stiffness of zero) in each horizontal direction as shown in Figure 7-3. The sliding rail system acts independently in each horizontal direction; thus a model with a square interaction surface was used instead of a bidirectionally coupled model. This assumption only affects the first yield mechanism since the model is perfectly plastic. The model initial stiffness of the CL bearing ( $K_{1s}$ ), where yield represents sliding of the bearing, was estimated as:

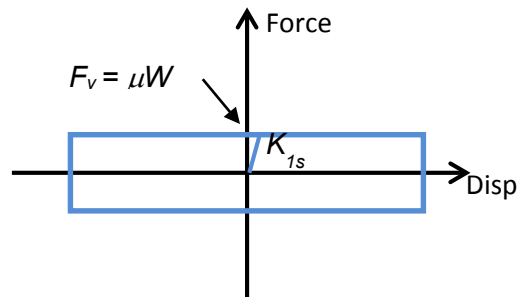


**Figure 7-3 Horizontal force-displacement of CL bearing for numerical simulation**

$$K_{1s} = \frac{\mu W}{D_y} \quad (7.6)$$

where  $\mu$  is the coefficient of friction,  $W$  is the weight (or static vertical force) on each isolator, and  $D_y$  is the yield displacement. The assumed friction coefficient for numerical simulation was 0.0025. Note that this differs from the value listed in Table 3-3, which reflects more recently acquired information about the CL bearing.

Under typical distribution of dead load based on tributary area, the center CL bearing would carry more weight than the CL bearings in corner positions. However, in the tested TP isolation system, the center bearing was lightly loaded compared to several of the other bearings (Dao, 2012). The warping at the base of the structure and the shimming procedure used to adjust the loads in the LR bearings affected the load distribution. The static vertical force in individual CL bearings was not measured during the test program. Since load distribution by tributary area was not a reasonable assumption, the total weight carried by the CL bearings (deduced from the weight of the structure and the measured weight on the LR bearings) was distributed evenly to individual CL bearings according to:

$$W = \frac{(W_{total} - \sum W_{LRBs})}{5} \quad (7.7)$$

Because of the uncertainty in the static axial loads in the CL bearings and the sensitivity of load transfer (Section 6.2) to the static equilibrium state, the developed numerical simulation model was not expected to accurately track axial forces in either LR or CL bearings. Trial and error variation of the vertical stiffness of these devices, which affects the balance of forces and load distribution over the isolators, was found to have little consequence to the predicted horizontal response of the isolation system.

### 7.2.2 Vertical Direction

The vertical force-deformation for the CL bearings was modeled using a similar parallel spring model as used for the LR bearing. In this case, the compression ( $K_{vc}$ ) and tension ( $K_{vt}$ ) stiffness were independent values provided by the manufacturer as listed in Table 3-3. Thus, the composite force-displacement relation was derived from an elastic-no tension spring with stiffness  $K_{vc} - K_{vt}$  (Figure 7.4(a)) and an elastic spring with stiffness  $K_{vt}$  (Figure 7.4(b)) to get the combined behavior of Figure 7.4(c).

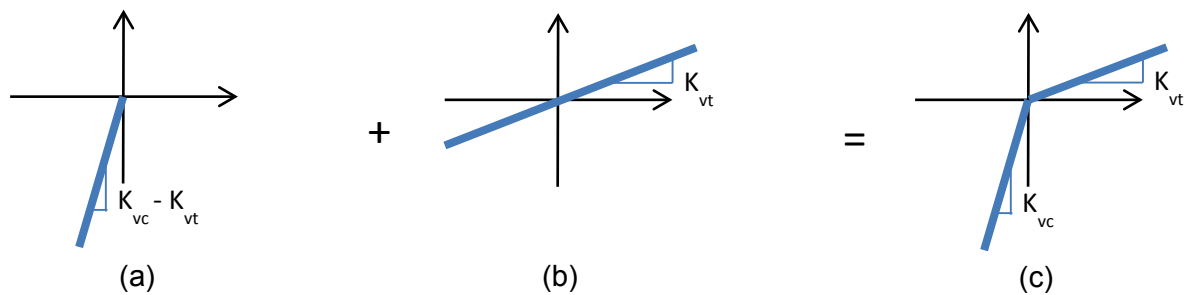


**Figure 7-4 Vertical force-deformation of CL bearing for analytical model: (a) elastic-no tension, (b) elastic, and (c) combined**

### 7.3 Composite Vertical Properties of the Isolation System

As part of our investigation, we considered the possibility that due to the flexibility of the load cell assemblies, the vertical stiffness (and fundamental frequency) did not represent a typical isolation system in the vertical direction. The following calculations support the conclusion that the hybrid LR isolation system was not uncharacteristically flexible in the vertical direction.

A typical “rigid body” vertical frequency of an elastomeric isolation system, computed from

$$\omega_{z,rigid} = \sqrt{\frac{g \cdot \sum K_v}{W}} \quad (7.8)$$

ranges from 10-15 Hz (Kasalanati 2012). Recall that the measured weight of the testbed building was 5,220 kN (1,174 kip), and the nominal (manufacturer supplied) vertical stiffnesses were 15,000 kN/cm (8,565 kip/in) for an LR bearing and 34,700 kN/cm (19,814 kip/in) for a CL bearing. The adjusted vertical stiffness of the LR bearing-load cell assembly was assumed to be 10,000 kN/cm (5,710 kip/in). Ignoring the influence of the CL bearings, suppose the isolation system had consisted of 4 LR bearings, which would be typical for the composite weight of the system, and not supported on load cells - thus representative of the expected field conditions for these LR bearings. The vertical frequency of the isolation system, computed from Equation (7.8), would be about 17 Hz (0.06 sec), which is on the stiff side of typical. Now, suppose the isolation system consisted of 4 LR bearings supported on load cells with the modified stiffness of 10,000 kN/cm (5,710 kip/in). In this case, the frequency would be reduced slightly to 14 Hz (0.07 sec), which is also stiff. However, the actual hybrid system tested in this experimental program, with 4 LR bearings on the load cell assemblies at 10,000 kN/mm (5,710 kip/in) and 5 CL bearings at 34,700 kN/cm (19,814 kip/in), had a vertical frequency of 31 Hz (0.032 sec). Thus, as asserted above, the fundamental vertical frequency of the tested hybrid isolation system was actually quite large, such that the system can be considered sufficiently stiff.

### 7.4 Characterization of Lead-Rubber Bearings

To predict the response of the isolation system for design of a nuclear power plant, one would ideally develop the modeling or numerical simulation parameters based on physical properties of the individual isolation devices. As discussed in Chapter 1,  $K_d$  is physically related to the stiffness of rubber and  $Q_d$  is physically related to the strength of the lead plug. For design, a single set of bilinear parameters ( $K_d$ ,  $Q_d$ ) is generally used to represent the bearing hysteresis loop over a wide range of displacement, supplemented by bounding analysis.

For the LR bearings tested as part of this experimental program, a single set of simulation parameters did not lead to sufficient accuracy in the model over the range of displacement amplitudes observed in the test program. Factors that contributed to the disparity in bearing hysteresis loop and best fit model parameters included the following. First, the test program included a few small amplitude simulations, such as Westmorland 80% that did not drive the isolators sufficiently into the nonlinear range to develop the full characteristic strength of the lead plug. Smaller amplitude motions would not normally be considered in design. Second, the pinching behavior induced by the smaller size lead plug, not seen in typical full scale LR bearings, meant that a bilinear model could not be fit closely to the observed hysteresis loop, which lacked a consistent backbone curve. Thus, more significant parameter variations induced by amplitude changes were observed throughout the test program. Finally, several a couple sources of characteristic strength variation were not incorporated into the bilinear model. For one, lack of a full recovery time between simulations meant that the response of the bearings was affected by temperature variation (as documented in Section 6.3), which could not be incorporated into the model easily due to the absence of measured temperature data. Furthermore, the response of the bearings was not representative of the real (unheated) state that would be experienced for a real earthquake when the isolation system is not excited in regular intervals. Second, the effective yield stress of the lead plug is rate dependent, wherein rate variation is a function of amplitude variation. Third, axial force variation affected the confinement of the lead plug, a dynamic effect that also was not accounted for in the bilinear model.

To obtain a consistently accurate prediction of isolator displacements and forces across the set of trials, we elected to characterize the bearing parameters independently for each simulation in the test program. As described above, this procedure was necessary only due to the special circumstances of the test program, and would not nor could not be attempted for design. Characterized bearing properties were determined both for pseudo-static cyclic tests conducted by DIS and for each simulation during the test program at E-Defense.

#### **7.4.1 Characterization by Dynamic Isolation Systems (DIS)**

The LR bearings were characterized by Dynamic Isolation Systems in their manufacturing facility prior to shipment to Japan. Bearings were tested in the machine two at a time; each pair of bearings was subjected to cyclic shear tests under constant compressive load and the measured horizontal force represents the sum of the horizontal forces in the two bearings. The tests were displacement controlled, such that the bearings were cycled back and forth to the target maximum displacement in each direction for the desired number of cycles. A series of four tests were conducted at different axial loads and displacements, as summarized in Table 7-1. Test C was added to accommodate E-Defense's safety protocol, given that a displacement demand of 55 cm (22 in) was to be targeted during the tests. Test D was a repeat of Test A and was intended to document any change in hysteresis loops as a result of repeated loading. A minimum fifteen minute interval was inserted after every test. As shown by the rate parameter in Table 7-1, these characterization tests were essentially static and thus do not include any rate effects on the bearing response. In particular, the lead plug heating effects would be smaller in a static simulation than in a high speed cyclic simulation.

**Table 7-1 Compression Shear Test Schedule.**

Test ID	Number of Cycles	Axial Load (kN)	$D_{max}$ (cm)	Shear Strain %	Rate (cycles/min)
A	3	600	30	125	1.15
B	3	1000	50	208	0.71
C	0.5	100	65	271	0.54
D	3	600	30	125	1.15

In the test report provided by Dynamic Isolation Systems (Appendix E), the isolator properties were determined by fitting a bilinear loop to the recorded hysteretic loop such that the energy dissipated and the effective stiffness of the two loops were equal. The fitted second-slope post-yield stiffness ( $K_d$ ) and characteristic strength ( $Q_d$ ) were determined directly from the fitted loop. The fitting procedure is described conceptually by Figure 7-5. The effective stiffness of the isolator ( $K_{eff}$ ) is equal to  $F_{max}/D_{max}$ , where  $D_{max}$  is the maximum isolator displacement and  $F_{max}$  is the maximum force measured in the isolator. If the cycle is unsymmetric, the peak-to-peak stiffness is used rather than the half cycle effective stiffness. The energy dissipated per cycle ( $EDC = \text{area of the loop}$ ) was determined by numerically integrating the force-displacement data. Fixing the corner points ( $F_{max}, D_{max}$  and  $F_{min}, D_{min}$ , which are the minimum isolator force and displacement, respectively) of the analytical model to match the test data,  $Q_d$  and  $K_d$  are adjusted until the energy dissipated in a cycle of the theoretical bilinear loop with initial stiffness  $K_1 = 10 K_d$  matches the numerically integrated energy dissipated from the recorded data.

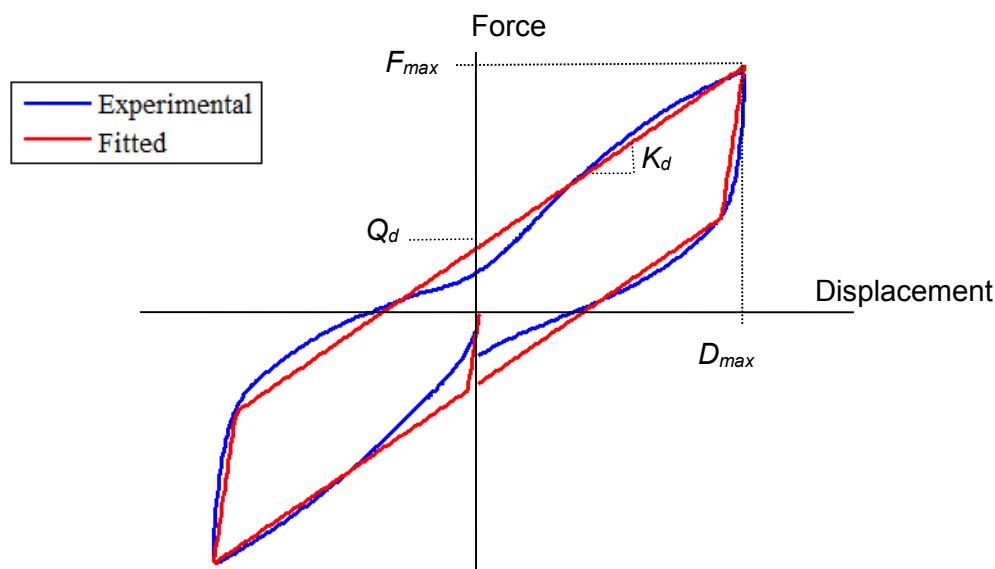


**Figure 7-5 Comparison of fitted hysteresis loop and parameters to test data**

The force-displacement relationship for one of the isolator pairs recorded during the Test A loading protocol is shown in Figure 7-6. Pinching of the hysteresis loop is observed around zero displacement, which is expected when the lead plug is small relative to the diameter of the bearing or simply small on an absolute scale. Pinching may be observed in full size or prototype LR bearings manufactured for real world projects, but far less pronounced than that observed here (Kasalanati, 2012).

The recorded and fitted parameters for the test data (Figure 7-6) are listed in Table 7-2 for each cycle as well as the average over all 3 cycles. The energy dissipation per cycle  $EDC$  and thus

fitted  $K_d$  and  $Q_d$  decrease after each cycle, with a large drop noted after the first cycle. As a result of the pinching, the fitted  $Q_d$  is significantly larger (by up to 70%) than the y-axis force intercept of the test data. The characterization procedure was carried out for each cycle of all four tests. The characterized values for each test (averaged over all cycles and over the two pairs of bearings) are reported in Table 7-3.

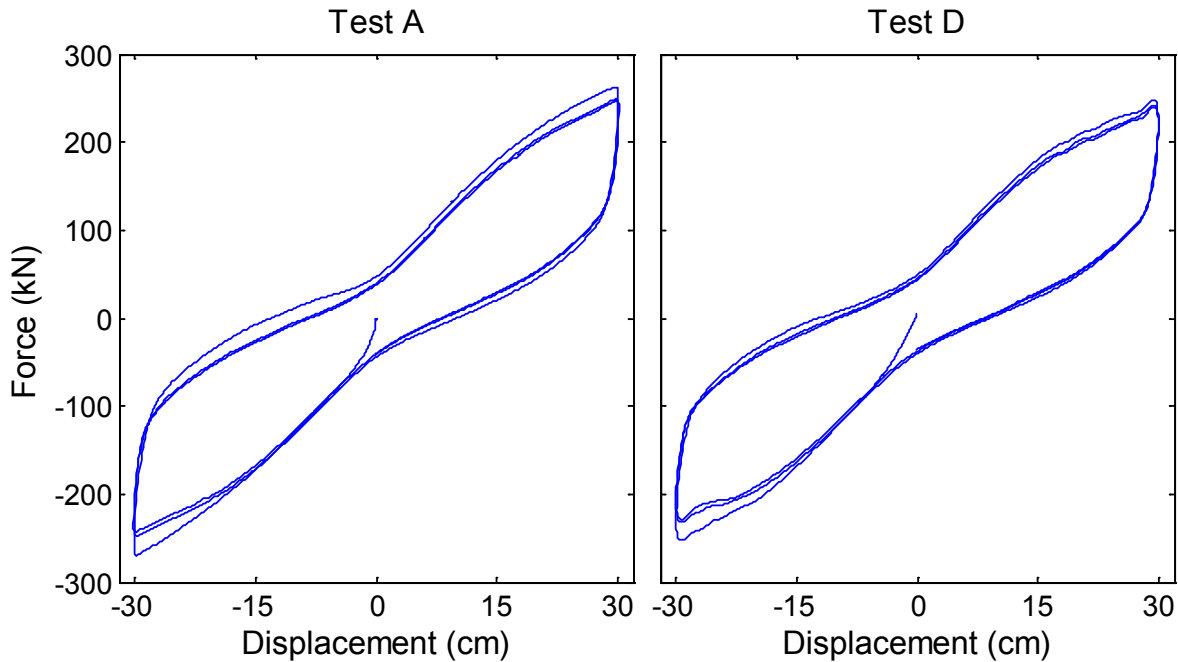


Figure 7-6 Hysteresis loop of Test A and D for one of the isolation pairs

Table 7-2 Recorded and fitted parameters for Test A.

Cycle	$D_{max}$ (cm)	$F_{max}$ (kN)	$K_{eff}$ (kN/cm)	$EDC$ (kN.cm)	$K_d$ (kN/cm)	$Q_d$ (kN)
1	30.1	266	8.8	8455	6.5	71.2
2	30.2	249	8.2	7486	6.2	62.9
3	30.2	245	8.1	7206	6.1	60.4
AVERAGE	30.2	253	8.4	7716	6.3	64.8

Table 7-3 Characterized isolator parameters for all tests in the sequence.

Test	Axial Load (kN)	$D_{max}$ (cm)	$K_d$ (kN/cm)	$Q_d$ (kN)	$K_{eff}$ (kN/cm)
A	600	30	6.3	64.7	8.4
B	1000	50	5.1	75.6	6.6
C	100	65	5.5	85.6	6.8
D	600	30	5.8	63.1	7.9

The isolator parameters given in the design specifications (Table 3-3) were stiffness  $K_d = 6.5$  kN/cm (3.7 kip/in), characteristic strength  $Q_d = 65.7$  kN (14.8 kips), and effective stiffness  $K_{eff} = 8.7$  kN/cm (5 kip/in). The fitted parameters are within 4% of the design specifications at a displacement of 30 cm (12 in). Note that the design specifications are just target values set by Dynamic Isolation Systems prior to their manufacture.

#### 7.4.2 Characterization Based on Experimental Data

The characterization of the bearings for the earthquake simulations was complicated by the fact that the experimental data was bidirectional, and the random earthquake excitation did not produce the smooth controlled hysteresis loops of cyclic data. We searched for a procedure to characterize the bearing parameters directly based on bidirectional data, but without success. Thus, the following alternative procedure was implemented to characterize the bearings for each test.

**Step1:** To obtain the best results for a unidirectional characterization procedure, the test data in both directions was rotated to an alternate coordinate system with a main axis that contained the largest displacement cycle of the record. The main axis was identified from the largest single cycle peak-to-peak excursion on the displacement trace. For instance, in Vogtle 100%, the main axis was identified at an approximate 45 degree rotation (Figure 7-7), consistent with the rotation of the input motion to generate the peak displacement demand along the diagonal (Section 3.3). Identification of the main axis was subjective if the displacement trace contained a large circular cycle of motion.

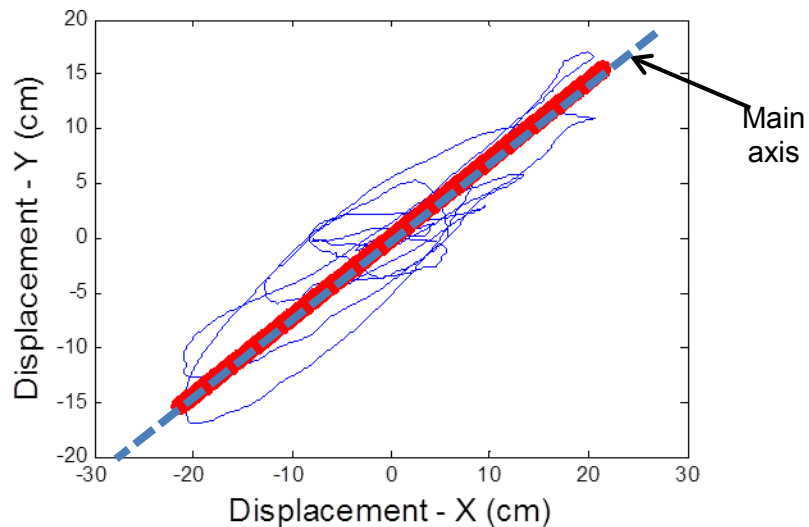


**Figure 7-7** Projection of displacement trace to main axis for Vogtle 100%

**Step 2:** The isolator displacement history was projected to the main axis direction of the rotated data, and the cycle containing the largest peak-to-peak displacement was selected for characterization. Figure 7-8 shows the selected cycle for LRB-E for Vogtle 100%.

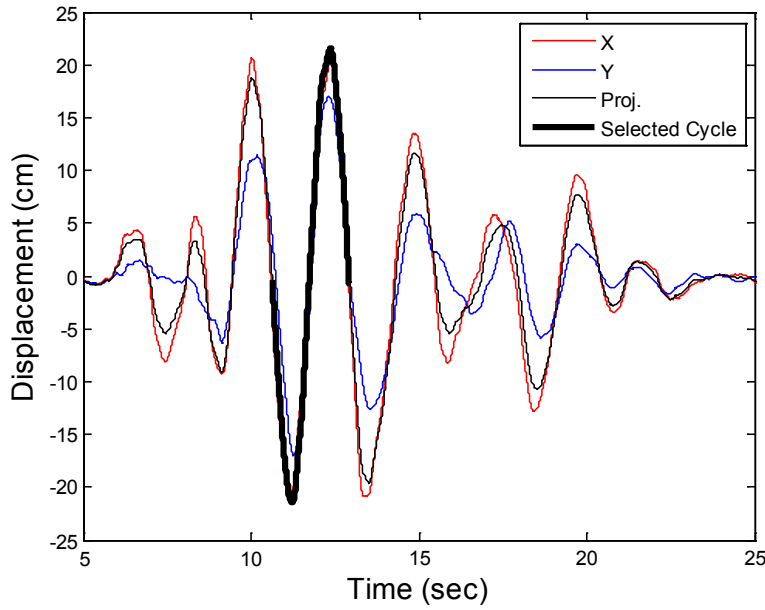


**Figure 7-8 Selection of cycle for characterization for Vogtle 100%**

**Step 3:** The energy dissipated ( $EDC_{test}$ ) for the selected cycle was determined by numerically integrating the shear force versus lateral displacement using a cumulative trapezoidal algorithm.

**Step 4:** The theoretical characteristic strength  $Q_d$ , post-yield stiffness  $K_d$  and yield displacement  $u_y$  were fitted to the projected test data using essentially the same algorithm employed by Dynamic Isolation Systems, and summarized as follows. The energy dissipated in a bilinear force-displacement loop  $EDC_{bilin}$  is determined by:

$$EDC_{bilin} = 4Q_d(uD_{peak} - Du_y) \quad (7.9)$$

where  $Q_d$  is the characteristic strength,  $u_{peak} D_{peak}$  is absolute peak displacement for the selected cycle, and  $Du_y$  is the yield displacement. The energy dissipated during the experiment ( $EDC_{test}$ ) is equated to the theoretical energy dissipated ( $EDC_{bilin}$ ), and Equation 7.9 is rearranged to solve for  $Q_d$ . The yield displacement  $u_y D_y$ , which is unknown, is dropped from the equation and replaced with a calibration factor  $\gamma\beta$  initialized to 1:

$$Q_d = \frac{\gamma\beta * EDC_{test}}{4 * Du_{peak}} \quad (7.10)$$

From the estimate of  $Q_d$ , the theoretical second-slope post-yield stiffness  $K_d$  and yield displacement  $u_y D_y$  are computed.

$$K_d = \frac{F_{peak} - Q_d}{u D_{peak}} \quad (7.11)$$

$$Du_y = \frac{Q_d}{K_1 - K_d} \quad (7.12)$$



where,  $F_{peak}$  is the absolute peak displacement force for the selected cycle, and  $K_1 = 10 K_d$ . Equations (7.9) – (7.12) are computed iteratively until convergence is obtained ( $EDC_{bilin} \approx EDC_{test}$ ). If  $EDC_{test} < EDC_{bilin}$ , then  $\gamma\beta$  is decreased by small increments, while if  $EDC_{test} > EDC_{bilin}$ , then  $\gamma\beta$  is increased by small increments.

Once the characterized values were computed by the above procedure, the model parameters (initial stiffness, kinematic hardening modulus and yield force) were computed from Equations 7.1 to 7.3.

The hysteresis loop for the projected experimental data and the fitted loop based on characterized parameters are compared in Figure 7-9 for Vogtle 100%. In Figure 7-9, no obvious bidirectional interaction is observed in the experimental data, which supports the idea that projecting the force-displacement data to a main axis improves the characterization compared to experimental data that has not been projected.

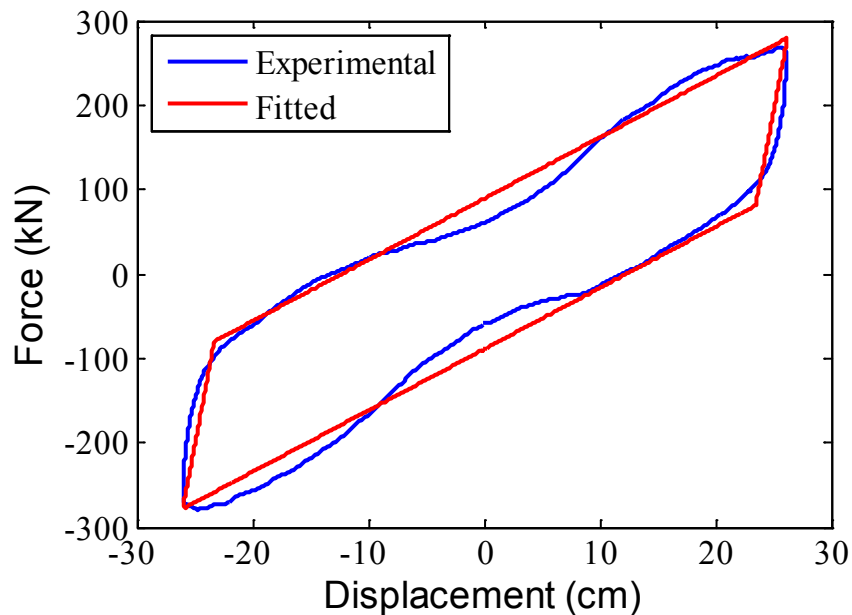


**Figure 7-9 Hysteresis loop of peak cycle for the projected-direction for East bearing for Vogtle 100%**

The characterized parameters  $Q_d$ ,  $K_d$ ,  $u_y$ ,  $D_y$  for each bearing and the average among all bearings for each simulation are summarized in Table 7-4. The numerical simulation model in OpenSees used the average values listed on the last column for each simulation, with some minor adjustment, which is described momentarily. The range of the parameters varied as follows. The average of  $Q_d$  ranged from 33.4 – 89.4 kN (7 - 20 kip), and the average  $K_d$  ranged from 5.7 - 11 kN/cm (3.2 - 6.3 kip/in). However, omitting WSM80 and ELC130, which produced only about 9 cm (4 in) and 21 cm (8 in) displacement, respectively,  $Q_d$  ranged from 62.0 - 89.4 kN (14.0 – 20.1 kip), and  $K_d$  ranged from 5.7 - 8.2 kN/cm (3.2 – 4.7 kip/in), where the displacement varied from 20 cm (8 in) to 55 cm (22 in). As a comparison, the target specifications at a displacement of 30 cm (12 in) were  $Q_d = 65.7$  kN (14.8 kip) and  $K_d = 6.5$  kN/cm (3.7 kip/in).

The numerical and experimental simulation hysteresis loops are compared using the design parameters (Figure 7-10(a),(c)) and the parameters determined by characterization (Figure 7-10(b),(d)) for the Westmorland 80% and Diablo 95% (XY) motion. The numerical simulation loops were determined by response history analysis of the complete specimen model (described in Chapter 8) subjected to the recorded table motion. The characterized parameters led to a clear improvement in prediction of the peak displacement for Westmorland 80%. On the other hand, since the characterized and design values of  $Q_d$  and  $K_d$  for Diablo 95% (XY) are about the same, the hysteresis loops and peak displacements generated by the two approaches were similar, as shown in Figure 7-10(c) and (d). Overall, Figure 7-10 confirms that the bilinear model is a reasonable assumption for the behavior of the bearing if the parameters are calibrated for each simulation.

**Table 7-4 Characterized bearing parameters for each earthquake simulation.**

Trial #	GM	Isolator	$Q_d$ (kN)	$K_d$ (kN/cm)	$K_1$ (kN/cm)	$u_y D_y$ (cm)	Average
1	WSM80	E	37.1	10.7	106.6	0.4	$F_y = 37.1$ kN $Q_d = 33.4$ kN $K_d = 11.0$ kN/cm
		S	31.5	10.7	107.0	0.3	
		N	33.6	11.0	110.3	0.3	
		W	31.5	11.5	115.1	0.3	
2	SIN100(Y)-1	E	78.2	8.4	83.8	1.0	$F_y = 86.0$ kN $Q_d = 77.4$ kN $K_d = 8.2$ kN/cm
		S	76.3	8.1	80.8	1.0	
		N	77.8	8.2	81.6	1.1	
		W	77.2	8.0	80.4	1.1	
3	VOG75-1	E	77.4	8.2	81.9	1.0	$F_y = 75.5$ kN $Q_d = 67.9$ kN $K_d = 8.2$ kN/cm
		S	61.6	8.7	87.2	0.8	
		N	70.8	8.2	81.8	1.0	
		W	61.8	7.6	75.9	0.9	
4	VOG100	E	86.3	7.4	73.5	1.3	$F_y = 88.6$ kN $Q_d = 79.7$ kN $K_d = 7.4$ kN/cm
		S	77.6	7.7	76.7	1.1	
		N	82.0	7.2	71.5	1.3	
		W	72.9	7.3	73.5	1.1	
5	VOG125	E	91.9	6.4	64.2	1.6	$F_y = 95.3$ kN $Q_d = 85.8$ kN $K_d = 6.5$ kN/cm
		S	83.0	6.4	63.8	1.4	
		N	86.9	6.4	64.3	1.5	
		W	81.3	6.7	67.4	1.3	
6	VOG150	E	92.4	6.0	59.8	1.7	$F_y = 98.5$ kN $Q_d = 88.7$ kN $K_d = 5.9$ kN/cm
		S	87.4	5.6	55.6	1.7	
		N	87.5	5.9	59.1	1.6	
		W	87.3	6.0	59.9	1.6	
7	VOG175	E	92.3	6.0	60.0	1.7	$F_y = 99.4$ kN $Q_d = 89.4$ kN $K_d = 5.7$ kN/cm
		S	90.5	5.4	53.8	1.9	
		N	87.8	5.7	56.7	1.7	
		W	87.1	5.6	56.1	1.7	
8	DIA80	E	79.2	6.6	65.7	1.3	$F_y = 74.8$ kN $Q_d = 67.3$ kN $K_d = 6.6$ kN/cm
		S	64.0	6.3	63.2	1.1	
		N	68.4	6.9	68.5	1.1	
		W	57.6	6.7	67.0	1.0	

**Table 7-4 (Cont.) Characterized bearing parameters for each earthquake simulation.**

<b>Trial #</b>	<b>GM</b>	<b>Isolator</b>	<b><math>Q_d</math> (kN)</b>	<b><math>K_d</math> (kN/cm)</b>	<b><math>K_1</math> (kN/cm)</b>	<b><math>u_y D_y</math> (cm)</b>	<b>Average</b>
9	DIA95(XY)	E	79.9	6.3	62.8	1.4	$F_y = 78.1$ kN $Q_d = 70.3$ kN $K_d = 6.2$ kN/cm
		S	65.7	6.0	59.9	1.2	
		N	74.4	6.2	62.4	1.3	
		W	60.9	6.3	63.0	1.1	
10	ELC130	E	61.0	7.7	77.2	0.9	$F_y = 59.5$ kN $Q_d = 53.5$ kN $K_d = 8.4$ kN/cm
		S	56.6	8.1	80.9	0.8	
		N	48.5	8.8	88.3	0.6	
		W	47.8	9.0	89.6	0.6	
11	IWA(XY)	E	81.3	6.7	66.7	1.4	$F_y = 87.6$ kN $Q_d = 78.8$ kN $K_d = 6.3$ kN/cm
		S	80.7	5.9	58.5	1.5	
		N	75.1	6.5	65.2	1.3	
		W	78.0	6.3	62.7	1.4	
12	RRS88(XY)	E	75.5	6.6	66.2	1.3	$F_y = 75.8$ kN $Q_d = 68.2$ kN $K_d = 6.6$ kN/cm
		S	65.1	6.4	63.6	1.1	
		N	68.8	6.7	66.9	1.1	
		W	63.3	6.6	65.9	1.1	
13	RRS88	E	74.3	6.5	65.3	1.3	$F_y = 74.7$ kN $Q_d = 67.2$ kN $K_d = 6.4$ kN/cm
		S	64.5	6.2	62.1	1.2	
		N	67.8	6.5	65.0	1.2	
		W	62.2	6.5	64.7	1.1	
14	VOG75-2	E	69.8	7.6	75.9	1.0	$F_y = 69.5$ kN $Q_d = 62.5$ kN $K_d = 7.4$ kN/cm
		S	61.3	7.6	75.7	0.9	
		N	64.3	7.2	72.5	1.0	
		W	54.8	7.2	72.4	0.8	
15	SIN100(Y)-2	E	75.5	7.7	76.5	1.1	$F_y = 79.7$ kN $Q_d = 71.8$ kN $K_d = 7.4$ kN/cm
		S	74.6	7.3	72.8	1.1	
		N	72.3	7.3	73.1	1.1	
		W	64.6	7.2	71.9	1.0	

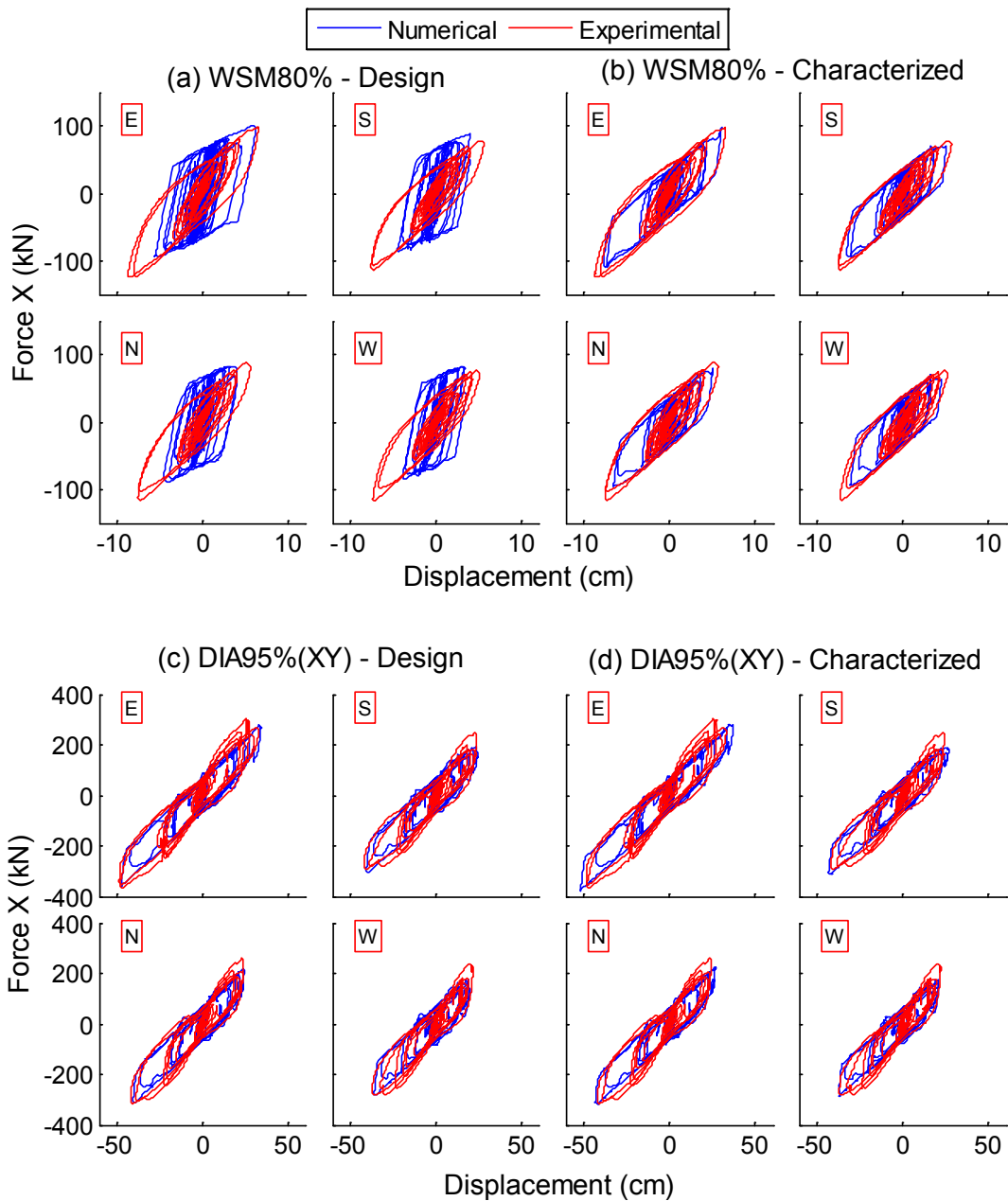


**Figure 7-10 Analytical and experimental hysteresis loop using (a),(c) isolator design parameters and (b),(d) characterized parameters**

The characterized model was calibrated for a cycle close to the peak displacement, but consequently did not improve the response prediction for cycles at smaller displacement. For example, the y-direction hysteresis loop and force history (test versus analysis) are shown in Figure 7-11 for the first sine wave trial. At small amplitudes (after 22 sec in Fig 7-11(b) and (d)), the actual force in the LR bearing was quite small, indicating the lead plug was not fully engaged. Thus, both numerical models significantly overestimated the force in this range. The characterized model gave a much better prediction of peak force than the design model at the expense of higher force error in the small amplitude part of the record. As another example, the x-direction mean square error in the design model was lower than the characterized model for Vogtle 175%. Based on the displacement history (Figure 7-12), the characterized model better

predicted the displacement for the largest cycle (around 10 sec), but the design model better predicted the displacement in subsequent cycles (compare Figures 7-12(a) and (b)).

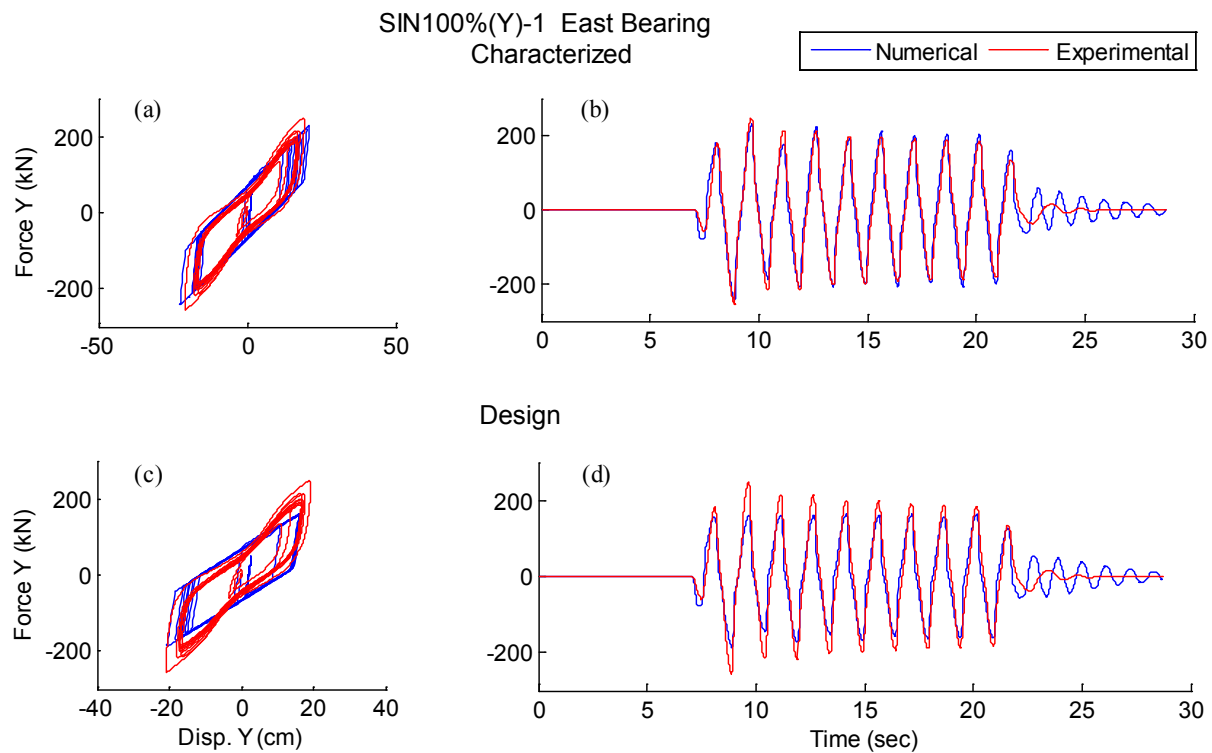


**Figure 7-11 Y-direction hysteresis and force history of test data of the East bearing compared to (a)-(b) characterization model, and (c)-(d) design model for Sine 100%(Y)-1**

The comparisons illustrate the challenge of predicting the bearing response using a single bilinear model that is insensitive to the characteristic strength variation due to axial force variation amplitude dependence and temperature change in the lead plug. The challenge was amplified by the pinching in the lead plug, which is not typical of full scale isolation bearings. When the bearing model was calibrated to the largest displacement cycle, it tended to overestimate the force and underestimate the displacement at smaller amplitudes. Development or use of existing models that account for the various effects such as pinching and, thermal, and axial force may significantly improve the fitted response that could be obtained from a model with a single set of parameters. One potential improvement was attempted, which was to model the bearings with trilinear force-deformation that may be able to represent a smoother transition to the fully-yielded state, and thus reduce the energy dissipated in the hysteresis loop for small cycles. This potential improvement was attempted, and is described in the next section.

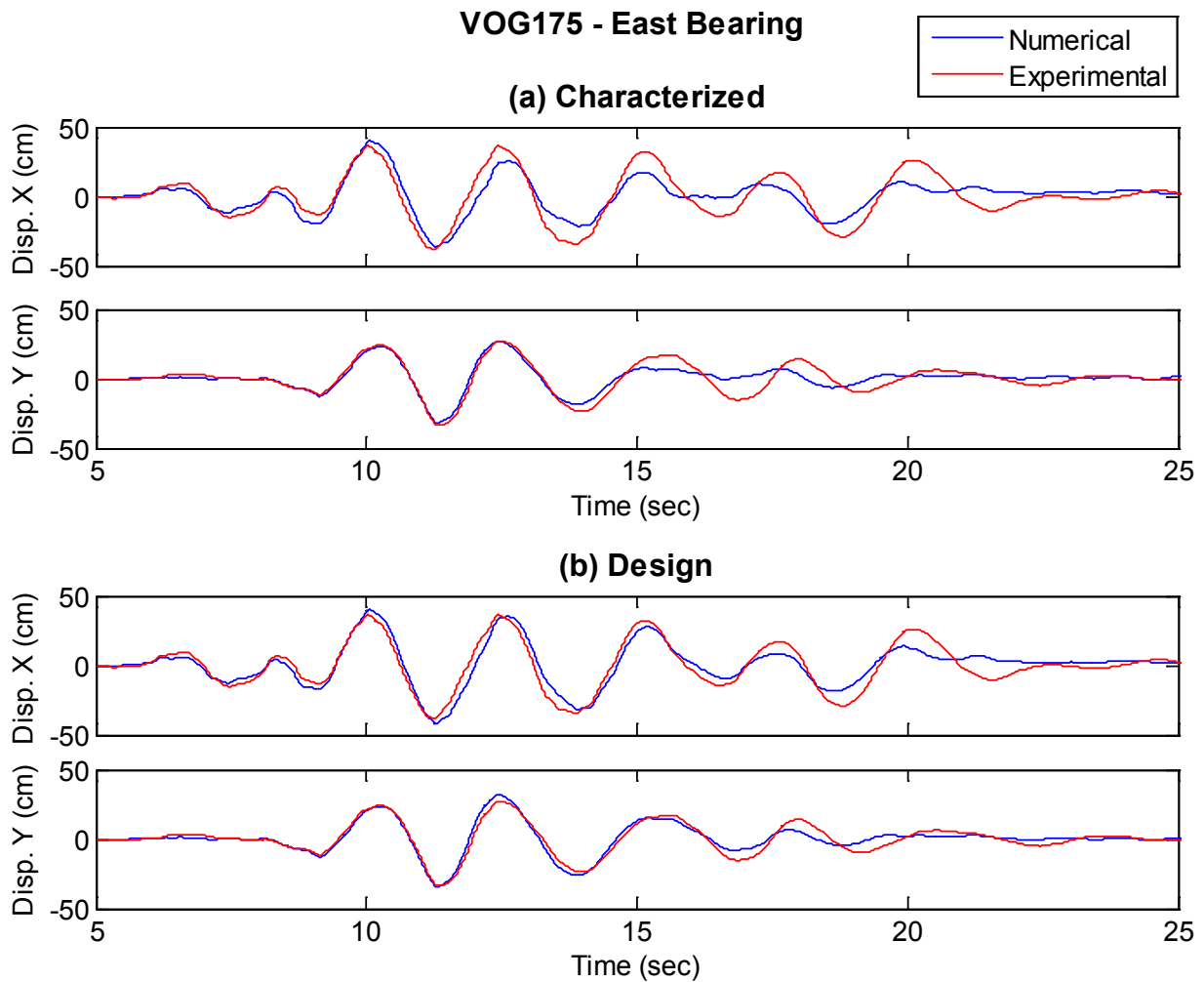


**Figure 7-12 X and y-direction displacement history of experimental data compared to (a) characterized model and (b) design model for Vogtle 175%, East bearing**

### 7.4.3 Trilinear Characterization

The elastic stiffness in a bilinear hysteretic model is determined by the stiffness of the lead plug, and the model assumes that the lead plug stiffness is linear. However, the experimental data exhibited a smooth transition from the linear to the post-yield state (e.g. Sine 100%(Y)-1, Figure 7-13), such that a numerical model defined by a sharp transition from the linear to post-yield state was overly stiff for large displacements. The gradual transition to the yielded state is a reflection of the true behavior of the lead plug (Figure 7-14). Thus, a trilinear model was attempted to improve the small displacement prediction without altering the large displacement response of the model. (A Bouc-Wen model (Park et al. 1986) is also known for smoothing the transition from the linear to the post-yield state, and is another approach that could have been attempted.)

SIN100%(Y)-1 East Bearing

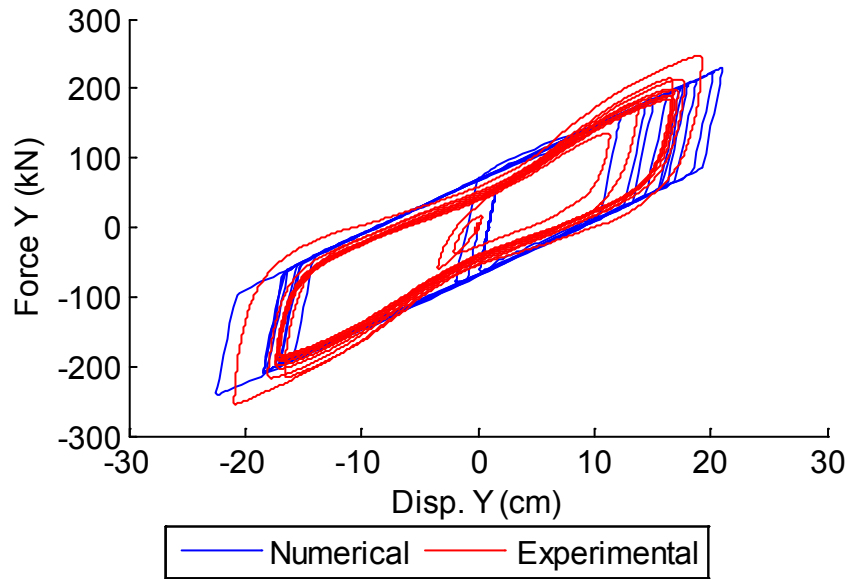


Figure 7-13 Force vs. displacement loop for the East LRB in Sine 100%(Y)-1

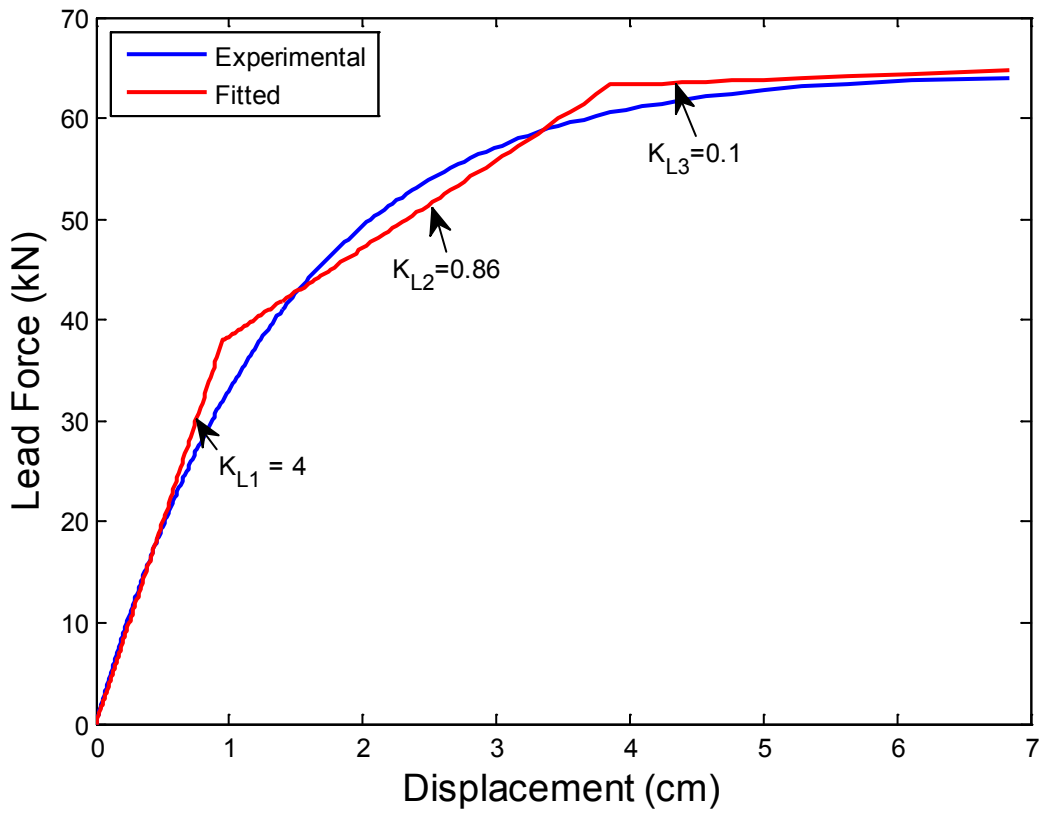


Figure 7-14 Conceptual force vs. displacement of lead plug for monotonic loading (courtesy of Dynamic Isolation Systems)

In the trilinear model, the stiffness of the lead-plug was modeled as piecewise linear with stiffness  $K_{L1}$ ,  $K_{L2}$  and  $K_{L3}$ . The values of  $K_{L1}$ ,  $K_{L2}$  and  $K_{L3}$  from Figure 7-14 were selected such that the tangent stiffness for the displacement less than 1 cm and greater than 6 cm matched the experimental data. Then,  $K_{L2}$  was selected such that the same area under the actual curve and the theoretical curve were equal area under the actual curve and the theoretical curve were equal.

The trilinear model was implemented in OpenSees as three bilinear springs in parallel, where each spring was assigned different properties and represented bidirectionally coupled behavior. Springs 1 and 2 represented the stiffness and energy dissipation in the lead plug while Spring 3 represented the stiffness of rubber. Springs 1 and 2 were elastic-perfectly plastic with initial stiffness and yield force as determined by Figure 7-14. The properties of the third spring representing the rubber were calculated as follows. The elastic stiffness of rubber ( $K_{1,rub}$ ) was computed as

$$K_{1,rub} = K_{1,char} - K_{1,lead} \quad (7.13)$$

where  $K_{1,char}$  is the characterized elastic stiffness described in Section 7.4 and  $K_{1,lead}$  is the elastic stiffness from Figure 7-15. The characteristic strength of rubber  $Q_{d,rub}$  was defined as:

$$Q_{d,rub} = Q_{d,char} - Q_{d,lead} \quad (7.14)$$

where  $Q_{d,char}$  is the characterized characteristic strength described in Section 7.4 and  $Q_{d,lead}$  is the characteristic strength of the lead from Figure 7-15. The yield displacement was defined as:

$$Du_{y,rub} = \frac{Q_{d,rub}}{K_{1,rub} - K_{d,char}} \quad (7.15)$$

where  $K_{d,char}$  is the characterized post yield stiffness described in Section 7.4.2. These properties were sufficient to determine the modeling parameters of the spring.

Results for numerical and experimental simulation with both the bilinear and trilinear bearing models are compared in Figure 7-15 for SIN 100(Y)-1 (Figure 7-15(a)-(b)) and Vogtle 100% (Figure 7-15(c)-(d)), where the influence of the multi-linear pivoting can be seen especially in the center of the loop and the large displacement transitions for Sine 100%. The trilinear model led to some improvement in the small displacement hysteresis for SIN100(Y)-1, but the improvement was negligible for Vogtle 100%. The same was true for the other earthquake simulations. In particular, the trilinear model did not appear to substantially change the prediction of the displacement over the majority of the record, and did not address the primary inconsistency of the model compared to the experimental data, which was the pinching of the lead plug through the center of the loop that extended into the post-yield behavior. Therefore, the trilinear model was not adopted for final numerical simulation to validate the experimental data.



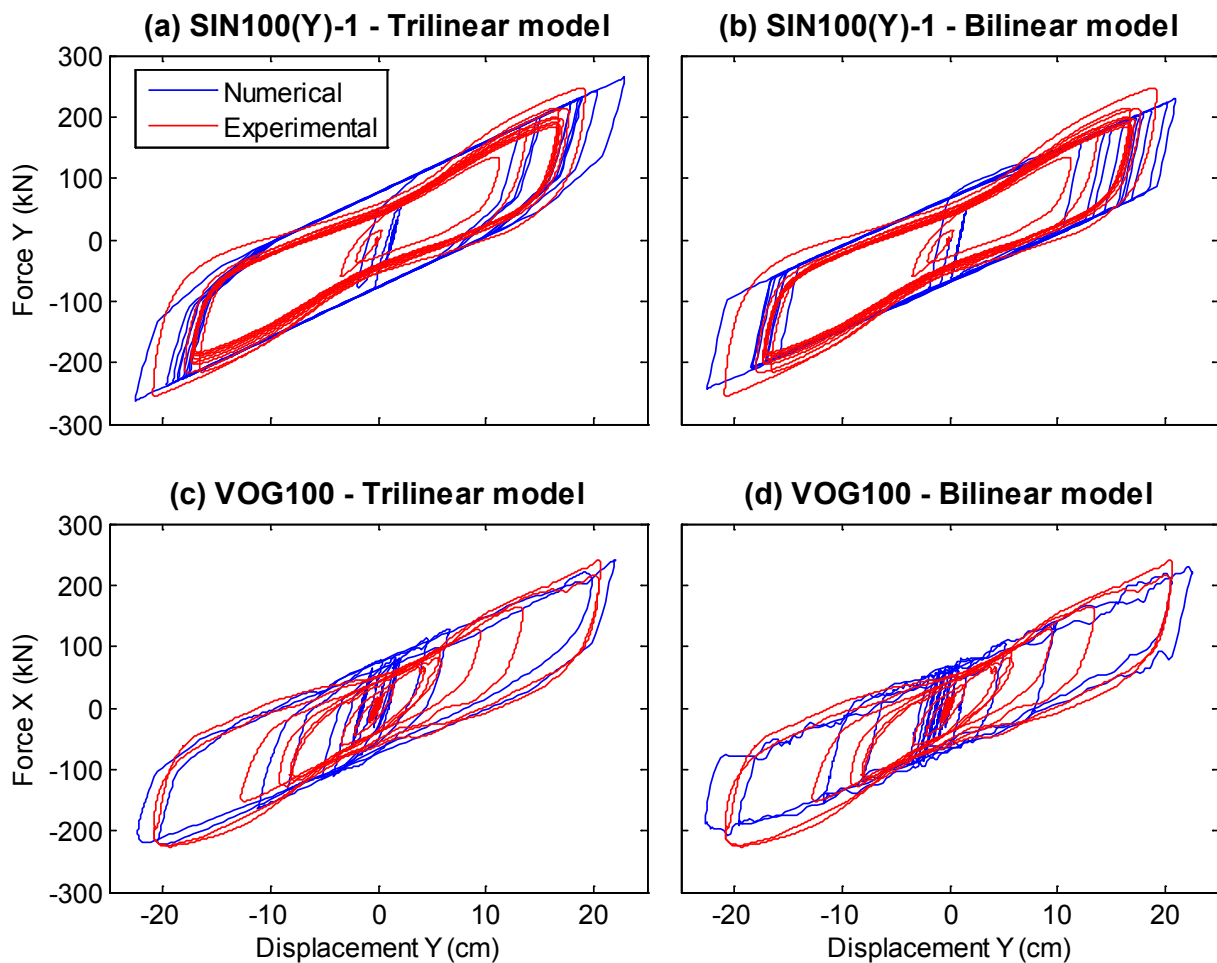


**Figure 7-15 Comparison of numerical and experimental simulation force versus displacement of the East bearing for SIN100(Y)-1 and VOG100 using (a), (c) a trilinear hysteretic model and (b), (d) a bilinear hysteretic model**

#### 7.4.4 Final Bearing Parameter Selection for Numerical Simulation

One slight modification was made to the characterized bearing parameters used in the final numerical simulation models, which are compared to the experimental results in Chapter 9. The peak displacements using the best fit parameters of Table 7-4 were often below the peak experimentally observed displacements. The problem seemed to result from the fact that the fitted  $Q_d$  (y-intercept) was larger than the actual  $Q_d$  of the LR bearings, thus increasing the energy dissipation at lower amplitudes and suppressing the higher displacement amplitudes from ever being reached. By trial and error, we observed that decreasing  $Q_d$  by a nominal amount relative to the best fit value improved the displacement prediction. As an example, Figure 7-16 compares simulation results using the best fit characterized model parameters and the model with  $Q_d$  reduced to 85% of the characterized value to the experimental data for Vogtle 100%. The model with reduced  $Q_d$  better predicted the peak displacement amplitude and followed the bearing hysteresis better than the best fit characterized model. Thus, the reduced value of  $Q_d$  was used for all simulation results presented in Chapter 9.

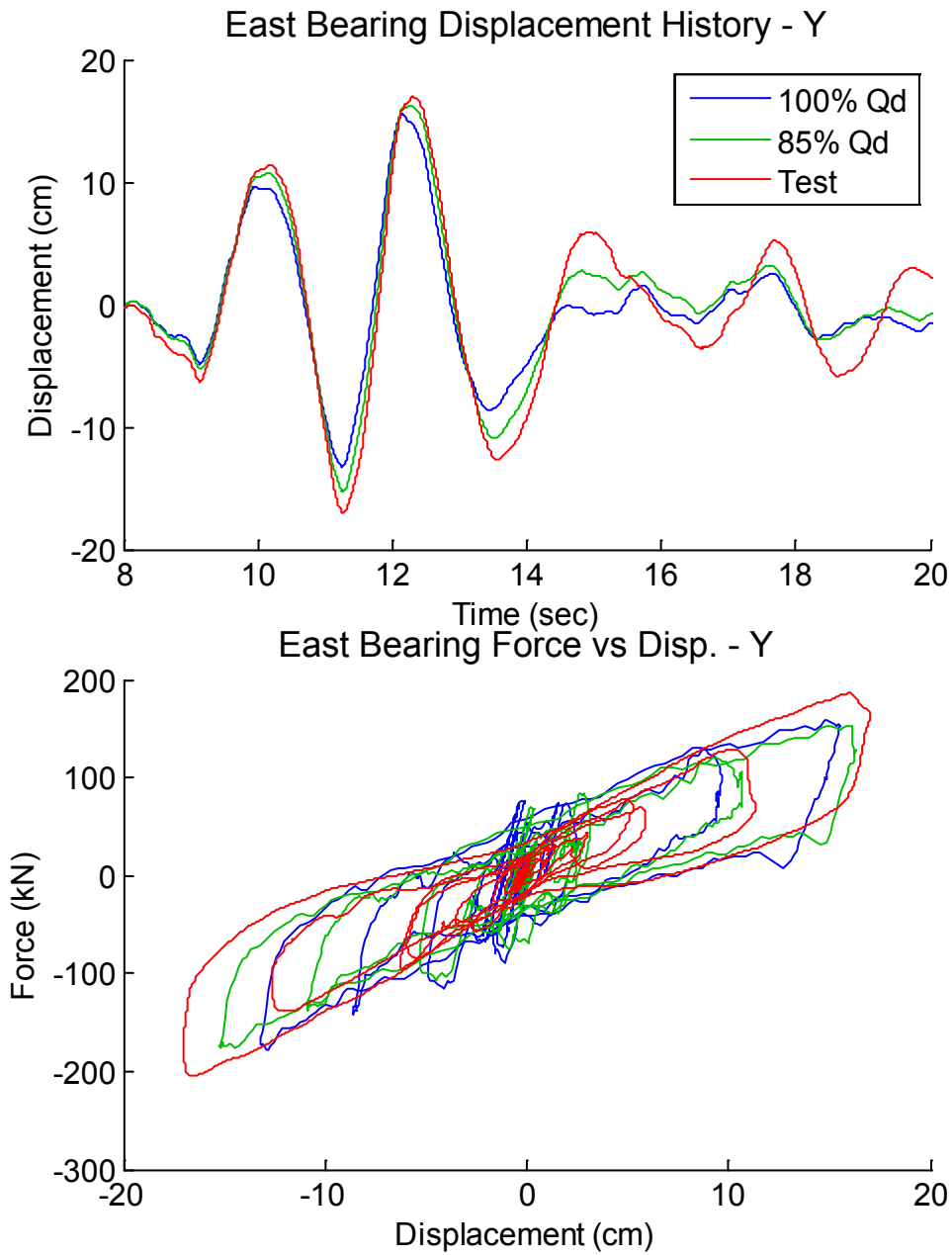


**Figure 7-16 Comparison of numerical simulation with 100% and 85% characterized values of  $Q_d$  to the experimental data for Vogtle 100%; displacement history and hysteresis loop in the y-direction for the East bearing**

## 8. NUMERICAL SIMULATION MODEL OF TESTBED STRUCTURE

As introduced in Chapter 7, a model for numerical simulation of the testbed building with the isolation system was developed in OpenSees. The assumptions used in developing the model of the building frame with floor slabs, shown in Figure 8-1(b), are described in this chapter. As an overview, the contribution of floor slabs to the bending stiffness was included in composite beam sections and their in-plane stiffness was accounted for through application of diaphragm constraints. The beam-column connection behavior was represented by a panel zone model. Material nonlinearity was considered through nonlinear material models, and some geometric nonlinearities were included through a P-Delta transformation. Mass and gravity loads were lumped to nodes. Rayleigh damping was applied to the superstructure with additional inter-story dampers to represent energy dissipation. The bearings were represented using the modeling assumptions and characterized parameters of LR bearings and CL bearings described in Sections 7.1 and 7.2, with calibrated bearing parameters of Table 7-4 Chapter 7.

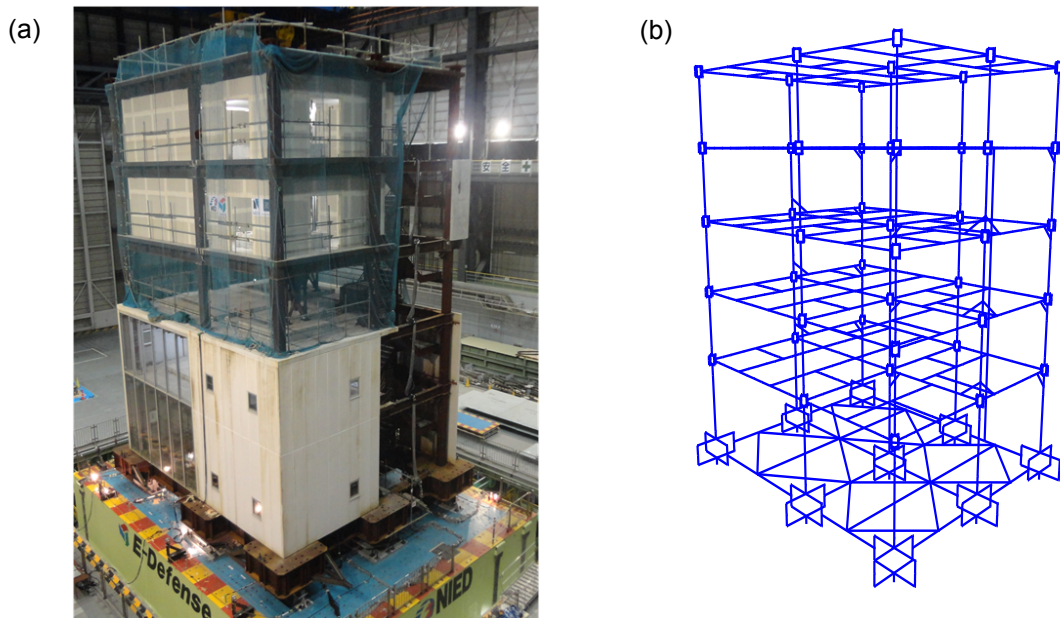


**Figure 8-1 (a) Photo and (b) OpenSees model of the testbed building without isolators**

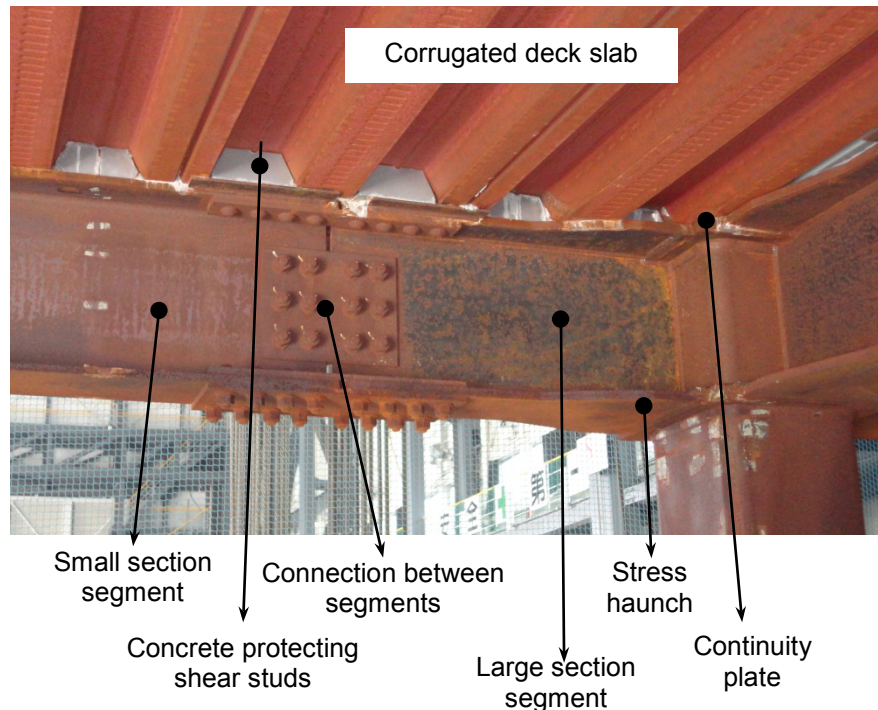


**Figure 8-2 Primary beam, beam-to-column connection, and slab**

### 8.1 Modeling Beams and Columns

The beams of the testbed building were composed of either rolled or built-up I-sections. Primary beams - supported by columns - consisted of a small section segment in the middle bolted to large section segments at the ends, all 40 cm (16 in) deep (Figure 8-2). The beam-column connections were fully restrained moment connections with beam flanges and webs welded to the column face. Generally, the primary beams were haunched at the ends for improved strength, and continuity plates protected the panel zones. Secondary beams - supported by primary beams - were connected to the primary beams through shear tabs. The columns were made of 35 cm (14 in) HSS sections with thickness varying from story to story (Appendix A).

Primary beams were modeled by displacement-based nonlinear frame elements with distributed plasticity. The displacement formulation was selected over advocated force formulations (Neuenhofer and Filippou 1997) to improve the convergence of the analytical model. To optimize the performance of displacement-based elements, each beam member was divided into at least 8 elements. Since mass was lumped at the nodes, the discretization also helped to distribute mass over the structure more realistically.

The nonlinear frame elements were accompanied by composite section models to account for the contribution of floor slabs, which were connected to the primary beams through shear studs (Figure 8-2). The effective slab width for each side of the composite section was the minimum of (1) one-eighth of the beam span, (2) one-half the distance between the beams and (3) the distance to the edge of the slab (AISC 2005). Longitudinal slab reinforcement was included in the section model. The Giuffre-Menegotto-Pinto (CEB, 1996) and Kent-Park concrete materials (Kent and Park 1971, Scott et al. 1982) are used to model the stress-strain relations of steel and unconfined concrete (applied to floor slabs), respectively. The tensile resistance of concrete was neglected in the concrete material model.

For these non-symmetric composite sections, when the material behavior becomes nonlinear, the neutral plane of the section moves and the geometric centerline deforms axially under pure bending loads. However, the rigid diaphragm constraint prevents the axial deformation of the centerline, thus introducing an axial force to the bent beam. The axial force changes the behavior of beams significantly, as demonstrated in Figure 8-3(b), where the bending behavior with and without axial deformation restraint are compared for a simply supported 5 m (16 ft) beam element with a composite section driven cyclically at the midpoint. To avoid the unintended effect of axial force on bending of the composite beam sections, the axial and bending behaviors were decoupled through the use of resultant section models for moment-curvature and axial force-strain. The resultant beam section behavior was determined from analysis of the composite fiber sections (e.g. Figure 8-3(a)). As an example, the pure bending cyclic behavior of the composite fiber section determined by section analysis (solid line in Figure 8-4(a)) was approximately represented by combining the steel material model (Figure 8-4(b)) with a hysteresis model (Figure 8-4(c)) in parallel.

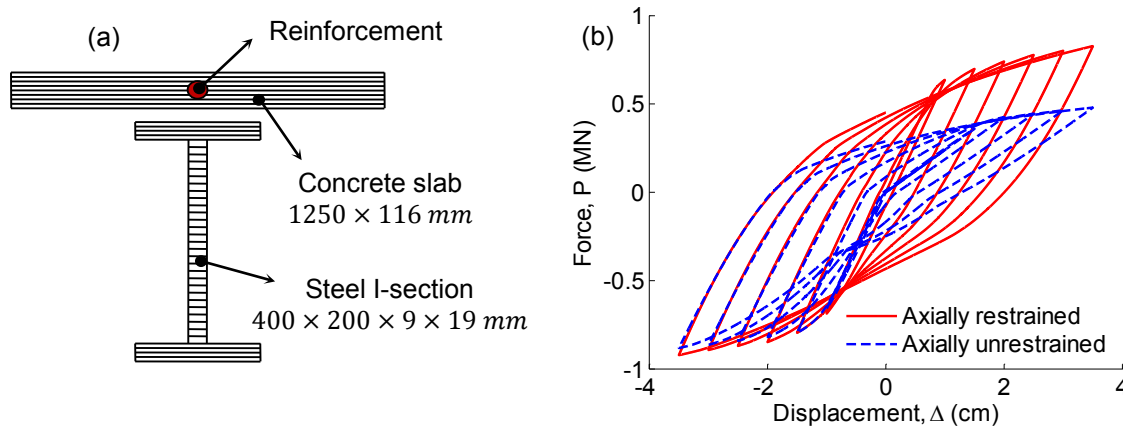


**Figure 8-3 Behavior of a representative composite fiber section beam with and without axial restraint: (a) fiber section geometry and (b) force-displacement relationship**

Secondary beams of the testbed were modeled as elastic beam elements with elastic composite sections. The secondary beams in the model were also divided into 8 elements to distribute mass realistically.

The testbed columns were also modeled by displacement-based nonlinear frame elements, but fiber sections were used to account for axial force-bending interaction in the columns. Each column member was modeled with 3 elements to improve the performance of the displacement-based elements. Because plasticity is mainly concentrated at the two ends of a column member, the length of the end elements was set equal to the section height (35 cm or 14 in). Three displacement-based elements were shown to give similar moment rotation behavior to the force-based element with 7 integration points (Dao 2012).

During the experimental simulation, the response of the testbed frame was essentially elastic. However, the floor system exhibited some nonlinearity due to the cyclic response of concrete between tension and compression. Dao et al. (2012b) demonstrated that the numerical simulation results more closely matched the experimental data when nonlinear modeling assumptions were considered, compared to an elastic frame model. Thus, we believe that the attention to detail and consideration of nonlinear effects in the model was justified.

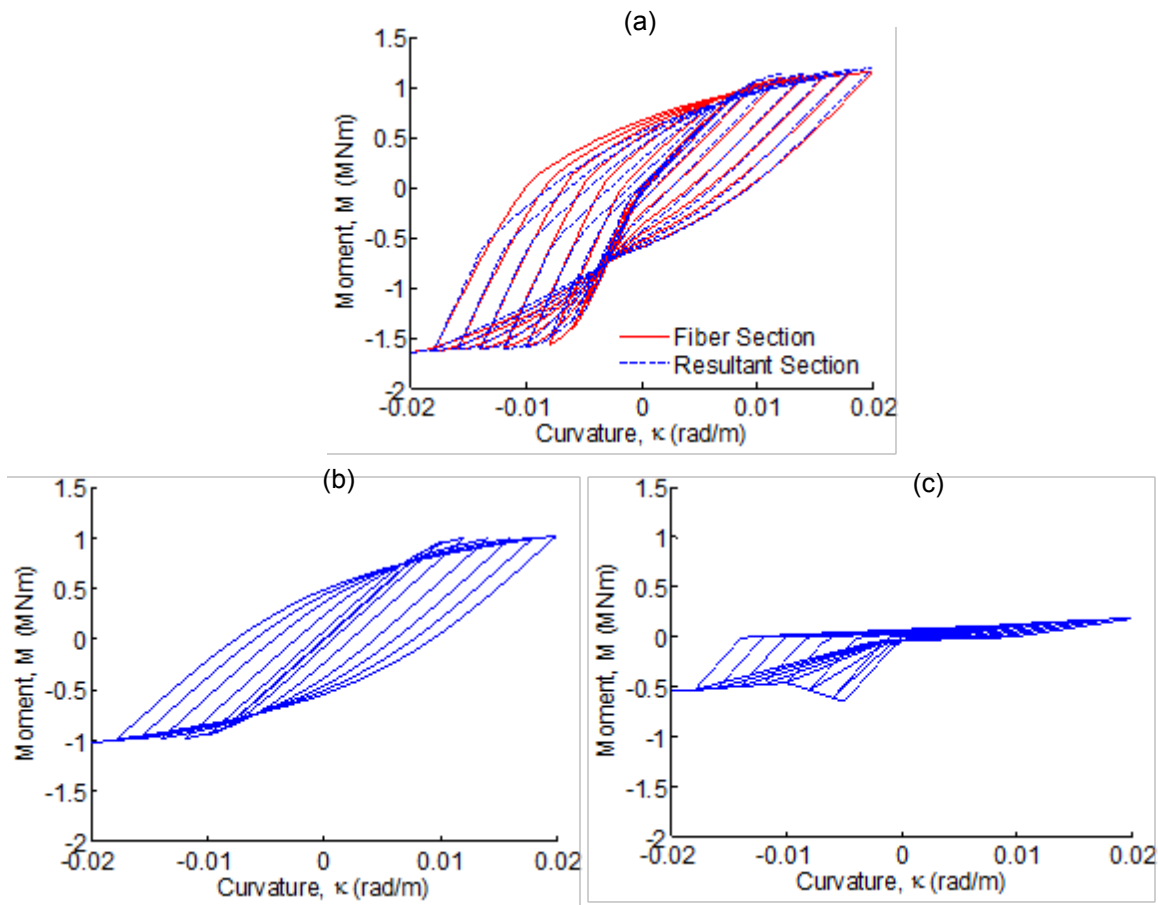


**Figure 8-4 Composite section behavior: (a) moment-curvature relationship of the section, (b) component 1 of resultant section modeled by steel material model, and (c) component 2 of resultant section modeled by hysteresis model**

## 8.2 Modeling Panel Zones

The Krawinkler panel zone model (Krawinkler 1978, Charney and Downs 2004) was used to model the connection between beams and columns. According to this model, each panel zone (Figure 8-5(a)) was modeled by 8 rigid elements and 2 elastic-perfectly plastic rotational springs, one representing the shear behavior of the panel zone (or the web, lying in the working plane) and one representing the bending behavior of the flanges (perpendicular to the working plane) (Figure 8-5(b)). Since the columns were fully welded to primary beams in both directions, the panel zones in two directions were independently modeled by two Krawinkler panel zone models.

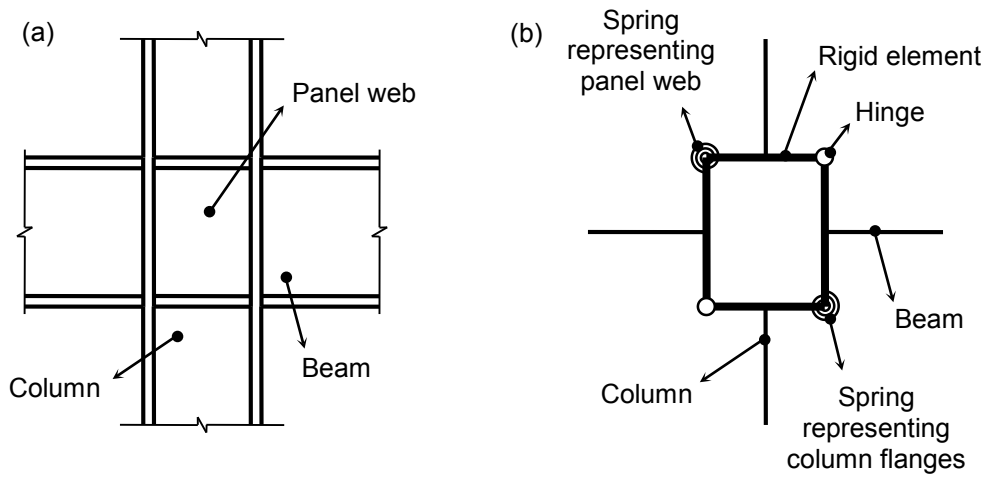


**Figure 8-5 Panel zone model for beam to column connection. (a) beam to column connection, (b) numerical model of panel zone**

The initial stiffness  $S_P$  and yield strength  $M_{yP}$  of the spring representing the shear behavior of the panel zone web were computed as:

$$S_P = GV_P \quad (8.1)$$

$$M_{yP} = 0.58F_Y V_P \quad (8.2)$$

where:  $G$  = shear modulus of steel,  $V_P$  = volume of the panel zone web, and  $F_{\sigma Y}$  = yield strength of steel material. The initial stiffness  $S_F$  and yield strength  $M_{yF}$  of the spring representing bending of the flanges are:

$$S_F = 0.75Gb_{cf}t_{cf}^2 \quad (8.3)$$

$$M_{yF} = 1.80F_Y b_{cf} t_{cf}^2 \quad (8.4)$$

where:  $b_{cf}$  = flange width of column and  $t_{cf}$  = flange thickness of column.

Elastic axial elements equivalent to the Krawinkler model were also used to model gusset plates (Figure 8-6(a)), which were an integral part of the specimen for attaching dampers in the March 2009 test (Kasai et al., 2010). The dampers were not present during the experimental simulation described in this report. Finite element analysis of a connection with gusset plate subjected to gravity load suggested that the gusset resistance is in the diagonal direction (Figure 8-6(b)), and can be modeled as a diagonal strut. The equivalent elastic stiffness  $k_{truss}$  of the axial element was:

$$k_{truss} = S_P \frac{(x^2 + y^2)}{x^2 y^2} \quad (8.5)$$

where  $x \times y$  = size of the gusset plate and  $S_P$  = initial shear stiffness of the gusset plate (Equation (8.1)).



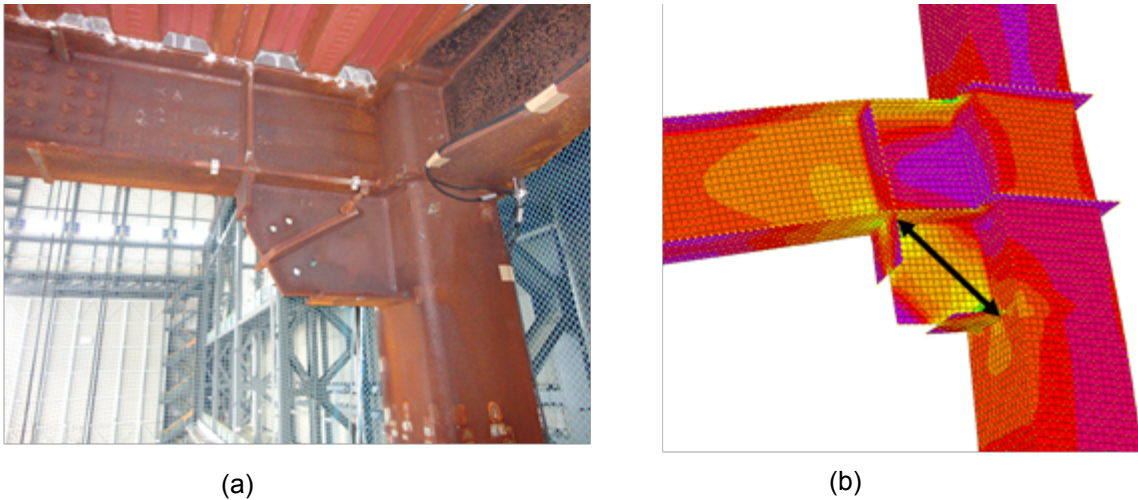


**Figure 8-6 Gusset plate and its finite element model: (a) gusset plate, (b) Von-Mises stress due to gravity load**

### 8.3 Modeling Gravity Load and Mass

As mentioned earlier, the testbed building was modeled as a bare frame without slabs so that gravity loads and mass were applied directly to beams and columns. Static analysis of a SAP2000 model subjected to gravity loads with slabs represented by general shell elements was used to compute beam internal forces and distributed loads. From the shear forces  $V_i$  and  $V_j$  at the two ends of a beam element, the equivalent uniform load  $v$  on the beam element was computed according to:

$$v = \frac{V_i - V_j}{L} \quad (8.6)$$

where  $V_i$  and  $V_j$  are shear forces at the two ends of the element, and  $L$  is the length of the element. The mass of the OpenSees model was directly derived from the computed distributed loads and lumped to every node of the model. Because of the bending stiffness of the slab, some of the slab gravity load transferred directly to the corner slab nodes. In the OpenSees model, these loads were applied as concentrated loads to the corresponding corners.

Table 8-1 summarizes the weight and the eccentricity of gravity center from the geometric center of the SAP and OpenSees models. The weight of all floors in SAP model, estimated directly from the nominal weight and dimension of all components of the testbed, is shown in column (2). By this approach, the total weight of the testbed building was 5122kN (1151 kips). However, as mentioned earlier, the measured weight of the testbed was actually 5250 kN (1180 kips), which was determined from the uplift investigation of the TP bearings. To match the measured weight, the weight in the numerical frame model was increased by a factor of  $5220/5122 = 1.019$ . The weight increase was assumed to be uniform over all nodes of the model. Column (3) indicates the factored weight at all floors applied to the OpenSees model.

Columns (4) and (5) indicate the mass eccentricity at every floor, or distance from the geometric center of the building to the center of mass. In general, the center of mass of each floor shifted toward the North-East relative to the geometric center. At the base, the center of mass shifted toward the West due to the weight of the column bases on the West side as well as the staircase on the SouthWest. The Y direction eccentricity at floor 5 increased relative to other floors due to the absence of the staircase in the 5th story. The eccentricity was greatest at the



roof due to the added steel blocks. As mentioned previously, this added weight was excessive compared to typical roof mounted equipment and influenced the seismic response of the testbed building.

**Table 8-1 Weight and eccentricity (distance from geometric center to center of mass) of numerical simulation model.**

Floor (1)	Weight from SAP (kN) (2)	Modified weight (kN) (3)	Eccentricity	
			X(cm) (4)	Y(cm) (5)
Roof	1153	1175	9	-85
5	771	786	20	-40
4	781	796	21	-24
3	782	797	27	-22
2	792	807	22	-24
Base	842	859	0	31
Sum	5122	5220	16	-32

#### 8.4 Modeling Damping

Rayleigh damping (combining mass and stiffness proportional components) was used to represent energy dissipation in the testbed building, based on specified damping ratios at two different frequencies. The experimental response of the fixed base building to white noise excitations was analyzed to find the periods and damping ratios of natural modes of the structure (Sasaki et al., 2012), which are listed in Table 8-2 for the first 3 modes in both directions. The Rayleigh damping curve passing through damping ratios of 2.2% at periods of 0.70 sec (frequency of 1.43 Hz), corresponding to the first mode period, and 0.15 sec (6.67 Hz) (Figure 8-7), was found to give a good match between experimental and numerical results of the fixed-base building.

Past experiments have shown that the damping ratios determined by the method described above include damping in the hydraulic actuators of the earthquake simulator and thus over-estimate the actual damping in the structural system. If determined from free vibration analysis, damping ratios on the order of 1% or less are expected for the first few modes of bare steel frame systems (e.g. Uang and Bertero 1986, Whittaker et al. 1990). The damping in the hydraulic actuators was not accounted for in the numerical modeling of the system. However, additional damping in the testbed building was present compared to a bare steel frame due to the concrete floor system, exterior concrete cladding, nonstructural components (partition walls, ceilings and piping system) and contents. Thus, the level of observed damping in the testbed building was partially justified.

The final “best fit” damping coefficients for the building with hybrid LR isolation system were determined by trial and error. The basic strategy behind the selection was to control damping between the periods of 0.1 sec (10 Hz) and 2 sec (0.5 Hz) and, which included the major response components that were observed in the floor spectra (see Section 9.3). The damping ratios were fixed at 1.9% and 1.93% at 0.15 sec (6.66 Hz) and 2.0 sec (0.5 Hz). The Rayleigh damping curve for the isolated building configuration is compared to that for the fixed-base building configuration in Figure 8-7.

**Table 8-2 Experimentally determined natural periods and damping ratios of the fixed-base building.**

	White noise X		White noise Y		White noise 3D	
	Period (s)	Damping ratio (%)	Period (s)	Damping ratio (%)	Period (s)	Damping ratio (%)
Mode 1 X	0.65	3.3	n/a	n/a	0.68	4.1
Mode 2 X	0.20	1.6	n/a	n/a	0.21	2.0
Mode 3 X	0.11	3.3	n/a	n/a	0.11	3.7
Mode 1 Y	n/a	n/a	0.68	2.5	0.69	3.5
Mode 2 Y	n/a	n/a	0.21	1.7	0.21	1.9
Mode 3 Y	n/a	n/a	0.11	2.6	0.11	3.6

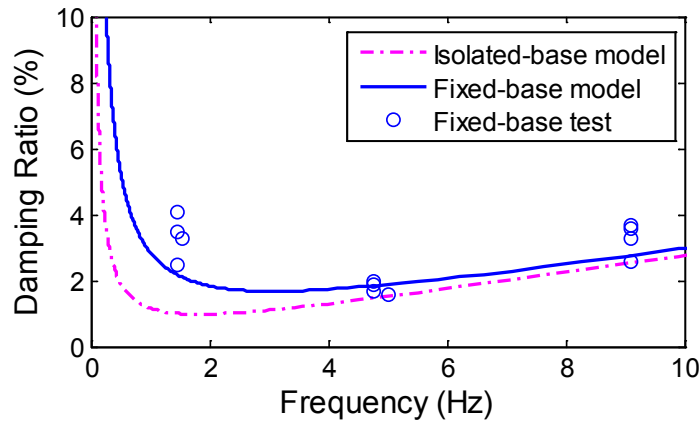


**Figure 8-7 Rayleigh damping model for the fixed-base and hybrid LR isolated building model**

The calibrated Rayleigh damping model produced low damping ratios at frequencies around 3 Hz (Figure 8-7), which were the frequencies of the first structural modes of the isolated structure in both directions, so that these frequency components of the numerically simulated response tended to be amplified compared to the experimental data. To solve this difficulty, additional dampers were added to apply extra damping to these modes (Dao 2012). From modal analysis, the relative horizontal displacement between the base and roof in the 1<sup>st</sup> structural mode in each direction was observed to be much larger than in other modes. Thus, additional dampers were connected between the center of stiffness nodes at the base and roof in each direction as shown in Figure 8-8. At these locations, the displacements in the 1<sup>st</sup> torsional mode were zero. The damping coefficient  $c$  for the damper in a given direction was computed as (Dao 2012):

$$c = \frac{2\zeta_n \omega_n m_{nn}^*}{\bar{c}_{nn}} \quad (8.7)$$

where  $n$  = mode number of the modified damping mode;  $\zeta_n$  = desired additional damping ratio;  $\omega_n$  = the angular frequency of the  $n^{th}$  mode;  $m_{nn}^*$  = modal mass of the  $n^{th}$  mode; and  $\bar{c}_{nn}$  = a constant dependent on  $n^{th}$  mode shape, computed by:

$$\bar{c}_{nn} = (\phi_{pn} - \phi_{qn})^2 \quad (8.8)$$

where  $\phi_{pn}, \phi_{qn}$  = horizontal displacements at base and roof in the  $n^{th}$  mode shape. Computation of  $[\bar{c}_{ij}]$  for the first 14 modes, including off diagonal terms, demonstrated that the extra damping contributed primarily to the intended mode (Dao 2012). The selected value of  $\zeta_n$  for numerical simulation was 2% for the for the hybrid LR isolation configuration.

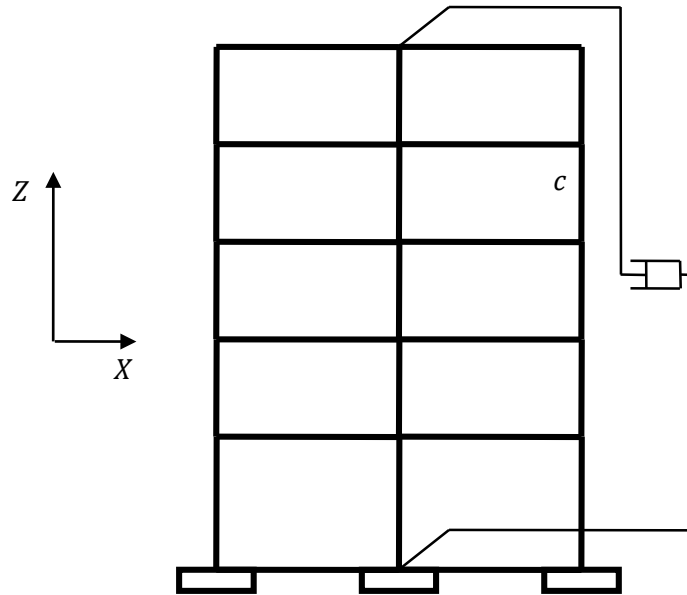


**Figure 8-8 Additional damper for adjusting the damping coefficient of the 2<sup>nd</sup> mode in the X direction**



## 9. COMPARISON OF EXPERIMENTAL AND NUMERICAL SIMULATION

In this chapter, we compare the predicted responses of the hybrid LR isolated building (both isolation system and structure) using the OpenSees model described in Chapters 7 and 8 to the experimental results. Response quantities examined include the isolator displacement and force, story drifts, floor accelerations, and floor response spectra. Four different input excitations have been chosen as a representative variety sample. These comparisons are shown for the following input excitations: El Centro 130%, Vogtle 100%, Vogtle 175%, Diablo Canyon 95%. Vogtle was selected because of its great interest to the research sponsor, and two different intensities were chosen to approximately represent the DBE and the beyond DBE. Diablo Canyon was chosen because of its secondary interest to the sponsor, and because it produced the largest displacement demand in the bearings. El Centro was chosen to be representative of a smaller earthquake. The earthquake records used as input to the numerical model are the recorded output at the base of the earthquake simulator. The target ground excitation for Diablo is bidirectional only (XY) excitation, while the other three excitations include vertical input. These motions have been selected as a representative variety sample, and focus on the particular excitations that are of greatest interest to the research sponsor. Reports comparing the experimental and numerical simulation results for every excitation are permanently archived in the NEEShub Project Warehouse (Ryan et al. 2012).

### 9.1 Isolator Response

Demonstration that the isolation system and overall structure demands of safety related nuclear structures can be accurately determined in analysis and design is an important milestone toward the acceptance and implementation of seismic isolation for nuclear structures. As discussed in Chapter 7, replication of the isolation system response using a single bearing model with physically determined parameters has been hampered by circumstances unique to the test program that would not normally be encountered in practice. These circumstances are: 1) the bearings were designed with an unusually small lead plug, resulting in pinching of the bearing hysteresis loops that is difficult to represent with a single bilinear model. 2) The sequence of closely spaced trials caused heating of the lead plugs. Since the bearing temperature was not measured, the influence of heating on the bearing response cannot be quantified. Under normal field conditions and in a strong earthquake, LR bearings would be activated in an unheated state. 3) The experimental simulation results include small intensity ground motions that induce limited displacement demands in the isolation systems. A bilinear bearing model would not be expected to replicate isolator demands in the small intensity simulations well.

As discussed in Chapter 7, in lieu of numerical simulation with a single bearing model, we independently calibrate the bearing modeling parameters for each experimental simulation to represent the largest displacement cycle that was observed. Use of this technique is helpful to interpret the data from this test program, but does not imply that a single bilinear model with physical parameters would not be suitable over a wide range of intensities in practice. Also discussed in Chapter 7, for all subsequent numerical simulation we substitute a model with  $Q_d$  equal to 85% of the best fit characterized model, based on the trial-and-error observation that it improves the results.

Displacement traces, displacement histories, and bearing force vs. displacement (hysteresis loops) for the four selected input motions are shown in Figures 9-1 to 9-8. This adjusted characterized model – with its acknowledged limitations – generally predicts the amplitude of the peak vector displacement in each LR bearing quite well; a prediction within 5% of the recorded peak is not uncommon. The model also tends to represent the largest cycles in the displacement traces well, and capture obvious differences among the 4 LR bearings that are the

result of the torsion in the system. For example, in Vogtle 100%, the numerical simulation correctly picks up a linear displacement along a diagonal axis in the East (E) and South (S) bearings, but more of a circular orbit pattern in the North (N) and West (W) bearings (Figure 9-3). Plots of the displacement history best illustrate the accuracy of the model throughout the records. As discussed in Chapter 7, the predicted displacement is most accurate at cycles close to the peak intensity for which it has been optimized. Thus, the numerical prediction of the displacement history is not as accurate over small intensity cycles in large intensity records (e.g. Vogtle 175%, Figure 9-5). However, the peak displacement – which is the most critical response parameter in the isolation system – is predicted very well by the model, and the prediction in the small displacement range is not too important. The numerical simulation also predicts well the peak base rotation angle in the isolation system, which is more sensitive to modeling errors. An example is shown for Vogtle 175% in Figure 9-9, which compares the history of base rotation angle as predicted by numerical and experimental simulation. As discussed earlier, the rotational demands in the isolation system that occurred in this testbed structure resulted from the limitations on number and placement of LR bearings, and could expect to be eliminated in practical buildings with many bearings distributed across the base plan.

The hysteresis loops confirm that, by inspection, the adjusted characterized numerical model is a good fit to the experimental data in most cases, and the fitted value of  $K_d$  looks reasonable. The numerical model tends to underestimate the force at the peak displacement. (e.g. consider the negative excursion of the bearings in both x and y-directions for El Centro, Figure 9-2), which results from the pinching behavior of the hysteresis loops due to a small diameter lead plug. Because of the pinching behavior, the best fit bilinear model parameter for  $Q_d$  exceeds the observed yield strength  $Q_d$  near the center of the loops, but is less than the physical  $Q_d$  (applicable at large displacements). Also, the numerically simulated loops show a tendency to be “wavy” compared to the experimental data. For example, in the El Centro motion, on the largest negative excursion in the x-direction, the numerically predicted force dips suddenly on the return for all 4 LR bearings, while the actual force recorded during the experimental simulation does not (Figure 9-2). In Vogtle 100%, the numerical hysteresis loops (Figure 9-4) are characterized by rapid up and down variations of force on a large displacement excursion that are absent from the experimental loops. We are not sure, but believe the waviness in the numerical hysteresis loops is related to the algorithm for bidirectional interaction.

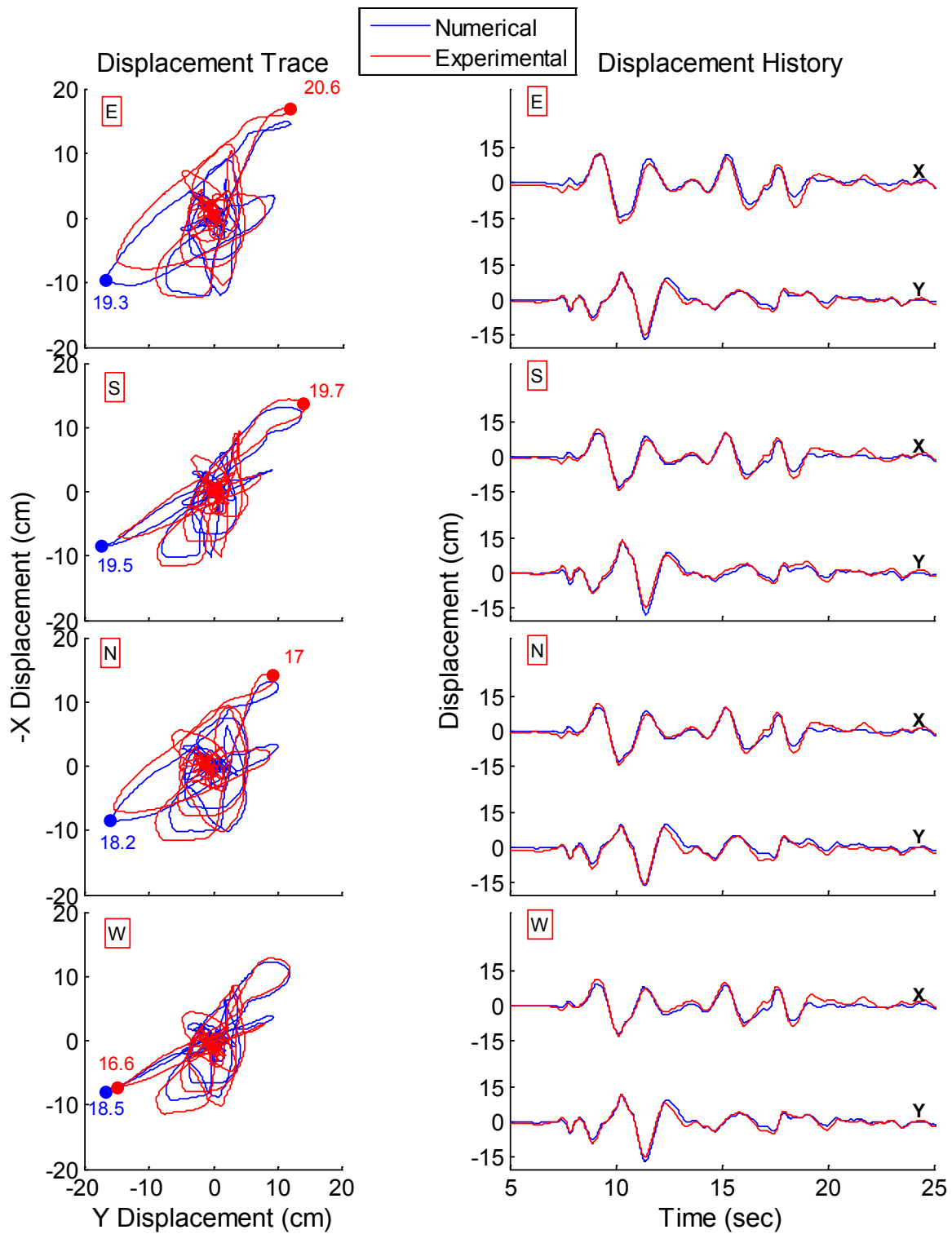


**Figure 9-1 Comparison of numerical and experimental simulation for El Centro 130%; displacement trace and displacement histories (x and y) in each LR bearing, labeled by position (E, S, N, W). Numerical simulation uses the characterized model with 85% of the characterized value for  $Q_d$**

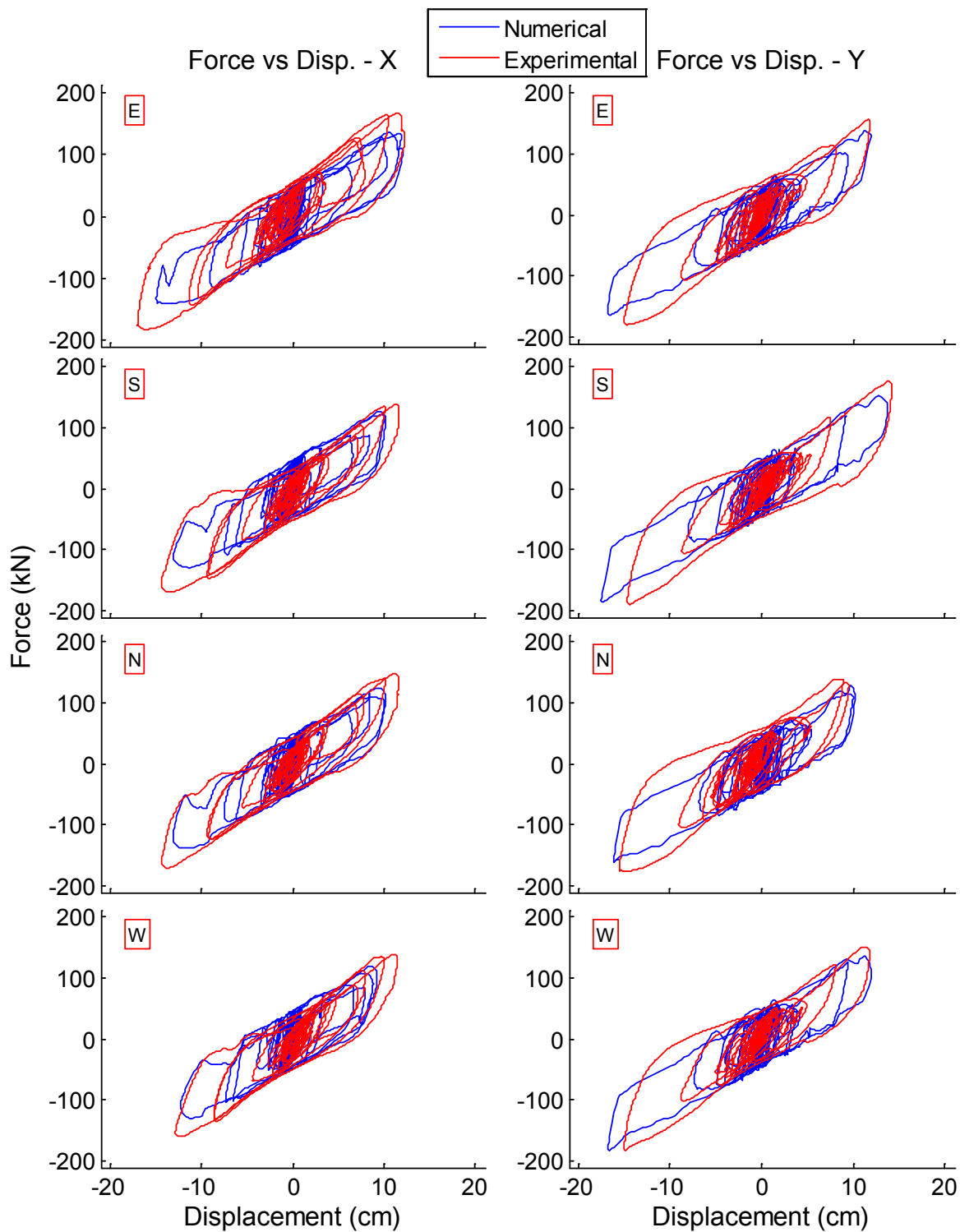


**Figure 9-2 Comparison of numerical and experimental simulation for El Centro 130%; bearing force vs. displacement or hysteresis loops (x and y) in each LR bearing, labeled by position (E, S, N, W). Numerical simulation uses the characterized model with 85% of the characterized value for  $Q_d$**



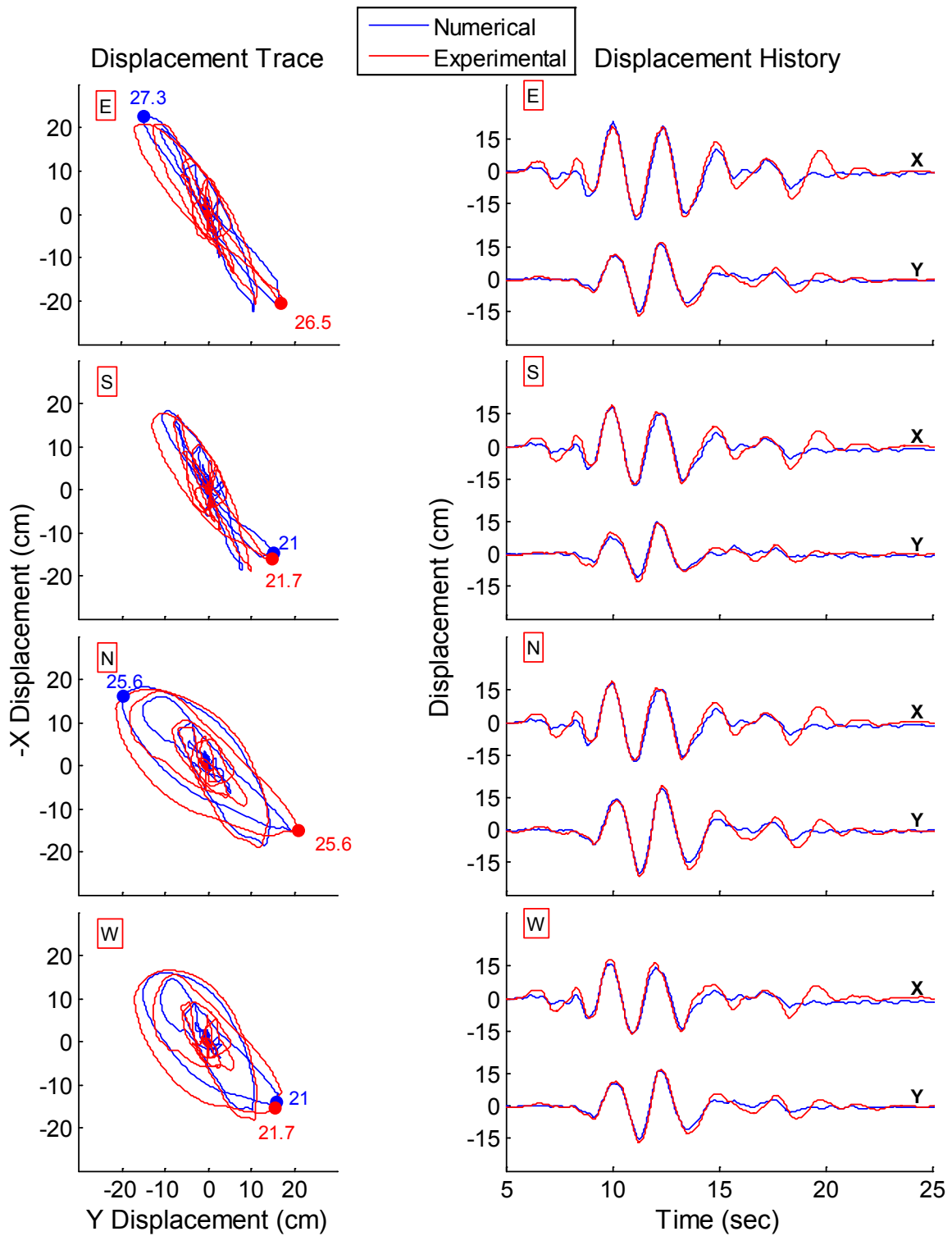


**Figure 9-3 Comparison of numerical and experimental simulation for Vogtle 100%; displacement trace and displacement histories (x and y) in each LR bearing, labeled by position (E, S, N, W). Numerical simulation uses the characterized model with 85% of the characterized value for  $Q_d$**

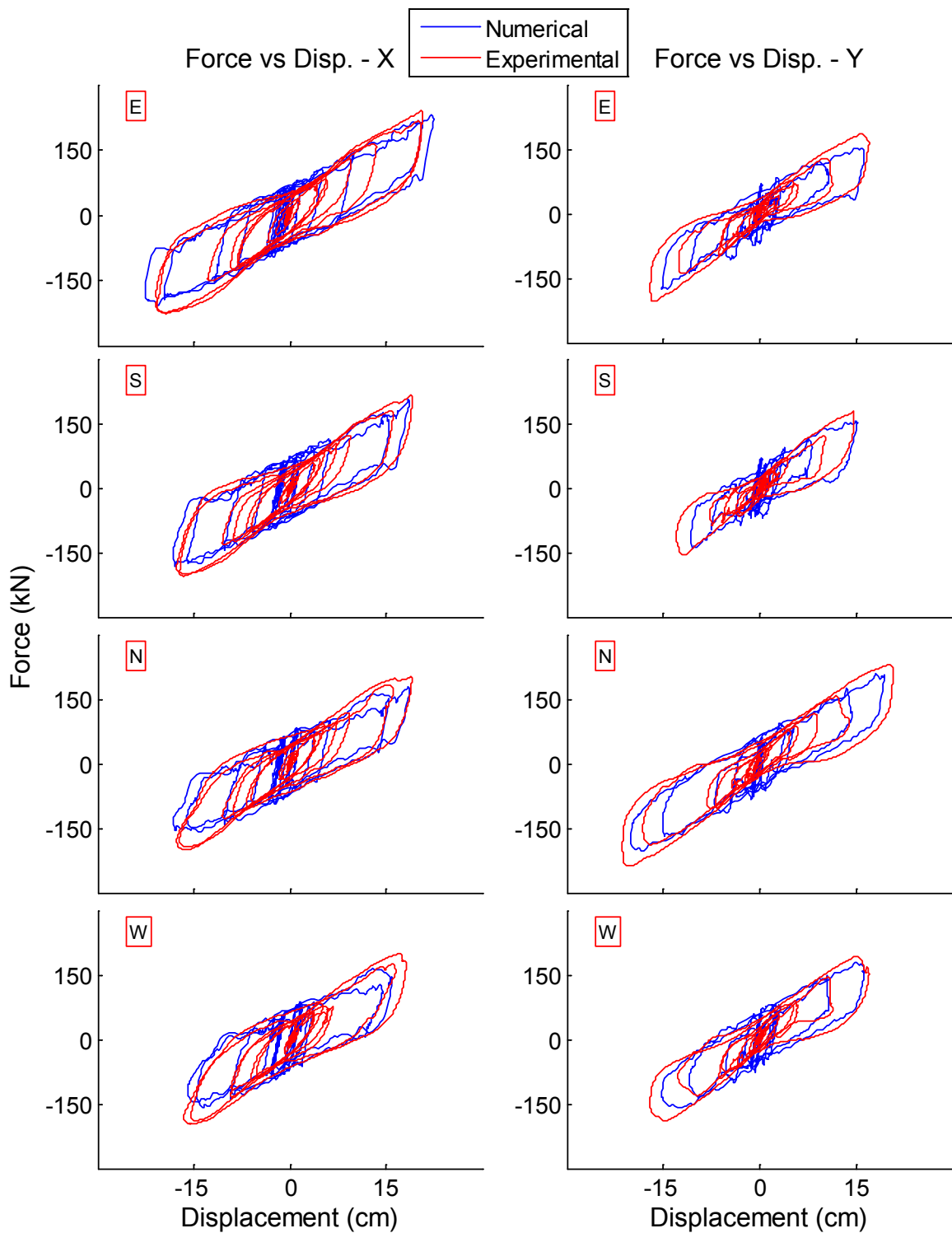


**Figure 9-4 Comparison displacement (x and y) histories of numerical and experimental simulation for Vogtle 100% in each LR bearing labeled by position (E, S, N, W). Numerical simulation uses the characterized model with 85% of the characterized value for  $Q_d$**

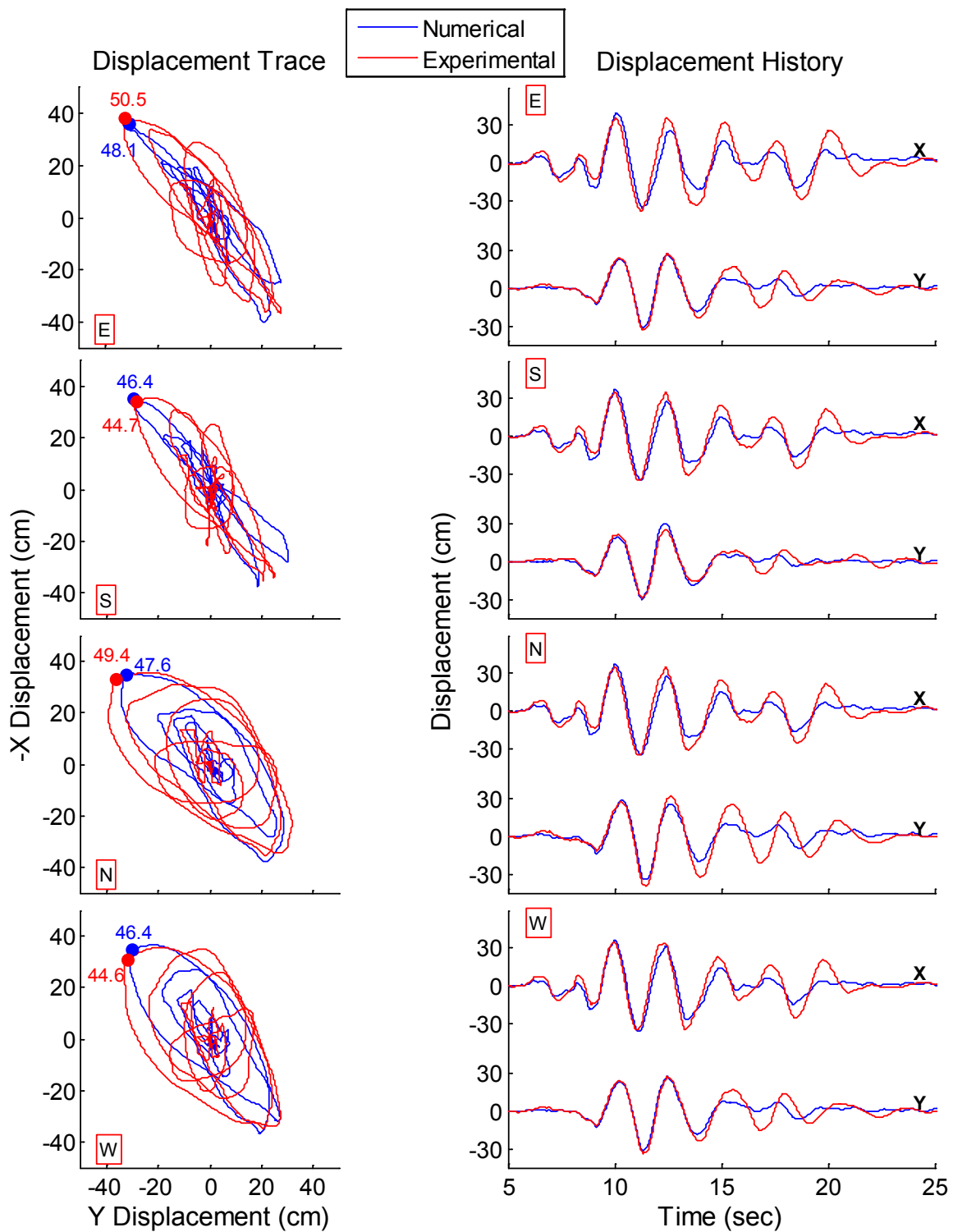
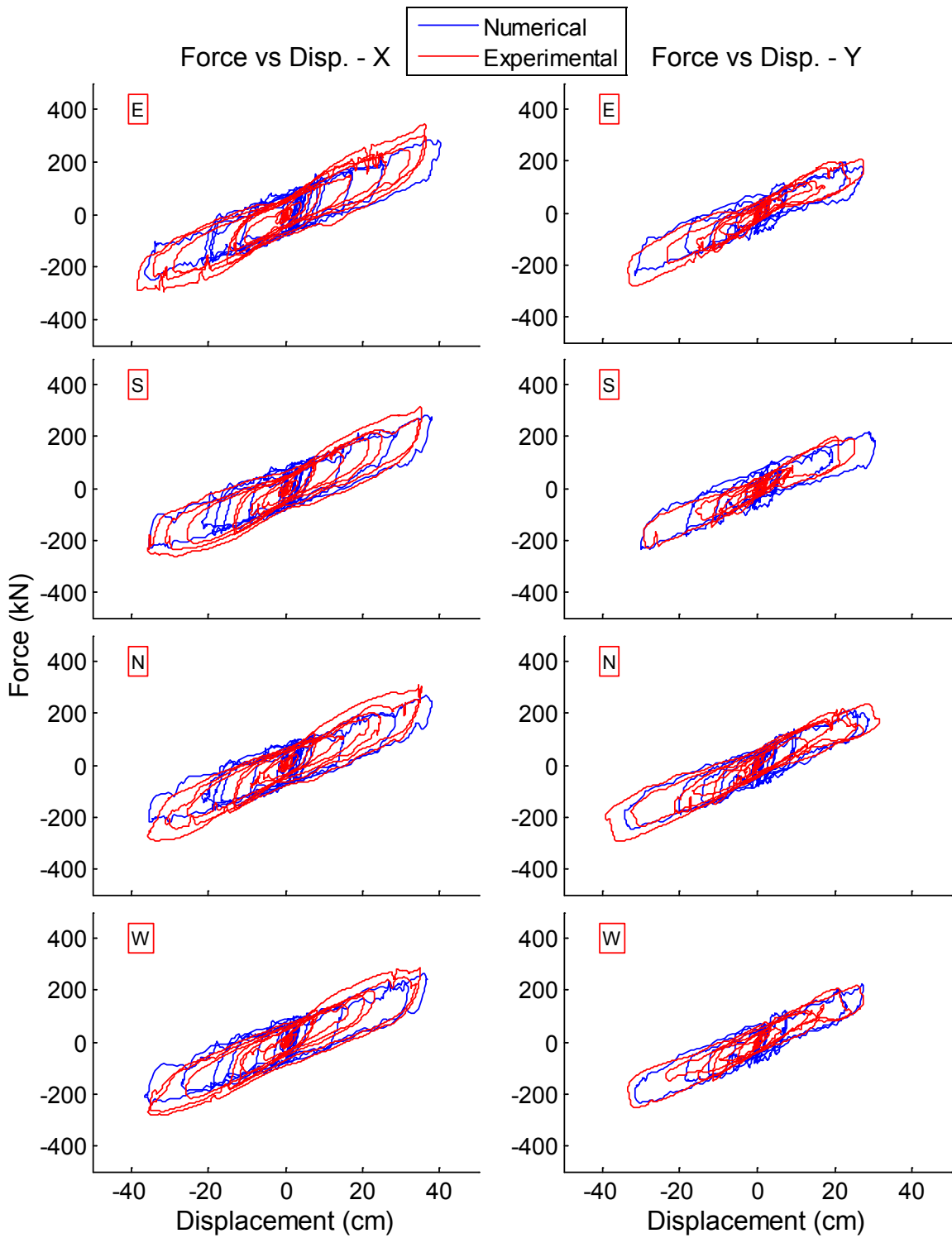
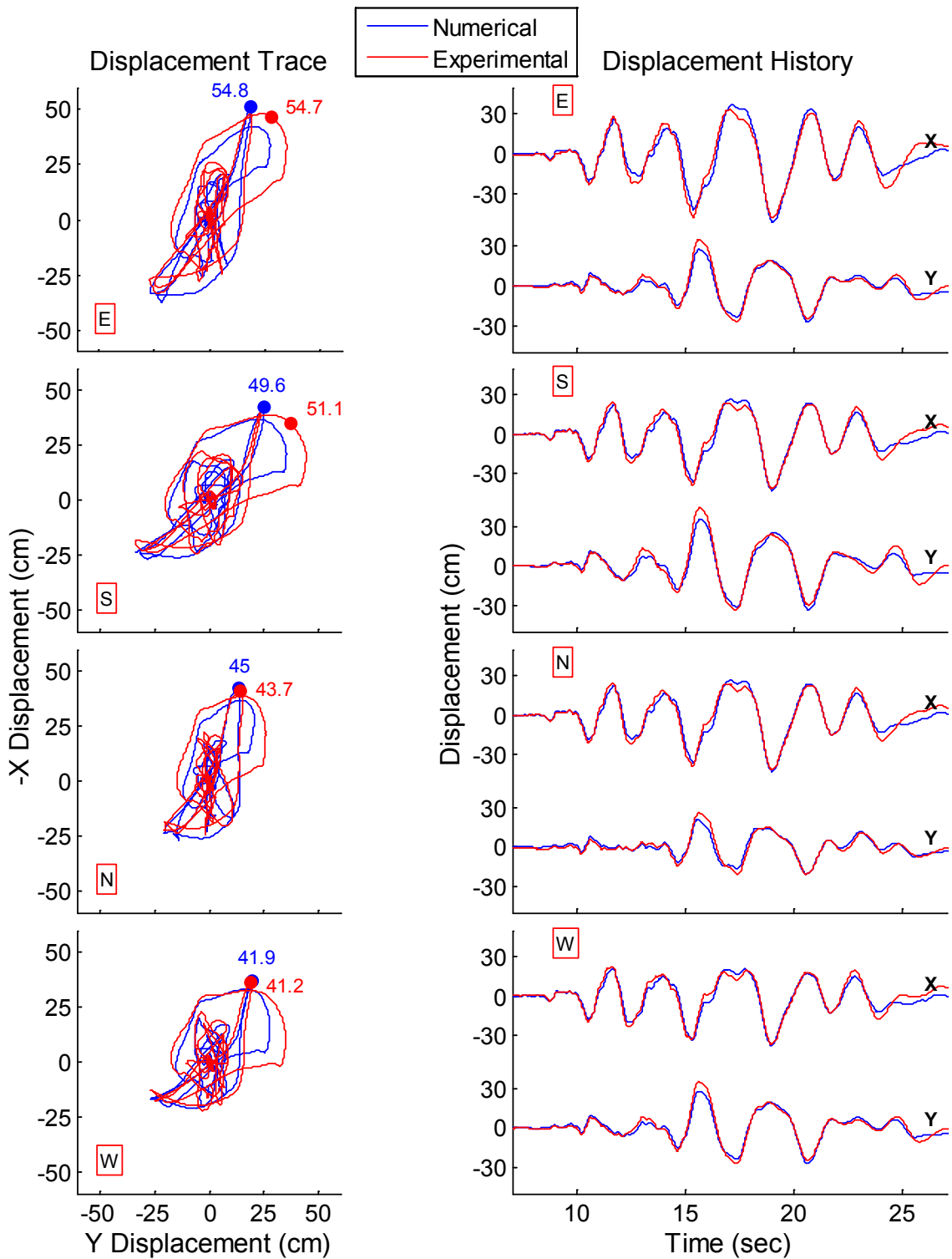


Figure 9-5 Comparison of numerical and experimental simulation for Vogtle 175%; displacement trace and displacement histories (x and y) in each LR bearing, labeled by position (E, S, N, W). Numerical simulation uses the characterized model with 85% of the characterized value for  $Q_d$



**Figure 9-6 Comparison of numerical and experimental simulation for Vogtle 175%; displacement trace and displacement histories (x and y) in each LR bearing, labeled by position (E, S, N, W). Numerical simulation uses the characterized model with 85% of the characterized value for  $Q_d$**



**Figure 9-7 Comparison of numerical and experimental simulation for Diablo 95%; displacement trace and displacement histories (x and y) in each LR bearing, labeled by position (E, S, N, W). Numerical simulation uses the characterized model with 85% of the characterized value for  $Q_d$**

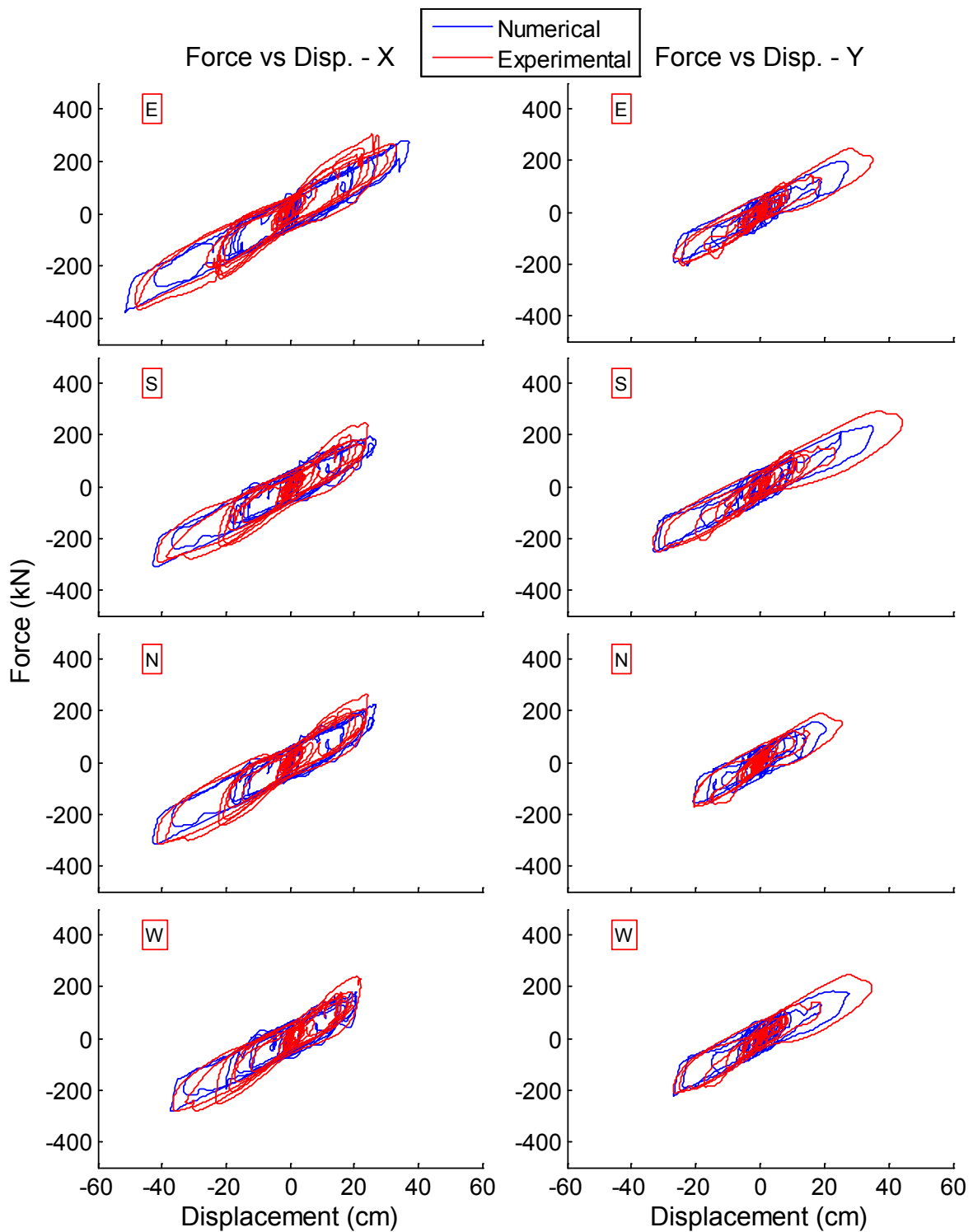


**Figure 9-8 Comparison displacement (x and y) histories of numerical and experimental simulation for Diablo 95% in each LR bearing labeled by position (E, S, N, W). Numerical simulation uses the characterized model with 85% of the characterized value for  $Q_d$**

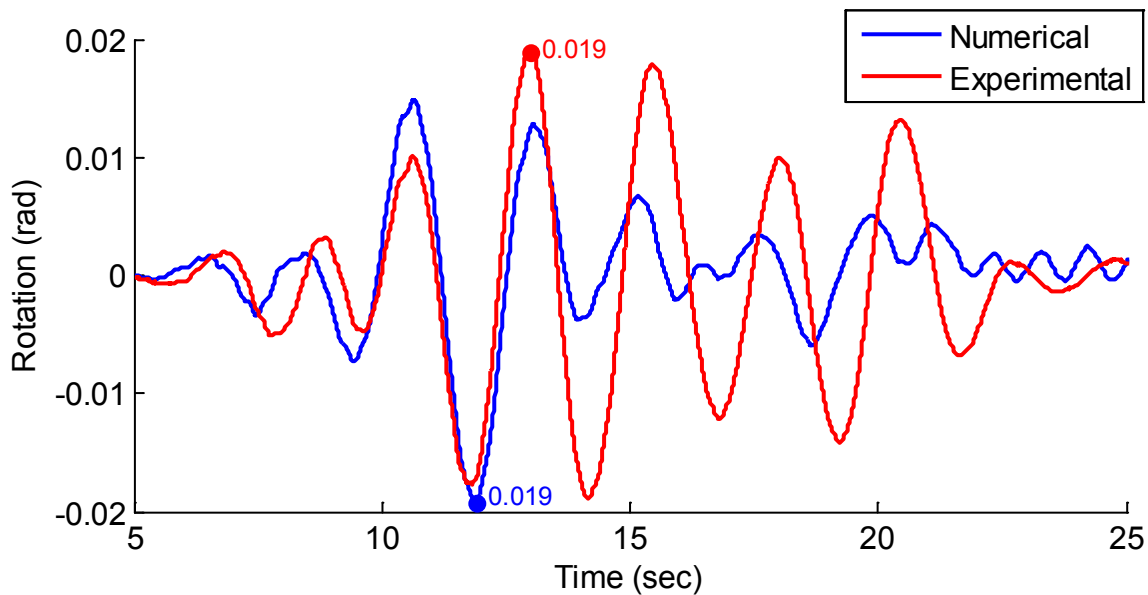


**Figure 9-9 Comparison of numerical and experimental simulation for Vogtle 175%; history of base rotation angle. Analysis uses the characterized model with 85% of the characterized value for  $Q_d$**

There is no evidence of loss of axial load carrying capacity in the bearing hysteresis loops. Such evidence would include a decrease of the stiffness at large horizontal displacements that occurred in combination with high overturning induced axial loads, and the inability of the numerical model, which does not include the interaction of horizontal shear and axial force, to simulate the response. Neither of these effects are observed in any of the hysteresis loops. In summary, the overall ability of the characterized model to predict the bearing displacement and bearing force is sufficient that this model can be expected to provide insight into the structural response, which is examined next.

Simulations of the axial force in the isolators as a function of time are not shown. Attempts to replicate the bearing axial force variation with the present numerical simulation model were unsuccessful. It may be possible to replicate the axial force variation and load transfer with a bearing model that predicts the horizontal-vertical coupling in the bearing. Such a model could also predict axial force instability in the bearing. Such models exist (e.g. Ryan et al. 2005, Yamamoto et al. 2009) but were not readily available to the authors and could not be implemented within the time constraints of the report. Because of the difficulties in reliable prediction of the LR bearing axial forces when used as a hybrid system, we recommend that hybrid LR isolation systems need not be applied to nuclear facilities. Isolation systems consisting solely of LR bearings and designed outside of the constraints of this test program will have similar response characteristics without the load transfer effects.

## 9.2 Modal Analysis

An analysis of the mode shapes and frequencies of the numerical model is useful for interpreting the floor spectra, and understanding the response to combined horizontal and vertical excitations (explored in depth in Chapter 10). For modal analysis, we assign equivalent linear parameters to the isolator models, which are horizontal stiffness  $k = 8.46$  kN/cm (4.83 kip/in) for the LR bearings (corresponding to period  $T = 2.5$  sec), horizontal stiffness  $k = 0.024$  kN/cm (0.014 kip/in) for the CL bearings (equal to the initial stiffness, Section 7.2.1), and vertical

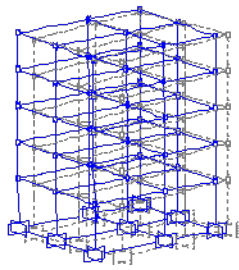
stiffness equal to the calibrated model compression stiffness for both LR bearings (Section 7.1.2) and CL bearings (Section 7.2.2). Because the isolator models are nonlinear, the actual mode shapes and frequencies of the testbed building vary dynamically such that the modes shown here are at best approximate. However, the higher modes, which are of greatest interest in the subsequent discussion, are relatively insensitive to variation of the isolator stiffness over a reasonable working range, such that an analysis based on equivalent linear mode shapes is meaningful. We will demonstrate that some of the higher frequency modes are observed in the responses of the building in some input excitations.

Figures 9-10 to 9-14 illustrate the first 20 modes of the numerical model, along with their associated frequencies and periods. For each mode, the following views are plotted: the deflected shape of the testbed framing in 3-dimensional space, the deflected shape of each of 3 frames in the x-direction, and the deflected shape of each of 3 frames in the y-direction. The undeflected shape of the system is shown in dashed lines for reference. The isolator displacement (displacement at base), frame deflection and panel zone deflection can be seen in the plots.

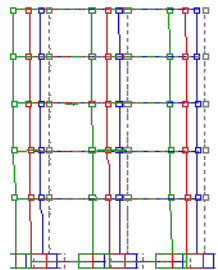
The first 3 modes are isolation modes that induce mainly horizontal deflection in the isolators, and almost no deflection in the testbed framing. Mode 1 ( $T = 2.72$  sec) is primarily an x-direction mode, mode 2 ( $T = 2.60$  sec) is primarily a y-direction mode, and mode 3 ( $T = 2.26$  sec) is a torsional mode. Mode 1 also includes torsional deflection due to several sources of stiffness and mass irregularity in the y-direction (e.g. unequal bay widths in y-direction, staircase at the SW corner of the building, and supplementary mass at the roof level on the E half of the building). The rotational demands observed at the base (Section 5.2) are not unexpected for this test structure, since the isolation system could not be configured to resist torsion, as pointed out in Section 3.3.2.

Modes 4-6 are the first structural modes, characterized by horizontal deflection in the isolation system, and linear deflection across the structural system with a single node (point of zero deformation) at approximately the 4<sup>th</sup> floor. Based on the assumed equivalent linear stiffness of the isolators, mode 4 ( $T = 0.38$  sec) is a y-direction mode, mode 5 ( $T = 0.36$  sec) is an x-direction mode, and mode 6 ( $T = 0.29$  sec) is a torsional mode. Likewise, modes 7, 8 and 10 are the second structural modes, characterized by structural deflection with 2 nodes at approximately the 2<sup>nd</sup> and 5<sup>th</sup> floors. Analogous to previous sets, modes 7 ( $T = 0.18$  sec) and 8 ( $T = 0.17$  sec) are primarily y-direction and x-direction modes, respectively, while mode 10 ( $T = 0.14$  sec) is a torsional mode. Modes 13 ( $T = 0.104$  sec) and 14 ( $T = 0.100$  sec) comprise a 3<sup>rd</sup> set of structural modes, with 3 nodes each in the 1st story, 3<sup>rd</sup> story and 5<sup>th</sup> story. Although these are primarily lateral modes, they also contain some notable slab vibration at the 4<sup>th</sup> and roof levels. A corresponding torsional mode does not appear in the first 20 modes that have been plotted.

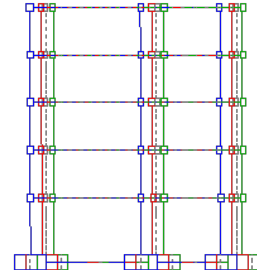




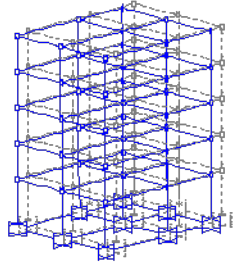
Mode 1:  $f = 0.37$  Hz;  $T = 2.72$  sec



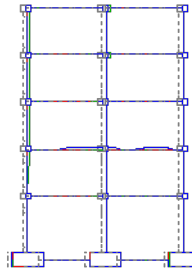
X



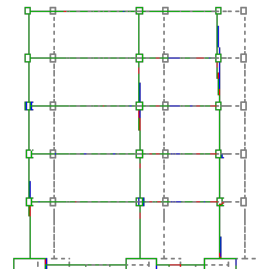
Y



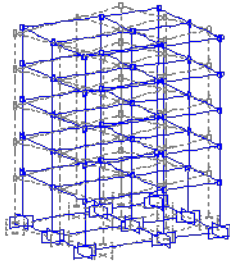
Mode 2:  $f = 0.38$  Hz;  $T = 2.61$  sec



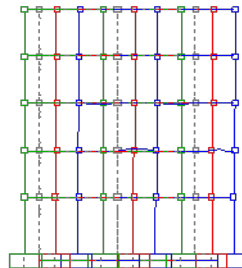
X



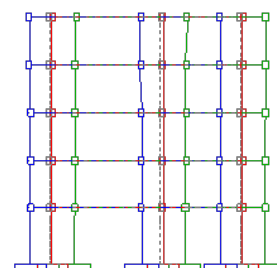
Y



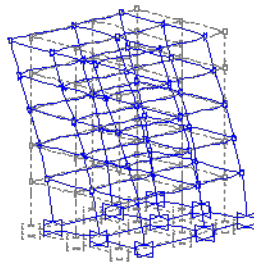
Mode 3:  $f = 0.44$  Hz;  $T = 2.26$  sec



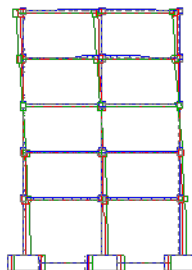
X



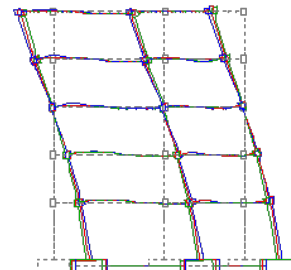
Y



Mode 4:  $f = 2.64$  Hz;  $T = 0.38$  sec



X



Y

**Figure 9-10 Modes 1-4 deflected shape of all the frames in 3-dimensional, x- and y-direction, along with their associated frequencies and periods. The undeflected shape of the system is shown in dashed lines**

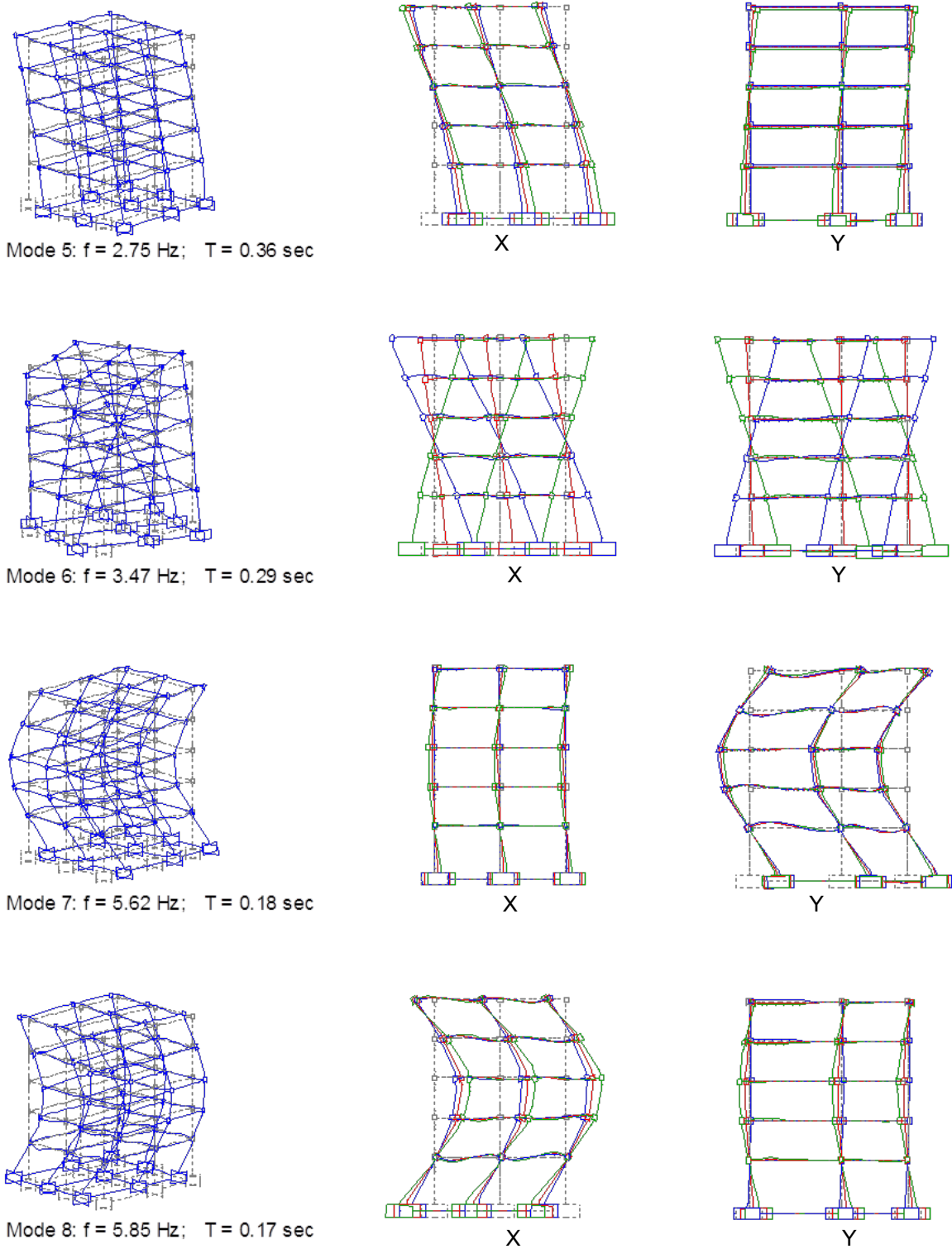


**Figure 9-11 Modes 5-8 deflected shape of all the frames in 3-dimensional, x- and y-direction, along with their associated frequencies and periods. The undeformed shape of the system is shown in dashed lines**

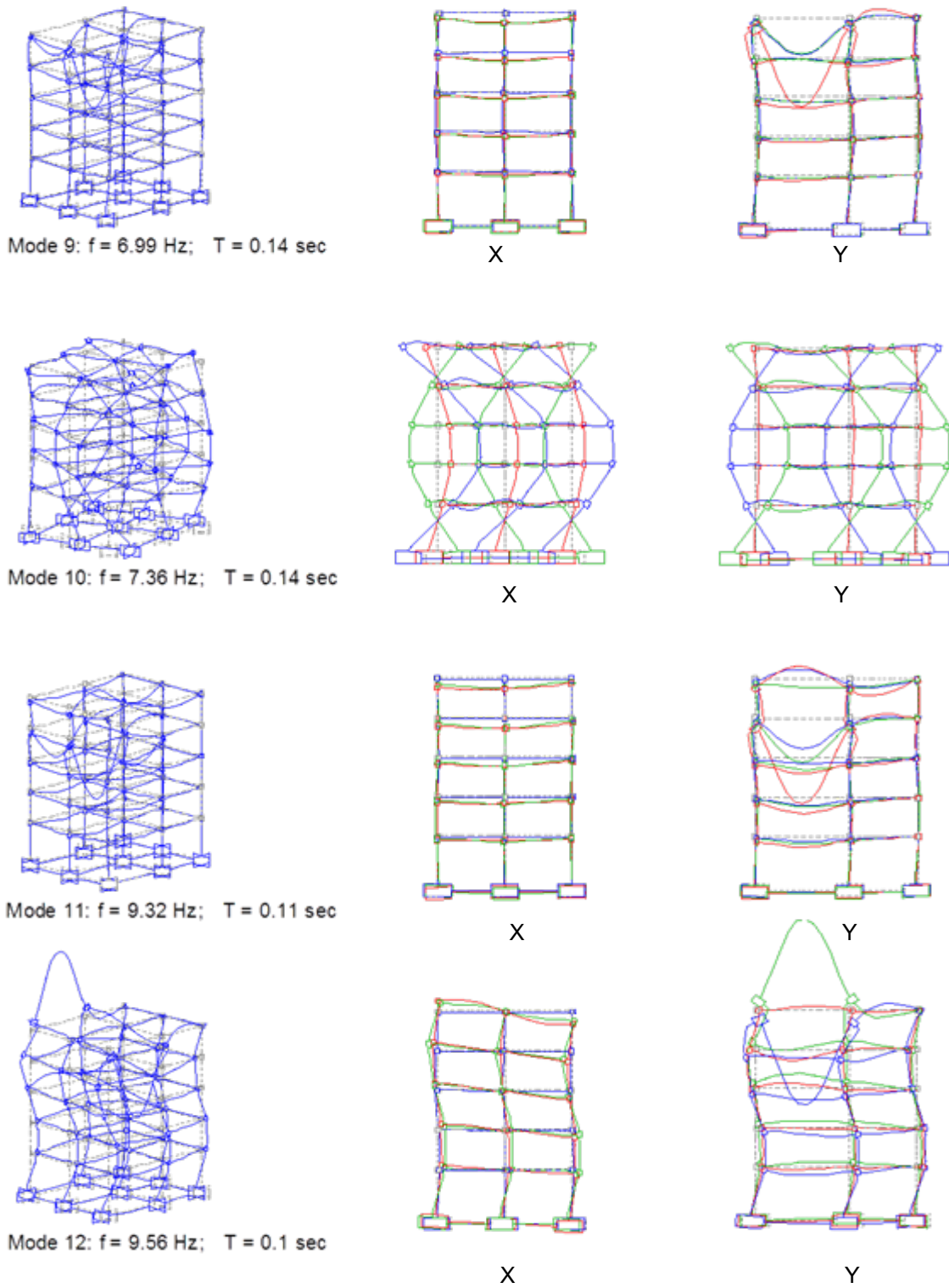
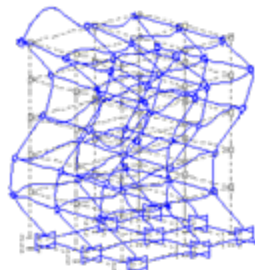
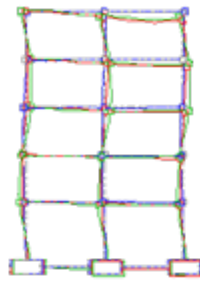


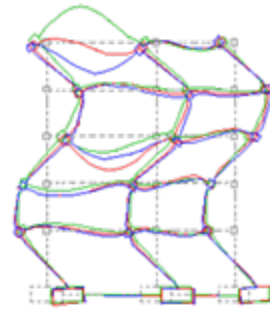
**Figure 9-12** Modes 9-12 deflected shape of all the frames in 3-dimensional, x- and y-direction, along with their associated frequencies and periods. The undeformed shape of the system is shown in dashed lines.



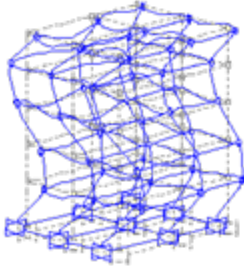
Mode 13:  $f = 9.66 \text{ Hz}$ ;  $T = 0.1 \text{ sec}$



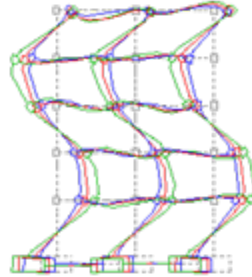
X



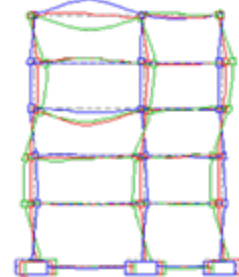
Y



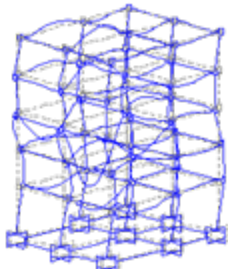
Mode 14:  $f = 9.97 \text{ Hz}$ ;  $T = 0.1 \text{ sec}$



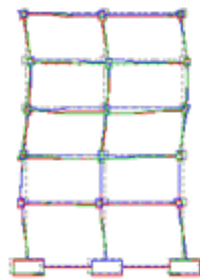
X



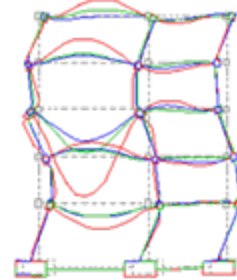
Y



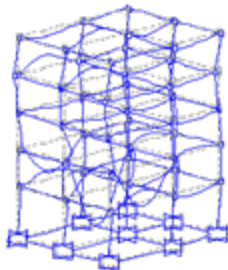
Mode 15:  $f = 10.18 \text{ Hz}$ ;  $T = 0.1 \text{ sec}$



X



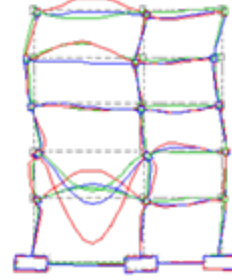
Y



Mode 16:  $f = 10.99 \text{ Hz}$ ;  $T = 0.09 \text{ sec}$



X



Y

**Figure 9-13** Modes 13-16 deflected shape of all the frames in 3-dimensional, x- and y-direction, along with their associated frequencies and periods. The undeflected shape of the system is shown in dashed lines

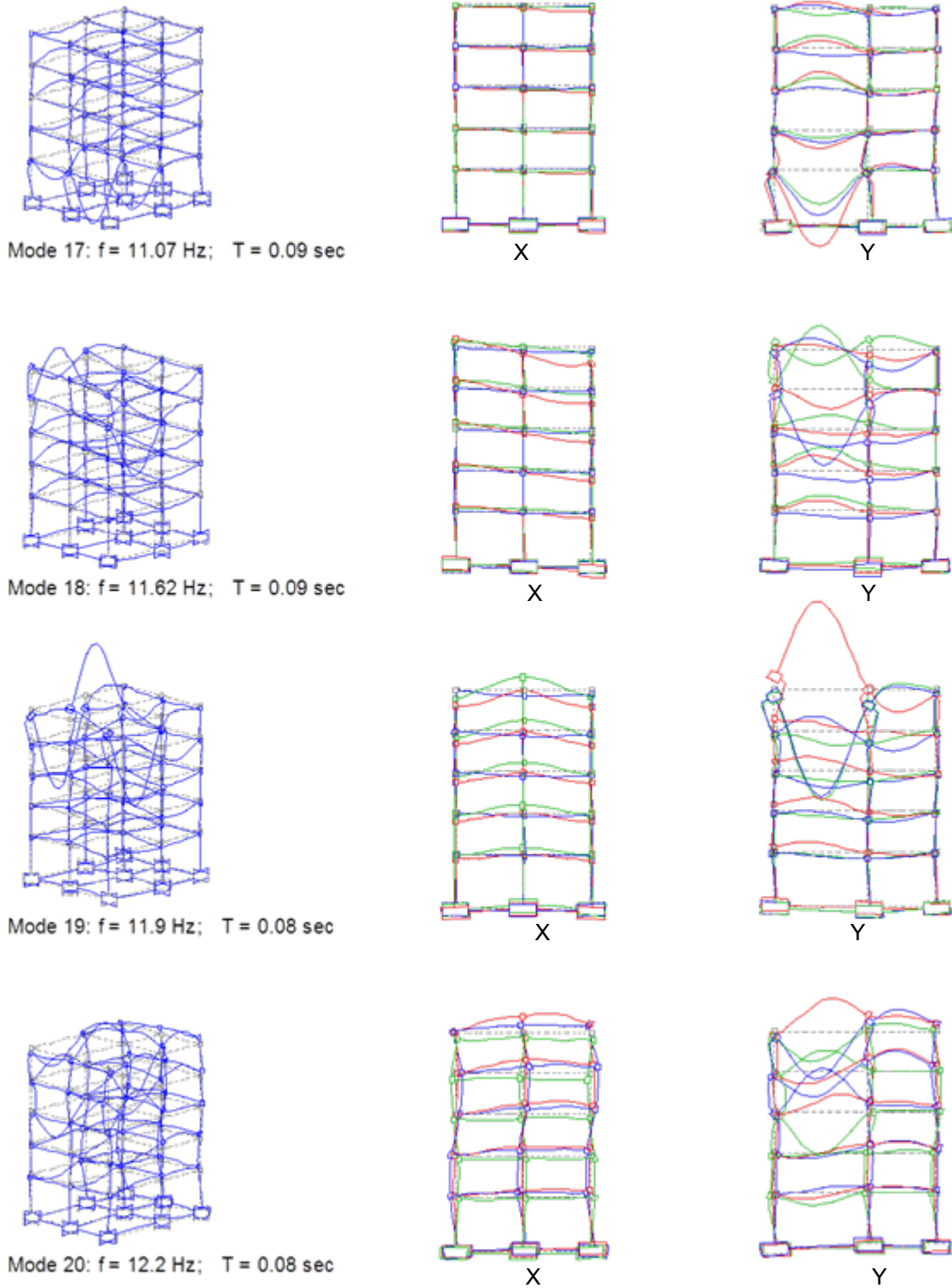


**Figure 9-14** Modes 17-20 deflected shape of all the frames in 3-dimensional, x- and y-direction, along with their associated frequencies and periods. The undeflected shape of the system is shown in dashed lines

As observed in Figures 9-12 to 9-14, the remaining modes (9,11,12,15-20) are local modes dominated by vertical vibration of individual slabs. Such modes are usually ignored when evaluating the dynamic characteristics of a building, but become more significant when the response to vertical excitation is evaluated. If movement of the horizontal degrees of freedom (DOFs) is present in the local modes, the horizontal floor accelerations and floor spectra will be amplified when the system is subjected to vertical excitation compared to horizontal only excitation. This phenomenon has not often been encountered in the literature. Mode 9 ( $T = 0.14$  sec, Figure 9-12) could be interpreted as the fundamental vertical mode. Uncharacteristic of a typical first vertical mode, Mode 9 is characterized primarily by vertical slab vibration at the roof level at the location directly beneath the supplementary mass. The supplementary mass has been confirmed (from SAP models not presented here) to increase the mass participation of Mode 9 as well as the slab vibration at the roof level relative to a typical building; however, the movement of horizontal DOFs in Mode 9 appears to be negligible (Figure 9-12). The influence of the supplementary mass on the response of the isolated testbed building is explored numerically in Chapter 10. Mode 11 ( $T = 0.107$  sec) is a local vertical mode dominated by slab vibration at the 5<sup>th</sup> floor. Mode 12 ( $T = 0.105$  sec) is a local mode dominated by slab vibration at the roof level that also contains movement of horizontal DOFs, especially at the 2<sup>nd</sup>, 3<sup>rd</sup> and 5<sup>th</sup> floors (Figure 9-12). Modes 15-20 (Figures 9-13 and 9-14) all appear to be local modes characterized by vertical slab vibration at several levels, but with little to no movement of horizontal DOFs except in Mode 15 ( $T = 0.098$  sec) in the y-direction. Modes 15 and above have low mass participation.

### 9.3 Structural Response

In this section, we compare the structural responses predicted by the numerical model to those recorded from the sensors. The x and y-direction roof acceleration histories, peak acceleration profiles (peak acceleration vs. story level), 2<sup>nd</sup> story drift histories, and peak drift profiles (peak drift vs. story level) are plotted for the four selected input motions in Figures 9-15 to 9-18. The response quantities are reported at the geometric center of the structure, obtained for the experimental data by averaging or linear interpolation of the filtered data from multiple sensors. The roof and 2<sup>nd</sup> story are chosen for plotting the acceleration and drift histories because the largest demands are observed at these locations, respectively.

Both low frequency and higher frequency components vibrations are visible in the roof acceleration and 2<sup>nd</sup> story drift histories (Figures 9-15 to 9-18). These signals have a low frequency motion vibration appears as a slow moving wave at the isolation frequency that determines the amplitude of oscillation through them that is indicative of the isolation frequency, while the higher frequency motions appear as rapid oscillations about the slower moving wave. As expected, the low frequency motion is strong in the drift histories, but obscured by higher frequency components in the acceleration histories. The observed isolation frequency is lower for El Centro (Figure 9-15) than for the other records, to reflect the nonlinearity of the system and thus the change in frequency with amplitude. A second component, strong in all signals, is deduced by visual inspection to be around 3 Hz (0.33 sec), and thus represents the first structural mode.



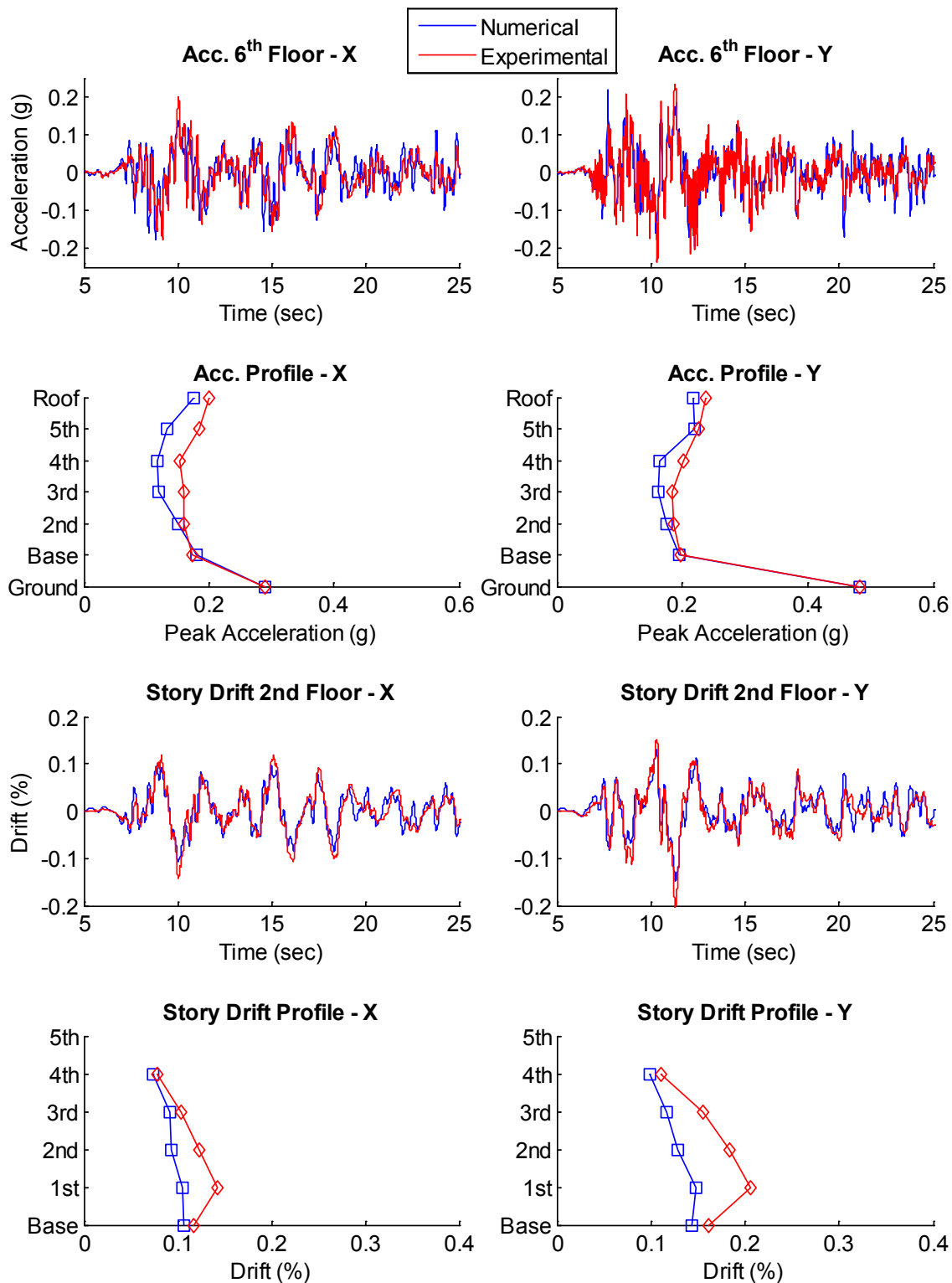


**Figure 9-15 Comparison of numerical and experimental simulation for El Centro 130%; x and y-direction roof acceleration histories, peak acceleration profiles, 2nd story drift histories, and peak drift profiles. Numerical simulation uses the characterized model with 85% of the characterized value for Qd**

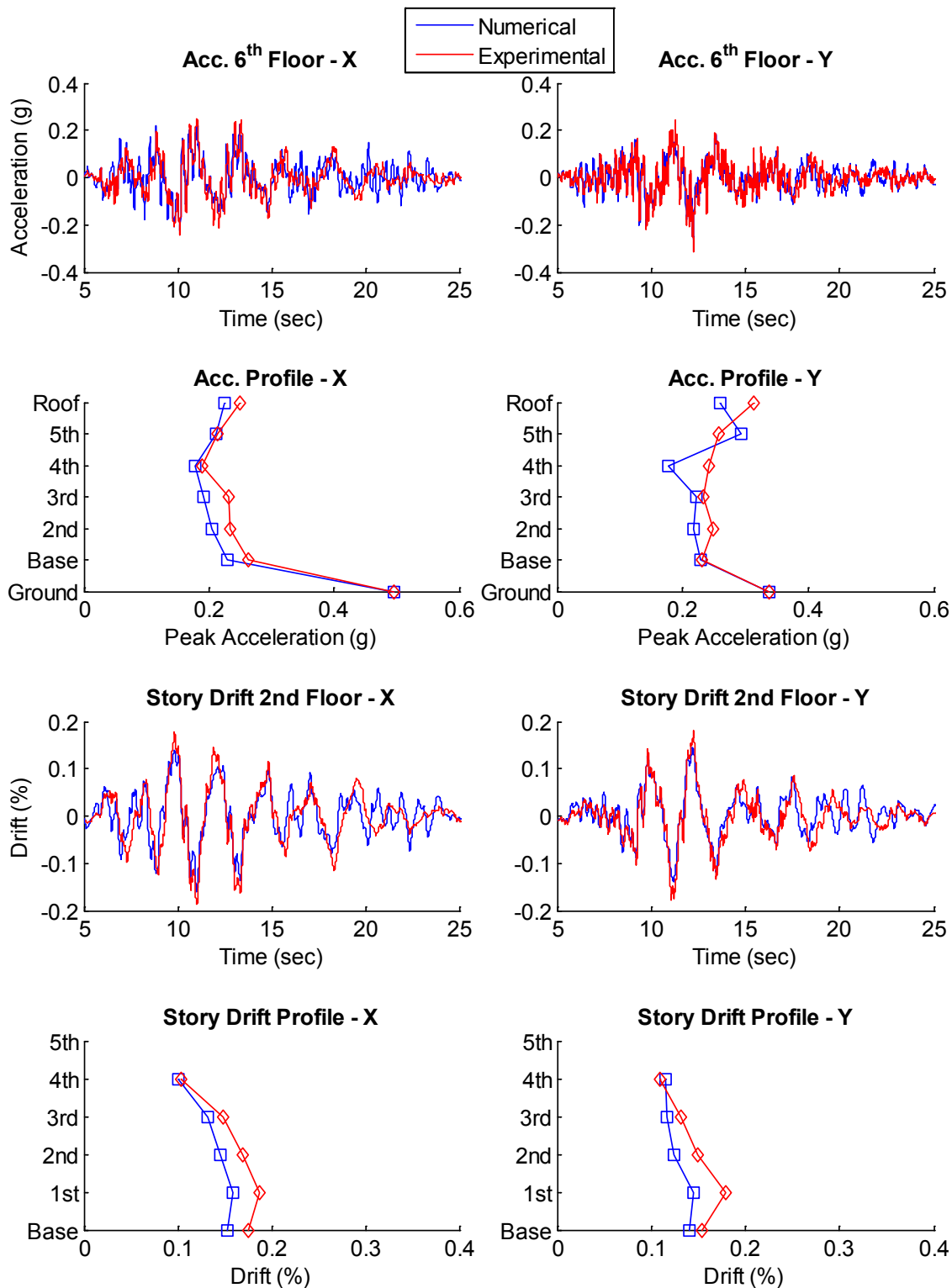


**Figure 9-16 Comparison of numerical and experimental simulation for Vogtle 100%; x and y-direction roof acceleration histories, peak acceleration profiles, 2nd story drift histories, and peak drift profiles. Numerical simulation uses the characterized model with 85% of the characterized value for  $Q_d$**



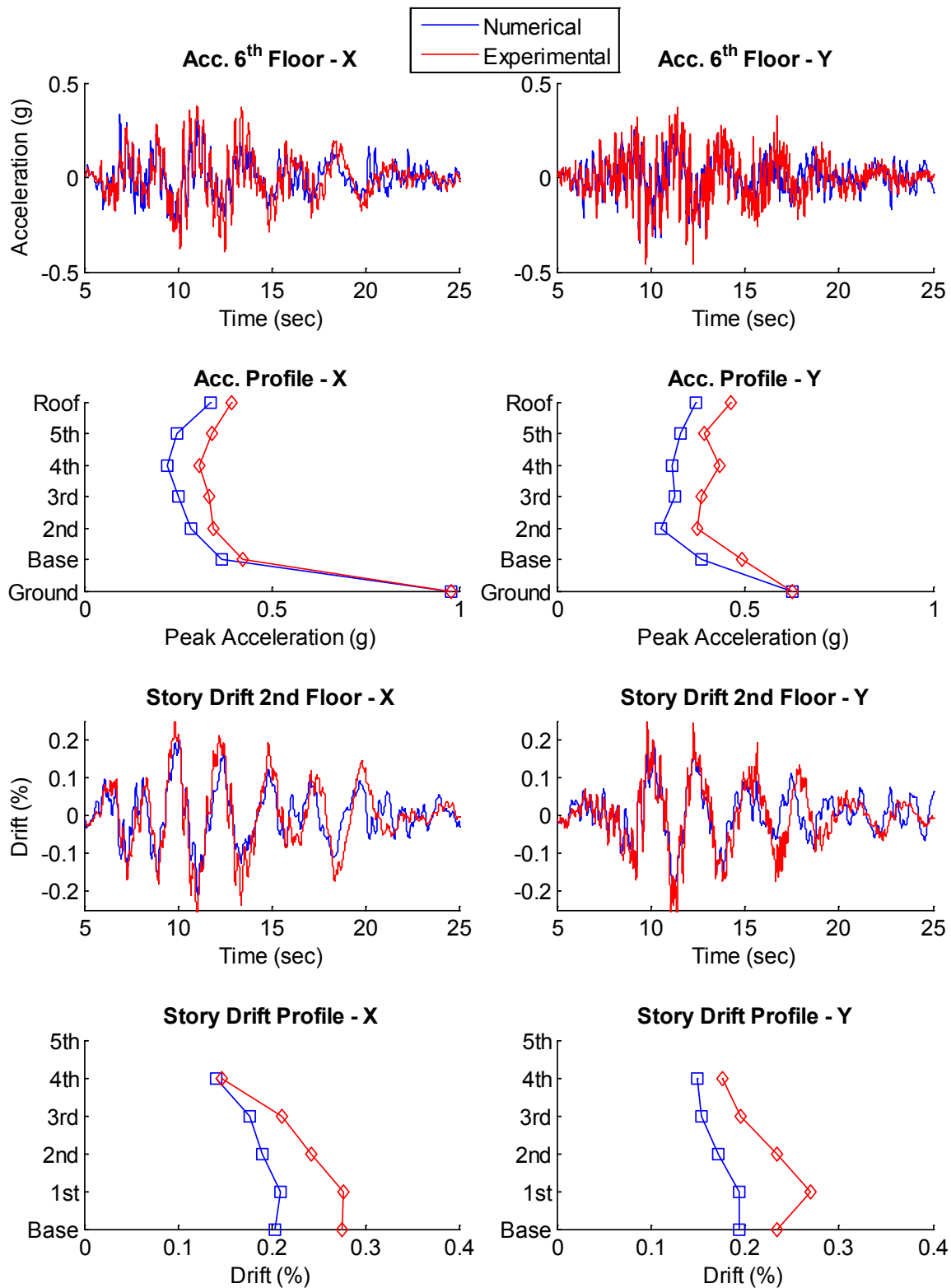


**Figure 9-17 Comparison of numerical and experimental simulation for Vogtle 175%; x and y-direction roof acceleration histories, peak acceleration profiles, 2nd story drift histories, and peak drift profiles. Numerical simulation uses the characterized model with 85% of the characterized value for  $Q_d$**

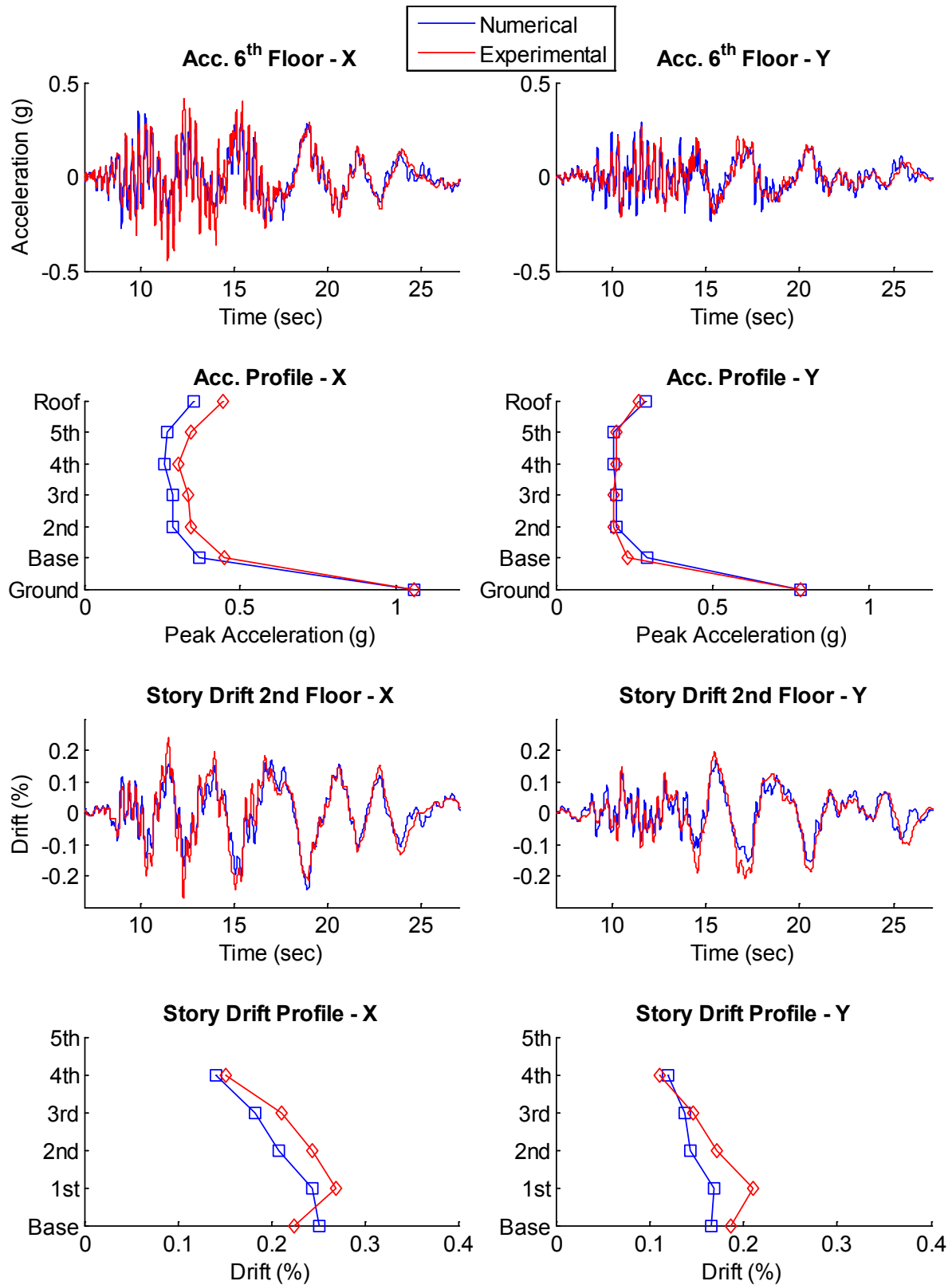


**Figure 9-18 Comparison of numerical and experimental simulation for Diablo 95%; x and y-direction roof acceleration histories, peak acceleration profiles, 2nd story drift histories, and peak drift profiles. Numerical simulation uses the characterized model with 85% of the characterized value for  $Q_d$**

The frequency components in the experimental response histories are clearly replicated in the numerically simulated responses, which is strong validation of the accuracy of the numerical simulation. The peak amplitude of response histories are difficult to simulate numerically due to inevitable noise and spikes in recorded experimental data, as well as the sensitivity of the response to the low values of damping in the calibrated numerical model. Given these difficulties, the numerically simulated peak amplitudes of floor acceleration and story drift are quite accurate, generally within about 20% of the experimentally observed values.

As further indication of the effectiveness of the numerical simulation, the numerically simulated acceleration profiles generally follow the trends observed in the experimental acceleration profiles. For instance, for all of the records except Diablo 95% (Figure 9-18), the accelerations in the y-direction are larger than in the x-direction, replicated in both experimental and numerical simulation data. The acceleration profile pattern in the x-direction is characterized by maxima at the base and the roof and a minimum at the 4<sup>th</sup> floor. This pattern is clearly indicative of the combination of an isolation mode (uniform) and a first structural mode (linear with a node at the 4<sup>th</sup> floor). A larger slope in the acceleration profile (or greater difference between the maximum and minimum acceleration over the height) indicates greater participation of the first structural mode. The shape of the acceleration profile through these control points is more jagged in the lower intensity motions (El Centro 130% and Vogtle 100%, Figures 9-15 and 9-16) and smoother in the larger motions (Vogtle 175% and Diablo 95%, Figures 9-17 and 9-18). All these trends are well captured by numerical simulation. In the y-direction, the acceleration profile shapes from the experimental data are not as consistent from record to record, which suggests that other modes may be participating. The numerical simulation seems to pick up a false peak at the 5<sup>th</sup> floor in the y-direction for some records such as Vogtle 100% (Figure 9-16). For further insight, the 5% damped x and y-direction floor spectra, obtained from the numerical and experimentally obtained floor acceleration histories, are plotted for every floor in Figures 9-19 to 9-22 for the same four selected input motions. Because the target input acceleration for Diablo 95% is bidirectional (without vertical), it is easiest to analyze. Peaks occurring at periods below about 0.1 sec are ignored and high frequency components (above 50 Hz or below 0.02 sec) are filtered out of the signals. In the Diablo 95% floor spectra (Figure 9-22), three distinct peaks appear. A first peak appears on every floor at a period between 2 and 3 sec (0.33 to 0.5 Hz), and represents the isolation mode in each direction. As mentioned previously, the period of this peak varies from record to record since the isolation system is nonlinear. A second peak appears on all floors except the 4<sup>th</sup> at a period between 0.3 and 0.4 sec (2.5 to 3.3 Hz), and represents the first structural mode in each direction. These modes (4 and 5), plotted in Figure 9-10 and 9-11 each have a node at the 4<sup>th</sup> floor. A third peak appears on all floors except the 2<sup>nd</sup> and 5<sup>th</sup> just below a period of 0.2 sec (5 Hz), and represents the second structural mode in each direction. These modes (7 and 8), plotted in Figure 9-11, each have nodes at the 2<sup>nd</sup> and 5<sup>th</sup> floor. These floor spectra confirm that participation of a 2<sup>nd</sup> structural mode in each direction, which could not be detected by visual inspection in the roof acceleration histories, is non-negligible in the acceleration response.

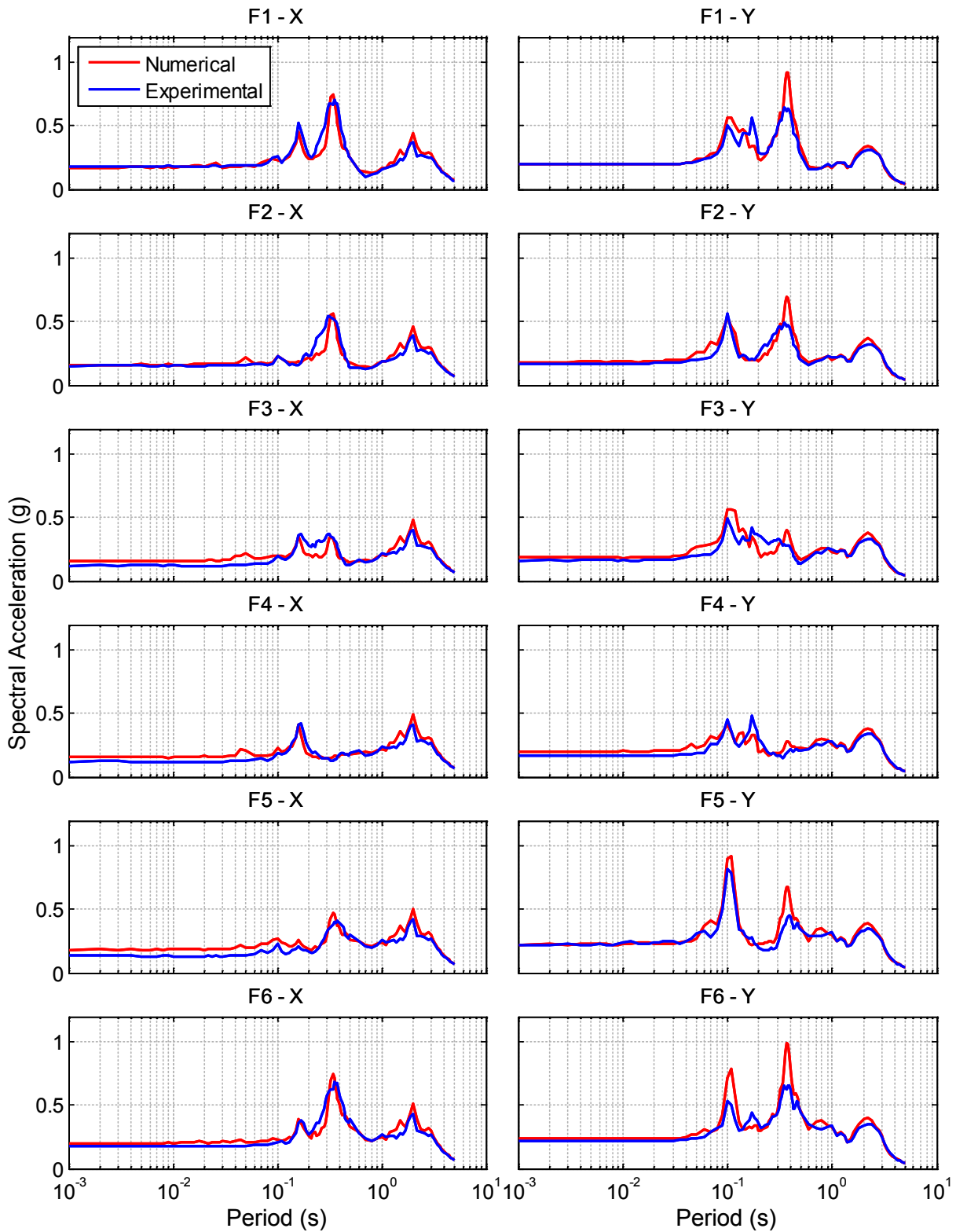


**Figure 9-19 Comparison of numerical and experimental simulation for El Centro 130%; x and y-direction spectral accelerations for 1st through 6th floors. Numerical simulation uses the characterized model with 85% of the characterized value for  $Q_d$**

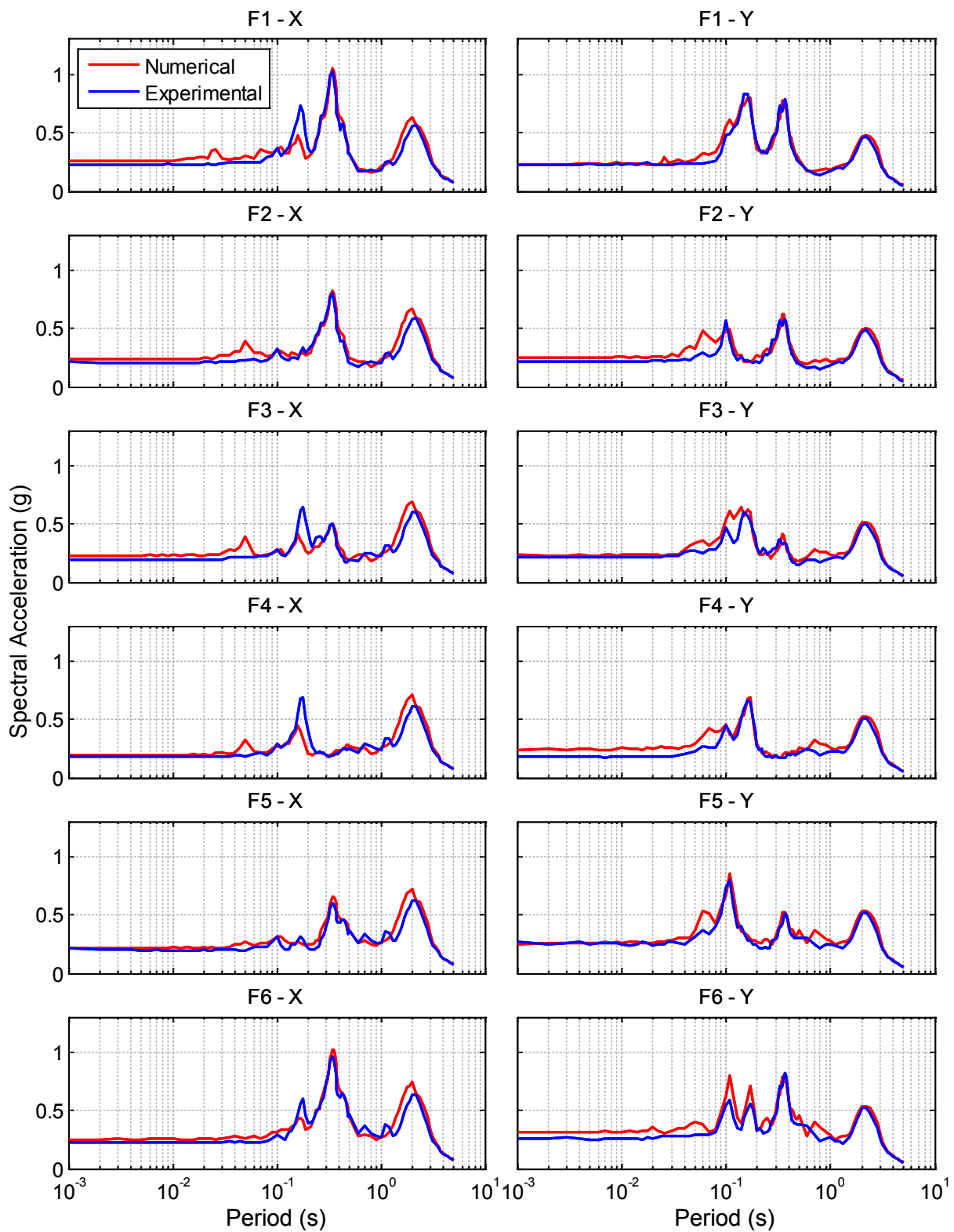


**Figure 9-20 Comparison of numerical and experimental simulation for Vogtle 100%; x and y-direction spectral accelerations for 1st through 6th floors. Numerical simulation uses the characterized model with 85% of the characterized value for  $Q_d$ .**

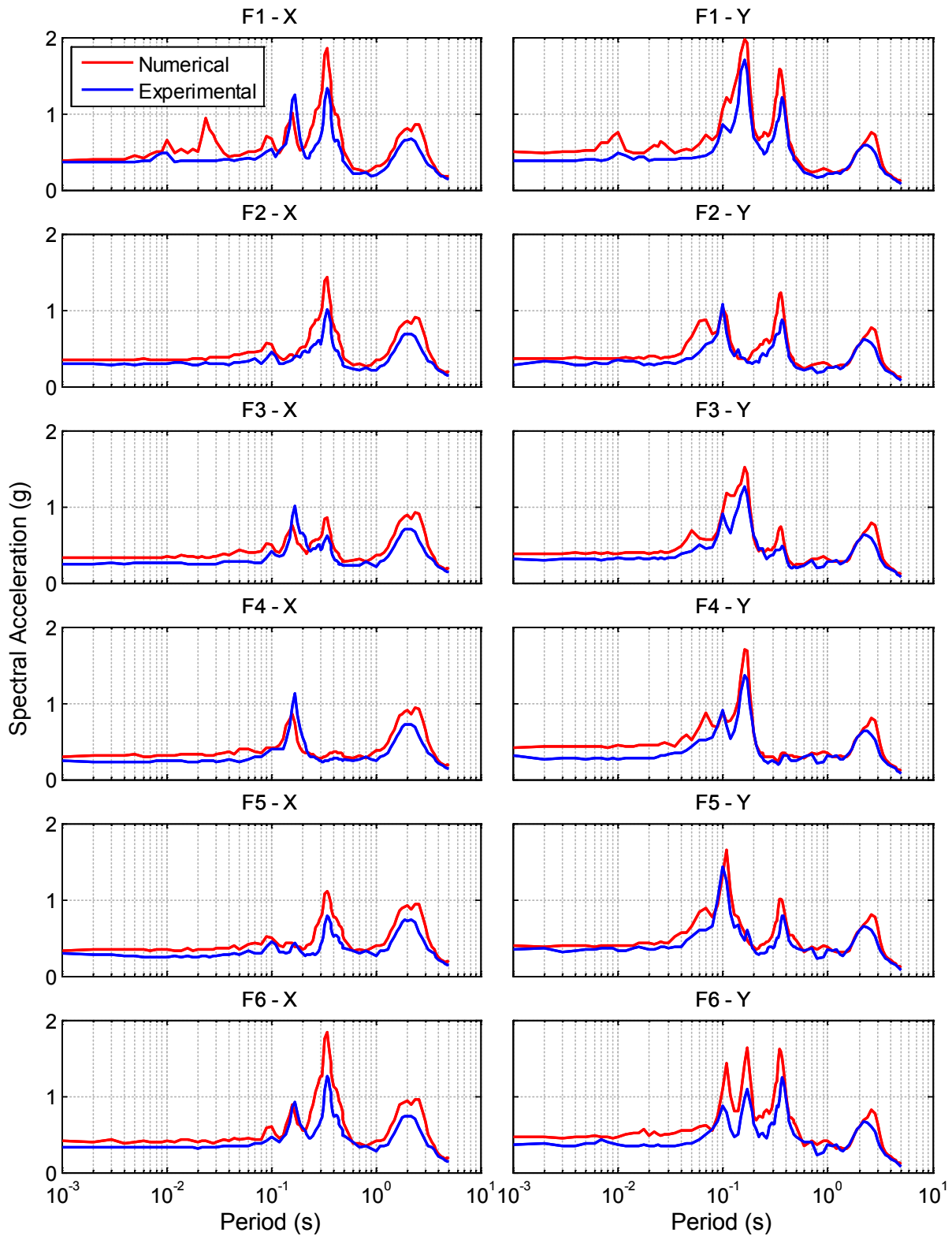


**Figure 9-21 Comparison of numerical and experimental simulation for Vogtle 175%; x and y-direction spectral accelerations for 1st through 6th floors. Numerical simulation uses the characterized model with 85% of the characterized value for  $Q_d$**

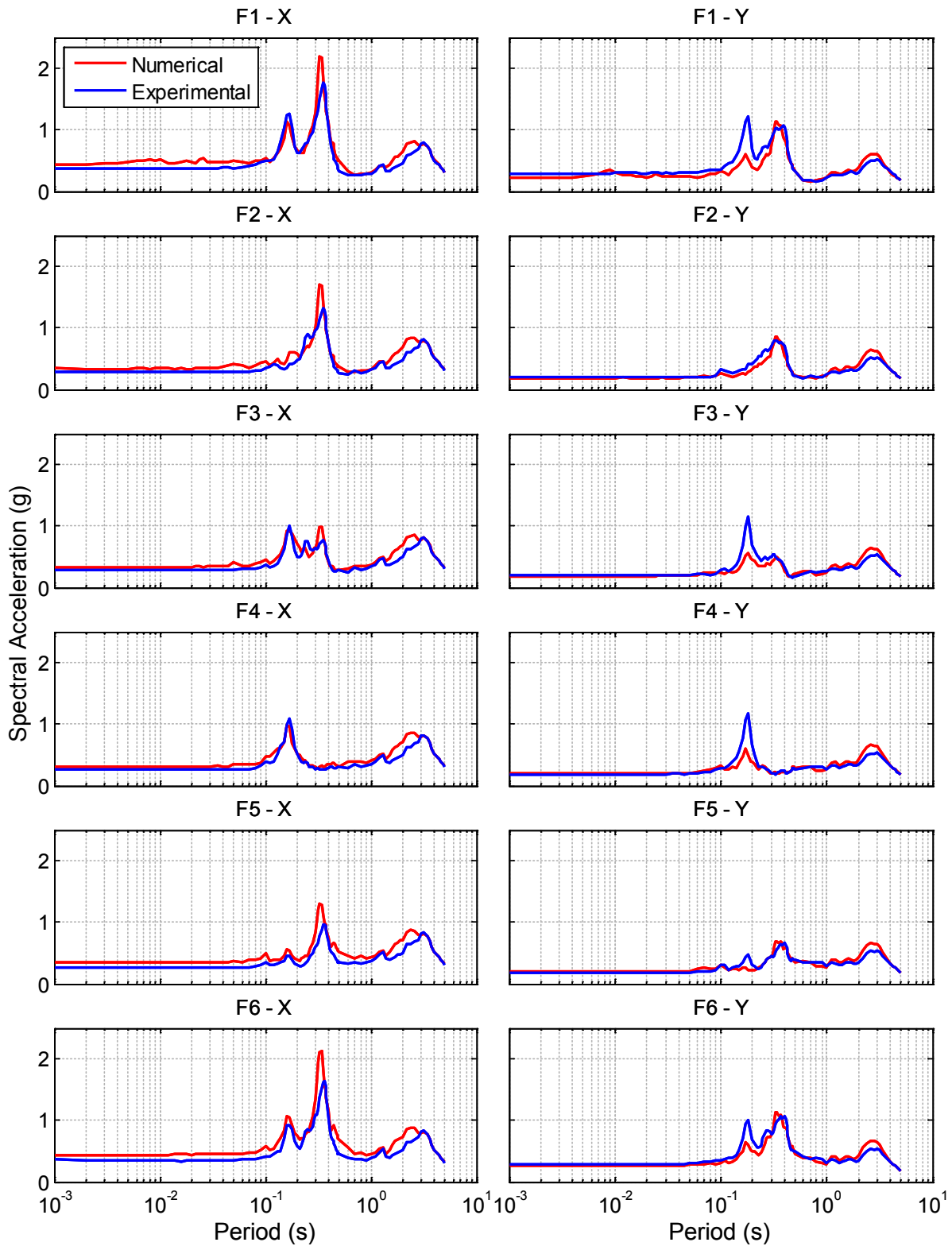


**Figure 9-22 Comparison of numerical and experimental simulation for Diablo 95% (XY); x and y-direction spectral accelerations for 1st through 6th floors. Numerical simulation uses the characterized model with 85% of the characterized value for  $Q_d$**

The same peaks in the floor spectra appear on the same floors at essentially the same periods for the three remaining motions (Figures 9-19 to 9-21). In the y-direction, an additional peak appears at a period of about 0.1 sec (10 Hz) on some floors. This peak is strongest on the 2<sup>nd</sup>, 3<sup>rd</sup>, 5<sup>th</sup> and roof floors. The most likely candidate for this peak is Mode 13 (Figure 9-13), which is the third structural mode in the y-direction. Although not suppressed on any floor, the horizontal deformation of Mode 13 is largest on the 2<sup>nd</sup>, 3<sup>rd</sup>, and 5<sup>th</sup> floors, corresponding approximately to the largest peaks in the spectra. Unlike the other structural modes, Mode 13 includes significant slab vibration at the 4<sup>th</sup> floor and (especially) roof, suggesting that this mode is driven by vertical excitation. The dominant slab vibration at the roof level is increased by the supplementary mass installed at the roof, which is explored further through numerical simulation in Chapter 10. The corresponding x-direction mode (Mode 14) contains much lower levels of slab vibration, and thus is not excited to the same extent by the vertical input. Although, small peaks in the x-direction floor spectra can sometimes be observed at this frequency (e.g. Vogtle 175%, Figure 9-21).

The peaks of the numerically predicted spectra generally occur at the same periods (or very close) to the spectra for the experimental data. As expected due to the nonlinearity of the isolation system, the periods at which these peaks occur do not exactly match the period of the modes shown in Figures 9-10 to 9-14. For instance, the peaks in the spectra occur at periods around 0.164 sec (6.1 Hz), while the periods of modes 7 and 8 are predicted to be 0.179 sec (5.6 Hz) and 0.169 sec (5.9 Hz), respectively. Since the stiffness assumed for the isolators does not reflect the actual frequency excited in a given motion, which changes continuously, the discrepancy in the periods of the numerically simulated spectral peaks compared to the modal peaks is quite reasonable. Indeed, the first mode period from modal analysis was 2.72 sec, while the actual first peaks of the floor spectra are closer to 2 sec for most motions, which confirms that a corresponding shift of periods throughout the modes is valid.

Strong higher mode participation is observed in the floor accelerations and floor spectra, which is a consequence of the low amount of energy dissipation in the steel frame. As described in Section 8.6, the Rayleigh damping model has been calibrated for 1.9% at the representative higher mode frequency of 6.6 Hz (0.15 sec). Measured damping ratios on the order of 1-2% are reasonable for a steel frame system that remains linear.

Calibration of the Rayleigh damping coefficients is difficult, which affects the accuracy of the numerical model in predicting the spectral peaks. The damping has been calibrated to achieve the best fit (by inspection) over all 15 simulations, but only a few are shown here. In the simulations shown here, the numerical model tends to be overdamped for the first structural mode (it underestimates the peak) and is underdamped for the second and higher structural modes (it overestimates the peaks). Recall that an additional damper was included in the numerical model to represent the first structural mode (Section 8.6). The calibrated value of this damper leads to accurate estimates of the first structural mode peaks for Vogtle 100% (Figure 9-20) and El Centro 130% x-direction (Figure 9-19), but underestimates the peaks for the other motions. Likewise, the calibrated Rayleigh damping coefficient at higher frequencies (2<sup>nd</sup> and 3<sup>rd</sup> structural modes) leads to accurate or over-estimated spectral peaks for El Centro 130% and both Vogtle records in the y-direction, but under-estimated spectral peaks for the rest. Thus, the observed energy dissipation in the system – quantified in terms of a viscous damping model – seems to vary from trial to trial, and no single assumption for the damping model is perfect. Improved accuracy of numerical simulation results relative to the experimental data may be achievable with computer programs that construct a damping matrix (even for nonlinear analysis) based on independent damping ratios in individual modes. Such approaches are infeasible for design since the damping properties of the building are not known in such detail.



Overall, the numerical simulation matches the experimental data with sufficient accuracy to a) build confidence in the modeling techniques used by the profession, and b) provide insight to help interpret the response of the test structure, as has been described above.

As discussed in Chapter 2, a nuclear facility would be substantially stiffer than the tested steel moment frame structure, with a natural period in the range of 0.1 to 0.25 sec, while the tested structure natural period exceeded 0.6 sec. Relative to the experimental data shown here, a stiffer structure with the same isolation period would experience lower overall accelerations and reduced higher mode effects. The expected evidence of reduced higher mode effects is a) reduced high frequency vibration in the acceleration histories (Figures 9-15 to 9-18), b) acceleration profiles that are more uniform (i.e. identical accelerations at all levels from base to roof (Figures 9-15 to 9-18), and c) reduction in the peaks of the floor spectra for periods less than 1.0 sec. In addition, higher mode effects may be reduced as a result of a simpler (single story) structural configuration. Without simulation, the extent of acceleration reduction cannot be predicted, but it is expected to be significant. These general trends can be verified by fundamental textbooks on the theory of seismic isolation (e.g. Kelly 1997, Chopra 2012).



## 10. INFLUENCE OF VERTICAL EXCITATION ON THE STRUCTURAL RESPONSE

In this chapter, the influence of vertical excitation on the overall response of the isolation system and the structure is evaluated. Several XY (horizontal only) and 3D excitations were included in the test program, and results for both types of motions have been discussed to date. To provide a direct assessment of the influence of vertical excitation, comparative simulations were conducted with input motions that included and neglected vertical shaking input. Specifically, the Northridge-Rinaldi record – scaled to 88% - was applied to the system as both an XY excitation (with target vertical excitation of zero) and as a 3D excitation. The Rinaldi 88% (XY) and Rinaldi 88% (understood to be 3D) simulations were applied back-to-back in the test program (Table 4-4). Similarly, the Diablo Canyon record was applied as an XY excitation with 95% scale factor (Diablo 95% XY) and as 3D excitation with 80% scale factor (Diablo 80%). The isolator and structural responses under the Rinaldi 88% (XY)/Rinaldi 88% and Diablo 95% (XY)/Diablo 80% pairings are compared in this chapter.

The substantial supplementary weight mounted at the roof level of the testbed structure, as described in Section 2.3, is believed to have influenced the response of the structure due to vertical excitations and the subsequent horizontal-vertical coupled response of the structure. As such, additional numerical simulations have been conducted using an augmented numerical simulation model of the structure. In the augmented model, all supplementary weight at the roof level has been removed and relocated at the base level (just above the isolators) in a regular configuration, or proportional to the existing mass at the base level. Thus, the augmented model essentially retains the same properties of the isolation system, and removes the substantial eccentricity and vertical irregularity associated with the roof weight. Numerical simulation results using the augmented model are included to provide the perspective on this effect. The simulations suggest that a good portion of the horizontal-vertical modal coupling and amplification of horizontal floor accelerations resulted from the supplementary mass that was placed at the roof level.

### 10.1 Response of LR Bearings under Axial Force Variation

The influence of the vertical excitation on the isolation system response is examined first. There was no evidence in any of the hysteretic data examined to date (see Section 9.1) that the bearing hysteresis loops were affected by loss of axial load carrying capacity under the combination of large displacements and increased axial loading due to overturning forces. Since the bearings were not subjected to the usual increase in axial force at large lateral displacements due to overturning, but rather tended to unload axially at large displacements (Section 6.2), loss of lateral load carrying capacity was not expected.

Comparative data from the Rinaldi 88% (XY) and Rinaldi 88% trials suggests that rapid strong axial force variation in the bearings affected the horizontal shear force in the bearings in the Rinaldi simulation. Figures 10-1 and 10-2 compare the bearing hysteresis loops in X and Y-directions for Rinaldi 88% XY and 3D for a single large displacement cycle. The vertical peak ground acceleration (V-PGA) for the 3D excitation is listed. While the displacements in the bearings are approximately the same for XY and 3D simulation, a small high frequency oscillation was present in the forces for the 3D simulation over certain parts of the hysteresis loop that was absent in the XY simulation. This oscillation is distinct from the effects of bolt slip documented in Section 6.1. For these simulations, the history of the shear force variation in LRB-S is plotted along with axial force variation in Figure 10-3, where the reference cycle shown in the hysteresis loops of Figures 10-1 and 10-2 is indicated in bold. Figure 10-3 indicates that the high frequency component of the shear force variation was in phase with the axial force variation. We do not know the cause of this small shear force variation; it could be a result of

instantaneous variation in confinement of the lead core as the axial force on the bearing cycles between a state of tension (axial force > 0 in Figure 10-3) to more than twice the initial static load in compression.

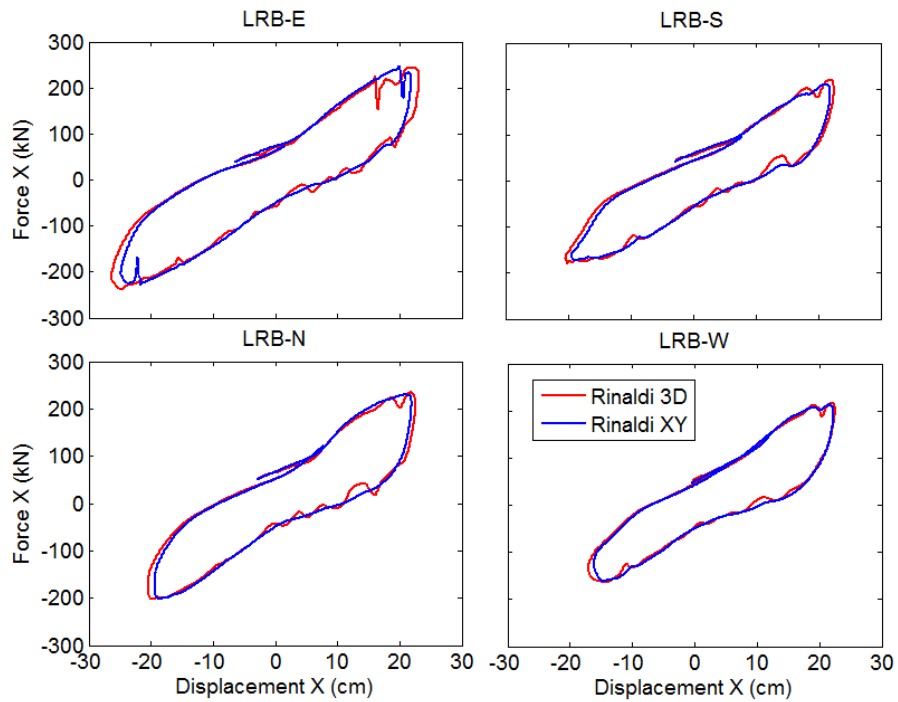


**Figure 10-1 Bearing force vs. displacement (hysteresis loops) in x-direction for a single large displacement cycle compared for Rinaldi 88% (XY) and Rinaldi 88% (V-PGA = 1.21g) excitations**

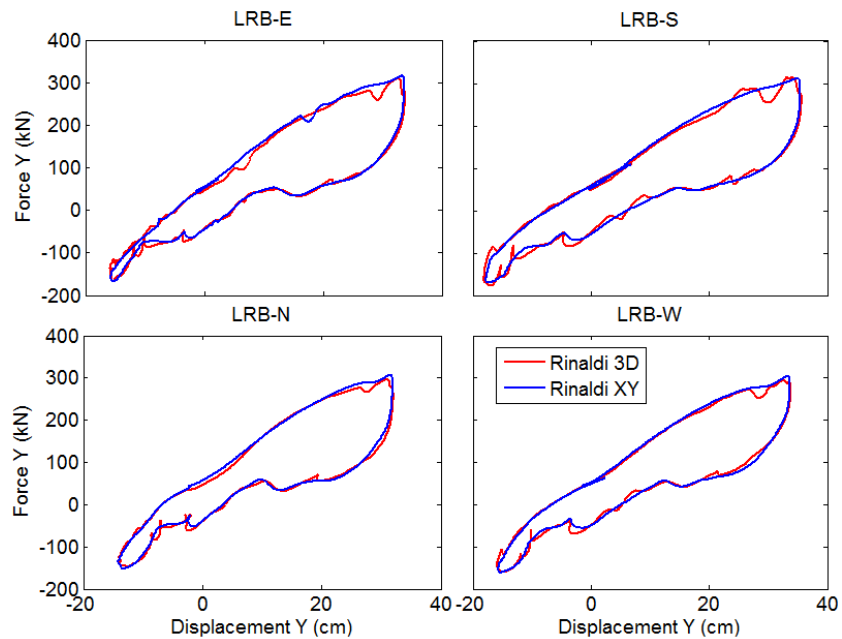


**Figure 10-2 Bearing force vs. displacement (hysteresis loops) in y-direction for a single large displacement cycle compared for Rinaldi 88% (XY) and Rinaldi 88% (V-PGA = 1.21g) excitations**

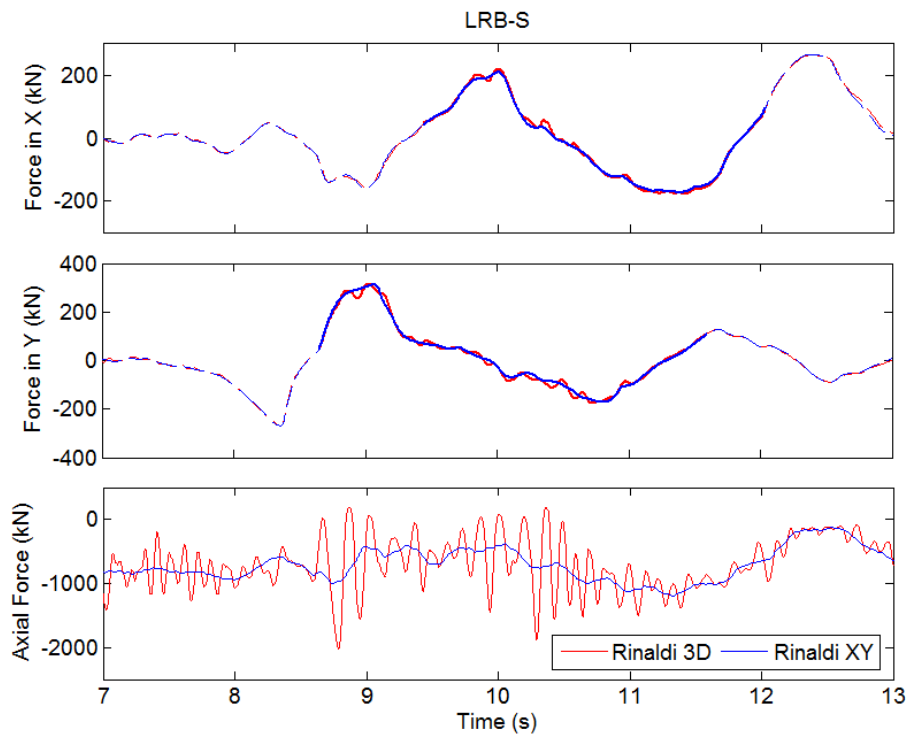


**Figure 10-3 History of shear force and axial force variation in LRB-S compared for Rinaldi 88% (XY) and Rinaldi 88% (V-PGA = 1.21g) excitations**

The high frequency shear force variation was not evident in any other records. Data analogous to Figures 10-1 to 10-3 (single loop bearing hysteresis and force histories for a single LRB in x, y and z-directions) are presented for Diablo 80%/Diablo 95% (XY) in Figures 10-4 to 10-6. Because the scale factors for the motions were different, the hysteresis loops do not align precisely and the same one-to-one comparison of XY versus 3D excitation was not possible for this simulation pairing. In the hysteresis loops of Figures 10-4 and 10-5, some oscillations in the shear force were present for both XY and 3D simulations (resulting from bolt slip or bidirectional interaction), but no local variations of the shear force could reasonably be attributed to vertical excitation.

The peak vertical ground acceleration observed in the Rinaldi 88% test (V-PGA = 1.26g) was more than twice that of any other record in the test program (Table 4-7), and local peaks exceeding about 0.75g were reached several times during the vertical history, including the part of the record when the horizontal acceleration became strong (Figure 4-18). The axial forces in the isolators cycled between a state of tension and more than twice the static load in compression, which is unusually large. The slight variation of the shear force that is correlated with this large intensity and high frequency variation of the axial force on the bearings, regardless of its cause, does not appear to be significant.

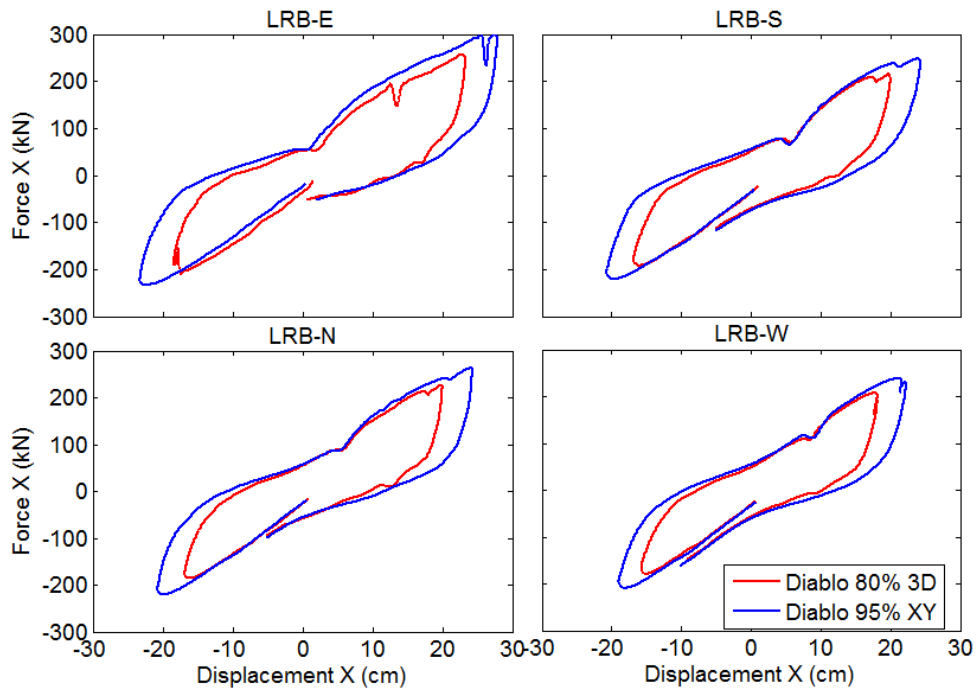


**Figure 10-4 Bearing force vs. displacement (hysteresis loops) in x-direction for a single cycle compared for Diablo 80% (V-PGA = 0.44g) and Diablo 95% (XY) excitations**

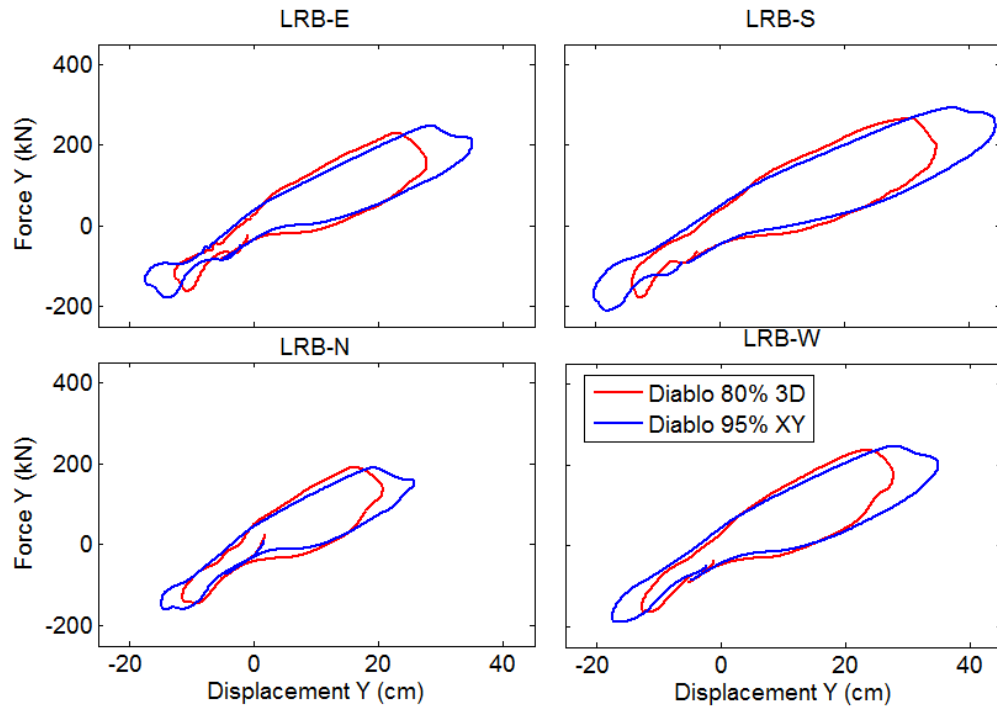


**Figure 10-5 Bearing force vs. displacement (hysteresis loops) in y-direction for a single cycle compared for Diablo 80% (V-PGA = 0.44g) and Diablo 95% (XY) excitations**

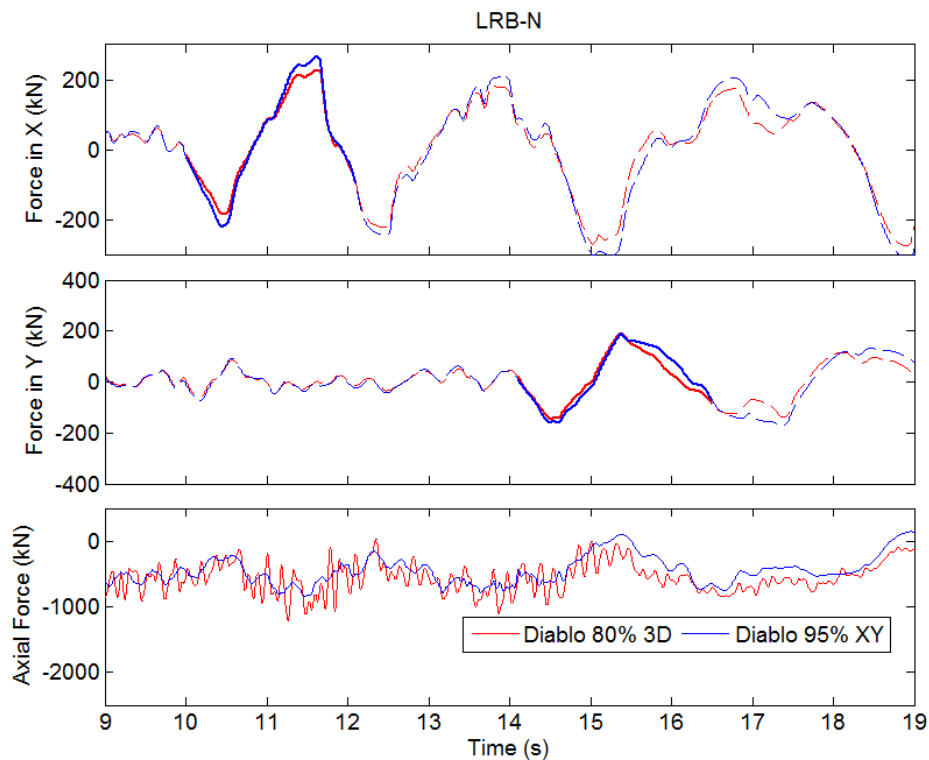


**Figure 10-6 History of shear force and axial force variation in LRB-N compared for Diablo 80% (V-PGA = 0.44g) and Diablo 95% (XY) excitations**

## 10.2 Horizontal and Vertical Floor System Vibration

Vertical acceleration produced by the earthquake simulator generated significant vertical vibration of the floor system (floor slabs). Figure 10-7 plots vertical accelerations recorded in the simulator platform and the middle of the floor slab at the 5<sup>th</sup> and roof levels for three different records: Vogtle 100% (V-PGA = 0.28g), Diablo 80% (V-PGA = 0.44g) and Rinaldi 88% (V-PGA = 1.21g). For these records, the peak slab accelerations were amplified relative to the V-PGA, and the amplification factor increased slightly as the intensity of V-PGA was increased. The 5<sup>th</sup> floor slab acceleration was amplified by a factor of 3.5 to 4.4, while the roof slab acceleration was amplified by a factor of 5.4 to 6.3. These amplification factors were determined by the slab vibration frequencies and were large due to the relatively low levels of damping. From Figure 10-7, the slab accelerations appeared to be dominated by single frequency vibration. The dominant slab vibration frequencies, confirmed by transfer function analysis (not shown here), were about 10 Hz for the 5<sup>th</sup> floor slab and 7 Hz for the roof slab. Thus, amplification was higher at the roof slab than for the 5<sup>th</sup> floor slab due to its lower natural frequency, which was a result of the supplementary weight that was attached at the roof level.

This suggests that individual local vertical modes were activated at each floor level. The numerical simulation did not replicate these floor slab vibrations – controlled by the local vertical modes – with as much precision as the horizontal response. In Figure 10-8, the numerical and experimental 5% damped vertical acceleration spectra at the roof level are compared for Diablo 80% and Rinaldi 88%. In this figure, both the numerically and experimentally determined spectra were dominated by a single spectral peak, which occurred at the frequencies mentioned above, thus verifying the single mode response. However, the amplitudes of the peaks were not predicted accurately by the numerical simulation model. The vibration intensity at the roof level was significantly under-estimated and the vibration intensity at the 5<sup>th</sup> floor level was

significantly over-estimated by the numerical simulation model. Although the intensity of local vertical modes could not be matched well by numerical simulation, this did not affect the ability of the model to predict horizontal floor accelerations and floor spectra in the building.

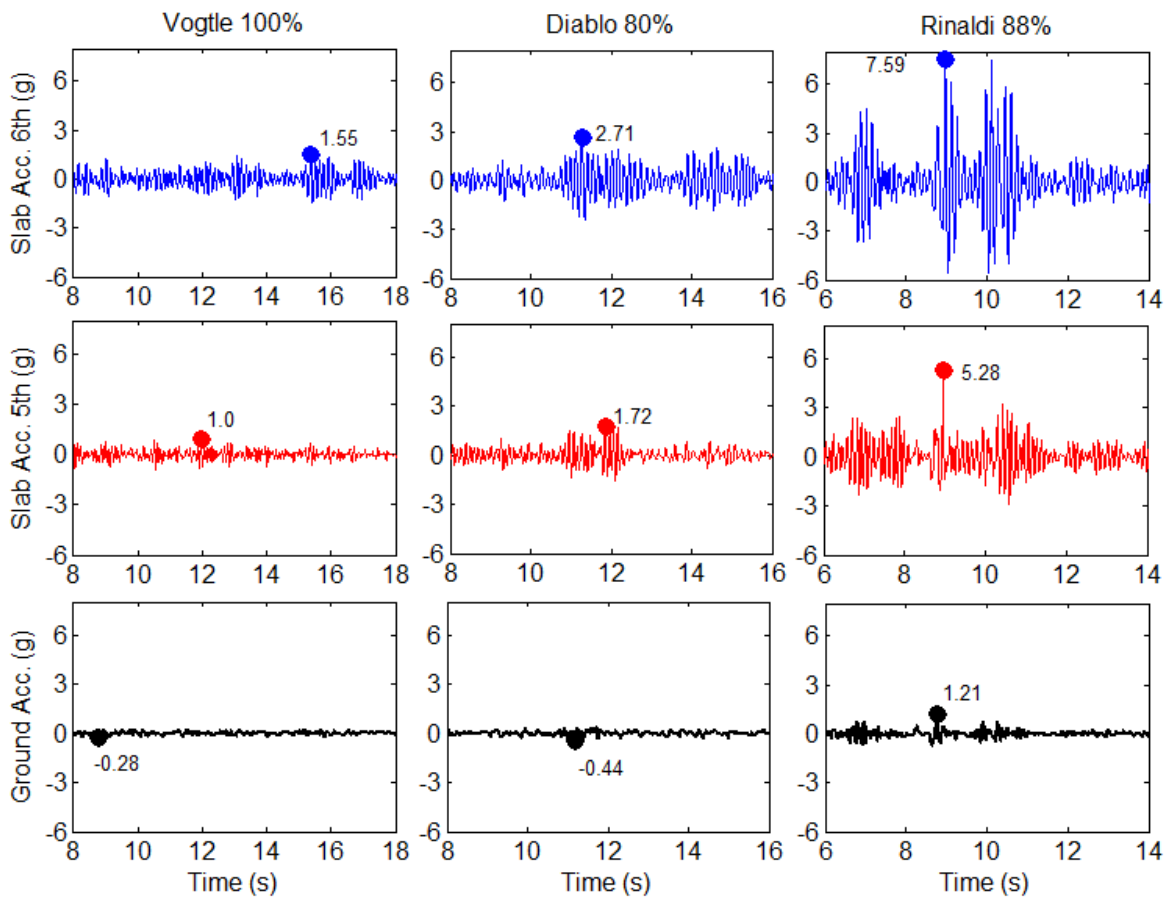


**Figure 10-7 Comparison of vertical roof slab acceleration (blue), 5<sup>th</sup> floor slab acceleration (red), and ground acceleration (black) for (a) Vogtle 100%, (b) Diablo 80%, and (c) Rinaldi 88%. Peak values indicated on graph**



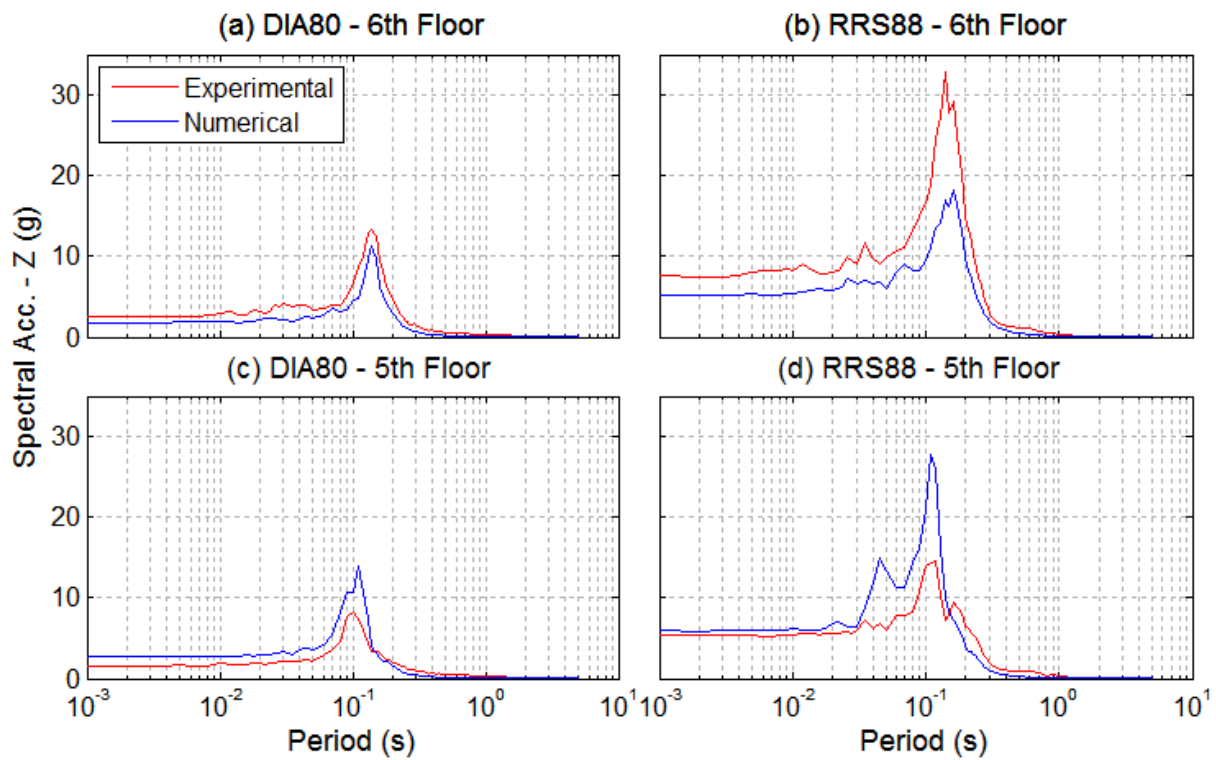


**Figure 10-8 Comparison of numerical simulation to experimental data for vertical slab acceleration; (a) roof floor and (c) 5<sup>th</sup> floor for Diablo 80%, and (b) roof floor and (d) 5<sup>th</sup> floor for Rinaldi 88%**

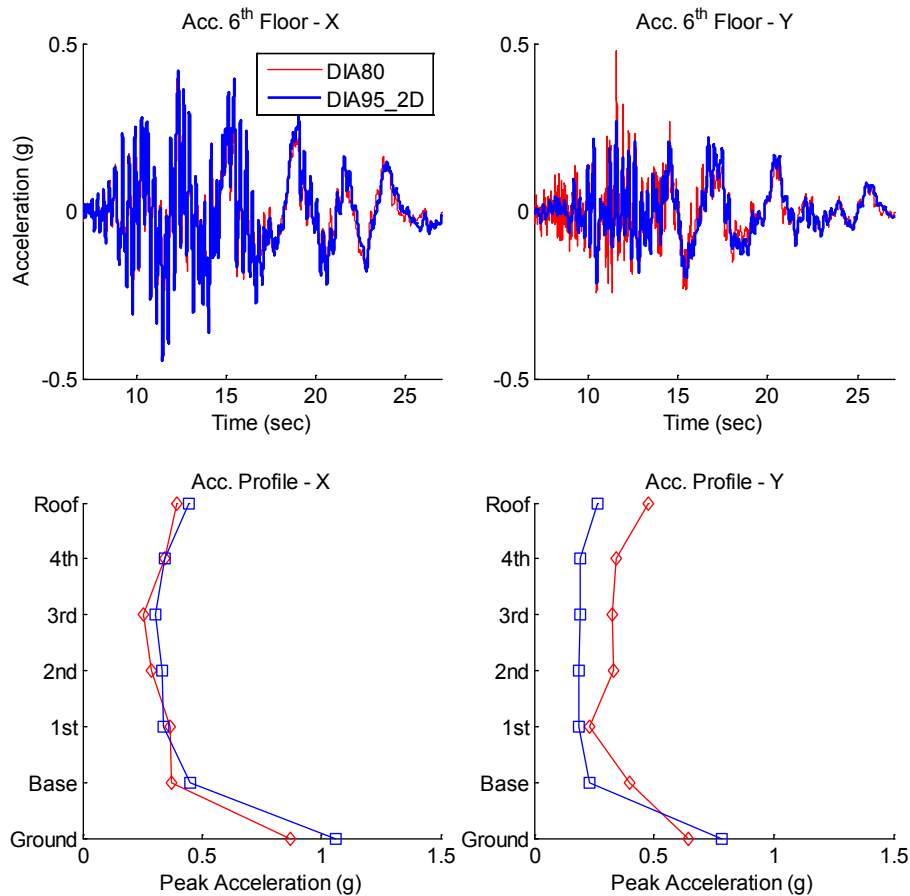


**Figure 10-9 Comparison of x and y-direction roof acceleration histories and peak acceleration profiles for Diablo 80% and Diablo 95% (XY)**

Besides the generation of significant vertical vibration of the floor system due to vertical excitation, the horizontal accelerations were also amplified for the 3D records relative to the XY records. This phenomenon is shown in Figures 10-9 and 10-10, which compare horizontal roof acceleration histories and peak acceleration profiles in x and y-directions for Diablo 80% /Diablo 95% (XY) and Rinaldi 88%/Rinaldi 88% (XY), respectively. For the Diablo record, the y-direction acceleration was larger for Diablo 80%, which included the vertical component of excitation, than for Diablo 95%, even though the scale factor applied to the motion was lower (Figure 10-9). The peak accelerations in the x-direction were approximately the same for Diablo 80% and Diablo 95% (XY). The amplification of horizontal floor acceleration under 3D excitation was even stronger for Rinaldi 88%. Peak horizontal accelerations were amplified by about 20% in the x-direction and about 100% in the y-direction (i.e. floor acceleration approximately doubled in the y-direction) (Figure 10-10). Part of this amplification was believed to be a coupled horizontal-vertical mode that was driven by the vertical acceleration (Section 9.3), which will be discussed further in Section 10.3. For interpreting the nonstructural component response, these floor accelerations were larger at the roof level than at the 5<sup>th</sup> floor level.

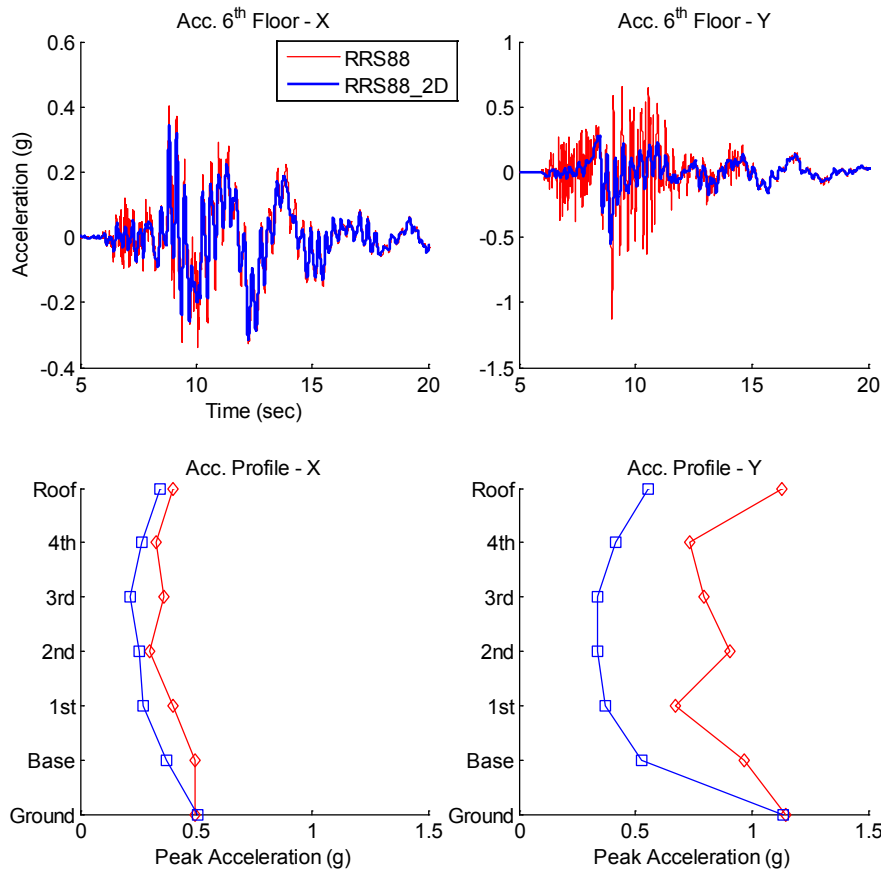


**Figure 10-10 Comparison of x and y-direction roof acceleration histories and peak acceleration profiles for Rinaldi 88% (XY) and Rinaldi 88%**

### 10.3 Source of Amplification of Horizontal Floor Acceleration under 3D Input

The amplification of horizontal floor accelerations described in Section 10.2 is best understood by considering horizontal floor spectra, and recalling the modal analysis that was presented in Chapter 9. The experimentally recorded horizontal floor spectra are compared for Diablo 80% and Diablo 95% (XY) in Figure 10-11, and for Rinaldi 88%/Rinaldi 88% (XY) in Figure 10-12. Note the difference in the amplitude for the two figures. In the x-direction, the floor spectra peaks were not amplified for Diablo 80% relative to Diablo 95% (XY). In the y-direction, however, acceleration peaks were amplified significantly at about 0.18 sec in the 1<sup>st</sup>, 3<sup>rd</sup>, 4<sup>th</sup> and 6<sup>th</sup> floors, and at about 0.1 sec in all floors, but especially 2<sup>nd</sup>, 3<sup>rd</sup>, 5<sup>th</sup> and 6<sup>th</sup> (Figure 10-11). The peak at 0.18 sec was associated with the 2<sup>nd</sup> structural mode (Mode 7 in Figure 9-11), and the peak at 0.1 sec was associated with the 3<sup>rd</sup> structural mode (Section 9.3 Mode 13 in Figure 9-13). Thus, the vertical component of acceleration amplified both the 2<sup>nd</sup> and 3<sup>rd</sup> structural modes.

For Rinaldi 88%, the x-direction spectral peaks at 0.18 and 0.10 sec at the associated floors were amplified very slightly for 3D excitation relative to XY excitation. The y-direction spectral peaks were amplified much more strongly at these two periods, especially the peaks at 0.18 sec (Figure 10-12). Thus, both 2<sup>nd</sup> and 3<sup>rd</sup> structural modes were amplified very slightly in the x-direction, while the 2<sup>nd</sup> structural mode was amplified most strongly and the 3<sup>rd</sup> structural mode

also amplified significantly in the y-direction. Spectral intensities greater than 5g were observed in the 2<sup>nd</sup> structural mode.

The floor spectra predicted by numerical simulation for Diablo 80% and Rinaldi 88% are compared to the experimental data in Figures 10-13 and 10-14, respectively. For Diablo 80%, the numerically predicted peaks at the 2<sup>nd</sup> and 3<sup>rd</sup> structural modes were close to those observed from the experimental data in both x and y-directions (Figure 10-13). For Rinaldi 88%, the numerically predicted peaks were close to those observed from the test data for all but the 2<sup>nd</sup> structural mode in the y-direction. (Figure 10-14).

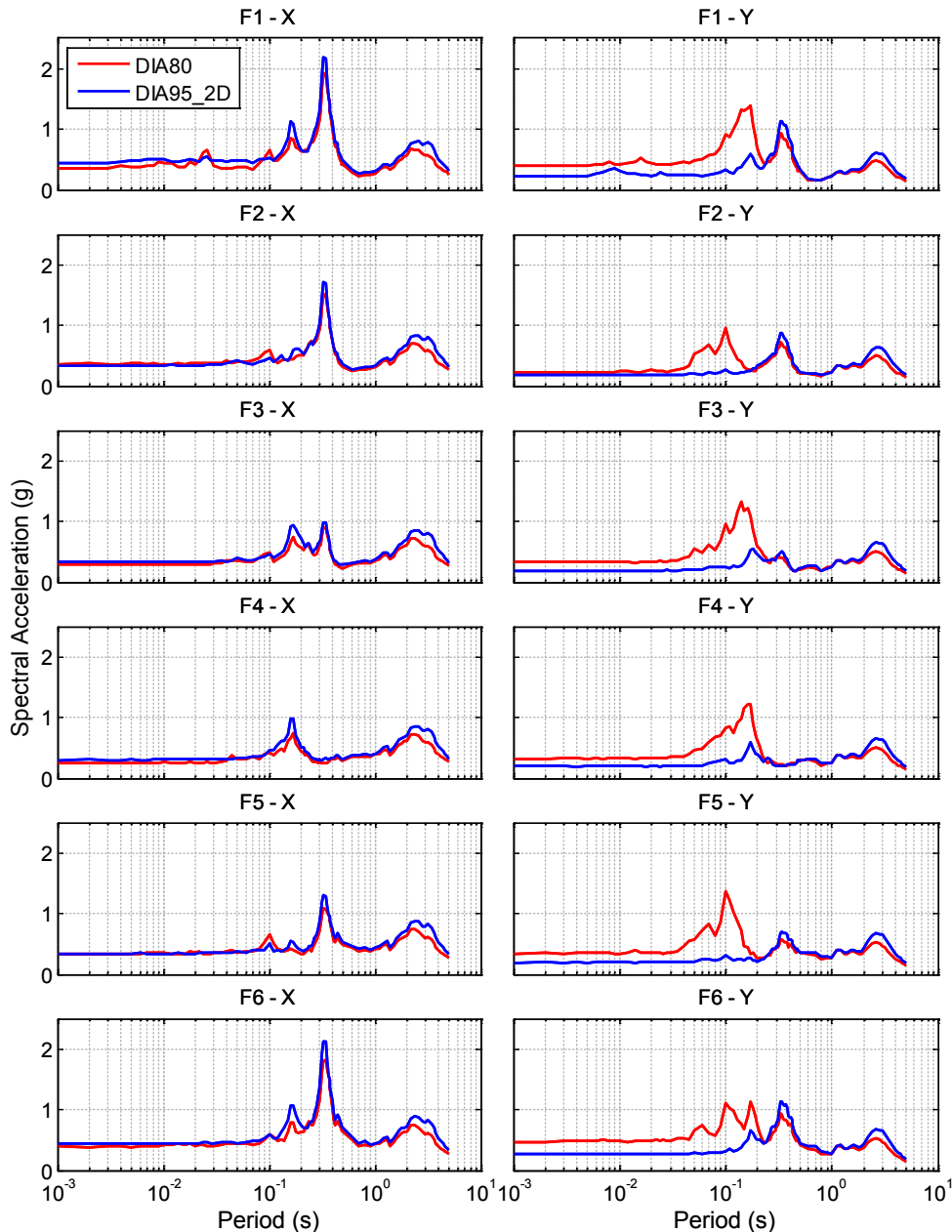


**Figure 10-11 Comparison of x and y-direction 5% damped spectral accelerations for 1<sup>st</sup> through 6<sup>th</sup> floors for Diablo 80% and Diablo 95% (XY). These spectra were derived from the experimentally recorded signals**

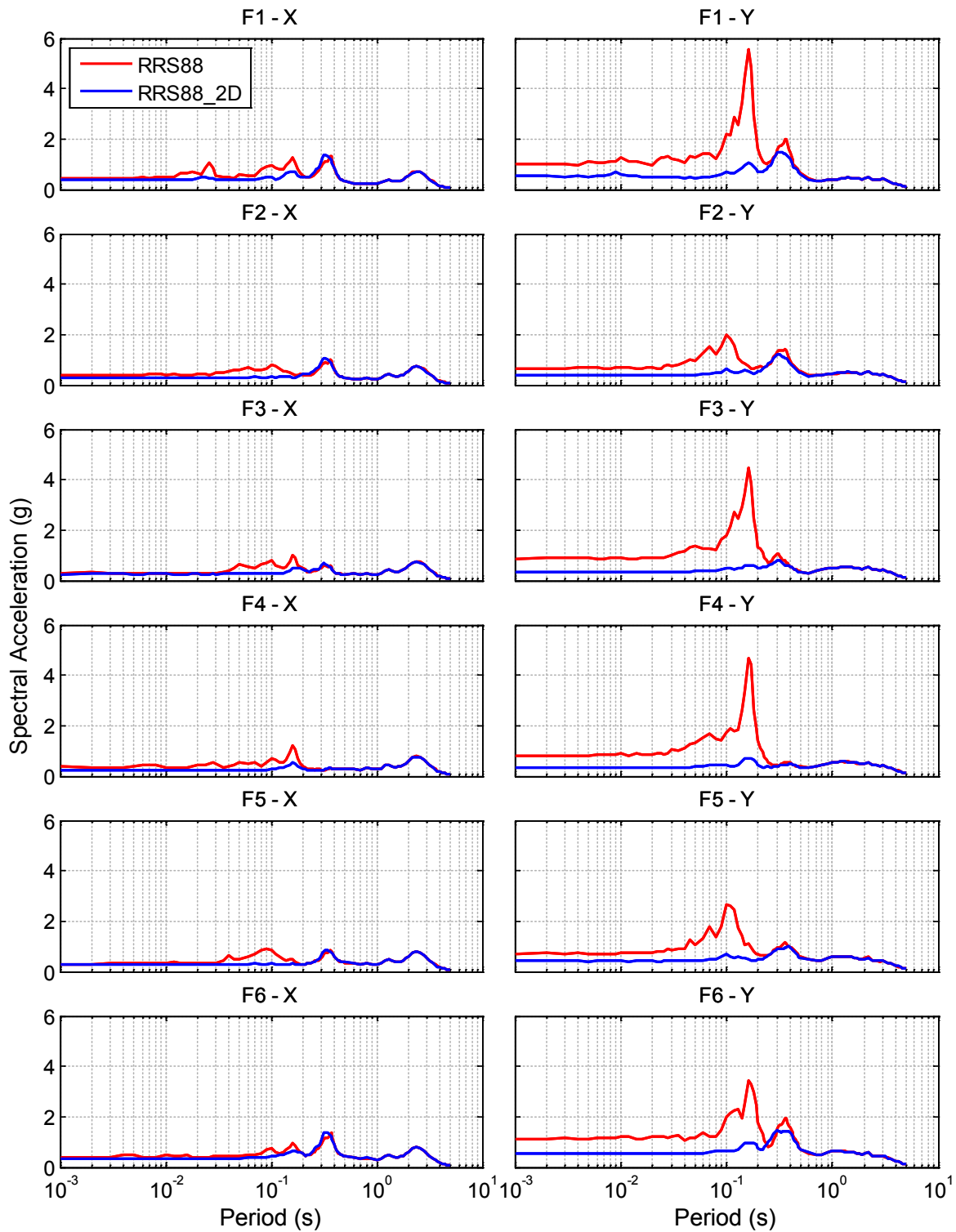


**Figure 10-12 Comparison of x and y-direction 5% damped spectral accelerations for 1<sup>st</sup> through 6<sup>th</sup> floors for Rinaldi 88% (XY) and Rinaldi 88%. These spectra were derived from the experimentally recorded signals**

The explanation for amplification of the 3<sup>rd</sup> structural mode (period = 0.1 sec) was introduced in Section 9.3. As described, this 3<sup>rd</sup> structural mode included substantial vertical slab vibration of the 4<sup>th</sup> and 6<sup>th</sup> floors, especially for the y-direction mode (mode 13 for y-direction and mode 14

for x-direction, Figure 9-14). Thus, the 3<sup>rd</sup> structural mode was driven by the vertical excitation, and the stronger the vertical excitation, the more this 3<sup>rd</sup> structural mode was amplified.

Horizontal-vertical modal interaction is not a feasible explanation for the amplification of what appears to be the 2<sup>nd</sup> structural mode. No vertical slab vibration was observed in the 2<sup>nd</sup> structural mode in either direction (mode 7 for y-direction and mode 8 for x-direction, Figure 9-12). We propose two possible theories regarding the source of amplification. They are simply theories that cannot be confirmed by the existing evidence. The first theory is that the 2<sup>nd</sup> structural mode was amplified by the high frequency oscillation in the base shear. Recall that a high frequency oscillation in the bearing shear force was clearly discernible for Rinaldi 88% (e.g., Figures 10-1 to 10-3), which could have been produced by the rapid change in the state of confinement of the lead core due to vertically induced axial load variation on the LR bearings. Thus, the variation of the yield force, tuned to the natural vertical frequency of the system (about 7 Hz or 0.14 sec), introduced a small harmonic to the base shear at 0.14 sec. This harmonic drove the overall structure in the nearest modes, which were around 0.17 to 0.18 sec.

The following arguments support this first theory that the slight axial load induced shear force fluctuation contributed to the large peaks in floor spectra coincident with the 2<sup>nd</sup> structural modes (around 0.18 sec): (1) The numerically simulated floor spectra, which could not capture the aforementioned shear force fluctuation, matched the experimental floor spectra for Diablo 80% well, since the shear force fluctuation was not evident in experimental data (Figure 10-12). However, the numerically simulated floor spectra fell well short of the experimental floor spectra at the 0.18 sec peak for Rinaldi 88% (Figure 10-12) when the shear force fluctuation was observed; (2) a similar amplification of the 2<sup>nd</sup> structural mode was observed in TP bearings that was quite evidently attributed to axial force induced fluctuations in the base shear throughout the experimental program (Dao 2012); (3) the amplification was strong in the y-direction (and essentially absent in the x-direction) for Rinaldi 88% because the input motion was much stronger in the y-direction than the x-direction.

The following arguments suggest that axial load induced shear force fluctuation could not have been singly responsible for the large peaks in the floor spectra coincident with the 2<sup>nd</sup> structural modes. (1) The numerical simulation model, which could not have captured the shear force fluctuation, predicted some amplification of the 2<sup>nd</sup> structural mode peak. (2) A base shear harmonic at 0.14 sec should have produced similar amplification of 2<sup>nd</sup> and 3<sup>rd</sup> structural modes, both about equally spaced from 0.14 sec (0.18 sec for 2<sup>nd</sup> structural mode and 0.10 sec for 3<sup>rd</sup> structural modes), yet the 2<sup>nd</sup> structural mode seemed to be amplified much more.

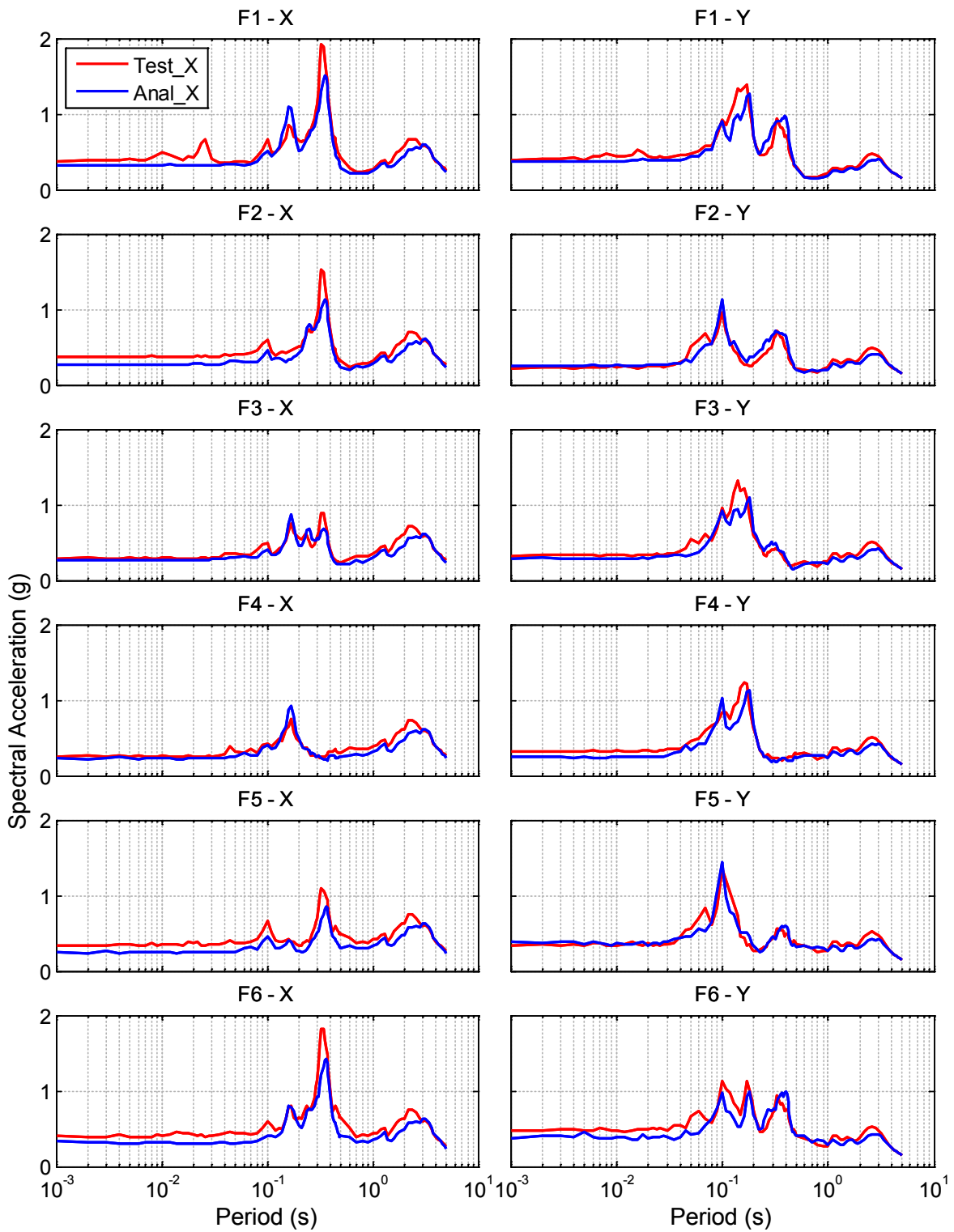


**Figure 10-13 Comparison of numerical simulation to experimental data for Diablo 80%; x and y-direction 5% damped spectral accelerations for 1st through 6th floors. Numerical simulation uses the characterized bearing model with 85% of the characterized value for  $Q_d$**

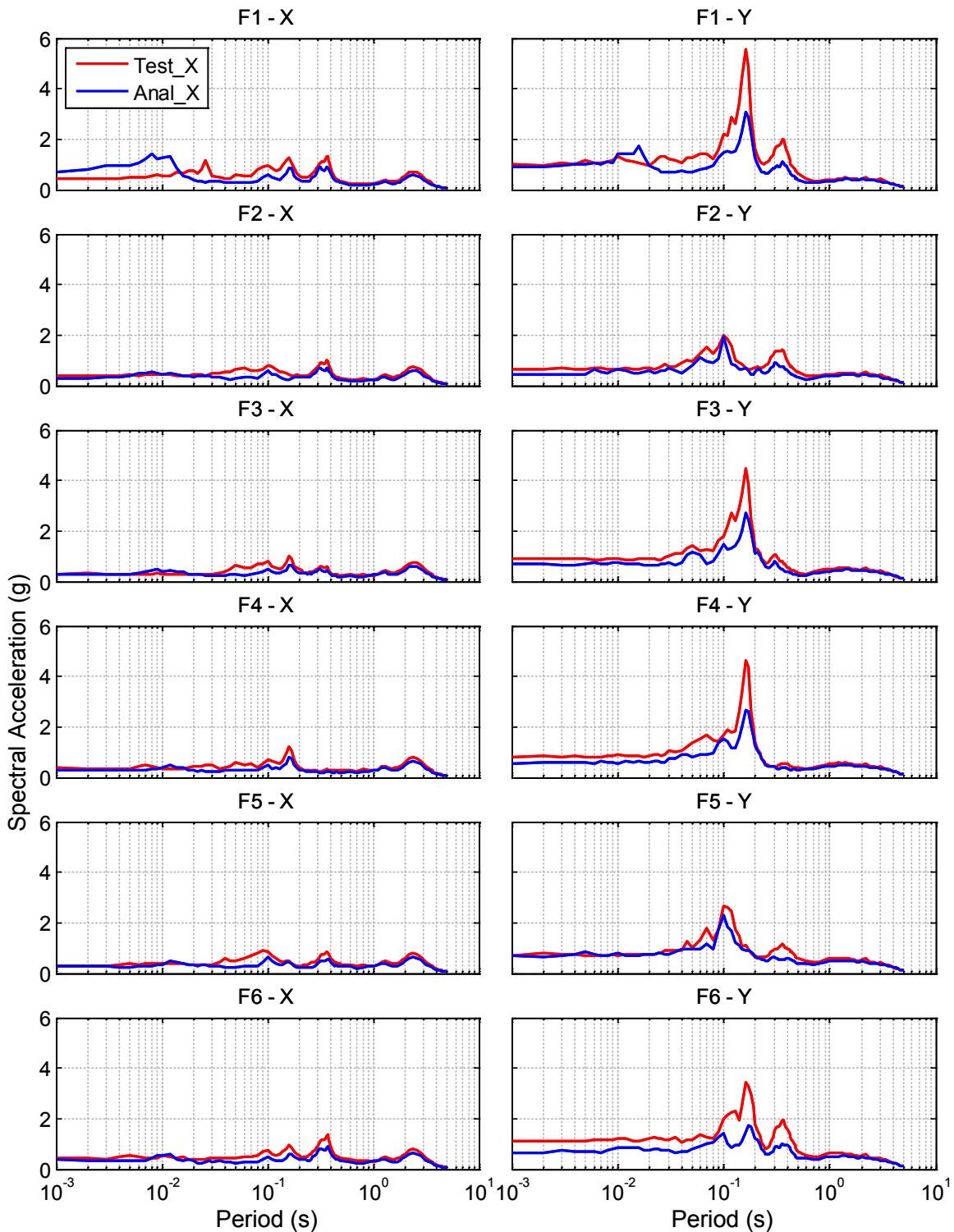


**Figure 10-14 Comparison of numerical simulation to experimental data for Rinaldi 88%; x and y-direction 5% damped spectral accelerations for 1<sup>st</sup> through 6<sup>th</sup> floors. Numerical simulation uses the characterized bearing model with 85% of the characterized value for  $Q_d$ .**

The foregoing considerations lead to the second theory, that amplification of a different mode also contributed to the amplified floor spectra peak at around 0.18 sec. Possible modes that



might have contributed are the 9<sup>th</sup> mode, which is a local vertical mode, or the 10<sup>th</sup> mode, which is a torsional mode with the same characteristic mode shape as the 2<sup>nd</sup> structural mode, but slightly more slab vibration (Figure 9-13). The 9<sup>th</sup> mode includes slight horizontal deflection and like the 2<sup>nd</sup> structural mode, appears to have nodes at the 2<sup>nd</sup> and 5<sup>th</sup> floor. The 9<sup>th</sup> mode includes a strong component of slab vibration at the roof and would thus be driven by vertical ground excitation.

In summary, the main source of amplification of horizontal acceleration was due to high frequency coupled horizontal-vertical modes of the structure that were driven by the vertical excitation input. A mode with frequency of 10 Hz or  $T = 0.1$  sec was positively identified and other modes may have contributed. Another possible source was that axial force variation in the isolators introduced a high frequency component into the base shear, which drove structural modes around 0.18 sec.

#### **10.4 Influence of Supplementary Roof Mass on Vertical Slab Vibration and Horizontal-Vertical Coupling**

Being mindful of the limitations of the numerical simulation model to predict vertical slab vibrations, the numerically simulated vertical acceleration at the 5<sup>th</sup> floor slab and roof slab are compared in Figure 10-15 for the tested building model, and the augmented model with the supplementary weight removed from the roof. This figure predicts that relocating the roof mass at the base level will not much reduce the intensity of vertical slab acceleration at the roof level and may actually increase the slab acceleration at the 5<sup>th</sup> floor. Given that the numerical simulation model was not shown to predict vertical acceleration well, we do not have high confidence in the prediction and expect that removing the roof mass would reduce the slab acceleration at the roof level.

Numerical simulation predicts that removing the supplementary roof mass reduces or eliminates the horizontal-vertical coupling that is manifested through amplified floor accelerations in 3D relative to XY simulations. Figures 10-16 to 10-19 utilize the augmented model with the supplementary roof mass moved to the base. The numerically simulated roof acceleration history and peak acceleration profiles are compared for Diablo 80%/Diablo 95% (XY) (Figure 10-16) and Rinaldi 88%/Rinaldi 88% (XY) (Figure 10-17). Comparing Figure 10-6 to Figure 10-9, almost no amplification of horizontal acceleration during 3D excitation is observed in the Diablo simulation when the mass was removed from the roof. The comparison is imprecise since the scale factors are different in the XY and 3D motions, consistent with the executed experiment. Comparing Figure 10-17 to Figure 10-10 (Rinaldi simulation), the peak horizontal floor accelerations are still amplified during 3D excitation when the mass was removed from the roof, but the amplification is substantially less than that observed in the experiment. These simulations support the theory that amplification of horizontal acceleration observed in 3D simulations throughout the test program are a result of horizontal-vertical coupling modes in the building, for which the supplementary roof mass is at least partially responsible.

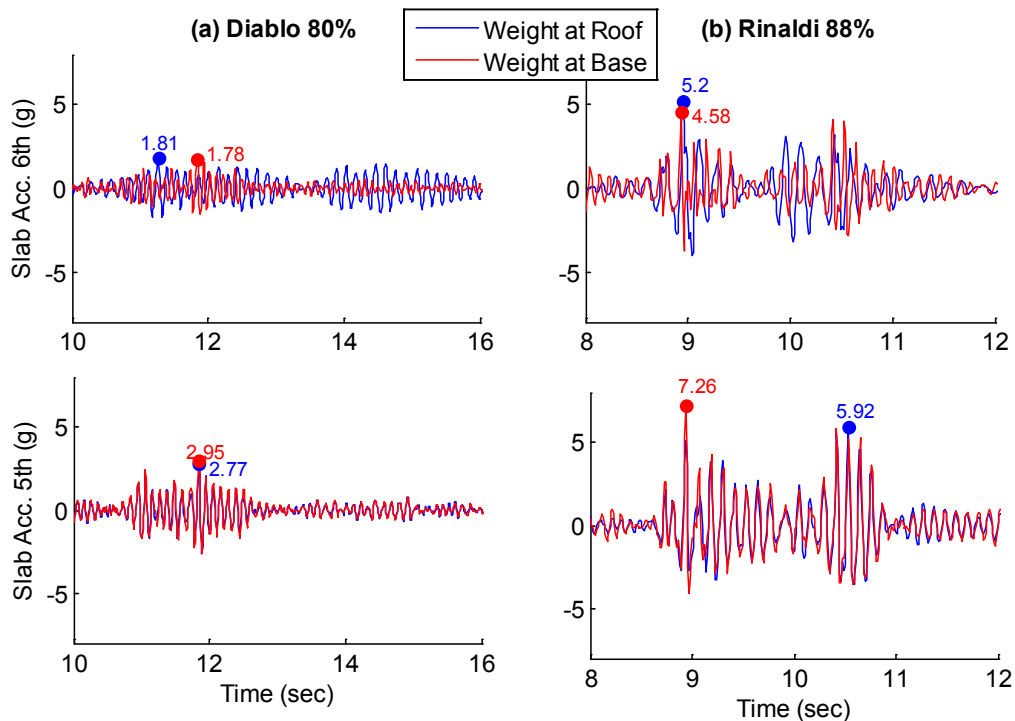


**Figure 10-15 Numerically simulated vertical slab acceleration for Diablo 80% and Rinaldi 88%; comparison using the testbed building model and the augmented model with supplementary mass removed from the roof and replaced at the base.**

The numerically simulated floor spectra in both x and y-directions are also compared for the Diablo 80%/Diablo 95% XY (Figure 10-18) and Rinaldi 88%/Rinaldi 88% XY (Figure 10-19) pairings. In the Diablo simulation, very slight amplification of spectral peaks at periods of 0.10 sec and below are observed, which suggests that a small amount of horizontal-vertical coupling may be present in what is the equivalent of a third structural mode, which is then driven by vertical excitation. However, comparing Figure 10-18 to Figure 10-11, the contribution of peaks at periods below 0.10 sec is much less when the mass was removed from the roof, such that the peak horizontal floor acceleration is not affected by vertical excitation (Figure 10-18). For the Rinaldi simulation, almost no amplification is observed in the critical period range of 0.10 to 0.20 sec when the mass was removed from the roof (Figure 10-19). The range of 0.10 to 0.20 sec comprises the range where amplification of spectral peaks in the 3D motion were significant for the tested building (Figure 10-11). The simulation results suggest that amplification would not be significant if the mass were removed from the roof, but recall that the simulation model did not capture all the coupling effects that were observed in the experiment. Meanwhile, the numerical simulation suggests that some amplification occurs at higher frequencies, or periods below 0.10 sec. The higher frequency peaks may not be significant.

Although it cannot be confirmed without further investigation, we expect that under typical levels of vertical excitation ( $V\text{-PGA} < 0.5g$ ) and torsional and vertical mass irregularities limited to accidental sources, amplification of horizontal acceleration would be negligible. Thus, the horizontal amplification observed in the experiments was not representative of typical practice. Fortunately, the numerical simulation data presented also suggests that effects of irregularities and amplification of horizontal acceleration can be identified during the design process.

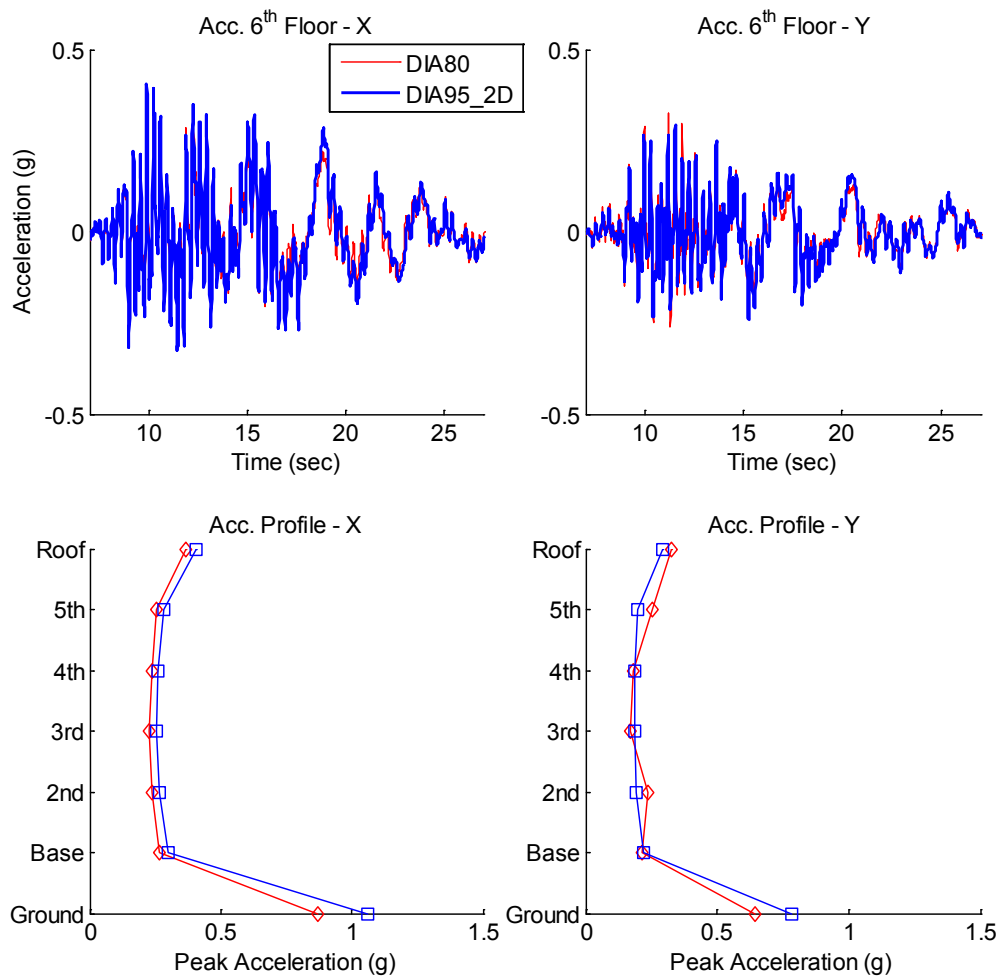


**Figure 10-16 Comparison of numerically simulated x and y-direction roof acceleration histories and peak acceleration profiles for Diablo 80% and Diablo 95% (XY) using the augmented model with supplementary mass removed from the roof and replaced at the base**

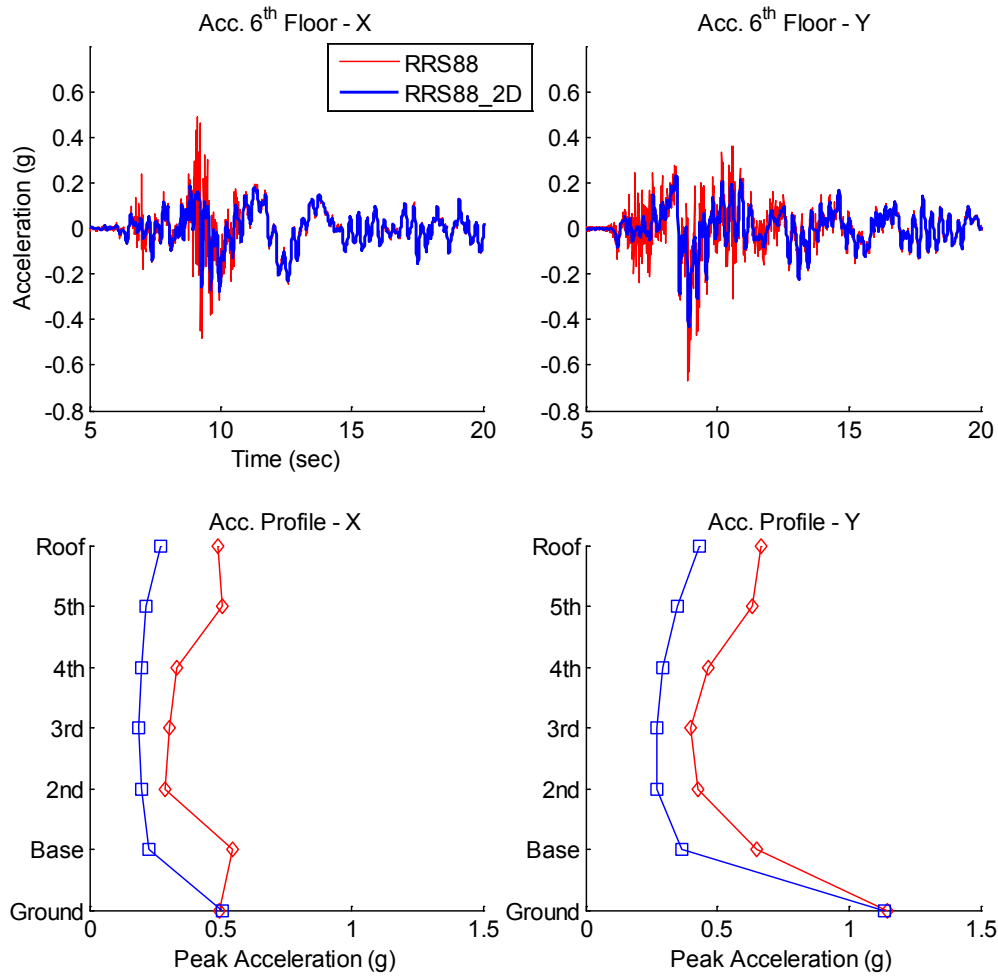


**Figure 10-17 Comparison of numerically simulated x and y-direction roof acceleration histories and peak acceleration profiles for Rinaldi 88% XY and Rinaldi 88% using the augmented model with supplementary mass removed from the roof and replaced at the base**

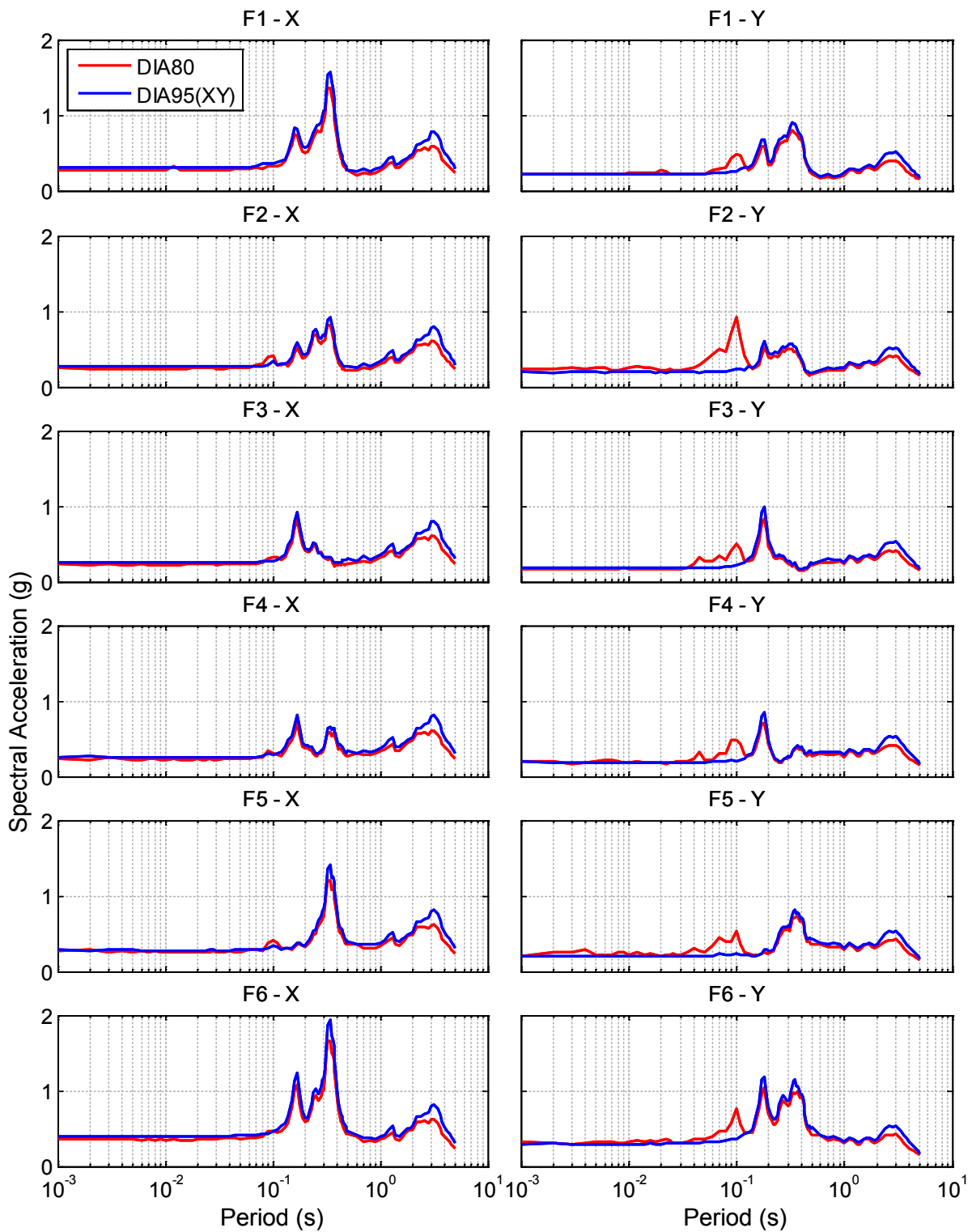


**Figure 10-18 Comparison of numerically simulated x and y-direction 5% damped spectral accelerations in 1<sup>st</sup> through 6<sup>th</sup> floors for Diablo 80% and Diablo 95% (XY) using the augmented model with supplementary mass removed from the roof and replaced at the base**

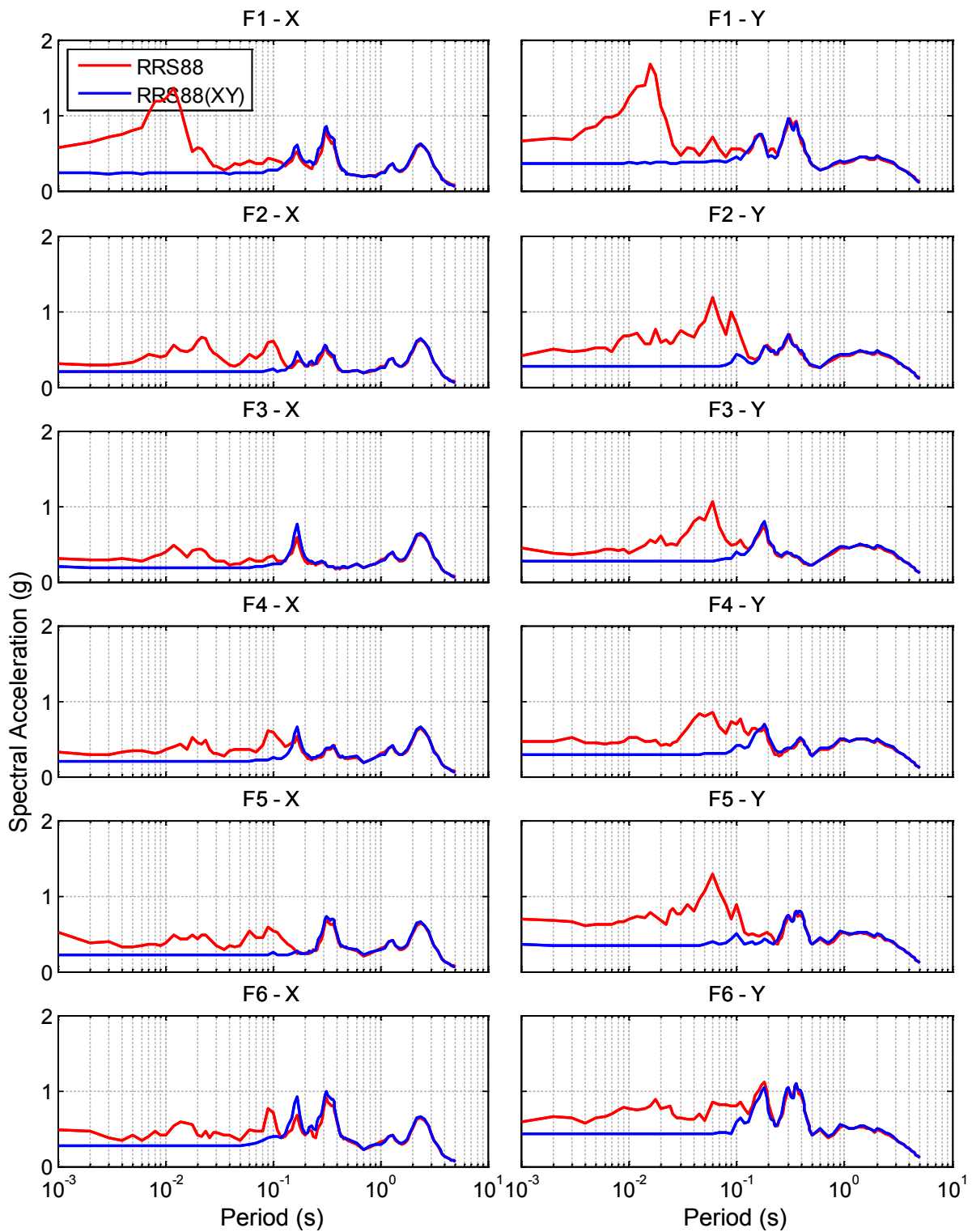


**Figure 10-19 Comparison of numerically simulated x and y-direction 5% damped spectral accelerations in 1<sup>st</sup> through 6<sup>th</sup> floors for Rinaldi 88% XY and 3D using the augmented model with supplementary mass removed from the roof and replaced at the base**

## 10.5 Implications for Design

This investigation of the response of the testbed structure for 3D excitations has shown that the influence of vertical excitations on the response of the seismic response of the system can be significant. Substantial vertical slab vibrations were generated, and horizontal floor accelerations were amplified by the input vertical motions. Fortunately, these effects were replicated by a properly crafted numerical simulation model of the structure and the isolators. The testbed structure was not best configured to minimize the effects of vertical excitation. Thus, the results have reinforced that good design practices should always be followed. Site specific horizontal and vertical acceleration histories should be used in the analysis and design of the structure, as is already done routinely for nuclear structures but is not required for conventional (non-nuclear) structures. The design of the base isolation system should consider and accommodate any sources of coupling in the structure, including horizontal-torsional and horizontal-vertical coupling effects.





## 11. STRUCTURAL AND ISOLATOR RESPONSE FOR THREE BUILDING CONFIGURATIONS

In this chapter, the general responses of the testbed building and isolation system are compared for the hybrid LR isolation system configuration, the TP isolation configuration, and the fixed-base configuration. When comparing the two isolation configurations, we emphasize that differences in isolator displacement demands and base shear are *primarily* determined by the design properties of the isolators and not related to the type of device. The normalized backbone curves (normalized base shear vs. isolator displacement) are compared for the hybrid LR isolation system and the TP isolation system in Figure 11-1. This figure is based on the design parameters of the hybrid LR isolation system (Table 3-3) rather than the characterized parameters. The normalized strength  $Q_d/W$  and post-yield period  $T_d$  represent the entire isolation system (i.e. strength and stiffness summed over all bearings); they are calculated using the measured weight of the testbed structure (Section 4.3) and thus differ from the design values given in Chapter 3. The backbone curve of the TP isolation system also reflects design parameters, wherein the multi-linear curve reflects the friction coefficients and pendulum lengths of the bearing's independent pendulum mechanisms. For more information about the design, refer to Dao (2012).

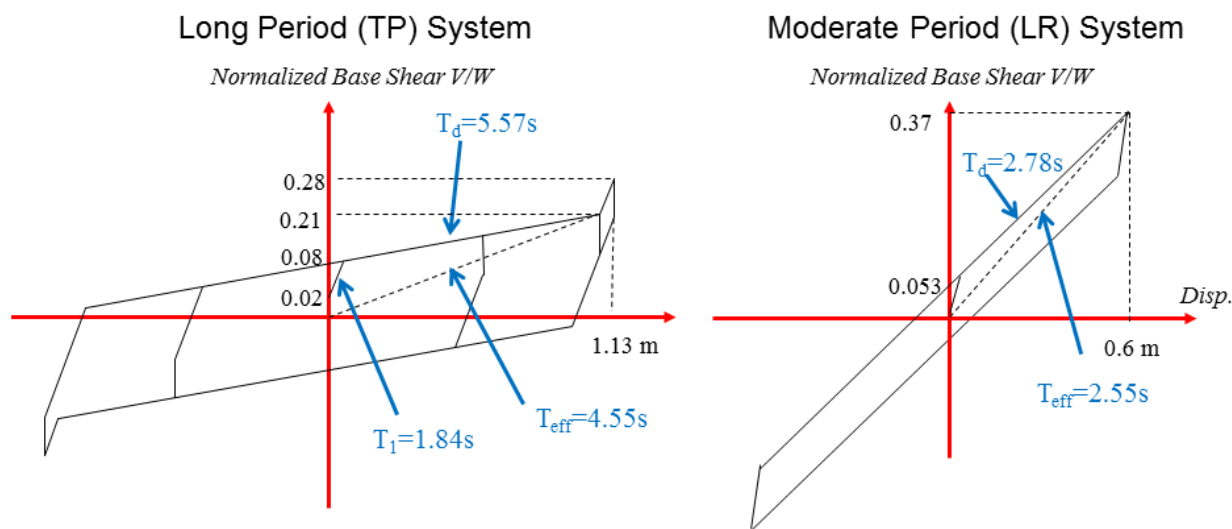


**Figure 11-1 Normalized backbone curves (base shear vs. displacement) for the Long Period TP isolation system and the Moderate Period LR isolation system, based on design properties of the bearings and measured mass**

With a post yield period  $T_d = 2.8$  sec, the as-designed hybrid LR isolation system provides a moderate period shift. In contrast, the TP isolation system when fully engaged ( $T_d = 5.6$  sec) provides a very long period shift. For the same seismic hazard, the lengthening of the isolation period is expected induce larger displacement demands, and as such the TP isolation system was designed with a large displacement capacity greater than 1 meter. While an LR isolation system could be designed to provide a backbone curve comparable to the tested TP isolation system, we remind the reader that providing this combination of flexibility and displacement capacity in a system designed with elastomeric or LR bearings might be challenging. On the other hand, significant penalties for large displacements would be incurred in the design of a safety related nuclear facility, and thus the isolation period of a nuclear structure is likely to be less than 3 sec. To emphasize that the response depends on the design parameters, we refer to

the hybrid LR isolation system as the “Moderate Period” system and the TP isolation system as “Long Period” system. However, some response trends are device specific and will be identified as such.

Several records were applied commonly to all three configurations to allow their responses to be compared objectively. Although the complete simulation schedule was summarized in Tables 4-3 to 4-5, the comparative simulations were not identified. Thus, the applied records, scale factors, target PGA and realized table PGA for all comparative simulations are summarized in Table 11-1. The Westmorland record (WSM80) from the 1987 Superstition Hills Earthquake was intended to represent a service level earthquake for the TP isolation configuration, Dao 2012) and was scaled to 80%. WSM80 is the only record that was applied to the three configurations at the same scale factor. The Iwanuma record (Iwanuma 100% (XY)) is a long period, long duration (approximately 200 sec) subduction record recorded in the 2011 Tohoku Earthquake, and was selected by our Japanese collaborators as it is typical of the seismicity in Japan. The record was scaled to 70% for the fixed-base building, which, as explained earlier, was selected to avoid any possibility of yielding in the moment frame structure. The vertical component of Iwanuma was not included since this would have precluded simulating the entire duration of the record due to limitations of the earthquake simulator. The Rinaldi record (Rinaldi 88%) is a well-known near-fault record from the 1994 Northridge Earthquake, which was scaled to 88% to represent a design level earthquake for the TP isolation configuration (Dao 2012). As explained earlier, this record was executed without the vertical component – denoted XY – and with the vertical input to assess the influence of vertical excitation in all three systems. The influence of vertical excitation for the hybrid LR configuration was examined thoroughly in Chapter 10; so that this chapter highlights the comparison between the systems. Note that the horizontal components of the Rinaldi record were scaled down to 35% for the fixed-base configuration, for the same reason described above, but the target vertical component was the same for all three system configurations. Recall that the realized peak accelerations of the earthquake simulator were generally larger than the target accelerations (Section 4.5), which is also observed in Table 11-1.

**Table 11-1 Ground Motions, Scale Factors and Peak Accelerations Common to 3 Configurations.**

Ground motion	System	Target Scale Factor	Target Peak $A_{xy}$ (g)	Realized Peak $A_{xy}$ (g)	Target Peak $A_z$ (g)	Realized Peak $A_z$ (g)
1987 Superstition Hills Westmorland	Hybrid	80%	0.17	0.19	0.20	0.14
	TP	80%	0.17	0.18	0.20	0.15
	Fixed	80%	0.17	0.24	0.20	0.14
2011 Tohoku Iwanuma (XY)	Hybrid	100%	0.43	0.59	0	0.02
	TP	100%	0.43	0.60	0	0.03
	Fixed	70%	0.30	0.39	0	0.01
1994 Northridge Rinaldi Rec. Sta. (XY)	Hybrid	88%	0.72	1.18	0	0.05
	TP	88%	0.72	1.24	0	0.10
	Fixed	35%	0.28	0.41	0	0.01
1994 Northridge Rinaldi Rec. Sta.	Hybrid	88%	0.72	1.19	0.73	1.25
	TP	88%	0.72	1.26	0.73	1.26
	Fixed	35% xy 88% z	0.28	0.42	0.73	1.10

## 11.1 Structural Response

Acceleration profiles (peak floor acceleration versus floor level) are compared in Figure 11-2 for each building configuration and each record. The accelerations plotted represent the peak instantaneous vector sum of floor acceleration at the center of the building (average over the NW and SE sensors). For a clearer impression of the level of attenuation or amplification of each building systems, the accelerations are normalized by PGA (different for each configuration) on the right graph. For the first three records (Figure 11-2(a) to (c)), the acceleration in the isolated building configurations was attenuated well below PGA – as expected – and the acceleration was essentially constant over the height. On the other hand, the acceleration increased with height in the fixed-base configuration, where at the roof level, the acceleration was amplified by a factor of about 2.5 to 3 with respect to PGA.

For the low level WSM80 excitation, the accelerations were better attenuated for the Moderate Period isolation system than for the Long Period isolation system, while for the larger intensity Iwanuma and Rinaldi XY excitations, the opposite was true. An explanation of this behavior is given in Section 11.2. For both systems, the attenuation of acceleration increased as the intensity of the record increased. Thus, the peak floor accelerations were about 60-70% of PGA in WSM80, 40-50% of PGA in Iwanuma, and 20-30% of PGA in Rinaldi XY. Thus, for Rinaldi XY, the acceleration at the roof level was reduced by about a factor of 10, which is compelling evidence of the effectiveness of base isolation.

The influence of a strong vertical excitation for all configurations can be ascertained by comparing the responses of each system observed during Rinaldi 88% to those observed during Rinaldi 88% (XY) (Figures 11-2(c) and (d)). The influence of vertical excitation was influenced by the type of isolation device and thus will be described with reference to the devices. To summarize observations for the hybrid LR system that have already been described, significant amplification of horizontal acceleration was observed in Rinaldi 88% (3D excitation) compared to Rinaldi 88% (XY) (Section 5.6), and the potential sources of amplification were identified (Section 10.3). The sources of amplification were: 1) high frequency coupled horizontal-vertical modes of the structure that were driven by the vertical excitation input (a mode with frequency of 10 Hz or  $T = 0.1$  sec was positively identified), and 2) axial force variation in the isolators introduced a high frequency component into the base shear, which drove structural modes around 0.18 sec. Based on Figure 11-2(c) and (d), the acceleration was also amplified in the fixed-base configuration for the Rinaldi 88% excitation; the roof acceleration increased from about 1g for XY input to 1.25g for 3D input. Thus, amplification of acceleration was noteworthy in the fixed-base configuration, but not as strong as for the hybrid LR isolation configuration since only the first source of amplification (modal coupling) would be present in the fixed-base building. As discussed earlier, the amplification of horizontal acceleration in the 3D excitation was largely a result of the supplementary roof mass, and was reduced significantly when the mass was removed from the roof in the numerical simulation model (Section 10.4).

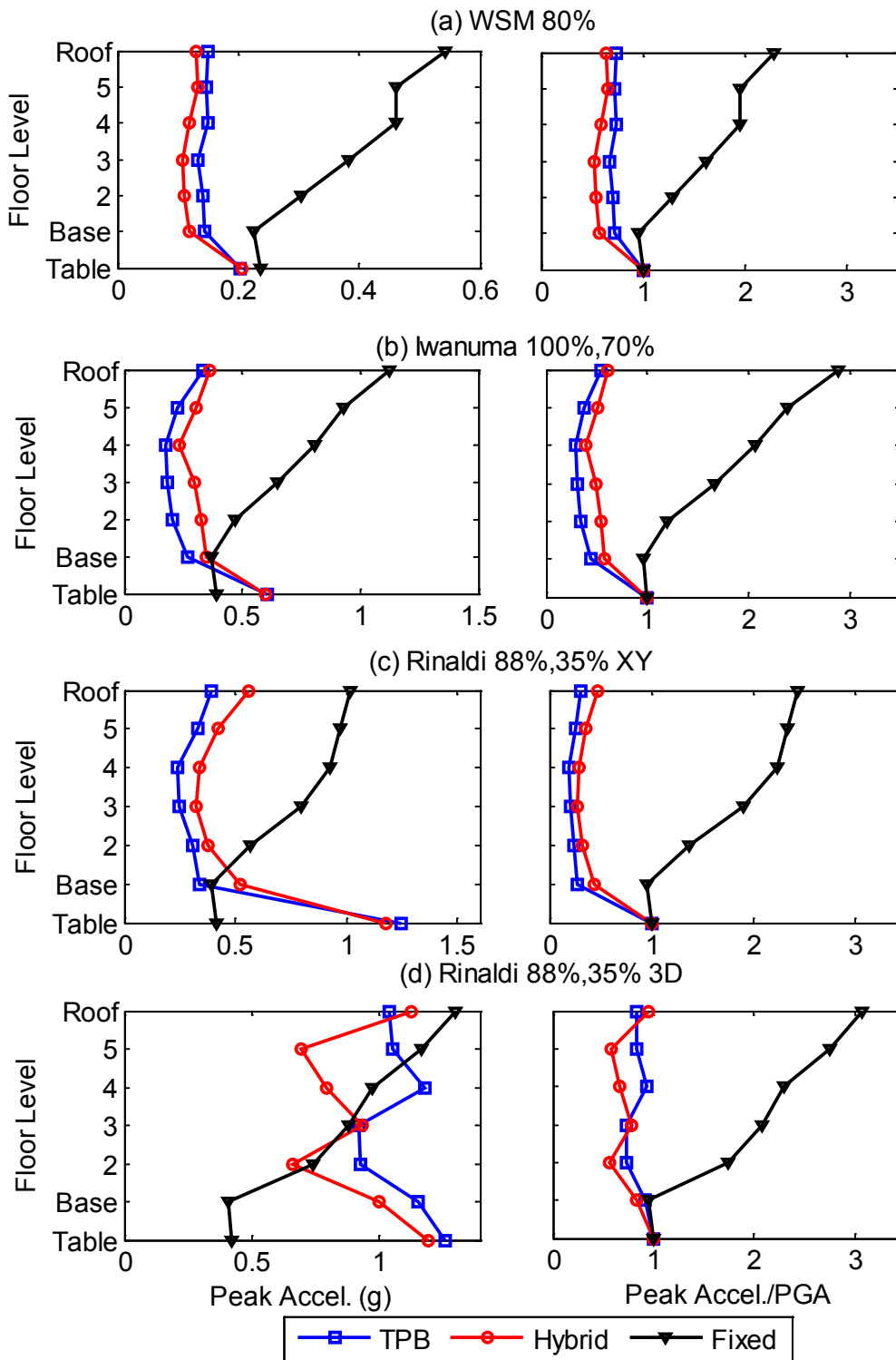


**Figure 11-2** Peak floor acceleration (vector sum) vs. floor level of the three building configurations for (a) WSM 80%, (b) IWA 100%/70%, (c) Rinaldi 88%/35% (XY) and (d) Rinaldi 88%/35% records. Accelerations are absolute on the left graph and normalized by PGA on the right.

As observed in Figure 11-2, the amplification of horizontal accelerations was greater for the Long Period TP isolation system than for the Moderate Period hybrid LR isolation system. The peak floor accelerations, which were lowest for Rinaldi XY in the TP isolation configuration as a result of its long period shift (Figure 11-2(c)), were generally larger in the TP isolation configuration than the hybrid LR isolation configuration for Rinaldi 3D (Figure 11-2(d)). The amplification was larger for TP bearings (a device specific effect) because an additional source of coupling is present in the bearings. In TP bearings or any friction devices, the horizontal force (base shear) is directly proportional to the vertical force (or axial load) carried by the bearing. Thus, the total axial force variation on the isolators due to vertical excitation is echoed as a high frequency oscillation in the total base shear. To demonstrate, the history of total base shear coefficient of the three building configurations for Rinaldi 88% (XY) and Rinaldi 88% motions is illustrated in Figure 11-3. For Rinaldi 88% (XY), the base shear of the isolated configurations oscillated at the natural frequency of the system, which was similar for the two configurations. The peak base shear of the hybrid LR isolated building was essentially unaffected by the vertical excitation (Figure 11-3(b)). On the other hand, the peak base shear coefficient of the TP isolated building increased from  $V/W = 0.13$  for XY input to  $V/W = 0.24$  for 3D input. This increase was caused by the high frequency oscillation observed in the base shear (Figure 11-3(b)). This oscillation has been confirmed to coincide with the fundamental vertical frequency of the structure, which was controlled by slab vibration at the roof level (similar to mode 9 in Figure 9-13).

Introduction of an additional frequency component into the base shear was offered as an explanation for the amplification of floor spectra peaks corresponding to the second structural mode in the hybrid LR isolation configuration under Rinaldi 88% (Section 10.4). However, the additional frequency component was quite small for the LR system, and is not even visually detectable in Figure 11-3. For many motions, the additional frequency component introduced to the base shear was strong for the TP isolation system, and the typical pattern was that the second structural mode of the TP isolated building, being close to the driving vertical frequency, was driven strongly by the base shear. However, because the vertical excitation in Rinaldi 88% ( $> 1g$ ) was strong enough to cause near complete uplift of the building from the isolators, the response of the system was complex. The 5% damped floor spectra for the TP isolation configuration observed in Rinaldi 88% (XY) and Rinaldi 88% (Figure 11-4) demonstrate the amplification of higher modes of the system over a range of frequencies. The reader is referred to Dao (2012) for a full documentation of the influence of vertical excitation in TP bearings. The results shown in Figures 11-2(d) and 11-4 are noted to be quite sensitive to the filtering parameters; a Butterworth filter with a cutoff frequency of 50 Hz was utilized.

Even under the influence of vertical excitation, the base shear of both isolated configurations was still significantly less than the base shear of the fixed-base configuration, which was subjected to only about 40% of the horizontal loading of the isolated configurations (ground motion scale factor of 35% compared to 88%). The base shear of the fixed-base structure was also sensitive to a high frequency component under Rinaldi 88% (Figure 11-3(b)) that was not present under Rinaldi 88% (XY) (Figure 11-3(a)). The comparison of the fixed-base and isolated building base shear was affected by the method used to derive the base shear in the respective configurations. In the fixed-base building, the base shear was derived from inertial forces (the sum of mass multiplied by floor accelerations) while the base shear was derived from the load cell measurements in the isolation configurations. When applied to the isolated buildings, the inertial force method was confirmed to agree closely with the load cell data for XY excitations, but deviate from the load cell measurements as the vertical intensity increased.

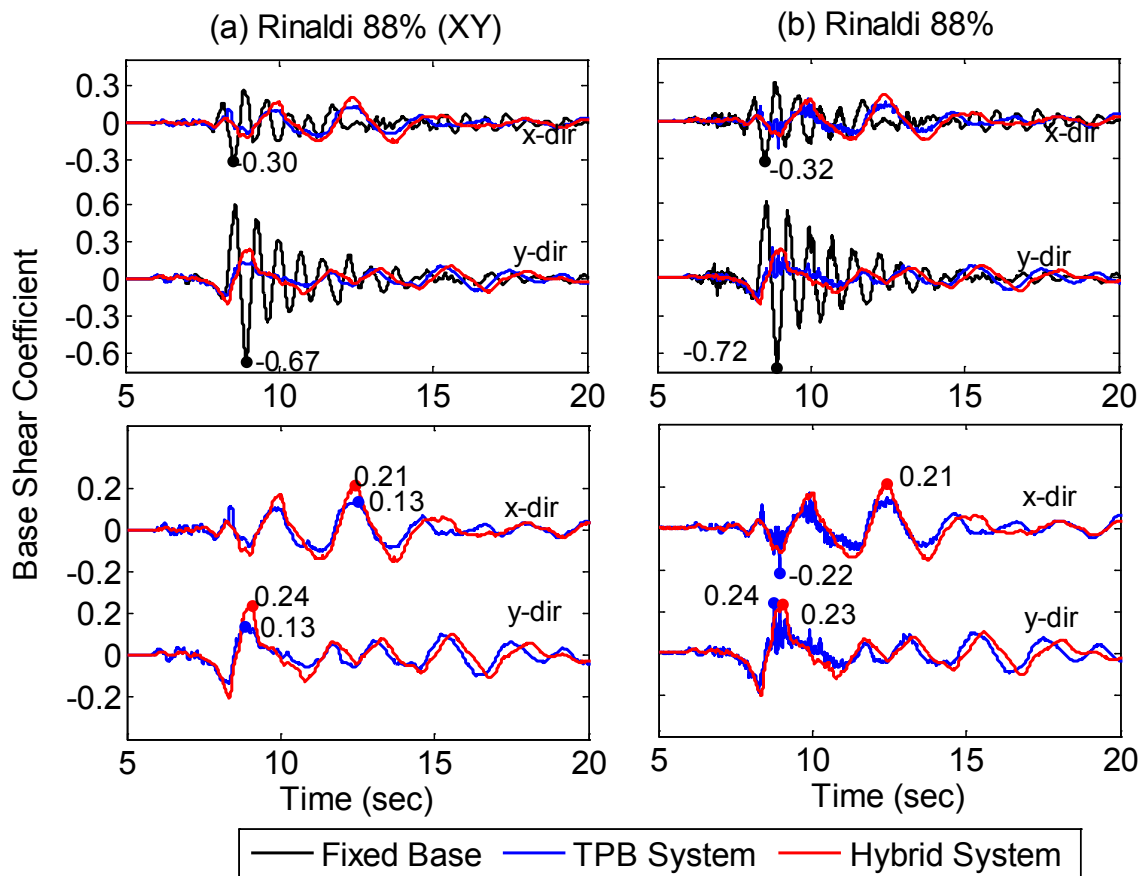


**Figure 11-3** History of total base shear in x and y-directions compared for the 3 system configurations in (a) Rinaldi 88% (XY) and (b) Rinaldi 88%. The bottom graphs provide a close-up of the isolated configurations; peak values are indicated

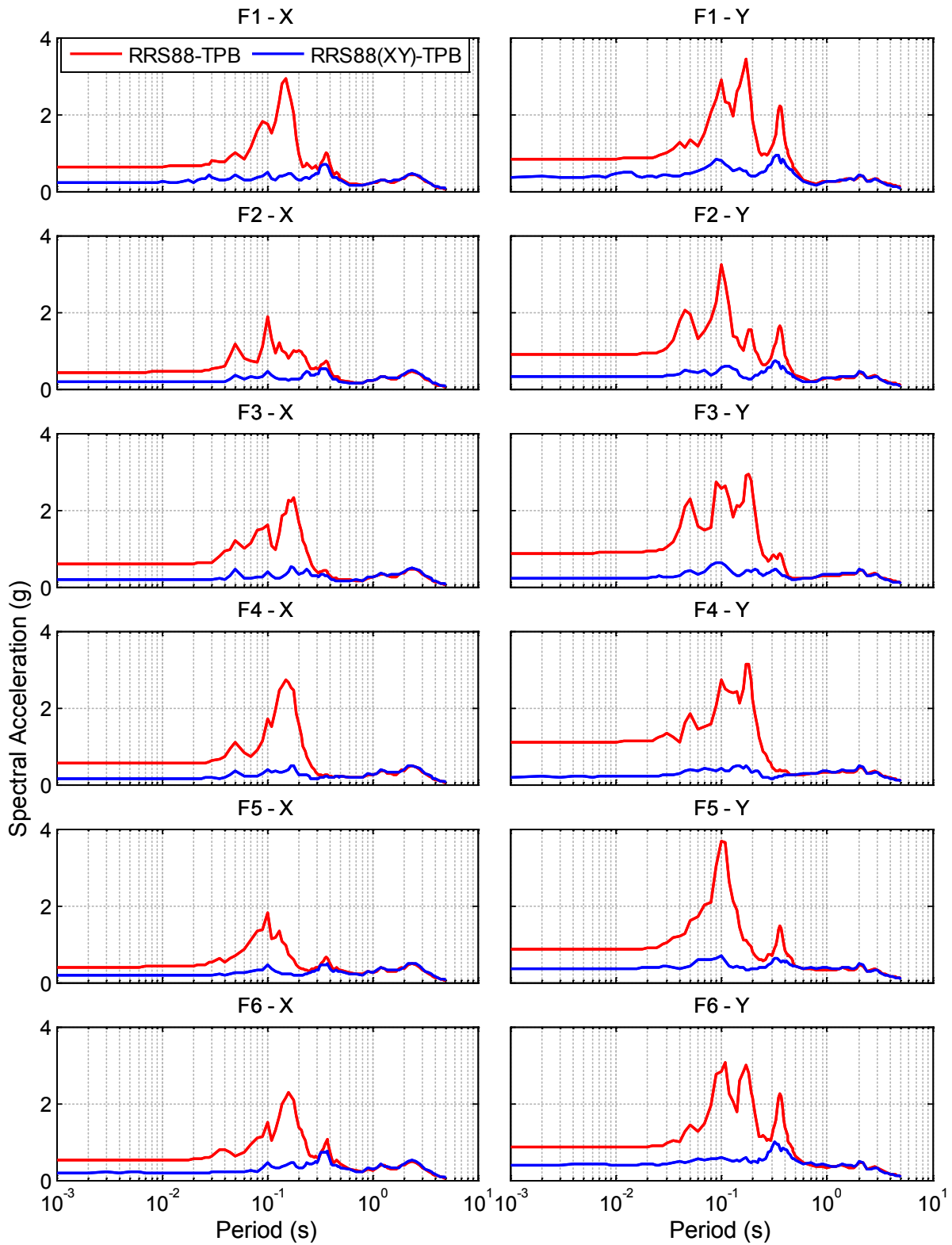


**Figure 11-4 Comparison of x and y-direction 5% damped spectral accelerations in the TP isolation configuration for 1<sup>st</sup> through 6<sup>th</sup> floors for Rinaldi 88% XY and Rinaldi 88%**

Besides the amplification of horizontal acceleration, the recorded vertical accelerations in the structure were significant in all three system configurations under Rinaldi 88% (RRS35(XY)88(Z) for the fixed-base structure). Figure 11-5 compares the input ground acceleration, column accelerations, and slab accelerations in the vertical direction at the 5<sup>th</sup> and roof level floors in all three system configurations. The peak ground acceleration in all three systems was similar with peak amplitude of about 1.2g.

In the TP configuration, a peak vertical acceleration of about 4g was observed in the columns (Fig 11-5(a),(d)), whereas only mild amplification of the vertical ground acceleration was observed in the hybrid LR isolation and fixed-base configurations (Figure 11-5(b-c),(e-f)). The source of the amplification in the TP isolated building was a vertical motion induced uplift that caused the entire building to lift off the bearings multiple times; the large accelerations were generated by the impact force that resulted when the building re-established contact with the simulator platform. Evidence of this uplift was observed in the force data for the bearings (simultaneous zero forces recorded in all but the SW bearing), but not shown here for brevity. However, the slab acceleration was dominated by vibration at its natural frequency (about 7 Hz at the roof level), and any high frequency input at the column level was not transmitted to the slabs. Thus, the amplitude of slab vibration was similar in all three configurations, and did not appear to be amplified in the isolation configurations over the fixed-base configuration except perhaps for some isolated spikes.

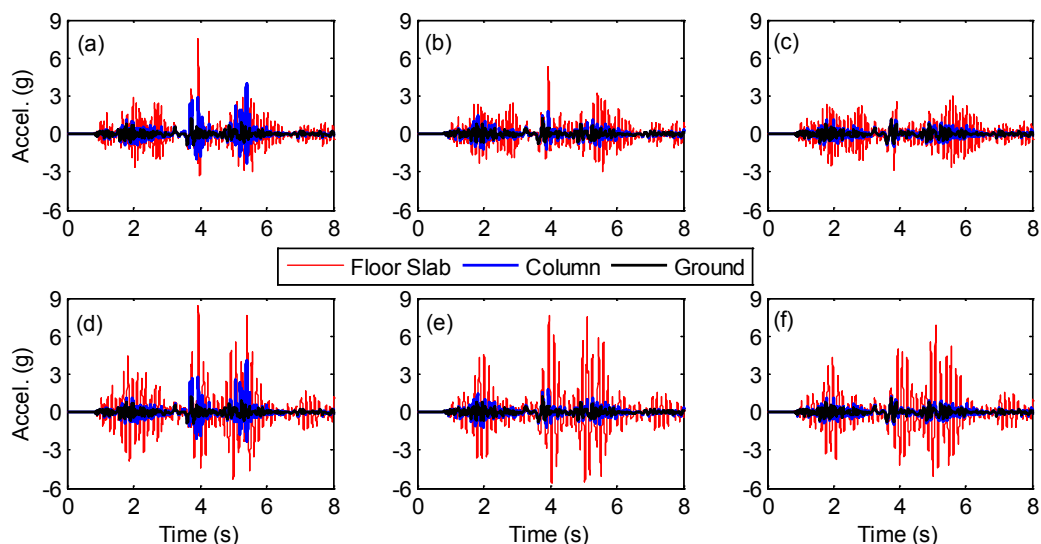


**Figure 11-5 Vertical acceleration history of floor slab (recorded at middle of the NE quadrant), column average, and ground acceleration average (recorded at simulator platform) for Rinaldi 88% for (a,d) TP isolation configuration, (b,e) hybrid LR isolation configuration, and (c,f) fixed-base configuration; (a-c) = 5<sup>th</sup> floor slab and (d-f) = roof slab**

Drift profiles (peak story drift vs story level) are compared in Figure 11-6 for each building configuration and each record. The peak drift represents the maximum relative story displacement in the x or y-directions at the center of the building determined by linear interpolation of the NW and SE displacement transducers, which directly measured relative story displacement. In the second story and above, a story drift of 3 cm corresponds to a drift angle of 0.01 rad. Because the 1<sup>st</sup> story was taller than 2<sup>nd</sup> to 5<sup>th</sup> stories (Figure 2-2), the peak drift angle was generally largest in the 2<sup>nd</sup> story and decreased substantially in the upper floors of the building. Substantial reductions in drift were observed in the isolated configurations



relative to the fixed-base configuration, recalling the reduced scale factors to the input motions for IWA 100% (70% for fixed-base, Figure 11-6(b)) and Rinaldi 88% XY (35% for fixed-base, Figure 11-6(c)). The drift demands in the hybrid LR system (Moderate Period) and TP system (Long Period) were about the same in Westmorland, but became increasingly lower in the hybrid LR system relative to the TP system as the intensity of the motion increased (e.g. Rinaldi 88% XY in Figure 11-6(c)), which was solely a function of the design properties of the system and not the specific type of isolation device. Unlike the floor acceleration, the peak drift was not too sensitive to vertical excitation (compare Figure 11-6(d) to Figure 11-6(c)), as the drift demands were determined by the fundamental or low frequency modes of the building.

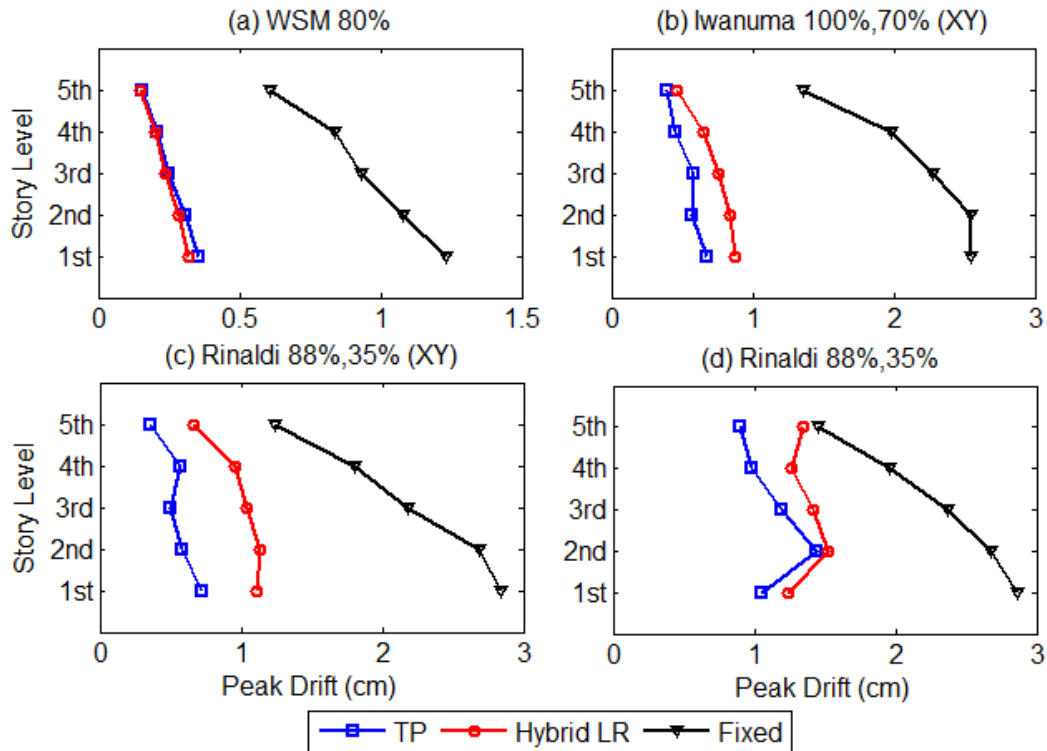


**Figure 11-6 Peak story drift (max in x or y-direction) vs. story level of the three building configurations for (a) WSM 80%, (b) IWA 100%/70%, (c) Rinaldi 88%/35% (XY) and (d) Rinaldi 88%/35% records**

## 11.2 Isolation System Response

As described above, the Long Period (TP) isolation system was designed with a displacement capacity of more than 1 meter. Several ground motions were selected that were intended to develop displacement demands close to the displacement limit of the isolation system. However, the peak displacement demand observed in the system was about 70 cm (27.6 in) under Tabas 100% (XY). The lower than projected displacement demands resulted from increased friction in the system; the measured friction coefficient for the outer pendulum mechanism (~0.10) exceeded the design friction coefficient (~0.08) for the outer pendulum mechanism. Besides the peak displacement demand, the suite of 19 ground motions (excluding sine waves) applied to the Long Period isolation system induced an average displacement demand of 42 cm (16.5 in), while the average displacement demand for the Moderate Period isolation system was 34 cm (13.4 in). Thus, the average displacement demands were not appreciably larger for the Long Period isolation system. This is not a fair comparison, since the suite of motions applied to the two systems contained little overlap. However, we observed that

for some of the near-fault motions, such as Takatori 100%, a peak in spectral displacement was observed in the 2-3 second range, such that further lengthening of the isolation system reduced the expected displacement demand. Takatori 100% induced a displacement demand of 56 cm (22 in) in the Long Period isolation system, while Takatori was not simulated for the Moderate Period isolation system, as it was predicted to exceed the safety limit. Thus, if justified by the seismicity, the period lengthening strategy used in the design of the Long Period isolation system might be used to increase the factor of safety in the design (provide extra displacement capacity) without much increase in the expected displacement demands.

The detailed responses of the Moderate Period (hybrid LR) isolation system and Long Period (TP) isolation system are compared for two excitations, WSM 80% and Rinaldi 88% (XY). The discussion is supported by the following figures, all of which directly compare the observed responses in the two systems: isolator displacement traces and displacement histories (Figure 11-7 for WSM 80% and Figure 11-8 for Rinaldi 88% (XY)), isolator force vs. displacement or hysteresis loops (Figure 11-9), and base rotation angle (Figure 11-10).

For WSM 80%, the peak vector sum isolator displacement, indicated on the displacement trace (Figure 11-7), was 8.8 cm for the Moderate Period system and 15.6 cm for the Long Period system, both occurring in the East bearing. The difference, however, was due primarily to a large residual displacement in the Long Period isolation system (-6 cm in x and 1 cm in y) that was present at the beginning of the record. The displacement traces and histories of the two isolation systems were similar. Visually, the two isolation systems appeared to be responding at the same or similar frequencies, as the larger displacement cycles were in phase throughout the record. The peak in both systems was determined by a circular orbit in the displacement trace. The Long Period (TP) system moved nearly exclusively on the inner sliders during WSM 80%, as indicated by the hysteresis loops for the East bearing (Figure 11-9(a)). As such, the isolation system did not re-center (TP bearings must be driven to the outer part of the hysteresis loop to re-center). For motion on the inner sliders, the TP system was stiffer than the Moderate Period LR isolation system (with a tangent period of 1.8 sec compared to 2.6 sec), and had a higher yield force coefficient, observed to be  $V/W \sim 0.10$  (Dao 2012, Dao et al. 2012a). On the other hand, the hybrid LR system yielded at a base shear coefficient  $V/W \sim 0.05$ , and thus engaged the softer second slope of the LR bearings. As a result, the Long Period TP system experienced larger base shear, and larger floor accelerations.

As the intensity of the input excitation increased, the outer pendulum mechanisms of the Long Period TP isolation system, with a tangent period of 5.6 sec, were engaged, and subsequently the base shear demand increased very slowly. This situation is well demonstrated by the response during Rinaldi 88% (XY). The peak vector sum displacement in the two isolation systems was comparable (38.8 cm or 15.3 in for the Moderate Period system and 36.6 cm or 14.4 in for the Long Period system – both in the South bearing, Figure 11-8). This displacement occurred at about 9 sec, which corresponded to the timing of the near-fault fling pulse (Figure 4-18). As expected, the base shear demand in the Moderate Period system at this displacement was larger than in the Long Period system (compare the hysteresis loops in Figure 11-9(b)), which affected the floor accelerations and story drifts, as discussed earlier. Aside from the instant of the large pulse, the displacement demand of the Long Period TP system was less than the Moderate Period LR system throughout the majority of the record (Figure 11-8), which suggests that the motion of the Long Period TP system was again dominated by sliding on the inner sliders.

Base rotation demands were affected by the isolation devices; however, as mentioned several times, the torsional properties of the tested hybrid LR isolation system were not representative of common practice, where it would be possible to configure the isolation system to minimize the eccentricities that induce torsion. The peak base rotation (Figure 11-10(a)) was larger in the

Long Period TP system for WSM 80%, which was primarily a result of the initial residual displacement. On the other hand, the oscillation of rotation angle was greater in the Moderate Period LR system, though not particularly large for this motion. The base rotation of the hybrid LR system during Rinaldi 88% (XY) was substantially larger than in the TP system, which was typical of many of the motions. As discussed earlier, the peak rotation angle of the hybrid LR system in any motion was 0.019 rad, which was observed in Vogtle 175%, while the peak rotation angle of the TP system in any motion was 0.005 rad.

Since the shear force in a TP bearing or any friction bearing is proportional to the axial force, the center of resistance naturally aligns with the center of mass and rotational demands are expected to be negligible. The observed rotation in the TP system was small, but not negligible. The distribution of gravity loads on the bearings did not follow the natural weight distribution in the building, but rather was constrained by the rigidity of the base diaphragm. The base diaphragm was believed to be warped by constant exposure to weather for more than 2 years before the tests. The misfit induced by the warping was accommodated by pre-stress, which ultimately caused the weight on the isolators to be redistributed. The expected and actual weights carried by the TP isolators are compared in Figure 11-11. The balance of loads depicted was achieved only after several iterations with shimming plates. Thus, the forces generated in the isolators did not correspond to the actual mass distribution in the building, causing a moderate torsional response to be generated. The rotational input observed in the earthquake simulator was negligible.

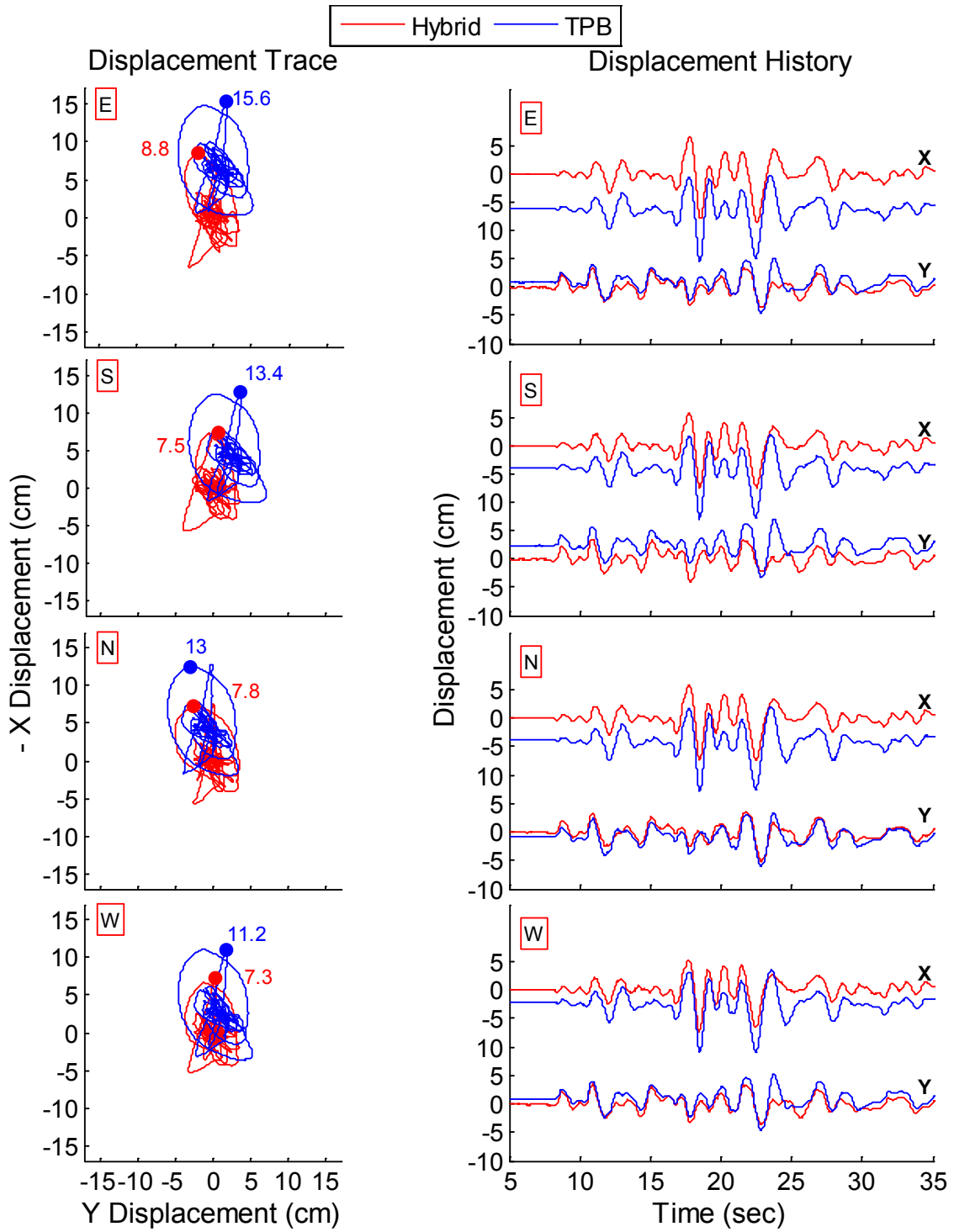


**Figure 11-7 Comparison of Moderate Period LR and Long Period TP systems for WSM 80%; displacement trace and displacement histories (x and y) in each bearing, labeled by position (E, S, N, W)**

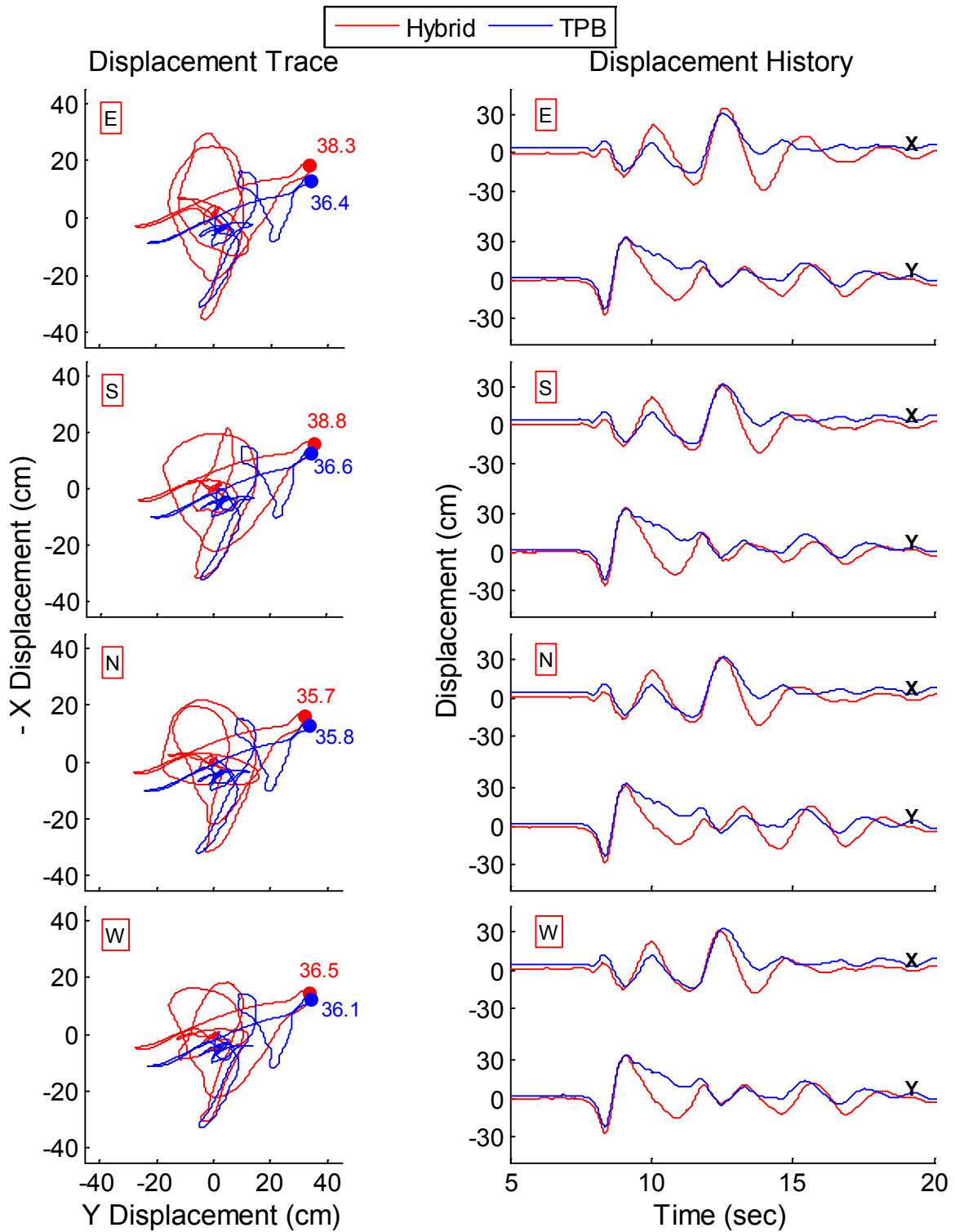


**Figure 11-8 Comparison of Moderate Period LR and Long Period TP systems for Rinaldi 88% (XY); displacement trace and displacement histories (x and y) in each bearing, labeled by position (E, S, N, W)**

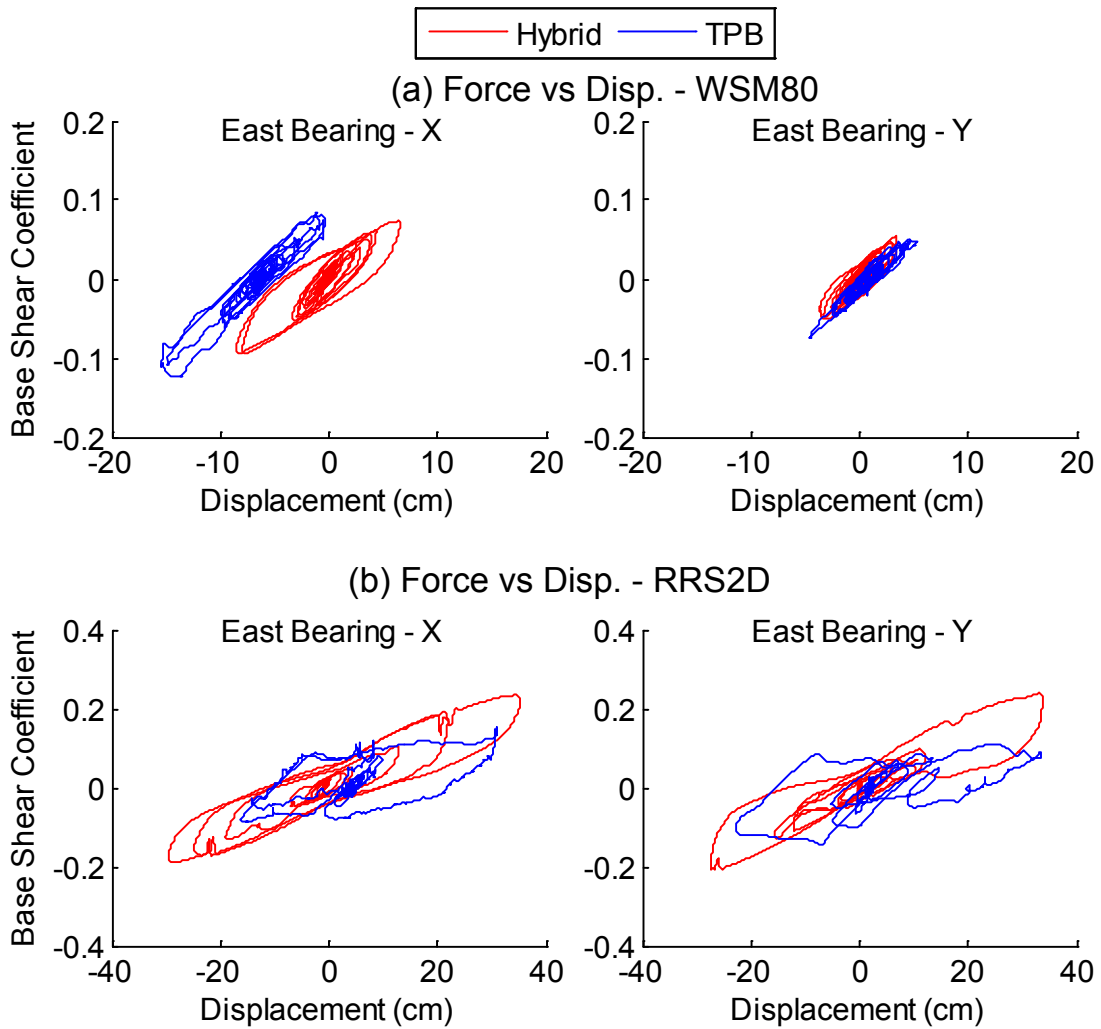


**Figure 11-9 Comparison of the base shear coefficient for Moderate Period LR and Long Period TP systems in the x- and y-directions for the East bearing; WSM 80% and Rinaldi 88% (XY)**

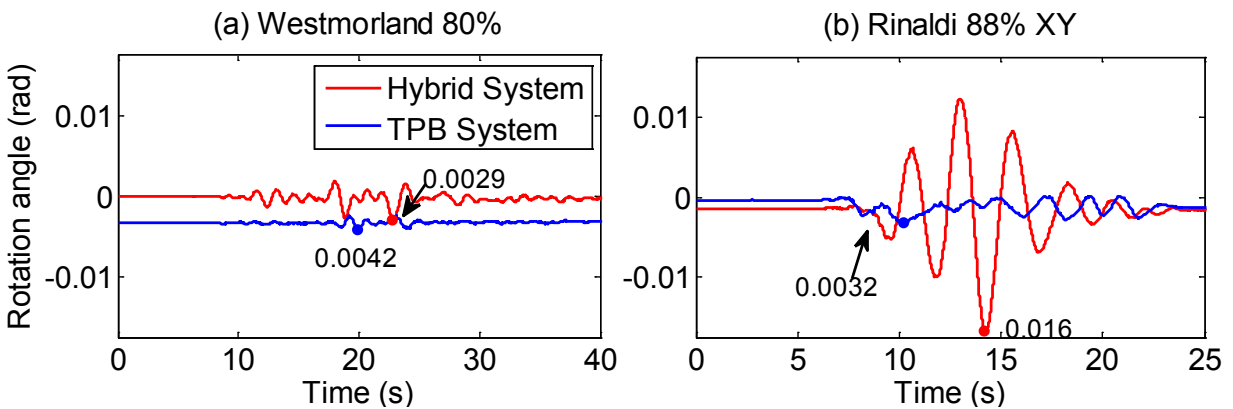


**Figure 11-10 Rotation angle at the base for Moderate Period LR and Long Period TP isolated configurations for (a) WSM 80% and (b) Rinaldi 88% (XY)**

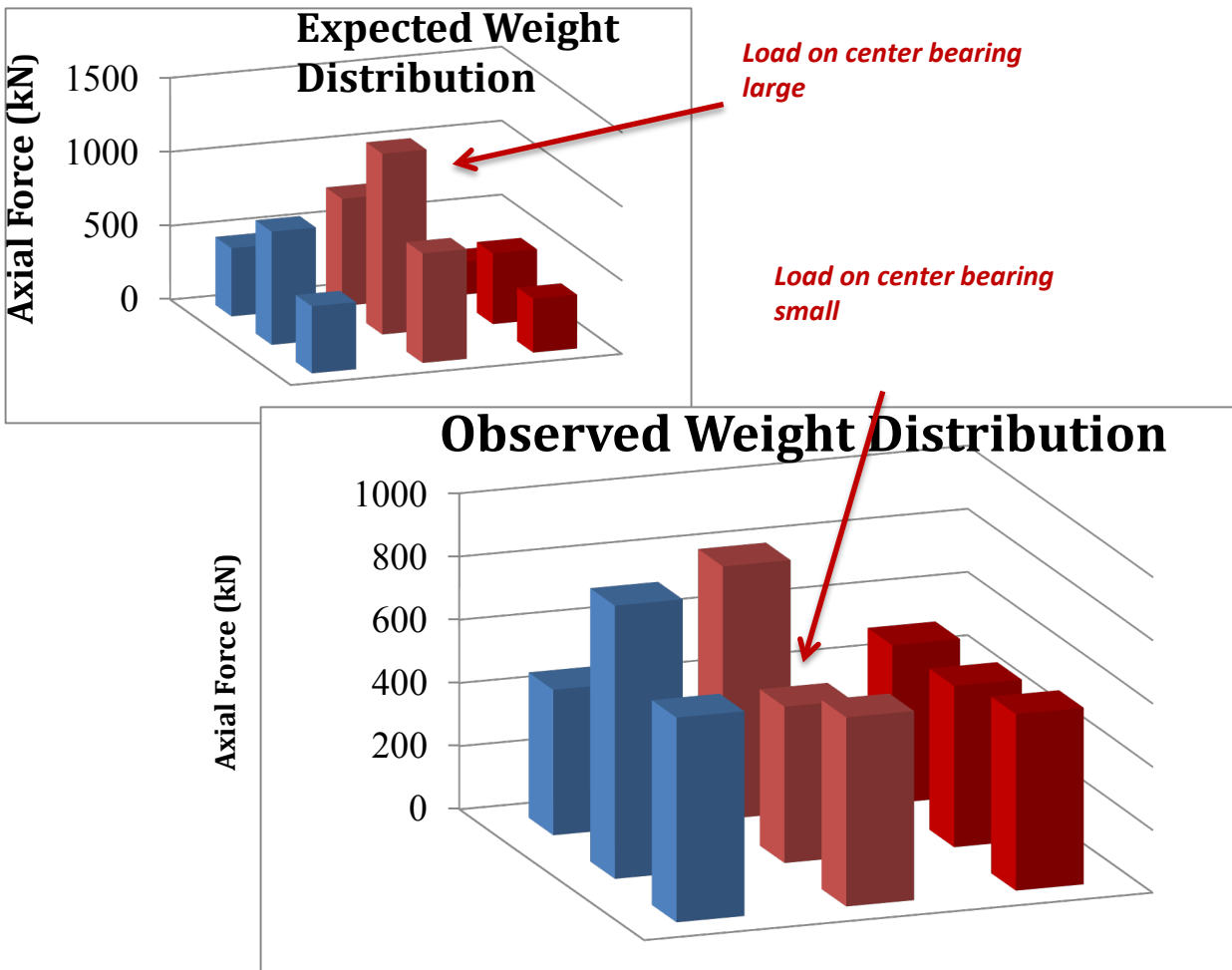
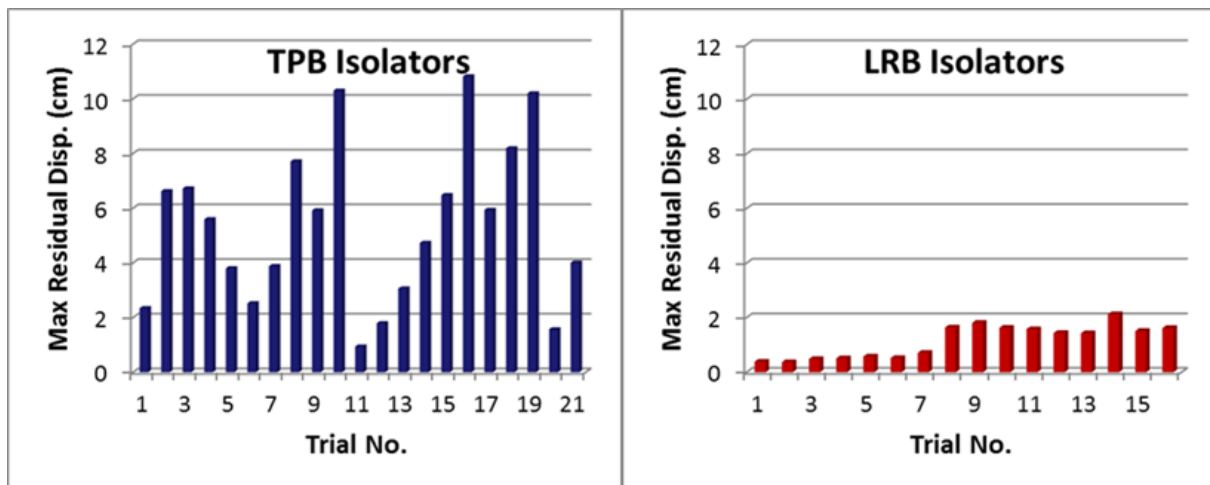


**Figure 11-11 Qualitative illustration of expected weight distribution (calculated by natural distribution of the weight) and observed weight distribution (measured in load cells) on TP isolation system**

The accumulation of residual or permanent displacements is distinctly a function of isolation period shift alone and completely independent of the isolation device. The bearing displacement histories shown in Figures 11-7 and 11-8 suggest that the Long Period isolation system was subjected to larger residual displacements than the Moderate Period isolation system. For both systems, the largest measured residual displacement over all the bearings after every trial is plotted in Figure 11-12, which confirms the observation. The largest residual displacement observed in the Moderate Period isolation system throughout the test program was about 2 cm (0.8 in), but as discussed in Section 5.5, was affected by slippage of the base plates so that the actual residual displacement was only about 0.5 cm (0.2 in). This residual displacement is small relative to the peak displacement of the system (55 cm (21.7 in) in Diablo 95%), and barely discernible on a cumulative displacement history of a bearing over the course of a single test day (Figure 11-13). On the other hand, the largest residual displacement observed in the Long Period isolation system throughout the test program was close to 11 cm (4.3 in), which is significant relative to the peak displacement of 70 cm (27.6 in). These residual displacements are a consequence of the flexibility of the system; the system was designed with a tangent period of 5.6 sec for motion on the outer pendulum mechanism.

Figure 11-14 illustrates the cumulative displacement history of a bearing in the Long Period isolation system over the course of a test day. Analysis of this figure suggests that the residual displacements did not accumulate. Near-fault motions (LGPC, ChiChi and Takatori) caused large residual displacements. Long duration motions or motions with typical frequency content (Iwanuma) helped re-center the bearings. When ChiChi 70% (denoted TCU in Table 4-3) was followed by ChiChi 80%, the residual displacement was larger in ChiChi, 80% but only because the peak displacement was larger in ChiChi 80%. The numerical simulation of the Long Period system (Dao 2012) suggested that these residual displacements were predictable. Furthermore, to reproduce the experimental histories through numerical simulation, it was not necessary and was in fact disadvantageous to zero correct the data. The experimental displacement histories (starting from the residual displacement) generally became aligned with the numerically simulated displacement histories (starting from zero) within the first few cycles of motion.

Although better control of the base shear demand is attractive, the accumulation of significant residual displacement is a noteworthy disadvantage of the Long Period design strategy. Re-centering the isolation system after a large earthquake could be problematic. An aftershock could help to re-center the system, provided it was strong enough to engage the post-yield period of the system (outer most sliding mechanism for TP bearings). The capacity of the structure to tolerate residual displacements must be considered when employing a Long Period design strategy utilizing large displacement capacity. In a nuclear facility, the structure could be jacked off the hard stops to eliminate the permanent displacement.



Long Period System  
 Peak Residual Disp. = 10.8 cm  
 Average Residual Disp. = 5.4 cm

Moderate Period System  
 Peak Residual Disp. = 2.01 cm  
 Average Residual Disp. = 1.2 cm

**Figure 11-12 Maximum residual displacement in the Long Period and Moderate Period isolation systems after each simulation**



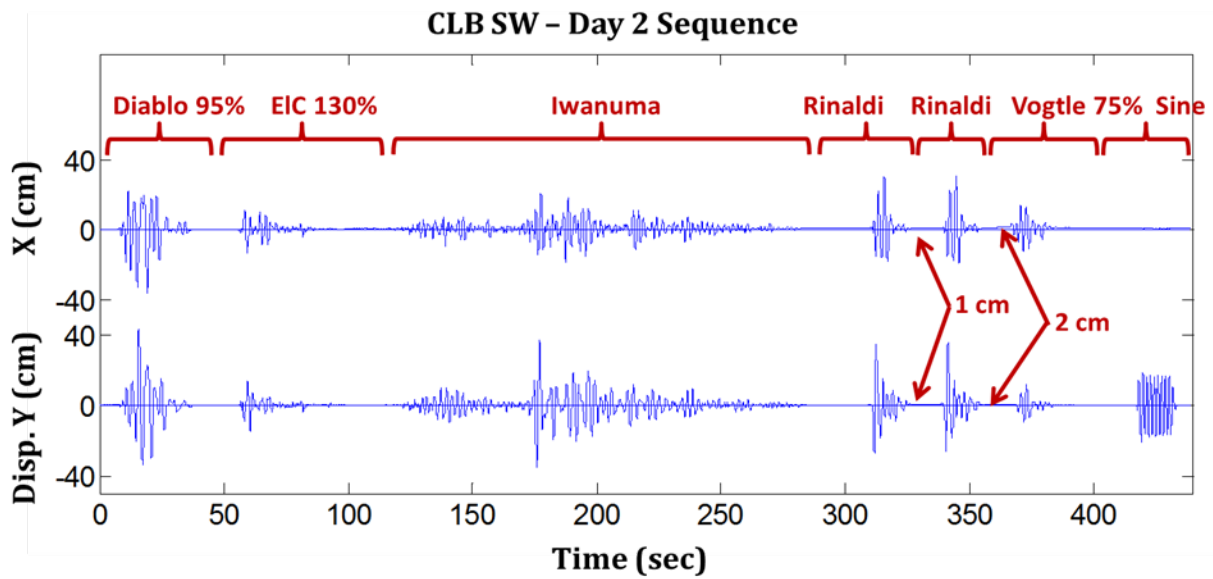


Figure 11-13 Displacement of the SW bearing in the Moderate Period isolation system over the course of a single test day, illustrating the residual displacement after each record

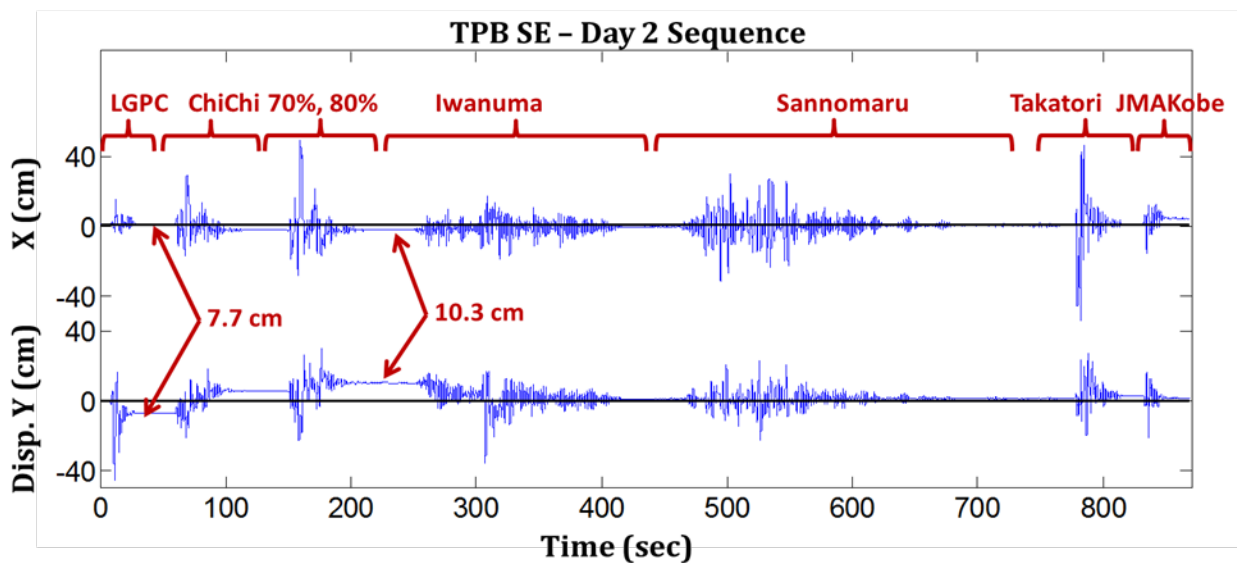


Figure 11-14 Displacement of the SE bearing in the Long Period isolation system over the course of a single test day, illustrating the residual displacement after each record



## **12. CONCLUSIONS AND CONSIDERATIONS FOR NUCLEAR POWER PLANTS**

As documented in this report, a hybrid elastomeric isolation system using lead-rubber (LR) bearings and cross-linear (CL) bearings was designed for a 5-story moment frame building and tested under a variety of earthquake excitations at E-Defense. The isolation system was designed to sustain displacement demands representative of extended or beyond design basis shaking at a potential nuclear site in central and eastern U.S., and such motions were prioritized in developing the test program. The experimentally observed response of the LR bearings was calibrated to a bidirectionally coupled, bilinear hysteretic model with uncoupled response in the horizontal and vertical directions. A realistic numerical simulation model of the 5-story building with isolators was built, tested and calibrated. This report has documented the overall test results, unusual response characteristics of the hybrid isolation system, the comparison of the numerical simulation to experimental data, the influence of vertical excitation, and the comparison of the hybrid LR isolation system to two other building configurations that were also tested. Key observations and considerations for nuclear power plants are discussed as follows.

### **12.1 Characteristics of Lead-Rubber Bearing Response**

The following behaviors, many of which have been observed before, were observed in the response of LR bearings during this test program.

1. Pinching near the center of the measured bearing hysteresis loop, attributed to the small size of the lead plug;
2. Loss of characteristic strength over the duration of an excitation, associated with heating of the lead plug;
3. Slight fluctuation of shear force during high frequency axial force variation; thought to be insignificant;
4. Small (negligible) permanent displacements at the end of the records;
5. Significant base rotation demands due to the inability to configure the system appropriately for torsion.;
6. No loss of shear resistance at large displacements due to the stabilizing influence of the CL bearings;
7. Transfer of axial forces from LR bearings to CL bearings at large displacements, causing the LR bearings to sustain tension;

Items 1-5 are not believed to be influenced by the presence of CL bearings. With regard to item 6, the stabilizing influence of the CL bearings prevented the loss of shear resistance of the LR bearings at displacement demands beyond their theoretically computed stability limits in this experiment. Normally, a system composed only of LR bearings can be designed to stay well within the stability limits, and under this scenario similar behavior would be expected. Item 7 is a behavior unique to the hybrid LR system.

### **12.2 Predictability of the System Response**

According to the recently developed NUREG (Kammerer et al. 2012), Predictability of response is perhaps the most has been identified as an important requirement for the application of

seismic isolation to nuclear power plants. Our numerical simulation and its comparison to experimental data cannot be directly applied to nuclear facilities due to difficulties in modeling the response of the tested LR bearings, and differences between the tested superstructure and a nuclear facility. Nonetheless, some of the observations and insights learned during this simulation exercise are applicable to isolated structures in general.

The following should be noted when evaluating the outcome of our numerical simulation to match the experimental data. A single amplitude-independent model with parameters based on physical theory is desirable to represent the response of the isolation system. Such an approach might be possible in general, but was not possible in this study due to the pinching of the hysteresis loops near zero displacement, which was a result of the small size of the lead plug. The pinching effect would greatly diminish or disappear for bearings with lead plugs designed to a minimum recommended diameter equal to at least  $1/6$  the bonded diameter of the bearing.

Second, the bearings were modeled using a rate independent bidirectionally coupled plasticity model that is commonly available in numerical simulation software. Improved models are available that can capture variation of the yield strength due to heating of the lead plug or pressure variation due to cyclic axial loading; both of these effects were observed during the experiments. Thus, the outcome of our simulation was to evaluate the accuracy of a readily available model to predict the bearing response, which would be desirable to use as a matter of convenience.

Lacking improved models, the parameters of the bilinear model were calibrated independently for each simulation. Using the calibrated model, the predicted displacement demand of the isolators was within 10% of the observed experimental displacement. When the model was calibrated for the peak displacement cycle, it did not capture the history of the displacement over smaller cycles very well. Since the demands could not be predicted a priori using this approach, an improved simulation model is needed.

The assumptions used in developing the numerical simulation model that led to a close match between the simulated and experimental responses (story drifts, floor accelerations and floor spectra) are summarized. The pre-test analytical model incorporated the following features:

- Nonlinear frame elements with composite sections were incorporated to represent the fully composite slab-beam interaction, including cyclic demands in the concrete slab.
- For application of nonlinear frame elements to beams and girders, resultant section behavior was modeled in lieu of using fiber sections. The resultant section behavior was calibrated based on section analysis of the appropriate fiber section, and the calibrated behavior was independent of axial force.
- Secondary beams were included in the model to represent the vertical vibration characteristics.
- Panel zone springs were included to represent the stiffness of the panel zone.

Though the structural framing remained essentially in its linear elastic range throughout the test series, rigorous assumptions improved the accuracy of the numerical simulations. A discussion of the influence of these assumptions, which supports the current conclusion, is given in Dao et al. (2012b).

Despite the attention to modeling detail, the pre-test model did not predict the structural drifts and accelerations well; the primary reason being that the model was overdamped. However, the

following adjustments were made to the post-test simulation model through an iterative trial and error process to calibrate the model to the test data.

- The frame elements (beams and girders) were further discretized to about 8 elements per structural member to more accurately distribute the mass, which was lumped at the nodes, to the system.
- The damping model for the structure was changed from stiffness-proportional damping, which damped out the higher mode response, to Rayleigh damping. The damping was calibrated to about 2% at the isolation frequency and the higher mode structural frequencies observed in the test data. (Note that no viscous damping was applied along the isolation system.) An additional damper was added to the model to control the first structural mode. The additional damper would not be needed in a program that accommodates constant modal damping.
- The isolator vertical stiffness was adjusted by inspection to represent the apparent vertical flexibility of the load cell assemblies. Such an adjustment would not be needed for nuclear structures.

Following these adjustments, the analytical model matched the floor spectra well; the frequency at which the peaks occurred were nearly identical for the analytical model and test data, and differences in amplitude occurred due to the lack of precision by which energy dissipation can be represented in the structural response. Higher mode participation was non-negligible, especially in vertical excitations.

For nuclear structures, the considerations are:

1. The test results have confirmed that the assumed damping model is probably the single most important component for accurate prediction of the structural response. For predictability, the modal damping ratios in a representative (e.g. certified design) safety related nuclear structure should be evaluated through testing to determine representative damping in nuclear structures for future design. The influence of the internal reactor and other equipment should be included in such an assessment as nonstructural components and content have been shown in the past to influence to markedly influence the damping in the system.
2. The damping in a nuclear structure is expected to be greater than in the tested structure at E-Defense.
3. The large base mat of a nuclear containment structure will filter out some of the higher frequency components of the ground motion relative to the free field motions that were considered in the test program. This also is expected to reduce higher mode response, perhaps significantly, relative to what was observed in the tested structure at E-Defense.

### **12.3 Hybrid Lead-Rubber (LR) and Cross-Linear (CL) Bearing System**

A hybrid isolation system of LR bearings and CL bearings was designed for the test program instead of a pure elastomeric isolation system to overcome the constraints of the utilized experimental setup. Such constraints would not be applicable in the design of a safety related nuclear structure, and thus a hybrid system approach would not be necessary. While a hybrid system can overcome stability issues, the vertical force demands in individual bearings are difficult to predict due to lack of compliance and subsequent load transfer between the two types of devices (LR bearings and CL bearings). Although hybrid systems are used routinely in Japan

for taller structures, the compliance issues suggest that the hybrid system should not be used in nuclear facilities.

The hybrid system was chosen for the following reasons. First, due to the light weight of the testbed structure, it was not possible to simultaneously provide the desired period elongation and the desired displacement demands with LR bearings alone. Second, the CL bearings provided significant tension resistance, which was needed to accommodate the expected tensile demands according to preliminary calculations.

In these tests, the hybrid system resulted in significant axial load transfer between the two types of devices; specifically, load redistributed from the LR bearings to the CL bearings as the lateral displacement increased, because the rigidity of the base diaphragm constrained the free downward movement of the LR bearings. As a positive benefit, the hybrid system eliminated the potential that the shear behavior of the LR bearings was affected by stability and post-buckling behavior. However, the tradeoff was that the tensile and compressive demands in the CL bearings were quite large, as they carried all the overturning induced axial forces, and significant tensile demands were observed in the LR bearings, which were constrained by the base diaphragm. Prediction of the axial force demands in the individual devices was not attempted in our simulation since the forces in the CL bearings were unknown. Inability to predict the force demands in design and protect the devices from excessive tension or compression is a drawback for the hybrid system.

## **12.4 Comparison of the Three Building Configurations**

These full scale experiments demonstrated the ability of two different isolation systems to significantly attenuate horizontal ground acceleration throughout the structure. Typically, peak floor accelerations in the isolated building were 25-50% of the peak input acceleration of the simulator platform, while the peak acceleration at the roof level of the fixed-base building under the same input motions was amplified by a factor of 2-3 relative to the peak input acceleration. This led to a reduction in roof acceleration demand of the isolated buildings by approximately a factor of 10 relative to the fixed-base building (Section 11.1).

Different strategies were employed in the design of the two isolation systems. Except for the multi-stage behavior of the TP isolation configuration, the design strategies are device independent, so that either strategy could be executed with either type of isolation device, especially in the absence of mass limitations, which are not a problem for nuclear structures. A Moderate Period design strategy was applied to the hybrid LR isolation system, targeting a post-yield period of 2.6 sec and a displacement demand of 0.6 meters (23.6 in). A Long Period design strategy was applied to the TP isolation system, targeting an “outer slider” period of 5.6 sec coupled with a displacement capacity exceeding 1 meter (40 in). Although the Long Period design allowed for very large displacement demands across the isolators, the benefit of this capacity was not fully realized in the test program, as the largest input motion produced a peak displacement demand of only 0.7 meter (27.6 in), which was not significantly greater than that observed in the Moderate Period design. In other words, the displacement demands for the Long Period design did not significantly exceed the displacement demands for the Moderate Period design even though some of the motions applied for the Long Period design were considered to be much larger intensity.

The Long Period design led to much larger residual displacements in the isolators than the Moderate Period design. The greatest residual displacement observed was about 0.5 cm (0.2 in) for the Moderate Period design and about 10 cm (4 in) for the Long Period design. (The input motions applied to the two systems were not comparable.) In summary, a Long Period design

strategy led to better attenuation of acceleration while not inducing substantially greater displacement demands, but at the expense of greater residual displacements.

Due to the asymmetry of the structural and isolator configuration, base rotation was observed in both isolation systems. The torsion in a TP isolation system is theoretically zero since any mass asymmetry is naturally balanced by the resisting force in the friction devices, which is a device specific effect. However, the “field conditions” introduced a small torsional response since the static axial force distribution on the isolators was inconsistent with the distribution of mass in the testbed structure. Nevertheless, the base rotation of the TP isolation system was relatively small. Greater rotation was observed in the hybrid LR isolation configuration due to the sub-optimal configuration of the bearings. This was a problem unique to the restrictive E-Defense test setup, and in realistic nuclear structures, base rotations could be eliminated by thoughtful placement of isolation devices beneath the base mat.

## **12.5 Influence of Vertical Excitation on the Structural Response**

Vertical excitation was observed to strongly influence the accelerations observed in the structure. Vertical accelerations in columns were amplified slightly relative to the input acceleration. The vertical slab accelerations were amplified by a factor of 4-6 compared to the input vertical acceleration, which was controlled by the slab vibration properties. The amplitude of column and slab vibrations were essentially the same in the hybrid LR isolation configuration and the fixed-base configuration. Thus, vertical accelerations in the structure were not amplified by the isolation system. The isolation system accommodated the multiple cycles of high frequency axial force variation due to vertical excitation. The vertical excitation had a very minor influence on the base shear when the intensity of vertical acceleration exceeded 1g (Section 10.1).

Horizontal floor accelerations were amplified in 3D excitations compared to XY (horizontal only) excitations. Amplification of horizontal acceleration occurred in both the isolated and fixed-base configurations. Through the analytical investigation, the following source of horizontal-vertical coupling was identified. The structural modes of the building, determined by modal analysis of the numerical simulation model, were coupled in the horizontal and vertical directions. Specifically, vertical floor slab movement was observed in some of the main horizontal structural modes of the building, causing those modes to be excited by vertical excitation. The coupling was primarily due to a mass irregularity; a large supplemental mass was placed at the roof level in an asymmetric configuration in plan. The spectral peaks associated with the coupling modes computed from analysis decreased significantly when the supplemental mass in the numerical model was moved from the roof and distributed in a regular configuration at the base level. Other sources of coupling in the hybrid LR isolation system were hypothesized but not confirmed.

The majority of the coupling effects were replicated by a well-crafted numerical simulation model that accounted for slab-frame interaction and refined distribution of mass over the floor system. The design of the base isolation system and structure should consider and accommodate these predictable horizontal-vertical coupling effects.





## 13. REFERENCES

1. Al-Hussaini TM, Constantinou MC, Zayas VA (1994). *Seismic Isolation of Multi-Story Frame Structures Using Spherical Sliding Isolation System*, Technical Report NCEER-94-0007, State University of New York at Buffalo: Buffalo, NY, USA.
2. American Association of State Highway and Transportation Officials (AASHTO), (2010). *Guide Specification for Seismic Isolation Design*, 3<sup>rd</sup> Edition.
3. American Institute of Steel Construction (AISC), (2005). *Steel Construction Manual*, 13rd edition.
4. American Society of Civil Engineers (ASCE), (2008). *Seismic Design Criteria for Structures, Systems and Components in Nuclear Facilities, ASCE 43-05*, ASCE, Reston, VA.
5. American Society of Civil Engineers (ASCE), (2010). *Minimum Design Loads for Buildings and Other Structures, ASCE/SEI 7-10*, ASCE, Reston, VA.
6. Buckle IG, Liu H (1994). "Experimental determination of critical loads of elastomeric isolators at high shear strain", *NCEER Bull.*, 8(3):1–5.
7. Buckle IG, Nagarajaiah S, Ferrell K (2002). "Stability of elastomeric isolation bearings: Experimental study", *ASCE J. Struct. Eng.* 128:3–11.
8. Charney FA, Downs WM (2004). "Modeling procedures for panel zone deformations in moment resisting frames", *Proc., ECCS/AISC workshop: Connections in Steel Structures V*, Amsterdam, Netherlands.
9. Chiou B, Darragh R, Gregor N, Silva W (2008). "NGA project strong-motion database", *Earthquake Spectra*, 24(1):23–44.
10. Chopra AK (2012). *Dynamics of Structures: Theory and Applications to Earthquake Engineering*, Fourth Edition, Prentice Hall.
11. Clark PW, Aiken ID, Kelly JM (1997). *Experimental Studies of the Ultimate Behavior of Seismically Isolated Structures*, Report No. UCB/EERC-97/18, University of California: Berkeley, CA, USA.
12. Comité Euro-international du Béton (CEB), (1996). *RC Elements under Cyclic Loading, State of the Art Report*. Thomas Telford Publications, London, England.
13. Constantinou MC, Mokha AS, Reinhorn AM (1990). *Experimental and Analytical Study of a Combined Sliding Disc Bearing and Helical Steel Spring Isolation System*, Technical Report NCEER-90-0019, State University of New York at Buffalo: Buffalo, NY, USA.
14. Constantinou MC, Whittaker AS, Kalpakidis Y, Fenz DM, Warn GP (2007). *Performance of Seismic Isolation Hardware under Service and Seismic Loading*, Technical Report MCEER-07-0012, Multidisciplinary Center for Earthquake Engineering Research, State University of New York at Buffalo: Buffalo, NY, USA.

15. Dao ND (2012). *Seismic response of a full-scale steel frame building isolated with triple pendulum bearings under 3D excitation*, PhD Dissertation, University of Nevada, Reno.
16. Dao ND, Ryan KL (2012). "Verification of computational simulation techniques for a full-scale steel moment frame building tested at E-Defense", Submitted to *ASCE Journal of Structural Engineering*.
17. Dao ND, Ryan KL, Sato E, Sasaki T (2013). "Predicting the displacement of triple pendulum bearings in a full scale shaking experiment using a three-dimensional element", Available in Early View, *Earthquake Engineering and Structural Dynamics*.
18. Fenz DM, Constantinou MC (2008). *Development, Implementation, and Verification of Dynamic Analysis Models for Multi-spherical Sliding Bearings*, Technical Report MCEER-08-0018, Multidisciplinary Center for Earthquake Engineering Research, State University of New York at Buffalo, Buffalo, NY, USA.
19. Griffith MC, Kelly JM, Coveney VA, Koh CG (1988a). *Experimental Evaluation of Seismic Isolation of Medium-Rise Structures Subjected to Uplift*, Report No. UCB-EERC 88-02, University of California: Berkeley, CA, USA.
20. Griffith MC, Aiken ID, Kelly JM (1988). *Experimental Evaluation of Seismic Isolation of a 9-story Braced Steel Frame Subjected to Uplift*, Report No. UCB-EERC 88-05, University of California: Berkeley, CA, USA.
21. Griffith MC, Aiken ID, Kelly JM (1990). "Displacement control and uplift restraint for base-isolated structures", *ASCE J. Struct. Eng.*, 116:1135–1148.
22. Huang NY, Whittaker AS, Kennedy RP, Mayes RL (2009) "Assessment of Base-Isolated Nuclear Structures for Design and Beyond-Design Basis Earthquake Shaking", *Tech. Report MCEER-09-0008*, University at Buffalo.
23. Kalpakidis IV, Constantinou MC (2009a). "Effects of heating on the behavior of lead-rubber bearings. I: Theory", *J. Struct. Eng.* 135:1440–1449.
24. Kalpakidis IV, Constantinou MC (2009b). "Effects of heating on the behavior of lead-rubber bearings. II: Verification of theory", *J. Struct. Eng.* 135:1450–1461.
25. Kalpakidis IV, Constantinou MC, Whittaker AS (2010). "Modeling strength degradation in lead-rubber bearings under earthquake shaking", *Earthq. Eng. Struct. Dyn.* 39:1533–1549.
26. Kalpakidis IV, Constantinou MC (2010). "Principles of scaling and similarity for testing of lead-rubber bearings", *Earthq. Eng. Struct. Dyn.* 39:1551–1568.
27. Kasai K, Ooki Y, Ishii M, Ozaki H, Ito H, Motoyui S, Hikino T, Sato E (2008). "Value-added 5-story steel frame and its components: Part 1 – full scale damper tests and analyses", *Proc., 14th World Conference on Earthquake Engineering*, Beijing, China.
28. Kasai K, Ito H, Ooki Y, Hikino T, Kajiwara K, Motoyui S, Ozaki H, Ishii M (2010). "Full scale shake table tests of 5-story steel building with various dampers," *Proc., 7th Intern. Conf. on Urban Earthquake Engin. & 5th Intern. Conf. on Earthquake Engin.* Tokyo Inst. Tech., Tokyo, Japan.

29. Kasai K, Murata S, Kato F, Hikino T, and Ooki Y (2011). "Evaluation rule for vibration period, damping, and mode vector of buildings tested by a shake table with inevitable rocking motions." *J. Struct. Const. Eng.*, AIJ, 76(270):2031-2040. (In Japanese).
30. Kasai K (2011). Personal Communication.
31. Kasalanati A, Constantinou MC (2005). "Testing and modeling of prestressed isolators", *ASCE J. Struct. Eng.* 131:857–866.
32. Kasalanati A (2012). Personal Communication.
33. Kelly JM, Skinner MS, Beucke KE (1980a). *Experimental Testing of an Energy Absorbing Seismic Isolation System*, Report No. UCB/EERC-80/35, University of California, Berkeley: CA, USA.
34. Kelly JM, Beucke KE, Skinner MS (1980b). *Experimental Testing of a Friction Damped Aseismic Base Isolation System with Fail-safe Characteristics*, Report No. UCB/EERC-80/18, University of California: Berkeley, USA.
35. Kelly JM, Hodder SB (1981). *Experimental Study of Lead and Elastomeric Dampers for Base Isolation Systems*, Report No. UCB/EERC-81/16, University of California: Berkeley, CA, USA.
36. Kelly JM (1988). *Base Isolation in Japan*, Report No. UCB/EERC-88/20, University of California: Berkeley, CA, USA.
37. Kelly JM, Chalhoub MS (1990). *Earthquake Simulator Testing of a Combined Sliding Bearing and Rubber Bearing Isolation System*, Report No. UCB/EERC-87/04, University of California: Berkeley, CA, USA.
38. Kelly JM (1997). *Earthquake-Resistant Design with Rubber*, 2<sup>nd</sup> Edition, Springer-Verlag.
39. Kent DC, Park R (1971). Flexural members with confined concrete. *Journal of the Structural Division, Proceedings of the ASCE* 97(ST7): 1969-1990.
40. Kikuchi M, Nakamura T, Aiken ID (2010). "Three-dimensional analysis for square seismic isolation bearings under large shear deformations and high axial loads", *Earthq. Eng. Struct. Dyn.* 39:1513–1531.
41. Koh C-G, Kelly JM (1987). *Effects of axial load on elastomeric isolation bearings*, Rep. No. UCB/EERC-86/12, Earthquake Engineering Research Center, Univ. of California, Berkeley, Calif.
42. Krawinkler H (1978). "Shear in beam-column joints in seismic design of steel frames", *Engineering Journal* (AISC), 15(3): 82-91.
43. Malushte S and Whittaker AS (2005). "Survey of past base isolation applications in nuclear power plants and challenges to industry/regulatory acceptance." *Proc. 18th International Conference on Structural Mechanics in Reactor Technology*, Beijing, China.
44. McGuire RK, Silva WJ and Costantino CJ (2001). *Technical Basis for Revision of Regulatory Guidance on Design Ground Motions: Hazard- and Risk-Consistent*

*Ground Motion Spectra Guidelines, NUREG/CR-6728*, U.S. Nuclear Regulatory Commission, Washington, D.C.

45. Mokha A, Constantinou MC, Reinhorn AM (1988). *Teflon Bearings in Aseismic Base Isolation: Experimental Studies and Analytical Modeling*, Technical Report NCEER-88-0038, State University of New York at Buffalo: Buffalo, NY, USA.
46. Mokha A, Constantinou MC, Reinhorn AM (1990). *Experimental Study and Analytical Prediction of Earthquake Response of a Sliding Isolation System with Spherical Surface*, Technical Report NCEER-90-0020, State University of New York at Buffalo: Buffalo, NY, USA.
47. Monzon EV, Buckle IG, Itani AM (2013). *Seismic Performance of Curved Steel Plate Girder Bridges with Seismic Isolation*, Report CCEER 13-06. Center for Civil Engineering Earthquake Research, University of Nevada, Reno, May, 2013.
48. Morgan TA and Mahin SA (2011). *The Use of Innovative Base Isolation Systems to Achieve Complex Seismic Performance Objectives*; Report No. PEER-2011/06, Pacific Earthquake Engineering Research Center, University of California, Berkeley, 2011.
49. Nagarajaiah S, Ferrell K (1999). "Stability of elastomeric isolation bearings", *J. Struct. Eng.* 125:946–954.
50. Neuenhofer A, Filippou FC (1997). "Evaluation of nonlinear frame finite-element models", *Journal of Structural Engineering* (ASCE), 123(7): 958-966.
51. Nishiyama I, Okawa I, Fukuyama H, Okuda Y (2011). "Building damage by the 2011 off the Pacific coast of Tohoku earthquake and coping activities by NILIM and BRI collaborated with the administration," *A Report to the U.S.-Japan Cooperative Program in Natural Resources (UJNR) Panel on Wind and Seismic Effects*, Japan Public Works Research Institute. Retrieved May 15, 2012, From [http://www.kenken.go.jp/english/contents/topics/pdf/report\\_ujnr2011.pdf](http://www.kenken.go.jp/english/contents/topics/pdf/report_ujnr2011.pdf)
52. Open System for Earthquake Engineering Simulation (OpenSees), Version 2.2.2. Pacific Earthquake Engineering Research Center, University of California, Berkeley. Retrieved May 15, 2010, From <http://opensees.berkeley.edu/>.
53. Park YJ, Wen YK, Ang AH-S (1986). "Random vibration of hysteretic systems under bi-directional ground motions", *Earthquake Engineering and Structural Dynamics* 14:543–557.
54. Ryan KL, Kelly JM, Chopra AK (2005). "Nonlinear model for lead-rubber bearings including axial-load effects", *J. Eng. Mech.* 131:1270–1278.
55. Ryan K, Sato E, Sasaki T, Okazaki T, Guzman T, Dao N, Soroushian S, Coria C (2013a). "Full Scale 5-story Building with Triple Pendulum Bearings at E-Defense", Network for Earthquake Engineering Simulation (database), Dataset, DOI:10.4231/D3X34MR7R
56. Ryan K, Sato E, Sasaki T, Okazaki T, Guzman T, Dao N, Soroushian S, Coria C (2013b). "Full Scale 5-story Building with LRB/CLB Isolation System at E-Defense", Network for Earthquake Engineering Simulation (database), Dataset, DOI:10.4231/D3SB3WZ43

57. Ryan K, Sato E, Sasaki T, Okazaki T, Guzman T, Dao N, Soroushian S, Coria C (2013c). "Full Scale 5-story Building in Fixed-Base Condition at E-Defense", Network for Earthquake Engineering Simulation (database), Dataset, DOI:10.4231/D3NP1WJ3P
58. Sanchez J, Masroor A, Mosqueda G, Ryan KL (2012). "Static and dynamic stability of elastomeric bearings for seismic protection of structures", *J. Struct. Eng.*, In Press.
59. Sasaki T, Sato E, Ryan KL, Okazaki T, Mahin SA, and Kajiwara K. "NEES/E-Defense base isolation tests: Effectiveness of friction pendulum and lead-rubber bearing systems", *Proc., 15th World Conference on Earthquake Engineering*, Lisbon, 2012.
60. Sato N, Kato A, Fukushima Y, Iizuka M (2002). "Shaking table tests on failure characteristics of base isolation system for a DFBR plant", *Nuclear Eng. Des.*, 212:293–305.
61. Sato E, Furukawa S, Kakehi A, Nakashima M (2011). "Full-scale shaking table test for examination of safety and functionality of base-isolated medical facilities", *Earthq. Eng. Struct. Dyn.* 40:1435–1453.
62. Scott BD, Park R, Priestley MJN (1982). "Stress-strain behavior of concrete confined by overlapping hoops at low and high strain rates", *ACI Journal Proceedings*, 79(1): 13-27.
63. Soroushian S, Ryan KL, Maragakis M, Sato E, Sasaki T, Okazaki T, Tedesco L, Zaghi AE, Mosqueda G, Alvarez D (2012). "Seismic response of ceiling/sprinkler piping nonstructural systems in NEES TIPS/NEES nonstructural/NIED collaborative tests on a full scale 5-story building", In *Proceedings of the 2012 ASCE Structures Congress*, Chicago, IL, USA, 29–31 March.
64. Tagawa Y and Kajiwara K (2007). "Controller development for the E-Defense shaking table", *Proc. IMechE Vol. 221, Part I, J. Systems and Control Engineering*.
65. Takaoka E, Takenaka Y, Nimura A (2011). "Shaking table tests and analysis method on ultimate behavior of slender base-isolated structure supported by laminated rubber bearings", *Earthq. Eng. Struct. Dyn.* 40:551–570.
66. Uang C-M, Bertero VB (1986). *Earthquake Simulation Tests and Associated Studies of a 0.3- Scale Model of a Six-Story Concentrically Braced Steel Structure*, Report No. UCB/EERC-86/10; University of California: Berkeley, CA, USA.
67. U.S. Code of Federal Regulations (CFR), (2011). Title 10, Part 50, Domestic Licensing of Production and Utilization Facilities, General Design Criterion (GDC) 2, Design Bases for Protection Against Natural Phenomena in Appendix A, General Design Criteria for Nuclear Power Plants, U.S. Nuclear Regulatory Commission, Washington, D.C.
68. Warn GP, Whittaker AS (2006). *A Study of the Coupled Horizontal-Vertical Behavior of Elastomeric and Lead-Rubber Seismic Isolation Bearings*, Technical Report MCEER-07-0012, Multidisciplinary Center for Earthquake Engineering Research, State University of New York at Buffalo: Buffalo, NY, USA.
69. Warn GP, Whittaker AS, Constantinou MC (2007). "Vertical stiffness of elastomeric and lead-rubber seismic isolation bearings", *ASCE J. Struct. Eng.* 133:1227–1236.

70. Warn GP, Ryan KL (2012). "A review of seismic isolation for buildings: historical developments and research needs", *Buildings (Open Access)*, In Press.
71. Weisman J, Warn GP (2012). "Stability of Elastomeric and Lead-Rubber Seismic Isolation Bearings", *J. Struct. Eng.*, 138(2), 215–223.
72. Whittaker AS, Uang C-M, Bertero VB (1990). *An Experimental Study of the Behavior of Dual Steel Systems*, Report No. UCB/EERC-88/14; University of California: Berkeley, CA, USA.
73. Yamamoto S, Kikuchi M, Ueda M, Aiken ID (2009). "A mechanical model for elastomeric seismic isolation bearings including the influence of axial load", *Earthq. Eng. Struct. Dyn.* 38:157–180.
74. Zayas V, Low S, Mahin S (1987). *The FPS Earthquake Resisting System*, Report No. UCB/EERC-87/01; University of California: Berkeley, CA, USA.

# APPENDIX A

## DESING & CONSTRUCTION DRAWING FOR TESTING OF VALUE-ADDED DAMPED BUILDING

Building Isolated with Hybrid Lead-Rubber Isolation System

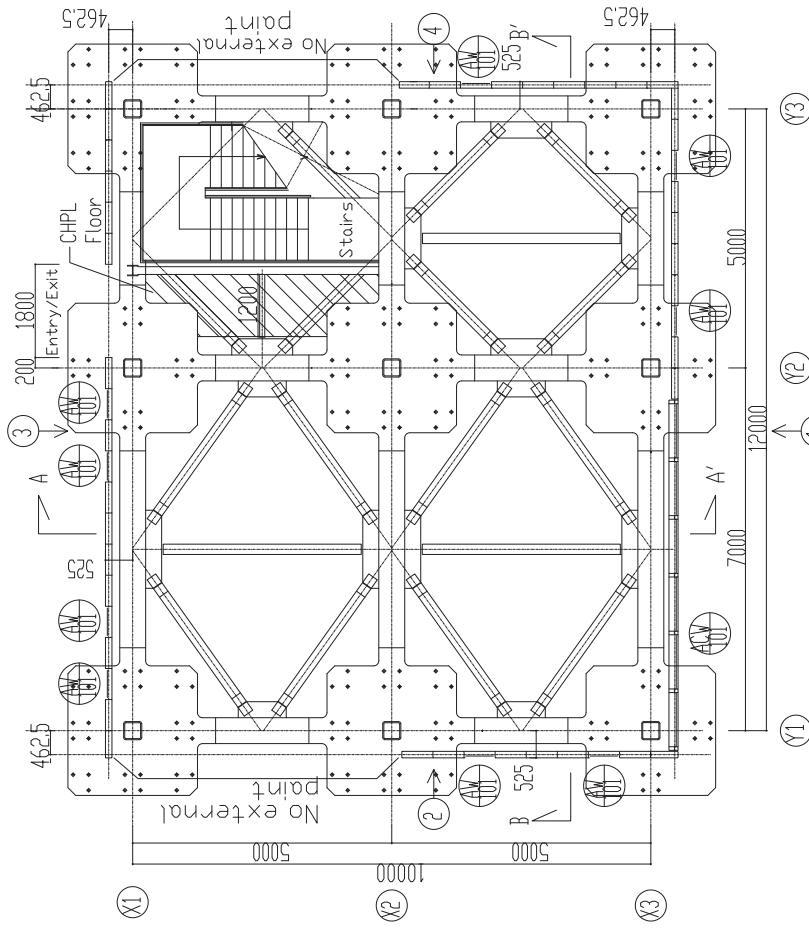
Originals developed by the National Research Institute for Earth Science and Disaster Prevention  
Hyogo Earthquake Engineering Research Center for Value Added Building Project, December 8,  
2008 Modified by NEES TIPS project for NEES/E-Defense Collaborative Test Program on  
Innovative Isolation Systems, 2011-2012

### Architectural Drawings

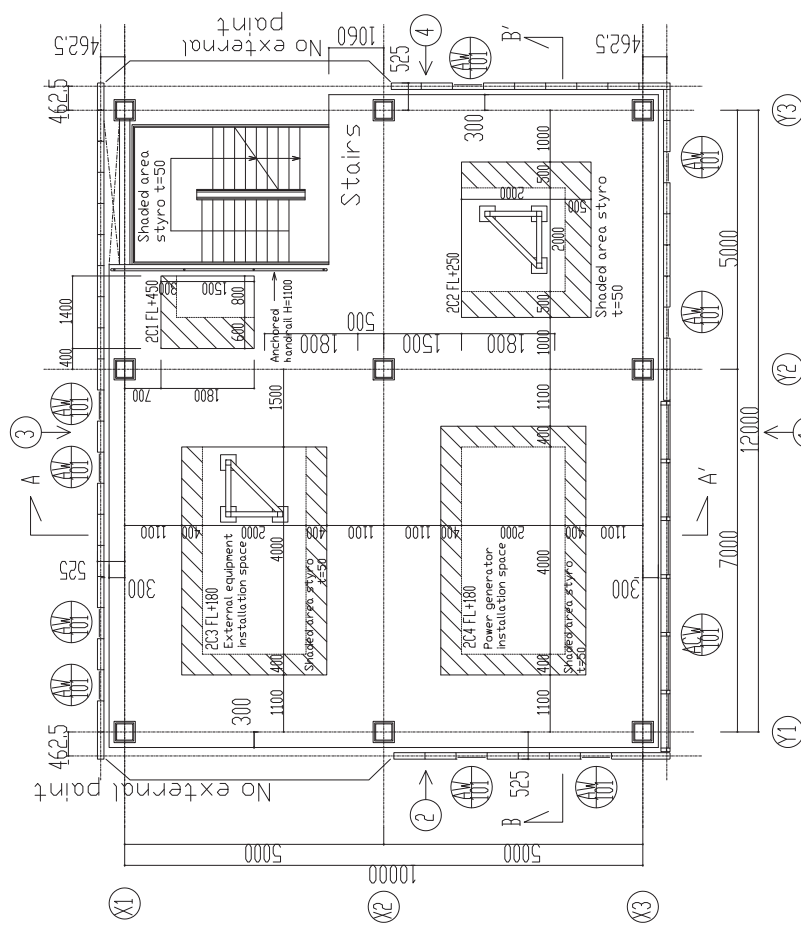
A-001	1F, 2F Plan
A-001a	3F, 4F Plan
A-002	5F, R Plan
A-003c	Elevation 1
A-004	Elevation 2
A-005	Section
A-006	Detailed Area 1
A-006a	Detailed Area 2
A-007	Stair Floor
A-008	Shaking Table Layout

### Structural Drawings

S-001	Structure and Particular Specification
S-002	Beam Plans, Framing Elevation
S-003	Material Cross-Sections
S-004	Steel Joint Standard, Test Hoisting Equipment
S-005	1F Column Base
S-006	Steel Structure (1)
S-007	Steel Structure (2)
S-008	Stud, Bolt Layout
S-009	QL Deck Layout
S-010	High Deck Layout



Front of specimen  
1F Plan



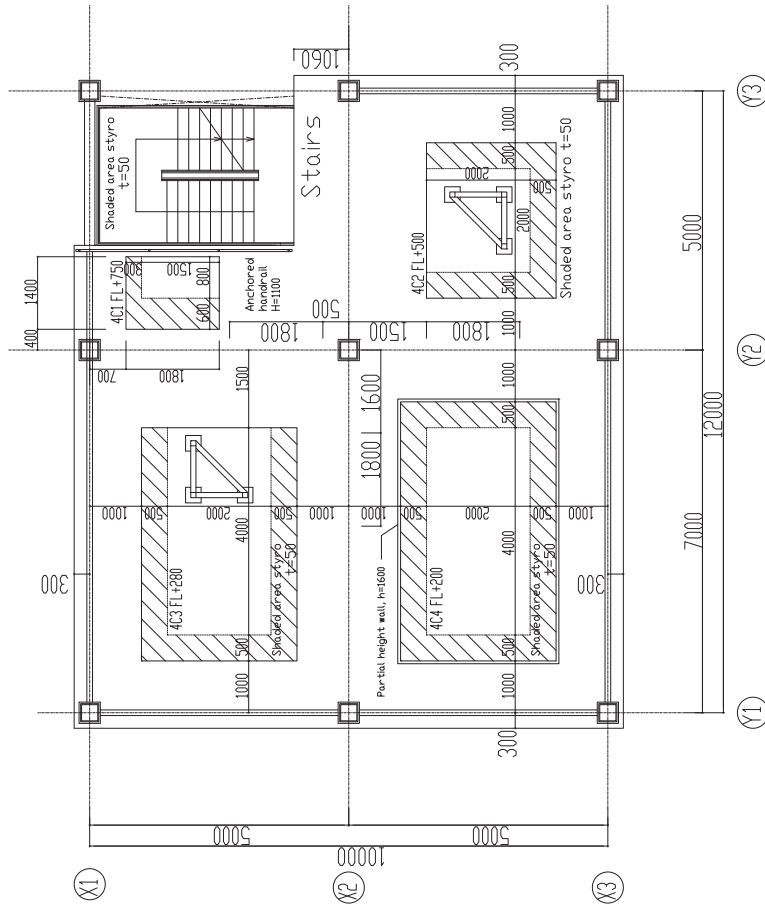
Front of specimen  
2F Plan

Internal Specification

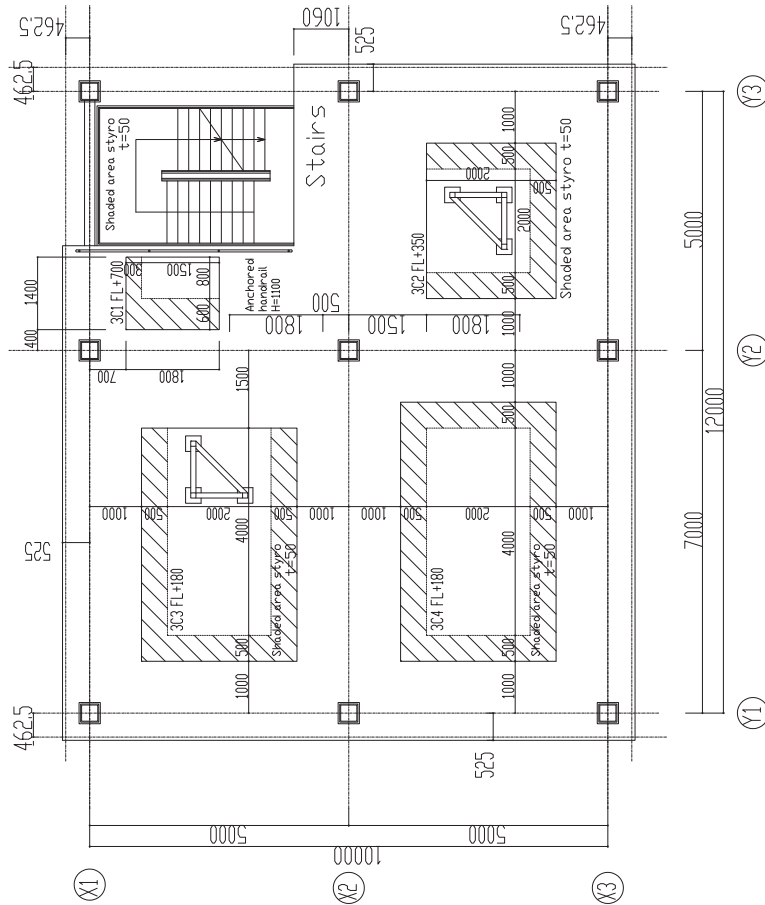
Room	Floor	Baseboard	Wall	Ceiling
Office	-	-	Plaster board t=9.5+12.5 LGS Backing	Installed only for non value-added experiment
Stairwell	Mortar finish with wood float	-	-	-

Code (Material)	Region	Type, Structure	Internal Dimensions (WxH)	Material, Finish	Note
AW	4F-5F	<input checked="" type="checkbox"/> Fixed window	W560xH560	Aluminum alumite	Glass FL-6
AW	4F-5F	Refer to Elevation		Aluminum alumite	Glass FL-10
AW	2F-5F	<input checked="" type="checkbox"/> Double sliding window	W1800xH2100	Steel	Glass FL-8 Threshold plate: steel t=20

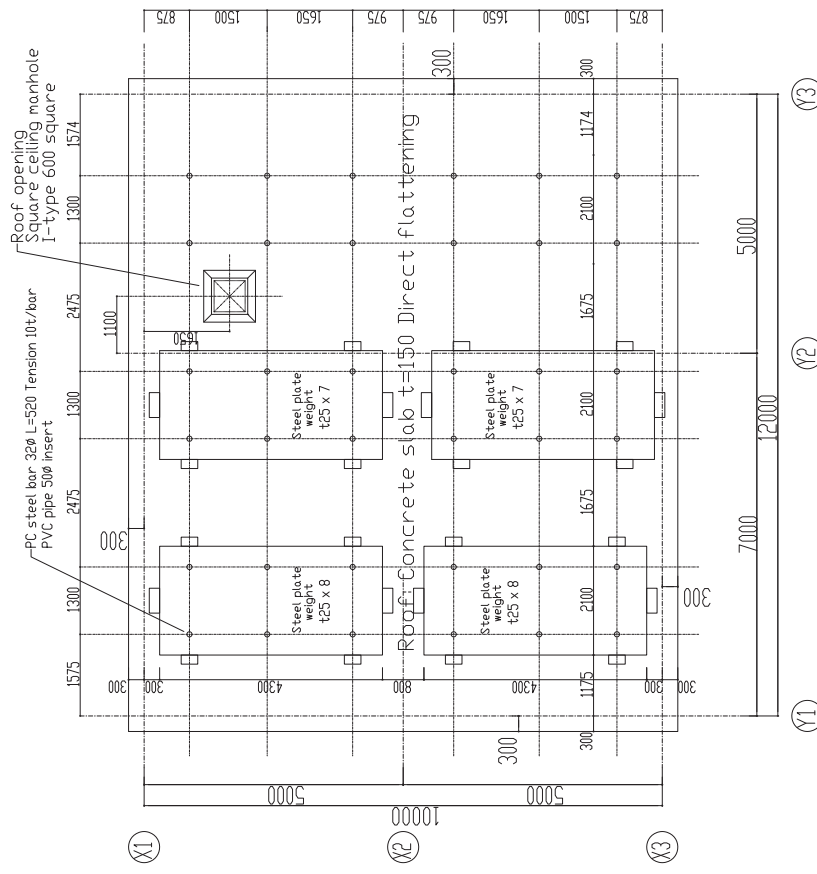




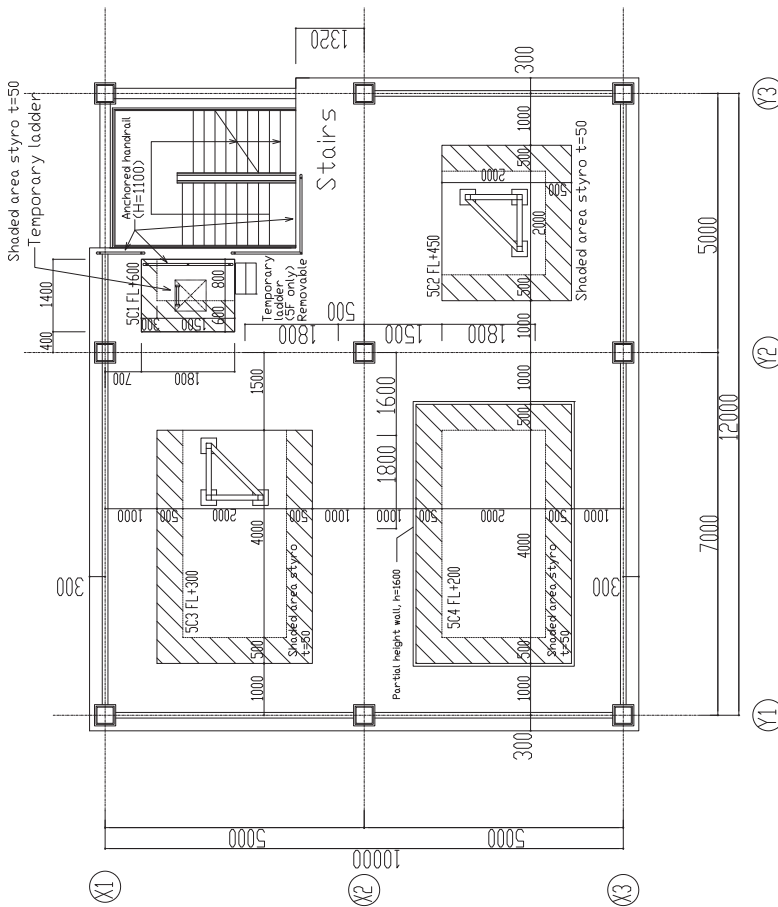
Front of specimen  
4F Plan



Front of specimen  
3F Plan

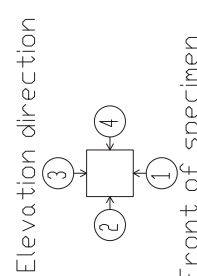
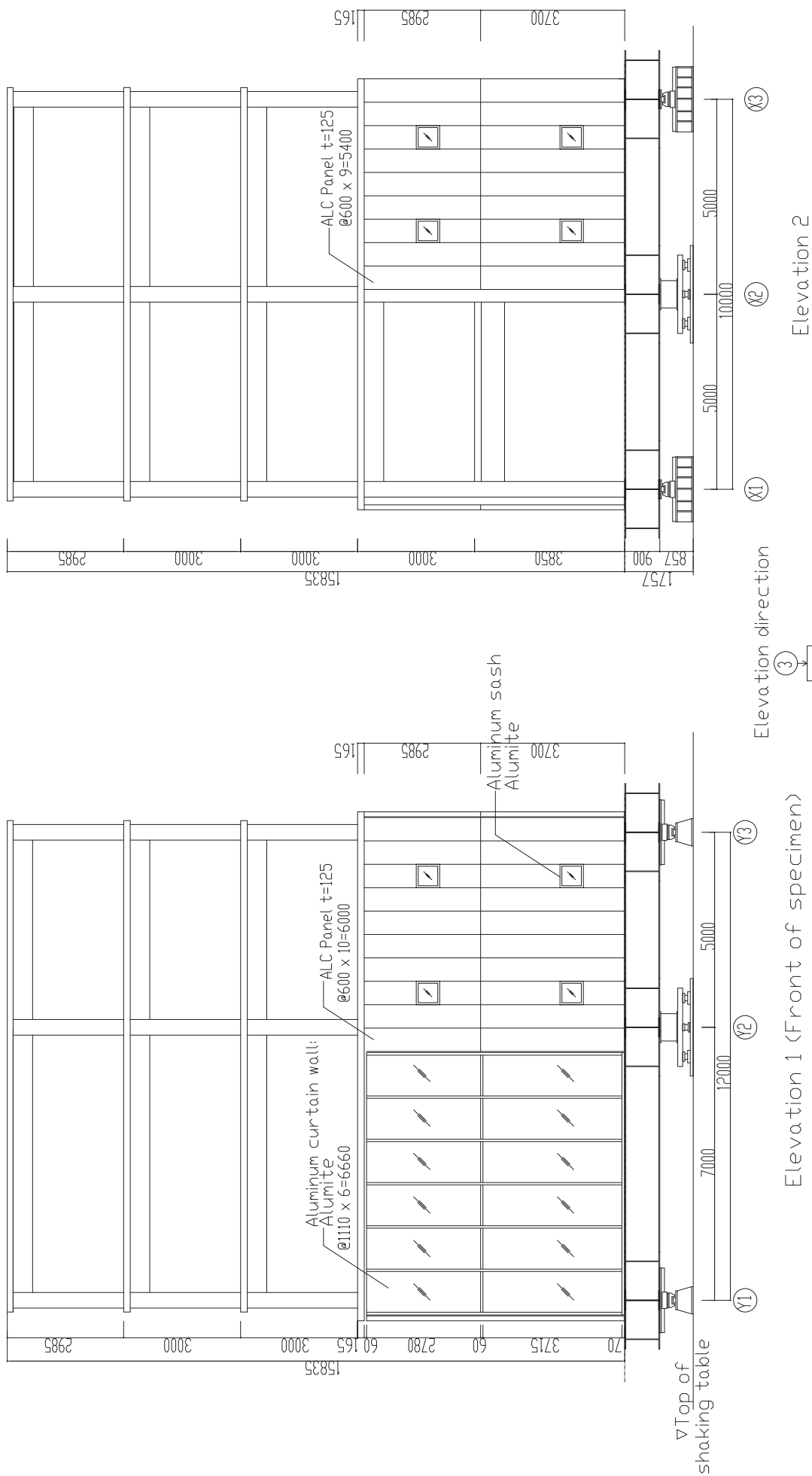


Front of specimen  
RF Plan



Front of specimen  
5F Plan

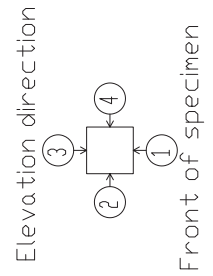
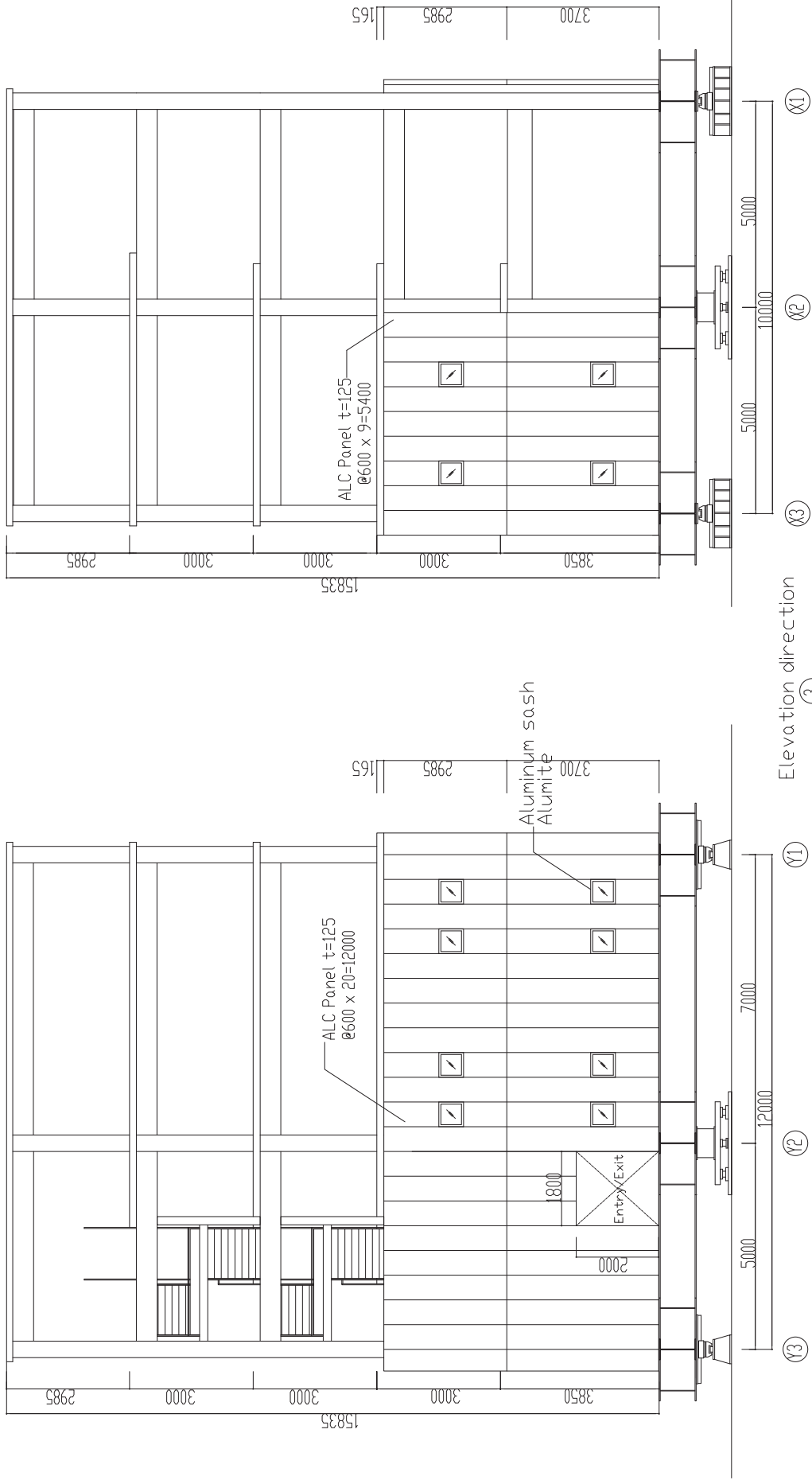
4	National Research Institute for Earth Science and Disaster Prevention Hyogo Earthquake Engineering Research Center Value-added Five-story Steel Frame Experiment Specimen Design Drawing
A-002	
A3/700	SF, RF Plan
A3/700	



Elevation 1 (Front of specimen)

Elevation 2

National Research Institute for Earthquake Engineering and Disaster Prevention Hyogo Earthquake Engineering Research Center Value-added Five-story Steel Frame Experiment Specimen Design Drawing	5
	2008.11.7
Elevation 1	A317/50
Elevation 2	A317/100
A-003c	



Revised	A-004	A37/100	Elevation 2	Value-added Five-story Steel Frame Experiment		2008.11.7	6
				Hyogo Earthquake Engineering Research Center			
				National Research Institute for Earth Science and Disaster Prevention			



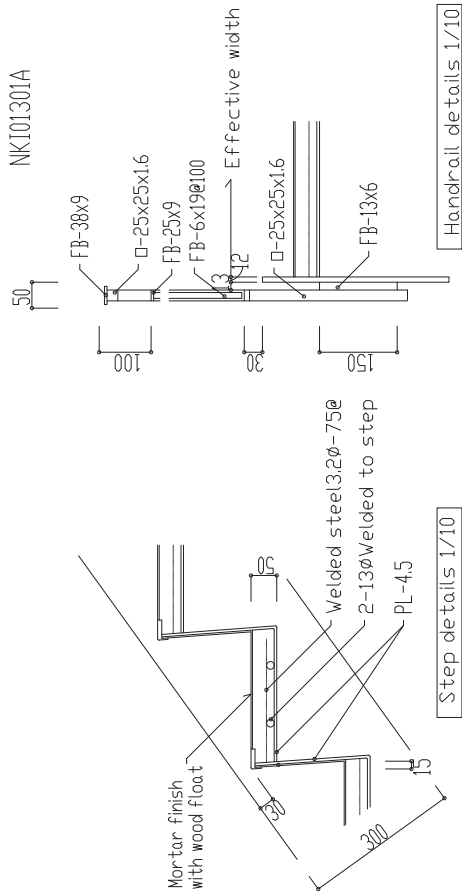
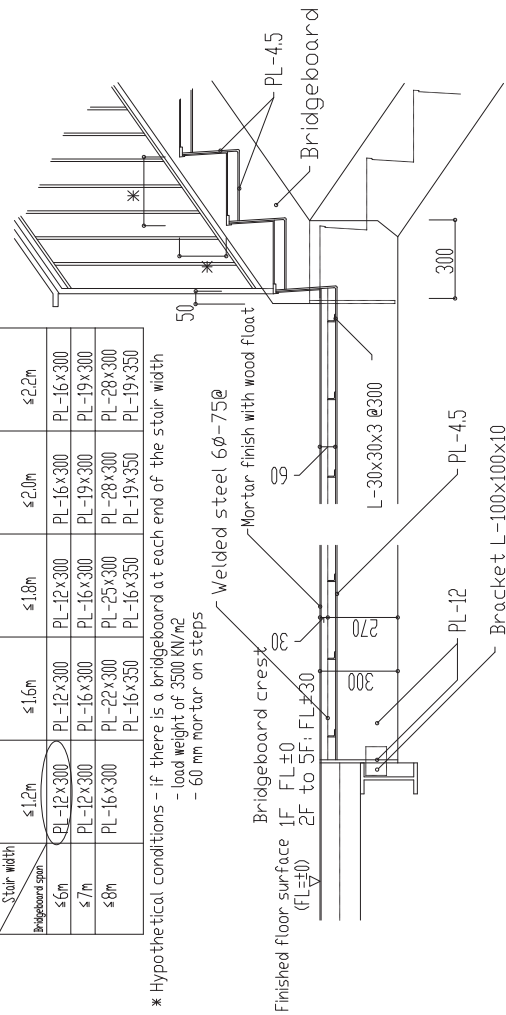




Bridgeboard required cross-section for each stair width and span (SS400)

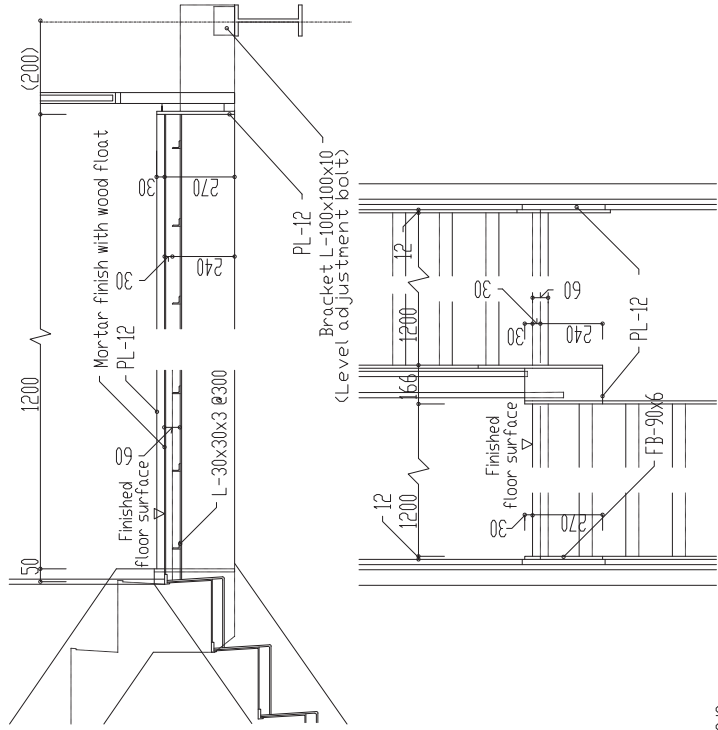
Stair width	≤ 1.2m	≤ 1.6m	≤ 1.8m	≤ 2.0m	≤ 2.2m
Bridgeboard span					
≤ 6m	PL-12x300	PL-12x300	PL-12x300	PL-16x300	PL-16x300
≤ 7m	PL-12x300	PL-16x300	PL-16x300	PL-19x300	PL-19x300
≤ 8m	PL-16x300	PL-22x300	PL-25x300	PL-28x300	PL-28x300
		PL-16x350	PL-16x350	PL-19x350	PL-19x350

\* Hypothetical conditions - if there is a bridgeboard at each end of the stair width  
 - load weight of 3500 KN/m<sup>2</sup>  
 - 60 mm mortar on steps

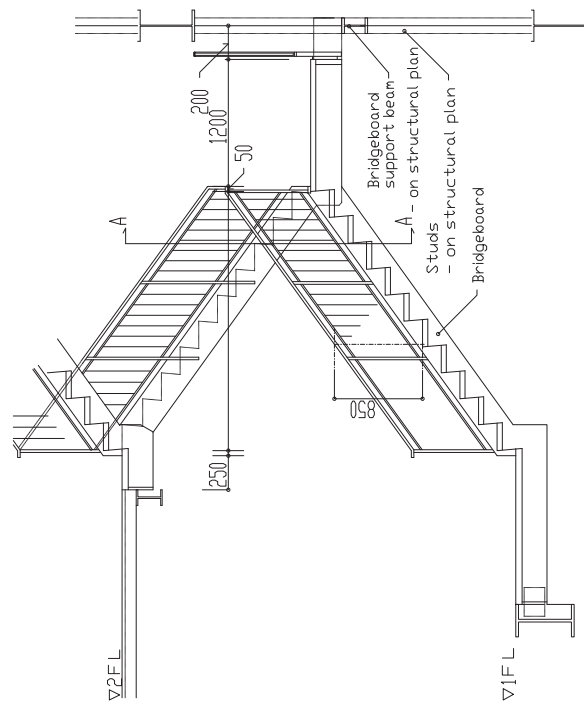


Step details 1/10

Handrail details 1/10

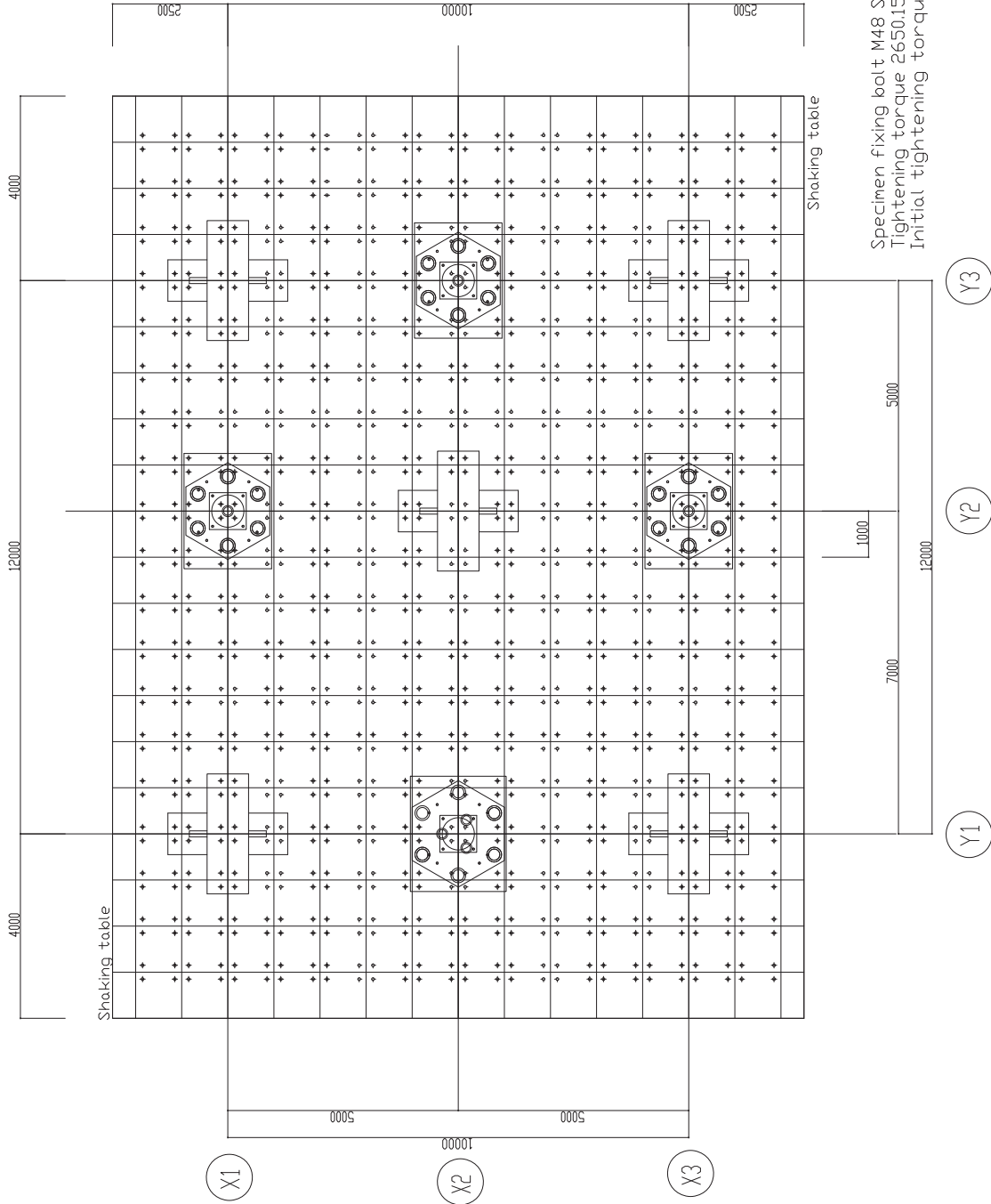


A-A Section 1/10



\* On different plan





Specimen fixing bolt M48 S45C, L=1570  
 Tightening torque 2650.15Nm  
 Initial tightening torque 42.470Nm(Using bolt tensioner)

Measurement Control Tower Side

National Research Institute for Earth Science and Disaster Prevention Hyogo Earthquake Engineering Research Center Value-added Five-story Steel Frame Experiment Specimen Design Drawing	11 2008.11.7
Shaking Table Layout	A11/50 A31/100

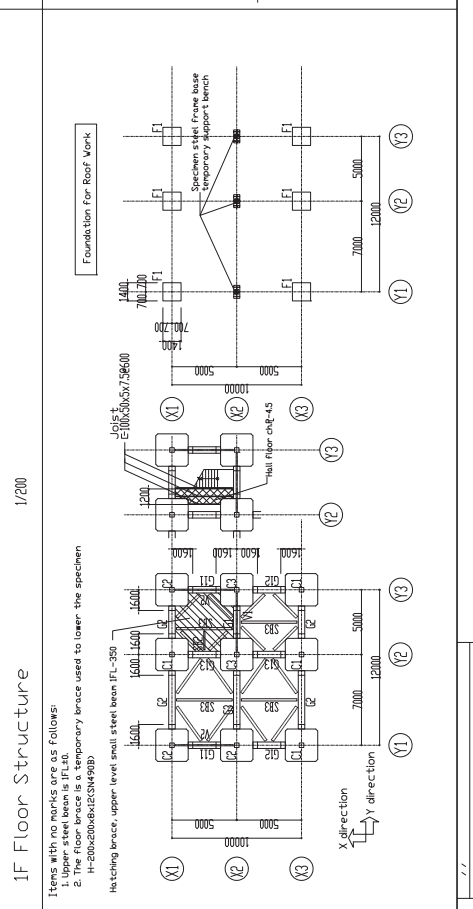
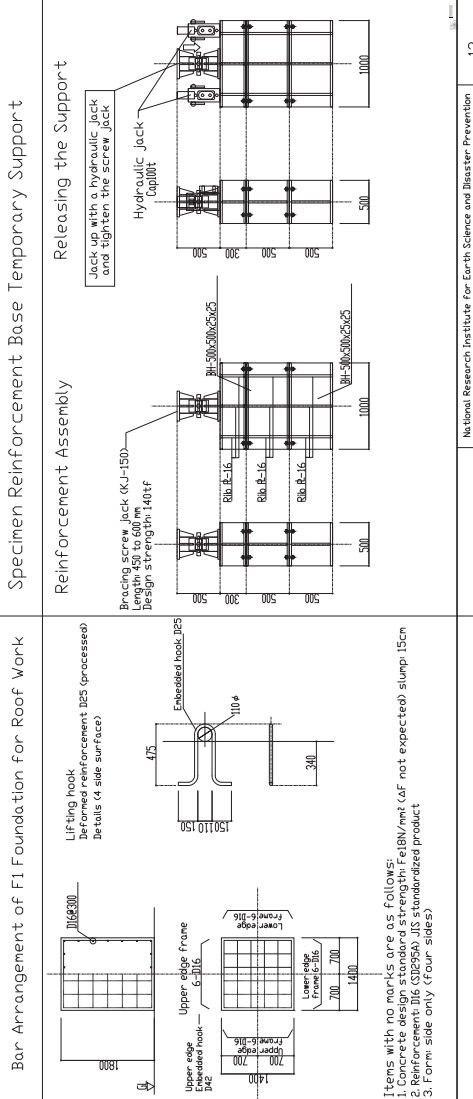
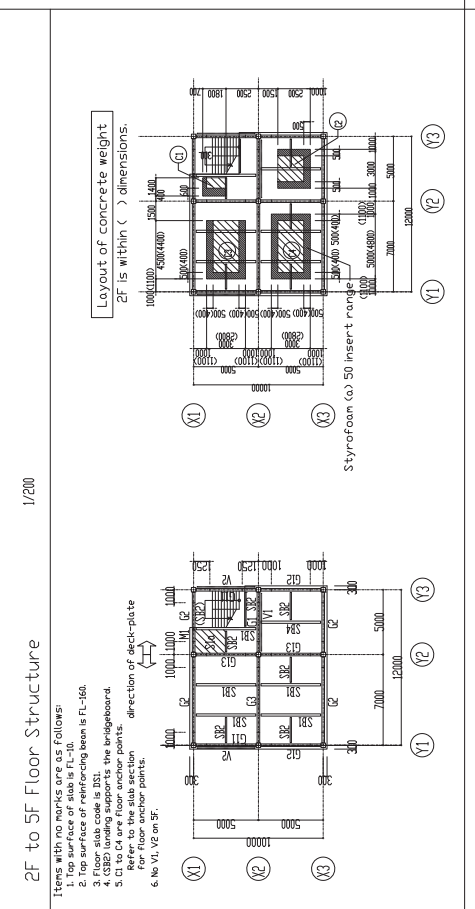
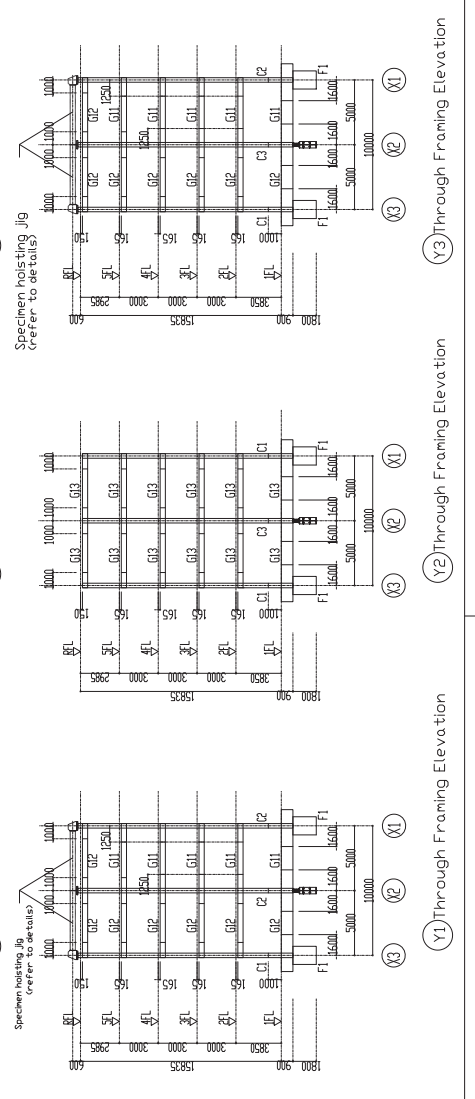
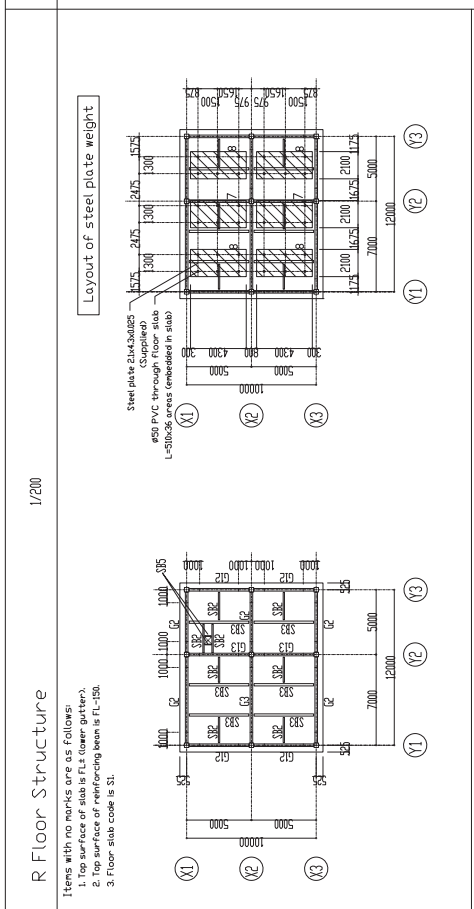
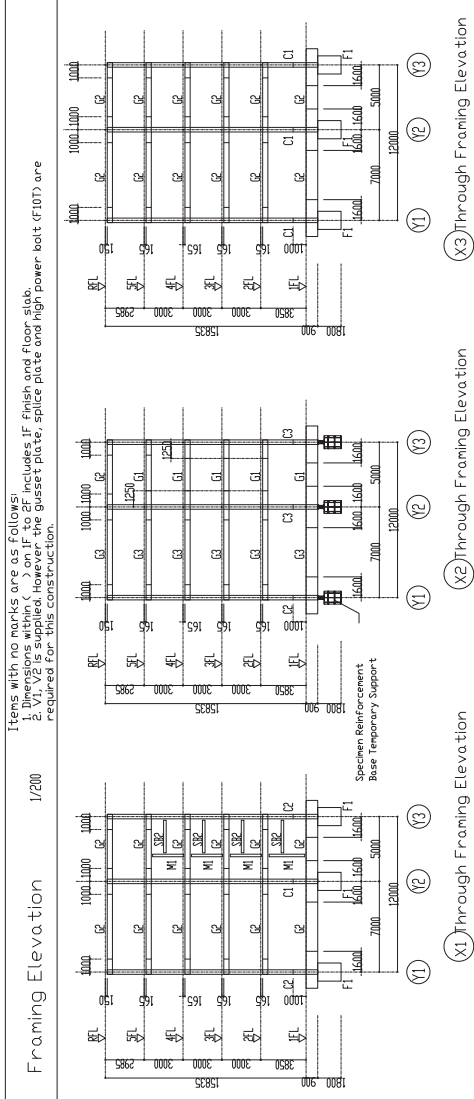
Revised	

Construction Summary	Value-added Five-story Steel Frame Specimen	Reinforcement Work	Steel Frame Construction	Welded Joints (Factory/Welded Joints)
Location	1501-21 Nishikameya, Sijimichonmura, Mitai City, Hyogo Prefecture National Research Institute for Earth Science and Disaster Prevention Hyogo Earthquake Engineering Research Center	5.2.1 Reinforcement 5.2.2 Materials, 5.2 Construction and Assembly	7.1 Common Items 7.2 Materials	7.6.3 Qualified welding technicians carrying out factory welding must have passed AW factory welding certification for the welding methods stipulated by AW (Welding position, end tab type) Flux (AW-4 certification required)
Building Use	Steel Structured Building Test (Value-added Five-story Steel Frame Specimen)	Area Used Concrete Weight Foundation for Roof Work	Area Used Material Welding	7.6.7 Input energy, interpass temperature Within material certification
No. of Floors	5 floors	Design Strength Type of Concrete	Material Welding	7.6.11 Welded Joint Test
Maximum Height	Specimen FL+14,935 (RFL slab ceiling)	Quantity Standard N/mm <sup>2</sup>	Material Welding	Inspection Item External Inspection Ultrasonic Inspection Inspector Sampling Rate Factory Welding Construction Factory
Bottom of Foundation	Specimen FL-900 (Foundation beam bottom)	Maximum Size Aggregate mm	Material Welding	Note Factory 100%, On-site 100% Factory 30%, On-site 100% CIW certified office
Construction Type	Steel construction	Floor Slab	Material Welding	Instructions for the Receiving Inspection of Complete Joint Penetration Welded Parts is created before the test and approved by construction management.
Structure Type	Long side Value-added moment steel frame (Y direction) Short side Value-added moment steel frame (X direction)	Concrete Weight	Material Welding	External Inspection, Factory Welding Ultrasonic Inspection, Sampling Rate 100%
Column	Steel construction	Foundation for Roof Work	Material Welding	Receiving Inspection Method by Factory Construction Inspection External Inspection Visual
Large beam	Steel construction	Workability and Slump	Material Welding	Ultrasonic Inspection Conform to "Standards for the Ultrasonic Inspection of Weld Defects in Steel Structures" by the Architectural Institute of Japan (if there is tensile stress created in the welded areas).
Small beam	Steel construction	Reinforcement for Roof Work	Material Welding	Attachment of non-constructed parts Non-constructed parts should be attached beforehand by factory welding plates and pieces designed for the non-constructed parts instead of welding the parts directly to the constructed material on-site.
Floor Plate	Composite deck plate floor	Workability and Slump	Material Welding	The attachment base for ALC, curtain wall and measurement apparatus base are entered into the single item plan.
Roof	Steel reinforced concrete slab (frame stack)	Workability and Slump	Material Welding	
Outer wall	ALC Plate (l=1.2m, vertical attachment, locking method), glass curtain wall	Workability and Slump	Material Welding	
Inner wall	LCS foundation board attachment	Workability and Slump	Material Welding	
Joined firmly to foundation beam	Joined firmly to foundation beam	Workability and Slump	Material Welding	
Joined firmly to steel foundation	Joined firmly to steel foundation	Workability and Slump	Material Welding	
Construction Method	Construction Method	Workability and Slump	Material Welding	
Particular Specifications (Building Construction) Structure	Particular Specifications (Building Construction) Structure	Workability and Slump	Material Welding	
Application of Japanese Architectural Standard Specifications	Application of Japanese Architectural Standard Specifications	Workability and Slump	Material Welding	
Specifications 1	Both the Particular Specification and the "Public Building Construction Standard Specifications (Building construction edition) 2007" (hereinafter referred to as the Ministry of Land, Infrastructure, Transport and Tourism Standard Specifications) apply to the construction of the Vibration Suppression Structure Specimen.	Workability and Slump	Material Welding	
Specifications 2	Items not listed in the design plan or particular specifications adhere to the Ministry of Land, Infrastructure, Transport and Tourism Standard Specifications (machinery equipment construction, electrical equipment construction). Particular specifications are linked to the relevant section in the Ministry Standard Specification.	Workability and Slump	Material Welding	
Documents for Submission	The following documents must be submitted to and approved by construction management before and after the relevant construction.	Workability and Slump	Material Welding	
No	Documents for Submission	Workability and Slump	Material Welding	
1	Instructions and Report for each test as shown in the Particular Specifications	Workability and Slump	Material Welding	
2	Steel Frame Plans	Workability and Slump	Material Welding	
3	Steel Frame Construction Factory and On-site Manufacturing Instructions	Workability and Slump	Material Welding	
4	Steel Frame Construction Factory and On-site Work Plans	Workability and Slump	Material Welding	
5	Steel Frame Welding Receiving Inspection	Workability and Slump	Material Welding	
6	Steel Frame Manufacturing Accuracy Measurement Plan and Report	Workability and Slump	Material Welding	
7	Steel Frame Work Accuracy Measurement Plan and Report	Workability and Slump	Material Welding	
8	Reinforced Concrete Work Instructions	Workability and Slump	Material Welding	

Reinforcement Work	Steel Frame Construction	Welded Joints (Factory/Welded Joints)
5.2.1 Reinforcement 5.2.2 Materials, 5.2 Construction and Assembly	7.1 Common Items 7.2 Materials	7.6.3 Qualified welding technicians carrying out factory welding must have passed AW factory welding certification for the welding methods stipulated by AW (Welding position, end tab type) Flux (AW-4 certification required)
Area Used Concrete Weight Foundation for Roof Work	Area Used Material Welding	7.6.7 Input energy, interpass temperature Within material certification
Design Strength Type of Concrete	Material Welding	7.6.11 Welded Joint Test
Quantity Standard N/mm <sup>2</sup>	Material Welding	Inspection Item External Inspection Ultrasonic Inspection Inspector Sampling Rate Factory Welding Construction Factory
Maximum Size Aggregate mm	Material Welding	Note Factory 100%, On-site 100% Factory 30%, On-site 100% CIW certified office
Instructions for the Receiving Inspection of Complete Joint Penetration Welded Parts is created before the test and approved by construction management.	Material Welding	Instructions for the Receiving Inspection of Complete Joint Penetration Welded Parts is created before the test and approved by construction management.
External Inspection, Factory Welding Ultrasonic Inspection, Sampling Rate 100%	Material Welding	External Inspection, Factory Welding Ultrasonic Inspection, Sampling Rate 100%
Receiving Inspection Method by Factory Construction Inspection External Inspection Visual	Material Welding	Receiving Inspection Method by Factory Construction Inspection External Inspection Visual
Ultrasonic Inspection Conform to "Standards for the Ultrasonic Inspection of Weld Defects in Steel Structures" by the Architectural Institute of Japan (if there is tensile stress created in the welded areas).	Material Welding	Ultrasonic Inspection Conform to "Standards for the Ultrasonic Inspection of Weld Defects in Steel Structures" by the Architectural Institute of Japan (if there is tensile stress created in the welded areas).
Attachment of non-constructed parts Non-constructed parts should be attached beforehand by factory welding plates and pieces designed for the non-constructed parts instead of welding the parts directly to the constructed material on-site.	Material Welding	Attachment of non-constructed parts Non-constructed parts should be attached beforehand by factory welding plates and pieces designed for the non-constructed parts instead of welding the parts directly to the constructed material on-site.
The attachment base for ALC, curtain wall and measurement apparatus base are entered into the single item plan.	Material Welding	The attachment base for ALC, curtain wall and measurement apparatus base are entered into the single item plan.

Reinforcement Work	Steel Frame Construction	Welded Joints (Factory/Welded Joints)
5.2.1 Reinforcement 5.2.2 Materials, 5.2 Construction and Assembly	7.1 Common Items 7.2 Materials	7.6.3 Qualified welding technicians carrying out factory welding must have passed AW factory welding certification for the welding methods stipulated by AW (Welding position, end tab type) Flux (AW-4 certification required)
Area Used Concrete Weight Foundation for Roof Work	Area Used Material Welding	7.6.7 Input energy, interpass temperature Within material certification
Design Strength Type of Concrete	Material Welding	7.6.11 Welded Joint Test
Quantity Standard N/mm <sup>2</sup>	Material Welding	Inspection Item External Inspection Ultrasonic Inspection Inspector Sampling Rate Factory Welding Construction Factory
Maximum Size Aggregate mm	Material Welding	Note Factory 100%, On-site 100% Factory 30%, On-site 100% CIW certified office
Instructions for the Receiving Inspection of Complete Joint Penetration Welded Parts is created before the test and approved by construction management.	Material Welding	Instructions for the Receiving Inspection of Complete Joint Penetration Welded Parts is created before the test and approved by construction management.
External Inspection, Factory Welding Ultrasonic Inspection, Sampling Rate 100%	Material Welding	External Inspection, Factory Welding Ultrasonic Inspection, Sampling Rate 100%
Receiving Inspection Method by Factory Construction Inspection External Inspection Visual	Material Welding	Receiving Inspection Method by Factory Construction Inspection External Inspection Visual
Ultrasonic Inspection Conform to "Standards for the Ultrasonic Inspection of Weld Defects in Steel Structures" by the Architectural Institute of Japan (if there is tensile stress created in the welded areas).	Material Welding	Ultrasonic Inspection Conform to "Standards for the Ultrasonic Inspection of Weld Defects in Steel Structures" by the Architectural Institute of Japan (if there is tensile stress created in the welded areas).
Attachment of non-constructed parts Non-constructed parts should be attached beforehand by factory welding plates and pieces designed for the non-constructed parts instead of welding the parts directly to the constructed material on-site.	Material Welding	Attachment of non-constructed parts Non-constructed parts should be attached beforehand by factory welding plates and pieces designed for the non-constructed parts instead of welding the parts directly to the constructed material on-site.
The attachment base for ALC, curtain wall and measurement apparatus base are entered into the single item plan.	Material Welding	The attachment base for ALC, curtain wall and measurement apparatus base are entered into the single item plan.

Reinforcement Work	Steel Frame Construction	Welded Joints (Factory/Welded Joints)
5.2.1 Reinforcement 5.2.2 Materials, 5.2 Construction and Assembly	7.1 Common Items 7.2 Materials	7.6.3 Qualified welding technicians carrying out factory welding must have passed AW factory welding certification for the welding methods stipulated by AW (Welding position, end tab type) Flux (AW-4 certification required)
Area Used Concrete Weight Foundation for Roof Work	Area Used Material Welding	7.6.7 Input energy, interpass temperature Within material certification
Design Strength Type of Concrete	Material Welding	7.6.11 Welded Joint Test
Quantity Standard N/mm <sup>2</sup>	Material Welding	Inspection Item External Inspection Ultrasonic Inspection Inspector Sampling Rate Factory Welding Construction Factory
Maximum Size Aggregate mm	Material Welding	Note Factory 100%, On-site 100% Factory 30%, On-site 100% CIW certified office
Instructions for the Receiving Inspection of Complete Joint Penetration Welded Parts is created before the test and approved by construction management.	Material Welding	Instructions for the Receiving Inspection of Complete Joint Penetration Welded Parts is created before the test and approved by construction management.
External Inspection, Factory Welding Ultrasonic Inspection, Sampling Rate 100%	Material Welding	External Inspection, Factory Welding Ultrasonic Inspection, Sampling Rate 100%
Receiving Inspection Method by Factory Construction Inspection External Inspection Visual	Material Welding	Receiving Inspection Method by Factory Construction Inspection External Inspection Visual
Ultrasonic Inspection Conform to "Standards for the Ultrasonic Inspection of Weld Defects in Steel Structures" by the Architectural Institute of Japan (if there is tensile stress created in the welded areas).	Material Welding	Ultrasonic Inspection Conform to "Standards for the Ultrasonic Inspection of Weld Defects in Steel Structures" by the Architectural Institute of Japan (if there is tensile stress created in the welded areas).
Attachment of non-constructed parts Non-constructed parts should be attached beforehand by factory welding plates and pieces designed for the non-constructed parts instead of welding the parts directly to the constructed material on-site.	Material Welding	Attachment of non-constructed parts Non-constructed parts should be attached beforehand by factory welding plates and pieces designed for the non-constructed parts instead of welding the parts directly to the constructed material on-site.
The attachment base for ALC, curtain wall and measurement apparatus base are entered into the single item plan.	Material Welding	The attachment base for ALC, curtain wall and measurement apparatus base are entered into the single item plan.



Items with no marks are as follows:

1. Top surface of slab is FL (lower girder).
2. Top surface of reinforcing beam is FL-150.
3. Floor slab code is S1.

Layout of steel plate weight

Steel plate 21x4.3x0.825 (Supplied)

slab PVC through floor slab L-50x5x8 areas embedded in slab

Layout of concrete weight

2F is within ( ) dimensions.

Styrofoam (a) 50 insert rounder

Items with no marks are as follows:

1. Top surface of slab is FL-10.
2. Top surface of reinforcing beam is FL-150.
3. Floor slab code is S1.
4. (S2) indicates the bridgeboard.
5. C1 to C4 are floor anchor points.
6. No V1, V2 on 5F.

Items with no marks are as follows:

1. Top surface of slab is FL-10.
2. Top surface of reinforcing beam is FL-150.
3. Floor slab code is S1.
4. (S2) indicates the bridgeboard.
5. C1 to C4 are floor anchor points.
6. No V1, V2 on 5F.

Items with no marks are as follows:

1. Top surface of slab is FL-10.
2. Top surface of reinforcing beam is FL-150.
3. Floor slab code is S1.
4. (S2) indicates the bridgeboard.
5. C1 to C4 are floor anchor points.
6. No V1, V2 on 5F.

Items with no marks are as follows:

1. Top surface of slab is FL-10.
2. Top surface of reinforcing beam is FL-150.
3. Floor slab code is S1.
4. (S2) indicates the bridgeboard.
5. C1 to C4 are floor anchor points.
6. No V1, V2 on 5F.

Items with no marks are as follows:

1. Top surface of slab is FL-10.
2. Top surface of reinforcing beam is FL-150.
3. Floor slab code is S1.
4. (S2) indicates the bridgeboard.
5. C1 to C4 are floor anchor points.
6. No V1, V2 on 5F.

Items with no marks are as follows:

1. Top surface of slab is FL-10.
2. Top surface of reinforcing beam is FL-150.
3. Floor slab code is S1.
4. (S2) indicates the bridgeboard.
5. C1 to C4 are floor anchor points.
6. No V1, V2 on 5F.

Items with no marks are as follows:

1. Top surface of slab is FL-10.
2. Top surface of reinforcing beam is FL-150.
3. Floor slab code is S1.
4. (S2) indicates the bridgeboard.
5. C1 to C4 are floor anchor points.
6. No V1, V2 on 5F.

Items with no marks are as follows:

1. Top surface of slab is FL-10.
2. Top surface of reinforcing beam is FL-150.
3. Floor slab code is S1.
4. (S2) indicates the bridgeboard.
5. C1 to C4 are floor anchor points.
6. No V1, V2 on 5F.

Items with no marks are as follows:

1. Top surface of slab is FL-10.
2. Top surface of reinforcing beam is FL-150.
3. Floor slab code is S1.
4. (S2) indicates the bridgeboard.
5. C1 to C4 are floor anchor points.
6. No V1, V2 on 5F.

Items with no marks are as follows:

1. Top surface of slab is FL-10.
2. Top surface of reinforcing beam is FL-150.
3. Floor slab code is S1.
4. (S2) indicates the bridgeboard.
5. C1 to C4 are floor anchor points.
6. No V1, V2 on 5F.

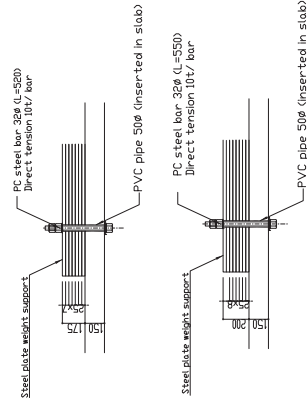
National Research Institute for Earth Science and Disaster Prevention Hyogo Earthquake Engineering Research Center Value-added Five-story Steel Frame Experiment Specimen Design Drawing No. 14/200 A3/400	13 2008.17 S-002
---	------------------------

Items with no mark are as follows:  
 1. Steel quality is SM490B.  
 2. 0 marks: SM490 material

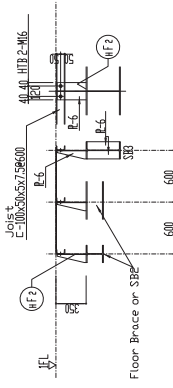
Girder Section

Code	Area	G1 (value-added plane plane)		G2 (non value-added plane)		G3 (non value-added plane)		Detail of stress haunch
		Full Section	End	Center	End	Center	End	
RF	H-400x200x94I2	H-400x200 x94I2	H-400x200 x94I2	H-400x200 x94I2	H-400x200 x94I2	H-400x200 x94I2	H-400x200 x94I2	
5F	BH-400x200x246	BH-400x200 x246	BH-400x200 x246	BH-400x200 x246	BH-400x200 x246	BH-400x200 x246	BH-400x200 x246	
4F	BH-400x200x249	BH-400x200 x249	BH-400x200 x249	BH-400x200 x249	BH-400x200 x249	BH-400x200 x249	BH-400x200 x249	
3F	H-400x200x242	H-400x200 x242	H-400x200 x242	H-400x200 x242	H-400x200 x242	H-400x200 x242	H-400x200 x242	
2F	H-400x200x222	H-400x200 x222	H-400x200 x222	H-400x200 x222	H-400x200 x222	H-400x200 x222	H-400x200 x222	
1F	OH-900x500x16x28	OH-900x500x16x28	OH-900x500x16x28	OH-900x500x16x28	OH-900x500x16x28	OH-900x500x16x28	OH-900x500x16x28	
Note	No Stress Haunch	Stress haunch installed on the 2F to 4F been flanges as shown on the right	Stress haunch installed on the 2F to 4F been flanges as shown on the right	Stress haunch installed on the 2F to 4F been flanges as shown on the right	Stress haunch installed on the 2F to 4F been flanges as shown on the right	Stress haunch installed on the 2F to 4F been flanges as shown on the right	Stress haunch installed on the 2F to 4F been flanges as shown on the right	

Roof Steel Plate Weight Attachment Guidelines



1F Hall Floor Details



Steel Column Section

Code	Area	C1		C2		C3		Note
		End, Center	End, Center	End, Center	End, Center	End, Center	End, Center	
1F	OH-900x500x16x28	OH-900x500x16x28	OH-900x500x16x28	OH-900x500x16x28	OH-900x500x16x28	OH-900x500x16x28	OH-900x500x16x28	(Note) Steel quality is BRC295.
2F	H-400x200x242	H-400x200x242	H-400x200x242	H-400x200x242	H-400x200x242	H-400x200x242	H-400x200x242	
3F	H-400x200x246	H-400x200x246	H-400x200x246	H-400x200x246	H-400x200x246	H-400x200x246	H-400x200x246	
4F	H-400x200x249	H-400x200x249	H-400x200x249	H-400x200x249	H-400x200x249	H-400x200x249	H-400x200x249	
5F	H-400x200x246	H-400x200x246	H-400x200x246	H-400x200x246	H-400x200x246	H-400x200x246	H-400x200x246	

Floor Slab Section

Code	Slab Thickness	Area	short direction reinforcement bar		long direction reinforcement bar		Note
			End, Center	End, Center	End, Center	End, Center	
S1	150	1000x1000	1000x200	1000x200	1000x200	1000x200	Flat deck is used instead of sacrifice formwork t=12
S1a	155	1000x1000	1000x200	1000x200	1000x200	1000x200	

2F to 5F Floor Anchoring					
Shape of Concrete Weight B x L x H					
Floor	C1	C2	C3	C4	Note
5F	14418x1616	3062x5045	45x30x103	50x30x102	
4F	14418x1616	3062x5045	45x30x103	50x30x102	
3F	14418x1616	3062x5045	45x30x103	50x30x102	
2F	14418x1616	3062x5045	45x30x103	50x30x102	

# Steel Joint Standards

**1 Standard High Strength Bolt Set**

Diameter	Pitch	Steel margin table for Bolt Symbol			
		S30	x 1	4	5
M16	60	35	40	18	44#
M20	60	40	50	22	44#
M22	60	48	50	24	44#

Note 1) The dimensions in steel margin apply if there are no fillet welds on the joint.  
 2) The high-strength bolts used are S305 F10T.

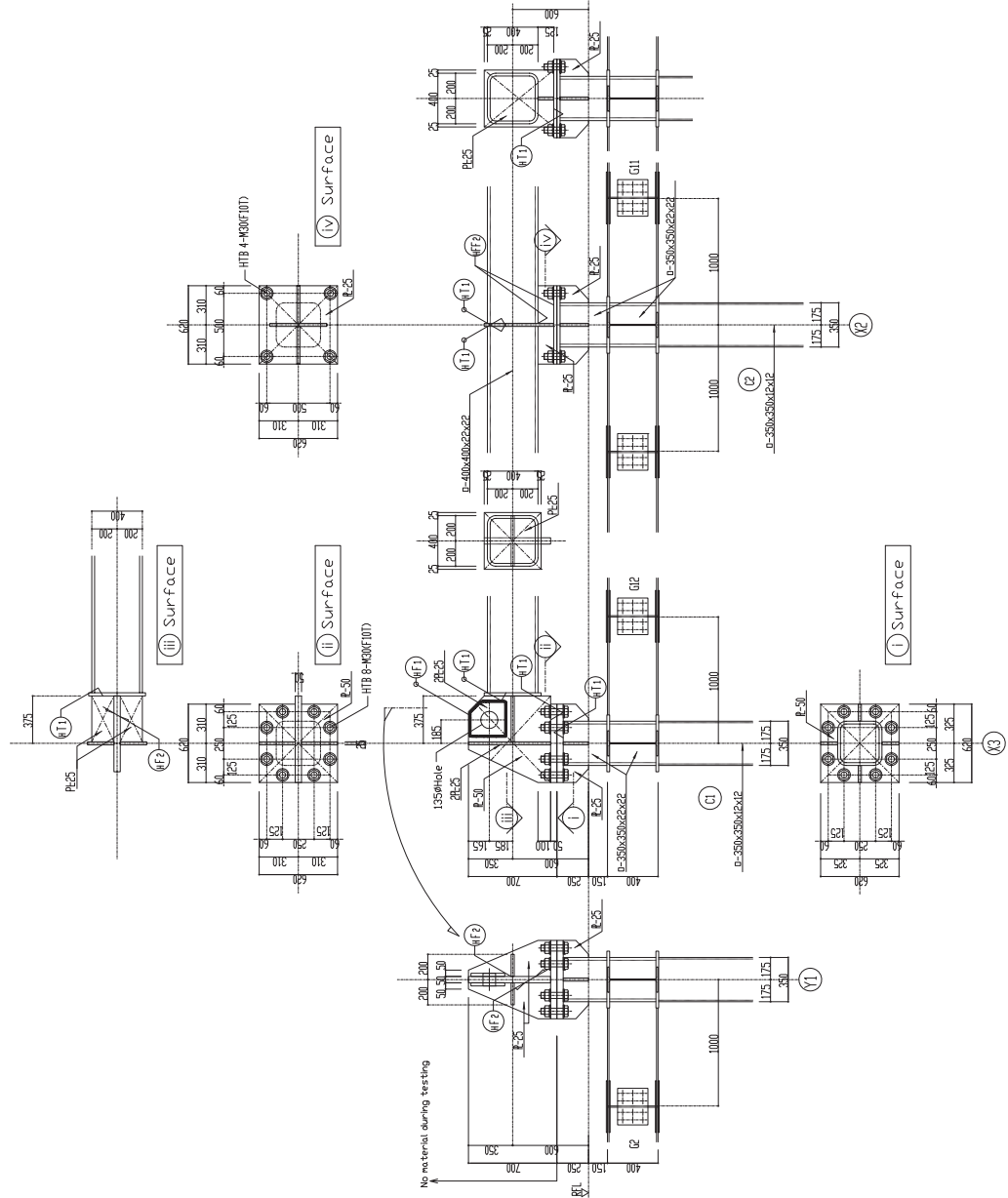
## 2 Standard Items for Joints

- 2-1 The high-strength bolts and splice plates for joints are determined by the number of the beam section.
- 2-2 The thickness of the splice plate is determined by the single side of the joint.
- 2-3 The length of the splice plate is determined by the distance between the joint plates. The length of the splice plate should be adjusted using a fillet plate.
- 2-4 The thickness of the splice plate should be the same as the base metal steel quality.
- 2-5 The thickness of the splice plate should be the same as the base metal steel quality.
- 2-6 Joints should be welded in the joint chart or the Steel Structure plans.
- 2-7 Erected plates for columns and beams that are welded should have 3 mm remaining after welding to be grinded after grinding.

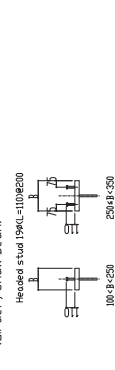
## 3 Column, Large Beam On-site Joint Positions

- 3-1 The column, large beam on-site joint positions are determined by the Steel Structure plans.
- 3-2 The column, large beam on-site joint positions are determined by the Steel Structure plans.
- 3-3 Rigid joints between the ends of small steel beams are determined by the column or the joint chart and detailed plans.

# Test Hoisting Equipment S-1/20



**1 Welding Guidelines For Steel Beam Headed Studs (Girder, Small Beam)**  
 Headed stud 19A(L)-110B(20)



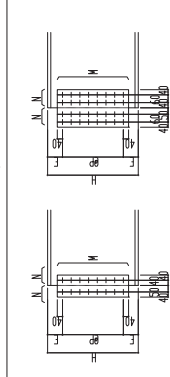
## 2 Standard Items for Joints

- 5-1 Steel columns and beam penetrating types are determined to be penetrating types if there is no special note on the detailed plans.
- 5-2 The length of the penetrating type is determined by the total column, beam flange material.
- 5-3 Thickness of material used is 6, 12, 18, 24, 30, 36, 42, 48, 54, 60, 66, 72, 78, 84, 90, 96, 102, 108, 114, 120 mm.
- 5-4 Refer to Welding Procedure Standards (WPS) and (PQR) for welded joints.

## Steel Beam Web Joint

Web Thickness	Web Height	HTB	Joint Type	Stainless Plate (SM490B)	SM113	SM114	SM115	SM116
400	9	20	6-M20	3x2	120	80	EP-9x20x240	EP-12x20x240
	12	20	8-M20	4x2	110	60	EP-12x20x240	EP-12x20x240
500	16	30	24-M20	8x3	135	90	EP-12x41x710	EP-12x41x710

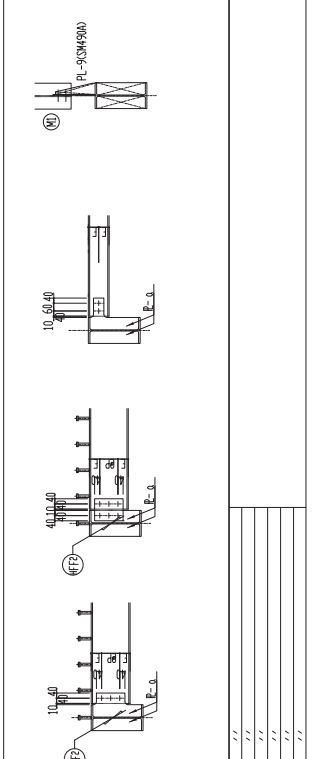
## Flange Bolt Layout



Items with no marks are as follows:  
 1. Steel quality is S3400.

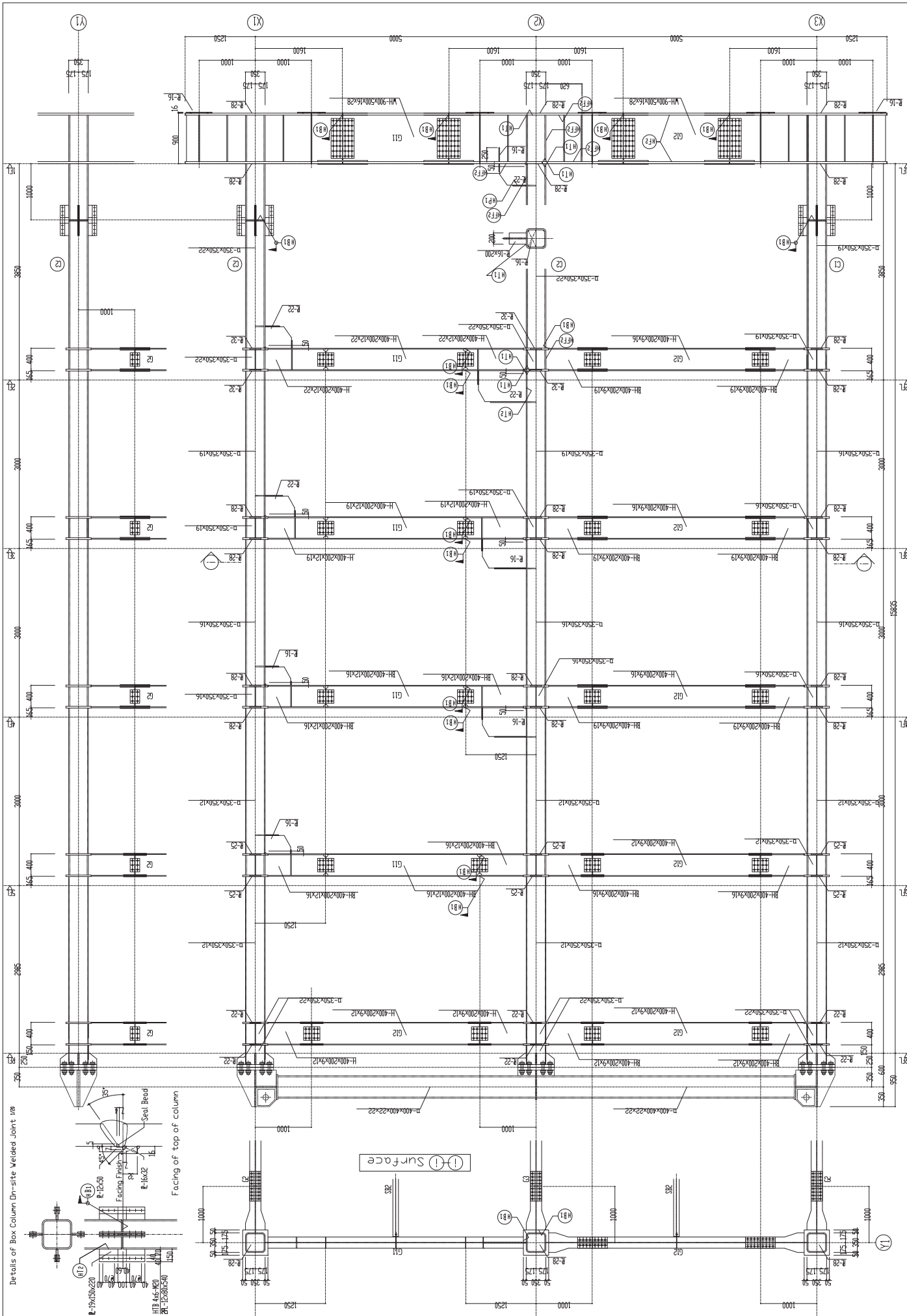
## Steel Beam, Floor Slab Section

Code	Material Section Dimensions	Joint		Web Surface Joint Standard		Note	
		HTB	M	E	Φ		
S81	H-300X306X59	A	3-M20	1x3	80	70	Splice plate (P3) E9 (EP4) E-9
S82	H-198X198X57	A	3-M20	1x2	69	60	E-9
S83	H-198X198X57	B	4-M20	1x4	70	60	2x-9x70x336 E-9 Refer to details
S84	H-250X250X71	A	4-M20	1x4	85	60	E-9
S85	L-100X100X57.5	C	2-M16	2x1	40	-	E-6 No studs, bolts SM99H
M1	H-200X200X84.2	D	4-M20	2x2	70	60	E-9

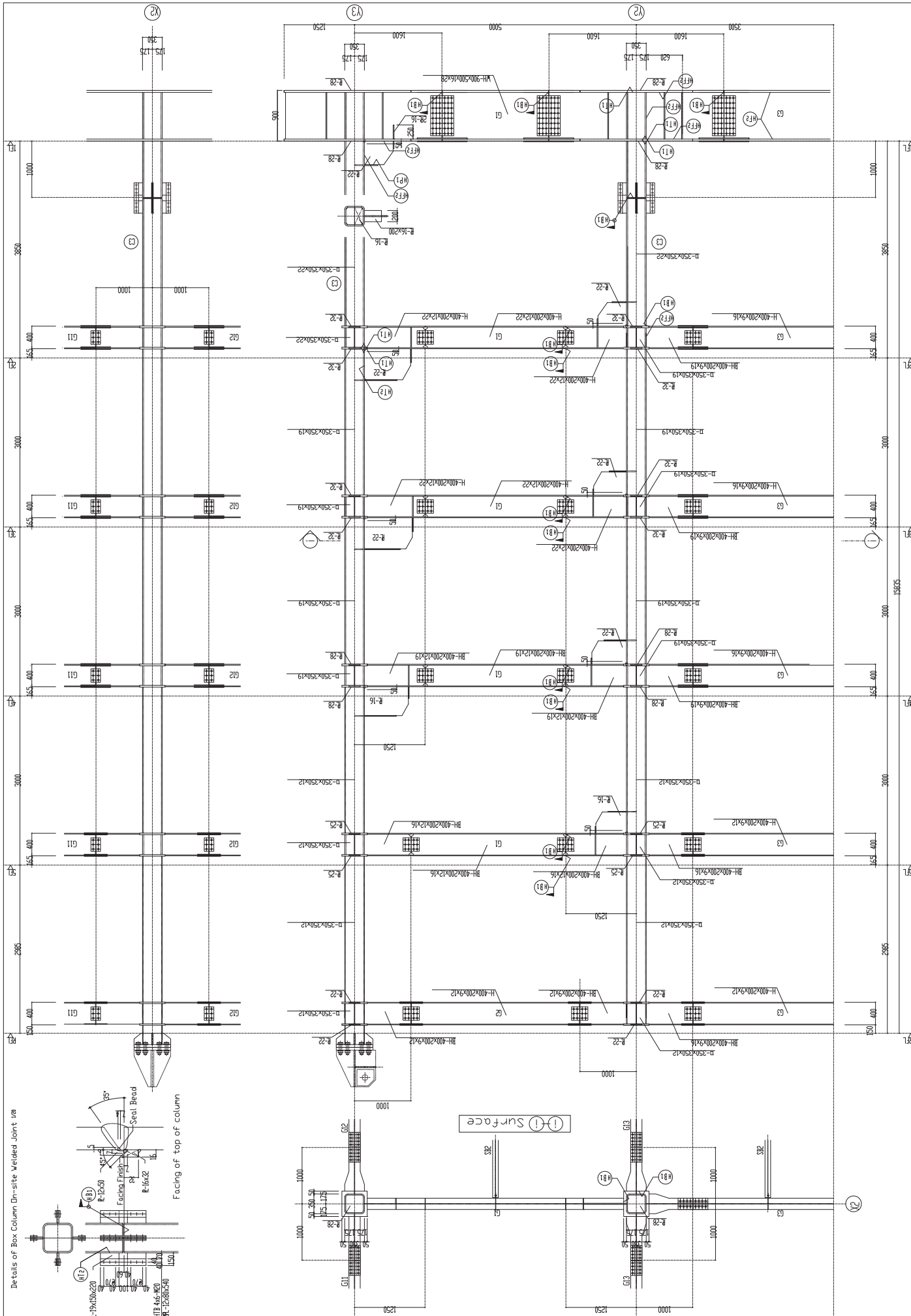








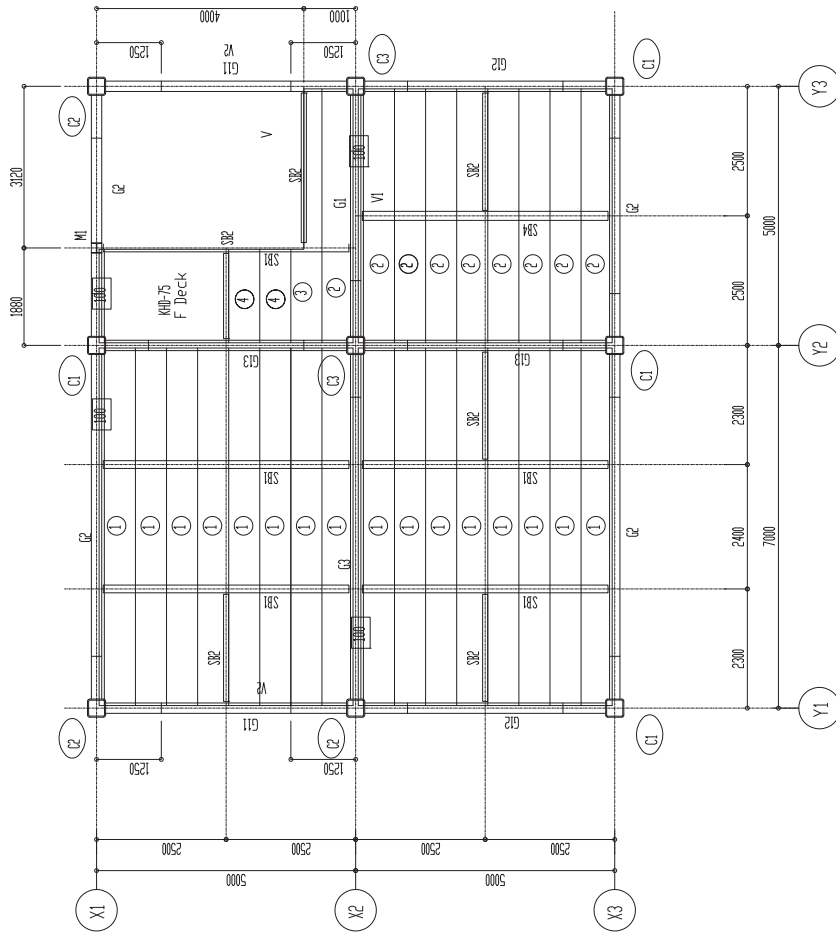
Revised	17	2008.11.7	S-106
17	2008.11.7	S-106	
National Research Institute for Earth Science and Disaster Prevention Hyogo Earthquake Engineering Research Center Value-added Five-story Steel Frame Experiment Specimen Design Drawing			
Steel Structure (1)			
A17/30			
A3/60			



Revised	18	National Research Institute for Earth Science and Disaster Prevention Hyogo Earthquake Engineering Research Center Value-added IT Network Steel Frame Experiment Specimen Design Drawing
	2008.11.7	
	AV/20	Steel Structure (2)
	A3/60	





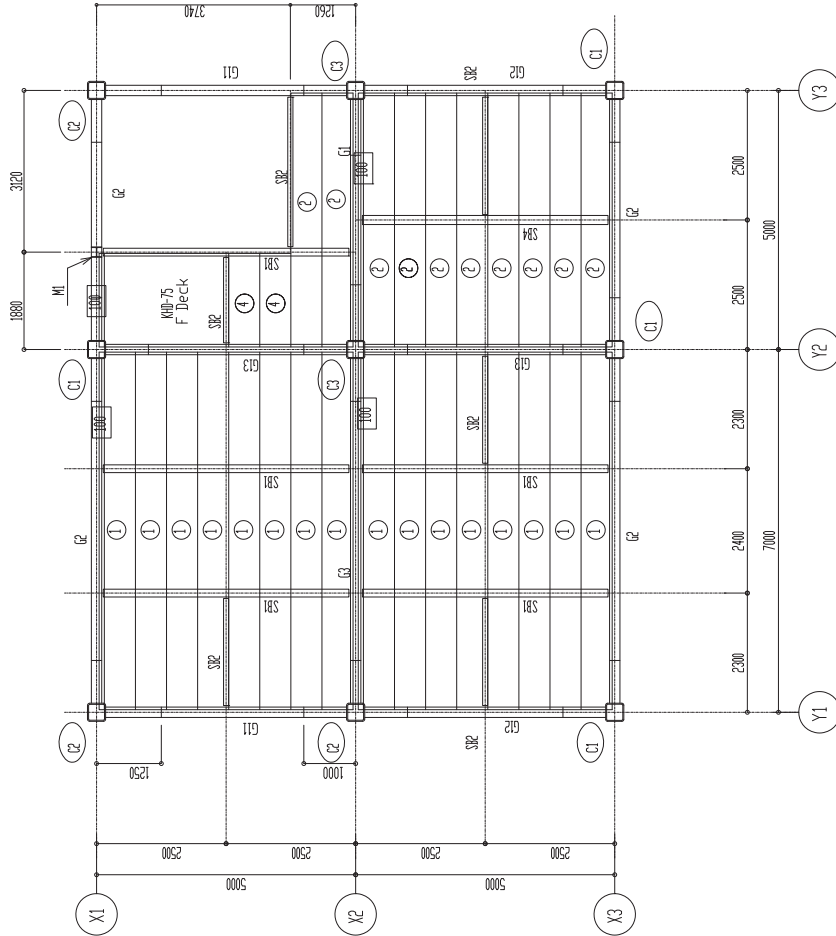


**2F, 3F, 4F Beam Structure**

Items with no marks are as follows:

1. Ceiling beam is FL-165.
2. Bracket length is 1000 from center of pillar.
3. Detail and placement of girder.

end haunch is based on 14CS-0032



**5F Beam Structure**

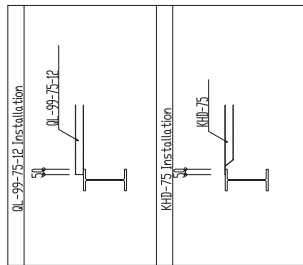
Items with no marks are as follows:

1. Ceiling beam is FL-165.
2. Bracket length is 1000 from center of pillar.
3. Detail and placement of girder.

end haunch is based on 14CS-0032

2F, 3F, 4F, 5F Deck Allocation Quantity

Code	Length	No.	Q Deck Allocation Quantity		Note
			Q1_99-75-12	Q1_99-75-12	
①	4900	64	16	48	3E
②	4900	37	9	28	3E
③	4900	3	1	2	U
④	1805	24	6	18	U
⑤	6500	8	2	6	2
⑥	1000	4900	4	4500	1
⑦	1000	1805	4	1405	1







# APPENDIX B

## DRAWINGS AND SPECIFICATIONS FOR LEAD-RUBBER BEARINGS AND CROSS LINEAR BEARINGS

Building Isolated with Hybrid Lead-Rubber Isolation System

Contributed by Dynamic Isolation Systems, Inc. and Aseismic Devices Co., Ltd.

Developed for NEES/E-Defense Collaborative Test Program on Innovative Isolation Systems, 2011-2012

### List of Documents

### Contributor

Type A Isolator (LRB Drawing)

Dynamic Isolation Systems, Inc.

Isolator Design Calculations

Dynamic Isolation Systems, Inc.

CLB 250 (CLB Drawing)

Aseismic Devices Co., Ltd.

CLB Specification

Aseismic Devices Co., Ltd.

APPR	REV	DATE	DESCRIPTION
AK	A	5/7/11	ISSUED FOR INFORMATION
AK	B	6/7/11	GEN. REV. - REISSUED FOR INFORMATION
TN	0	6/10/11	REV. DWG. # - ISSUED FOR APPROVAL
MG	1	6/10/11	ISSUED FOR FABRICATION
AK	2	6/24/11	REV. EXT. ENDP. - REISSUED FOR APPROVAL
AK	3	6/29/11	REV. EXT. ENDP. - REISSUED FOR APPROVAL

**NOTES:**

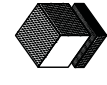
1. MATERIALS:  
ALL STEEL PL's ASTM A36.  
ALL STEEL SHIMS ASTM A1011 GR. 36.  
INTERNAL RUBBER IS DIS TYPE T.  
EXTERNAL RUBBER IS DIS TYPE E100S.  
DIMENSIONS ARE IN UNITS NOTED.  
DIMENSIONS IN BRACKETS ARE EQUIVALENTS FOR REFERENCE ONLY.
2. DO NOT SCALE THIS DRAWING.
3. FINISH: TO BE DETERMINED.

ISOLATOR DIMENSION TABLE	
TYPE A ISOLATOR	C698.5/459.8/101.6
QUANTITY	4+0
TARGET	TOL./ALLOWABLE
A Isolator Diameter	698.5mm ± 2mm ± 4mm
B Overall Isolator Ht.	459.8mm ± 4mm ± 6.35mm
C Lead Core Diameter	101.6mm ± 2mm
D Parallelity	1/300 1/200
Estimated Weight	1,864 lb./847 kg
Measurements are taken at 20°C.	

**GENERAL TOLERANCES:**

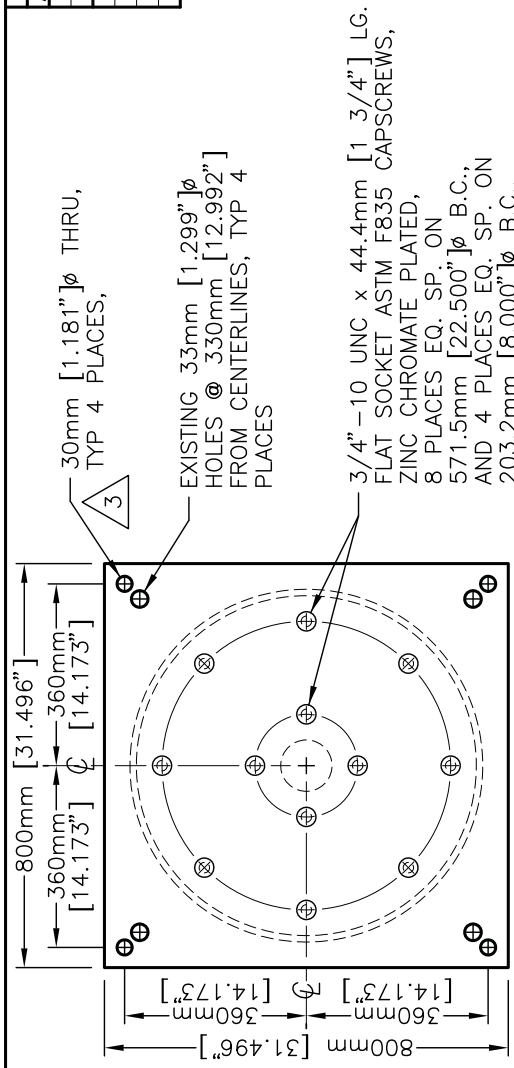
1. ENDP. OVERALL DIMENSIONS: ± 3.18mm.
2. BOLT HOLE LOCATIONS: ± 0.8mm.
3. PLATE THICKNESS: ± 1.6mm.
4. PLATE FLATNESS: ± 3.18mm.

THIS DRAWING IS THE PROPERTY OF DYNAMIC ISOLATION SYSTEMS, INC.  
INFORMATION AND KNOW-HOW HEREON ARE CONFIDENTIAL AND MAY NOT BE USED, REPRODUCED OR REVEALED TO OTHERS  
EXCEPT IN ACCORDANCE WITH THE CONTRACT OR OTHER WRITTEN PERMISSION OF DYNAMIC ISOLATION SYSTEMS, INC.  
ANY REPRODUCTIONS IN WHOLE OR IN PART SHALL INCLUDE THIS NOTATION.

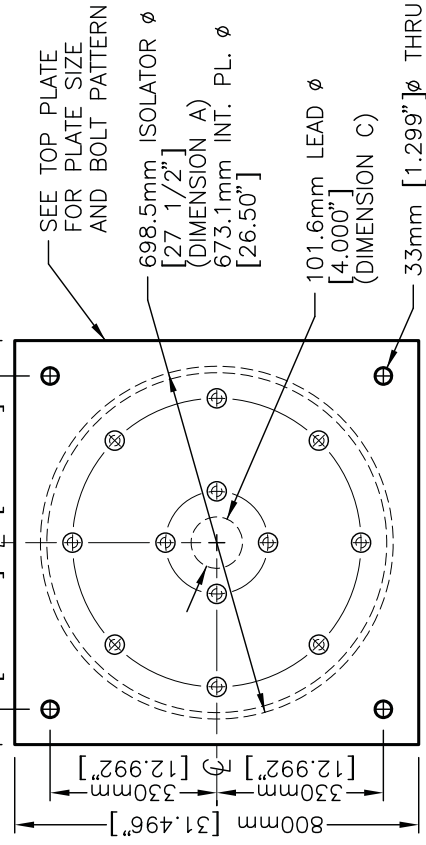
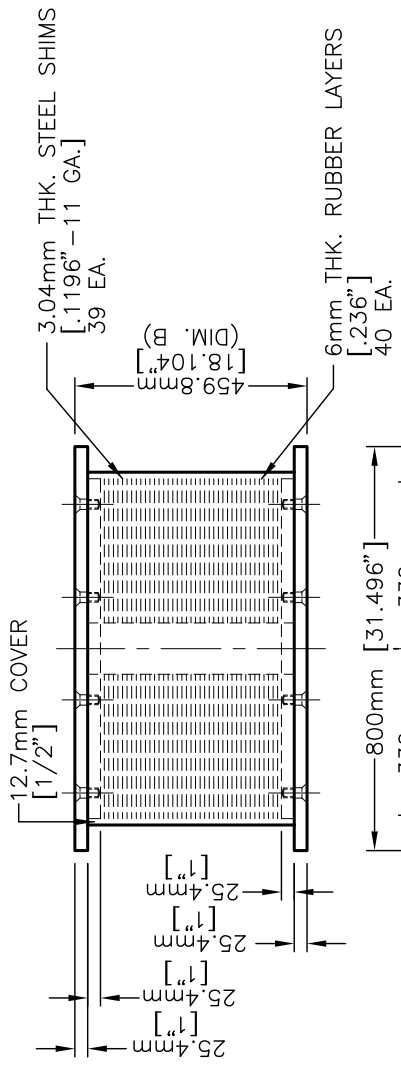


**DYNAMIC ISOLATION SYSTEMS**  
DIS SEISMIC ISOLATORS  
NRC Project at EDefense  
Type A Isolator  
**DWG. NO. 152-100** SHEET: 1 of 1  
ORIG: 5/6/11

DESIGNER APPROVAL	AK
PROJECT MANAGER APPROVAL	-
PLANT MANAGER APPROVAL	MG



TOP VIEW



BOTTOM VIEW

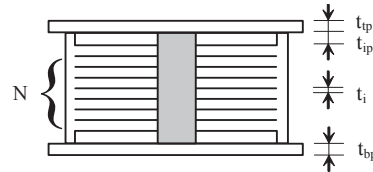


### Isolator Design Calculations

**Job No. :** \_\_\_\_\_ **Job :** EDefense - Final **By :** AK **Date :** June 9, 2011  
**Client :** \_\_\_\_\_ **Subject :** Seismic Isolator Calculations, LRB **Checked :** \_\_\_\_\_ **Date :** \_\_\_\_\_

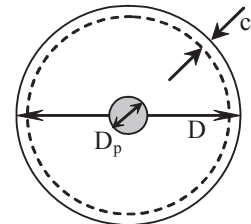
**Rubber Properties**

Rubber Shear Modulus  $G := 0.060 \cdot \text{ksi}$   $G = 0.414 \text{ MPa}$   
 Rubber's Elongation-at-break  $\epsilon_u := 5.5$



**Bearing Dimensions**

Overall Diameter  $D := 27.5 \cdot \text{in}$   $D = 698.5 \text{ mm}$   
 Number of Rubber Layers  $N := 40$   
 Lead Diameter  $D_p := 4.0 \cdot \text{in}$   $D_p = 101.6 \text{ mm}$   
 Shim Thickness  $t_s := 0.1196 \cdot \text{in}$   $t_s = 3 \text{ mm}$   
 Layer Thickness  $t_i := 0.236 \cdot \text{in}$   $t_i = 6 \text{ mm}$   
 Side Cover Rubber Thickness  $c_s := 0.5 \cdot \text{in}$   $c_s = 12.7 \text{ mm}$   
 Top Mounting Plate Thickness  $t_{tp} := 1 \cdot \text{in}$   $t_{tp} = 25.4 \text{ mm}$   
 Bottom Mounting Plate Thickness  $t_{bp} := 1 \cdot \text{in}$   $t_{bp} = 25.4 \text{ mm}$   
 Internal Plate Thickness  $t_{ip} := 1 \cdot \text{in}$   $t_{ip} = 25.4 \text{ mm}$



Isolator Height  $H_{isol} := N \cdot t_i + (N - 1) \cdot t_s + t_{bp} + t_{tp} + 2 \cdot t_{ip}$   $H_{isol} = 18.104 \text{ in}$   $H_{isol} = 460 \text{ mm}$

800 mm SQ Ext plates; 4 x 1"  $\phi$  Ext holes, 8 x 0.75"  $\phi$  internal connection

**Design Displacement**

Design Displacement  $D_D := 300 \cdot \text{mm}$  Properties are checked at this displacement.  
 Maximum Displacement  $D_{TM} := 600 \cdot \text{mm}$  Capacity is checked at this displacement.

**Project Loads**

Rotation applied on the bearing  $\theta_0 := 0.0$   $\theta_{DTM} := 0.0$  No rotations are applied on the isolators  
 Load at undeformed condition  $P_{zero} := 50 \cdot t$  Assumed  
 Load at maximum displacement  $P_{DTM} := 50 \cdot t$

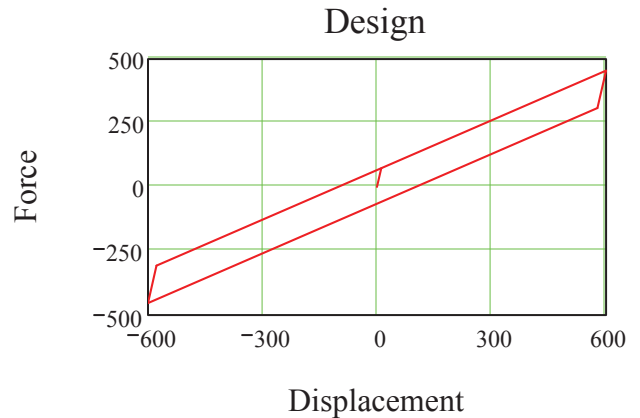
**Summary**

**Isolator Dimensions**

Overall Diameter	D = 27.5 in	D = 698.5 mm
Number of Rubber Layers	N = 40	N = 40
Lead Diameter	D <sub>p</sub> = 4 in	D <sub>p</sub> = 101.6 mm
Shim Thickness	t <sub>s</sub> = 0.12 in	t <sub>s</sub> = 3 mm
Layer Thickness	t <sub>i</sub> = 0.236 in	t <sub>i</sub> = 6 mm
Side Cover Rubber Thickness	c <sub>s</sub> = 0.5 in	c <sub>s</sub> = 12.7 mm
Top Mounting Plate Thickness	t <sub>tp</sub> = 1 in	t <sub>tp</sub> = 25.4 mm
Bottom Mounting Plate Thickness	t <sub>bp</sub> = 1 in	t <sub>bp</sub> = 25.4 mm
Internal Plate Thickness	t <sub>ip</sub> = 1 in	t <sub>ip</sub> = 25.4 mm
Isolator Overall Height	H <sub>isol</sub> = 18.104 in	H <sub>isol</sub> = 459.9 mm

**Isolator Properties**

Design Maximum Displacement	D <sub>D</sub> = 300 mm
Maximum Corner Displacement	D <sub>TM</sub> = 600 mm
Yielded Stiffness	K <sub>d</sub> = 0.65 $\frac{\text{kN}}{\text{mm}}$
Elastic Stiffness	K <sub>e</sub> = 6.5 $\frac{\text{kN}}{\text{mm}}$
Characteristic Strength	Q <sub>d</sub> = 65.7 kN
Yield Force	F <sub>y</sub> = 73 kN
Yield Displacement	Δ <sub>y</sub> = 11.28 mm
Vertical Stiffness	K <sub>v</sub> = 1500 $\frac{\text{kN}}{\text{mm}}$
Shear Force	F <sub>max</sub> (D <sub>D</sub> ) = 259.8 kN
Effective Stiffness	K <sub>eff</sub> (D <sub>D</sub> ) = 0.87 $\frac{\text{kN}}{\text{mm}}$
Energy Dissipated per Cycle	EDC(D <sub>D</sub> ) = 76 kN·m



Equivalent Viscous Damping Ratio at Design Displacement	$\beta(D_D) = 0.155$	$\beta_m(D_{TM}) = 0.094$
Shear Strain in Rubber at Design Displacement	$\gamma(D_D) = 1.25$	
Shear Strain in Rubber at Maximum Displacement	$\gamma(D_{TM}) = 2.5$	
Allowable Load at Undeformed Condition (with a FS of 3.0)	Pallowable <sub>zero</sub> = 4197 kN	
Allowable Load at Maximum Displacement	Pallowable <sub>D<sub>TM</sub></sub> = 532 kN	



**Summary**

**Isolator Dimensions**

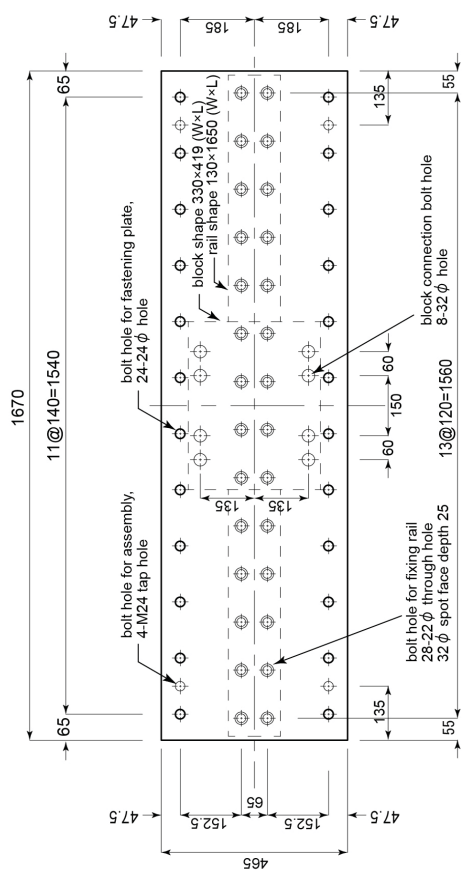
Overall Diameter	$D = 27.5 \text{ in}$	$D = 698.5 \text{ mm}$
Number of Rubber Layers	$N = 40$	$N = 40$
Lead Diameter	$D_p = 4 \text{ in}$	$D_p = 101.6 \text{ mm}$
Shim Thickness	$t_s = 0.12 \text{ in}$	$t_s = 3 \text{ mm}$
Layer Thickness	$t_l = 0.236 \text{ in}$	$t_l = 6 \text{ mm}$
Side Cover Rubber Thickness	$c_s = 0.5 \text{ in}$	$c_s = 12.7 \text{ mm}$
Isolator Overall Height	$H_{isol} = 18.104 \text{ in}$	$H_{isol} = 459.9 \text{ mm}$
Yielded Stiffness	$K_d = 3.7 \frac{\text{kip}}{\text{in}}$	$K_d = 0.6 \frac{\text{kN}}{\text{mm}}$
Elastic Stiffness	$K_e = 37 \frac{\text{kip}}{\text{in}}$	$K_e = 6.5 \frac{\text{kN}}{\text{mm}}$
Characteristic Strength	$Q_d = 14.8 \text{ kip}$	$Q_d = 65.7 \text{ kN}$
Yield Force	$F_y = 16.4 \text{ kip}$	$F_y = 73 \text{ kN}$
Yield Displacement	$\Delta_y = 0.44 \text{ in}$	$\Delta_y = 11.28 \text{ mm}$
Vertical Stiffness	$K_v = 8566 \frac{\text{kip}}{\text{in}}$	$K_v = 1500 \frac{\text{kN}}{\text{mm}}$
Undisplaced condition	$Pallowable_{zero} = 4197 \text{ kN}$	FS of 3.0

**Displacement**

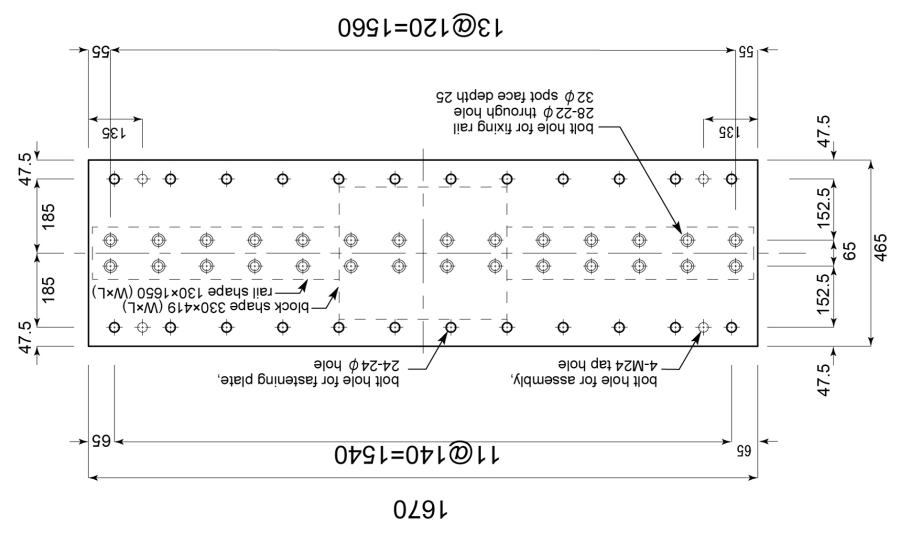
- $D_{TM} := 300 \text{ mm}$
- $D_{TM} := 350 \text{ mm}$
- $D_{TM} := 400 \text{ mm}$
- $D_{TM} := 450 \text{ mm}$
- $D_{TM} := 475 \text{ mm}$
- $D_{TM} := 500 \text{ mm}$
- $D_{TM} := 525 \text{ mm}$
- $D_{TM} := 550 \text{ mm}$
- $D_{TM} := 575 \text{ mm}$
- $D_{TM} := 600 \text{ mm}$

**Minimum of buckling, elastomer limit or a stress limit**

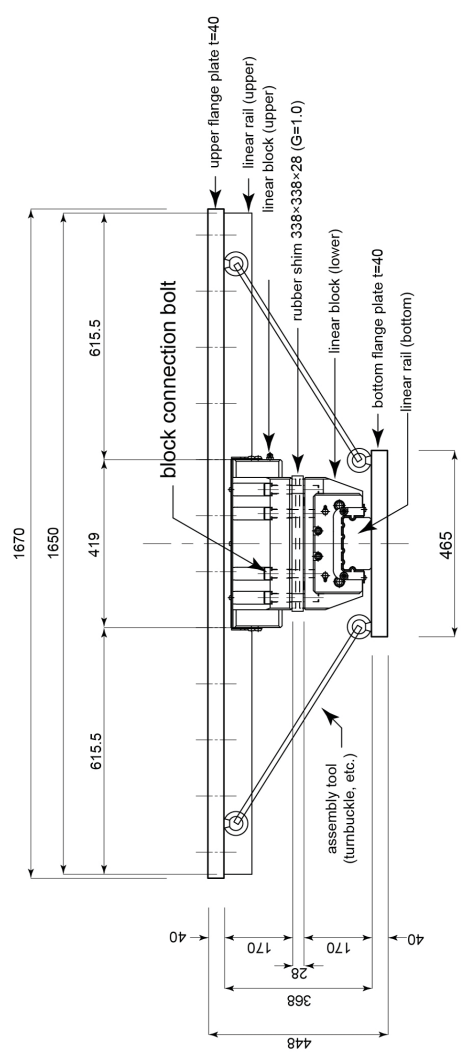
- $Pallowable(D_{TM}) = 4795 \text{ kN}$
- $Pallowable(D_{TM}) = 4648 \text{ kN}$
- $Pallowable(D_{TM}) = 3659 \text{ kN}$
- $Pallowable(D_{TM}) = 2736 \text{ kN}$
- $Pallowable(D_{TM}) = 2304 \text{ kN}$
- $Pallowable(D_{TM}) = 1893 \text{ kN}$
- $Pallowable(D_{TM}) = 1507 \text{ kN}$
- $Pallowable(D_{TM}) = 1149 \text{ kN}$
- $Pallowable(D_{TM}) = 822 \text{ kN}$
- $Pallowable(D_{TM}) = 532 \text{ kN}$



CLB250 Upper Flange Plate



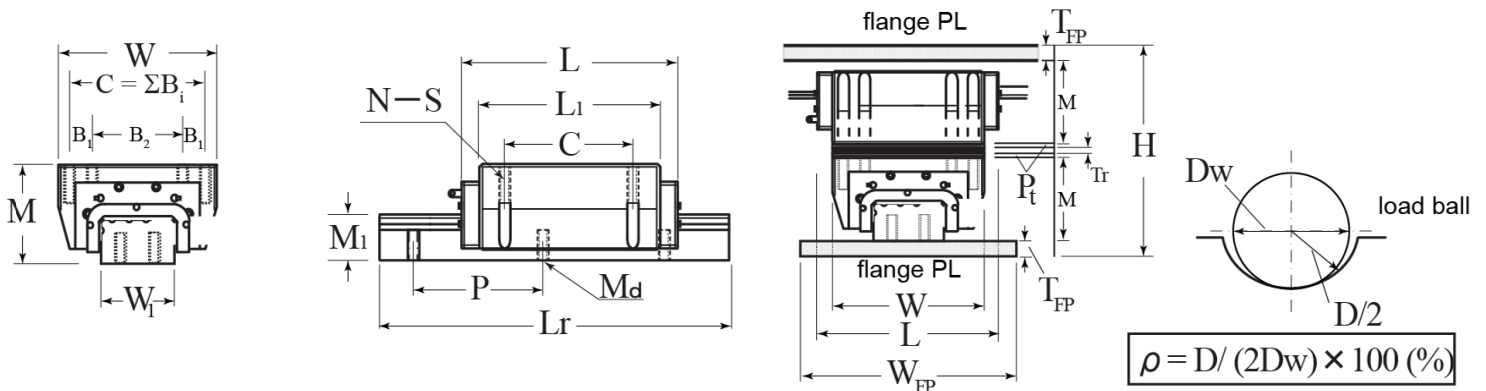
CLB250 Bottom Flange Plate



CLB250 Entire Assembly Cross Section

## Device Dimensions and Loading Properties

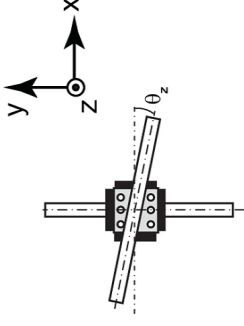
Basic Model Number		CLB099	CLB133	CLB250	CLB385	CLB500	CLB780
Standard Load (kN)		972	1300	2451	3775	4903	7649
Static Load (kN)	Compression	972	1300	2451	3775	4903	7649
	Tension	687	919	833	1324	1716	2649
Short-term Allowable Load (kN)	Compression	1944	2600	4902	7550	9806	15298
	Tension	188	257	410	481	588	880
Ultimate Strength (kN)	Compression	3246	4342	8186	12609	16376	25548
	Tension	282	385	615	722	882	1320
Vertical Stiffnes (kN/mm)	Compression	2106	2242	3471	5171	6120	7957
	Tension	262	282	245	315	388	468
External Dimensions (mm)	M	90	105	170	210	235	290
	W	215	260	330	410	465	560
	L	300.4	322.8	419	519	584	722
	H	264	308	448	538	599	730
Block Dimensions (mm)	$\Sigma B_i$	2×92.5	2×110	2×60+150	2×80+180	2×90+200	2×110+250
	C	185	220	270	340	380	470
	N-S	6-M16	6-M18	8-M20	8-M24	8-M27	8-M30
Rail Dimensions (mm)	W <sub>1</sub>	85	100	130	160	180	230
	M <sub>1</sub>	48	57	70	85	98	120
	M <sub>d</sub>	M22	M24	2×M20	2×M24	2×M27	2×M30
	P	90	105	120	150	150	200
Load Ball	D <sub>w</sub> (mm)	11.113	13.494	16.669	20.638	23.813	30.163
	Number	21×(2×2)	20×(2×2)	19×(4×2)	19×(4×2)	19×(4×2)	18×(4×2)
	$\rho$ (%)	51	51	52	52	52	52
Rubber Shim	P <sub>t</sub> (mm)	7	9	9	9	9	9
	G (N/mm <sup>2</sup> )	0.8	1.0	1.0	1.0	1.0	1.2
	T <sub>r</sub> (mm)	6	8	10	10	11	12
Flange PL (mm)	W <sub>FP</sub> ×T <sub>FP</sub>	425×32	465×36	465×40	555×45	630×50	740×60
	Bolt & Pitch	2-M20@125	2-M22@150	2-M22@140	2-M24@150	2-M27@150	2-M30@200



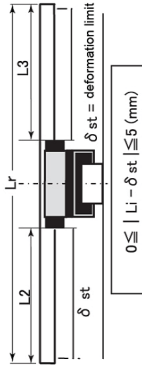
### 8.3 Installation tolerances for seismic isolation devices

#### Standard values for installation tolerance

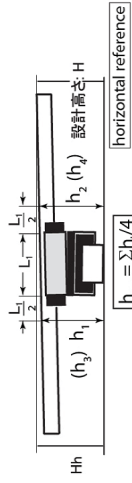
Item	Standard Tolerance	Remarks
rust, scratch, dirt	none	visual inspection
block movement (play)	$\leq \pm 5 \text{ mm}$	
rail incline angle $\theta_x$	$\theta_x \leq 1/500 \text{ rad}$	(-6.3, 6.4) : limit angle : 10/1000 rad
rail orthogonal tilt angle $\theta_y$	$\theta_y \leq 1/500 \text{ rad}$	(-6.5, 6.6) : limit angle : 10/1000 rad
rail twist angle $\theta_z$	$\theta_z \leq 1/300 \text{ rad}$	(-6.7, 6.8) : torsion limit : 18/1000 rad
構造芯平行ずれ、振れずれ 設置レベル差	$\pm 5\text{mm}$ 以下、 $\theta_x, \theta_y, \theta_z \leq 1/300\text{rad}$ $\Delta h \leq \pm 0.01H$ , $\Delta h \leq 1.5\text{mm}$	to ensure consistency with analysis $\Delta h$ : deviation from design level, construction accuracy
based on level and JIS1 class measure		



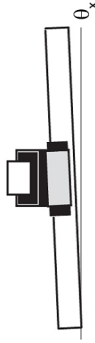
Definition of rail twist angle



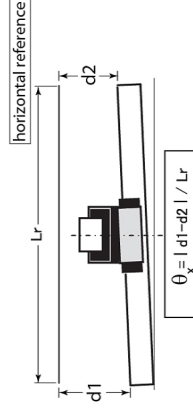
Block position shift measurement method



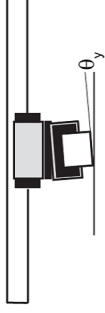
Installation level difference measurement method



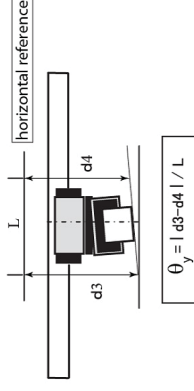
Definition of rail incline angle



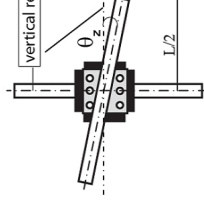
Rail incline angle measurement method



Definition of rail orthogonal tilt angle



Rail orthogonal tilt angle measurement method



$$\theta_z = 2d_r / L \text{ (rad)}$$

Rail twist angle measurement

### 8.4 Seismic design criteria for material rigidity and strength

#### Reference value for seismic design

Item	Reference Tolerance	Remarks (inspection procedure, acceptance criteria)
Tilt angle	Rail incline angle $\theta_x$	$\theta_x \leq 8/1000 \text{ rad}$ Limit angle : 10/1000 rad (-6.3, 6.4), installation error
	Rail orthogonal tilt angle $\theta_y$	$\theta_y \leq 8/1000 \text{ rad}$ Limit angle : 10/1000 rad (-6.5, 6.6), installation error
	Rail twist angle $\theta_z$	$\theta_z \leq 14/1000 \text{ rad}$ Torsion limit: 18/1000 rad (-6.7, 6.8) at static allowable moment ( $M_0$ ) 18/1000rad (CLB250)

# APPENDIX C

## DRAWINGS FOR LOAD CELL ASSEMBLIES AND CONNECTION TO THE SIMULATOR PLATFORM

Building Isolated with Hybrid Lead-Rubber Isolation System

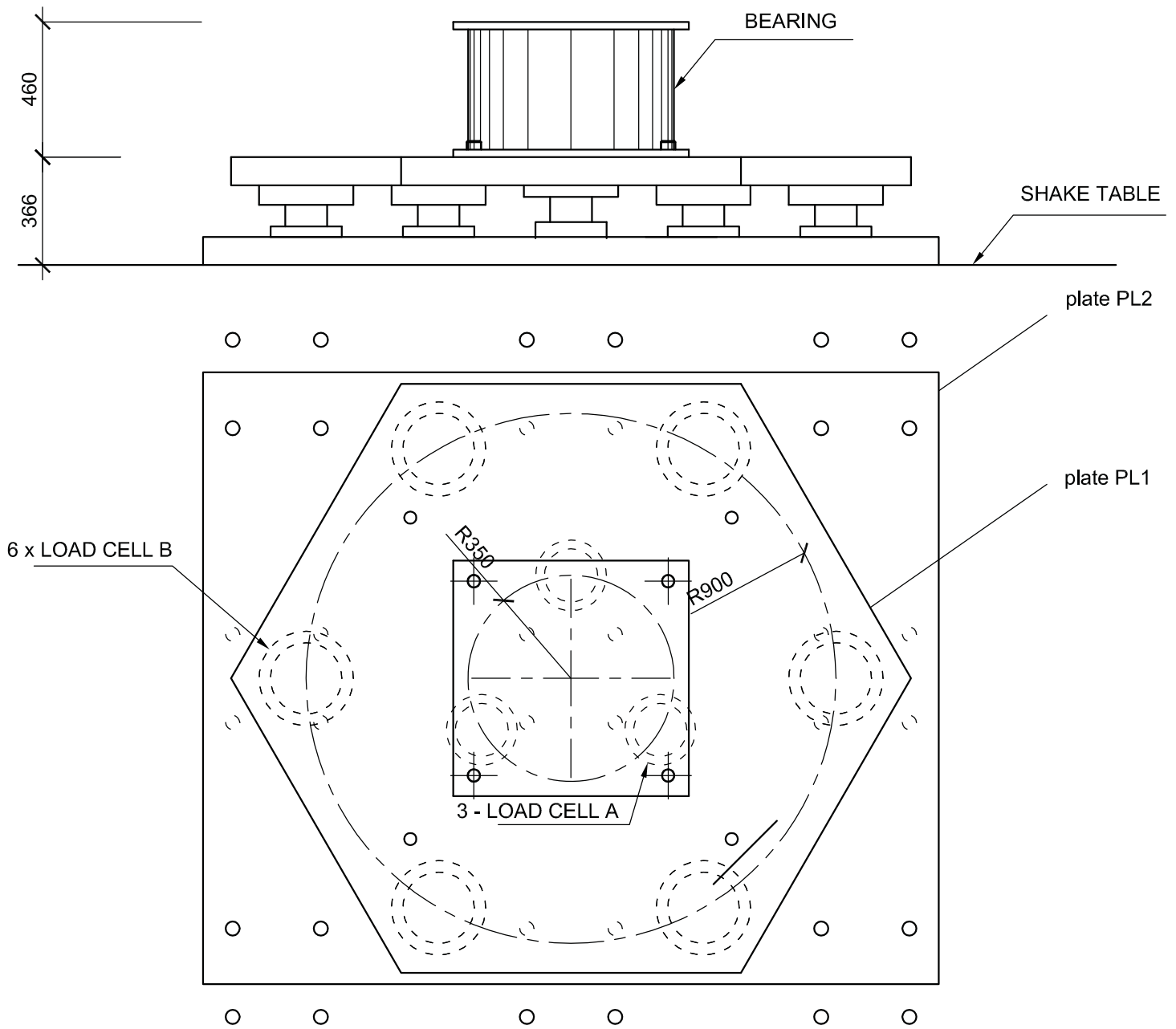
Developed by NEES TIPS Project for NEES/E-Defense Collaborative Test Program on

Innovative Isolation Systems, 2011-2012

Lead Contributor: Nhan D. Dao

### Connection Drawings

B-001	Connecting Plate PL1 – East Column
B-002	Connecting Plate PL1 – East Column
B-003	Connecting Plate PL2 – East Column and Placer
B-004	Connecting Plate PL2 – North, South, West Columns
B-005	Connecting Plate PL2 – North, South, West Columns
B-006	Connecting Plate PL2 – North, South, West Columns
B-007	Elevation of Load Cell Connection
B-008	Connecting Bearing to Structure



**BEARING CONNECTION - EAST COLUMN (1 UNIT)**

SCALE: 1/20



UNIVERSITY OF NEVADA, RENO  
1664 N. Virginia St, Reno, NV 89557

EXPERIMENTAL EVALUATION OF  
AN INNOVATIVE ISOLATION SYSTEM  
FOR A LIGHTWEIGHT STEEL MOMENT FRAME BUILDING

CONNECTING PLATE PL1 - EAST COLUMN

Drawing: B-001  
Scale: As Shown  
Drawn by: N. D. Dao  
Checked by:  
Date: 28 Apr 2011

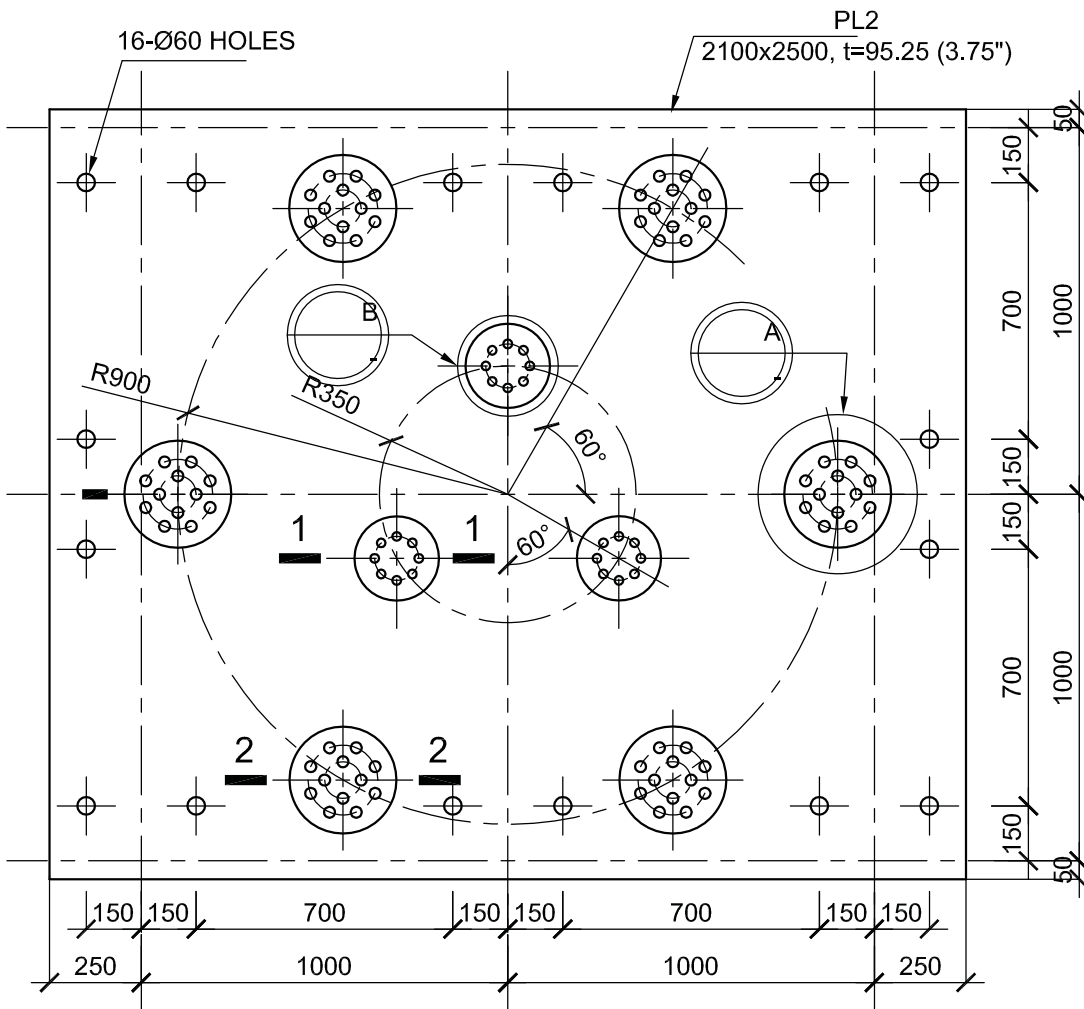
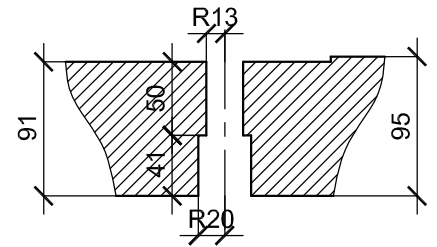


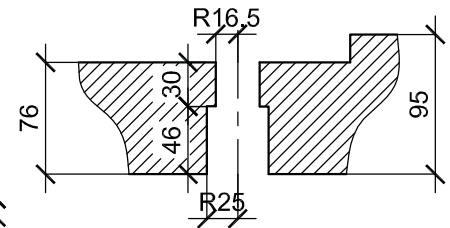
**PLATE PL2 - EAST COLUMN (1 UNIT)**

SCALE: 1/20



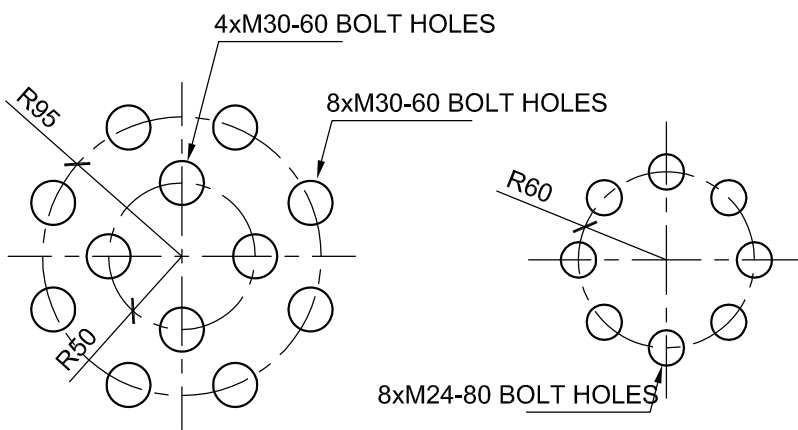
**M24-80 BOLT HOLE**

SCALE: 1/5



**M30-60 BOLT HOLE**

SCALE: 1/5

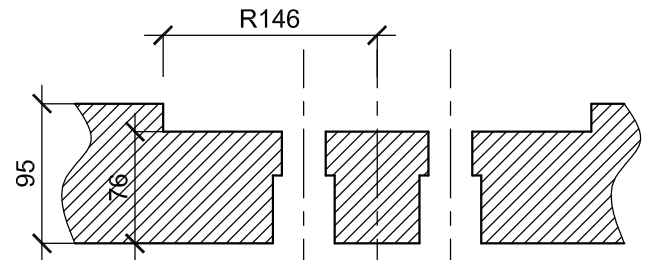


**DETAIL A**

SCALE: 1/5

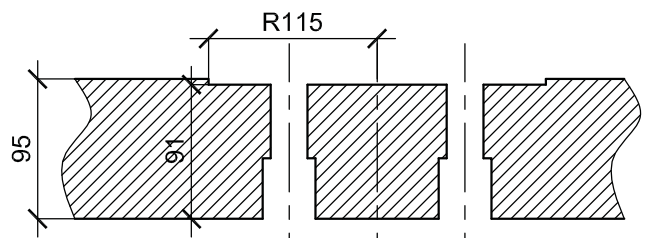
**DETAIL B**

SCALE: 1/5



**SECTION 2-2**

SCALE: 1/5



**SECTION 1-1**

SCALE: 1/5

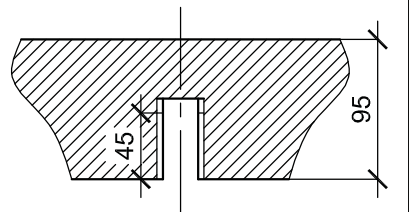
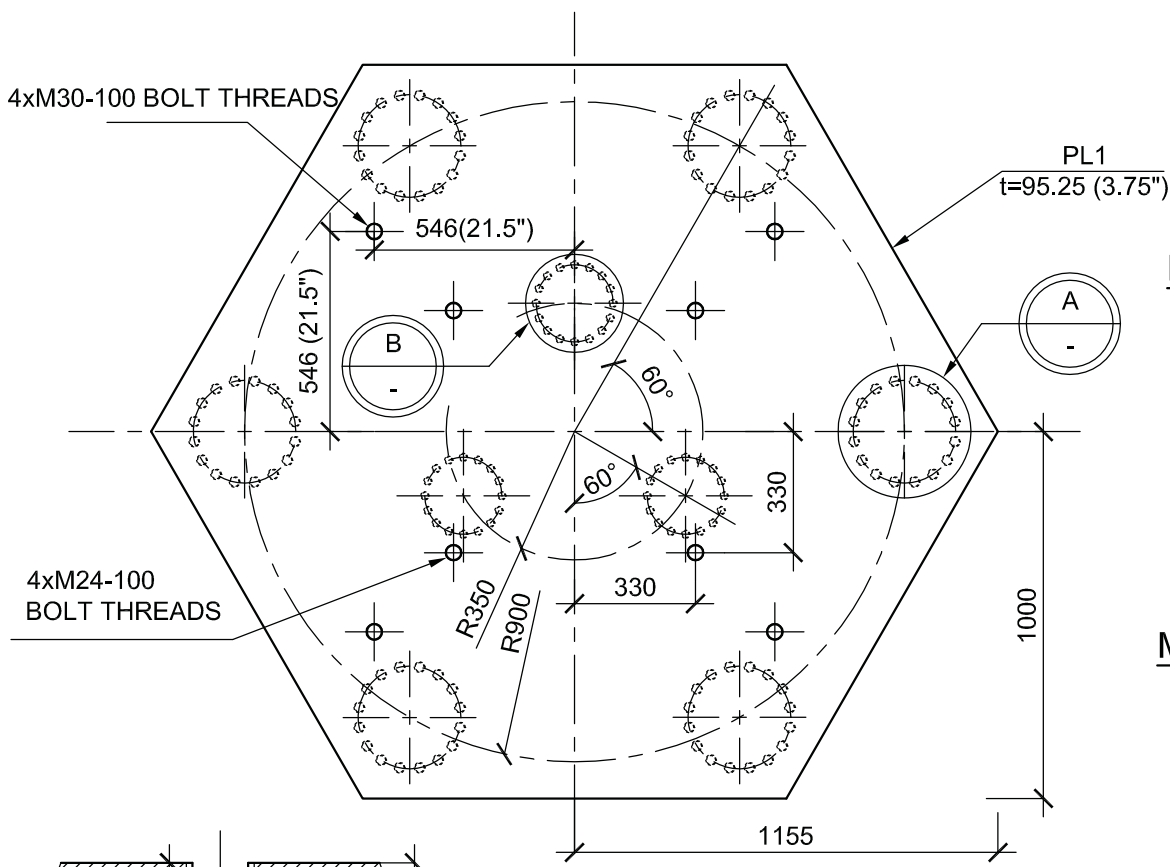


UNIVERSITY OF NEVADA, RENO  
1664 N. Virginia St, Reno, NV 89557

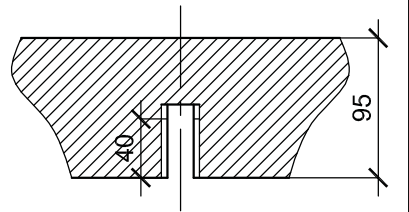
EXPERIMENTAL EVALUATION OF  
AN INNOVATIVE ISOLATION SYSTEM  
FOR A LIGHTWEIGHT STEEL MOMENT FRAME BUILDING

CONNECTING PLATE PL2 - EAST COLUMN  
And PLACER

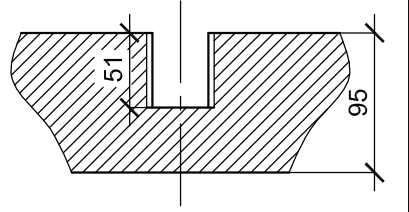
Drawing: B-003  
Scale: As Shown  
Drawn by: N. D. Dao  
Checked by:  
Date: 28 Apr 2011



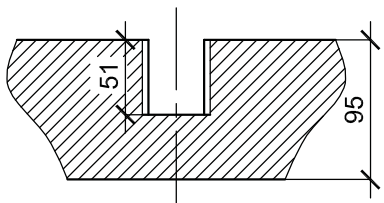
**M24-100 BOLT THREAD**  
SCALE: 1/5



**M18-80 BOLT THREAD**  
SCALE: 1/5

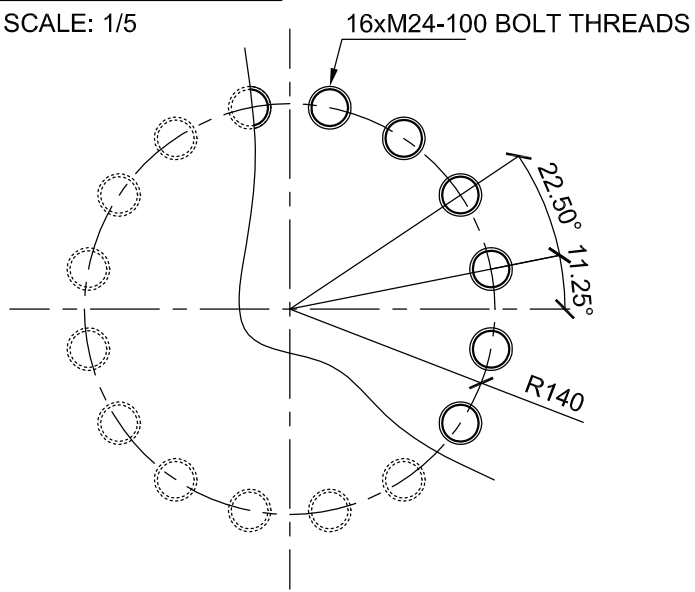


**M30-100 BOLT THREAD**  
SCALE: 1/5

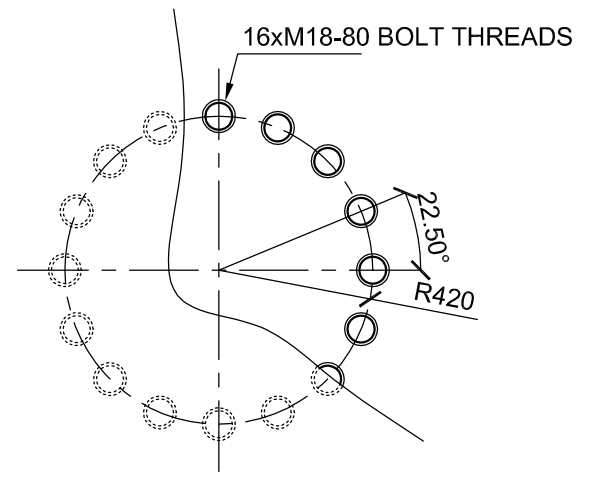


**M24-100 BOLT THREAD**  
SCALE: 1/5

**PLATE PL1 - EAST COLUMN (1 UNIT)**  
SCALE: 1/20

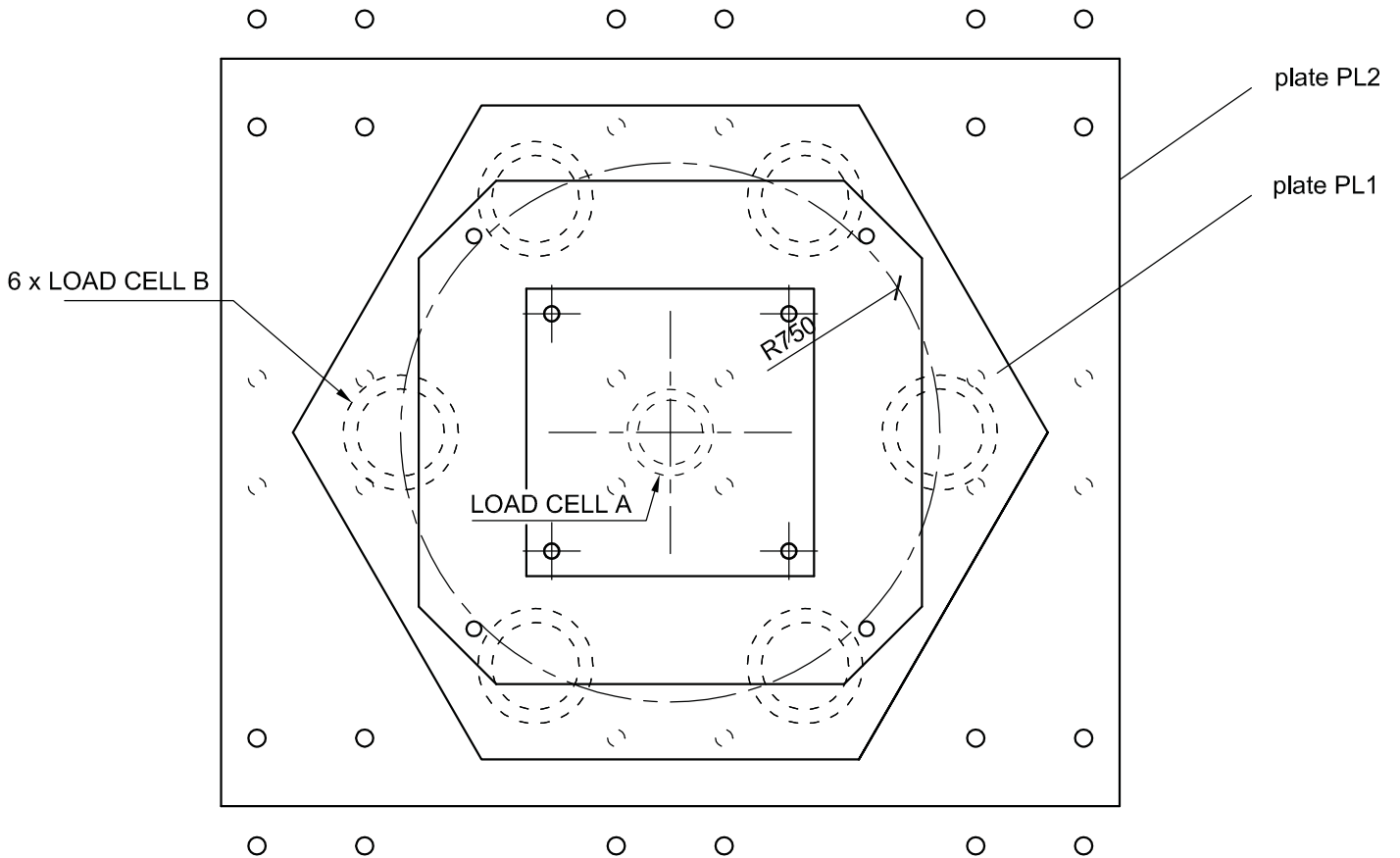
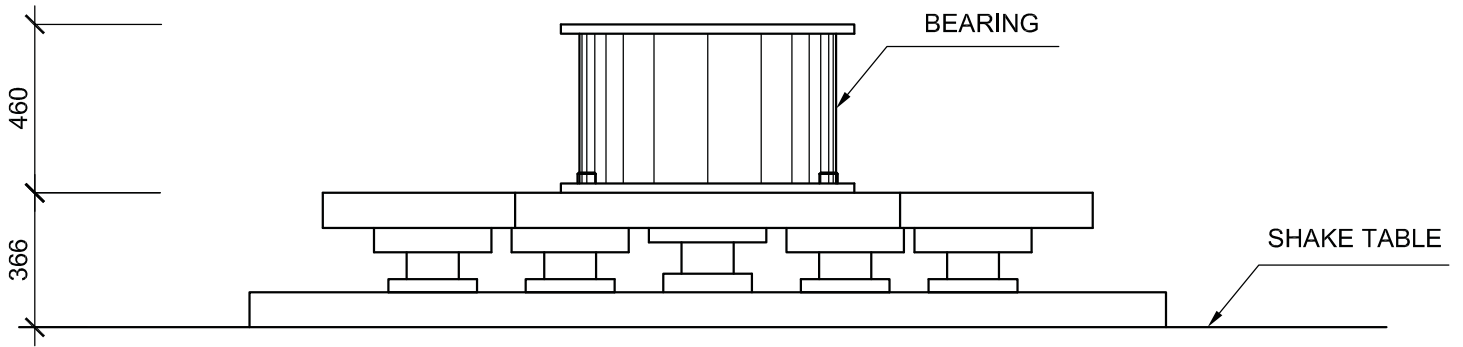


**DETAIL A**  
SCALE: 1/5



**DETAIL B**  
SCALE: 1/5





**BEARING CONNECTION - N, S, W COLUMNS (3 UNITS)**

SCALE: 1/20



UNIVERSITY OF NEVADA, RENO  
1664 N. Virginia St, Reno, NV 89557

EXPERIMENTAL EVALUATION OF  
AN INNOVATIVE ISOLATION SYSTEM  
FOR A LIGHTWEIGHT STEEL MOMENT FRAME BUILDING

CONNECTING PLATE PL2 -  
NORTH, SOUTH, WEST COLUMNS

Drawing: B-004  
Scale: As Shown  
Drawn by: N. D. Dao  
Checked by:  
Date: 28 Apr 2011

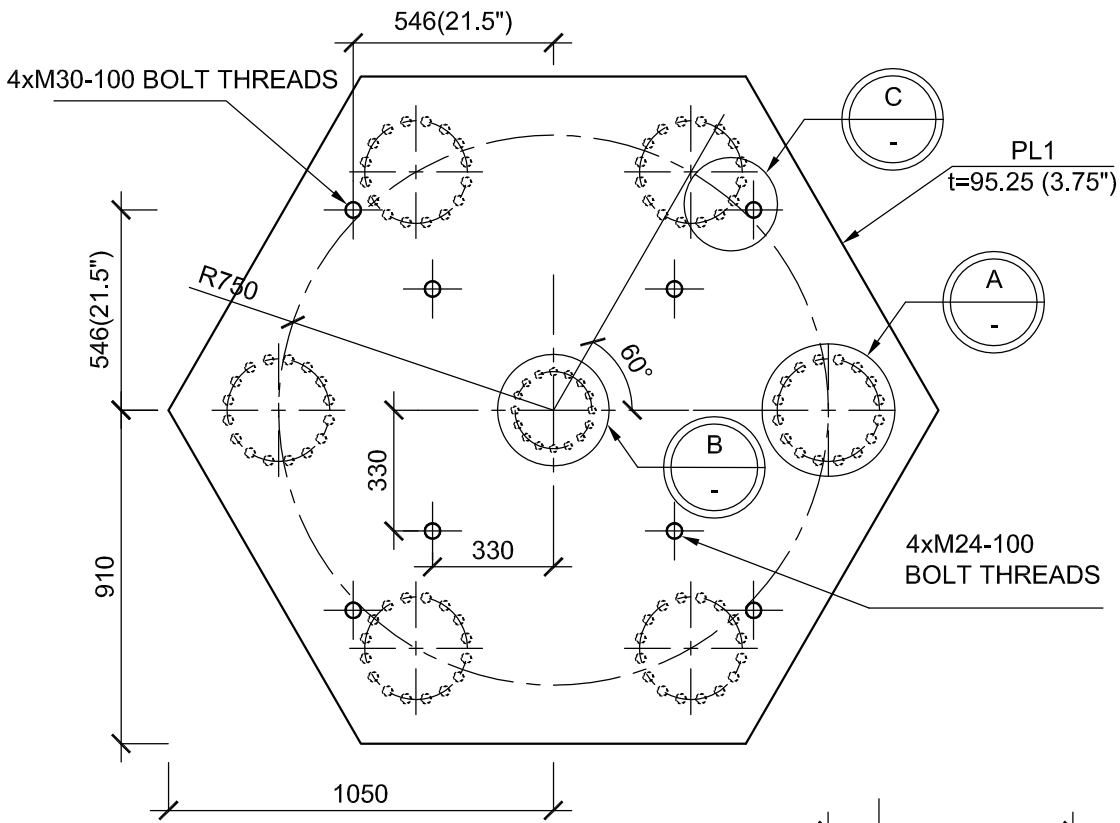
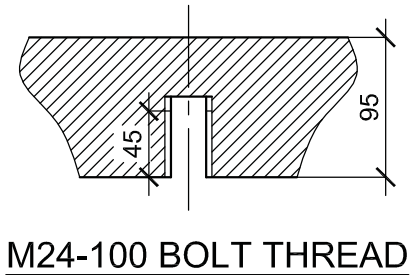
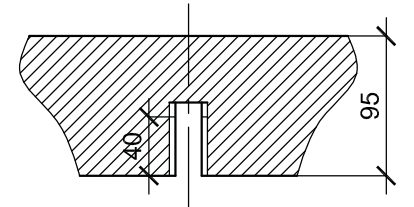


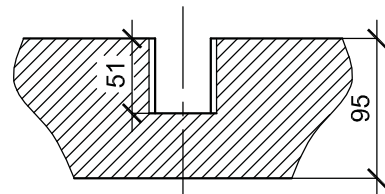
**PLATE PL1 - N, S, W COLUMNS (3 UNITS)**  
SCALE: 1/20



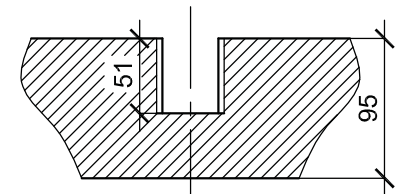
SCALE: 1/5



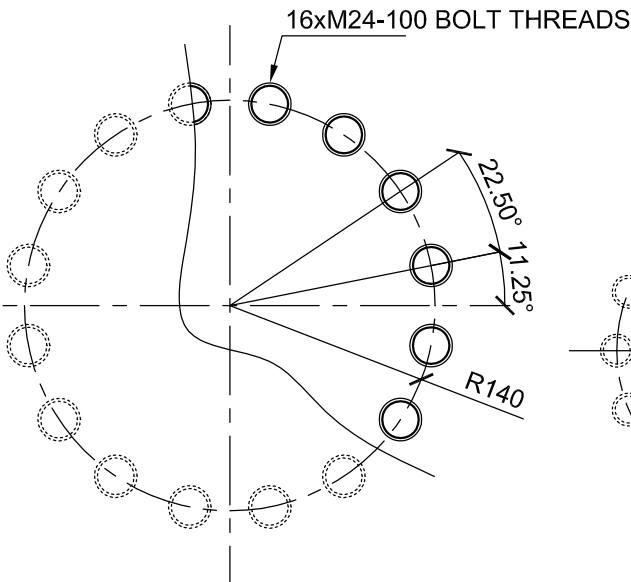
SCALE: 1/5



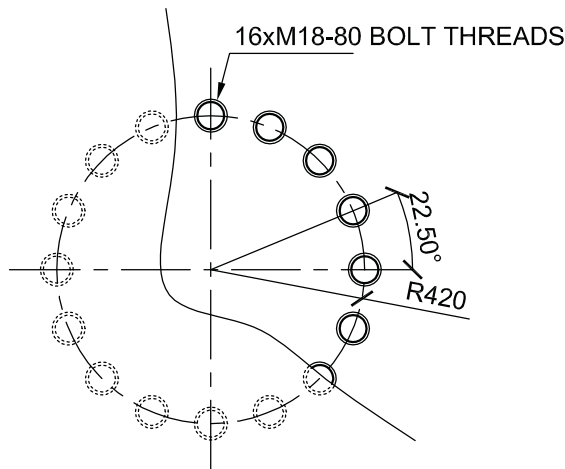
**M24-100 BOLT THREAD**  
SCALE: 1/5



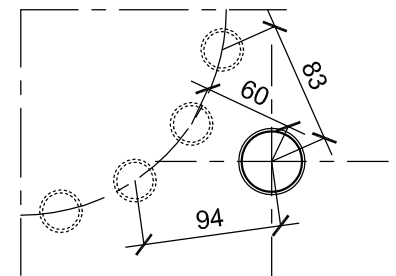
**M30-100 BOLT THREAD**  
SCALE: 1/5



**DETAIL A**  
SCALE: 1/5



**DETAIL B**  
SCALE: 1/5



**DETAIL C**  
SCALE: 1/5



UNIVERSITY OF NEVADA, RENO  
1664 N. Virginia St, Reno, NV 89557

EXPERIMENTAL EVALUATION OF  
AN INNOVATIVE ISOLATION SYSTEM  
FOR A LIGHTWEIGHT STEEL MOMENT FRAME BUILDING

CONNECTING PLATE PL2 -  
NORTH, SOUTH, WEST COLUMNS

Drawing: B-005  
Scale: As Shown  
Drawn by: N. D. Dao  
Checked by:  
Date: 28 Apr 2011

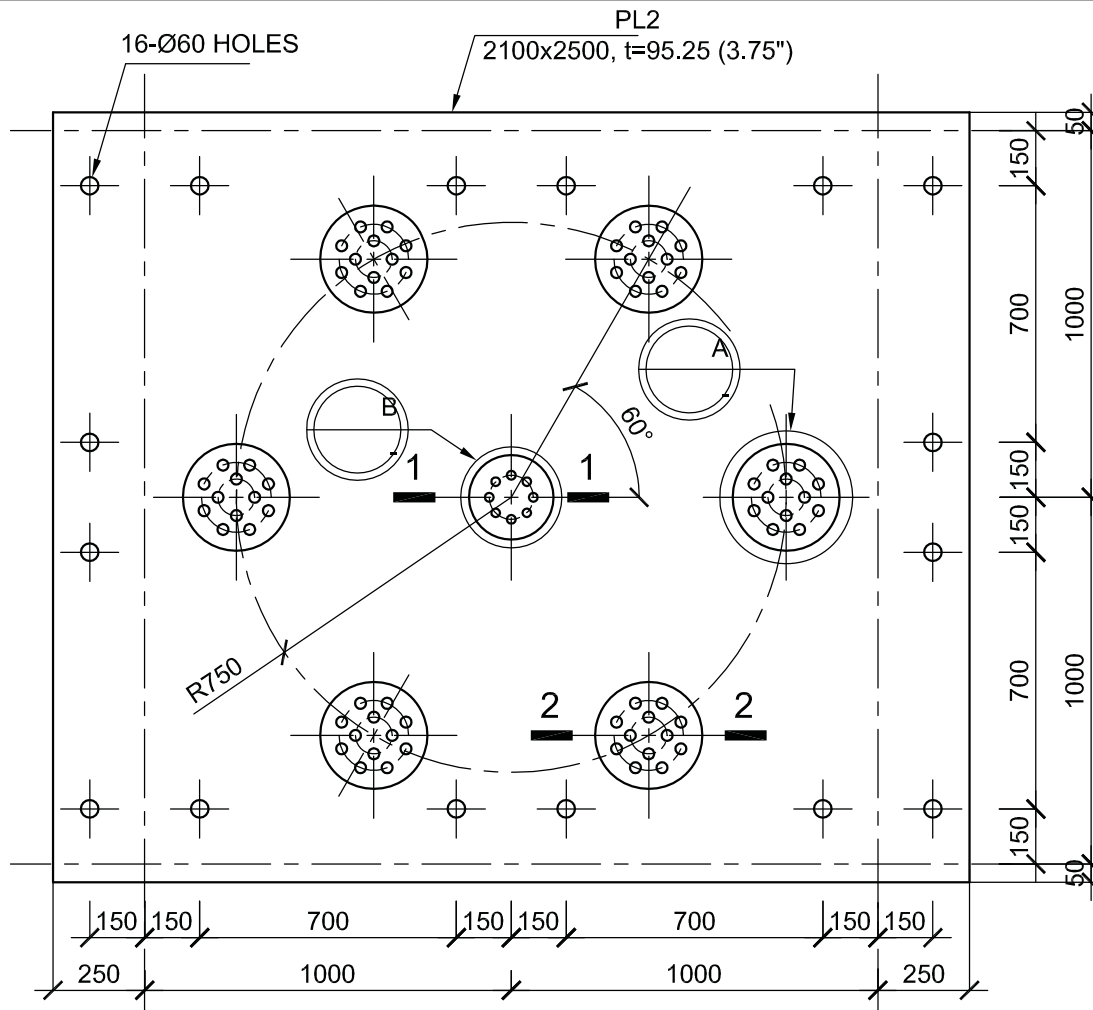
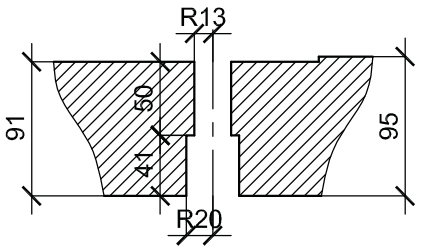


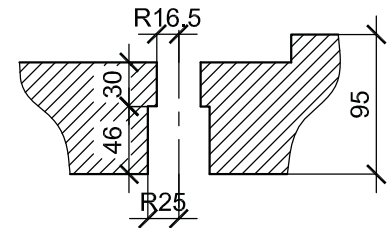
**PLATE PL2, N, S, W COLUMNS (3 UNITS)**

SCALE: 1/20



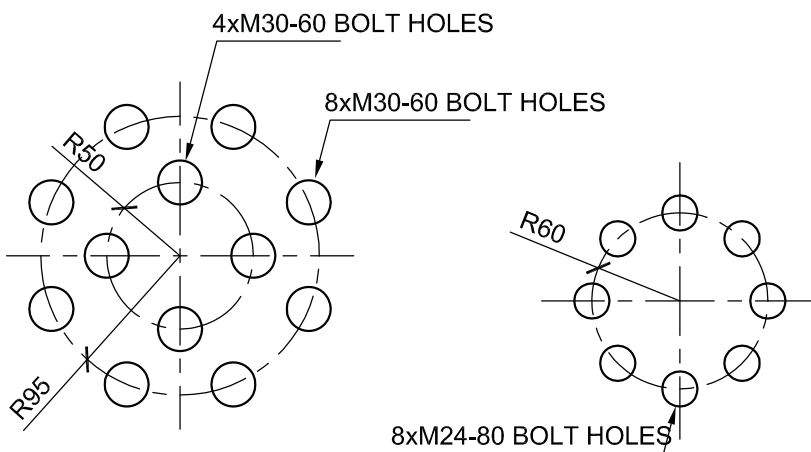
**M24-80 BOLT HOLE**

SCALE: 1/5



**M30-60 BOLT HOLE**

SCALE: 1/5

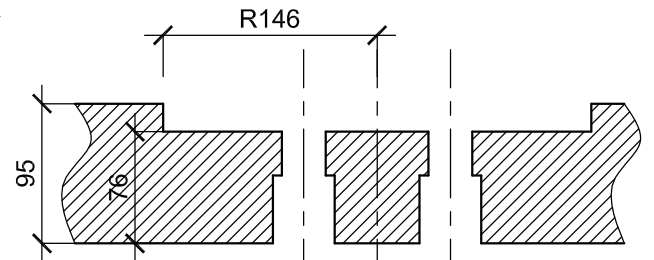


**DETAIL A**

SCALE: 1/5

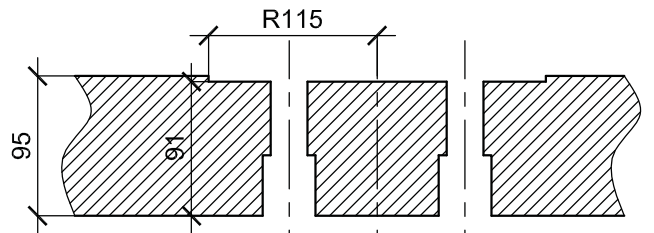
**DETAIL B**

SCALE: 1/5



**SECTION 2-2**

SCALE: 1/5



**SECTION 1-1**

SCALE: 1/5

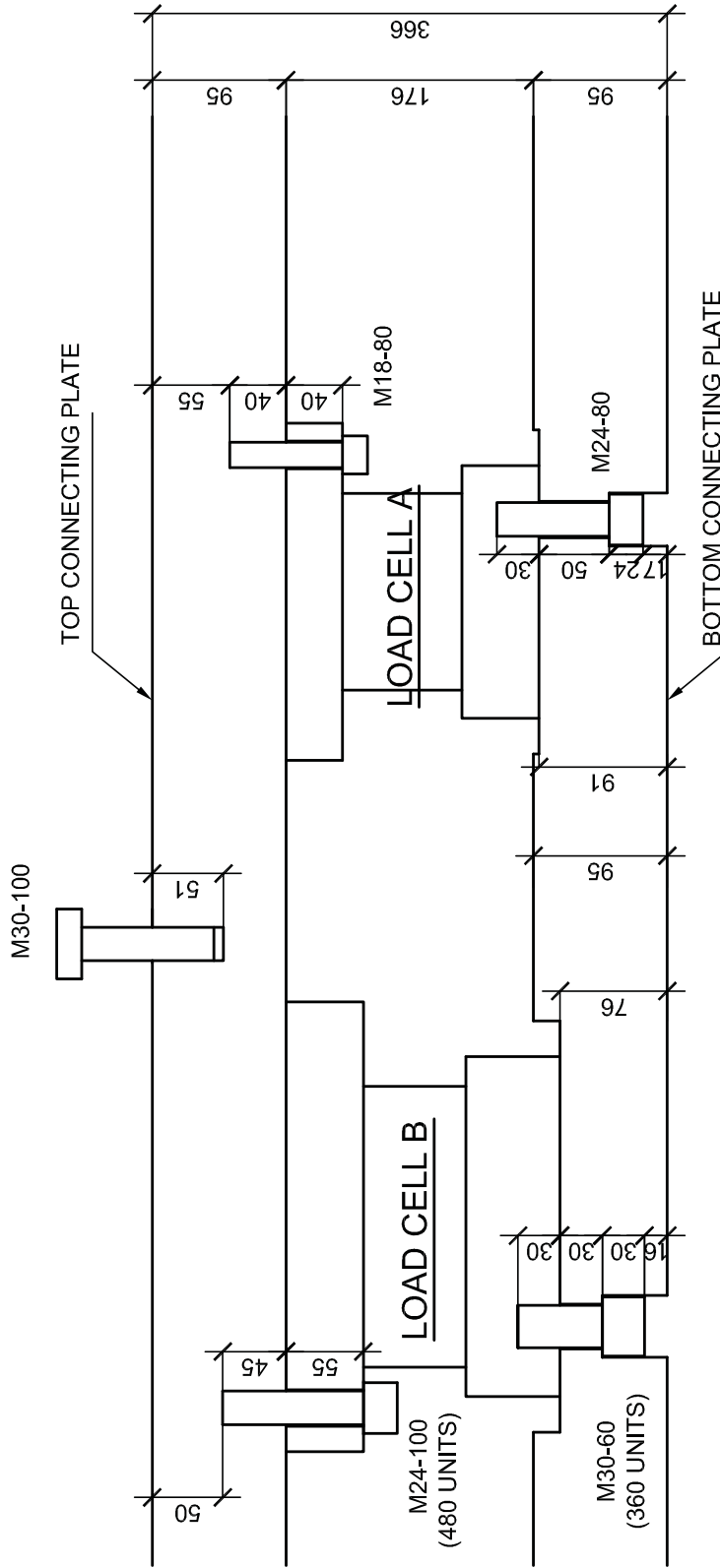


UNIVERSITY OF NEVADA, RENO  
1664 N. Virginia St, Reno, NV 89557

EXPERIMENTAL EVALUATION OF  
AN INNOVATIVE ISOLATION SYSTEM  
FOR A LIGHTWEIGHT STEEL MOMENT FRAME BUILDING

CONNECTING PLATE PL2 -  
NORTH, SOUTH, WEST COLUMNS

Drawing: B-006  
Scale: As Shown  
Drawn by: N. D. Dao  
Checked by:  
Date: 28 Apr 2011



C-8



UNIVERSITY OF NEVADA, RENO  
1664 N. Virginia St, Reno, NV 89557

EXPERIMENTAL EVALUATION OF  
AN INNOVATIVE ISOLATION SYSTEM  
FOR A LIGHTWEIGHT STEEL MOMENT FRAME BUILDING

ELEVATION OF LOAD CELL CONNECTING

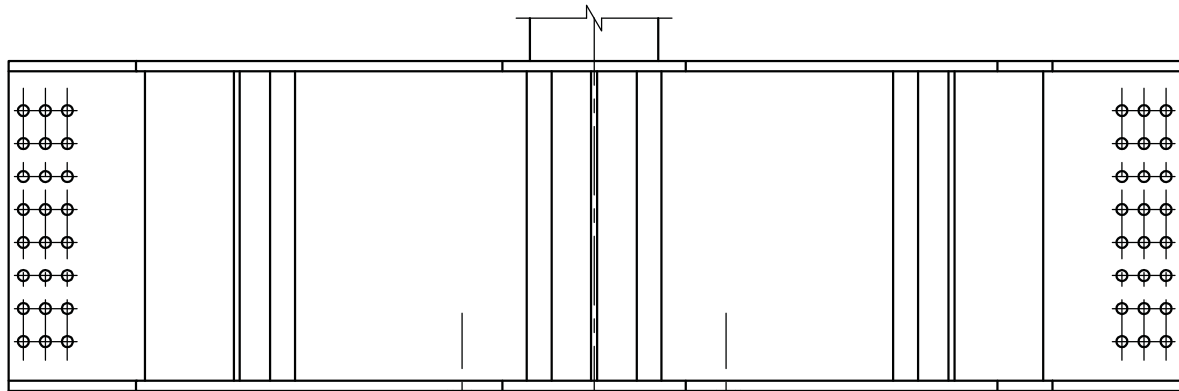
Drawing: B-007

Scale: As Shown

Drawn by: N. D. Dao

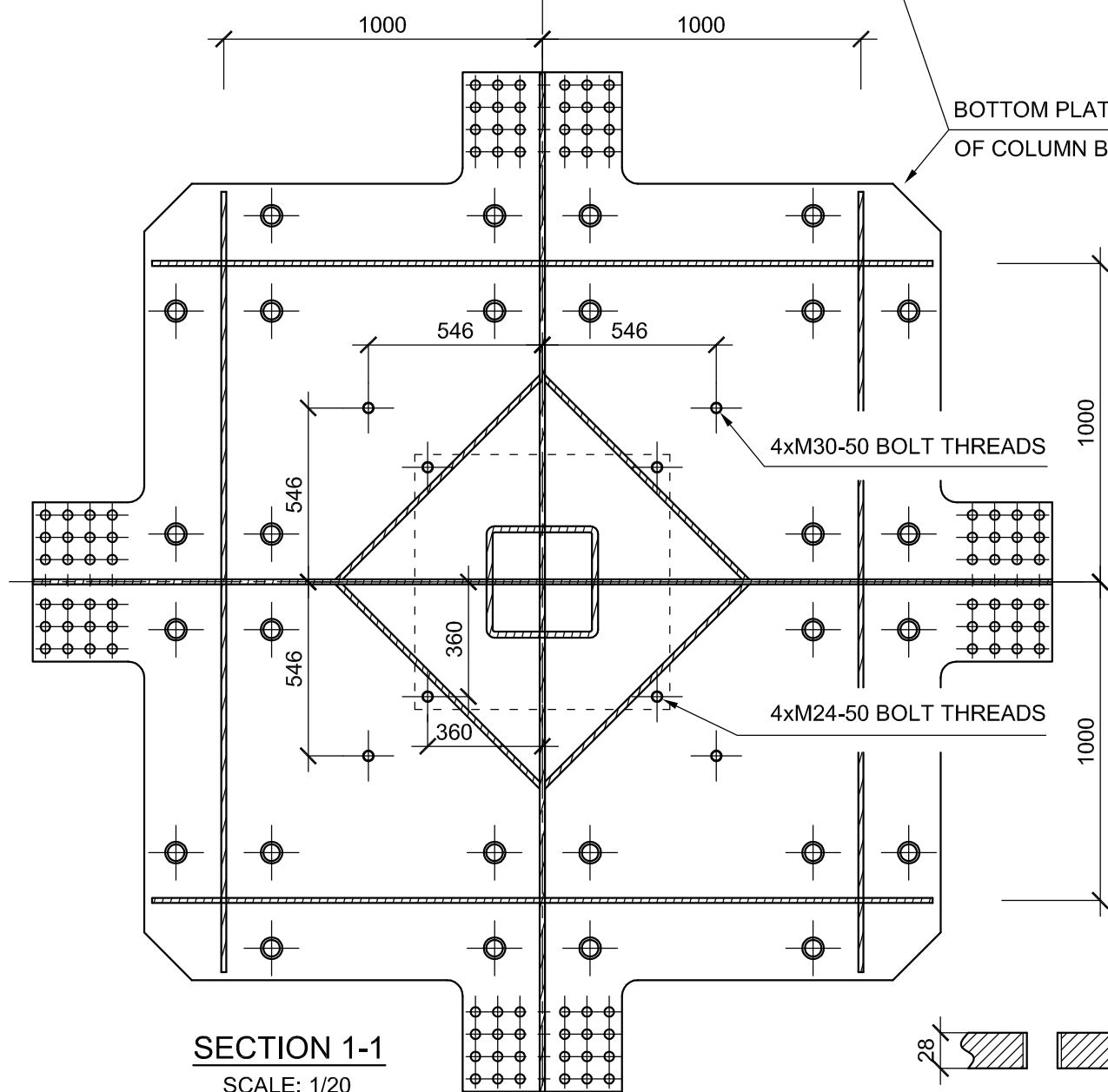
Checked by:

Date: 28 Apr 2011



STEEL PLATE OF BEARING

BOTTOM PLATE OF COLUMN BASE

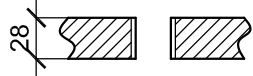


SECTION 1-1

SCALE: 1/20

4xM30-50 BOLT THREADS

4xM24-50 BOLT THREADS



M30-50 and M24-50 BOLT THREAD

SCALE: 1/5



# APPENDIX D

## DRAWINGS FOR STRUCTURAL INSTRUMENTATION PLAN

Building Isolated with Hybrid Lead-Rubber Isolation System

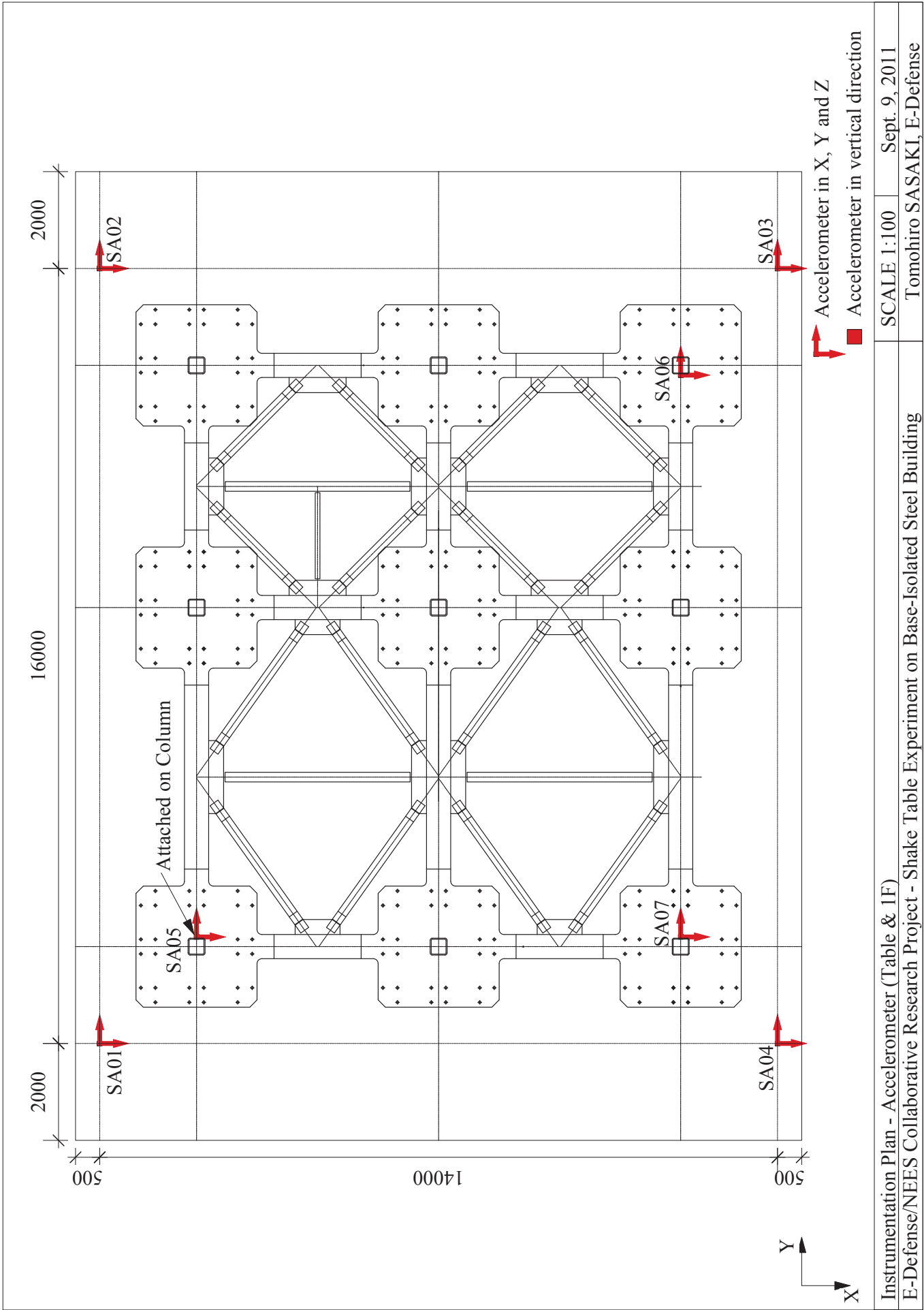
Developed by Hyogo Earthquake Engineering Research Center for NEES/E-Defense Collaborative

Test Program on Innovative Isolation Systems, 2011-2012

Lead Contributor: Tomohiro Sasaki

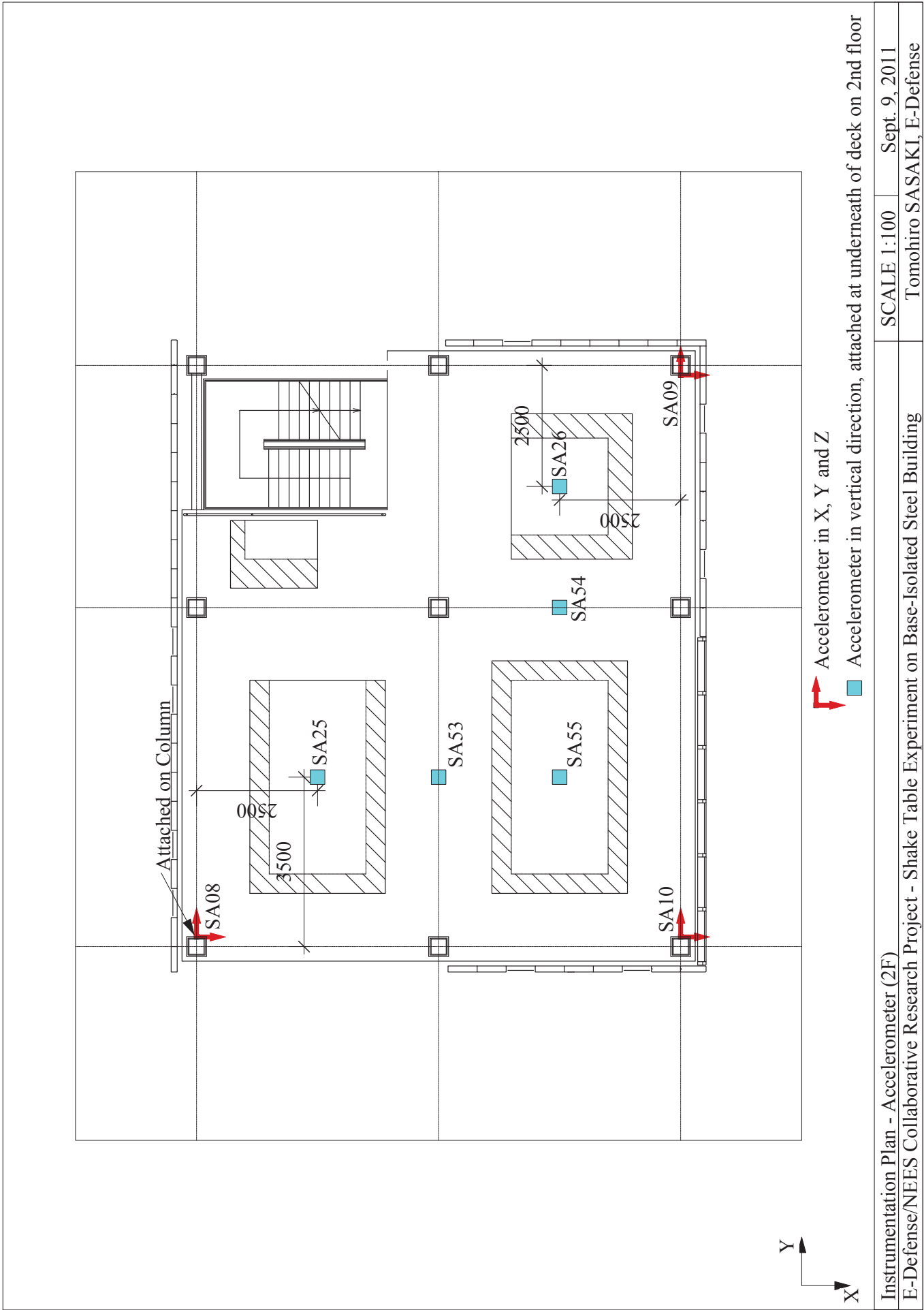
### Instrumentation Drawings

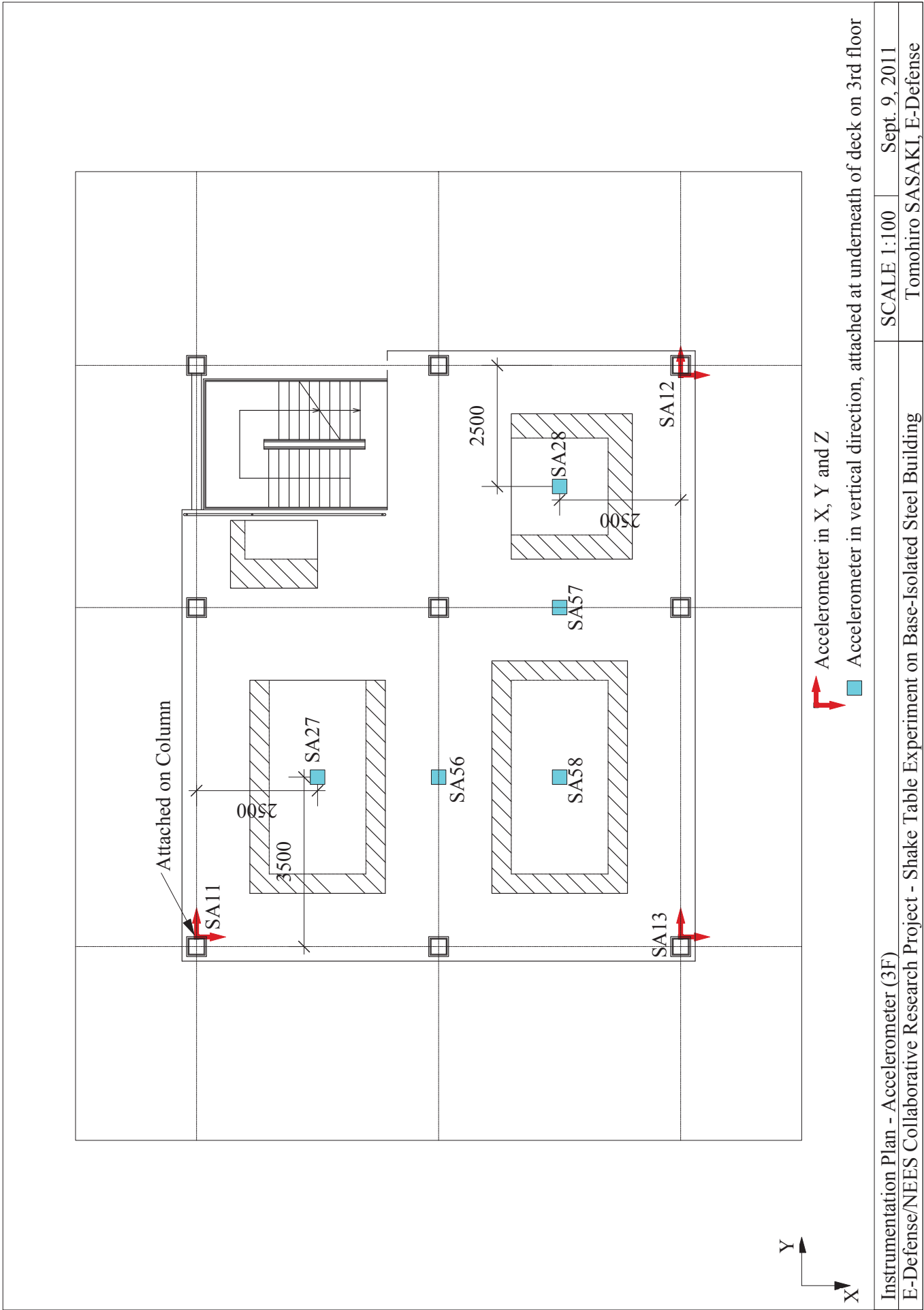
Sheet 1	Accelerometer (Table & 1F)
Sheet 2	Accelerometer (2F)
Sheet 3	Accelerometer (3F)
Sheet 4	Accelerometer (4F)
Sheet 5	Accelerometer (5F)
Sheet 6	Accelerometer (RF)
Sheet 7	Accelerometers for Hexagon-shaped Steel Plates
Sheet 8	Displacement Transducers for Bearings
Sheet 9	Displacement Transducers (1F)
Sheet 10	Displacement Transducers (2F)
Sheet 11	Displacement Transducers (3F)
Sheet 12	Displacement Transducers (4F)
Sheet 13	Displacement Transducers (5F)
Sheet 14	Load cells for Bearings (LRB/CLB)
Sheet 15	Strain Gages on Column Faces (1F)
Sheet 16	Strain Gages on Column Faces (2F)
Sheet 17	Strain Gages on Column Faces (3F)
Sheet 18	Strain Gages on Column Faces (4F)
Sheet 19	Strain Gages on Column Faces (5F)



Instrumentation Plan - Accelerometer (Table & 1F)  
 E-Defense/NEES Collaborative Research Project - Shake Table Experiment on Base-Isolated Steel Building







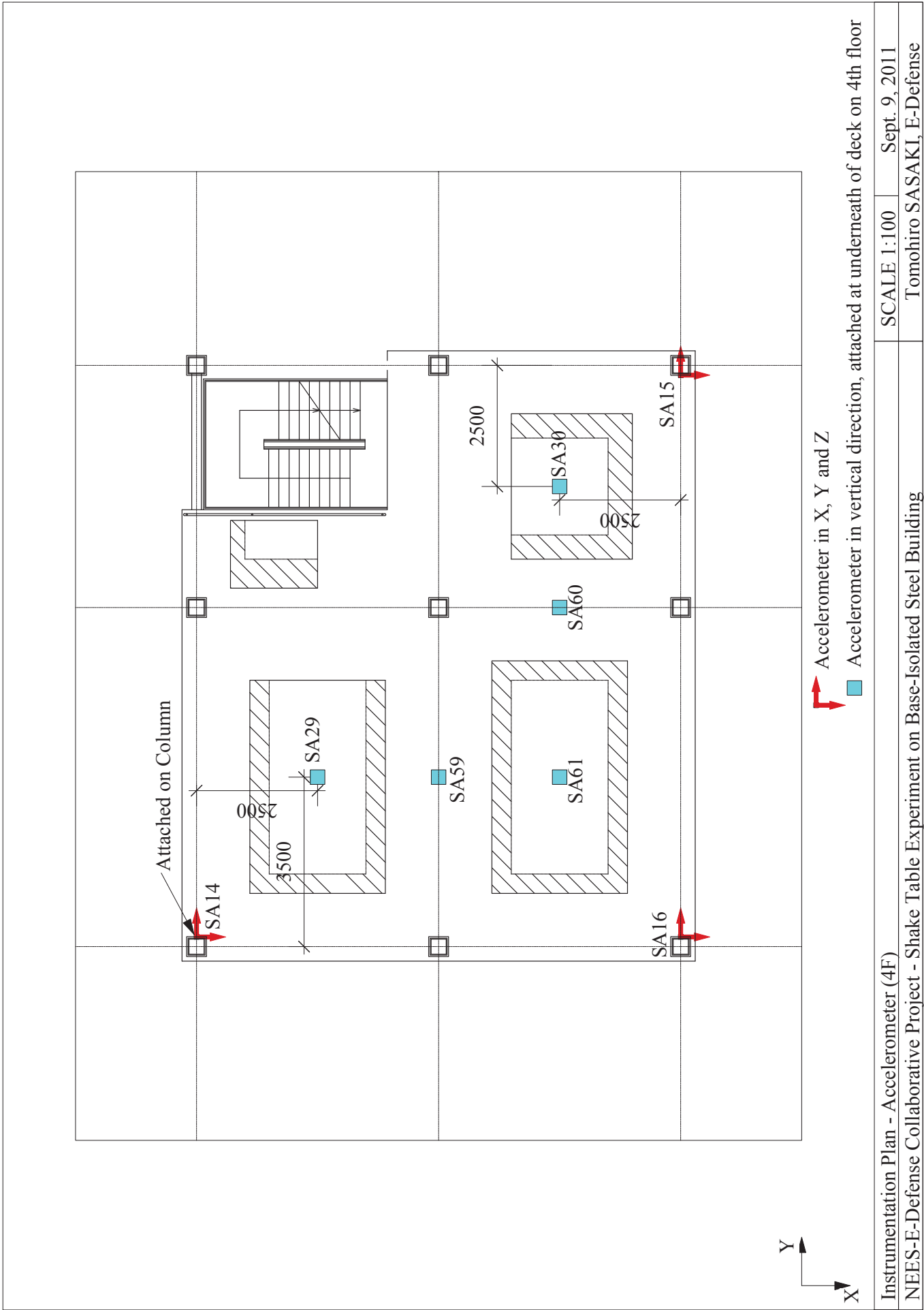
Instrumentation Plan - Accelerometer (3F)

E-Defense/NEES Collaborative Research Project - Shake Table Experiment on Base-Isolated Steel Building

SCALE 1:100

Sept. 9, 2011

Tomohiro SASAKI, E-Defense



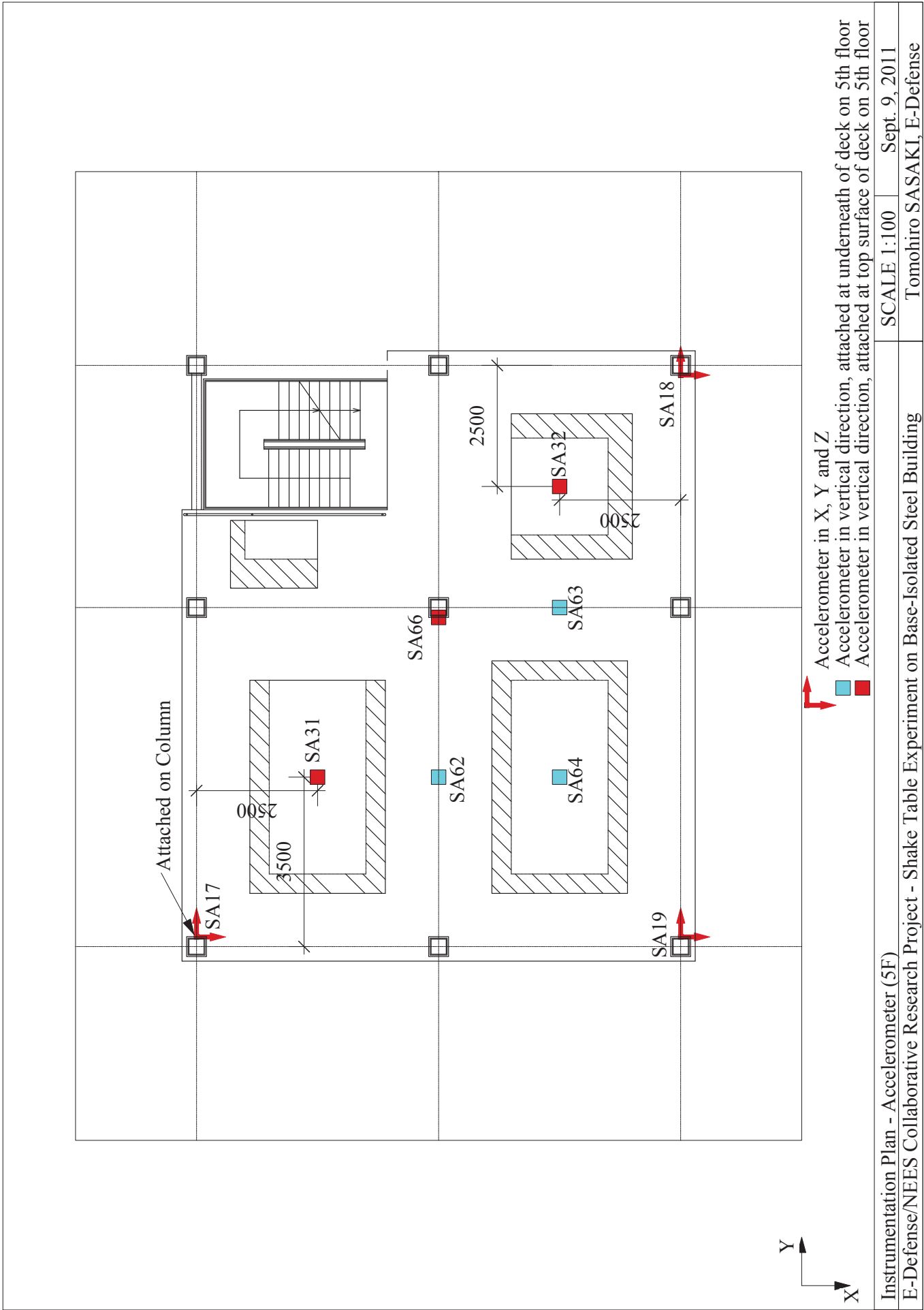
Instrumentation Plan - Accelerometer (4F)

NEES-E-Defense Collaborative Project - Shake Table Experiment on Base-Isolated Steel Building

SCALE 1:100

Sept. 9, 2011

Tomohiro SASAKI, E-Defense

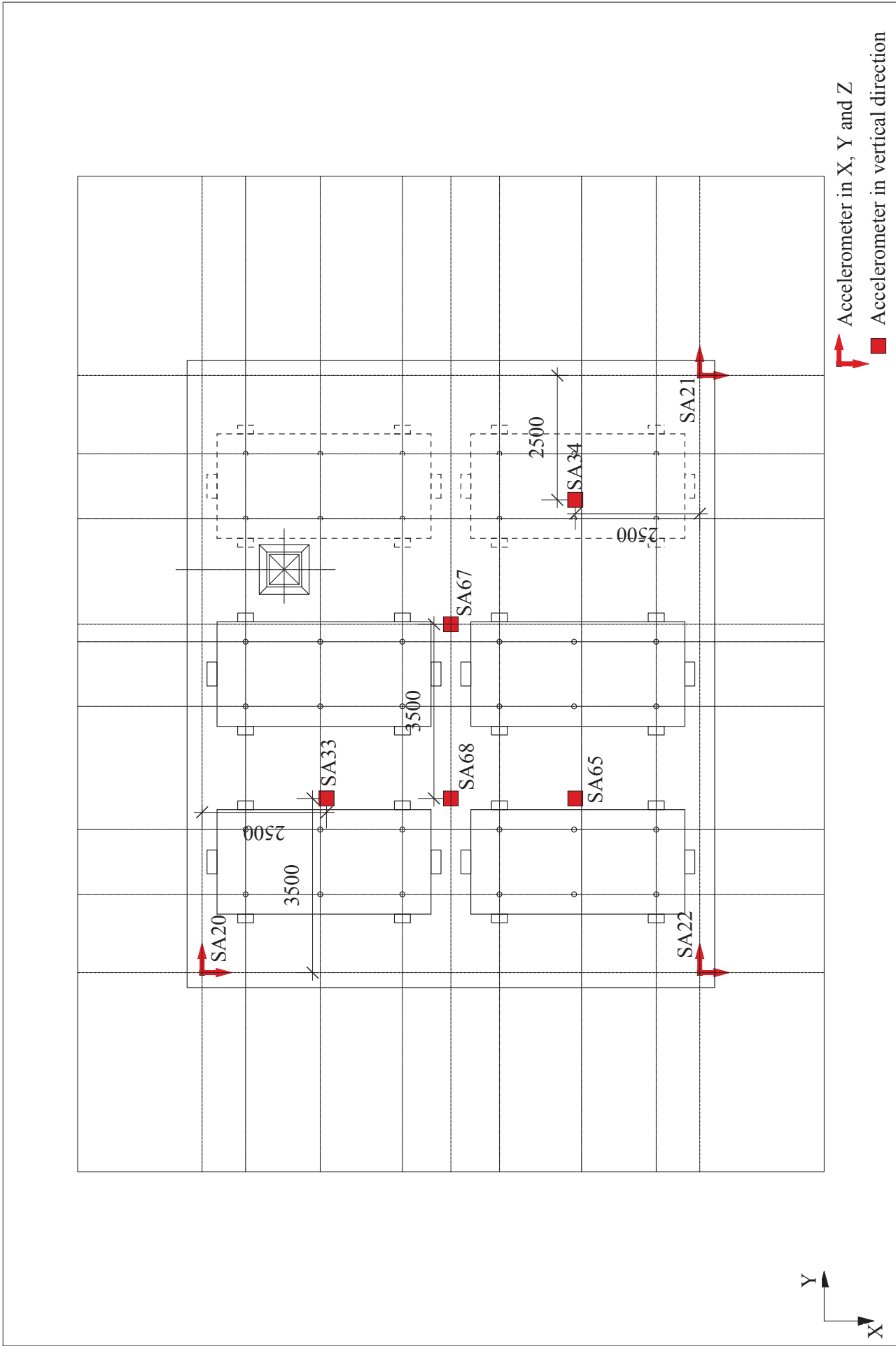


Instrumentation Plan - Accelerometer (5F)

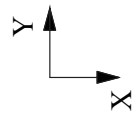
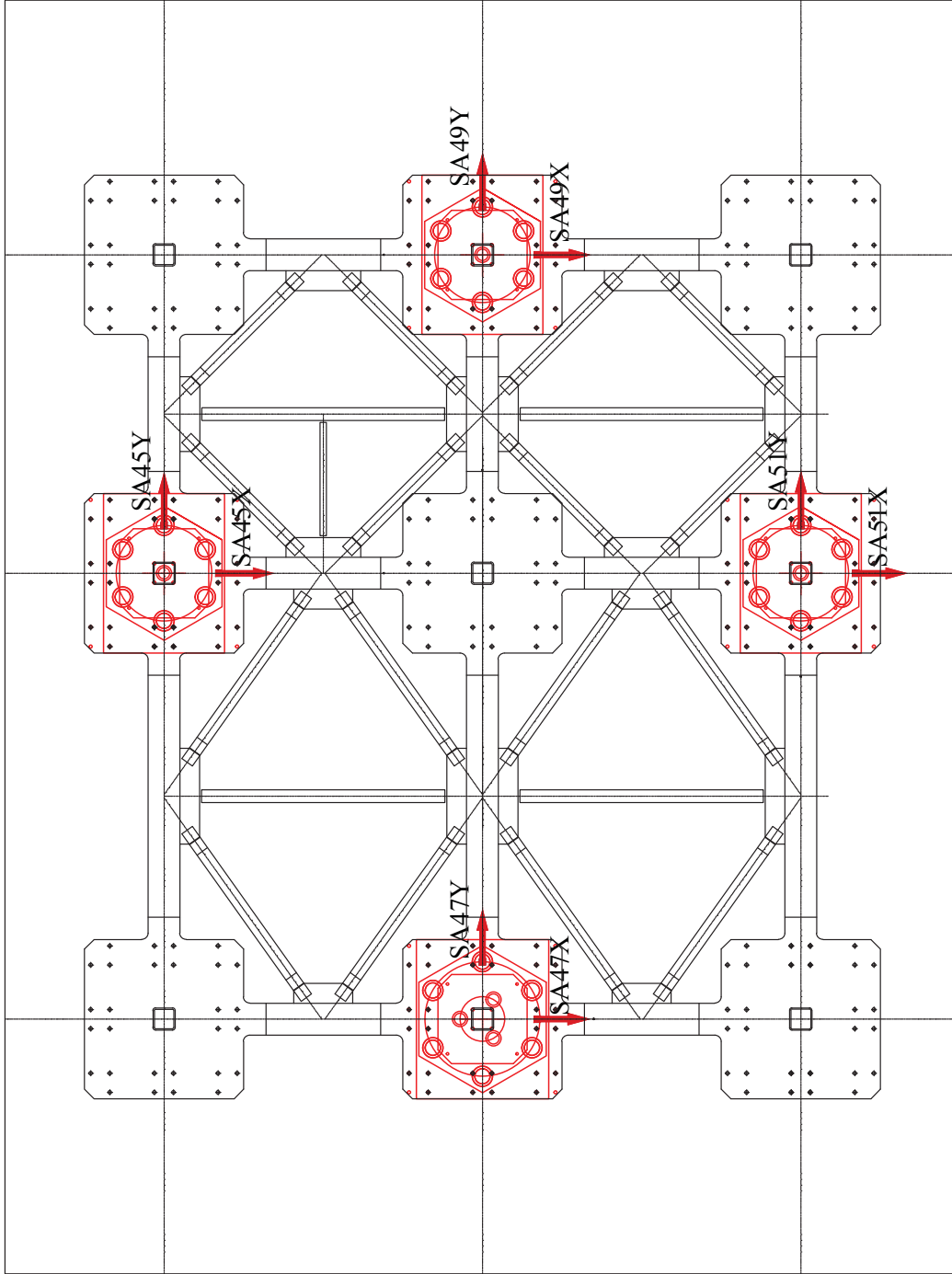
E-Defense/NEES Collaborative Research Project - Shake Table Experiment on Base-Isolated Steel Building

SCALE 1:100 Sept. 9, 2011

Tomohiro SASAKI, E-Defense



Instrumentation Plan - Accelerometer (RF)	SCALE 1:100	Sept. 9, 2011
E-Defense/NEES Collaborative Research Project - Shake Table Experiment on Base-Isolated Steel Building	Tomohiro SASAKI, E-Defense	

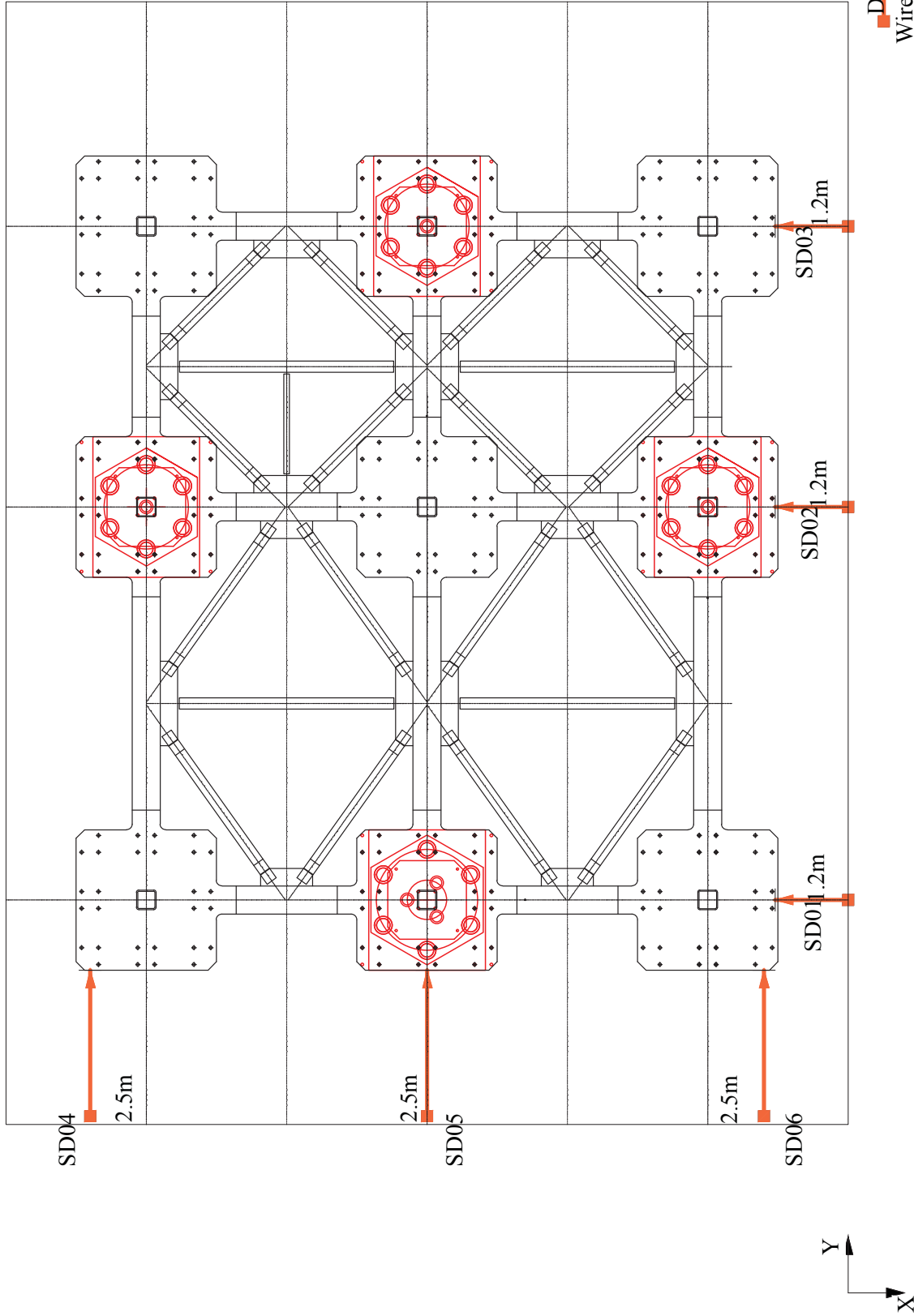


Accelerometer (Horizontal)

Instrumentation Plan - Accelerometers for Hexagon-shaped Steel Plates  
 E-Defense/NEES Collaborative Research Project - Shake Table Experiment on Base-Isolated Steel Building

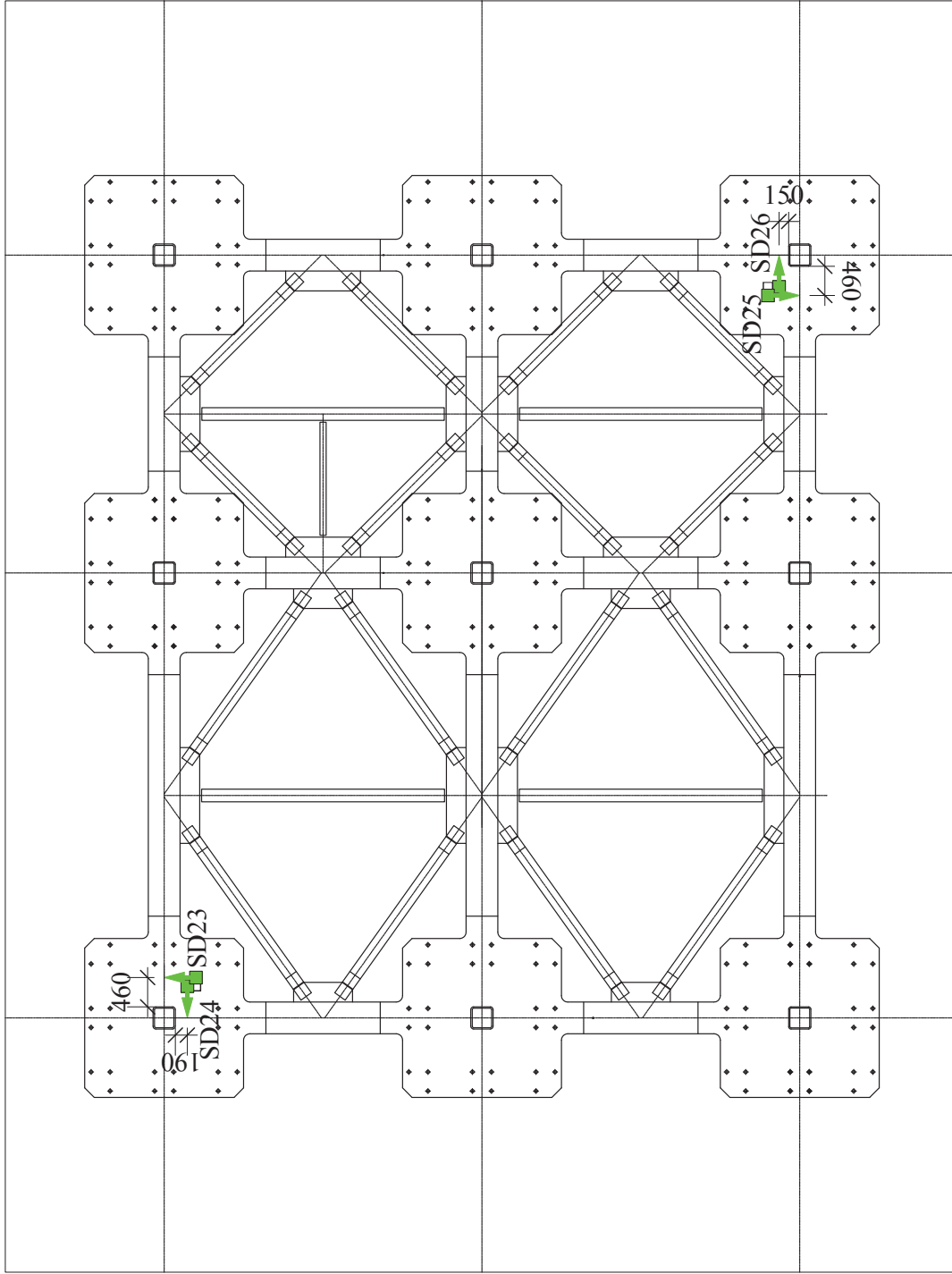
SCALE 1:100

Sept. 9, 2011  
 Tomohiro SASAKI, E-Defense



→ Direction of wire  
■ WirePod  
○ Target

Instrumentation Plan - Displacement Transducers for Bearings E-Defense/NEES Collaborative Research Project - Shake Table Experiment on Base-Isolated Steel Building	SCALE 1:100	Sept. 9, 2011
	Tomohiro SASAKI, E-Defense	



 Direction of laser  
 Laser DT      Target

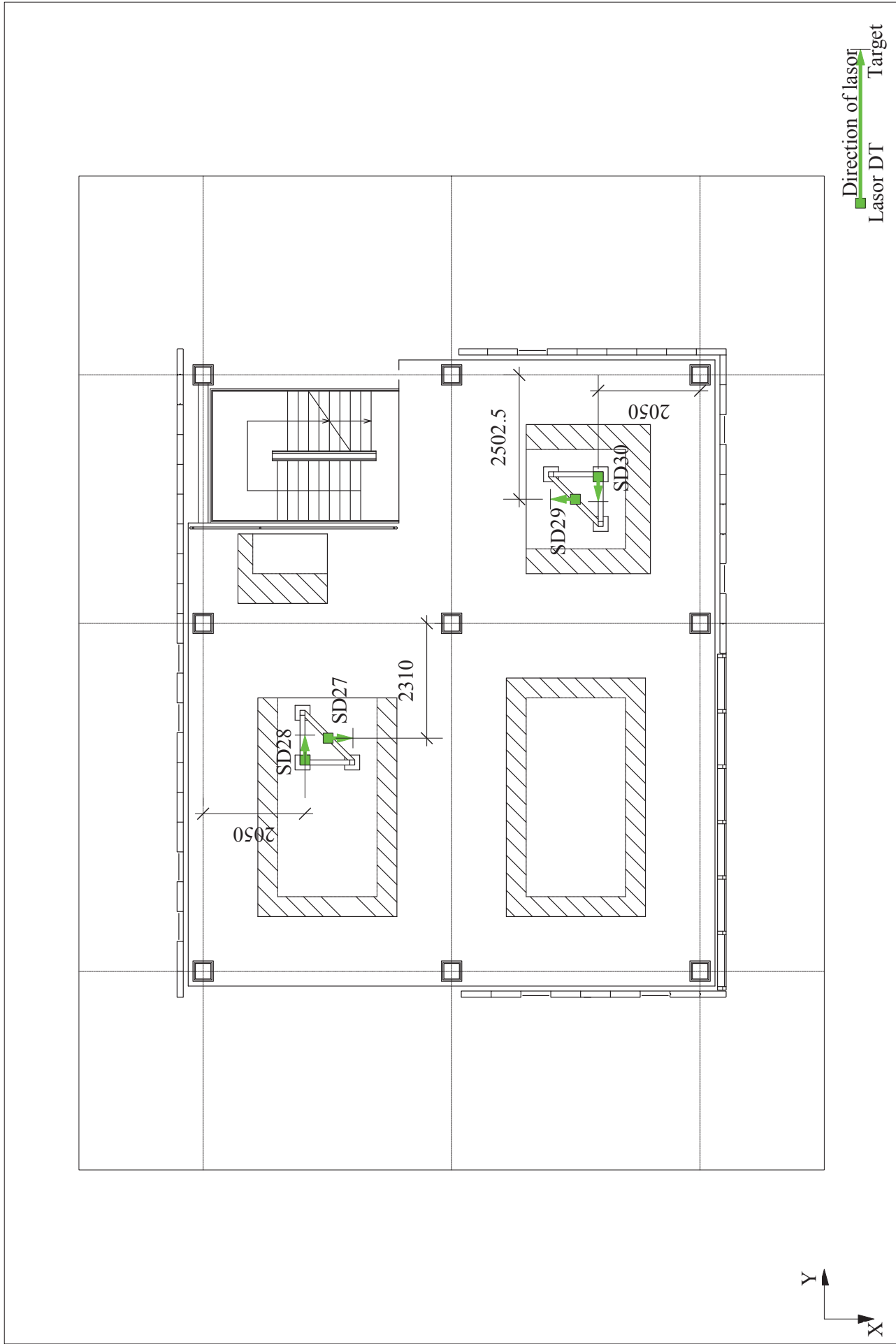
Instrumentation Plan - Displacement Transducers (1F)

E-Defense/NEES Collaborative Research Project - Shake Table Experiment on Base-Isolated Steel Building

SCALE 1:100      Sept. 9, 2011

Tomohiro SASAKI, E-Defense





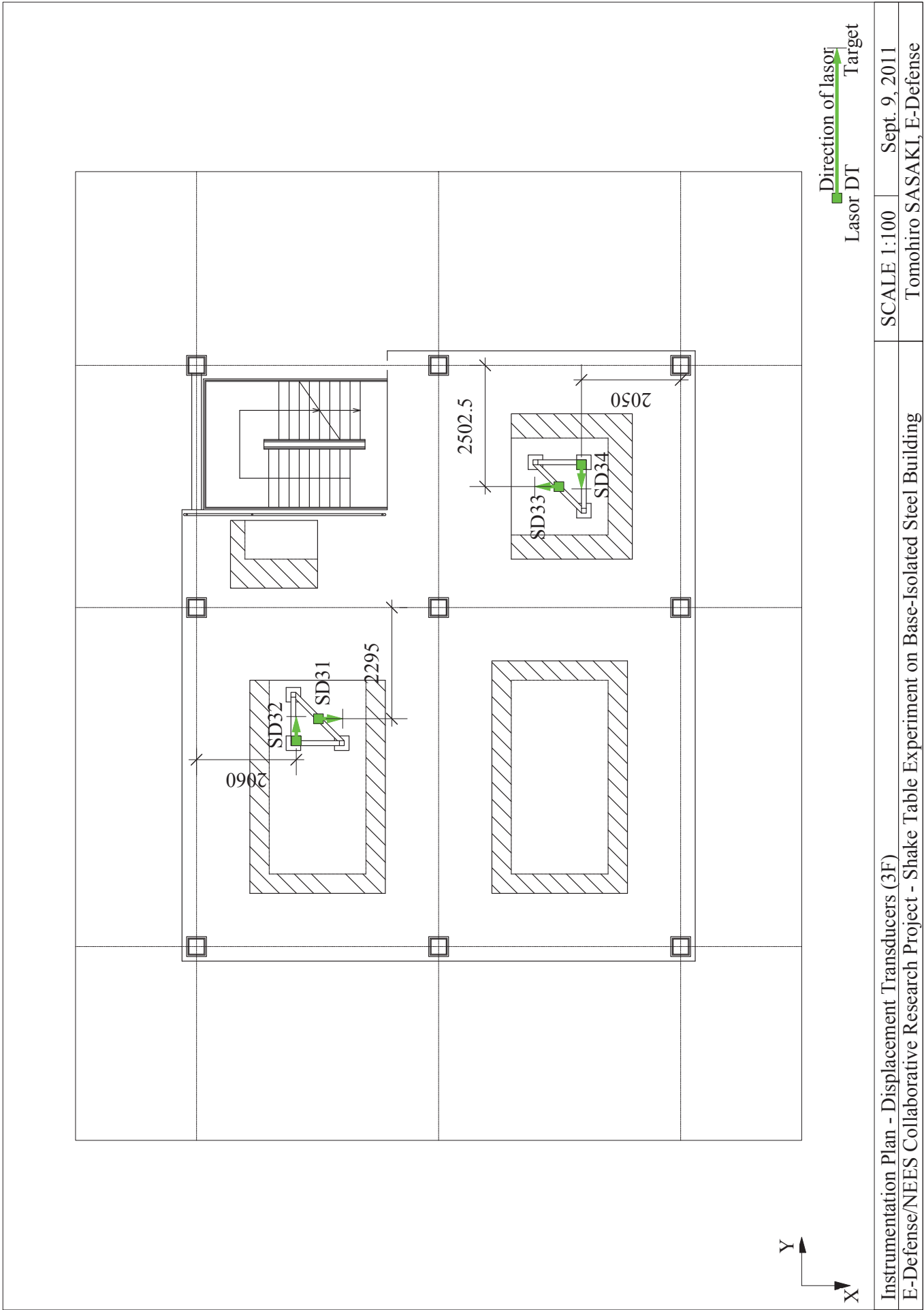
Instrumentation Plan - Displacement Transducers (2F)

E-Defense/NEES Collaborative Research Project - Shake Table Experiment on Base-Isolated Steel Building

SCALE 1:100

Sept. 9, 2011

Tomohiro SASAKI, E-Defense



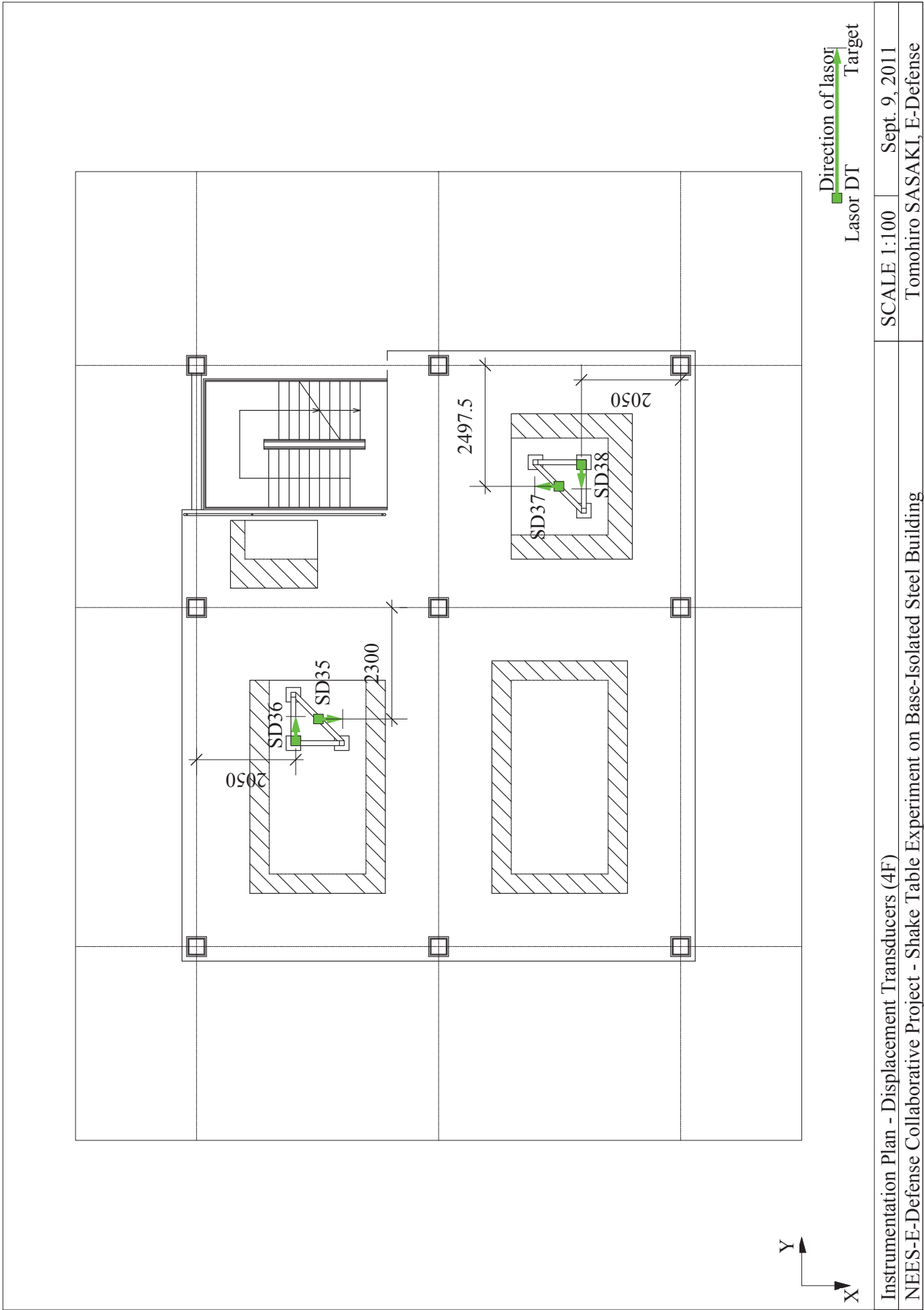
Instrumentation Plan - Displacement Transducers (3F)

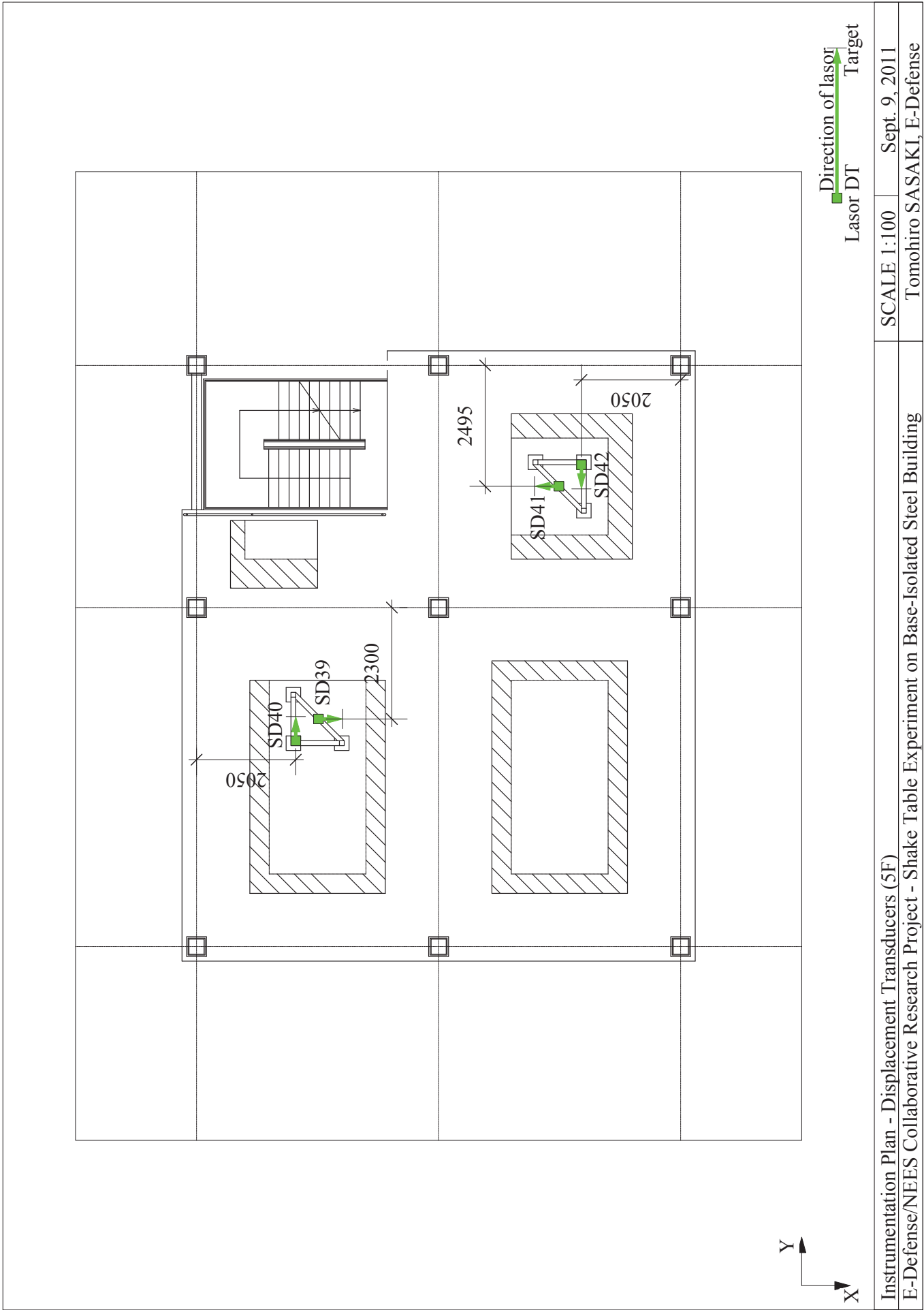
E-Defense/NEES Collaborative Research Project - Shake Table Experiment on Base-Isolated Steel Building

SCALE 1:100

Sept. 9, 2011

Tomohiro SASAKI, E-Defense





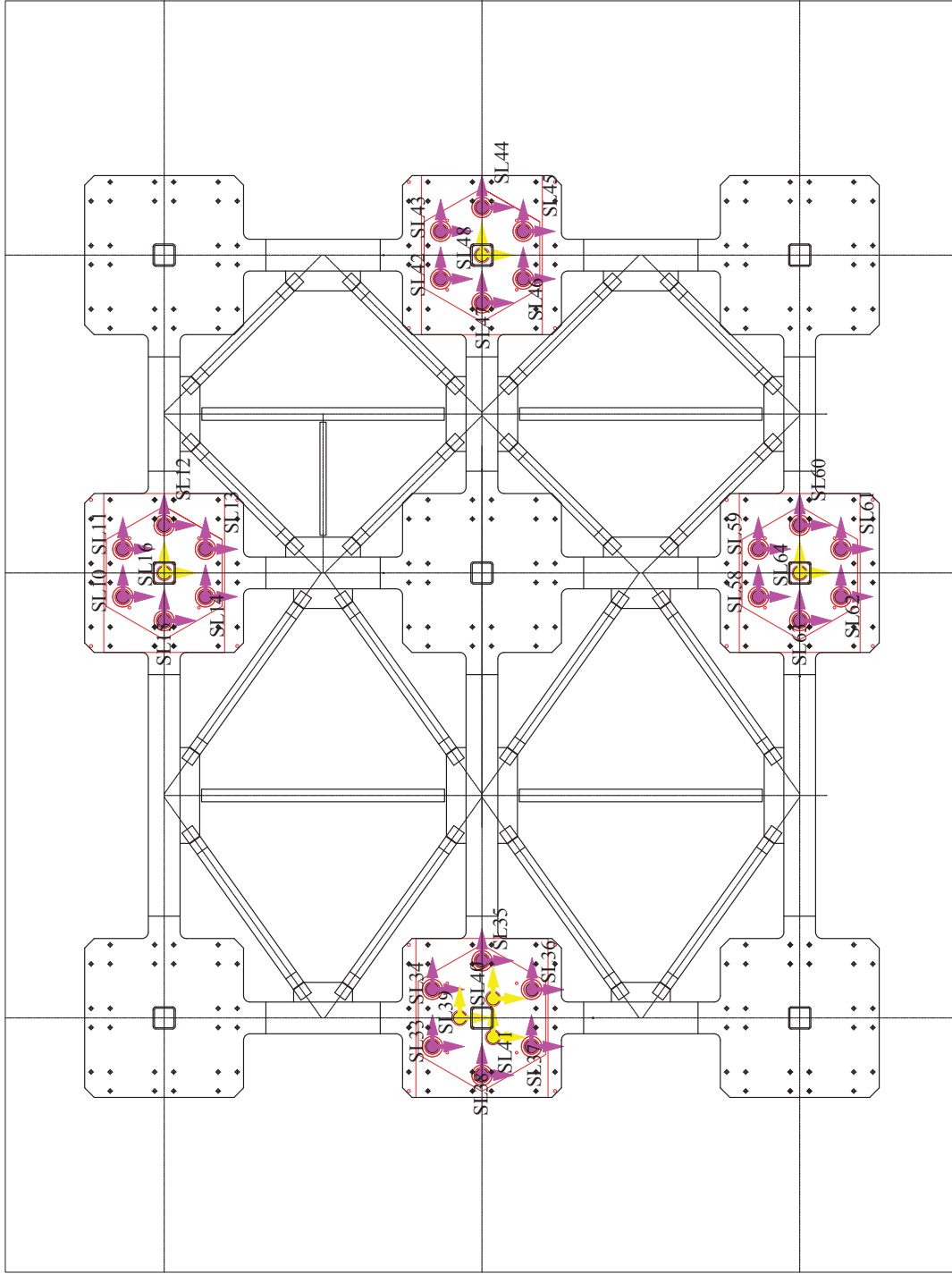
Instrumentation Plan - Displacement Transducers (5F)

E-Defense/NEES Collaborative Research Project - Shake Table Experiment on Base-Isolated Steel Building

SCALE 1:100

Sept. 9, 2011

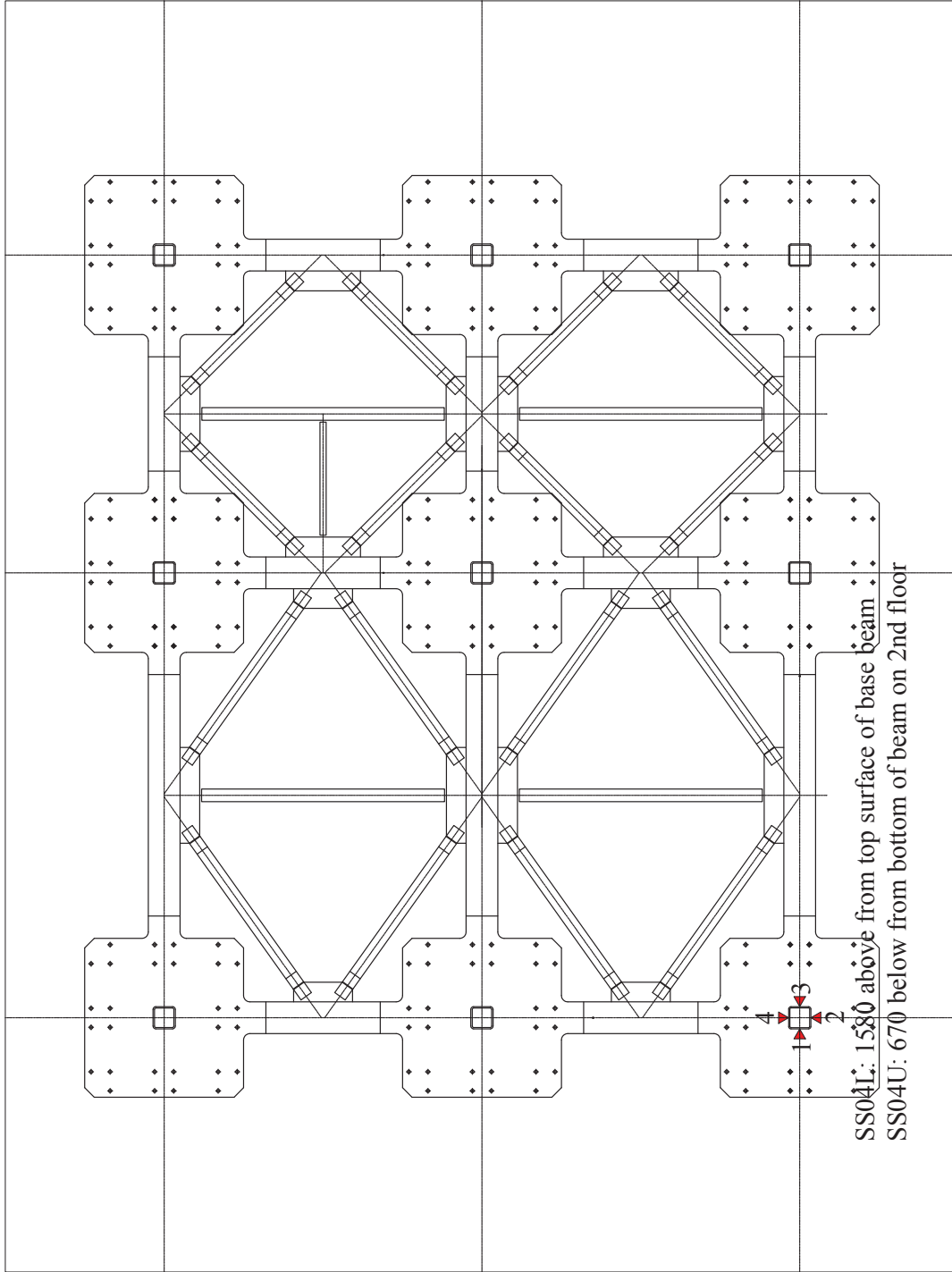
Tomohiro SASAKI, E-Defense



 Loadcell A (xy250kN/z400kN)  
 Loadcell B (xy400kN/z700kN)

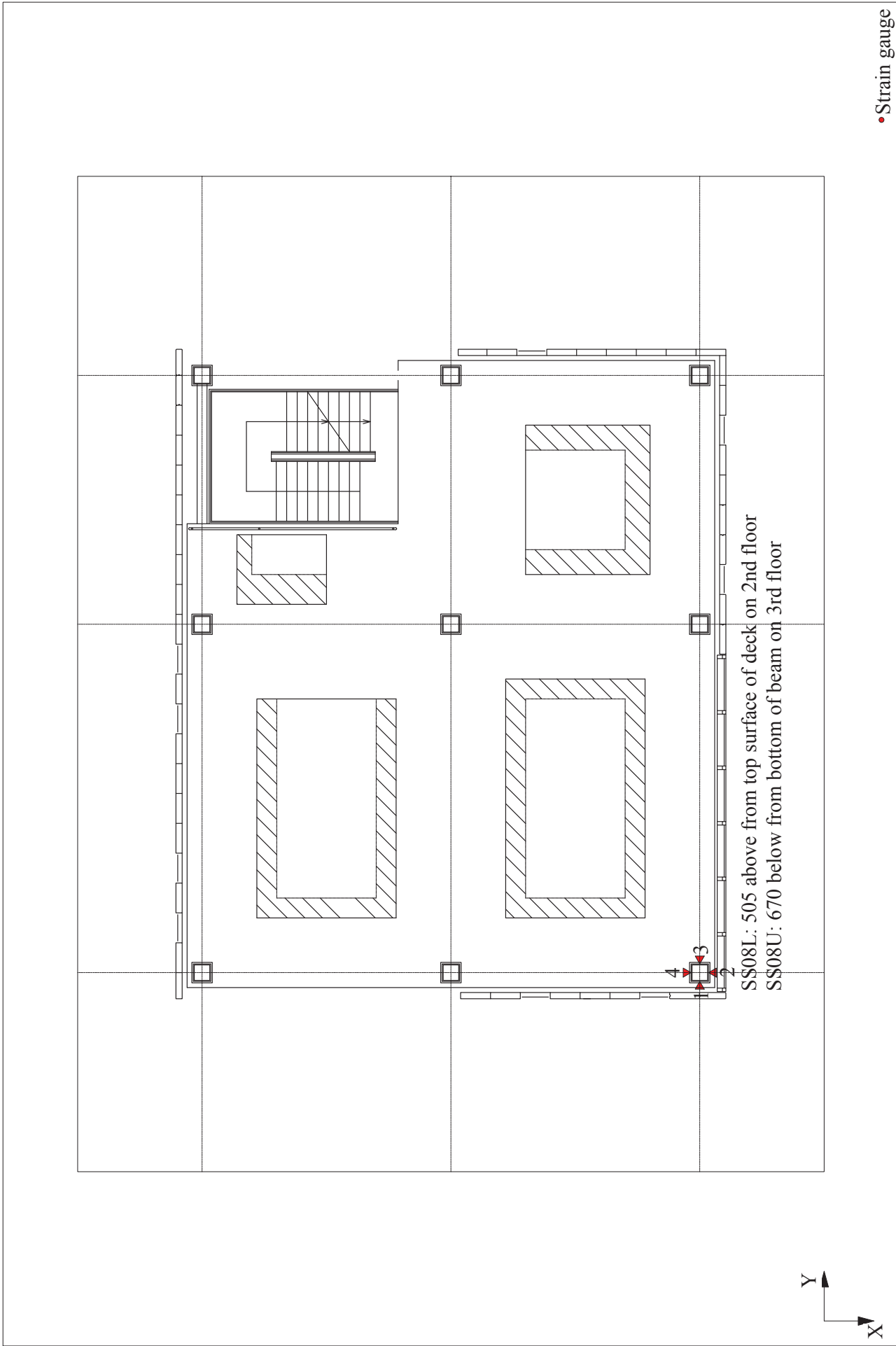
Instrumentation Plan - Loadcells for Bearings (LRB/CLB)  
 E-Defense/NEES Collaborative Research Project - Shake Table Experiment on Base-Isolated Steel Building

SCALE 1:100      Sept. 9, 2011  
 Tomohiro SASAKI, E-Defense

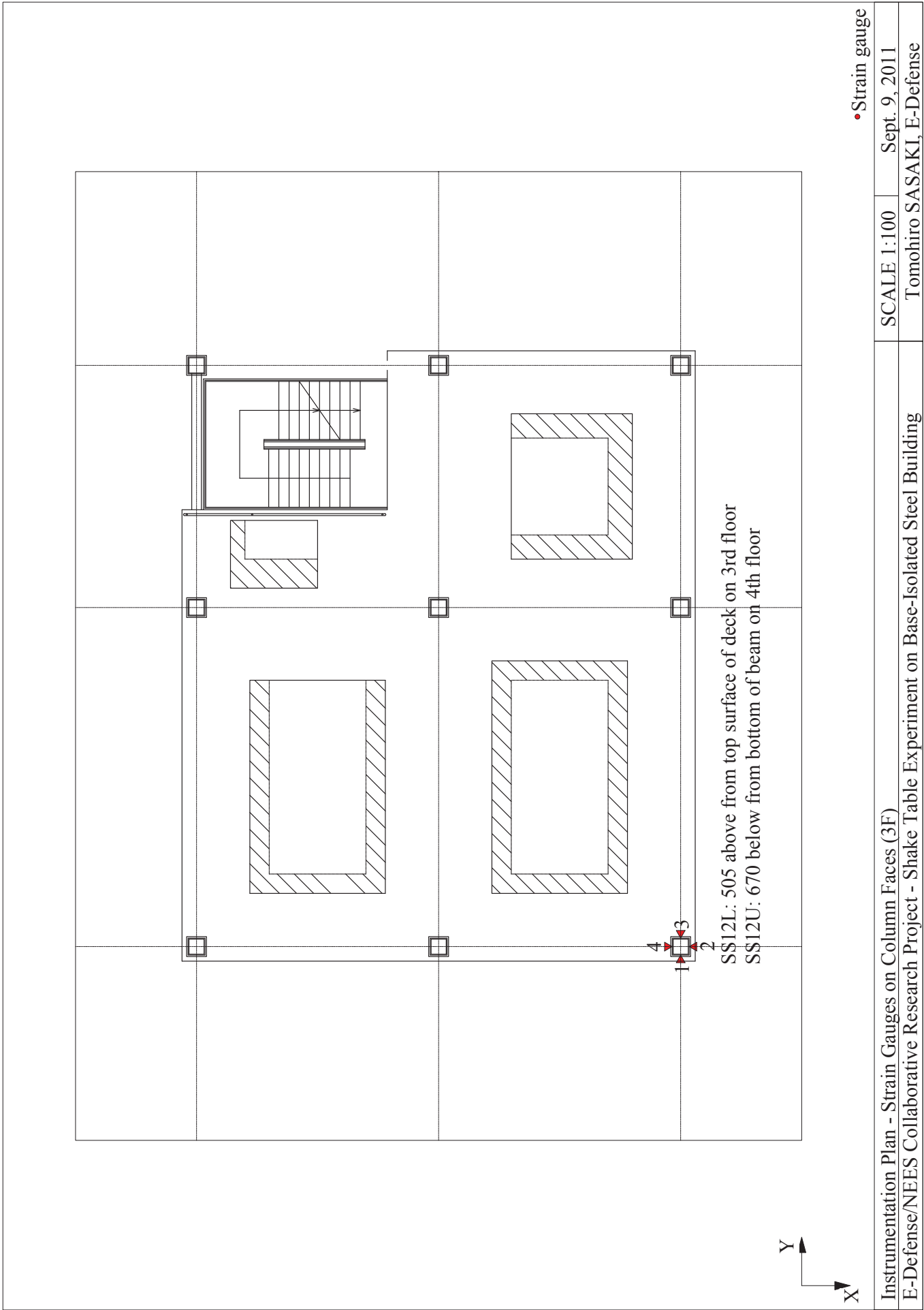


• Strain gauge

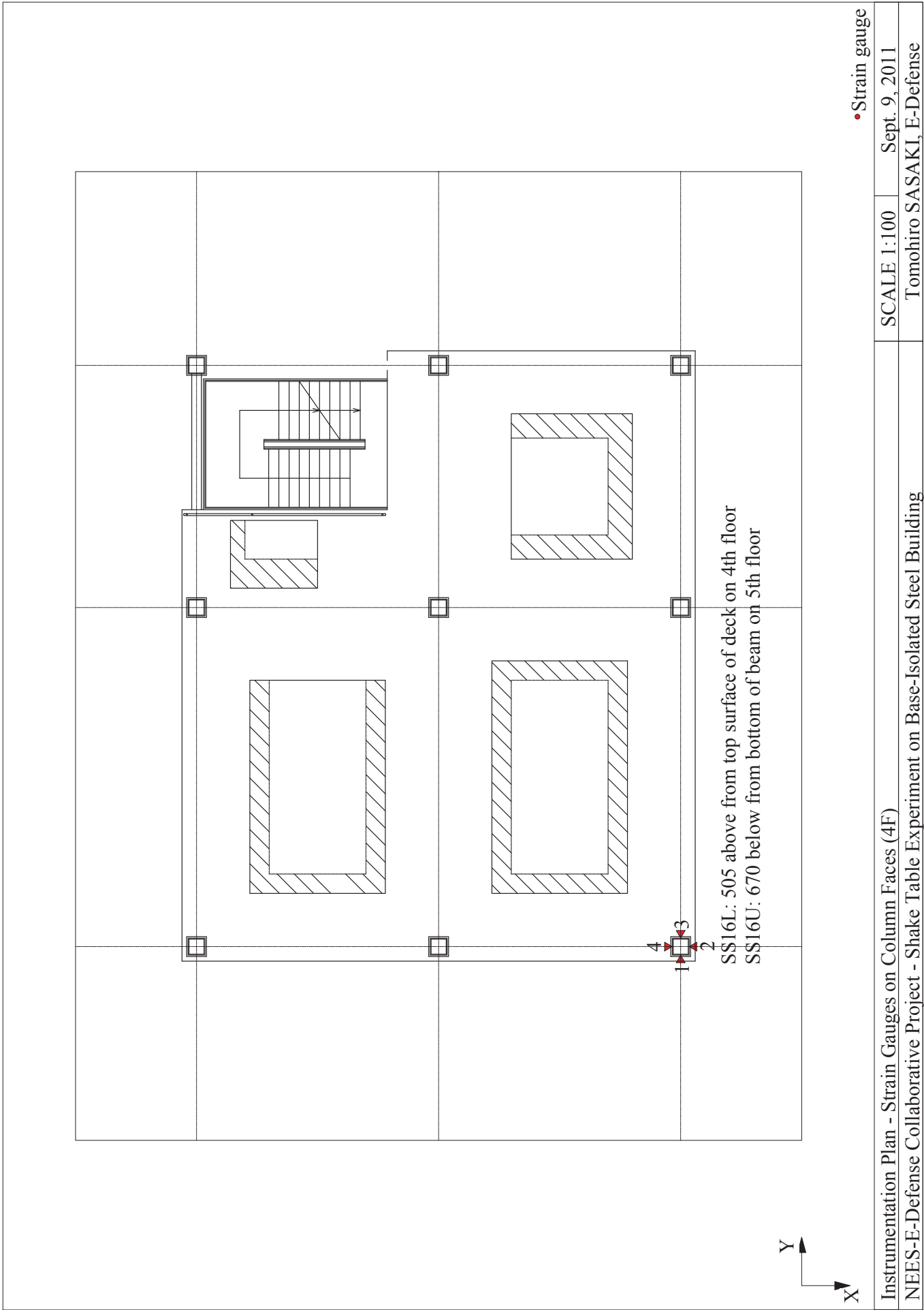
Instrumentation Plan - Strain Gauges on Column Faces (1F)	SCALE 1:100	Sept. 9, 2011
E-Defense/NEES Collaborative Research Project - Shake Table Experiment on Base-Isolated Steel Building	Tomohiro SASAKI, E-Defense	

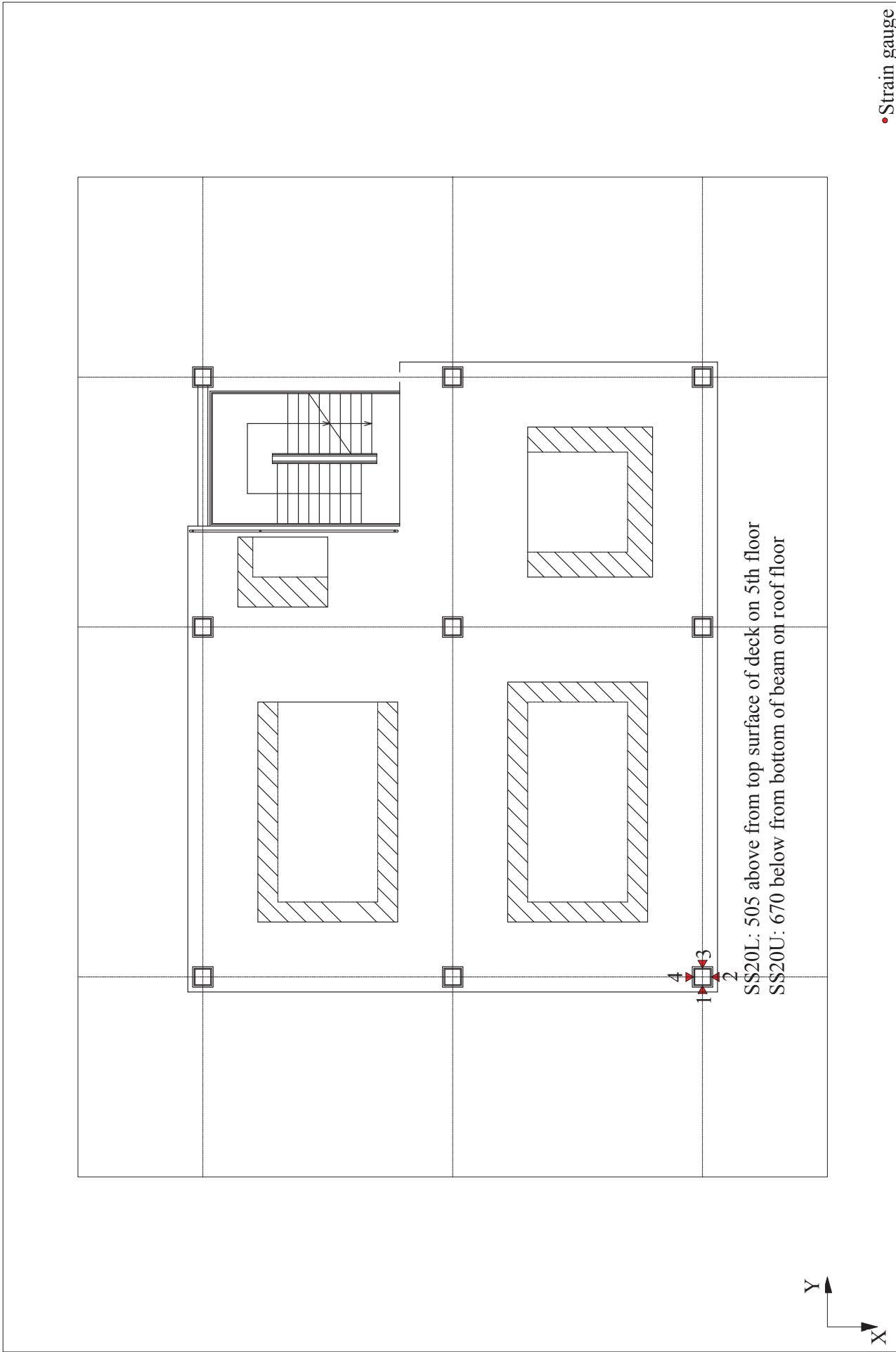


Instrumentation Plan - Strain Gauges on Column Faces (2F)  
 E-Defense/NEES Collaborative Research Project - Shake Table Experiment on Base-Isolated Steel Building









SCALE 1:100      Sept. 9, 2011

Instrumentation Plan - Strain Gauges on Column Faces (5F)  
 E-Defense/NEES Collaborative Research Project - Shake Table Experiment on Base-Isolated Steel Building

Tomohiro SASAKI, E-Defense

SS20L: 505 above from top surface of deck on 5th floor  
 SS20U: 670 below from bottom of beam on roof floor

# **APPENDIX E**

## **ISOLATOR TEST REPORT FOR LEAD-RUBBER BEARINGS**

Building Isolated with Hybrid Lead-Rubber Isolation System

Contributed by Dynamic Isolation Systems, Inc.

Developed for NEES/E-Defense Collaborative Test Program on

Innovative Isolation Systems, 2011-2012



## **ISOLATOR TEST REPORT**

**PROJECT NAME: NRC**

**DATE ISSUED: JULY 11, 2011**

**REPORT NUMBER: 152-10**

---

**PREPARED BY: DIS INC.**



## Introduction

This report has been prepared for Isolator Types A and B for the NRC project. Included in this report are the isolator testing plans, testing results, drawings, an overview of the testing facility, and the test rig calibration certificates.

The testing was performed on July 7, 2011 at DIS' test facility in McCarran, NV.

**Table 1 - Tested Bearing Serial Numbers**

Bearing Type	Serial Number
A	16439
	16443
B	16450
	16458



## Table of Contents

LIST OF TABLES .....	ii
LIST OF FIGURES.....	ii
<b>TEST MATRIX TABLE .....</b>	<b>1</b>
TEST MATRIX .....	1
COMPRESSION SHEAR TESTS.....	1
<b>MEASUREMENT &amp; CALCULATION PROCEDURES .....</b>	<b>4</b>
COMPRESSION SHEAR TESTS.....	4
<b>TEST RESULTS AND HYSTERESIS LOOPS .....</b>	<b>5</b>
DISCUSSION OF TEST RESULTS .....	5
SUMMARY OF TEST RESULTS .....	6
HYSTERESIS LOOPS .....	7
<b>TEST APPARATUS .....</b>	<b>16</b>
OVERVIEW OF TEST FACILITY .....	16
TEST RIG CALIBRATION .....	17

## List of Tables

Table 1 - Tested Bearing Serial Numbers.....	i
Table 2 - Isolator Type A - Test A Results .....	6
Table 3 - Isolator Type A - Test B Results .....	6
Table 4 - Isolator Type A - Test C Results.....	6
Table 5 - Isolator Type A - Test D Results .....	6

## List of Figures

Figure 1 - Combined Compression and Shear Test Matrix.....	2
Figure 2 - Isolator Type A Drawing .....	3
Figure 3 - Graphical Display of Isolator Shear Properties.....	4
Figure 4 - DIS Big Rig Photo.....	16
Figure 5 - DIS Big Rig Drawing.....	16

## **Test Matrix Table**

### **Test Matrix**

The test procedure is determined by a compilation of test information called "Test Matrix". The contents of the test matrix, such as the order of testing and number of tests, are determined by the designer (or the parties involved in the project). The test matrices for this project are presented in this section.

### **Compression Shear Tests**

Each test is described by one row of information in the test matrix table. Each test performed bears a test ID, shown in the first column of the test matrix table.

The testing parameters are:

- a) Compression load on the bearing to be maintained during the test.
- b) Displacement deformation to be imposed on the isolator.
- c) Number of fully-reversed-cycles of testing.
- d) The acceptance criteria for the test, if any.

One cycle of shear deformation consists of movement from the zero position to the maximum specified displacement in the positive direction ( $D_{max}$ ), then to the maximum specified displacement in the negative direction ( $D_{min}$ ), and back to the zero position. This movement is applied in a smooth continuous way, similar to a constant velocity saw-tooth shape.

**Combined Compression and Shear Test**

**Isolator Type A**

Test ID	Test Order	C. Stress (N/mm <sup>2</sup> )	Load (kN)	Number of Cycles	Shear Strain (%)	Displ. (mm)	Notes
A	1	1.7	600	3	125	300	Note 1
B	2	2.8	1000	3	208	500	Note 1
C	3	0.3	100	0.5	271	650	Note 1
D	4	1.7	600	3	125	300	Note 1

Revision Status		
Approval	Rev	Date
KF	0	06/29/11
		Issued for Approval
		Description

**Notes:**

1. Wait 15 minutes between tests

Customer Approval	
Des. Eng. Approval	
Proj. Mng. Approval	
Test Sup. Approval	



**DYNAMIC ISOLATION SYSTEMS**

**NRC**

**Production Isolators**

**Combined Compression & Shear  
Test Matrix No. 152-100-01**



APPR	REV	DATE	DESCRIPTION
AK	A	5/6/11	ISSUED FOR INFORMATION
AK	B	6/7/11	GEN. REV. - REISSUED FOR INFORMATION
TN	0	6/10/11	REV. DWG. # - ISSUED FOR APPROVAL
MG	1	6/10/11	ISSUED FOR FABRICATION
AK	2	6/24/11	REV. EXT. ENDP. - REISSUED FOR APPROVAL

**NOTES:**

1. MATERIALS:  
ALL STEEL PL's ASTM A36.  
ALL STEEL SHIMS ASTM A1011 GR. 36.  
INTERNAL RUBBER IS DIS TYPE T.  
EXTERNAL RUBBER IS DIS TYPE E100S.
2. DIMENSIONS ARE IN UNITS NOTED.  
DIMENSIONS IN BRACKETS ARE EQUIVALENTS  
FOR REFERENCE ONLY.
3. DO NOT SCALE THIS DRAWING.
4. FINISH: TO BE DETERMINED.

ISOLATOR DIMENSION TABLE	
TYPE A ISOLATOR	
C698.5/459.8/101.6	
QUANTITY	4+0
TARGET	TOL./ALLOWABLE
A Isolator Diameter	698.5mm ± 2mm ± 4mm
B Overall Isolator Ht.	459.8mm ± 4mm ± 6.35mm
C Lead Core Diameter	101.6mm ± 2mm
D Parallelity	1/300 1/200
Estimated Weight	1,864 lb./847 kg
Measurements are taken at 20°C.	

**GENERAL TOLERANCES:**

1. ENDPATE OVERALL DIMENSIONS: ± 3.18mm.
2. BOLT HOLE LOCATIONS: ± 0.8mm.
3. PLATE THICKNESS: ± 1.6mm.
4. PLATE FLATNESS: ± 3.18mm.

THIS DRAWING IS THE PROPERTY OF DYNAMIC ISOLATION SYSTEMS, INC.  
INFORMATION AND KNOW-HOW HEREON ARE CONFIDENTIAL AND MAY NOT BE USED, REPRODUCED OR REVEALED TO OTHERS  
EXCEPT IN ACCORDANCE WITH THE CONTRACT OR OTHER WRITTEN PERMISSION OF DYNAMIC ISOLATION SYSTEMS, INC.  
ANY REPRODUCTIONS IN WHOLE OR IN PART SHALL INCLUDE THIS NOTATION.



**DYNAMIC ISOLATION SYSTEMS**

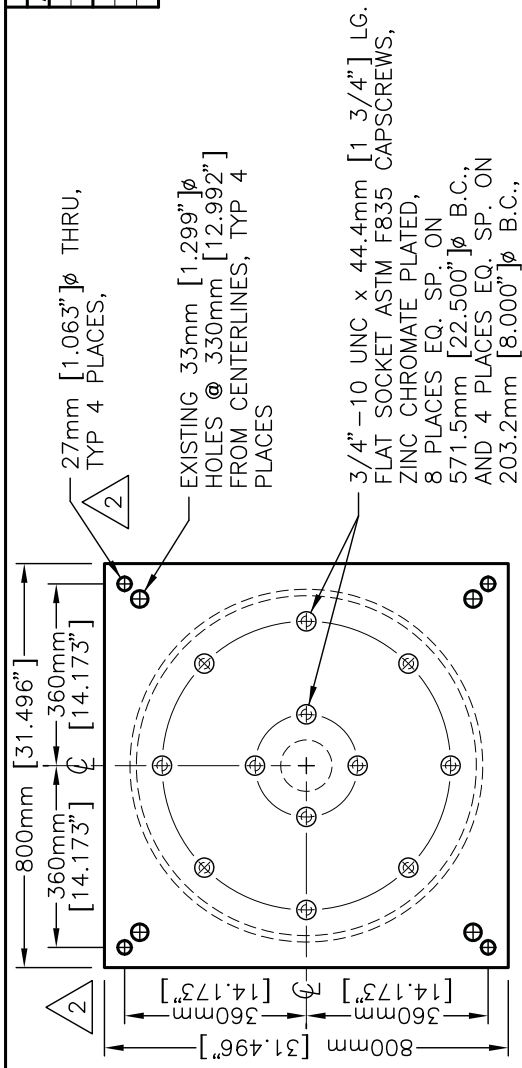
DIS SEISMIC ISOLATORS

NRC Project at EDefense

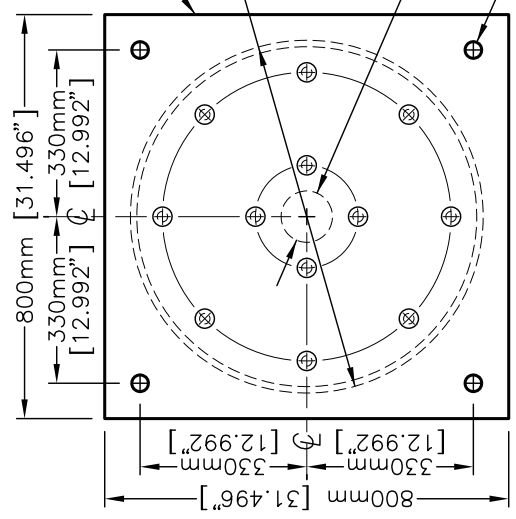
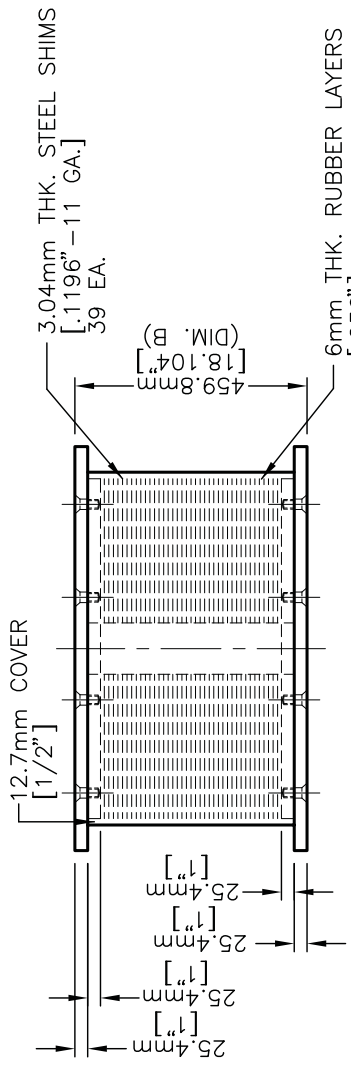
Type A Isolator

**DWG. NO. 152-100**

SHEET: 1 of 1  
ORIG: 5/6/11



TOP VIEW



BOTTOM VIEW

DESIGNER APPROVAL	AK
PROJECT MANAGER APPROVAL	-
PLANT MANAGER APPROVAL	MG

## Measurement & Calculation Procedures

### Compression Shear Tests

Testing begins when the axial load is applied to the isolators. Maintaining the axial load, the isolators are sheared to the specified displacement for the appropriate number of cycles. Using the recorded shear force and displacements from the test, shear force-displacement plots (hysteresis loops) are generated. Since two isolators of the same type are tested simultaneously, the total measured shear force has been multiplied by one half during processing to produce hysteresis loops for a single isolator.

The essential properties of an isolator can be extracted from a hysteresis loop. Figure 2 shows an example of a hysteresis loop generated after a compression shear test and some of the isolator properties that are obtained from it. Three properties are measured directly from the recorded data, the maximum isolator displacement ( $D_{max}$ ), the maximum force required to displace the isolator ( $F_{max}$ ), and the area of the hysteresis loop which gives the total energy dissipated per cycle (EDC). The effective stiffness of the isolator ( $K_{eff}$ ) is equal to  $F_{max}/D_{max}$ . There is no engineering judgment or estimation involved in the determination of  $F_{max}$ ,  $D_{max}$ ,  $K_{eff}$ , or EDC.  $F_{max}$  and  $D_{max}$  are self-evident and EDC is determined by numerical integration of the recorded force-displacement data file.

The hysteresis loop has the following properties in addition to the measured properties listed above. These are the hysteretic force at zero displacement ( $Q_d$ ), the yielded stiffness of the isolator ( $K_2$ ), and the unloading stiffness of the isolator ( $K_1$ ). A bi-linear loop is fitted to the actual hysteresis loop such that the fitted loop has identical measured properties ( $K_{eff}$  and EDC) as the actual hysteresis loop.

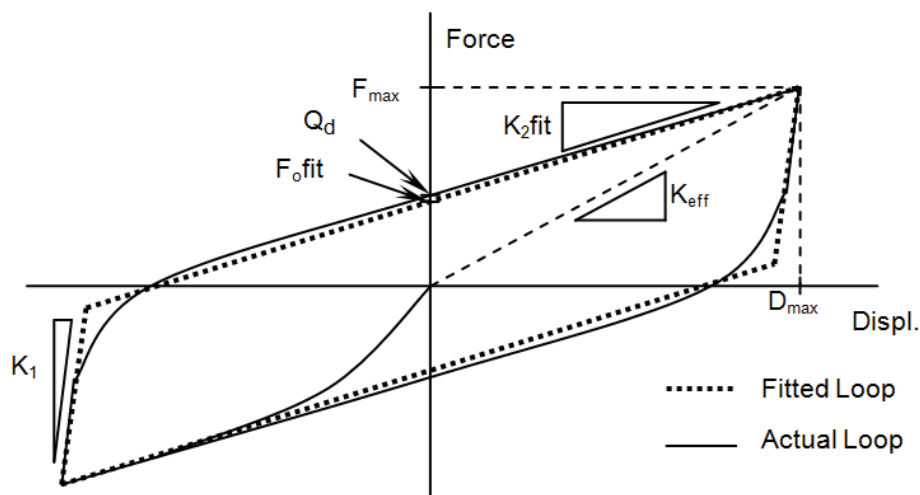


Figure 2 - Graphical Display of Isolator Shear Properties



## Test Results and Hysteresis Loops

### Discussion of Test Results

The compression shear and compression stiffness test results are summarized in Table 2 and **Error! Reference source not found.** as well the corresponding hysteresis loops. The hysteresis loops exhibit positive incremental stiffness and the isolators remained stable during testing.

**Summary of Test Results**
**Table 2 - Isolator Type A - Test A Results**

Serial Numbers	Axial Load	$D_{max}$	$K_d$	$Q_d$	$F_0$	$K_{eff}$
	(kN)	(mm)	(kN/cm)	(kN)	(kN)	(kN/cm)
16439	600	300	6.3	41.4	64.8	8.4
16443	600	300	6.3	41.4	64.8	8.4
16450	600	300	6.2	39.2	64.5	8.3
16458	600	300	6.2	39.2	64.5	8.3
<b>Average</b>	<b>600</b>	<b>300</b>	<b>6.3</b>	<b>40.3</b>	<b>64.7</b>	<b>8.4</b>

**Table 3 - Isolator Type A - Test B Results**

Serial Numbers	Axial Load	$D_{max}$	$K_d$	$Q_d$	$F_0$	$K_{eff}$
	(kN)	(mm)	(kN/cm)	(kN)	(kN)	(kN/cm)
16439	1000	500	5.1	45.9	75.7	6.6
16443	1000	500	5.1	45.9	75.7	6.6
16450	1000	500	5.0	43.6	75.5	6.5
16458	1000	500	5.0	43.6	75.5	6.5
<b>Average</b>	<b>1000</b>	<b>500</b>	<b>5.1</b>	<b>44.8</b>	<b>75.6</b>	<b>6.6</b>

**Table 4 - Isolator Type A - Test C Results**

Serial Numbers	Axial Load	$D_{max}$	$K_d$	$Q_d$	$F_0$	$K_{eff}$
	(kN)	(mm)	(kN/cm)	(kN)	(kN)	(kN/cm)
16439	100	650	5.5	56.2	85.1	6.8
16443	100	650	5.5	56.2	85.1	6.8
16450	100	650	5.4	53.1	86.1	6.8
16458	100	650	5.4	53.1	86.1	6.8
<b>Average</b>	<b>100</b>	<b>650</b>	<b>5.5</b>	<b>54.7</b>	<b>85.6</b>	<b>6.8</b>

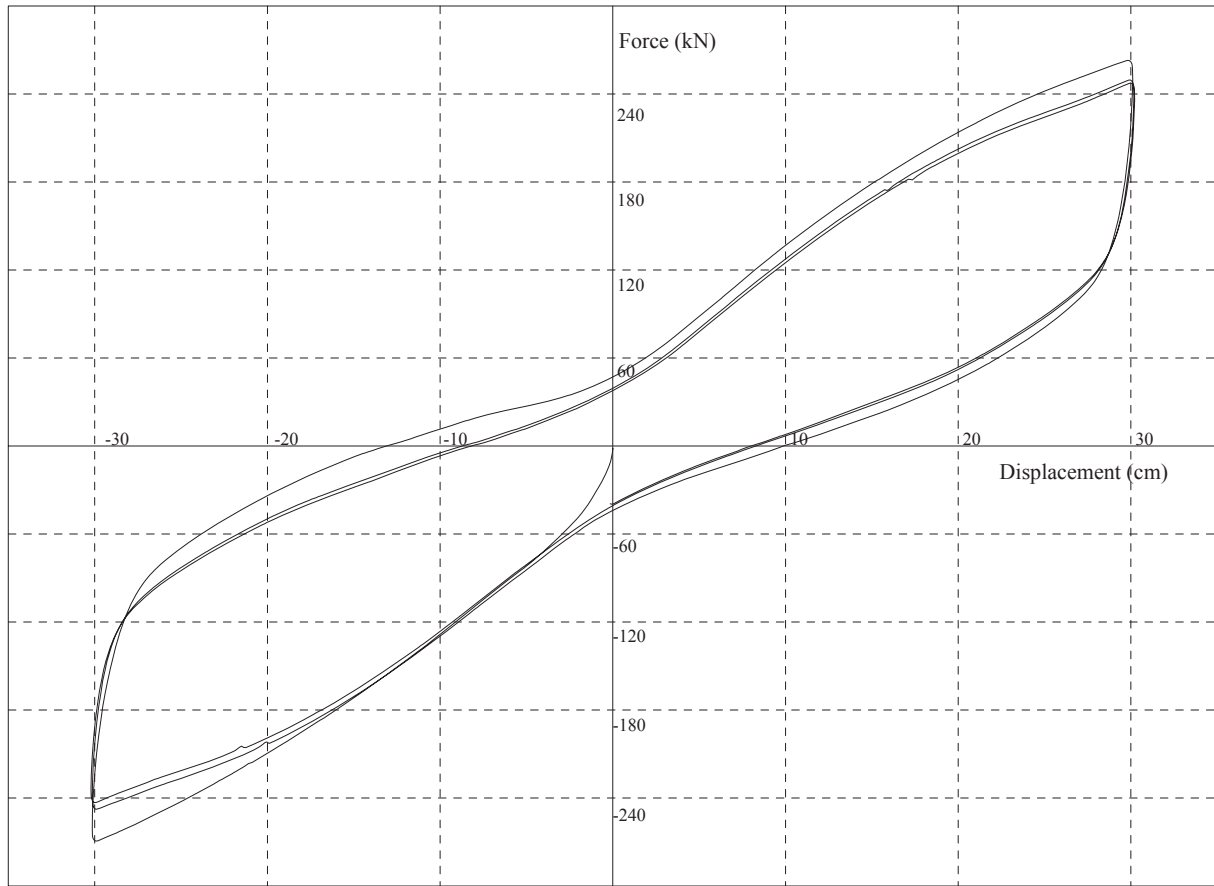
**Table 5 - Isolator Type A - Test D Results**

Serial Numbers	Axial Load	$D_{max}$	$K_d$	$Q_d$	$F_0$	$K_{eff}$
	(kN)	(mm)	(kN/cm)	(kN)	(kN)	(kN/cm)
16439	600	300	5.8	41.7	63.4	7.9
16443	600	300	5.8	41.7	63.4	7.9
16450	600	300	5.8	40.1	62.8	7.9
16458	600	300	5.8	40.1	62.8	7.9
<b>Average</b>	<b>600</b>	<b>300</b>	<b>5.8</b>	<b>40.9</b>	<b>63.1</b>	<b>7.9</b>



## **Hysteresis Loops**

---

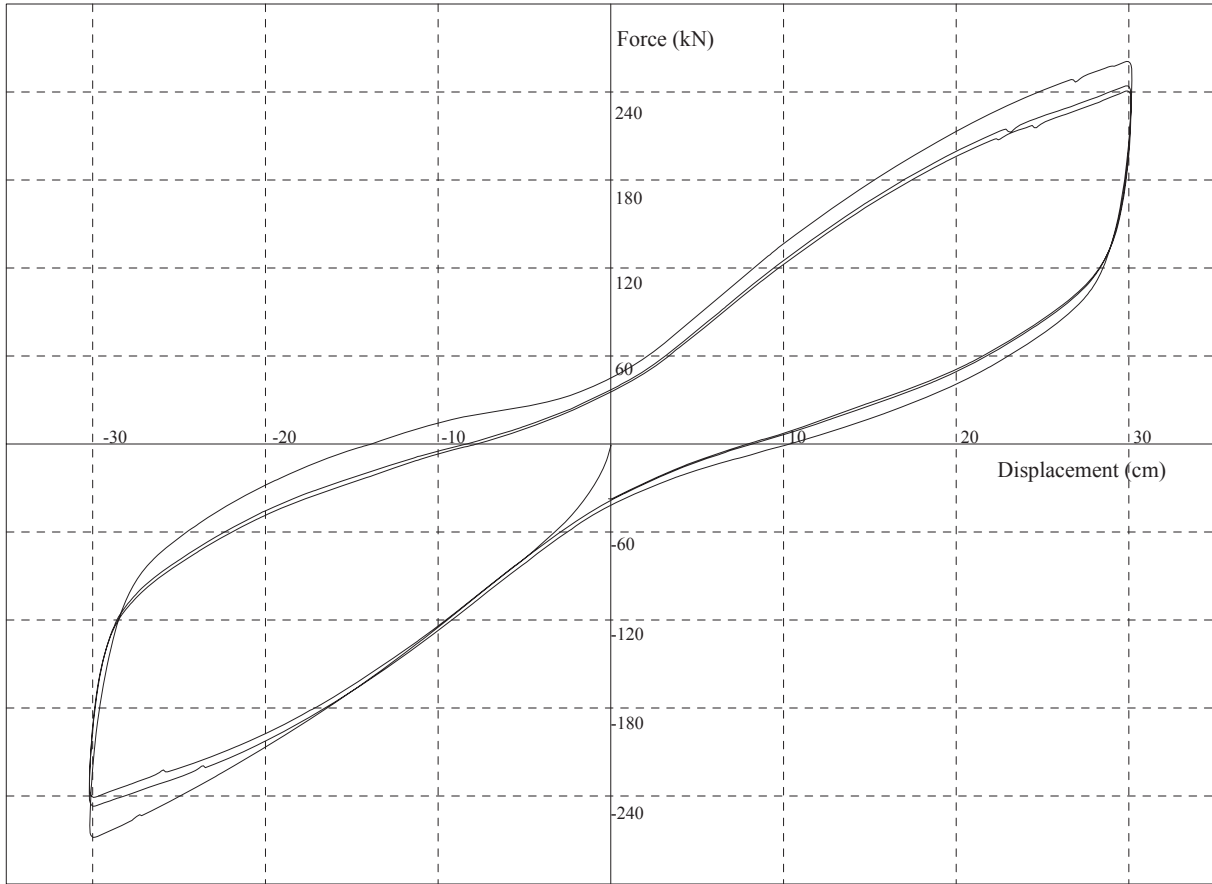


Job: 152 (NRC) Test Name : 25838-001.dat

Class: Production Type: A Isolators 16439 & 16443 Tested: 7/7/2011 5:55:42 PM

Test Type: Production Test Matrix ID: A (Stress: 1.7N/mm<sup>2</sup>, Strain: 125%)

<u>Cycle</u>	<u>Dmax(cm)</u>	<u>Fmax(kN)</u>	<u>Keff(kN/cm)</u>	<u>Qd(kN)</u>	<u>EDC(kN.cm)</u>	<u>K2fit(kN/cm)</u>	<u>Fofit(kN)</u>	<u>V(cm/min)</u>
1	30.12	266.15	8.84	45.46	8454.7	6.47	71.24	136.09
2	30.15	248.61	8.24	40.03	7486.1	6.16	62.90	140.41
3	30.21	245.26	8.12	38.61	7206.2	6.12	60.40	140.41
<b>AVERAGE</b>	<b>30.16</b>	<b>253.34</b>	<b>8.40</b>	<b>41.4</b>	<b>7715.7</b>	<b>6.25</b>	<b>64.84</b>	<b>139.0</b>

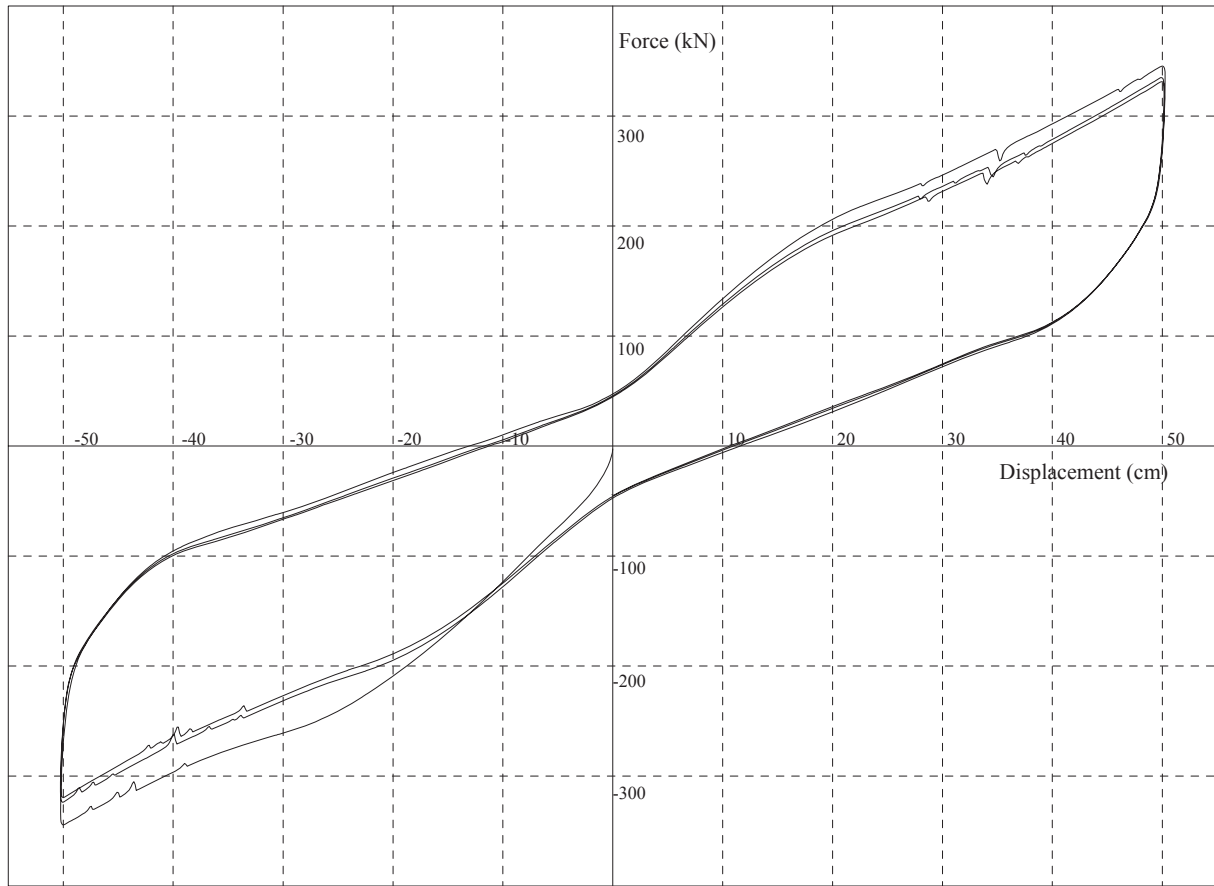


Job: 152 (NRC) Test Name : 25834-001.dat

Class: Production Type: A Isolators 16450 & 16458 Tested: 7/7/2011 2:28:21 PM

Test Type: Production Test Matrix ID: A (Stress: 1.7N/mm<sup>2</sup>, Strain: 125%)

<u>Cycle</u>	<u>Dmax(cm)</u>	<u>Fmax(kN)</u>	<u>Keff(kN/cm)</u>	<u>Qd(kN)</u>	<u>EDC(kN.cm)</u>	<u>K2fit(kN/cm)</u>	<u>Fofit(kN)</u>	<u>V(cm/min)</u>
1	30.17	264.55	8.77	43.29	8505.8	6.40	71.49	136.33
2	30.16	245.63	8.14	37.70	7433.0	6.08	62.38	140.40
3	30.16	240.83	7.99	36.49	7108.8	6.01	59.63	140.46
<b>AVERAGE</b>	<b>30.16</b>	<b>250.33</b>	<b>8.30</b>	<b>39.2</b>	<b>7682.5</b>	<b>6.16</b>	<b>64.49</b>	<b>139.1</b>



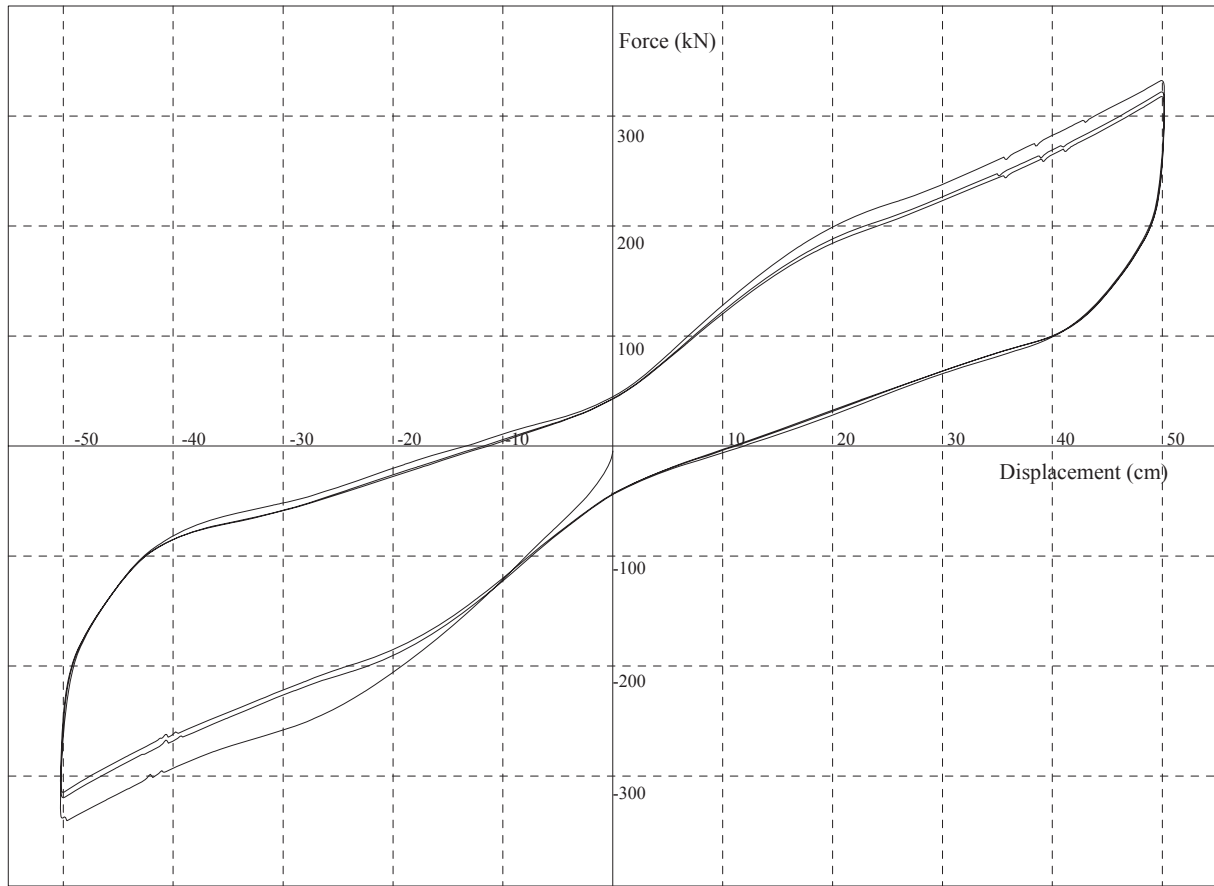
Job: 152 (NRC) Test Name : 25839-001.dat

Class: Production Type: A Isolators 16439 & 16443 Tested: 7/7/2011 6:27:49 PM

Test Type: Production Test Matrix ID: B (Stress: 2.8N/mm<sup>2</sup>, Strain: 208%)

<u>Cycle</u>	<u>Dmax(cm)</u>	<u>Fmax(kN)</u>	<u>Keff(kN/cm)</u>	<u>Qd(kN)</u>	<u>EDC(kN.cm)</u>	<u>K2fit(kN/cm)</u>	<u>Fofit(kN)</u>	<u>V(cm/min)</u>
1	50.25	344.95	6.86	47.36	16181.4	5.25	81.19	138.12
2	50.21	329.41	6.56	45.74	14809.4	5.08	74.31	140.96
3	50.21	325.42	6.48	44.73	14284.9	5.05	71.65	140.94
<b>AVERAGE</b>	<b>50.23</b>	<b>333.26</b>	<b>6.64</b>	<b>45.9</b>	<b>15091.9</b>	<b>5.13</b>	<b>75.72</b>	<b>140.0</b>



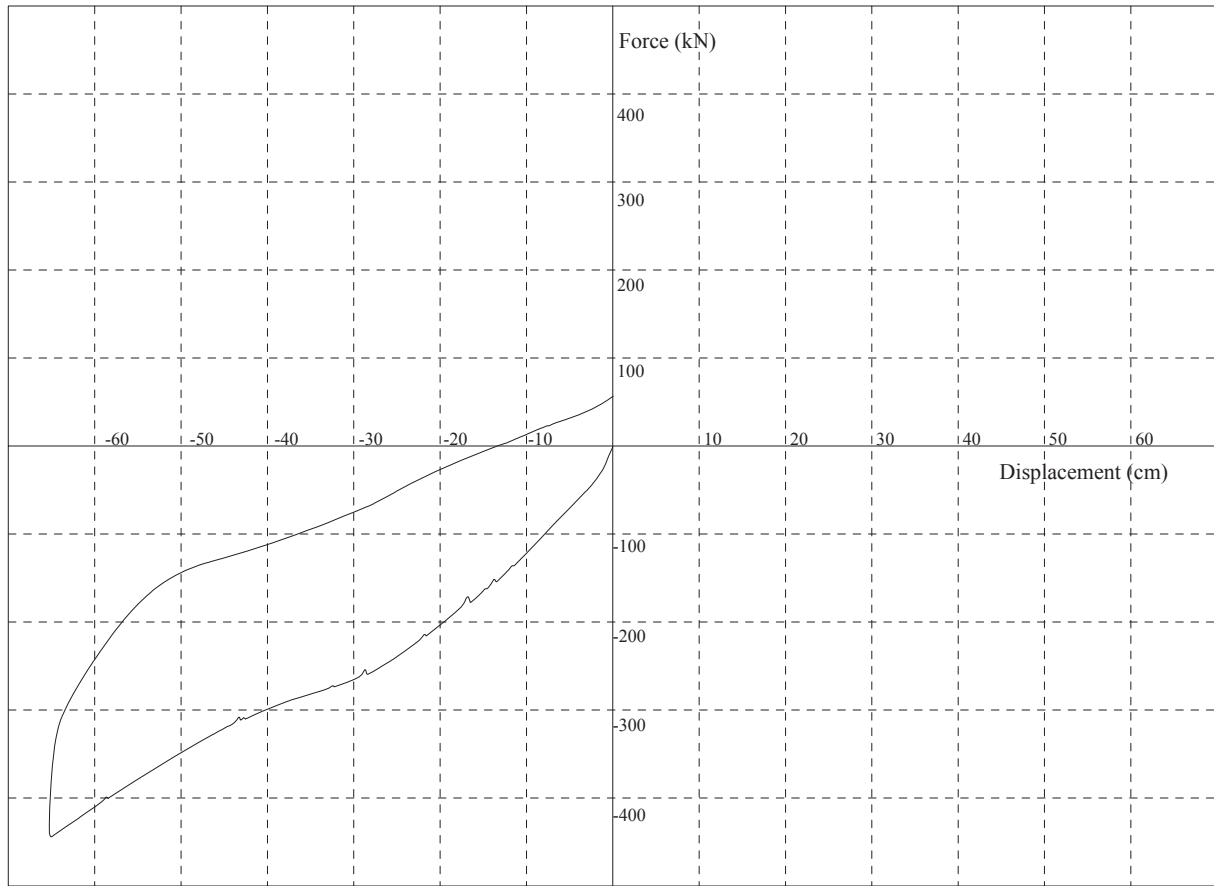


Job: 152 (NRC) Test Name : 25835-001.dat

Class: Production Type: A Isolators 16450 & 16458 Tested: 7/7/2011 2:54:06 PM

Test Type: Production Test Matrix ID: B (Stress: 2.8N/mm<sup>2</sup>, Strain: 208%)

<u>Cycle</u>	<u>Dmax(cm)</u>	<u>Fmax(kN)</u>	<u>Keff(kN/cm)</u>	<u>Qd(kN)</u>	<u>EDC(kN.cm)</u>	<u>K2fit(kN/cm)</u>	<u>Fofit(kN)</u>	<u>V(cm/min)</u>
1	50.22	336.42	6.70	44.52	16198.4	5.08	81.26	138.25
2	50.20	320.95	6.39	43.31	14690.8	4.93	73.67	141.01
3	50.21	316.35	6.30	42.97	14278.0	4.88	71.57	141.03
<b>AVERAGE</b>	<b>50.21</b>	<b>324.57</b>	<b>6.46</b>	<b>43.6</b>	<b>15055.7</b>	<b>4.96</b>	<b>75.50</b>	<b>140.1</b>

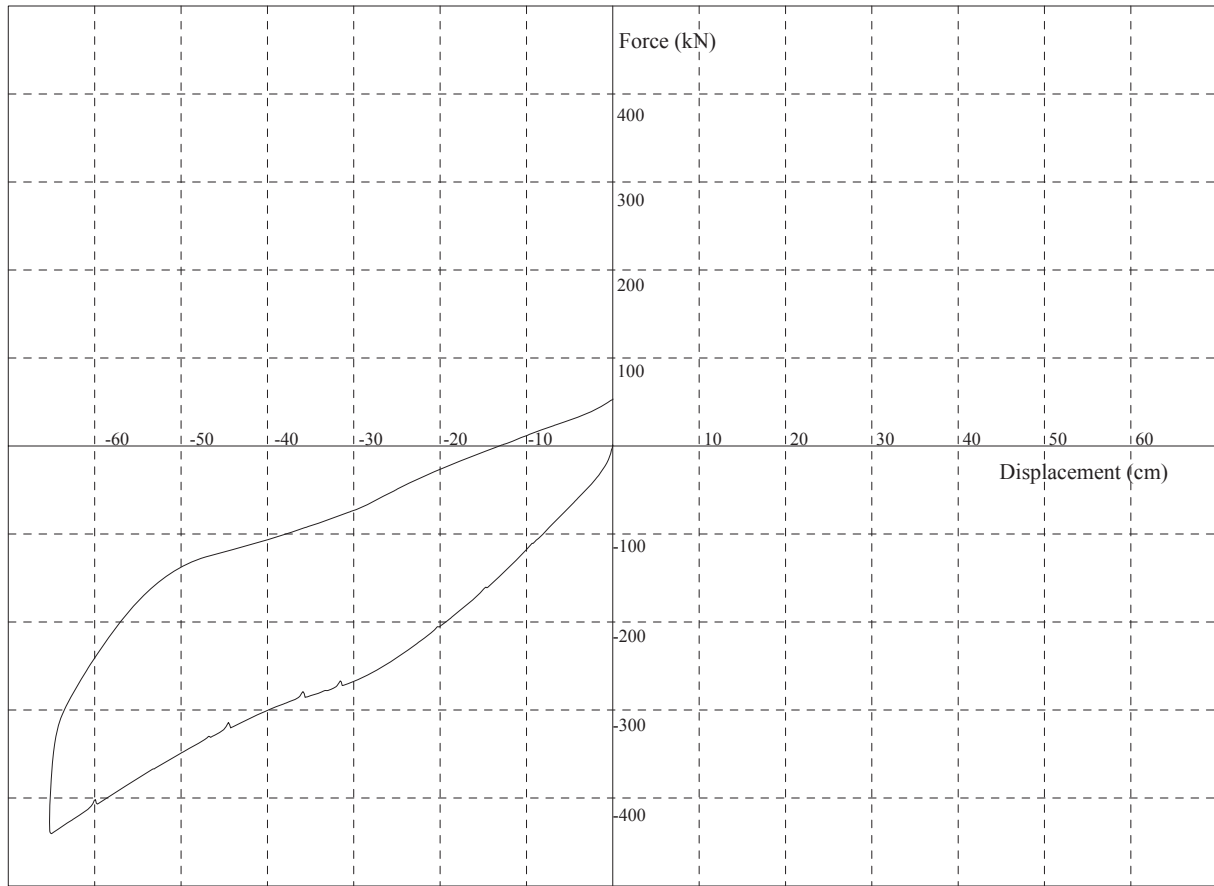


Job: 152 (NRC) Test Name : 25840-001a.dat

Class: Production Type: D6 Isolators 16439 & 16443 Tested: 7/14/2011 8:43:12 AM

Test Type: Production Test Matrix ID: C (Stress:0.3N/mm<sup>2</sup>, Strain: 271%)

<u>H.Cyc</u>	<u>Dmax(cm)</u>	<u>Fmax(kN)</u>	<u>Keff(kN/cm)</u>	<u>Qd(kN)</u>	<u>EDC(kN.cm)</u>	<u>K2fit(kN/cm)</u>	<u>Fofit(kN)</u>	<u>V(cm/min)</u>
1	-65.26	-444.11	6.80	56.19	10926.7	5.50	85.06	-136.44

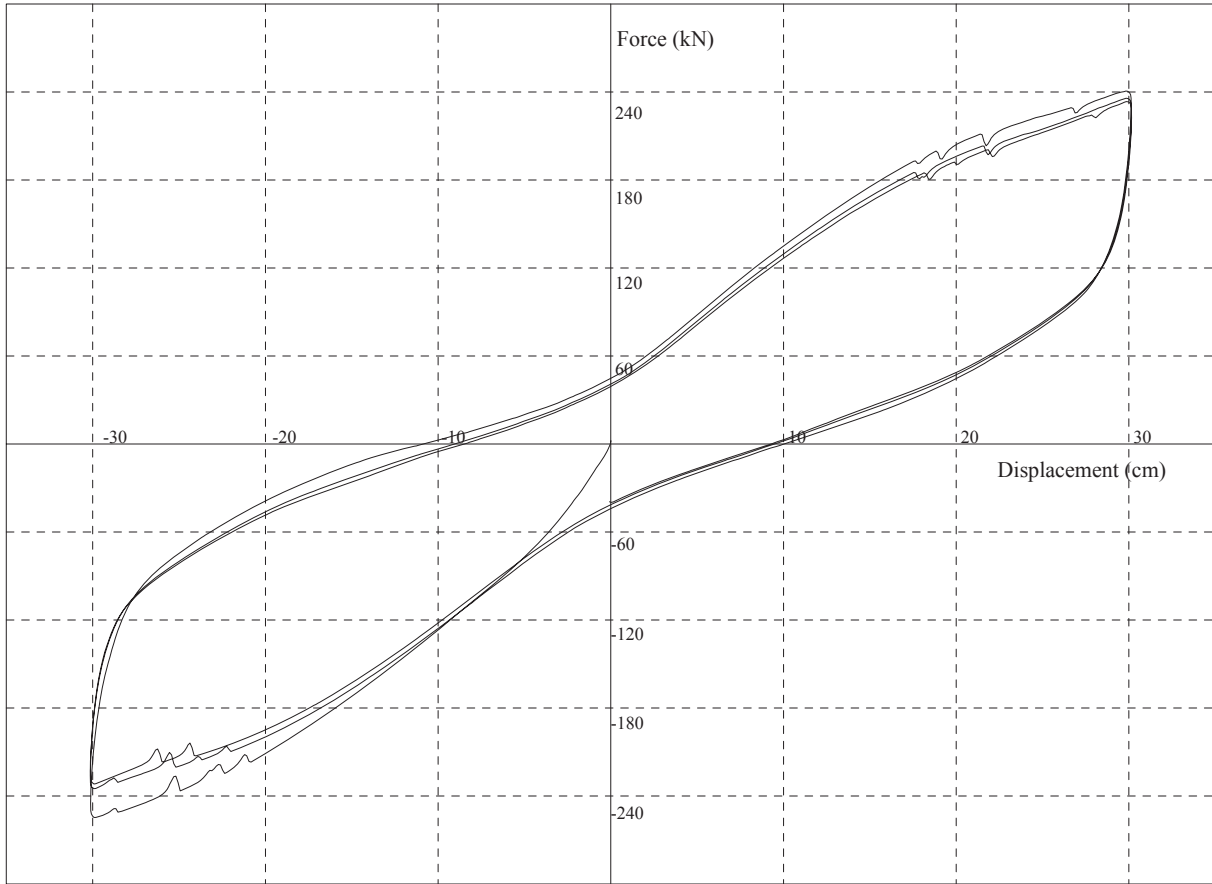


Job: 152 (NRC) Test Name : 25836-001a.dat

Class: Production Type: D6 Isolators 16450 & 16458 Tested: 7/14/2011 8:44:24 AM

Test Type: Production Test Matrix ID: C (Stress:0.3N/mm<sup>2</sup>, Strain: 271%)

<u>H.Cyc</u>	<u>Dmax(cm)</u>	<u>Fmax(kN)</u>	<u>Keff(kN/cm)</u>	<u>Qd(kN)</u>	<u>EDC(kN.cm)</u>	<u>K2fit(kN/cm)</u>	<u>Fofit(kN)</u>	<u>V(cm/min)</u>
1	-65.24	-440.48	6.75	53.11	11058.8	5.43	86.14	- 136.15

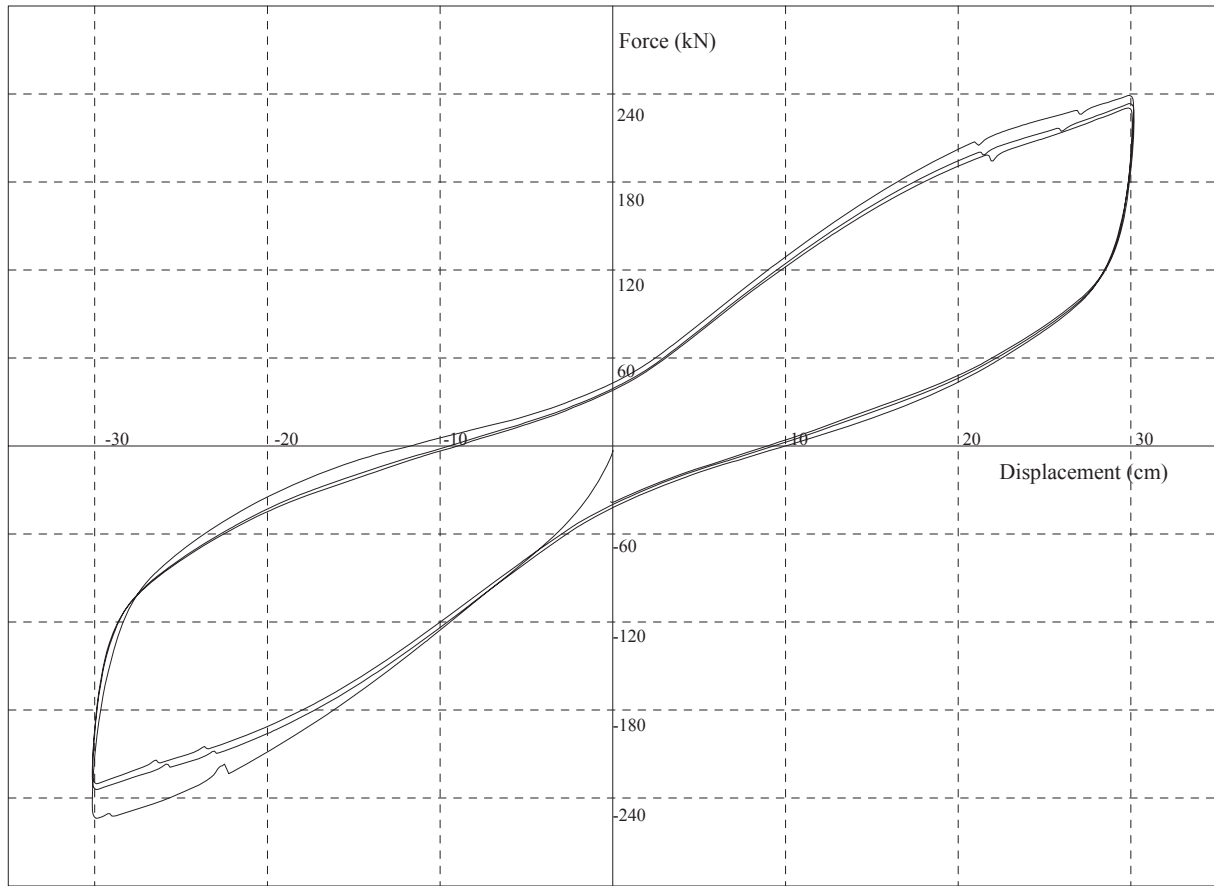


Job: 152 (NRC) Test Name : 25841-001.dat

Class: Production Type: A Isolators 16439 & 16443 Tested: 7/7/2011 7:16:44 PM

Test Type: Production Test Matrix ID: D (Stress: 1.7N/mm<sup>2</sup>, Strain: 125%)

Cycle	Dmax(cm)	Fmax(kN)	Keff(kN/cm)	Qd(kN)	EDC(kN.cm)	K2fit(kN/cm)	Fofit(kN)	V(cm/min)
1	30.13	247.63	8.22	44.42	7954.8	5.99	67.20	135.77
2	30.14	235.37	7.81	41.13	7439.2	5.73	62.74	140.41
3	30.14	232.66	7.72	39.48	7146.6	5.72	60.23	140.43
<b>AVERAGE</b>	<b>30.14</b>	<b>238.55</b>	<b>7.92</b>	<b>41.7</b>	<b>7513.6</b>	<b>5.81</b>	<b>63.39</b>	<b>138.9</b>



Job: 152 (NRC) Test Name : 25837-001.dat

Class: Production Type: A Isolators 16450 & 16458 Tested: 7/7/2011 3:38:45 PM

Test Type: Production Test Matrix ID: D (Stress: 1.7N/mm<sup>2</sup>, Strain: 125%)

<u>Cycle</u>	<u>Dmax(cm)</u>	<u>Fmax(kN)</u>	<u>Keff(kN/cm)</u>	<u>Qd(kN)</u>	<u>EDC(kN.cm)</u>	<u>K2fit(kN/cm)</u>	<u>Fofit(kN)</u>	<u>V(cm/min)</u>
1	30.15	246.41	8.17	42.47	7938.8	5.95	66.97	135.85
2	30.17	233.82	7.75	39.54	7350.9	5.70	61.89	140.58
3	30.10	230.44	7.65	38.24	7058.4	5.68	59.51	140.56
<b>AVERAGE</b>	<b>30.14</b>	<b>236.89</b>	<b>7.86</b>	<b>40.1</b>	<b>7449.3</b>	<b>5.78</b>	<b>62.79</b>	<b>139.0</b>

## Test Apparatus

### Overview of Test Facility

The DIS test facility is located at its manufacturing plant in McCarran, NV. The testing laboratory has approximately 4,000 square feet of available floor space and houses two combined compression and shear test rigs along with their support hardware and is serviced by a 10-ton overhead crane. The big test rig is illustrated in Figure 3 and Figure 4 below. As shown in the figures, two isolators are tested together in the hydraulically powered test rig. The isolators can be examined for both their shear and compression properties in the test rig.

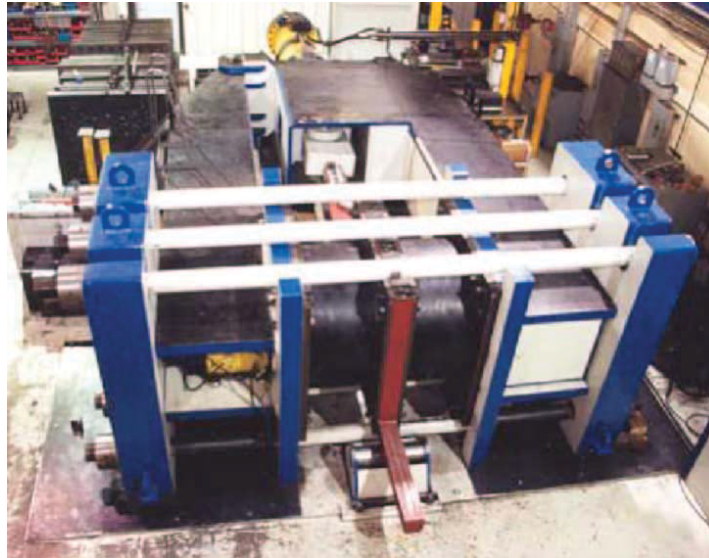


Figure 3 - DIS Big Rig Photo

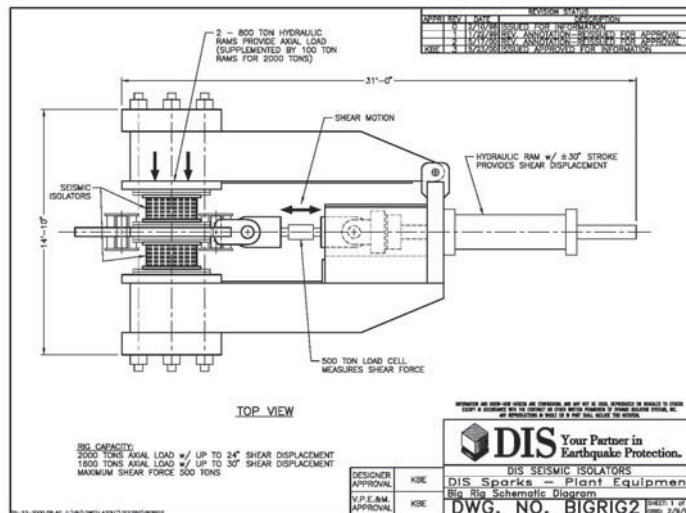


Figure 4 - DIS Big Rig Drawing



## **Test Rig Calibration**

---

C E R T I F I C A T E   O F   V E R I F I C A T I O N

This is to Certify that the

Big Rig - Axial Mode                      3.2Mlb Nominal Capacity  
 Test Rig No. 3                              2 - Enerpac 800T Rams  
 APGroup Digital Gage Model: PG-10000    Serial: X3566

Located at

Dynamic Isolation Systems, Inc.  
 885 Denmark Drive  
 McCarran Nevada 89434

was calibrated on 25 March 2011 according to applicable procedures of ASTM Specification E4, and the fitted load table values determined to be within the required 1.0 % tolerance, or Gage resolution limits, of the true loads applied to the system over the following range(s):

MACHINE RANGE, LB	LOADING RANGE, LB Minimum - Maximum	Gage Reading...psi Minimum - Maximum
3,600,000	300,365 - 3,370,873	1,002 - 9,518

Systems used were verified according to ASTM Specification E 74 by the National Standards Testing Laboratory as indicated below:

INSTRUMENTS.... USED.....	CAPACITY. .....LB	SERIAL... .....NO	VERIFIED. .....DATE
E M E Load Cell	1,500,000	8512.03	17 Mar 11
E M E Load Cell	1,500,000	9709.05	21 Sep 10
E M E Load Cell	1,500,000	9709.06	21 Sep 11

RCN Enterprises, Inc.  
 371 Bowler Road  
 Waller Texas 77484

25 March 2011





C E R T I F I C A T E   O F   V E R I F I C A T I O N

This is to Certify that the

Big Rig - Axial Mode                      4.8Mlb Nominal Capacity  
 Test Rig No 3            10 Enerpac Rams: 2-800T and 8-100T  
 APGroup Digital Gage Model: PG-10000    Serial: X3566

Located at

Dynamic Isolation Systems, Inc.  
 885 Denmark Drive  
 McCarran Nevada 89434

was calibrated on 25 March 2011 according to applicable procedures of ASTM Specification E4, and the fitted load table values determined to be within the required 1.0 % tolerance, or Gage resolution limits, of the true loads applied to the system over the following range(s):

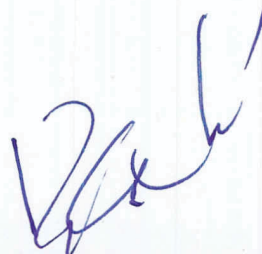
MACHINE RANGE, LB	LOADING RANGE, LB Minimum - Maximum	Gage Reading...psi Minimum - Maximum
4,800,000	433,786 - 4,304,681	998 - 8,551

Systems used were verified according to ASTM Specification E 74 by the National Standards Testing Laboratory as indicated below:

INSTRUMENTS.... USED.....	CAPACITY. .....LB	SERIAL... .....NO	VERIFIED. .....DATE
E M E Load Cell	1,500,000	8512.03	17 Mar 11
E M E Load Cell	1,500,000	9709.05	21 Sep 10
E M E Load Cell	1,500,000	9709.06	21 Sep 11

RCN Enterprises, Inc.  
 371 Bowler Road  
 Waller Texas 77484

25 March 2011



# Certificate of Verification

This is to certify that the:

HSI Universal Load Cell – Capacity: 1.0Mlbs – Tension Loading  
HSI Load Cell            Model: 3100-1000        Serial: 9951-001  
National Instruments Data Acquisition System  
LabView Software displaying Force on Load Cell

Located At:

Dynamic Isolation Systems  
885 Denmark Drive  
McCarran Nevada 89434

Was calibrated on 17 September 2009 according to the ASTM Standard E-4-10 and determined to indicate load within the specified 1.0 percent tolerance on the ranges listed below. This Certificate accompanies a Calibration Report which details the specific errors. The maximum error observed was 0.56 percent.

Machine Range, lb:	Loading Range, lb:
1,000,000	53,522 – 1,228,859

Ambient temperature recorded during this calibration: 66.0 F

Devices used were verified as noted below by National Standards Testing Laboratory or Morehouse Instrument Company according to ASTM Standard E-74-06.

Device:	Serial:	Class "A" Range, in Lbs:	Verified:
HSI Load Cell	3335-006	20,800 – 400,000	21 Jul 2009
HSI Load Cell	3335-006B	27,942.2 – 400,000	24 Aug 2010
EME Load Cell	9709.06	94,694.7 – 1,500,000	21 Sep 2010
EME Load Cell	9709.05	99,360.3 – 1,500,000	21 Sep 2010

RCN Enterprises, Inc.  
371 Bowler Road  
Waller, Texas 77484

25 March 2011

 Digitally  
signed by  
Roy Nash

# Certificate of Verification

This is to certify that the:

HSI Universal Load Cell – Capacity: 1.0Mlbs – Compression Loading  
HSI Load Cell            Model: 3100-1000    Serial: 9951-001  
National Instruments Data Acquisition System  
LabView Software displaying Force on Load Cell

Located At:

Dynamic Isolation Systems  
885 Denmark Drive  
McCarran Nevada 89434

Was calibrated on 22 March 2011 according to ASTM Standard E-4-10 and determined to indicate load within the specified 1.0 percent tolerance on the ranges listed below. This Certificate accompanies a Calibration Report which details the specific errors. The maximum error observed was 0.61 percent.

Machine Range, lb:	Loading Range, lb:
1,000,000	40,019 – 1,200,891

Ambient temperature recorded during this calibration: 65.0 F

Devices used were verified as noted below by Morehouse Instrument Company according to ASTM Standard E-74-06.

Device:	Serial:	Class "A" Range, in Lbs:	Verified:
HSI Load Cell	3335-006B	27,942.2 – 400,000	24 Aug 2010
EME Load Cell	9709.05	94,694.7 – 1,500,000	21 Sep 2010

RCN Enterprises, Inc.  
371 Bowler Road  
Waller, Texas 77484

22 March 2011



Digitally  
signed by  
Roy Nash







<p><b>NRC FORM 335</b> (12-2010) NRCMD 3.7</p> <p style="text-align: center;"><b>U.S. NUCLEAR REGULATORY COMMISSION</b></p> <p style="text-align: center;"><b>BIBLIOGRAPHIC DATA SHEET</b> (See instructions on the reverse)</p>	<p><b>1. REPORT NUMBER</b> (Assigned by NRC, Add Vol., Supp., Rev., and Addendum Numbers, if any.) <b>NUREG/CR- 7196</b></p>				
<p><b>2. TITLE AND SUBTITLE</b></p> <p>Large Scale Earthquake Simulation of a Hybrid Lead Rubber Isolation System Designed with Consideration of Nuclear Seismicity</p>	<p><b>3. DATE REPORT PUBLISHED</b></p> <table border="1"> <tr> <td>MONTH</td> <td>YEAR</td> </tr> <tr> <td>08</td> <td>2015</td> </tr> </table> <p><b>4. FIN OR GRANT NUMBER</b></p>	MONTH	YEAR	08	2015
MONTH	YEAR				
08	2015				
<p><b>5. AUTHOR(S)</b></p> <p>Ryan, K.L., Coria, C.B., Dao, N.D.</p>	<p><b>6. TYPE OF REPORT</b></p> <p style="text-align: center;">Technical</p> <p><b>7. PERIOD COVERED (Inclusive Dates)</b></p> <p style="text-align: center;">August 2011 to April 2013</p>				
<p><b>8. PERFORMING ORGANIZATION - NAME AND ADDRESS</b> (If NRC, provide Division, Office or Region, U. S. Nuclear Regulatory Commission, and mailing address; if contractor, provide name and mailing address.)</p> <p>Center for Civil Engineering Earthquake Research (CCEER) University of Nevada, Reno/MS 0258 Reno, Nevada 89557-0258</p>					
<p><b>9. SPONSORING ORGANIZATION - NAME AND ADDRESS</b> (If NRC, type "Same as above", if contractor, provide NRC Division, Office or Region, U. S. Nuclear Regulatory Commission, and mailing address.)</p> <p>U.S. Nuclear Regulatory Commission Office of Nuclear Regulatory Research Washington, DC 20555</p>					
<p><b>10. SUPPLEMENTARY NOTES</b></p>					
<p><b>11. ABSTRACT (200 words or less)</b></p> <p>This report provides technical information and comprehensive test data that can be used by the NRC staff to support new regulatory guidance related to seismic isolation (SI) technology on future nuclear power plant structures. The study focus on lead-rubber (LR) SI system test subjected to 2D/3D displacements representing beyond design basis ground motions in Central and Eastern United States sites and design basis ground motions for a Western United States. It is anticipated the data acquired can address the gap in the NRC staff's ability to review applications that include the use of LB bearing SI devices and the performance of these isolators under the extreme beyond-design-basis ground motions for the staff review of seismic safety margins, confirmatory analysis, and numerical simulation benchmark.</p> <p>The primary finding with OpenSees simulation is that the LR bearing characterized with a bilinear force-displacement relation needs to be re-calibrated independently for each simulation to match the test data. This indicates the need of improved models that can capture others nonlinear parameters such as the effects of heating of the lead core, pressure variation, and rate dependence. Despite its drawback, the analysis still provides some useful insight of the behavior of SI system and structure responses.</p>					
<p><b>12. KEY WORDS/DESCRIPTORS</b> (List words or phrases that will assist researchers in locating the report.)</p> <p>Acceleration; Bearing; Beyond Design Basis; Cross Linear; Diablo; Drift; Dynamic Isolation Systems; Earthquake; Eccentricity; El Centro; Excitation; Experimental; Feedback; Ground Motion; Lead-Rubber Bearing; Load Cell; Modeling; Nuclear Power Plant; OpenSees; Panel Zone; PGA; Propagation; Rinaldi; Seismic Isolation; Shear Test; Simulator; Slab-Frame Interaction; Spectral; Structural Response; Testbed; Total Base Shear; Transducer; Vogle</p>	<p><b>13. AVAILABILITY STATEMENT</b></p> <p style="text-align: center;">unlimited</p> <p><b>14 SECURITY CLASSIFICATION</b></p> <p>(This Page) unclassified</p> <p>(This Report) unclassified</p> <p><b>15. NUMBER OF PAGES</b></p> <p><b>16. PRICE</b></p>				



Federal Recycling Program







**UNITED STATES  
NUCLEAR REGULATORY COMMISSION**  
WASHINGTON, DC 20555-0001  
\_\_\_\_\_  
OFFICIAL BUSINESS



**NUREG/CR-7196**

**Large Scale Earthquake Simulation of a Hybrid Lead Rubber Isolation System  
Designed with Consideration of Nuclear Seismicity**

**August 2015**